

A Thesis Submitted for the Degree of PhD at the University of Warwick

Permanent WRAP URL:

<http://wrap.warwick.ac.uk/174969>

Copyright and reuse:

This thesis is made available online and is protected by original copyright.

Please scroll down to view the document itself.

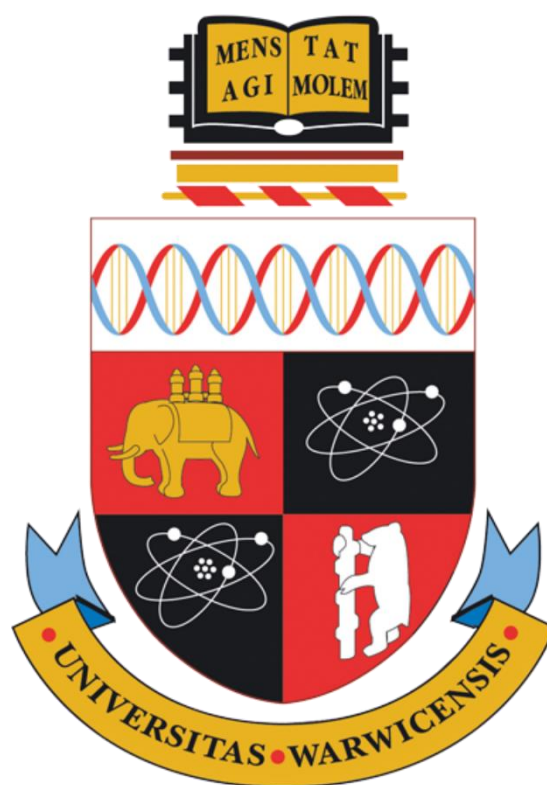
Please refer to the repository record for this item for information to help you to cite it.

Our policy information is available from the repository home page.

For more information, please contact the WRAP Team at: wrap@warwick.ac.uk

Development of non-invasive analytical techniques for the detection of iron in the human brain

Ziedo Solomon



Submitted for the degree of Doctor of Philosophy in Analytical Science

Molecular Analytical Science Centre for Doctoral Training

July 2022

Contents

Contents	2
Declaration.....	5
Figures and Tables.....	7
List of abbreviations.....	24
Acknowledgements	26
Abstract.....	27
Chapter 1 – Introduction and Background	29
1.1 Introduction.....	29
1.1.1 Motivation.....	29
1.1.2 Aims.....	30
1.2 Literature Review	31
1.2.1 Iron in the brain	31
1.2.2 Iron in Alzheimer’s Disease	33
1.3 Iron in the Human Brain.....	37
1.3.1 Substantia Nigra.....	37
1.3.2 Red Nucleus	39
1.3.3 Putamen	40
1.3.4 Globus Pallidus.....	41
1.3.5 Age and Iron concentration	42
1.3 Description of study	44
Chapter 2 – Methods, principles, and instrumentation.....	45
2.1 Introduction.....	45
2.2 MRI	45
2.2.1 Nuclear magnetic resonance – NMR.....	45
2.2.2 Relaxation and relaxometry	48
2.2.3 Imaging	49
2.2.4 MRI Equipment	54
2.2.5 Pulse Sequences.....	58
2.2.6 Iron in MRI	59
2.2.7 GE Discovery 750W 3T MRI Scanner - Overview	61
2.2.8 MR Microscopy	63
2.3 Computed Tomography	65
2.3.1 X-Ray generation and detection	65
2.3.2 Types of photon production	66

2.3.3 Relationship between Bremsstrahlung photons and kVp	67
2.3.4 Absorption and scattering	68
2.3.4 Beam hardening	70
2.3.5 CT Scan	71
2.3.6 Dual Energy Computed Tomography - DECT	78
2.4 ICP-MS	82
Chapter 3 – Quantifying iron concentration in the brain of post-chemotherapy patients suffering from ChemoBrain symptoms.....	84
3.1 Summary.....	84
3.2 Introduction.....	85
3.2.1 Chemotherapy	85
3.2.2 CICI or “ChemoBrain”	86
3.2.3 Iron in CICI.....	87
3.2.4 Study Design	88
3.3 Literature review	89
3.3.1 Neuroimaging studies in CICI	89
3.3.2 Iron in CICI.....	94
3.4 T2 Relaxometry.....	97
3.5 Method	98
3.5.1 Echo time selection.....	98
3.5.2 Control Brain Regions – typical T2 relaxation times	104
3.5.3 Calculating iron concentration from R2.....	105
3.5.4 Calculating test-case brain iron concentration.....	106
3.5.6 Image Acquisition	107
3.5.7 Image Processing.....	108
3.6 Results	112
3.6.1 Results and data	112
3.6.2 Analysis and Discussion.....	120
3.6.3 Future work - Improving the study methodology.....	123
3.10 Individual contribution.....	124
Chapter 4 - DECT Phantom Studies	125
4.1 Summary.....	125
4.2 Introduction.....	126
4.3 Literature Review	127
4.3.1 DECT for material specificity with monochromatic reconstruction.....	128
4.3.2 DECT iron	129
4.3.3 Detection limits.....	134
4.3.4 ASIR.....	135

4.3.5 CT Energy.....	137
4.4 Studies.....	139
4.4.1 Layered experiment.....	139
4.4.2 Agarose 5 gels.....	151
4.4.3 Aqueous Phantom Study.....	155
4.4.4 ASIR study.....	162
4.5 MRI Phantom Study.....	170
4.5.1 Summary and aims.....	170
4.5.2 Method.....	170
4.5.3 Results.....	172
4.5.4 Analysis and discussion.....	173
4.6 Discussion and further work.....	173
4.7 Individual contribution.....	176
Chapter 5 - Cadaver Study.....	177
5.1 Summary.....	177
5.2 Introduction.....	177
5.3 Literature review.....	178
5.3.1 Imaging in post-mortem tissue.....	178
5.3.2 In-vivo DECT.....	179
5.4 Method.....	182
5.5 Image processing.....	185
5.5.1 ITK-Snap ROIs.....	185
5.5.2 Thresholding.....	186
5.6 Results.....	191
5.6.1 T2 calculation from MRI.....	192
5.6.2 Dual energy CT Results.....	195
5.7 Analysis.....	198
5.7.1 Results and figures.....	198
5.7.2 Comparing DECT and MRI data.....	199
5.7.3 Statistical Analysis.....	202
5.7.4 Spectral imaging consideration of brain images.....	203
5.8 Discussion.....	204
5.8.1 Practical limitations.....	204
5.8.2 Accurate iron determination.....	205
5.8.3 Additional sources of error.....	206
5.9 Conclusions.....	207
5.9.1 Other literature.....	207

5.10 Further work	209
5.11 Individual contribution	211
Chapter 6 - Conclusions and Future Work	212
6.1 Summary	212
6.2 Future work experimental designs	215
References	218
Appendices	245
Appendix 1	245
Appendix 2	253
Appendix 3	264
Appendix 4	264
Patient 01	265
Patient 03	271
Patient 04	279
Patient 05	287
Patient 07	294
Patient 1	301
Patient 3	308
Patient 4	314
Patient 5	321
Patient 7	326
Appendix 5	330
5.1 Patient A.....	330
5.2 Patient B.....	335
5.3 Patient C.....	340
5.4 Patient D.....	345
Appendix 6	350
Appendix 7	359

Declaration

This thesis is submitted to the University of Warwick in support of my application for the
degree of Doctor of Philosophy.

It has been composed by myself and has not been submitted in any previous application for
any degree

The work presented (including data generated and data analysis) was carried out by the
author except in the cases outlined below:

Chapter 3, ChemoBrain MR images provided by Dr Sarah Wayte

Figures and Tables

Figure 1.2.2.1: The amyloid cascade hypothesis, reproduced from Reitz' 2012 paper. (Reitz, 2012)
Amyloid precursor protein (APP) leads to A β aggregation which causes oxidative stress leading to cell death.

Table 1.2.2.1: A summary of various brain region studies from a collection of papers. Reproduced from Haacke 2005 (Haacke et al., 2005)

Figure 1.2.1.1: Relationship between Fe brain levels ($\mu\text{g/g}$, dry weight) and age (years): mean value of the different 14 brain regions for each individual ($n = 42$) (a) and Fe levels in putamen (b), globus pallidus (c) and caudate nucleus (d). Figure and caption reproduced from (Ramos et al., 2014).

Figure 1.3.1.1: Substantia Nigra, highlighted in purple and indicated. Figure adapted from atlas.brain-map.org. (Hawrylycz et al., 2012)

Figure 1.3.2.1: The Red Nucleus is easy to see as two dark black spots in the midbrain on T2 weighted MR images. Figure adapted from Zecca et al. (Zecca et al., 2004)

Figure 1.3.3.1: Brain anatomy including the Putamen and Globus Pallidus. Figure adapted from Sandstrom and Dunbar's textbook ("Huntington's Dis. - Core Concepts Curr. Adv.," 2012)

Figure 1.3.5.1: Non-haem iron in the globus pallidus at different ages. Filled circles represent cases with large intestinal haemorrhages. Figure and caption reproduced from (B. Hallgren & Sourander, 1958).

Figure 2.2.1.1: The hydrogen atom's magnetic moment, μ , aligns with the external magnetic field, B_0 , and begins to precess with angular frequency ω . This ω is known as the Larmor frequency. The angle is exaggerated in the figure.

Figure 2.2.1.2: (A) No external field. Hydrogen atoms are randomly distributed and there is no overall net magnetisation. (B) An external field is applied and the nuclei align with the external field. Some align "with", and some align "against" the field, with respect to the direction of the magnetic moment of the external field.

Figure 2.2.3.1.1: At a short TR = 500ms, the difference in overall contrast, Mz, between the material labelled "Short T1" and the material labelled "Long T1", is larger compared to the difference in the same material at TR=2000ms. Thus, the T1 weighting is reduced, by increasing TR. Figure reproduced from (Weishaupt, 2003).

Figure 2.2.3.2.1: at a short TE = 20ms, there is little difference between the signal received from the sample labelled "Long T2", and the sample labelled "Short T2". There has not been sufficient elapsed time for the short T2 time of the "Short T2" material to have differed greatly from the "Long T2" material. At a longer TE=80ms, the "Short T2" material's signal has decayed much more, meaning the contrast between short and long T2 materials is amplified. In this way, longer TE means more heavily weighted T2-image, where darker means a shorter T2 time (since the signal has decayed much more and so appears less bright in the image reconstruction). Figure reproduced from (Weishaupt, 2003)

Figure 2.2.3.5.1: The top of the scalp, containing fat, is super-imposed on the bottom of the skull, due to that part of the skull extending past the FOV. Image used from web reference (AD Elster, 2021)

Figure 2.2.4.1: (A) 3T with iPAT reconstruction algorithm, (B) 3T without iPAT, (C) 1.5T with iPAT, (D) 1.5T without iPAT. The authors indicate that when comparing (A) with (C), and (B) with (D), smaller vessels and delineation of small regions of detail are rated as significantly superior by radiologists reviewing the images. Figure reproduced from (Gaa et al., 2004).

Figure 2.2.4.2: A field plot obtained using a human brain. Reproduced from Jezzard, 2006 (Jezzard, 2006)

Figure 2.2.6.1: Dependence on field strength for 2.01mg/mL iron in aqueous solution Reproduced from Vymazal 1995. (Vymazal et al., 1995)

Figure 2.2.7.1: GE Healthcare Discovery MR750 3T MRI scanner. Figure reproduced from GE healthcare (GE-Healthcare, 2009)

Figure 2.2.7.2: 5-Gauss line for 1.5T and 3T MRI Scanners. Figure reproduced from GE Discovery MR750W Datasheet. (GE-Healthcare, 2009)

Figure 2.2.8a (left) and (b) right. The cooling mechanism is connected via pipes (a) to the MR probe which it inserted into the underside of the NMR spectrometer. The cooling pump (b) maintains constant temperature of the coolant water at 16.5 degrees Celsius during operation.

Figure 2.3.1.1: Schematic of an X-Ray tube as used in a clinical CT scanner. Reproduced from (FCRPhysics, 2012)

Figure 2.3.3.1: Application of the optical transfer function in X-ray computed tomography – a review. Reproduced from (N Flay, 2012)

Figure 2.3.3.2: A photon counter detector combined with a linear actuator is used to turn the incoming light into a digital signal, which is processed by a connected computer.

Figure 2.3.5.1.1: The intensity of X-ray beam after passing through material 1 is the input X-ray to material 2. The resulting attenuation is a combination of effects. By substituting the middle equation for I_1 into the equation for I_2 , the additive law of attenuation coefficients is clear. Figure reproduced from (Bubba, 2019)

Figure 2.3.5.3.1 Typical setup for an X-ray source and detector pair. Reproduced from (Herman, 2009)

Figure 2.3.5.3.2: A diagram to show the formation of greyscale images from CT numbers determined by X-Ray. Reproduced from s (S. W. Smith, 1998)

Figure 2.3.5.3.3. (a) Standard X-Ray image with a horizontal line marking the level at which the CT cross section will be taken, (b) sinogram produced from projection data, (c) Convolved projection data (a step in the image construction process), (d) final image of cross-sectional slice of the patient's abdomen. Reproduced from (Herman, 2009).

Figure 2.3.5.3.4: Filtered back projection reconstructs an image by filtering each view before backprojection. This removes the blurring seen in simple backprojection, and results in a mathematically exact reconstruction of the image. Filtered backprojection is the most commonly used algorithm for computed tomography systems. Image and caption Reproduced from Technical Principles of Dual Source CT, 2008.

Figure 2.3.6.2.1: A figure demonstrating the fast-kVp switching of the DECT scanner from 140kVp to 80kVp, allowing image reconstruction at any monochromatic energy range from 40keV to 140keV, while also reducing artifacts and obtaining accurate CT numbers. Figure reproduced from (GE-Healthcare, 2011)

Figure 2.3.6.2.2: Number of views per rotation of the scanner. Figure reproduced from (GE-Healthcare, 2011)

Figure 3.3.1.1.1: Evaluation of changes in abnormal white matter in the four participants who completed the study. Abnormal white matter is expressed as a count of abnormal pixels. Abnormal white matter volume is estimated using an assumed 10,000 pixels = 50cm³ of abnormal white matter. Reproduced from Brown et al. 1998

Figure 3.3.1.1.2: One slice from T2 weighted MRI of one study participant. Numerical labels on the figure refer to months after high-dose chemotherapy (E=Entry point = 0 months). Reproduced from Brown et al. 1998

Figure 3.3.1.1.3 The hyperintensities were read by the study neuroradiologist as of uncertain clinical significance, but they appeared somewhat more prominent throughout white matter in (A) the chemotherapy-treated twin than in (B) the twin who did not receive chemotherapy as confirmed by volumetric analysis. Reproduced from Ferguson et al. 2007

Figure 3.3.2.1: Experimental design for animal study. Reproduced from (Cardoso et al., 2020)

Figure 3.3.2.2 (left) Comparison of [Fe] between control group and treatment group, and (right) comparison of ferritin concentration between control group and treatment group. Reproduced from Cardoso et al 2020.

Figure 3.4.1: Linear relationship between R2 and Iron concentration in human neurological tissue. Note the units of R2 in 1/s rather than 1/ms. Figure reproduced from (Mary E. Finnegan, 2013).

Figure 3.5.1.1.1: Top left: One slice of Substantia Nigra (Left) from my brain MRI. Top right: The 3D volumetric reconstruction of multiple slices (3 slices were used in these regions). Bottom left and bottom right: As previously, but for Substantia Nigra (Right).

Figure 3.5.1.1.2: Top left: One slice of Red Nucleus (Left) from my brain MRI. Top right: The 3D volumetric reconstruction of multiple slices (3 slices were used in these regions). Bottom left and bottom right: As previously, but for Red Nucleus (Right).

Figure 3.5.1.1.2: Monoexponential decay fit to echo time data for my brain. The above datapoints are for Substantia Nigra (Left side), with resulting $R^2 = 0.025$. Error propagation is used to calculate resulting T2 values, shown in Table 3.5.1.1.1

Table 3.5.1.2.1: ANOVA results for comparison of echo time methodology.

Figure 3.5.3.1: Calibration measure from literature values of R2 and [Fe]. There are very few sources of segmented human brain R2 values at 3T. Data is sourced from (Haacke et al., 2005). [Fe] measurements are verified using ICP-MS.

Table 3.5.3.1 Linear fit statistics (3 significant figures) for the calibration curve.

Table 3.5.4.1: Measured T2 values with calculated [Fe] values for my brain regions.

Table 3.5.6.1: MRI scanner parameters for image acquisition

Figure 3.5.6.1 Left: Segmentation of the Red Nucleus (Left) for a study participant (Patient 1). Right: The 3D reconstruction produced with ITK-Snap. The segmentation is exported to ImageJ for analysis.

Figure 3.5.7.1: Top, image echo times split into Blue, Green and Red Channels. Bottom: Recombined image would be completely greyscale if the images were identical. Hues can help visually identify regions of faster decay as well as image registration issues.

Figure 3.5.7.4: Patients 4,5, and 7 do not show significant registration mismatch.

Table 3.6.1.1: Measured T2 values across each of the 5 participants.

Table 3.6.2.1.1 Measured [Fe] values based on T2 value. Error displayed is standard deviation.

Table 3.6.2.1.2 Comparison table for mean region with literature value. P-value obtained from one-sample t-test.

Figure 4.3.1.1 Reproduced from (Kumar et al., 2018) HU against monochromatic keV for each phantom. The authors did not use this data in order to plot HU against concentration over a range of energies, which would have allowed them to see which energy was best at determining concentration change among their sample size.

Figure 4.3.2.1 Reproduced from (Tsai et al., 2014) Linear relationship between HU and iron concentration in the heart (Top) and liver (Bottom).

Figure 4.3.2.2 Reproduced from (E.-S. Ibrahim & Bowman, 2014) Linear relationship between iron content and HU depends on the energy level chosen in the monochromatic reconstructed image. (Right) The authors fit a linear model to the data, whereas a mono-exponential fit would usually be most appropriate. If they had included energy levels down to 40keV it is possible that this mono-exponential relationship would be apparent.

Figure 4.3.2.3: Reproduced from (Luo et al., 2015) Comparison of CT measurements at 80 kV, 140 kV and 120 kV with virtual iron content (VIC) measurements derived from dual-energy CT for iron quantification in fat-free phantoms.

Figure 4.3.2.4: CNR increases with kV with mA held constant. Figure reproduced from (Pauwels et al., 2014).

Figure 4.3.4.1: Reproduced from (Hara et al., 2009) Noise reduction in images reconstructed with adaptive statistical iterative reconstruction in phantom. Graph shows linear decrease in image noise (SD) as percentage adaptive statistical iterative reconstruction increases. Images acquired with 50% dose reduction (half dose) have 1.4 times SD value (28.57 compared with 20.39) without adaptive statistical iterative reconstruction. Reconstructing images with 30% adaptive statistical iterative reconstruction for half-dose acquisitions produces images with noise nearly equivalent to that of full dose images without adaptive statistical iterative reconstruction (double arrow) (SD 20.52 compared with 20.39).

Table 4.3.4.1: Reproduced from (Hara et al., 2009). Results of 12 patient study into CT dose index reduction as a result of using ASIR.

Figure 4.3.4.2: Reduction in noise due to ASIR observed in brain CT scan. Reproduced from (Beister et al., 2012)

Figure 4.3.5.1 Reproduced from (Malvarosa et al., 2014) (Left) The gradient of the linear fit increases as the energy level decreases. This is shown as the variable (S) in the Table 4.3 (Right).

Figure 4.4.1.2.1: Layered agarose gel, with concentrations ranging from 0 to 7681 $\mu\text{g}/\text{mL}$ Iron (III) Chloride

Table 4.4.1.4.1: Iron concentrations in each layer at the time of ICP-MS analysis.

Table 4.4.1.5.1: Mean HU and corresponding standard deviation for 80keV and 140keV monochromatic reconstructions of images taken for the layered agarose gel.

Figure 4.4.1.5.1: Layered agarose gel, with concentrations ranging from 0 to 7681 $\mu\text{g}/\text{mL}$ Iron (III) Chloride. Top: 80keV monochromatic reconstruction with $R2=0.77$. Bottom: 140keV monochromatic reconstruction with $R2=0.10$.

Figure 4.4.1.5.1: $R2$ against Concentration for each of the layered gels. It was not possible to fit an exponential decay for the highest concentration sample, due to the $T2$ signal decay at 9.4T being faster than the gap between the first and 2nd echo time.

Figure 4.4.1.5.2: Concentrations ranging from 0 to 500 $\mu\text{g}/\text{mL}$ Iron (III) Chloride. Top: 80keV. Bottom: 140keV.

Figure 4.4.1.5.3: The bottom layer has 10 random circular samples taken from it. The same is done with the 4th, 8th and 11th layers. The 10 values for each layer are then compared using a t-test.

Table 4.4.1.5.2: 10 samples taken from each of the 4 layers indicated above, with mean HU from each compared across layers.

Figure 4.4.1.6.1a: Layer 11, with concentration = 7681 $\mu\text{g/g}$. The MR signal at the 2nd echo time has already decayed to background. So, no T2 measurement is possible for this layer.

Figure 4.4.1.6.2: Layer 10 with concentration = 2851 $\mu\text{g/g}$. Note that measurement error in the signal is very small at high resolution high field MRI.

Table 4.4.2.3.1: HU values for each of the five agarose phantoms at 80 and 140keV, along with corresponding standard deviation values.

Figure 4.4.2.3.1: Top (previous page): Attenuation (HU) against concentration for 5 phantoms using 80keV monochromatic reconstruction. Bottom (this page): As above but using 140keV monochromatic reconstruction.

Figure 4.4.3.3.1 For each phantom, the attenuation was greater at higher energy. This attenuating effect is mostly due to Compton scattering and Photoelectric effect

Figure 4.4.3.3.2 The same dataset from Figure 1, showing dependency of attenuation on iron concentration for a selected range of energies. For any given energy, attenuation was greater for

higher concentration of iron. Note however that the gradient is greater for the lowest energies, indicating that the greatest scope for sensitivity to iron is at 40keV.

Figure 4.4.3.4.1.1: Research into measured HU variation with kVp across a range of CT manufacturers shows that increased energy can lead to increased attenuation in certain polymer-based phantoms – that is, the plastic casing of the aqueous phantom. In this figure, the sample is water, and the casing is made of polystyrene. Additionally, the phantom has $HU < 0$. Figure reproduced from (Sande et al., 2010)

Figure 4.4.3.4.1.2: A comparison of HU values using two different methods of image reconstruction (filtered back projection, labelled FPB, and iterative reconstruction, labelled as ADIR). Image (a) is Polypropylene, (b) is nylon, (c) is acrylic, and (d) is Delrin. The numbers 1, 2 3 and 4 refer to 135kVp, 120kVp, 100kVp and 80kVp respectively, i.e., the energy decreases from left to right, while the attenuation also decreases in each case. Figure reproduced from (Suyudi et al., 2020)

Figure 4.4.4.2.1: Flow diagram of ASIR process. Based on the same diagram in GE Healthcare white paper, Reproduced from (Jiahua Fan, 2014)

Table 4.4.4.4.1: Mean attenuation values and standard error of the mean for each of the 6 phantoms with no ASIR.

Figure 4.4.4.4.1: The result of scanning with no ASIR. Error bars show the standard error of the mean within the chosen region of interest. $R^2 = 0.64$.

Table 4.4.4.4.2: Statistics of the linear fit shown in Figure 5.4. RSS = residual sum of squares

Table 4.4.4.4.3: Mean attenuation values and standard error of the mean for each of the 6 phantoms with 50% ASIR.

Figure 4.4.4.4.2: Scanning with 50% ASIR. Error bars show the standard deviation of the mean within the chosen region of interest. $R^2 = 0.96$.

Table 4.4.4.4.4: Statistics for the linear fit shown in Figure 5.5. RSS = residual sum of squares.

Figure 4.4.4.4.3: Residual plot for both No-ASIR (top) and 50% ASIR (bottom).

Figure 4.6.2.1: Left: The result of the localizer scan. The phantom is off centre within the imaging probe. The sequence for the localiser is not optimised for a clean image, simply as a fast and practical image registration tool for the spectrometer operator, so there are image artifacts present in the localiser image. Right: The final image as obtained once the image registration is complete.

Figure 4.6.2.2: Free induction decay follows a mono-exponential decay when the scanner is correctly tuned via the shim coils.

Figure 5.3.1.1: This non-contrast CT image shows loss of the grey-white differentiation, as well as an inability to see the sulci of the brain. Figure reproduced from (A. B. Smith et al., 2012)

Figure 5.3.1.3: Axial T2 weighted fast spin-echo MRI sequence of a cadaver with temperature reduced due to storage in a mortuary. Figure reproduced from (A. B. Smith et al., 2012)

Table 5.4.1: The four heads used in the study for analysis

Table 5.4.2: MRI scan parameters for study

Table 5.4.3: DECT parameters used in study

Figure 5.5.1.1: Substantia Nigra segmentation from Patient A. This region is then exported to ImageJ for analysis.

Figure 5.5.2.1: (Left) The slice of the brain of Patient B which was used for analysis of Globus Pallidus and Putamen. (Right) a histogram showing the total distribution of pixels in the image. By thresholding all pixels in the leftmost peak, all “noise” pixels are effectively removed from the image.

Figure 5.5.2.1 a, b: Patient E, large areas of damage and gas.

Figure 5.5.2.1 c, d: Patient F, large areas of damage and gas.

Figure 5.5.2.1e, f: Patient G, large areas of damage and gas.

Figure 5.5.2.1g, h: Patient H, large areas of damage and gas.

Figure 5.6.1: Images are manually registered using a transparent overlay, and ROIs are drawn on the MR image from the 3D regions produced from ITK-Snap 3D reconstructions. These then correspond to the same location on the DECT image. Shown above: Red Nucleus and Substantia Nigra.

Table 5.6.1.1: T2 relaxation time found in brain regions of cadaveric heads. This data is then used to produce corresponding iron concentration values shown in Table 5.6.1.2. Given to 2sf

Table 5.6.1.2: Calculated Iron concentration ($\mu\text{g/g}$) in each patient and each brain region

Figure 5.6.1.1: Brain iron concentration calculated from T2 relaxation times for each head and for each brain region.

Figure 5.6.2.1a: Distribution of pixel values in each ROI on DECT images for patient A.

Figure 5.6.2.1b: Distribution of pixel values in each ROI on DECT images for patient B.

Figure 5.6.2.1c: Distribution of pixel values in each ROI on DECT images for patient C.

Figure 5.6.2.1d: Distribution of pixel values in each ROI on DECT images for patient D.

Figure 5.7.1.1a: Attenuation against [Fe] concentration in 40keV (50% ASIR) DECT images for patient A.

Figure 5.7.1.1b: Attenuation against [Fe] concentration in 40keV (50% ASIR) DECT images for patient B.

Figure 5.7.1.1c: Attenuation against [Fe] concentration in 40keV (50% ASIR) DECT images for patient C.

Figure 5.7.1.1d: Attenuation against [Fe] concentration in 40keV (50% ASIR) DECT images for patient D.

Figure 5.7.2.1a: Attenuation against R2 in 40keV (50% ASIR) DECT images for patient A

Figure 5.7.2.1b: Attenuation against R2 in 40keV (50% ASIR) DECT images for patient B

Figure 5.7.2.1c: Attenuation against R2 in 40keV (50% ASIR) DECT images for patient C

Figure 5.7.2.1d: Attenuation against R2 in 40keV (50% ASIR) DECT images for patient D

Figure 5.8.3.1: Reproduced from Dr Mary Finnegan's PhD thesis, a former group member, showing how the segmentation was mapped using MR imaging and then the samples underwent ICP-MS for accurate concentration determination.

List of abbreviations.

Abbreviations used are listed here, and are defined on first use within the text.

A β	Amyloid Beta
APP	Amyloid precursor protein
ASIR	Adaptive Statistical Iterative Reconstruction
CICI	Chemotherapy-induced cognitive impairment
CT	Computed Tomography
DC	Direct Current
DECT	Dual Energy Computed Tomography
FBP	Filtered Back Projection
[Fe]	[Concentration of] Iron
FDA	(United States) Food and Drug Authority
FID	Free Induction Decay
FOV	Field of View
GE	General Electric
GP	Globus Pallidus
HU	Hounsfield Units - also called CT Numbers
ICP MS	Inductively Coupled Plasma Mass Spectrometry
keV	Kilo-electron volt
kVp	Kilovoltage peak
mAs	Milliamp seconds
MRI	Magnetic Resonance Imaging
NFT	Neurofibrillary Tangle
NMR	Nuclear Magnetic Resonance
NMV	Net Magnetisation Vector
PUT	Putamen
QSM	Quantitative Susceptibility Mapping

R1	Longitudinal relaxation rate = $1/T1$
R2	Transverse relaxation rate = $1/T2$
RF	Radio Frequency
RN	Red Nucleus
ROI	Region of Interest
SN	Substantia Nigra
T	Tesla
TE	Echo time (example usage: TE = 80ms means Echo time of 80 milliseconds)
T1	Longitudinal relaxation time
T2	Transverse relaxation time

Acknowledgements

Thank you to my two supervisors, Prof Joanna Collingwood and Dr Sarah Wayte, for their guidance, wisdom, and seemingly infinite patience.

Thank you to all of the incredible staff at University Hospitals Coventry and Warwickshire. Though far too numerous to list, without them none of the studies outlined in the pages to follow would have been possible.

Thank you to my parents, Torrick and Ann, who raised me to think for myself and to strive for greatness.

Thank you to my brothers Adam and Riad for being a source of often needed (and often not) distraction.

Thank you to my wonderful Denise, for her endless support.

Thank you to all of the MOAC and MAS staff and students over the years who made my time so enjoyable, and to the countless academics who have inspired and often confused me.

“Strange about learning; the farther I go the more I see that I never knew even existed. A short while ago I foolishly thought I could learn everything - all the knowledge in the world. Now I hope only to be able to know of its existence, and to understand one grain of it.”

Daniel Keyes, Flowers for Algernon

Abstract

In a range of neurodegenerative diseases including Alzheimer's Disease and Parkinson's Disease, iron is found in increased concentrations in various regions of the human brain. Quantitative analysis of iron in the brain is a difficult task – while post-mortem study using highly sensitive analytical techniques such as Inductively Coupled Plasma Mass Spectrometry (ICP-MS) is somewhat straightforward, accurately quantifying brain iron in living patients, necessitating the use of clinical imaging, presents a range of unique challenges.

In this thesis, one of the current standard techniques of non-invasive brain iron quantification, Transverse Relaxometry (T2 Relaxometry) using a clinical 3T MRI scanner, is compared with a challenger technique, Dual Energy Computed Tomography. DECT is cheaper and faster than Magnetic Resonance Imaging (MRI) (a standard T2 Relaxometry experiment can take 30-40 minutes, while a DECT scan takes under 20 seconds), and can be used on patients that have some ferromagnetic or electronic implants while MRI cannot. In addition, T2 relaxometry is used to attempt to provide a case for iron concentration quantification as a novel method of diagnosing Chemo Brain, a term that describes a set of symptoms experienced by some patients that have undergone chemotherapy.

9.4T Magnetic Resonance Microscopy was used to investigate the relationship between iron concentrations in aqueous phantoms and the relaxation parameters, to support translational work with 3T clinical MRI.

The results of studies into the use of DECT for brain iron quantification show, for the first time, that the technique can be used for sensitive analysis of neurologically relevant iron concentrations in aqueous phantoms, but that there is still work needed to establish whether this is also true in the human brain. The results of the novel human cadaver study described in Chapter 5 indicate that there is no correlation with DECT-acquired CT Number data and iron concentration in cadaveric human brain tissue, but that the discussed limitations of the available cadaver samples (including post-

mortem tissue decay and putrefactive gas accumulation) may confound the results from DECT imaging studies.

Chapter 1 – Introduction and Background

1.1 Introduction

1.1.1 Motivation

The link between iron overload in the brain and a range of neurodegenerative diseases has been well established over the past few decades (J. F. Collingwood & Davidson, 2014; Finnegan et al., 2019; Ke & Qian, 2003; Thompson et al., 2001). Numerous studies have concluded that iron concentration, location, and speciation may play a role in neurodegenerative disease pathogenesis (J. F. Collingwood & Davidson, 2014; LaVaute et al., 2001). The importance of accurately quantifying iron concentration in the brain to support diagnosis is clear – but this is not a straightforward task. The gold standard of iron quantification is to take post-mortem biopsies of brain regions of interest and use high-specificity analytical techniques such as Inductively Coupled Plasma Mass Spectrometry (ICP-MS). The obvious problem, of course, is that this cannot be applied to a living patient. The development of non-invasive techniques for accurate, quantitative measurement of iron concentration in the human brain is potentially key for early diagnosis which would feed into prospective therapies for these diseases. There have not been any additional US Food and Drug Agency (FDA) approved drugs to treat Alzheimer’s disease since 2003, and many drug trials have failed (Yiannopoulou et al., 2019).

In this thesis, the context of analytical Magnetic Resonance Imaging (MRI) is examined, with particular interest in the role of quantifying iron concentration in the brain. A novel pilot study is carried out looking into whether or not ChemoBrain patients exhibit increased levels of neurological iron, as measured by these techniques. The technique of Dual Energy Computed Tomography (DECT) is examined, and numerous phantom studies presented, offering a potential alternative to MRI. Finally, a cadaver study using four human brains with varying confirmed levels of Alzheimer’s Disease compares the efficacy of quantitative MR imaging with DECT.

1.1.2 Aims

The aim of this thesis is to examine the methods in quantitative neuroimaging for determination of iron concentration in the human brain. This is addressed in three distinct ways. Firstly, Chapter 3 aims to determine whether or not T2 (transverse relaxation) relaxometry can be used to determine the presence of Chemotherapy-induced cognitive impairment (CICI), or “ChemoBrain”, in a human trial (Chapter 3). Further study (Chapter 4) then aims to develop a Dual Energy Computed Tomography (DECT) approach which would allow quantitative analysis and determination of iron concentration at neurologically relevant concentration levels (Chapter 4). Finally, the approach that was developed in chapter 4 is used in a clinical human cadaver trial in order to determine whether or not the technique developed in Chapter 4 can be used to assess brain iron concentration in human cadavers (Chapter 5).

1.2 Literature Review

Each of chapters 3, 4 and 5 contains a review of relevant literature. A shorter general review is presented here in addition to the literature review work presented in Section 3.3, Section 4.3 and Section 5.3.

1.2.1 Iron in the brain

Iron plays an important role in numerous metabolic processes in the human body. In the brain, iron is involved in oxygen transportation, DNA synthesis, mitochondrial respiration, myelin synthesis, and neurotransmitter synthesis and metabolism (Ward et al., 2014). Iron in the brain can be categorised in two groups: heme-iron and nonheme-iron. As long ago as 1886, Zaleski reported this finding, and investigated the structure of these two types (Koeppen, 1995) .

Heme iron is usually found in the form of Fe^{2+} within an organic complex, while nonheme-iron exists in the form of ionic iron, or combined to generate low-molecular-weight complexes (Haacke et al., 2005). 90% of brain iron is stored in the form of ferritin. (Ward et al., 2014)

Iron concentration in the brain can be affected by brain region, age, and the presence of neurodegenerative disease (Ramos et al., 2014). Ramos et al (Ramos et al., 2014) collected brain tissue samples from men ($n = 27$; 67 ± 11 years old) and women ($n = 15$; 77 ± 12 years old) who were *not* registered in the Portuguese National Registry of Refusal to Organ Donation. Inclusion criteria were the absence of neurodegenerative disease, absence of injuries involving the central nervous system, and macroscopically normal tissue. The authors also collected three samples from individuals with documented neurodegenerative disease, Alzheimer's disease ($n=2$, female, 73 and 85 years old) and Parkinson's disease ($n=1$, female, 91 years old). The authors produced linear regressions relating concentration of iron in various brain regions with age. These are shown in Figure 1.2.1.1.

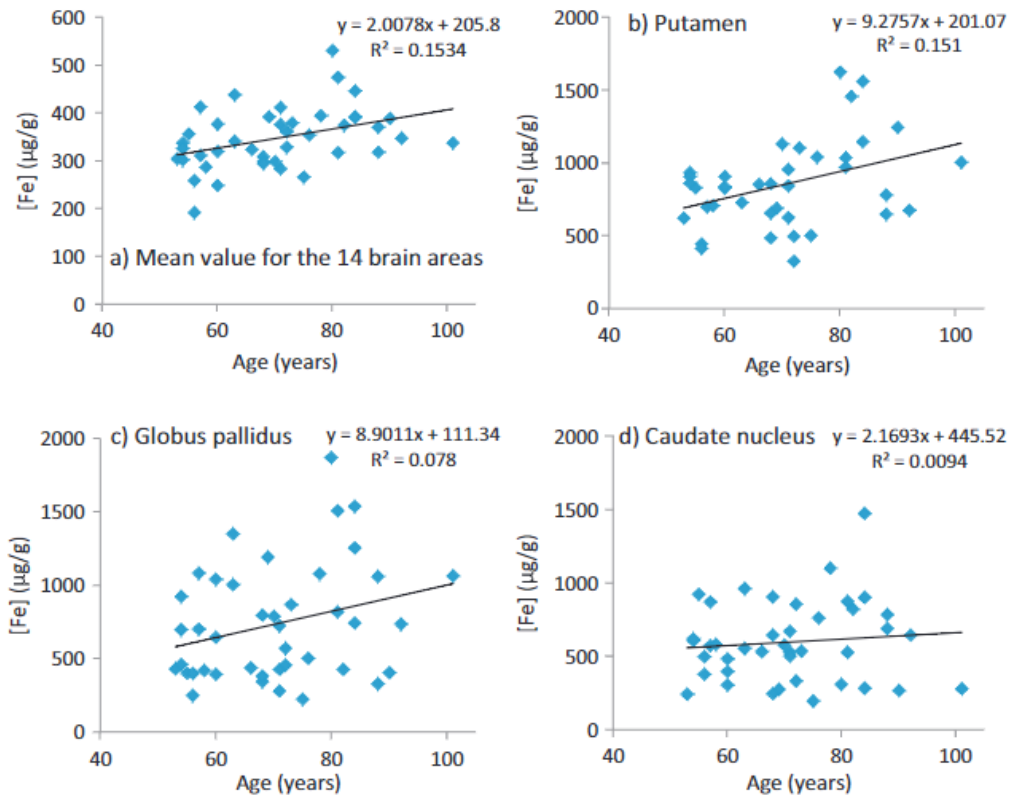


Figure 1.2.1.1: Relationship between Fe brain levels ($\mu\text{g/g}$, dry weight) and age (years): mean value of the different 14 brain regions for each individual ($n = 42$) (a) and Fe levels in putamen (b), globus pallidus (c) and caudate nucleus (d). Figure and caption reproduced from (Ramos et al., 2014).

The authors state that this data represents a significant relationship between age and iron content in the brain. However, the plots above show R^2 values of 0.1534 for all brain regions, and 0.151, 0.078 and 0.0094 for putamen, globus pallidus and caudate nucleus respectively. In a linear regression, the R^2 represents the amount of the variance observed in the dependent variable, which is explained by the variance in the independent variable. In this case, for instance, these results illustrate that only ~15% of the variance in brain iron is explained by age overall, and for caudate nucleus this is <1. This is evident from the plots in Figure 1.2.1.1 if the linear regression trendline is ignored, i.e. simply looking at the scatter of points – there is not a clear and obvious positive linear trend found, and the low value of R^2 reflects this. Nonetheless, this is only one paper, and the result does not align with some other studies into age related brain iron content (B. Hallgren & Sourander, 1958).

While age has been shown to have an effect on brain iron (B. Hallgren & Sourander, 1958; P. A. Hardy et al., 2005), it is not clear from the literature that this is a dominating effect. A recent large-cohort study (Ayton et al., 2021) reaffirmed the role of neurodegenerative disease in increased levels of brain iron. Therefore, the clinical significance of this research is evident – iron concentration is more than a function of age, and the ability to detect increased levels of iron concentration could play a key role in the development of non-invasive diagnostic techniques for the diagnosis of neurodegenerative diseases.

1.2.2 Iron in Alzheimer’s Disease

Alzheimer’s disease is a progressive neurodegenerative disease, and the most common form of dementia (Q. Li et al., 2018). It is categorised by extensive neuronal and synaptic loss (Tan et al., 2013), (Gao et al., 2016), as well as neurofibrillary tangles (Lovell et al., 1998) and senile plaques (J. Hardy & Selkoe, 2002) (Everett et al., 2018). The specific pathogenesis of the disease is still debated, however there is evidence that supports the so called “amyloid cascade hypothesis”, as described in Figure 1.2.2.1. This outlines a potential pathway for the disease progression of Alzheimer’s disease. The proposition is that an aggregation of APP (Amyloid Precursor Protein), presenilin1 (PSEN1) and presenilin 2 (PSEN2) causes aggregation of A β (Amyloid Beta). This aggregation, which leads to both soluble forms of A β as well as deposited forms of A β as a peptide, causes neuron stress. This, combined with the aggregate stress when including Tau and NFT (neurofibrillary tangles) leads to neuronal dysfunction and ultimately neuronal death. It is this loss of neurons that is posited to cause the symptoms of dementia. There is still debate over whether the amyloid hypothesis is a primary factor in diseases pathogenesis, outlined in a recent article arguing against the hypothesis (Makin, 2018)).

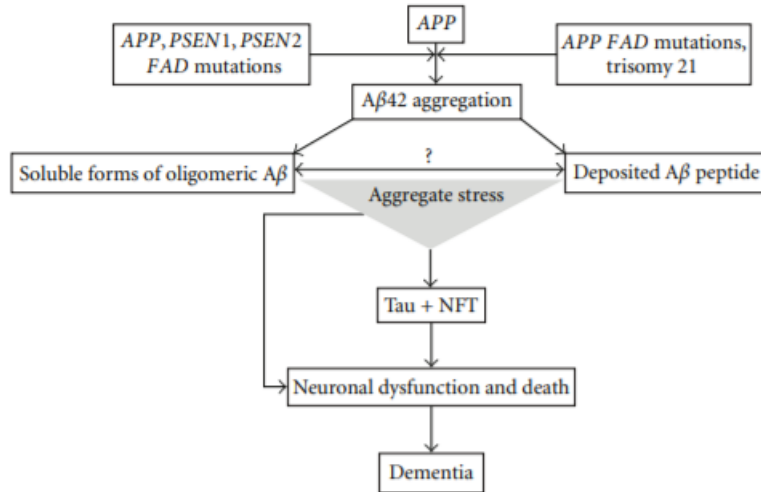


Figure 1.2.2.1: The amyloid cascade hypothesis, reproduced from Reitz' 2012 paper. (Reitz, 2012) Amyloid precursor protein (APP) leads to A β aggregation which causes oxidative stress leading to cell death.

Two of the most significant advancements in the understanding of Alzheimer's Disease (AD) led to the amyloid hypotheses: Firstly, that Amyloid β (A β) is a main component portion of senile plaques, described by Glenner and Wong in their 1984 paper which attributed a "92% reliability" on the use of A β as a biomarker for Alzheimer's Disease (Glenner & Wong, 1984) as well as more recently Palmqvist et al. concluding that "Amyloid PET and CSF biomarkers can identify early AD with high accuracy" (Palmqvist et al., 2015), and secondly that people with a family history of early-onset Alzheimer's Disease frequently shared the same gene mutations of APP, PSEN1 and PSEN2 (Goate et al., 1991)(Levy-Lahad et al., 1995) (Sherrington et al., 1995) (Lanoiselée et al., 2017). In the most recent literature, debate is still active. Herrup makes a case in a 2015 Nature paper that the Amyloid Hypothesis is unable to explain enough of the disease pathology to be held as the current leading theory on the progression of Alzheimer's Disease (Herrup, 2015). Despite this, Herrup also clarifies that even if A β is ultimately proven to merely correlate with (rather than be a contributing cause of) Alzheimer's Disease, this correlation is still a reliable biomarker. The extent to which A β is related to Alzheimer's Disease is still unclear. Regardless of disease pathogenesis, it is however commonly found that A β plaque build-up is a present in the Alzheimer's Disease patient (Deture & Dickson, 2019; Ronald et al., 2009).

Another candidate biomarker for AD is increased concentration of brain iron. Iron is stored throughout the body (including the brain) inside the protein ferritin. ferritin is a globular (spherical) protein complex, consisting of 24 protein sub-units, and is the primary iron storage protein in almost living organisms including algae, bacteria, plants and animals. ferritin's cage-like structure allows each individual protein to hold up to approx. 4500 Fe atoms, though 20% saturation is typical (Reif, 1992). ferritin acts as a protective buffer to protect the human body from both iron deficiency and iron overload. If the integrity of ferritin proteins in the body is compromised, iron may fail to be properly regulated in the body, leading to the possibility of iron overload. In their 2010 paper, Duce et al. describe a strong correlation between brain iron content and APP expression (Duce et al., 2010).

Haacke (Haacke et al., 2005) describes methods of analysing iron in the brain using imaging techniques, as well as giving an overview of the role that iron is potentially playing in the pathogenesis of a number of neurodegenerative diseases. The measurement of non-heme brain iron may also lead to the ability to predict disease outcome (Haacke et al., 2005). Histochemical techniques showed that the iron within the brain was heterogeneous, with further study clarifying the precise distribution of iron throughout the brain. In particular, Haacke notes that from the various studies, which are summarised in Table 1.0, the highest iron concentrations are found in the Globus Pallidus (GP), Red Nucleus (RN), Substantia Nigra (SN) and Putamen (PT).

A range of brain iron sources are provided in the literature. The most widely cited source remains Hallgren and Sourander's 1958 paper (B. Hallgren & Sourander, 1958). A collection of sources is presented in Table 1.2.2.1

Brain Region	Iron µg Fe/g ww	Ratio to GM cortex	No. of samples	Analysis technique	Sample analyzed	Reference
<i>Gray matter</i>						
Globus pallidus	213.0	4.2	55	Colorimetry	Whole	Hallgren and Sourander (1958)
Globus pallidus	175.3	3.8	10	AAS	Whole	Chen et al. (1989)
Globus pallidus	182.0		6	AAS	Whole	Chen et al. (1993)
Globus pallidus lateral	159.4		24	ICP	Whole	Dexter et al. (1991)
Globus pallidus lateral	207.0		6	AAS	Whole	Griffiths and Crossman (1993)
Globus pallidus medial	141.2		23	ICP	Whole	Dexter et al. (1991)
Globus pallidus medial	163.8		6	AAS	Whole	Griffiths and Crossman (1993)
Globus pallidus total	300.6	5.0	23	ICP	Whole	Dexter et al. (1991)
Globus pallidus total	370.8	7.4	6	AAS	Whole	Griffiths and Crossman (1993)
Globus pallidus	108.0		4	AAS	Uncertain	Riederer et al. (1989)
Globus pallidus	81.0	2.9	8	Colorimetry	Supernatant	Riederer et al. (1989)
Substantia nigra	185.0	3.7	52	Colorimetry	Whole	Hallgren and Sourander (1958)
Substantia nigra ZC	159.4	2.6	59	ICP	Whole	Dexter et al. (1991)
Substantia nigra	139.8	2.8	6	AAS	Whole	Griffiths and Crossman (1993)
Substantia nigra oral	65.0		4	AAS	Uncertain	Riederer et al. (1989)
Substantia nigra caudal	45.0		4	AAS	Uncertain	Riederer et al. (1989)
Substantia nigra	48.0	1.7	8	Colorimetry	Supernatant	Riederer et al. (1989)
Substantia nigra ZC	63.0		9	Colorimetry	Supernatant	Sofic et al. (1991)
Substantia nigra ZR	94.0		9	Colorimetry	Supernatant	Sofic et al. (1991)
Substantia nigra ZC+ZR	157.0		9	Colorimetry	Supernatant	Sofic et al. (1991)
Substantia nigra	84.0		6	Colorimetry	Uncertain	Thomas et al. (1993)
Putamen	130.0	2.6	56	Colorimetry	Whole	Hallgren and Sourander (1958)
Putamen	120.8	2.6	10	AAS	Whole	Chen et al. (1989)
Putamen	110.0		6	AAS	Whole	Chen et al. (1993)
Putamen	164.8	2.7	31	ICP	Whole	Dexter et al. (1991)
Putamen	119.8	2.4	6	AAS	Whole	Griffiths and Crossman (1993)
Putamen	76.0		4	AAS	Uncertain	Riederer et al. (1989)
Putamen	96.0	3.4	8	Colorimetry	Supernatant	Riederer et al. (1989)
Putamen	78.0		6	Colorimetry	Uncertain	Thomas et al. (1993)
Caudate	93.0	1.8	58	Colorimetry	Whole	Hallgren and Sourander (1958)
Caudate	115.6	2.2	4	INAA	Whole	Brooks et al. (1989)
Caudate	92.5	2.0	10	AAS	Whole	Chen et al. (1989)
Caudate	117.4	1.9	59	ICP	Whole	Dexter et al. (1991)
Caudate	99.6	2.0	6	AAS	Whole	Griffiths and Crossman (1993)
Caudate	76.0		4	AAS	Uncertain	Riederer et al. (1989)
Caudate	56.0		6	Colorimetry	Uncertain	Thomas et al. (1993)
Hippocampus	52.0		21	INAA	Whole	Cornett et al. (1998)
Hippocampus	43.2		11	INAA	Whole	Deibel et al. (1996)
Hippocampus	42.1		15	INAA	Whole	Thompson et al. (1988)
Hippocampus	24.0	0.9	8	Colorimetry	Supernatant	Riederer et al. (1989)
Amygdala	49.0		21	INAA	Whole	Cornett et al. (1998)
Amygdala	48.6		11	INAA	Whole	Deibel et al. (1996)
Amygdala	48.9		15	INAA	Whole	Thompson et al. (1988)
Amygdala	20.0		4	AAS	Uncertain	Riederer et al. (1989)
Parietal cortex	38.0		37	Colorimetry	Whole	Hallgren and Sourander (1958)
Inferior parietal	56.0		21	INAA	Whole	Cornett et al. (1998)
Inferior parietal	54.4		11	INAA	Whole	Deibel et al. (1996)
Parietal cortex	30.2		6	AAS	Whole	Griffiths and Crossman (1993)
Prefrontal cortex	29.2		52	Colorimetry	Whole	Hallgren and Sourander (1958)
Frontal cortex	53.6		4	INAA	Whole	Brooks et al. (1989)
Frontal lobe	46.0		10	AAS	Whole	Chen et al. (1989)
Frontal cortex	52.0		21	INAA	Whole	Cornett et al. (1998)
Frontal cortex	41.8		6	AAS	Whole	Griffiths and Crossman (1993)
Temporal cortex	31.3		38	Colorimetry	Whole	Hallgren and Sourander (1958)
Temporal pole	51.0		21	INAA	Whole	Cornett et al. (1998)
Temporal gyrus	53.2		11	INAA	Whole	Deibel et al. (1996)
Temporal cortex	50.1		6	AAS	Whole	Griffiths and Crossman (1993)
Temporal cortex	28.0		8	Colorimetry	Supernatant	Riederer et al. (1989)
Motor cortex	50.3		46	Colorimetry	Whole	Hallgren and Sourander (1958)
Occipital cortex	45.5		38	Colorimetry	Whole	Hallgren and Sourander (1958)

(continued on next page)

Table 1.2.2.1: A summary of various brain region studies from a collection of papers. Reproduced from Haacke 2005 (Haacke et al., 2005)

It is noted that ferritin, and the abnormal ferritin molecular pathway molecule hemosiderin, are considered to be the only forms of non-heme iron storage in sufficiently high quantities to affect MR contrast in the human brain (Schenck, 2003).

1.3 Iron in the Human Brain

Iron distribution is not homogeneous throughout the brain, and specific brain regions have been observed to manifest iron dysregulation in response to certain neurodegenerative disorders (Zhu et al., 2009).

As evidenced from the literature (Haacke et al., 2005), four specific brain regions that are observed to have typically high levels of iron (Perl & Good, 1992)(B. Hallgren & Sourander, 1958) are tracked and compared. A brief summary and justification for each is given below.

1.3.1 Substantia Nigra

The Substantia Nigra (SN) is a component of the basal ganglia, as shown in figure 1.3.1.1, which is split into the Substantia Nigra pars compacta and the Substantia Nigra pars reticulata. It is involved in movement, motor control, and the reward dopamine response. The loss of SN neurons is a classic hallmark of Parkinson's disease, and the accumulation and dysregulation of iron in individual neurons in this region was found to also correlate with the disease (Oakley et al., 2007) (Dias et al., 2013).

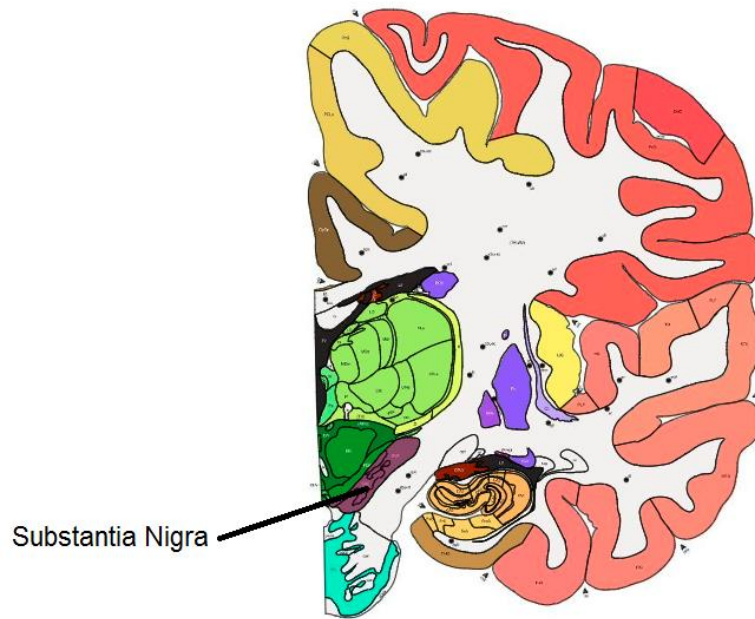


Figure 1.3.1.1: Substantia Nigra, highlighted in purple and indicated. Figure adapted from atlas.brain-map.org. (Hawrylycz et al., 2012)

There has been conflicting evidence in the literature regarding iron concentration in Substantia Nigra. Griffiths et al. observed that iron concentration in SN was more than double healthy controls in Parkinson's Disease patients (Griffiths et al., 1999), while Zhu et al. failed to see significant elevation of iron levels in the SN in Alzheimer's Disease patients (Zhu et al., 2009). Further, for patients with both AD and PD, the iron level detected in the SN was significantly elevated compared to patients with only AD (Brar et al., 2009). These results support and strengthen the evidence for a disease-specific iron dysregulation response in the brain, allowing the potential differentiation of neurodegenerative diseases.

Finally, SN is one of the highest iron concentration brain regions in adult humans (B. Hallgren & Sourander, 1958)(Zecca et al., 2004), meaning that it is a good region to test an emerging technique with an unknown sensitivity limit in human neurological tissue, in this case Dual Energy Computed Tomography.

1.3.2 Red Nucleus

The Red Nucleus is a structure in the midbrain involved in motor control. This region is naturally high in iron (B. Hallgren & Sourander, 1958; Lewis et al., 2013), and is easy to spot on T2 weighted MR images due to this, as in Figure 1.3.2.1.

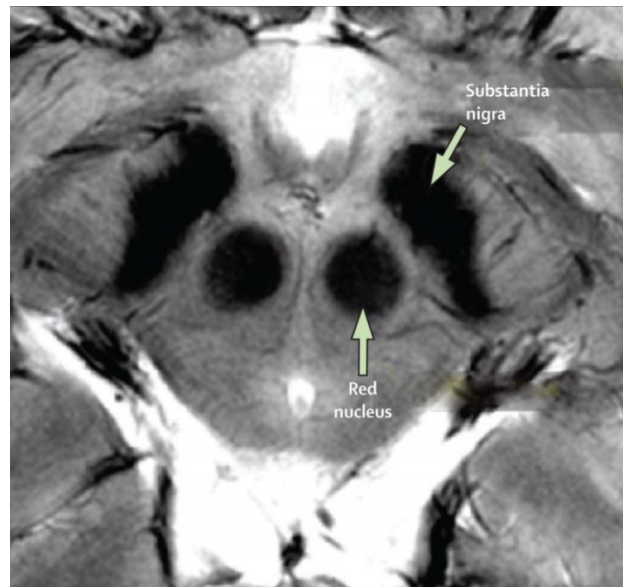


Figure 1.3.2.1: The Red Nucleus is easy to see as two dark black spots in the midbrain on T2 weighted MR images. Figure adapted from Zecca et al. (Zecca et al., 2004)

Lewis et al. find that Red Nucleus iron content is positively correlated with Parkinson's Disease (Lewis et al., 2013). Further to this, evidence of Alzheimer's Disease related senile plaques have been found in the Red Nucleus (Iseki et al., 1989). As the region has naturally high iron content, then as with Substantia Nigra it makes an excellent candidate for study when attempting to establish a detection limit of a new technique.

1.3.3 Putamen

The putamen belongs to the basal ganglia as shown in figure 1.3.3.1, and along with the Caudate Nucleus is primarily responsible for coordinating movement and learning (Alkinoos et al., 2016)(C. S. R. Li, 2000)(Seger & Cincotta, 2005). The putamen is another brain region that is typically high in iron content (B. Hallgren & Sourander, 1958)(Drayer et al., 1987), while also showing significantly elevated levels of iron concentration in patients with some neurodegenerative diseases including Alzheimer's disease and Parkinson's disease (George Bartzokis et al., 2004)(G. Bartzokis & Tishler, 2000).

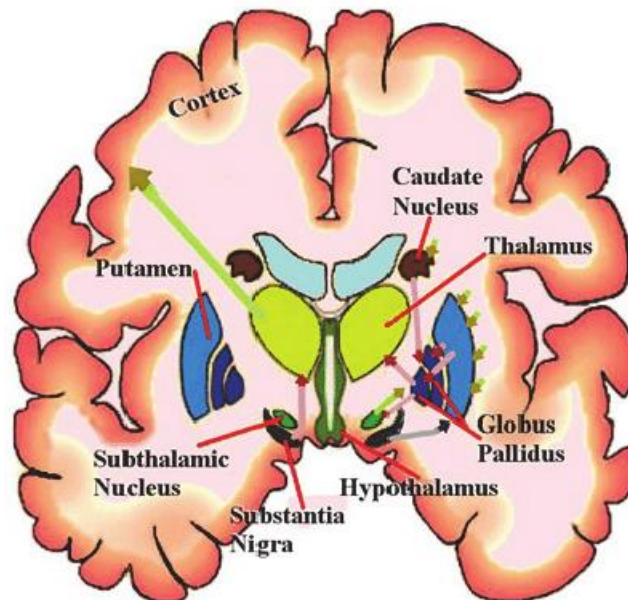


Figure 1.3.3.1: Brain anatomy including the Putamen and Globus Pallidus. Figure adapted from Sandstrom and Dunbar's textbook ("Huntington's Dis. - Core Concepts Curr. Adv.," 2012)

1.3.4 Globus Pallidus

The Globus Pallidus, shown in Figure 1.3.3.1, is involved with movement, and is also part of the basal ganglia. The Globus Pallidus has the highest iron concentration of any brain region for a healthy adult, with Hallgren and Sourander measuring an average 213 $\mu\text{g/g}$ as iron content per fresh tissue weight (B. Hallgren & Sourander, 1958). There are conflicting results in the literature for the iron-regulatory response of the Globus Pallidus in the case of various neurodegenerative diseases. For example, House et al. found no significant iron content increase for Alzheimer's Disease patients in the globus pallidus using MRI (House et al., 2008), while Bartzokis in multiple MRI studies found that there was a significant increase (G. Bartzokis & Tishler, 2000; George Bartzokis et al., 2004), confirming the result from Loeffler's 1995 paper (Loeffler et al., 1995).

Despite these conflicting observations, as the most iron rich region of the brain, it is naturally included in our study as a target to support method development for a potentially iron-sensitive scanning technique.

1.3.5 Age and Iron concentration

As described in section 1.2.1, there have been numerous attempts to accurately model iron concentration in the brain as a function of age. There are a number of practical reasons why this is a difficult process, and suggests at least a partial explanation for conflict in the literature.

In general, iron content has been observed to vary with age (Ramos et al., 2014) (B. Hallgren & Sourander, 1958), tending to increase with age at least up to a certain point, and with Hallgren & Sourander also determining a model for iron concentration as a function of age in specific regions of the brain (Figure 1.3.5.1).

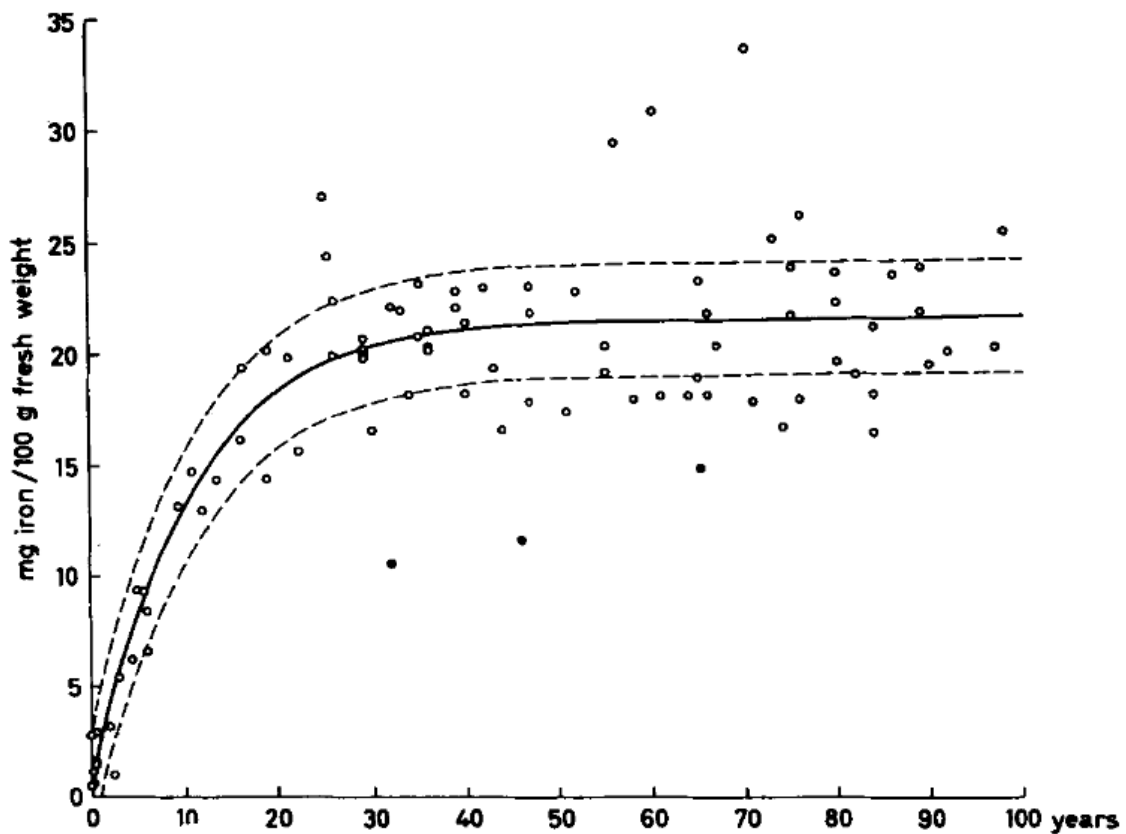


Figure 1.3.5.1: Non-haem iron in the globus pallidus at different ages. Filled circles represent cases with large intestinal haemorrhages. Figure and caption reproduced from (B. Hallgren & Sourander, 1958).

One of the challenges with this analysis is that iron concentration can vary greatly between individuals. Furthermore, until recent developments in quantitative MRI, it has been impossible to obtain accurate brain-iron measurements without waiting for a post-mortem biopsy, meaning a person cannot have had more than one datapoint in their lifetime. This means that collating literature results and comparing data across studies leads to high uncertainty and large standard deviation. Recent MRI techniques have made accurate iron concentration determination possible in living individuals – and such techniques will be discussed and compared in this thesis. However, this still requires individuals to be enlisted in longitudinal MRI studies with regular iron concentration measurements being made. A review article identifies the issue and raises the point that longitudinal brain iron data on *individuals* is still very rare (Degremont et al., 2021).

1.3 Description of study

The main study in this thesis in Chapter 5 will scan 4 cadaveric human heads using both T2 relaxometry and DECT in order to determine the concentration of iron present in each of the four brain regions detailed above. T2 Relaxometry was used as the iron-determining method, with DECT being the test method. Two cohorts of 4 heads are used, however the second cohort turned out to have significant damage and putrefactive gas build-up, making the images unusable for analysis.

Chapter 2 outlines the methods behind techniques used in this thesis and describes how each technique is relevant or suited to iron concentration quantification.

Chapter 3 is a results chapter for the CICI study. It first presents relevant literature on similar studies, and then presents novel data and insights in the use of T2 relaxometry attempt to quantify iron concentration in brain regions in CICI patients.

Chapter 4 is a results chapter for the DECT phantom study. It first presents relevant literature on similar studies, and then presents novel data and insights from a number of developmental studies in order to provide a technique that can be used to quantify iron at neurologically relevant concentration levels.

Chapter 5 is a results chapter for the cadaver study. It presents brain scans from cadavers where we attempt to calculate iron concentration using DECT in order to illustrate and compare the technique to T2 relaxometry.

Chapter 6 discusses the overall conclusions of thesis. Where there was a negative result, we discuss if this was likely to be the underlying hypothesis or technology that caused the failure. We also discuss which techniques show promise for iron concentration quantification in living patients in the future.

Chapter 2 – Methods, principles, and instrumentation

2.1 Introduction

The research and results contained in this thesis aim to answer questions relating to the detection and measurement of iron concentration in tissue or other media. This chapter introduces the methodologies used, the instrumentation used in measurement, and describes the underlying physics principles involved.

The principal techniques used are clinical MRI at 3T (3 Tesla), and clinical Dual Energy CT.

Additional research and development using 9.4T MR Microscopy (Magnetic Resonance Microscopy) as well as the use of Inductively Coupled Plasma Mass Spectrometry (ICP-MS) for accurate iron-concentration determination in some phantom studies are also used, and are introduced in this section.

This section will introduce and discuss the clinical hardware itself, as well as the underlying physical principles and the way in which images are captured, stored, processed and analysed.

2.2 MRI

The MRI system used in all studies presented in this thesis is a clinical 3T MRI scanner (GE Discovery MR750W) located at University Hospitals Coventry and Warwickshire.

2.2.1 Nuclear magnetic resonance – NMR

All hadrons and elementary particles have an intrinsic angular momentum property called spin, s . This value is intrinsic to the particle itself, much like rest mass or charge. Nucleons (neutrons and protons) both have a spin value of $s = \frac{1}{2}$. Atomic nuclei have an overall spin, called the spin quantum number, S . However, two protons in a nucleus are at a lower (and thus more desirable) energy state when they are anti-parallel, not when they are parallel, which allows spins to cancel each other out within the atom. The lower energy state means that they are more likely to be found in this configuration. In fact, 147 out of the 152 stable even-numbered nuclei (nuclei with an even number of protons) have spin 0, meaning all spins have cancelled each other out. The 5 remaining ones are odd-proton, odd-neutron

nuclei which have non-zero spin, namely: ${}^2_1\text{H}$, ${}^6_3\text{Li}$, ${}^{10}_5\text{B}$, ${}^{14}_7\text{N}$, ${}^{180}_{73}\text{Tl}$. Odd numbered nuclei, however, all necessarily have non-integer spin, e.g., ${}^1_1\text{H}$ has spin $s = \frac{1}{2}$.

Spin plays an important role in magnetic resonance. Any nucleus with non-zero spin will give rise to a magnetic moment, μ , because of the positive charge found within all nuclei. Magnetic moment is the vector that describes the magnetic strength and orientation of any object that produces a magnetic field. When a nucleus with a magnetic moment is placed into an external magnetic field, the magnetic moment aligns with the field and will precess around the magnetic field, illustrated in 2.2.1.1.

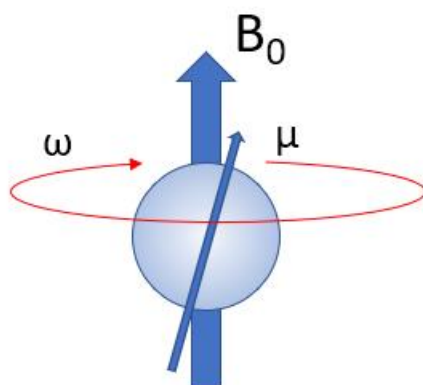


Figure 2.2.1.1: The hydrogen atom's magnetic moment, μ , aligns with the external magnetic field, B_0 , and begins to precess with angular frequency ω . This ω is known as the Larmor frequency. The angle is exaggerated in the figure.

In a general population of, say, ${}^1_1\text{H}$ atoms (with $s = \frac{1}{2}$), these magnetic moments are all pointing in random directions, and so the net magnetisation (i.e., the vector sum of the population) at thermal equilibrium is 0. However, if this population is placed into a strong magnetic field B_0 , the magnetic moments will align either *with* (called parallel, spin-up, or low energy) or *against* (antiparallel, spin down, or high energy) the magnetic field. See figure 2.2.1.2.

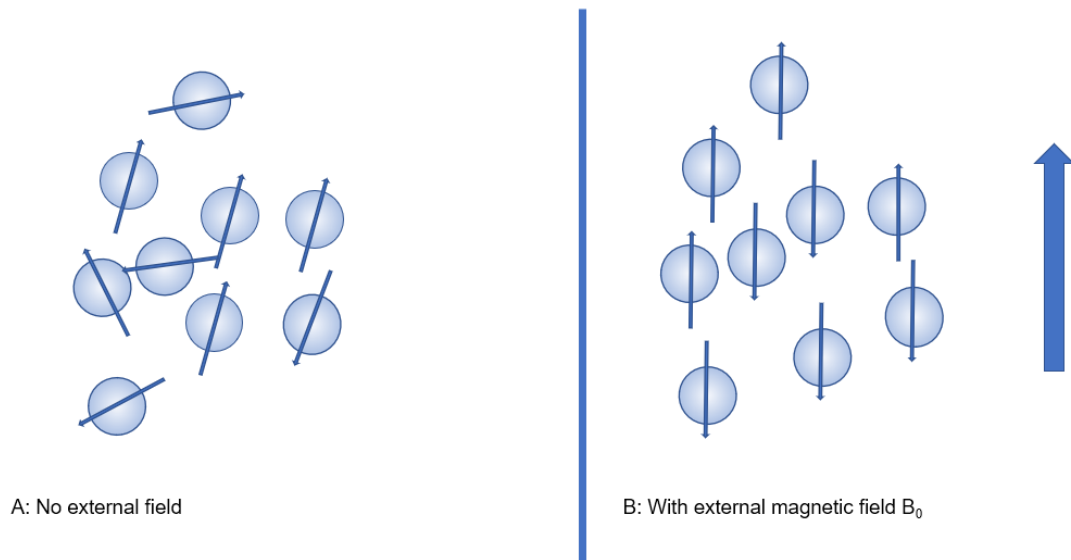


Figure 2.2.1.2: (A) No external field. Hydrogen atoms are randomly distributed and there is no overall net magnetisation. (B) An external field is applied, and the nuclei align with the external field. Some align “with”, and some align “against” the field, with respect to the direction of the magnetic moment of the external field.

Due to the lower energy requirement for parallel / spin-up / “with the field” alignment, there will always be more of these low energy nuclei, each of which can cancel out the magnetic moment of precisely one high energy nucleus. The remaining *excess* low energy nuclei form the Net Magnetisation Vector. The stronger the magnetic field, the more nuclei are in the spin-up state.

As protons are being influenced by the strong external magnetic field, they do not simply sit still – they precess around the magnetic field lines of B_0 , at a particular frequency called the Larmor frequency (ω_0). In fact, the stronger the magnetic field, the higher the frequency, and this is detailed in the Larmor equation, $\omega_0 = \gamma B_0$, where γ is the gyromagnetic ratio of a particular atomic species. This is what is meant by, for example, a 400MHz NMR spectrometer – it means that the field strength of the magnet is such that hydrogen will precess at 400MHz (this corresponds to around 9.4T). NMR can be conducted with any atom that possesses nonzero spin, but since hydrogen is so abundant in the human body, it is the obvious choice for MR imaging.

By applying a pulse of energy with a frequency equal to the Larmor frequency, the system energy is increased, forcing a population of low energy nuclei to excite to a high energy state. The mechanism

by which this pulse of energy is applied is by activating another external field, B_1 , which is perpendicular to B_0 . This B_1 field rotates at the Larmor frequency and causes the NMV to align into the xy plane and to rotate around the B_0 field. This rotating NMW is then detectable by the RF coil via the induced voltage and resulting current. When the RF pulse is switched off, the nuclei begin to regress back to their original state aligned with B_0 , reducing the induced voltage in the RF coil. This is Free Induction Decay (FID) and is the source of the “signal” in an NMR experiment.

2.2.2 Relaxation and relaxometry

Relaxation is the physical process of a nucleus returning to its ground state after excitation by an RF pulse. The individual components of relaxation can be understood by the Bloch equations; all of the nuclei in a sample can be modelled as a single vector, M , known as the net magnetisation vector (NMV). M can then be resolved into its longitudinal (T1) and latitudinal (T2) components.

2.2.2.1 T1 Relaxation

Longitudinal recovery of the net magnetisation vector, or T1 recovery, is the process describing how the NVM returns to its original maximal value, parallel to the external B_0 field. In 1946, Felix Bloch et al. (Bloch et al., 1946) described this process mathematically as a mono-exponential recovery, which can be modelled as $M = M_0(1 - e^{-\frac{t}{T_1}})$. When $t=T_1$, this becomes $M = M_0(1 - e^{-1}) = M_0(1 - \frac{1}{e})$. Thus, one T1 time is equal to the amount of time for the recovery of roughly 63% of the overall net magnetisation vector. As the NMV returns to alignment with the B_0 field, the system loses energy as more spins become aligned to the spin-up orientation of the field. This energy is lost as heat, which is passed into the surrounding atoms and molecules within the field, i.e., passed into the lattice, hence the name spin-lattice relaxation.

2.2.2.2 T2 Relaxation and use for quantifying iron

Spin-spin relaxation, or T2 relaxation, is the transverse component of the NMV. This decays exponentially towards its default equilibrium value. It is characterised by the mono-exponential decay equation $M = M_0 e^{-\frac{t}{T_2}}$. When $t=T_2$, this becomes $M = M_0 e^{-1}$. The T2 time is defined as the amount of time taken to reach $1/e$, or approximately 37% of the original value.

The presence of iron in a sample has been shown to not only decrease T2 time (Vymazal et al., 1996), but to also be linearly correlated to iron concentration (House et al., 2007a; St Pierre et al., 2004; Vymazal et al., 1996). This principle allows accurate iron quantification based on T2 value to be carried out in biological tissue (Drayer et al., 1987; House et al., 2007b).

The reciprocal of T2 is R2, i.e., transverse relaxation rate, measured in s^{-1} .

2.2.3 Imaging

Magnetic Resonance Imaging, MRI, is the process by which we can visualise the manipulation of nuclear magnetic moments by our application of magnetic fields. A general view of MRI is that it is simply a Hydrogen-NMR experiment, where we use additional coils (gradients) to spatially locate the source material, in order to build up a pixel-wise greyscale image.

There are three intrinsic properties of biological material that dictate the MR contrast:

1. The proton density, that is, how many hydrogen atoms are available to contribute to the net magnetisation vector. Images that are primarily generated by minimising the effect of T1 and T2 times on the resulting image are known as proton density weighted images.
2. T1 time. This is the time taken for excited spins to recover and be available to be re-excited by the RF pulse. Images that are primarily generated from T1 recovery are called T1-weighted images,
3. T2 time. This determines the time taken for the MR signal to fade after excitation. Images that are primarily generated from T2 decay are called T2-weighted images.

2.2.3.1 T1-weighted imaging

In order to actually generate an image of a biological sample, a slice of that material must be excited by the external field, and the resulting signal recorded. Repetition time, TR, describes the length of the relaxation period between excitation pulses. This is important in T1 weighted images, as incomplete relaxation will reduce the available net magnetisation for the next pulse, which reduces the overall MR signal that can be collected. By using a short TR, say 500ms, tissue with a short T1 time is

able to recover fully before the next pulse, meaning they produce a strong signal in the subsequent pulses, and appear brighter on the image. Tissue that does not fully recover cannot contribute to the MR signal as much, due to a resulting smaller net magnetisation, and so appear darker.

If a longer TR is selected, say TR=2500ms, then all tissue (both short and long T1 tissue) will have recovered fully in between each repetition, meaning the “advantage” of the short T1 tissue is lost, and so the overall effect of T1 time of the tissue is much lower, as shown in figure 2.2.3.1.1. So, by adjusting TR, we can adjust the effect of T1 weighting on the image.

Short TR = strong T1 weighting

Long TR = low T1 weighting

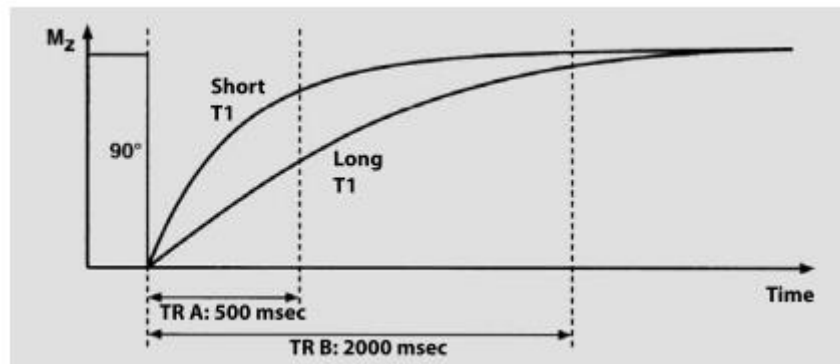


Figure 2.2.3.1.1: At a short TR = 500ms, the difference in overall contrast, M_z , between the material labelled “Short T1” and the material labelled “Long T1”, is larger compared to the difference in the same material at TR=2000ms. Thus the T1 weighting is reduced, by increasing TR. Figure reproduced from (Weishaupt, 2003).

2.2.3.2 T2-weighted imaging

As different gradients are applied, they induce magnetic field inhomogeneities. These inhomogeneities are required to spatially encode the MR signal. These gradients also contribute to spin dephasing, which means a refocusing pulse is required to obtain an MR signal. The signal which is induced at the end of this process, in the receiver coil, after re-establishing phase coherence with the refocusing pulse, can itself be measured – and this is called *spin echo*.

Echo time, TE, is a measure of how long the instrument waits between applying the excitation pulse and collecting the MR signal from the receiver coil. Where Figure 2.2.3 showed that shortening of the TR helps to add more weight to T1-weighted images, the reverse is true of the TE \leftrightarrow T2 relationship i.e., a longer TE results in a more heavily weighted T2 image. This is clear from Figure 2.2.3.2.1.

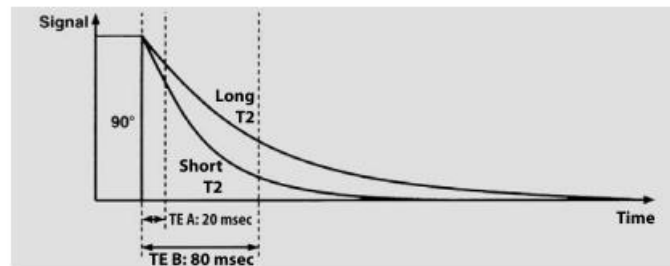


Figure 2.2.3,2,1: at a short TE = 20ms, there is little difference between the signal received from the sample labelled “Long T2”, and the sample labelled “Short T2”. There has not been sufficient elapsed time for the short T2 time of the “Short T2” material to have differed greatly from the “Long T2” material. At a longer TE=80ms, the “Short T2” material’s signal has decayed much more, meaning the contrast between short and long T2 materials is amplified. In this way, longer TE means more heavily weighted T2-image, where darker means a shorter T2 time (since the signal has decayed much more and so appears less bright in the image reconstruction). Figure reproduced from (Weishaupt, 2003)

Short TE = low T2-weighting

Long TE = strong T2-weighting

It follows that tissues with short T2 time appear darker on more heavily T2-weighted images i.e., longer TE times, and tissues with longer T2 time appear brighter.

2.2.3.3 Slice selection and spatial encoding

In order to achieve slice-wise images of the sample, we need some method of precisely affecting the magnetic field of a cross-section of the sample only. If a uniform magnetic field were applied across an entire biological sample (say, a person’s body), then all protons would be excited at once by the RF pulse, meaning it would be impossible to determine the spatial information of any particular set of

protons. Instead, by deliberately inducing a magnetic field inhomogeneity with the use of gradient coils, a linear magnetic field gradient is applied across the entire sample. At one end of the sample (say, the person's head) the magnetic field will be stronger, and at the other end, will be weaker. By carefully moving and placing the field gradient, a perfect "slice" which is at precisely the field strength required to excite protons with an RF pulse at the Larmor frequency can be created.

Therefore, the RF pulse will excite only those protons, and not the others, meaning the signal detected will be from the intended cross-sectional slice of the material. A gradient which changes slowly will create thicker slices, while a gradient that drops quickly from one side of the sample to the other will produce thinner slices.

So far only slice selection has been discussed i.e., magnetic field gradient in the Z direction. The more difficult problem is X and Y spatial encoding. A similar physical principle is involved i.e., the use of magnetic field gradients to adjust the magnetic field such that only a select range of protons in the sample are excited.

For y-axis spatial encoding, *phase encoding* is used. This is a magnetic field gradient in the Y direction, which is switched on after the protons have been excited. This way, phase encoding alters the Larmor frequency of the spins, along the Y axis. Excited spins which are towards the stronger end of the magnetic field gradient experience a stronger magnetic field, which causes them to gain phase, while lower down the gradient there is a loss of phase. This is called a *phase shift* and the detection of signal from protons in different phase states is what allows Y-axis spatial encoding.

X-axis spatial encoding is done via a *frequency encoding*, where a 3rd and final magnetic field gradient is applied. If the higher field strength end of the gradient is on the left, then protons from the left of the sample will precess faster than those on the right, and this frequency difference is again detected in the receiver coil, since we always receive the *entire* frequency spectrum (each pixel can be thought of as an independent NMR experiment).

2.2.3.4 K-Space

As described in 2.2.3.3, X and Y axis data are detected in the form of *phase encoding* and *frequency encoding*. As data is fed into the computer which is attached to the MRI scanner, it is received in the form of a *phase-frequency coordinate system*. In order to convert from phase-frequency to (x, y), a 2D Fourier transform is used.

2.2.3.5 Real world limitations.

MR images can suffer from image artifacts. This is spurious signal that manifests in the image, despite *not* being as a result of free induction decay from the sample recorded in the receiver coil.

Some of the common causes of artefacts are:

Ambient temperature and consistency of DC power supply to the instrument. This can cause a *central point artefact* where a dot in the centre of an image is very bright due to a constant offset in the DC current, which after Fourier transform, appears as a bright spot in the centre of the image.

Electric fields that interfere with the scanner, for instance in a hospital room with insufficient shielding, or a patient with electronic devices near the scanner. This can cause so called *zipper artefacts* which appear as a black and white striped band across the image. The gradient coils themselves will have imperfections in their ability to create and maintain a constant electric and magnetic field, and fluctuations can cause the Herringbone artifact, which again looks like a striped pattern. This effect can also be caused by fluctuations in the power supply to the instrument.

Inhomogeneity in the main B_0 magnetic field (aside from the *intentional* inhomogeneity introduced by the gradient coils) can cause super-imposition of pixels, where a particular signal is erroneously assigned the wrong spatial coordinates. This results in an effect known as *Moire fringes*.

Uneven excitation of nuclei by the RF pulse due to flip angles other than 90 or 180 degrees. This can cause a *shading artefact* if the correct coil size is not used for the given sample or patient.

Incorrect field of view (FOV), for example attempting to image a patient whose body extends past the FOV. This can be corrected by over-sampling the data, however if this is not addressed, then aliasing can occur. Aliasing is also known as a *wrap-around* effect. This is shown in Figure 2.2.3.5.1

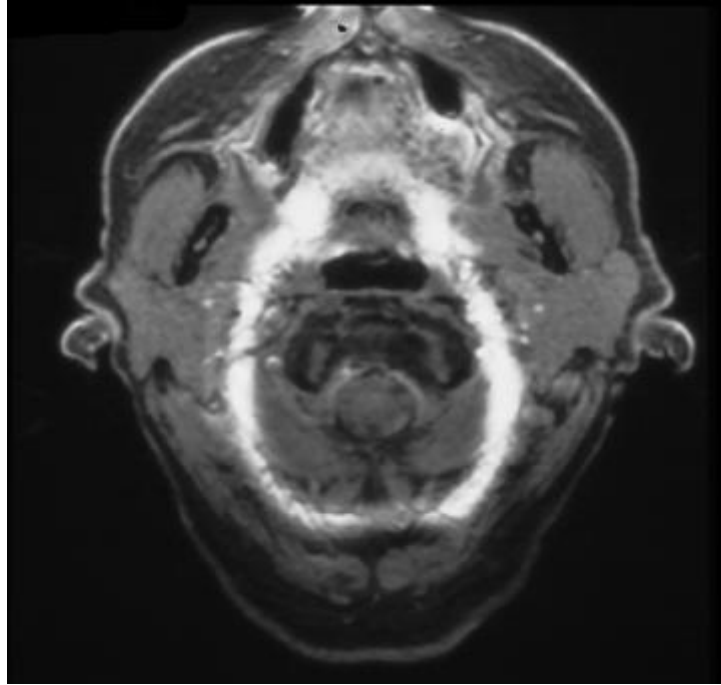


Figure 2.2.3.5.1: The top of the scalp, containing fat, is super-imposed on the bottom of the skull, due to that part of the skull extending past the FOV. Image used from web reference (AD Elster, 2021)

2.2.4 MRI Equipment

This study uses a GE Healthcare Discovery 750W 3T Clinical MRI scanner along with a head coil to ensure uniform excitation across the brain. It is generally desirable to have a higher field strength in an MRI system. The higher field strength means that a larger NMV is produced when a sample is placed in the bore of the magnet, and so the benefit is seen in the signal-to-noise ratio (SNR). NB: Wattjes argues in a 2012 paper that this may not always result in an increased level of diagnostic

ability, and the research publications they reviewed producing results on 1.5T systems have produced equally accurate diagnoses compared to 3T systems (Wattjes & Barkhof, 2012)).

However, even work cited within that review paper would conclude that diagnostic accuracy was more often increased by using 3T MRI, and that signal-to-noise ratio was increased by 1.8-2.3 times for 3T systems compared to 1.5T systems (Wardlaw et al., 2012).

Work by Gaa et al (Gaa et al., 2004) illustrate the difference in figure 2.2.4.1

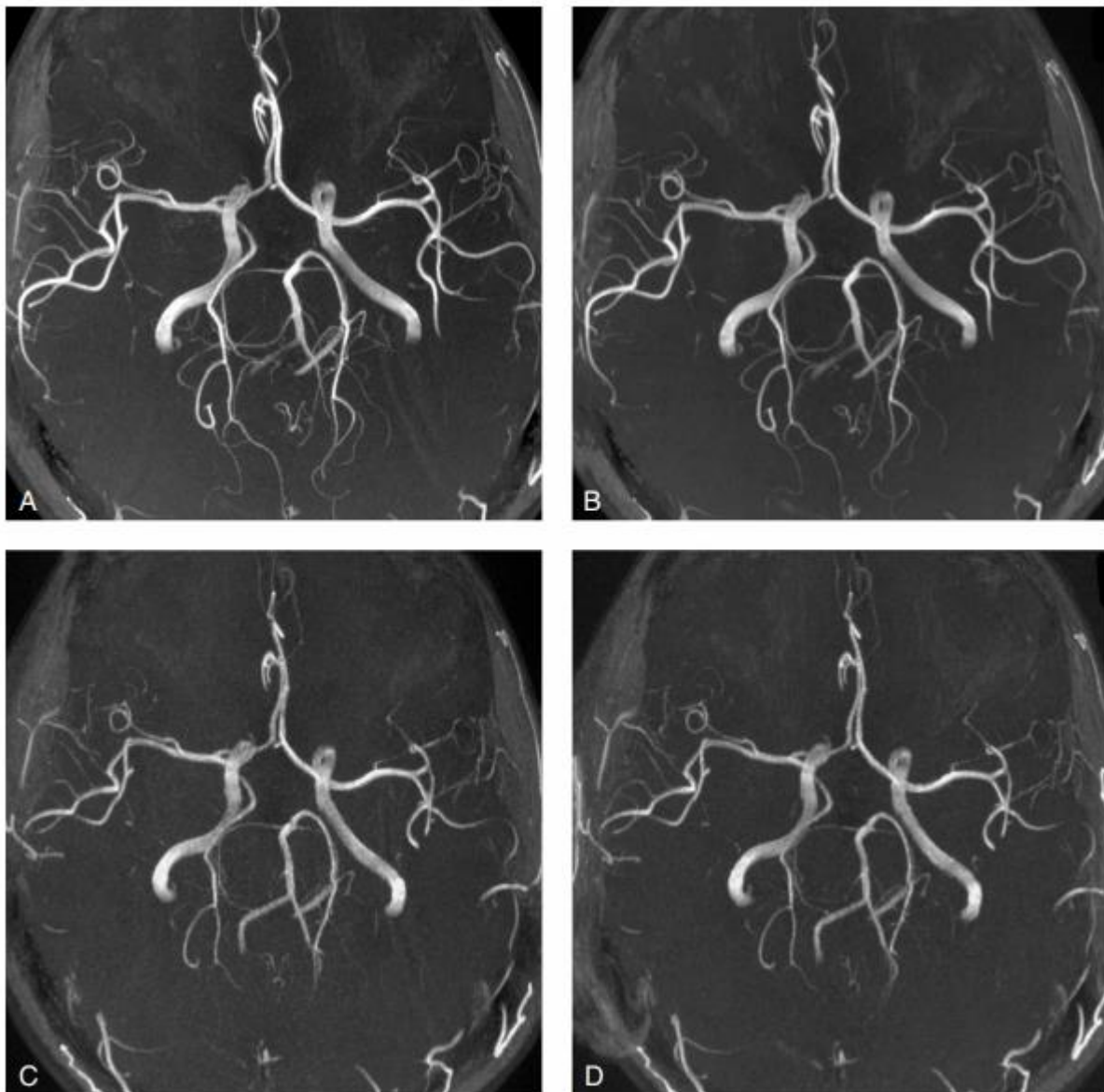


Figure 2.2.4.1: (A) 3T with iPAT reconstruction algorithm, (B) 3T without iPAT, (C) 1.5T with iPAT, (D) 1.5T without iPAT. The authors indicate that when comparing (A) with (C), and (B) with (D), smaller vessels and delineation of small regions of detail are rated as significantly superior by radiologists reviewing the images. Figure reproduced from (Gaa et al., 2004).

Shimming

One of the properties of an MR system is field homogeneity. This will be measured in ppm over a specific diameter of spherical volume (DSV). For example, say a magnet is claimed to have <1ppm over a 30cm DSV, this means that any point within 15cm of the magnet isocentre will experience a field strength of $3 \pm 3 \times 10^{-6}$ T (1 part per million). The reason this is so important will be clear in the next section regarding gradient coils and localisation. What's important, though, is that if you were to buy a magnet and install it in a hospital, you would probably find that the magnetic field strength would vary by over 100ppm at first. This is due to the location of the scanner in the building, the electrical wires running through the walls, the placement of metallic objects in the vicinity, and even other magnets from nearby MRI scanners. The installation will therefore include a shimming process, both active and passive, which aims to reduce the field inhomogeneity to within an acceptable level.

Passive shimming involves installing magnetic materials around the bore of the magnet which counteract the local field inhomogeneities. The full mathematical detail was given by Romeó and Hoult in their 1984 paper which addressed the specific issue of vector field inhomogeneity applied to MRI scanners that need high degrees of accuracy in order to perform high resolution imaging (Roméo & Hoult, 1984). While passive shimming provides a huge amount of correction to local field inhomogeneities, the magnetic material itself is sensitive to temperature, and so the ambient temperature of the room and the temperature of the sample affects how much the material can contribute to the field corrections. Furthermore, each sample that is placed in the bore of the magnet will interact with the B_0 field and produce its own field inhomogeneities. Therefore, active shimming is also used. This is done by a series of coils, known as shim coils, through which current can be automatically or manually varied. Naturally the shim settings must be adjusted and modified for every sample. In clinical MRI, this is normally done automatically by the MRI software package attached to the scanner, which is able to detect and apply the optimal settings after an iteration process.

Gradient Coils

The gradient coils are what turns an NMR experiment into MR Imaging. They slightly alter the magnetic field in the X, Y or Z direction in a predictable way, forming a gradient from one end of the axis to the other. The coils can be used in combination to alter the gradient in any direction in 3D space. In this way, when the FID is detected, the specific magnetic field strength at that precise location will change the Larmor frequency of the corresponding voxel. This allows us to spatially encode the MR signal. By applying an RF pulse that matches a slice of the sample at the newly modified Larmor frequencies, slice selection is achieved. A Fourier transformation is used to separate out the combined signal into frequency and amplitude. In this way the Fourier transformed signal is used to uniquely identify the position of the signal source. It is clear now why shimming is so crucially important – if there is uncertainty about the source of the signal, the image will not be an accurate representation of the sample. Regardless of how perfectly the MRI system is shimmed, once a sample is placed into the bore, magnetic field inhomogeneities are introduced by the sample itself. Figure 2.2.4.2 shows the process of tracking a head scan as the shim is manually adjusted from -0.6ppm to +0.6ppm. These images are from one slice, but the spatial registration is adjusted as the shim coil is adjusted.

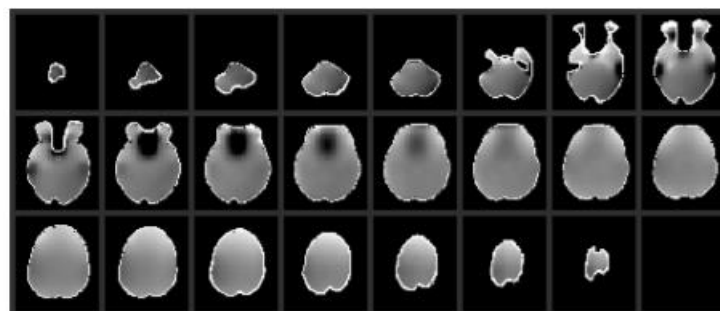


Figure 2.2.4.2: A field plot obtained using a human brain. Reproduced from Jezzard, 2006 (Jezzard, 2006)

The values of magnetic field strength variation across the gradient coils can be determined by adjusting the amount of current through them. This variance simply adds to, or detracts from, the B_0 field.

Taking this concept further, as the gradient coils determine the Larmor frequency at a particular location, and the RF pulse will excite nuclei at their resonant frequency, the gradient coils also allow individual slice selection. The slice through the object formed from a plane composed of specific (x, y, z) magnetic field strength coordinates can be selectively excited and therefore the FID comes only from a given plane. This plane can be angled and placed in any way, as it is simply a collection of coordinates on which we send an excitation pulse, and then collect the resulting FID. Contrast this to CT, where the X-ray emitter and detector pair limit the geometries of slices that can be achieved.

To achieve high resolution imaging, steep gradients are required to have sufficient differentiation of the magnetic field strength in 3 dimensions.

2.2.5 Pulse Sequences

The original MRI experiments by Bloch and Purcell (Bloch et al., 1946)(Purcell et al., 1946) used continuous wave fixed frequency B_1 field, while the main magnetic field B_0 was varied, and resonance was detected as coil voltage fluctuations. After that, it was noticed that immediately after the resonance was detected, there was a small oscillating signal that was left behind. From this observation came the progression of pulsed MRI sequences, where the B_0 field was fixed, and the B_1 field was pulsed on and off at the Larmor frequency. Hahn then discovered that after the B_1 field RF pulse, the same oscillating signal was present (Hahn, 1950). He called it “nuclear induction decay”, now referred to as free induction decay (FID). In reality, the FID is only one kind of NMR signal.

There are four basic types: FID generated by a single RF pulse, Gradient Echo (GRE) generated by an RF pulse followed by a gradient coil reversal, Spin Echo (SE) generated by two RF pulses, and finally Stimulated Echo generated by 3 or more RF pulses.

Gradient Echo

For Gradient Echo, a 90-degree RF pulse is applied to the sample, followed by a gradient reversal via the gradient coils. In this way, the resulting signal has both a net magnetisation vector which is decaying, and also specific spatial information on the sample. Gradient echo sequences do not account for local field inhomogeneities, and therefore measure $T2^*$ rather than $T2$.

Spin Echo

A spin echo sequence accounts for field inhomogeneity by first applying a 90-degree pulse, and then a flip via a 180-degree pulse. In this way, the sample has regained spin phasing, ensuring that the signal is due to spin-spin relaxation and not due to local field inhomogeneities.

Our study uses a collection of single echo spin echo sequences, one for each echo time. Collecting resulting T2 relaxation time allowed exponential decay curves to be fit and graphed separately using statistics and graphing software OriginPro 2016 (OriginLab Corporation, Northampton, MA, USA).

2.2.6 Iron in MRI

Brain iron is found in the iron storage protein ferritin. ferritin is not ferromagnetic (permanently exhibiting magnetism) but is paramagnetic (requiring an external magnetic field to exhibit magnetism) (Vogt, 2016). In their 1995 paper, Vymazal et al. quote Hallgren and Sourander as saying that total brain non-haem iron accounts for 1/3 of all iron content, however then also go on to point out that more recent studies from Brookes and Bauminger confirm that the overall impact on T2 signal decay from ferritin is much higher in the iron rich grey matter (R. A. Brooks et al., 1995)(Bauminger et al., 1994) (Vymazal et al., 1995). Thus, Vymazal et al. conclude that iron-related MRI signal changes in these areas are due to ferritin. As shown in Figure 2.2.6.1, R2 relaxation rate for ferritin displays a linear dependence on magnetic field strength. R2 is the reciprocal of T2, i.e., transverse relaxation rate, measured in s^{-1} .

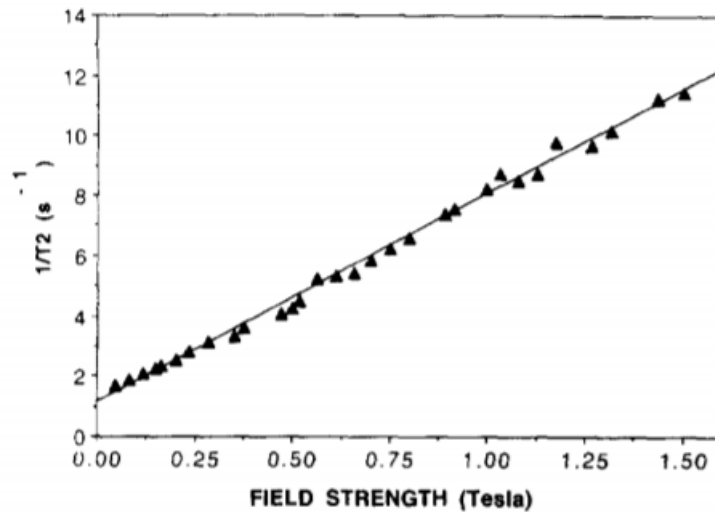


Figure 2.2.6.1: Dependence on field strength for 2.01mg/mL iron in aqueous solution Reproduced from Vymazal 1995.

(Vymazal et al., 1995)

This linear dependence also holds at higher fields. Work by Finnegan et al (Finnegan et al., 2019) involved the use of 9.4T magnetic resonance microscopy to calculate parametric maps of post-mortem brain tissue from Alzheimer’s disease (n=3, ages 73, 75, 98) and healthy controls (n=2, ages 76, 78). The tissue samples were analysed using ICP-MS to determine accurate iron content in the given brain regions. A linear relationship was identified in all brain regions studied with correlation coefficient $r = 0.87$, with experimental uncertainty of 12%. This study published the first set of results that demonstrate the linear relationship between R2 and iron concentration at field strength above 7T.

It is important to note that this is a model system, which is dependent only on iron, and there are no additional effects from paramagnetic radicals. Any additional paramagnetic material in a real-world system will contribute some non-zero effect in decreasing the T2 relaxation rate, meaning that Figure 2.2.6.1. represents an idealised “best case” scenario, whereas in reality the observed R2 would be higher.

Iron that is found in neurodegenerative disease pathways are ferrous iron (Iron(II)) and ferric iron (Iron(III)), as well as magnetite and ferrihydrite (P. Kumar et al., 2016). Iron in its metallic form, as well as Iron (III) are paramagnetic. Iron(II) is usually also paramagnetic, but due to the two free

electrons, can be found in diamagnetic complexes. In 2020, Birkl et al (Birkl et al., 2020) found that the change in oxidation state from ferric to ferrous iron showed no influence on R1, but led to a decrease of 18% in white matter and 13% in cortex tissue for R2.

2.2.7 GE Discovery 750W 3T MRI Scanner - Overview

The MRI scanner used in this thesis is a GE Discovery 750W 3T MRI scanner located at the Department of Nuclear Medicine, University Hospitals Coventry and Warwickshire NHS Trust, Coventry, UK. Figure 2.2.7.1.



Figure 2.2.7.1: GE Healthcare Discovery MR750 3T MRI scanner. Figure reproduced from GE healthcare (GE-Healthcare, 2009)

This system uses a 3T magnet to create the main magnetic field. The magnet specifications are detailed in Table 2.2.7.1.

Operating field strength The Magnetic field strength of the magnet	3.0T (127.8 MHz)
Number of Shim coils	18 superconducting
Magnet shielding Whether active or passive shielding is used	Active
EMI shielding factor EMI = Electromagnetic Interference. The EMI Shielding Factor is used (along with magnetic field strength) to calculate the 5 Gauss Line, i.e., the physical “line” around an MRI scanner at which the stray magnetic field is equivalent to 5 gauss (0.5mT).	97%
Magnet size (without enclosures) (L x W)	173 cm x 206 cm
Magnet length with enclosures	196 cm
Magnet weight with cryogenes	9,750kg
Long-term stability This describes the MRI Scanner Drift, which is the gradual degradation of signal and scan intensity over time. This is corrected with regular calibration.	0.1ppm/hr over 24-hour period
Fringe field (axial x radial) The 5-Gauss line and the 1-Gauss line of this system.	5 Gauss = 5.0 m x 2.8 m 1 Gauss = 7.4 m x 4.4 m

Table 2.2.7.1: List of MR system parameters (GE-Healthcare, 2009)

The 5-Gauss line is further away (i.e., the magnetic field strength remains stronger, for a greater distance) for stronger magnetic fields. Figure 2.2.7.2 shows this effect compared between a 1.5T and 3T GE Healthcare MRI scanner system.

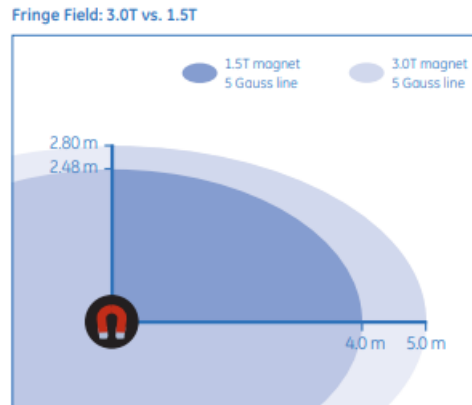


Figure 2.2.7.2: 5-Gauss line for 1.5T and 3T MRI Scanners. Figure reproduced from GE Discovery MR750W Datasheet.

(GE-Healthcare, 2009)

2.2.7.1 Calibration

MR Scanners at UHCW undergo daily calibration checks by radiographers using a GE Healthcare-provided phantom and standard calibration pulse sequence (Daily Quality Assurance sequence). This ranges through various pre-programmed image acquisition modes including T1-weighted imaging and T2-weighted imaging. Mean and standard deviation of expected MR signal are recorded and a signal-to-noise ratio is calculated and compared to a reference. The system warns the operator if any values are outside of normal ranges.

Throughout the course of this project, the machine was never re-calibrated, although daily checks were being done and so no parameters had fallen outside of normal ranges. Changes over time to signal-to-noise, field strength or field inhomogeneity were not recorded.

2.2.8 MR Microscopy

MR Microscopy is effectively MRI at micron-level resolution. It is defined as MRI with spatial resolution lower than 100 microns (Glover & Mansfield, 2002).

MR Microscopy is a useful non-clinical environment to test assumptions about the behaviour of phantoms without using clinical scanner time. However, the MR probe that was available was attached to a 9.4T NMR spectrometer, which means there will be field-dependent differences to account for when comparing findings from the 9.4T MR microscopy probe with those from the 3T clinical scanner.

In addition to the clinical scanner at UHCW, a Bruker 400MHz 9.4T NMR spectrometer with Bruker Micro 2.5 gradient system (ID/OD = 40/72 mm), compatible with the 89 mm wide-bore magnet (MICWB40) was also used to test and develop MR pulse sequences outside of the clinical environment. The imaging probe was used in this thesis to image 1.5mL to 15mL polypropylene test tubes with aqueous and agarose gel-based phantoms.

This probe requires an external cooling system, pictured in Figures 2.2.8a-b.



Figure 2.2.8a (left) and (b) right. The cooling mechanism is connected via pipes (a) to the MR probe which it inserted into the underside of the NMR spectrometer. The cooling pump (b) maintains constant temperature of the coolant water at 16.5 degrees Celsius during operation.

2.3 Computed Tomography

2.3.1 X-Ray generation and detection

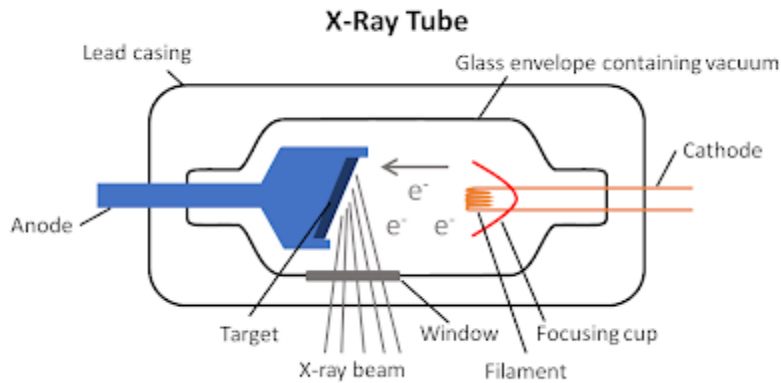


Figure 2.3.1.1: Schematic of an X-Ray tube as used in a clinical CT scanner. Reproduced from (FCRPhysics, 2012)

X-rays for medical imaging are generated by an X-Ray tube. This device is effectively an energy converter; it takes electrical energy from the power supply and transforms this into X-rays and heat. Heat is an unwanted by-product of the interaction, and there are various mechanisms that a CT scanner manufacturer must put in place to deal with this build-up of thermal energy (Alvarez & Macovski, 1976).

As shown in Figure 2.3.1.1, the X-ray tube consists of a hot wire cathode on one side, and a rotating anode on the other. The heat in the cathode results in thermionic emission of electrons, while a potential difference across the cathode anode configuration causes electrons to accelerate towards the anode. The tube is kept at high vacuum so that electrons do not hit molecules in the air and lose energy (Alvarez & Macovski, 1976). The amount of energy carried by an electron is dependent on the voltage between the cathode and anode. A voltage of 1kV provides 1keV of energy to the electron. Collisions with the anode resulting in a sharp decrease in kinetic energy release X-ray radiation. Only 1% of the energy of the electrons is converted to X-rays, with the rest being converted to heat (Yoshizumi, 2011). For this reason, the anode rotates to distribute heat across it.

The factors affecting how many photons are produced at the anode are anode material, tube current, and electron energy. Historically, tungsten was used for the anode, as it has a high Z number (74) and the ability for the metal to retain its strength at very high temperatures. In recent years, research into material science has shown that a more effective anode is a tungsten-rhenium alloy, on top of a graphite or molybdenum base. The base provides heat storage for the system allowing longer continuous use.

The X-ray tube, schematic shown in figure 2.3.1.1, has casing typically made of some heavily attenuating material like lead. This is to protect users from harmful radiation outside of the X-ray beam, and is also used as a means of heat dissipation. Typically, there will be a layer of oil between the glass envelope and the lead casing, in order to absorb thermal energy from the anode.

2.3.2 Types of photon production

The two main types of photon production within the X-ray tube are ‘characteristic x-rays’ and ‘Bremsstrahlung x-rays’.

Characteristic x-rays occur when an electron released by the cathode via thermionic emission interacts with the electron shell of an atom on the anode. One of the incoming electrons hits a bound electron in the anode, causing it to get ejected from a low valence level. This leaves a gap, which must be filled by an electron from a higher energy state. This electron drops down to fill the gap, causing a photon to be released.

Bremsstrahlung x-rays account for the majority (80%) of emitted photons from the x-ray tube (Jiahua Fan, 2014; Yoshizumi, 2011), and occur from interaction with the nucleus of the anode atoms.

Electrons that pass close to the positively charged nucleus of an anode atom experience significant deceleration as the electrostatic forces pull the electron towards the nucleus. This loss of energy manifests as an X-ray photon. X-rays produced in this way are not all of the same energy – the nature of Bremsstrahlung radiation is that different electrons will experience different amounts of

deceleration depending on how close they are to anode nuclei, meaning a wide spectrum of X-ray photons are released in this way.

2.3.3 Relationship between Bremsstrahlung photons and kVp

Very few photons in the X-ray tube will emit with the energy of the incoming electrons. Electrons that pass very close to an anode nucleus will experience strong deceleration, and therefore release a photon close to the maximum energy. Conversely, an electron narrowly passing by will only be slowed a small amount, releasing a low energy photon. The distribution of photon energies released is shown in Figure 2.3.3.1.

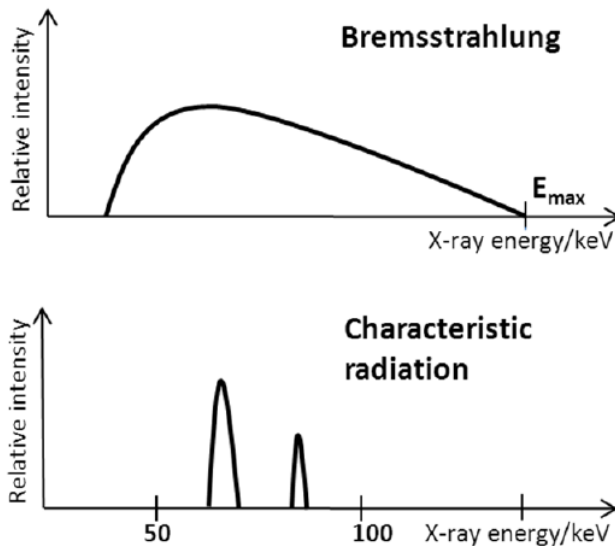


Figure 2.3.3.1: Application of the optical transfer function in X-ray computed tomography – a review. Reproduced from (N Flay, 2012)

It is not possible for X-rays beyond the kVp to be released via bremsstrahlung radiation, however any energy level continuously over the interval can be released. Characteristic radiation, on the other hand, can only take specific energy levels due to quantisation of electronic energy levels present in the anode material. Figure 2.3.3.1 is a general example, however each characteristic radiation spectra is unique to each material. The peaks represent the $K\alpha$ and $K\beta$ peaks. This refers to the quanta of energy which is released when an incident electron collides with a K-shell electron, ejecting it, and an outer shell electron fills this vacancy in the K shell. Figure 2.3.3.2 shows a specific example for X-rays

pass through a filter to remove low energy photons which would not contribute to the imaging process (but would contribute to patient dose)

Once X-rays pass out of the X-ray tube, through the filter and into the sample, they are either absorbed, scattered, or pass through the sample without interaction.

The maximum possible energy in the GE 750W DECT clinical scanner is 140kVp resulting in a maximum energy of 140keV.

While there are various specific methodologies for X-ray detection, the mechanism used in the scanner used in this research is as follows: X-ray detection is accomplished by a series of flat panel detectors along the other side of the scanner. These work by a layer of scintillation material which absorbs X-rays and converts them to light via luminescence. This light is absorbed by a photodetector array which generates an electrical signal proportional to the amount of light received. This data, after reconstruction, is what produces voxel specific intensity data which is given in Hounsfield Units.

Figure 2.3.3.2 shows a schematic for a simple scintillator and photodiode CT setup (Leng et al., 2019)

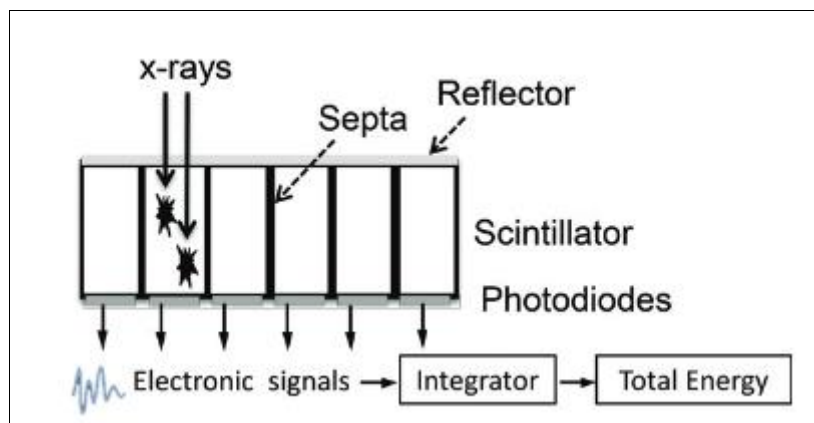


Figure 2.3.3.2: A diagram showing a scintillator and photodiode CT detection setup. Figure reproduced from (Leng et al., 2019)

2.3.4 Absorption and scattering

The differentiation of material in computed tomography (CT) is based on their X-ray attenuation as quantified in Hounsfield Units (HU) and displayed via greyscale images. The two main mechanisms

responsible for these effects in the photon energy range used in CT are Compton scattering and the photoelectric effect(Yoshizumi, 2011). For the energy range in a CT scan, the Compton effect is independent of photon energy, whereas the photoelectric effect is strongly energy dependent. As will be shown in results sections later, the HU value of tissue does not vary terribly much for tissue, but does vary considerably more for iron, due to the increased impact of the photoelectric effect on this material.

A simple analysis of X-Ray absorption is possible for the idealised case of a narrow monochromatic well collimated X-Ray beam. The x-ray beam intensity follows the exponential attenuation law:

$$I = I_0 e^{-\mu s}$$

Where I_0 is the incident intensity of the monoenergetic beam of photons, s is the material thickness, μ is the linear attenuation coefficient, and I is the final intensity of the photon beam(Hubbell, 1996).

Absorption in CT experiments occurs due to Compton scattering, and the photoelectric effect. The photoelectric effect is where an incoming photon is absorbed by a nucleus, resulting in an electron being excited to a state where it has sufficient energy to be released from the atom (known as a photoelectron).

And so, a narrow, well collimated beam of X-Rays will decay exponentially with distance travelled through a material. However, in a more typical broad beam case, this analysis does not hold; there are now competing effects, since having some X-rays scattered does not mean that they are no longer considered at all, but rather they may or may not be detected at another location. It is important therefore to understand how scatter occurs and what proportion of photons can be expected to scatter for a given material with a given density.

Compton scattering is where an incident photon is deflected by the electric charge on a sub-atomic particle, typically an electron, when it interacts with the atom, thus changing its energy and direction.

The formula for the wavelength after Compton scattering is as follows:

$$\lambda' - \lambda = \frac{h}{m_e c} (1 - \cos \theta)$$

Where:

λ is the initial wavelength of the photon

λ' is the wavelength after scattering

h is the Planck constant

m_e is the electron rest mass

c is the speed of light

θ is the scattering angle.

2.3.4 Beam hardening

The X-ray source used in CT scanning is polychromatic, that is to say there is a distribution of photon energies that are emitted, and which pass through the object material. If the beam of radiation were monochromatic, this effect would be simple to understand and quantify – there would be some linear attenuation coefficient which would predict the intensity seen at the detector. However, in a polychromatic energy environment, the photons that happen to have a lower energy are more likely to be absorbed or scattered than the higher ones. In this way, the distribution of energies *itself* is changed by the material. This phenomenon is known as beam hardening. The results of beam hardening are a streak artifact (where the resulting image contains dark bands) and cupping artifacts (where at the boundary between a dense object and a non-dense object, such as bone and air, the high levels of beam hardening due to the bone causes the boundary to show up very brightly). The ways that CT scanner manufacturers have come up with to avoid this effect are varied, but generally are a combination of pre-hardening the beam using some form of metallic filter, in addition to calibration with manufacturer-specific phantoms which effectively normalise the distribution on the assumption that some predetermined “standard” amount of beam hardening has occurred.

2.3.5 CT Scan

2.3.5.1 Measuring attenuation

Attenuation is the reduction of intensity of an x-ray beam as it passes through matter.

The attenuation of photons moving through a medium is described as a function of the *linear attenuation coefficient* μ , and the length of the material the photons pass through. This is described by the *Beer-Lambert Law*:

$$I = I_0 e^{-\mu s}$$

Where:

I = intensity of X-ray after passing through the material, a function of wavelength (λ).

I_0 = intensity of initial X-ray beam, a function of wavelength (λ).

μ = linear attenuation coefficient of the material

s = the length of the material that the photons pass through

The effect of multiple media is to attenuate one after another, i.e., the resultant x-ray attenuation after being attenuated by material 1 is the input to material 2. This is shown in figure 2.3.5.1.1.

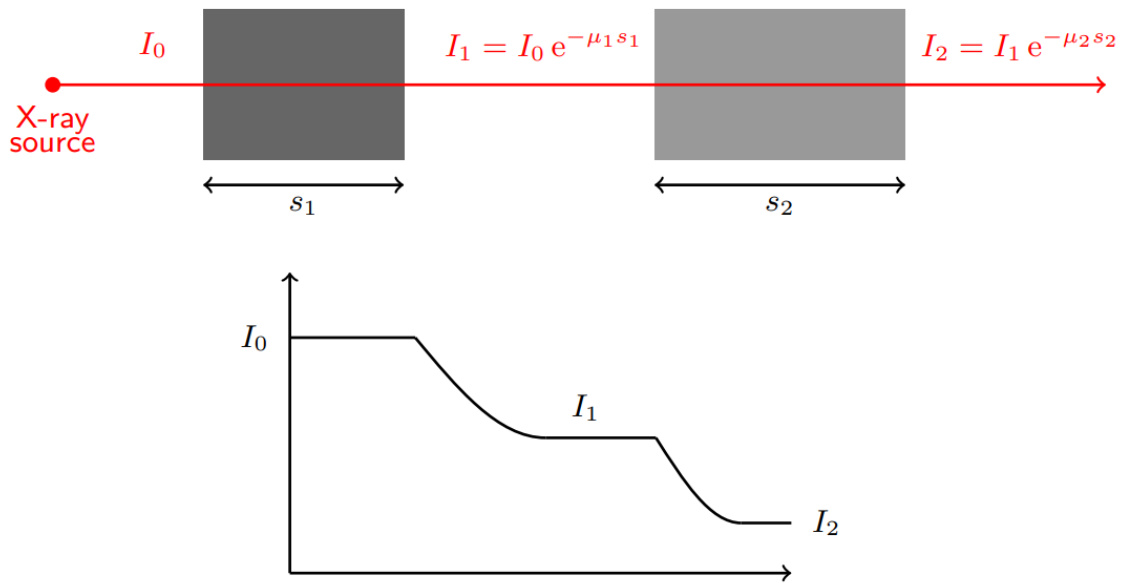


Figure 2.3.5.1.1: The intensity of X-ray beam after passing through material 1 is the input X-ray to material 2. The resulting attenuation is a combination of effects. By substituting the middle equation for I_1 into the equation for I_2 , the additive law of attenuation coefficients is clear. Note that the figure above uses the linear attenuation coefficient, rather than the mass attenuation coefficient. Figure reproduced from (Bubba, 2019)

The *mass attenuation coefficient* for a given material is defined as $(\frac{\mu}{\rho_m})$ where μ is the linear attenuation coefficient of the material and ρ_m is the material density. Using the mass attenuation coefficient, the attenuation coefficient can be calculated for a given heterogeneous material as follows:

$$\mu = (\frac{\mu}{\rho})_1 \rho_1 + (\frac{\mu}{\rho})_2 \rho_2 + \dots$$

Where each term in the sum above is the *mass attenuation coefficient* of a given component of the material, multiplied by the material density. When using mass attenuation coefficient, for example in radiology, the beer lambert law is then stated in an alternate form as follows:

$$I = I_0 e^{-(\frac{\mu}{\rho_m})\lambda}$$

Where $\lambda = s \times \rho_m$ is defined as the area density, i.e. the length of material multiplied by the density.

2.3.5.1 Hounsfield Units

In the above workflow, a CT image is produced by mapping signal from a photomultiplier on to a pixel value in the range [0,255]. Hounsfield Units (HU) are a convenient way to express CT numbers. The linear attenuation coefficient of radiation within a given material produces a grayscale image. The Hounsfield Unit is an arbitrary definition where distilled water is defined to have a value of 0, and air has a value of -1000. All material values are linearly mapped onto this scale. Therefore HU is defined as:

$$HU = 1000 \times \frac{\mu - \mu_{water}}{\mu_{water} - \mu_{air}}$$

where μ_{water} and μ_{air} are the linear attenuation coefficients of water and air, respectively.

Some additional HU values are given for reference in table 2.3.5.1.1.

Material	HU
Dense cortical bone	1000
Fat	-30 to -70
White matter	25
Grey matter	35
Soft tissue	20 to 30

Table 2.3.5.1.1: Some typical HU values for various materials. (Kamalian et al., 2016)

Limitations of HU include the fact that different X-ray beam energies result in different absorption, and therefore different HU values. Therefore, to ensure that HU values are reliable, machine calibration is required.

Software that is used to analyse CT images often automatically adjusts pixel values into Hounsfield Units. This is a property of the DICOM image format, where information in the DICOM header

(specifically Attribute Name: Rescale Intercept, DICOM Tag: (0028, 1052)) is used to establish that pixel values are to be reported in Hounsfield Units (DICOM Nema, 2016). ImageJ, which is used for image analysis in this thesis, uses this setting by default.

2.3.5.3 Image construction

A Computed Tomography (CT) scan is a process by which a computer combines X-Ray attenuation data, gathered from multiple angles, to construct cross-sectional slices of an object. Original CT scanners would take one snapshot using a source-detector pair, then be manually moved, take another snapshot, and so on. CT scans were incredibly lengthy and if the object to be imaged was a person, as is the typical use for a CT scanner, any movement in between scans made imaging difficult. CT technology improved and in 1998 the modern multi slice helical scanning system was introduced, where multiple detectors are mounted on a circular array which spins as the object to be images moves through the bore of the scanner. A schematic of the source-detector pair is shown in Figure 2.3.5.3.1.

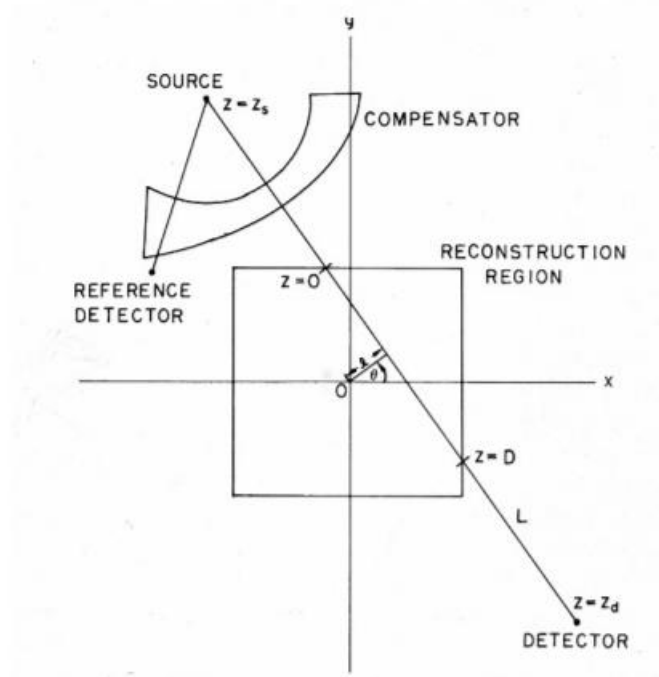


Figure 2.3.5.3.1 Typical setup for an X-ray source and detector pair. Reproduced from (Herman, 2009)

Absorption of X-ray radiation, as outlined above, forms the basis of CT image reconstruction. For a given image, each pixel is given a greyscale value which is based on the CT number that is assigned to a particular voxel. The way of assigning that CT number is a function of the attenuation experienced through that region of space.

It is shown in figure 2.3.5.3.2 that an individual slice of a CT reconstruction is a matrix of CT numbers, measured in Hounsfield Units, with each number given a greyscale value.

The way that CT number is calculated from this matrix is using a sinogram. Shown in Figure 2.7b, the sinogram is a collection of all the line integrals from each source-detector pair as the object is scanned. Taking them all together produces a full image, shown in Figure 2.3.5.3.3d. Since different tissues and materials have different attenuation characteristics, their sinograms will also be different, meaning the ultimate reconstructed image will show areas of contrast that allow diagnostic analysis.

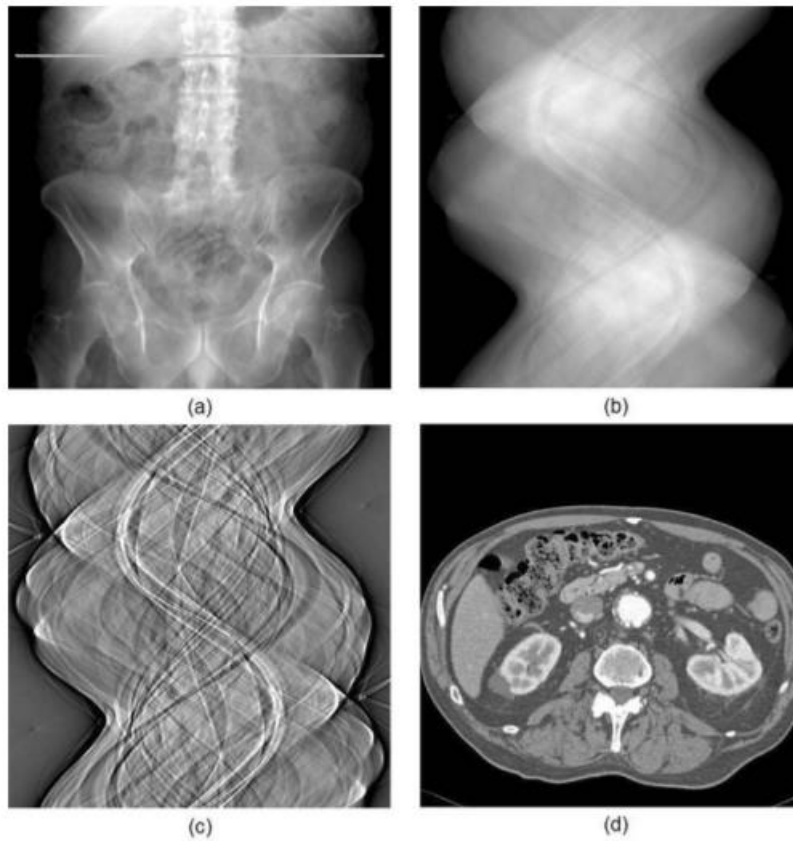


Figure 2.3.5.3.3. (a) Standard X-Ray image with a horizontal line marking the level at which the CT cross section will be taken, (b) sinogram produced from projection data, (c) Convolved projection data (a step in the image construction process), (d) final image of cross-sectional slice of the patient's abdomen. Reproduced from (Herman, 2009).

Finally, image reconstruction itself takes two main forms. Traditional CT uses a process known as filtered back projection, while more modern iterative reconstruction techniques can produce images with lower noise at the expense of additional computing power (Ter-Pogossian, 1984).

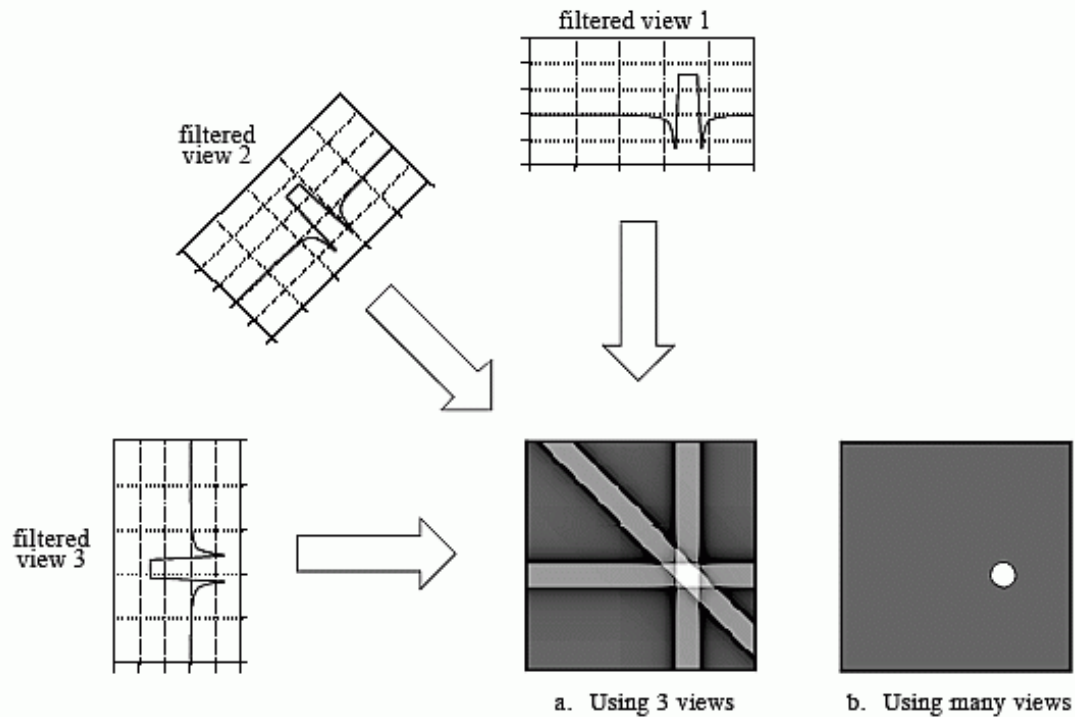


Figure 2.3.5.3.4: Filtered back projection reconstructs an image by filtering each view before backprojection. This removes the blurring seen in simple backprojection, and results in a mathematically exact reconstruction of the image. Filtered backprojection is the most commonly used algorithm for computed tomography systems. Image and caption Reproduced from *Technical Principles of Dual Source CT*, 2008.

Back projection is effectively a way of taking enough averages of a sample that eventually the image must resemble the original object to within a certain degree of error. With enough views combined and averaged, the resulting CT numbers in each pixel will approach the true value, as shown in Figure 2.3.5.3.4. Applying a filtering kernel to this process completes what is known as filtered back projection (FBP).

Filtered back projection is an intuitive way of recreating spatial data with a large number of single-track sources, however it leaves the resulting images open to a number of issues. If no filtering was applied at all, and simple back projection used, the areas of overlap between the beams would always have a huge amount of noise. In particular, regions of overlap between source-detector pairs will always result in a circular “dot” of image data, which fades away towards the edges. There is no reason that this is necessarily a true reflection of reality (and in biological tissue imaging this almost certainly is not the case), and so appropriate filters are used to counteract this effect. In fact, with

infinite source-detector pairs, the filtered back projected image would be *identical* to the real image. This would be the most comprehensive and exhaustive way of imaging a piece of 3D space.

Iterative reconstruction is notable in its ability to reduce patient dose while maintaining or even enhancing image quality compared to traditional FBP reconstruction methods. One of the most important considerations in choosing to scan a patient is the dose that is being delivered to that person. In a low-dose scan, traditional FBP suffers from noise and artifacts. IR techniques have been known to be possible since the 1970s, but only in recent years has processing power been sufficient to make these techniques feasible in the clinical setting. To understand what IR does, first consider a standard filtered back projection reconstruction. Effectively, we are trying (impossibly) to solve $\mathbf{Ax} = \mathbf{p}$ for \mathbf{x} , where \mathbf{A} the forward projection matrix, \mathbf{x} is the forward projected “artificial” image, and \mathbf{p} is the measured FBP image. However, while we cannot solve this system of equations due to the system being overdetermined, we can optimise $\hat{\mathbf{x}} = \mathit{min}\|\mathbf{Ax} - \mathbf{p}\|$. (Jiahua Fan, 2014) Simply, this means that while we cannot algorithmically find an exact solution for the “best” image that fits the data from a single CT scan, we can take a low dose scan, use standard FBP to construct an image, and then iterate that image multiple times until we find the lowest possible difference between the image we constructed with FBP and the image we constructed using forward projection. The true image lies somewhere between these two.

2.3.6 Dual Energy Computed Tomography - DECT

The idea of using more than one x-ray energy in CT imaging is not a new one – since the 1970s, it was known that using two energy sources for the purpose of obtaining spectral image data from CT scanning was possible (Hara et al., 2009), and the benefits were being discussed. With over 1,800 citations, the well-known 1976 paper from Alvarez and Macovski (Alvarez & Macovski, 1976) “Energy-selective Reconstructions in X-ray Computerized Tomography” documents this fact and details that researchers have long been aware of the possibility to use some form of DECT, typically by producing two successive CT scans with different energies and combining the resulting images via some form of postprocessing. In modern systems, the idea is to have an emission and detection setup

that is capable of producing x-rays at two different kVp values while also having a detector that is capable of differentiating between the two different x-ray sources. There are three main ways this is implemented, though the first two (Dual Source CT and rapid kVp switching) are more commonly used than the third (layer detector technology).

2.3.6.1 Dual Source CT

Dual Source CT is employed in Siemens DECT scanners, and the setup is probably the most intuitive one; if you want two different x-ray sources and a detector setup that knows which photons came from which source, the simplest way to do it is to have two different x-ray tubes at 90 degrees to one another, complete with their own detectors in the array around the gantry. As the system rotates, the entire object is imaged by both detectors and the composite image can be reconstructed. One evident benefit is that patient motion should not produce a large effect due to fast rotation time. Typically, these scans are done with an 80kVp and a 140kVp x-ray source. Conventional CT images can be obtained from averaging the scans, however more than just that can be reconstructed (McCollough et al., 2015).

The low kVp scan in the dual source setup is typically the one with more noise, because a smaller proportion of photons are able to penetrate the object being imaged (which is usually a person)(T. R. C. Johnson, 2012). On the other hand, for iodine enhanced images, contrast is typically better at lower kVp since the average keV of an 80kVp x-ray source is closer to the k-edge of iodine (33keV).

2.3.6.2 Gemstone detector and fast kVp switching – GE Discovery 750HD

The scanner used in all original DECT work presented this thesis is a GE Healthcare Discovery 750HD Dual Energy CT scanner, located at University Hospitals Coventry and Warwickshire. It is notable that the majority of DECT studies performed in the wider community, some of which are reviewed in Chapter 2, use the Siemen's Dual Source DECT system. The GE scanner has two main

technological advances over similar scanners, namely rapid kVp switching and the gemstone detector. (GE-Healthcare, 2011)

The Discovery CT750 HD was the first quantitative dual energy spectral imaging scanner on the market. (GE-Healthcare, 2011).

Image acquisition is powered by the Gemstone detector, and its ability to recreate monochromatic reconstructions from a dual source CT. This is shown in figure 2.3.6.1.

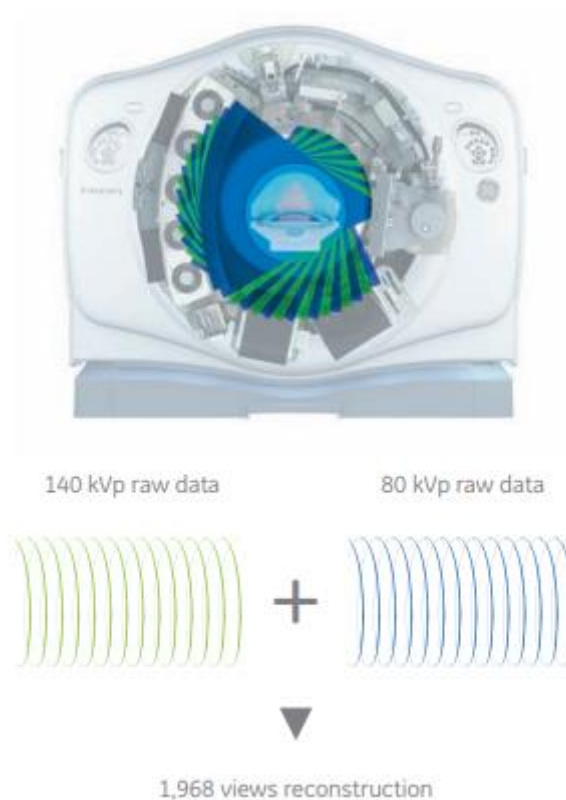


Figure 2.3.6.2.1: A figure demonstrating the fast-kVp switching of the DECT scanner from 140kVp to 80kVp, allowing image reconstruction at any monochromatic energy range from 40keV to 140keV, while also reducing artifacts and obtaining accurate CT numbers. Figure reproduced from (GE-Healthcare, 2011)

The number of views per rotation of the scanner is increased compared to a traditional scanner also, allowing for a higher amount of data acquisition which is used in the reconstruction algorithm to produce images with reduced artifacts (GE-Healthcare, 2011). See figure 2.3.6.2.2.



Figure 2.3.6.2.2: Number of views per rotation of the scanner. Figure reproduced from (GE-Healthcare, 2011)

The scintillator in a CT scanner absorbs a photon from the resulting beam of x-rays that have passed through the sample, which causes the material to experience luminescence. This light is then converted to current and produces the signal that is then fed into a computer for reconstruction. Some issues that can arise are that the scintillator therefore has a time required to “ramp up” to luminescence, i.e. the time delay from the photon hitting the detector to the light being produced, and a “ramp down” delay, i.e. the time that the scintillator is still producing light, rendering it unable to record another signal in that position until it has stopped (Svensson et al., 2020). GE therefore developed a proprietary material that would have desirable properties for a fast scintillator. The material is a complex rare-earth based oxide, which has a chemically replicated garnet crystalline structure (GE-Healthcare, 2011). The main features of the material are very fast primary speed (the speed at which luminescence occurs given an incident photon), and very low afterglow (the “ramp down” time for the luminescence). In fact, compared to the previous gold standard scintillator material used by GE called GOS (Gd_2O_2S), the new Gemstone material is 100 times faster in primary speed (30ns), and has an afterglow 4 times shorter (Karçaaltincaba & Aktaş, 2011). If this scintillator were not used, then incident photons from the ‘new’ energy would be hitting the detector plate while previous photons were still being dealt with, either by still inducing luminescence or by the presence of afterglow. The GE scanner can switch between kVp values approximately once every 0.25 milliseconds, and they report this as “near simultaneous” dual energy acquisition.

Dual Energy CT is able to not only enhance material differentiation by acquiring CT Number data at two different energies for each voxel, but also reduce the effects of beam hardening (Da Zhang et al., 2011).

Svensson et al used fast kVp switching DECT to be better able to detect urate build-up in gout patients, and attributed this ability to the gemstone detector's low afterglow and inbuilt algorithmic reconstruction which combines the 140kVp and 80kVp images in order to recreate monochromatic reconstructions with lower artifact levels. (Svensson et al., 2020)

2.3.6.3 Calibration

All CT scanners at UHCW have daily air calibration performed by the radiographers. The X-Ray beam hits the detector through air only, and the machine steps through a range of tube voltages and currents in order to calibrate the detector. As described in 2.3.5.1, the HU of air is defined to be 0.

Radiographers also perform daily QA using an inbuilt GE Healthcare protocol, which checks that the HU of water is within 5HU of baseline, and that noise is within 10% of baseline. These are measured as mean and standard deviation of an ROI which obstructs 75% of the FOV. The phantom used is made of Perspex and has various chambers filled with either water or air, and the calibration protocol steps through each of them in turn.

Engineers perform quarterly (4x per year) calibration of the CT numbers for water and air.

No additional calibration was done before or during any of the experiments in this thesis.

2.4 ICP-MS

Inductively Coupled Plasma Mass Spectrometry is an analytical technique used for accurately determining the elemental content of a sample. Electrical current provided by electromagnetic induction to energise and ionise a sample, which then allows an attached mass spectrometer to detect the Mass/Charge ratio. Samples are digested in nitric acid prior to analysis, and then heated to approx. 10,000 K. This ensures total dissociation of atoms within the sample, and the energy applied to the system causes ionisation.

The device used in these studies is an Agilent 7500cx Inductively Coupled Plasma Mass Spectrometer (ICP-MS). A schematic is shown in Figure 2.4.1

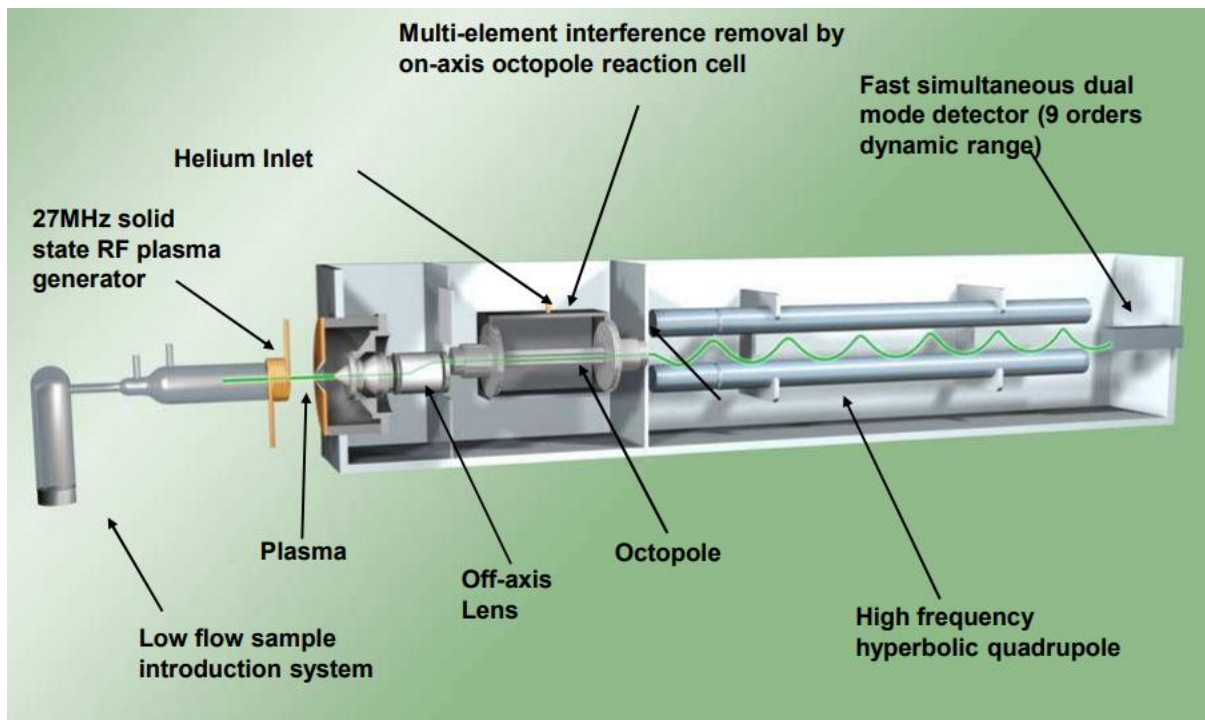


Figure 2.4.1: Agilent 7500cx ICP-MS system. Figure reproduced from (Agilent, 2022).

ICP-MS has the ability to determine iron concentration with high accuracy and with a low detection limit, as low as 1.5 ng/L (Chemnitzer, 2019; Quemet et al., 2012). This technique is used in later phantom studies in order to obtain accurate iron concentration measurements in phantoms.

Chapter 3 – Quantifying iron concentration in the brain of post-chemotherapy patients suffering from ChemoBrain symptoms

3.1 Summary

After receiving chemotherapy, patients sometimes express symptoms of cognitive impairment including memory loss and processing speed (H.C., 2014). The purpose of this pilot study was to use clinical MRI to observe whether or not R2 values in brain regions often associated with neurodegenerative disease were affected in such patients, possibly suggesting elevated concentrations of iron in these brain regions.

This chapter will present the methods and results of the pilot study. Patients (n=5) with ages ranging from 40 to 73 were scanned on a GE Discovery 750W 3T MRI scanner, using three single echo sequences: TR=2500ms, TE=10, 45, 80ms respectively, where the image size was 256x256 pixels. The four brain regions investigated were Substantia Nigra, Red Nucleus, Globus Pallidus, and Putamen.

This chapter will outline how manual segmentation of image data was performed, and then exponential decay curves were fit in order to derive T2 values. Evidence will be presented that T2 is decreased in most regions, and that all patients have at least one reduced region. Statistical analysis shows that all 5 patients had significantly ($p < 0.05$) elevated levels of brain iron. It was decided that these results merit further study and were used in a funding application for a longitudinal study at University Hospitals Coventry and Warwickshire.

3.2 Introduction

3.2.1 Chemotherapy

Cancer – characterised by uncontrollable cellular growth, is one of the deadliest diseases in the world. In 2018, an estimated 1 in 6 deaths was caused by a form of cancer (World Health Organisation, 2018).

Cancer can be treated in a number of ways, including surgery (removal of cancerous tissue), radiotherapy (the use of ionising radiation in order to kill cancer cells), or chemotherapy (the use of cancer-targeting drugs to kill cancer cells).

A full review of the field of chemotherapeutics is beyond the scope of this thesis – but a few fundamental principles can be summarised as follows:

1. Chemotherapy drugs are toxic

Cancer drugs produce several side effects due to their toxicity in humans. Research has indicated that drug toxicity is one of the leading causes of poor therapeutic outcomes in cancer patients (G. Tao et al., 2020), and so work is active in trying to reduce toxic side effects. As an example, one avenue of active research into chemotherapeutics involves the drug Doxorubicin (Dox). While an effective anti-cancer drug, it's highly toxic side effects on non-cancer tissue makes it unsuitable for clinical application (Y. Chen et al., 2007) (S. Li et al., 2018). Therefore, research is active in combining Dox with other treatments (other drugs, as well as other types of treatment including bone marrow rescue) in order to reduce its toxicity while maintaining its effectiveness (S. Li et al., 2018)

2. High-dose chemotherapy can be more effective in improving cancer patient outcomes

Numerous studies have shown an improvement in patient outcome when high-dose chemotherapy is used as part of their cancer treatment (Bacci, 2001; Nieboer et al., 2005; R. L. Smith et al., 2012). In order for high-dose chemotherapy to be successful and not overwhelm the patient with toxic side effects, this type of treatment is usually combined with some form of stem cell transplant or bone

marrow rescue (Bock et al., 2006; R. L. Smith et al., 2012) – re-transplanting the patient’s own bone marrow pre-treatment into their body post-treatment.

Due to the potential for more effective treatment, it is desirable to utilise high-dose chemotherapy for cancer treatment. However, due to the inherent toxicity of the drugs themselves, there has been some concern over the accentuated side-effects as a result of high-dose chemotherapy (Cetkovská et al., 2002; Tavčar et al., 2010).

3.2.2 CICI or “ChemoBrain”

Understanding the side-effects of high-dose chemotherapy has a great deal of importance due to the advent of using bone marrow rescue (transplant). This technique allows modern chemotherapy treatment to utilise chemotherapy drugs at much higher doses than before – potentially reaching levels that would otherwise be lethal (M. S. Brown et al., 1995). But while bone marrow rescue techniques can mitigate the potentially harmful effects of the chemotherapy itself (Garaventa et al., 1996), they are not necessarily involved in protecting against the mechanism of the side effects. This leaves open the possibility that side effects are potentially worse as a result of the increased dose (Bock et al., 2006; Nieboer et al., 2005).

Some of the adverse side-effects following chemotherapy are well known, for example hair loss, hot flushes and fatigue. However, far less is known about the decline in neurological function after treatment. Chemotherapy-induced cognitive impairment (CICI) or ‘ChemoBrain’ is a collective term for a set of symptoms experienced by some people after undergoing chemotherapy, with estimates that the condition affects anywhere from 15% to 75% of patients (Kovalchuk & Kolb, 2017; Wieneke & Dienst, 1995). Further, these symptoms can remain with patients for many years after treatment (Koppelmans et al., 2012). Patient studies in the past have shown that in addition to cognitive

difficulties, often the residual cognitive dysfunction has a negative impact on patient wellbeing (Boykoff et al., 2009).

Although the existence of CICI itself is well documented, the specific pathophysiology is still uncertain (El-Agamy et al., 2019; Walker et al., 2012). In Kovalchuk and Kolb's 2017 review paper (Kovalchuk & Kolb, 2017), they identify that a growing number of studies appear to attribute CICI symptoms to the use of chemotherapy drugs, and in particular oxidative stress associated with them (Y. Chen et al., 2007; Gaman et al., 2016). Even if the initial cause were to be determined, the disease mechanism itself is still another unknown. One area of research is into voxel-based morphometry, where shrinking of the brain post chemotherapy has been observed (Blommaert et al., 2019; Mark S. Brown et al., 1998). This involves a volumetric comparison of grey and white matter between a test subject and a control in order to determine neurological atrophy. While this shines crucial light on the potential macro-physical changes of the brain post-chemotherapy, one shortcoming of this approach is the inability to determine material-specific composition of that grey of white matter.

3.2.3 Iron in CICI

Iron accumulation in the brain has long been associated with neurodegenerative diseases (Kruer et al., 2012), (Schipper, 2012). For example, though there is still debate over the cause and progression of Alzheimer's Disease, iron accumulation in the brain is a classic hallmark, and the extent to which iron deposits are found in the brains of dementia patients has been (and continues to be) widely studied (G Bartzokis et al., 1994), (Jellinger et al., 1990).

Despite this, there is little existing literature pointing towards iron as a cause or biomarker for CICI. In their 2005 paper, Joshi et al. conclude that free radical mediated oxidative stress from the chemotherapy drug Adriamycin is a potential cause of CICI (Joshi et al., 2005). They point towards the fact that Fe^{2+} catalyses free radical production, acting as a catalyst for oxidative stress leading to neurodegenerative disorders (Schipper, 2012), however do not go on to hypothesise that concentration

of iron build-up in the brain could be related to onset of CICI. It is, therefore, the aim of this chapter to establish whether or not a link exists between the onset of CICI and elevated iron concentration measured using T2 relaxometry.

3.2.4 Study Design

Given the above, this chapter documents a study designed to determine the iron concentration in four key brain regions in a set of five patients who have received chemotherapy and are exhibiting symptoms of CICI, and to further determine whether there exists a relationship between the existence of CICI symptoms and transverse R2 relaxation rate. Using established analytical quantitative MR techniques, this R2 value is used to estimate iron content in each brain region, which is compared between the study participants and reference literature values.

We assume that prior to chemotherapy, each patient has an age-typical amount of brain iron in each region. This assumption is necessary due to the lack of pre-chemotherapy head MRI scans with suitable sequences for T2 analysis, and indeed the difficulty of finding patients that would fit such a criterion. We also acknowledge the limitations of this pilot study in that we are deriving results from only 5 patients. Following this proof-of-concept investigation, a longitudinal study should be carried out with a larger population and where a head MRI scan of each patient is taken before they begin treatment.

3.3 Literature review

3.3.1 Neuroimaging studies in CICI

Previous neuroimaging studies in the field of CICI research have aimed to quantify the change in volume associated with CICI symptoms of various regions of the brain (Blommaert et al., 2019; B. T. Chen et al., 2018; Inagaki et al., 2007), with little research in the wider literature into structural change on a material or trace-element-composition level (*recent studies that do address this are examined in Section 3.3.2*). This literature imbalance is echoed in various systematic reviews (M. Li & Caeyenberghs, 2018; Simó et al., 2013). It was found that while there were indeed studies into the manifestation of CICI as a physical change in the brain, these were mostly centred around measuring atrophy of white matter, rather than measuring change in the composition of the brain tissue (Simó et al., 2013).

3.3.1.1 White matter volume

Structural neuroimaging studies require manual brain-region segmentation in order to directly measure regions of interest. Early research from the late 1990s (M. S. Brown et al., 1995; Mark S. Brown et al., 1998) found that patients treated with chemotherapy exhibited volumetric differences in white matter lesion volume compared to controls. A longitudinal study was conducted (13 months), treating participants (N=8, Age 47.4 ± 8.6 years) with high-dose chemotherapy (cyclophosphamide at 1875 mg/m^2 per day for 3 days as a 1-hour intravenous infusion, cisplatin at 55 mg/m^2 per day as a continuous intravenous infusion for 72 hours, and carmustine at 600 mg/m^2 as a 2-hour intravenous infusion on the fourth day, followed by autologous hematopoietic progenitor cell support (AHPCS)), and measured the participants volumetric white matter brain regions over time using images obtained from T2 weighted MRI. The authors note that this treatment regime was used effectively to treat stage II-IV breast cancer. Six of the participants completed the initial round of chemotherapy, and all 6 presented as normal when measuring white matter volume on structural MR images. Four patients

completed the study in its entirety. It was found that the volume of abnormal white matter increased over time in three of the four participants (Figure 3.3.1.1.1). Visual confirmation with T2 weighted MRI scans agreed that white matter appeared to stop expanding at around 6 months into the study (Figure 3.3.1.1.2).

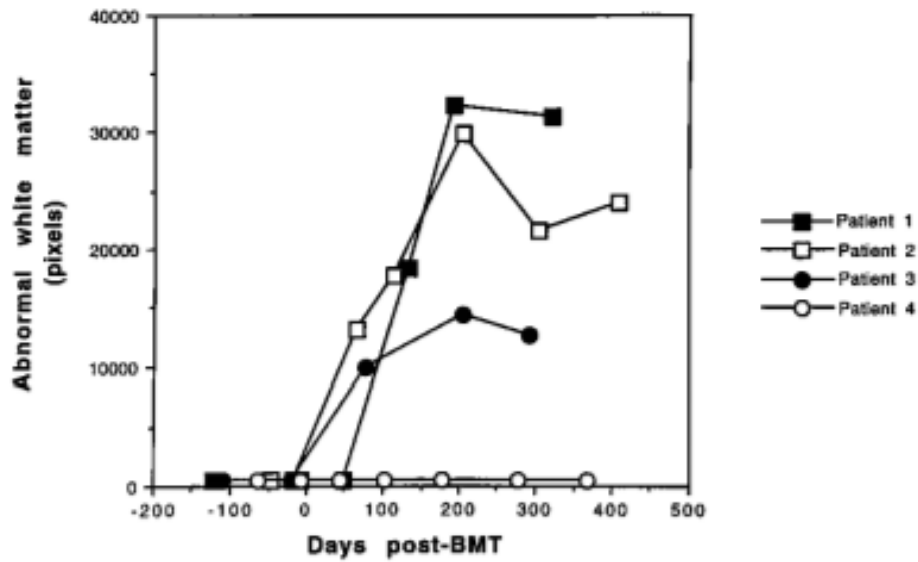


Figure 3.3.1.1.1: Evaluation of changes in abnormal white matter in the four participants who completed the study. Abnormal white matter is expressed as a count of abnormal pixels. Abnormal white matter volume is estimated using an assumed 10,000 pixels = 50cm³ of abnormal white matter. Reproduced from Brown et al. 1998

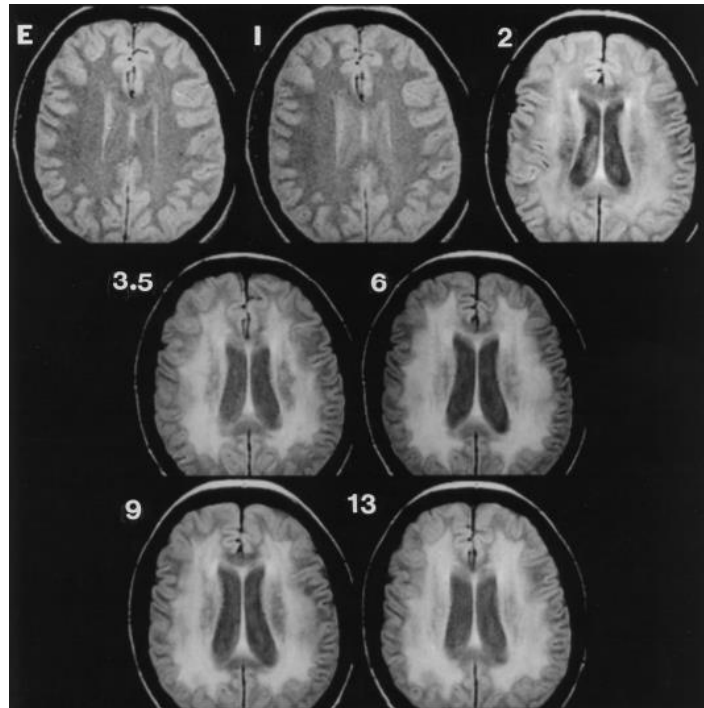


Figure 3.3.1.1.2: One slice from T2 weighted MRI of one study participant. Numerical labels on the figure refer to months after high-dose chemotherapy (E=Entry point = 0 months). Reproduced from Brown et al. 1998

So, while there is some evidence in the literature for white matter changes associated with CICI, there are also conflicting reports. A 2007 paper (Ferguson et al., 2007) looked into possible effects in brain structure in identical twins (Twin A and Twin B, age = 60), one of which had stage II breast cancer and received high-dose chemotherapy. Twin A underwent 22 months of high-dose chemotherapy for stage II breast cancer prior to the study, four cycles of doxorubicin 108.6 mg and cyclophosphamide 1,086 mg, with each cycle administered every 3 weeks. She also received four cycles of docetaxel 178 mg over a 1-hour infusion administered every 3 weeks. Her post-treatment hormonal therapy consisted of oral tamoxifen at 20 mg/day. The presence of CICI was clinically diagnosed using a MASQ (Mood and Anxiety Questionnaire) score, a 77-item report used in psychiatric diagnoses. Structural MRI was acquired in the same session at 1.5T. A gradient echo, echo-planar sequence was used to provide whole-brain coverage for functional MRI (repetition time [TE], 2,500 msec; echo time [TE], 40 msec; field of view [FOV], 24 cm; number of excitations [NEX], 1.29; 5-mm-thick

sagittal slices with no skip, yielding a 64×64 matrix with 3.75 mm² in-plane resolution). Finally, functional MRI scans were obtained by asking the participants to match a string of letters that were being fed into an earpiece and respond on an answer button while in the MRI scanner.

The results of the tests were not conclusive: Twin A had significantly higher MASQ scores than twin B, indicating that she was indeed suffering from CICI symptoms and was therefore correctly diagnosed. However, there were minimal differences in neuropsychological testing prior to the MASQ, with Twin A scoring higher in some areas and lower in others than twin B. Furthermore, the structural MRI shown in Figure 3.3.1.1.3 does show areas of white matter hyperintensity, which the authors classified as a “nonspecific finding of uncertain clinical significance by a neuroradiologist blinded to participant identity”. They also clarify that while white matter hyperintensity would be an indicator of brain tissue atrophy, it is also characteristic of carriers of the APOE ϵ -4 gene, which both twins are. Brain activity was noted to be *higher* in twin A who underwent chemotherapy.

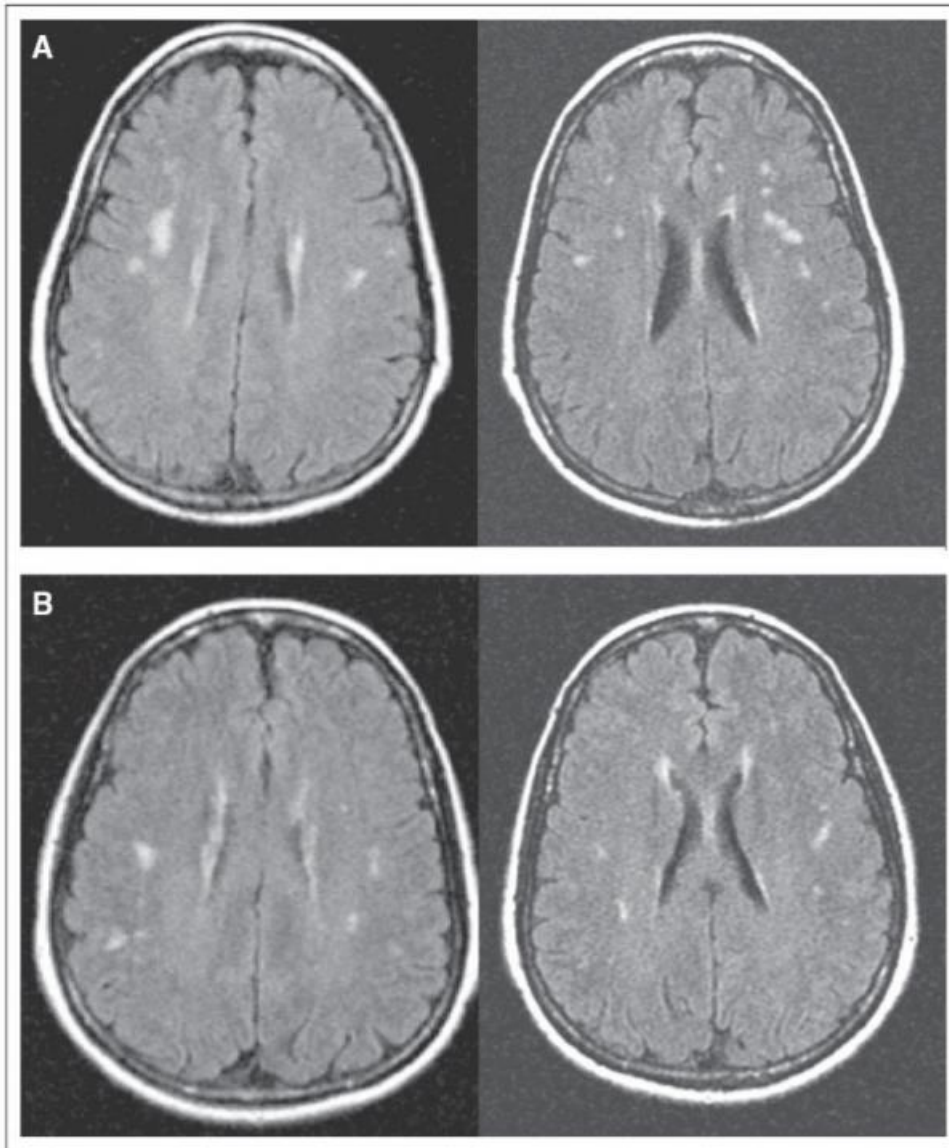


Figure 3.3.1.1.3 The hyperintensities were read by the study neuroradiologist as of uncertain clinical significance, but they appeared somewhat more prominent throughout white matter in (A) the chemotherapy-treated twin than in (B) the twin who did not receive chemotherapy as confirmed by volumetric analysis. Reproduced from Ferguson et al. 2007

The results of this study offer an example that despite the wider literature having a focus on structural and volumetric change of white matter in the brain, the results of these studies are not necessarily conclusive and cannot be used to reliably detect presence of CICI. The authors acknowledge that it is unclear whether or not the observed white matter structural changes are a result of normal aging versus CICI. This gives further merit to an imaging study that looks at potential neurophysiological damage that is *not* limited simply to white matter volume and/or density reduction.

3.3.1.2 Hippocampal volume

Another possible but contested explanation that has been offered in the wider literature is hippocampal volume change as a result of chemotherapy (Peukert et al., 2020). In Yoshikawa et al.'s 2005 paper (Yoshikawa et al., 2005) the authors find that decreased hippocampal brain volume is not responsible for CICI symptoms, while a number of subsequent studies (Bergouignan et al., 2011; Chaddock-Heyman et al., 2015; X. Chen et al., 2017; Perrier et al., 2020) found weak links between hippocampal deformation and/or volume reduction as a potential contributing factor to CICI. The novel study presented in this chapter does not aim to reproduce or involve structural studies into brain regions, and instead focuses on iron concentration in tissue.

3.3.2 Iron in CICI

From the structural studies reviewed and understood in section 3.2.2, it is clear that there is some evidence that CICI is at least in part a physical condition with associated morphological change in the brain, and not entirely contained as a mental illness. Finally, as discussed in 3.2.3, oxidative stress has been hypothesised as a potential disease mechanism for CICI (Schipper, 2012). In other neurological diseases, iron plays a role in the oxidative stress associated with disease pathogenesis, including Parkinson's disease, Alzheimer's disease, Huntington's chorea and Amyotrophic Lateral Sclerosis (Carocci et al., 2018).

To date, only one animal study (Cardoso et al., 2020) has approached the topic of quantitative brain iron measurement in post-chemotherapy drug use. In this study, Doxorubicin (DOX) was administered to an experimental group (N=20) of rats. There was an equal sized control group (N=20). A number of indicators were measured, including antioxidant enzyme activity and Nitrite content, but of particular interest to my own research was the inclusion of measures of both iron content and ferritin content.

The researchers had the following experimental design:

40 male Wistar rats, 3 months of age and weighing 290±20g, were housed in polypropylene cages and temperature controlled to 22±2 degrees Celsius. Artificial lighting produced a 12-hour day-night cycle and all treatments were administered between 9am and 12am to account for the possible effects of difference in circadian rhythm between the individuals.

Rats in the control group were administered 2.5mg/kg of DOX weekly, for 4 weeks. The control group were injected with the same volume of 0.9% saline solution for the same period. For reference, the recommended human dose for most cancer patients is 60-75mg once every 21 days ([Doxorubicin Dosage Guide + Max Dose, Adjustments - Drugs.com](#)), i.e. a dose that is 24-30 times stronger, though delivered 3 times less frequently, and a 75kg human would have approximately 259 times greater body mass. Experimental design is shown in Figure 3.3.2.1

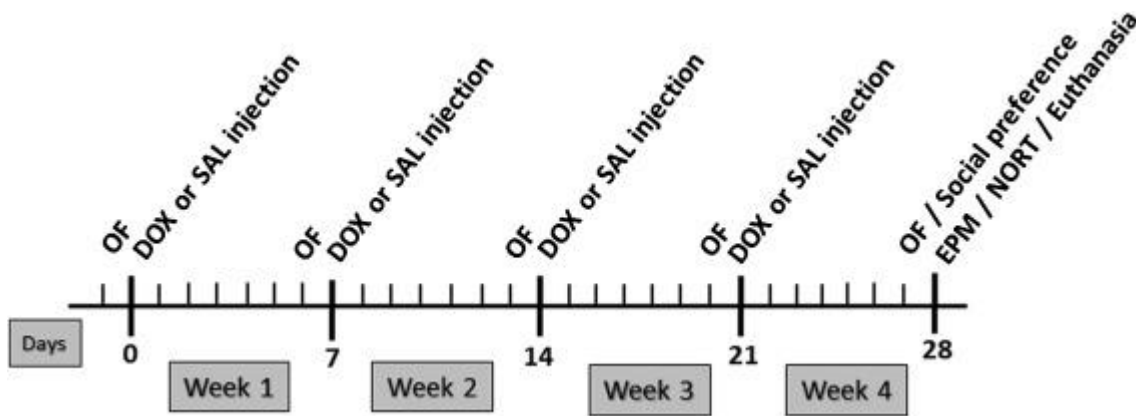


Figure 3.3.2.1: Experimental design for animal study. Reproduced from (Cardoso et al., 2020)

Total brain iron in tissue was estimated using the modified Goodwin and Murphy (Goodwin & Murphy, 1966) method, using colorimetric iron estimation.

ferritin was measured using a Turbilatex ferritin kit (Spinreact, Sant Esteve de Pas, Spain), according to the recommendations provided by the manufacturer.

Results are shown in Figure 3.3.2.2.



Figure 3.3.2.2 (left) Comparison of [Fe] between control group and treatment group, and (right) comparison of ferritin concentration between control group and treatment group. Reproduced from Cardoso et al 2020.

No significant ($p < 0.05$) difference in Fe concentration was measured between the two groups using an unpaired 2-tailed t-test.

The difference in ferritin was significant ($p < 0.05$), although decreased rather than increased.

In 2020, Spence et al (Spence et al., 2020) documented in their review paper that there is consistent evidence that brain iron is detrimental to cognitive health. The authors concede that it is not known whether iron build-up is a primary cause or a secondary effect of brain atrophy, but that MRI techniques show promise to continue providing iron determination as a biomarker for cognitive decline.

There has never been a quantitative MR investigation into relating brain iron concentration in human CICI patients in Globus Pallidus, Red Nucleus, Substantia Nigra, and Putamen, to presence of CICI, which the results of this chapter will present.

3.4 T2 Relaxometry

T2 relaxometry was used to determine iron concentration in specific brain regions of each patient.

Theory is detailed in **Section 2.1.5**.

In this study, we employ the use of a single-echo T2 MRI sequence at three different echo times in order to produce an exponential decay curve from which a T2 relaxation time can be measured.

Previous research within the group (Collingwood et al. 2014) has shown the dependency of R2 on iron concentration within the basal ganglia, of which the Globus Pallidus, Substantia Nigra, and Putamen are a part. The summary of this work is that there is a linear relationship between R2 measured at multiple field strengths (1.5T – 9.4T) and iron concentration in human neurological tissue, illustrated in Figure 3.4.1. Furthermore, individual single echo times, rather than a multi-echo sequence, are used in order to reduce the impact of B₁ field inhomogeneity.

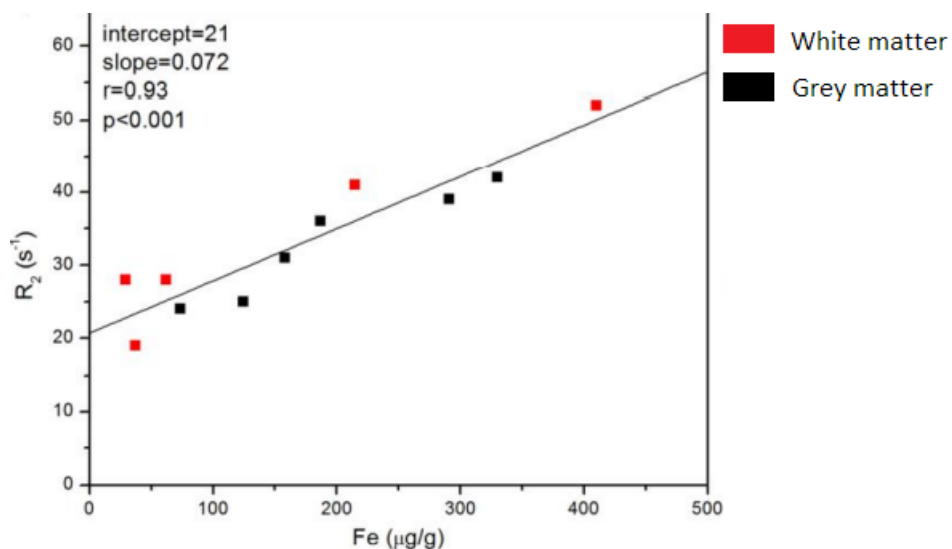


Figure 3.4.1: Linear relationship between R2 and Iron concentration in human neurological tissue. Note the units of R2 in 1/s rather than 1/ms. Figure reproduced from (Mary E. Finnegan, 2013).

3.4.1 Dependency of T2 on Iron concentration

The linear dependence of R2 on iron concentration has been shown from 1.5T to 7T (Gossuin et al., 2004), and this dependency has been used repeatedly in the wider literature in order to obtain non-invasive iron concentration measurements from T2 relaxometry data (Ghadery et al., 2015; Langkammer et al., 2014; X. Tang et al., 2018). A full description of using T2 relaxometry to measure iron concentration is given in **Section 2.1.5**.

3.5 Method

3.5.1 Echo time selection

In order to improve the feasibility of this study, image alignment between spin echo sequences is crucial. While a limited amount of image post-processing can correct for minor translational errors, having participants lay still in the MRI scanner is the most effective method of ensuring well-aligned image slices. Since each single echo sequence takes around 6.5minutes, a reduction in the number of echoes would be beneficial provided it did not give rise to a significantly worse exponential fit through the data, nor to a T2 value that was significantly different to the value obtained with more echo times.

This section shows the results of an initial study that was conducted in order to determine whether decreasing the number of echoes from 4 to 3 would make a significant difference to the calculation of T2 value. Using the author of this thesis as a participant, an initial test of the study protocol was carried out using 1 participant (Male, 27),

Figure 3.5 shows a scan of my brain, scanned using four echo times (10, 27.5, 45, 80ms) on a 3 Tesla GE Discovery MR750W MRI scanner, using the same settings that were to be used in the ChemoBrain study itself.

3.5.1.1 Brain image segmentation

In order to make measurements from MR images, manual image segmentation was carried out. This is a highly laborious process, but ensures accuracy when focusing on specific brain regions. 3D images were produced using ITK-Snap (Yushkevich et al., 2006), which were then exported to ImageJ for analysis. Figures 3.5.1.1.1 and 3.5.1.1.2 show the segmentation process and resulting 3D volume.

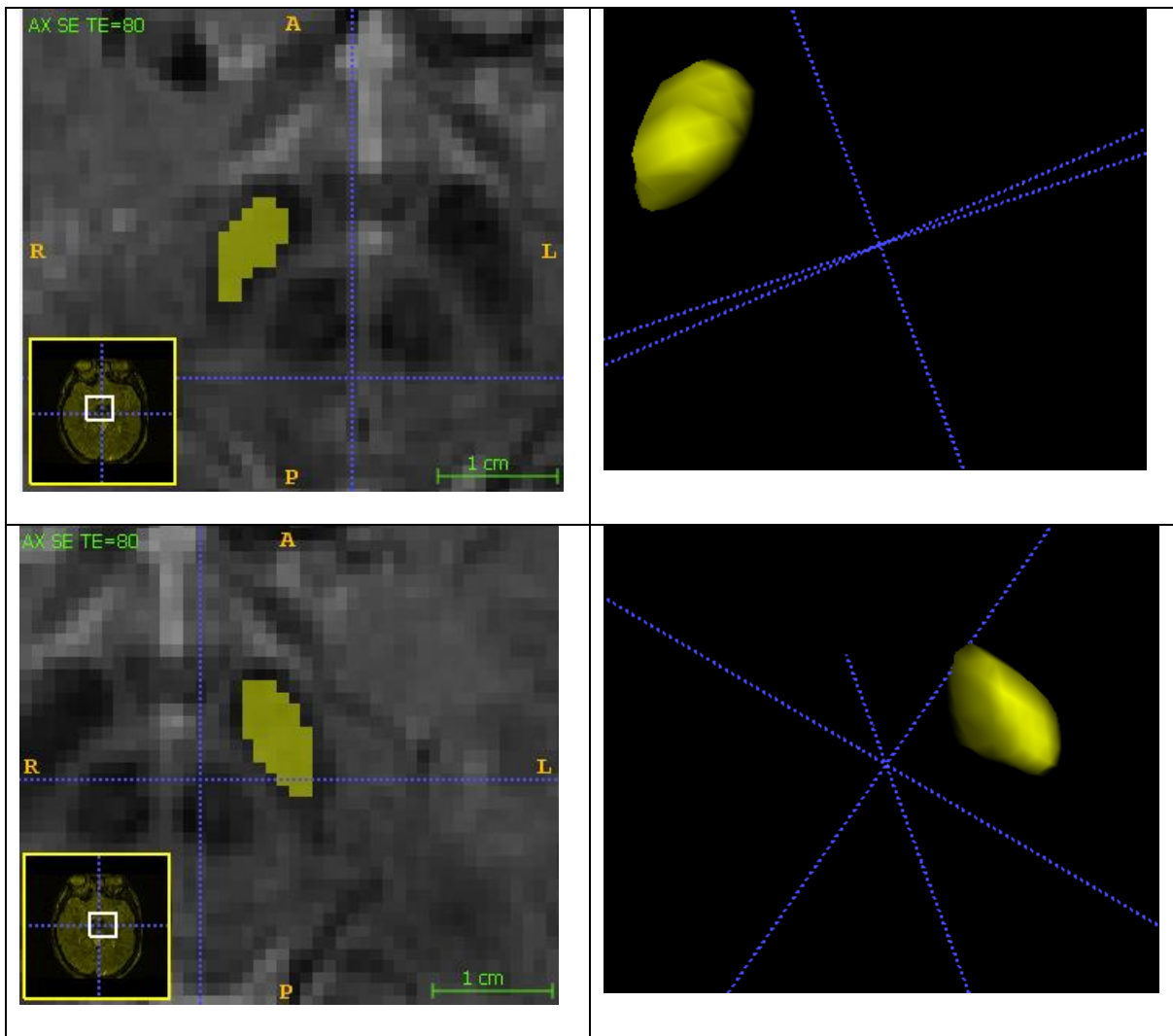


Figure 3.5.1.1.1: Top left: One slice of Substantia Nigra (Left) from my brain MRI. Top right: The 3D volumetric reconstruction of multiple slices (3 slices were used in these regions). Bottom left and bottom right: As previously, but for Substantia Nigra (Right).

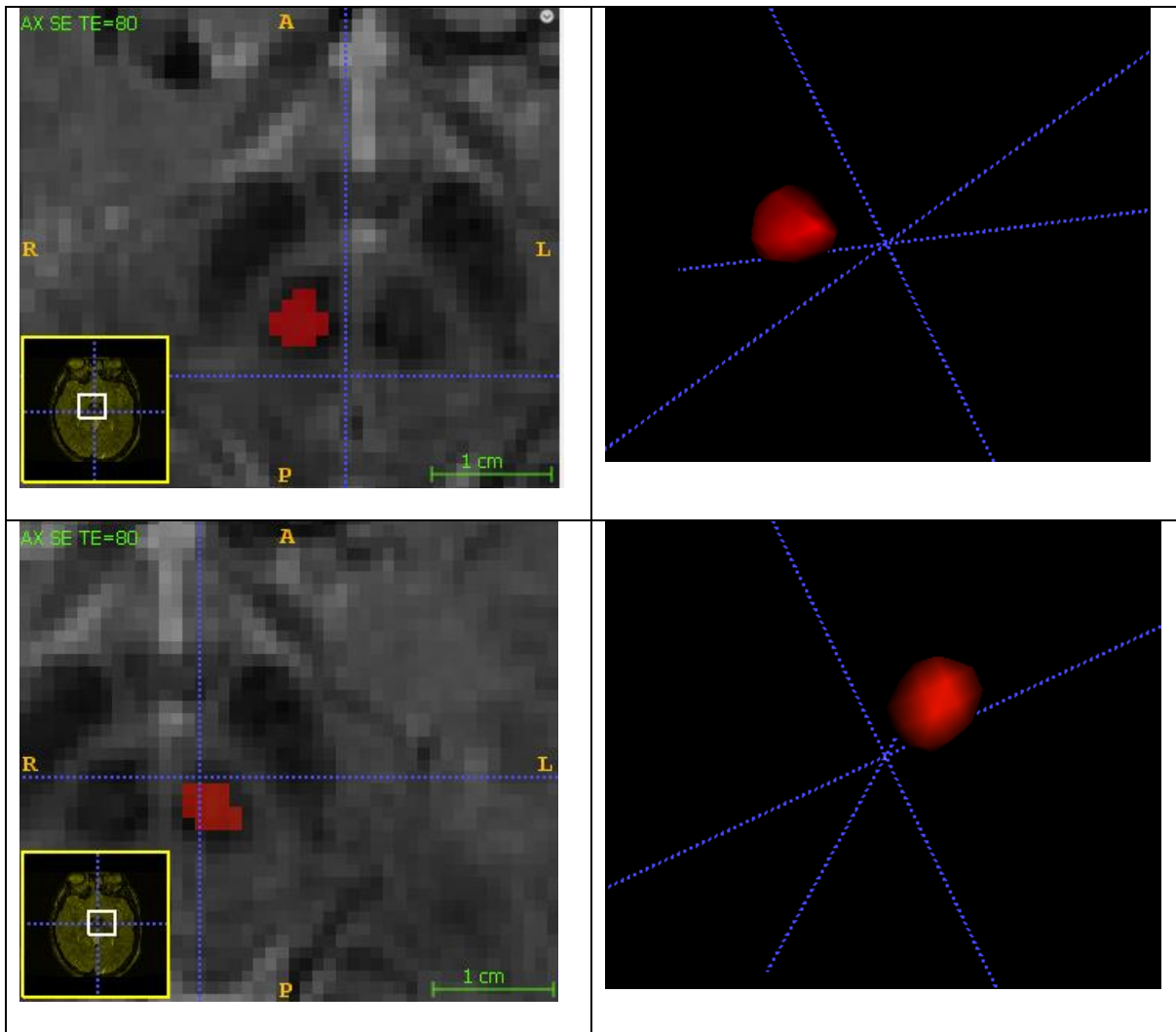


Figure 3.5.1.1.2: Top left: One slice of Red Nucleus (Left) from my brain MRI. Top right: The 3D volumetric reconstruction of multiple slices (3 slices were used in these regions). Bottom left and bottom right: As previously, but for Red Nucleus (Right).

Slice Thickness: 2.5mm, Repetition time (TR): 2500, Echo times: 10, 27.5, 45, 80ms, FOV: 256*192, Flip angle: 90 degrees.

The data was analysed firstly as a whole set of 4, and then in the triplets (10, 45, 80) and (10, 27.5, 80), shown in Table 3.5.1.1.1. Exponential decays were fit to the data. An example fit is shown in figure 3.5.1.1.2. Mean T2 values from each of the 3 sets are compared with an ANOVA test, to check

if there is significant difference when using three images rather than four, or if there is a difference with dropping the 27.5ms echo time rather than the 45ms echo time.

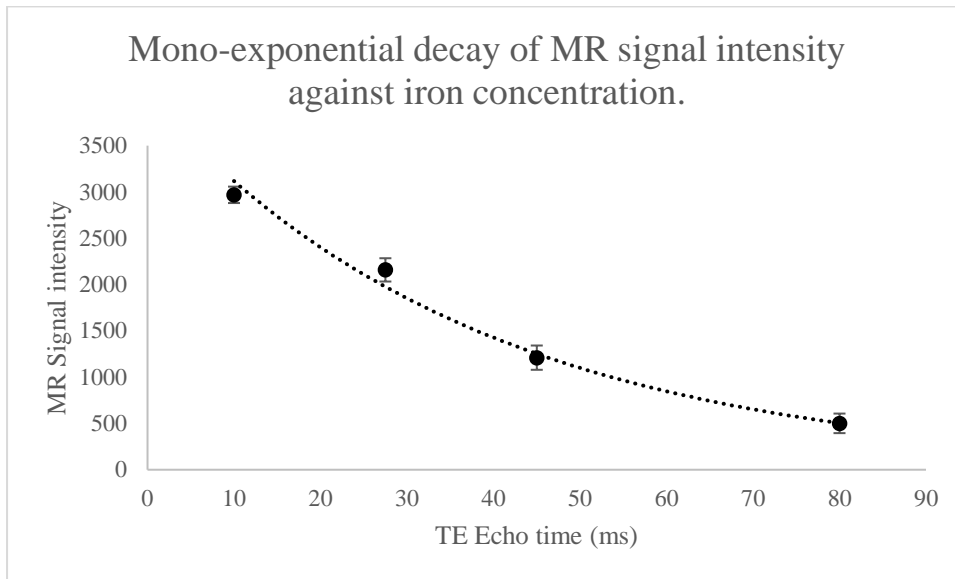


Figure 3.5.1.1.2: Mono-exponential decay fit to echo time data for my brain. The above datapoints are for Substantia Nigra (Left side), with resulting $R^2 = 0.025$. Error propagation is used to calculate resulting T2 values, shown in Table 3.5.1.1.1

Brain Region	All 4 times used		TE=10,45,80ms		TE=10,27.5,80ms	
	Mean T2 (ms)	SD	Mean T2 (ms)	SD	Mean T2 (ms)	SD
RN_L	45.20	6.91	45.63	6.67	45.35	7.37
RN_R	43.34	6.57	43.36	6.03	43.24	6.69
SN_L	40.51	4.68	40.59	4.70	40.58	4.84
SN_R	40.73	5.14	40.89	5.14	40.79	5.38

Table 3.5.1.1.1: Mean T2 value measured when using all 4 echo times, only using TE=10,45,80ms, or only using TE=10,27.5,80ms

3.5.1.2 Analysis of Variance (ANOVA)

To see whether there are any differences between the three calculated sets of values, an ANOVA test was carried out for each of the 4 regions measured, across each of the three sets of echo times. Results are shown in Table 3.5.1.2.1.

A p-value of 0.05 would be required to reject the null hypothesis and provide a positive result that the groups were different.

ANOVA – Analysis of Variance			
Brain Region	No. Voxels	F-statistic	p value
RN_L	46	0.045	0.956
RN_R	42	0.004	0.996
SN_L	82	0.007	0.993
SN_R	96	0.023	0.978

Table 3.5.1.2.1: ANOVA results for comparison of echo time methodology.

The groups were found *not* to be significantly different with a very high p-value ($p=0.956-0.996$), providing strong evidence that we fail to reject the null hypothesis.

Therefore, using 3 echo times obtains a statistically significantly *similar* result for T2 as using 4 echo times. The TE=10,45,80ms set was chosen as the SD was slightly smaller in each case.

This data showed that with 3 echo times, the quality of the exponential fit was always at least $R^2=0.98$, with a 25% reduction in scan time. A Mann-Whitney U test confirmed that each of the 3 outputs are not significantly different. This test was chosen as its purpose is to determine if two groups are significantly different from each other, however unlike a t-test, it does not require that the data be normally distributed. In the interest of time availability with the clinical scanner, the decision was made to eliminate the 27.5ms single echo sequence. The result shows that 3 echo times (plus a

background reading) are sufficient to fit an exponential decay and accurately determine T2 in this context.

3.5.2 Control Brain Regions – typical T2 relaxation times

In order to produce Iron concentration estimates, some typical T2 relaxation times to use as control values are required per region.

Control values for T2 at 3 Tesla for human brain tissue are uncommon in literature – the majority of clinical scanners are 1.5T scanners. There is a scarcity of literature values for fully segmented human brain regions at 3T, so it is difficult to compare across multiple studies. Haacke's 2005 study collated, at that time, the most comprehensive list of human brain region T2 values from a variety of studies, most of which were at 1.5T.

3T values are used here as literature reference values. Globus Pallidus, Putamen and Red Nucleus only had 1 study reporting values (Gelman et al., 1999). Substantia Nigra had three sources (D. J. Brooks et al., 1989; Gelman et al., 1999; Ordidge et al., 1994) and so an average was used.

To date there have been no additional studies reporting brain region-specific values in segmented Red Nucleus, Globus Pallidus, Substantia Nigra or Putamen at 3T in human brain tissue.

Values obtained were used to form a calibration curve. Since the number of samples is low, there is a large Standard Error of Slope (see discussion for more details on this).

3.5.3 Calculating iron concentration from R2

Given the linear relationship between iron concentration, literature values are used to form a linear regression to calculate the slope and intercept of the linear model in brain tissue. The linear model will take the form:

$$(1) [Fe] = m * R_2 + C$$

It is therefore necessary to find a value of m and C , which is the slope of the linear relationship between R_2 and $[Fe]$ at 3T and the intercept. This is shown in Figure 3.5.3.1, using linear regression based on literature values of both R_2 and $[Fe]$. This relationship is then used as a calibration curve for further $[Fe]$ measurement from R_2 values.

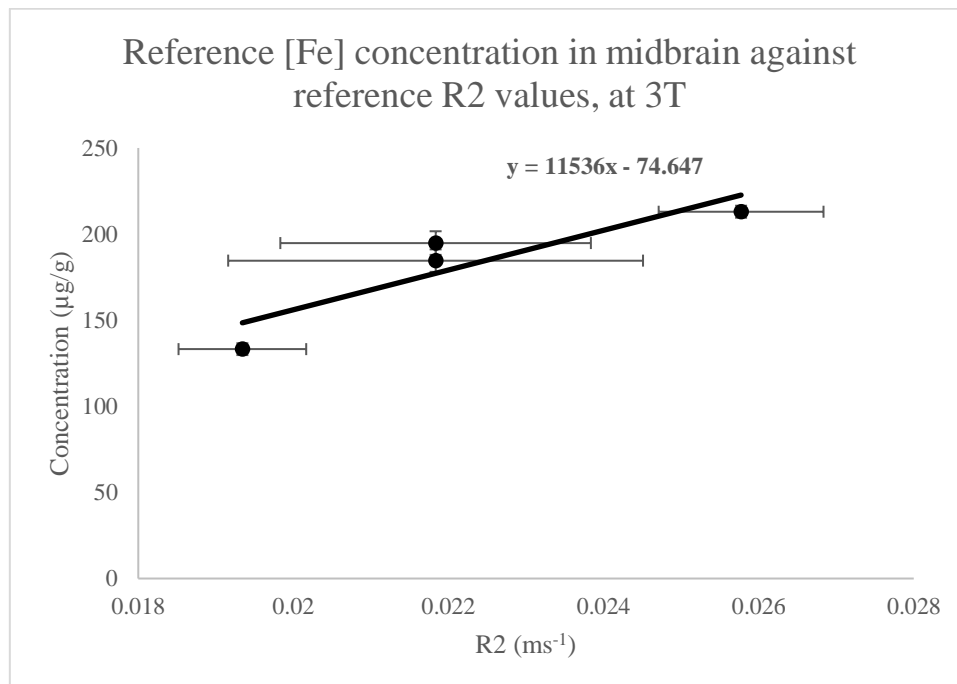


Figure 3.5.3.1: Calibration measure from literature values of R_2 and $[Fe]$. There are very few sources of segmented human brain R_2 values at 3T. Data is sourced from (Haacke et al., 2005). $[Fe]$ measurements are verified using ICP-MS.

Linear fit statistics (3 significant figures)	
Gradient	11500
Intercept	-74.6
Standard Error of Slope	4030
Correlation coefficient r^2	0.803

Table 3.5.3.1 Linear fit statistics (3 significant figures) for the calibration curve.

The linear model fit to the literature data has properties summarised in Table 3.5.3.1.

The gradient value of $m = 11,500$ (3 s. f.) can then be used in the calibration curve equation for measuring Iron concentration:

$$[Fe]_{observed} = 11500 * (R2_{observed}) - 74.6$$

Note that the standard error of the slope is large, due to the large relative error sizes on literature R2 values.

3.5.4 Calculating test-case brain iron concentration

In order to test the protocol itself, I used the methodology to calculate my own brain iron in four regions (Substantia Nigra Left and Right (**SN_L**, **SN_R**), Red Nucleus Left and Right (**RN_L**, **RN_R**)) shown in Table 3.5.4.1 along with standard deviation and propagated error. This used the relationship above along with error propagation in order to achieve confidence intervals on the stated value.

Propagated error is calculated using:

$$(\Delta[Fe]_{observed})^2 = (R2)^2(\Delta m)^2 + m^2(\Delta R2)^2 + (\Delta c)^2$$

Where Δc is estimated as 75, approximately equal to the linear offset of the intercept.

Region	T2 (ms)	SD	Propagated	
			Concentration ($\mu\text{g/g}$)	Error ($\mu\text{g/g}$)
RN_L	45.2	6.9	180	123
RN_R	43.3	6.6	191	126
SN_L	40.5	4.7	209	129
SN_R	40.7	5.1	208	129

Table 3.5.4.1: Measured T2 values with calculated [Fe] values for my brain regions.

3.5.6 Image Acquisition

Five patients, aged 73, 50, 40, 57 and 52, were scanned using a GE Discovery 750W 3T MRI scanner, using three single echo sequences: TR=2500ms, TE=10, 45, 80ms respectively. Image analysis was carried out using ImageJ, and exponential decays were fit using MATLAB.

MRI Scan parameters are described in Table 3.5.6.1

Parameter	Value
Slice Thickness (mm)	2.5
Repetition Time (ms)	2500
Echo Time (ms)	10, 45, 80
Number Of Averages	1
Imaging Frequency (MHz)	127.8
Imaged Nucleus	1H
Magnetic Field Strength (T)	3
Spacing Between Slices (mm)	2.5
Pixel Bandwidth (Hz)	244.141
Rows	256
Columns	256

Table 3.5.6.1: MRI scanner parameters for image acquisition

Image segmentation was carried out manually with assistance from the Harvard Brain Atlas (K. Johnson, 1999). Each brain region was manually traced in software ITK Snap (Yushkevich et al., 2006).

Using ITK-Snap, multi-slice 3D regions can be traced slice-by-slice and reconstructed into a 3D region. This can then be exported to ImageJ for pixel-wise analysis.

Each individual voxel in each brain region therefore has a value for each of 10ms, 45ms, 80ms, and exponential decay curves fit to each triplet using non-linear least squares regression, fitting to an exponential function of the form $y = Ae^{\frac{-t}{T_2}}$. This approach of calculating the T2 map slice-pixel-wise allows calculation not only of an overall R2 value, but also the full distribution of values contained within a given ROI, allowing for error propagation and analysis (see Results for details). One example is detailed in figure 3.5.6.1, while all others are found in Appendix 2.

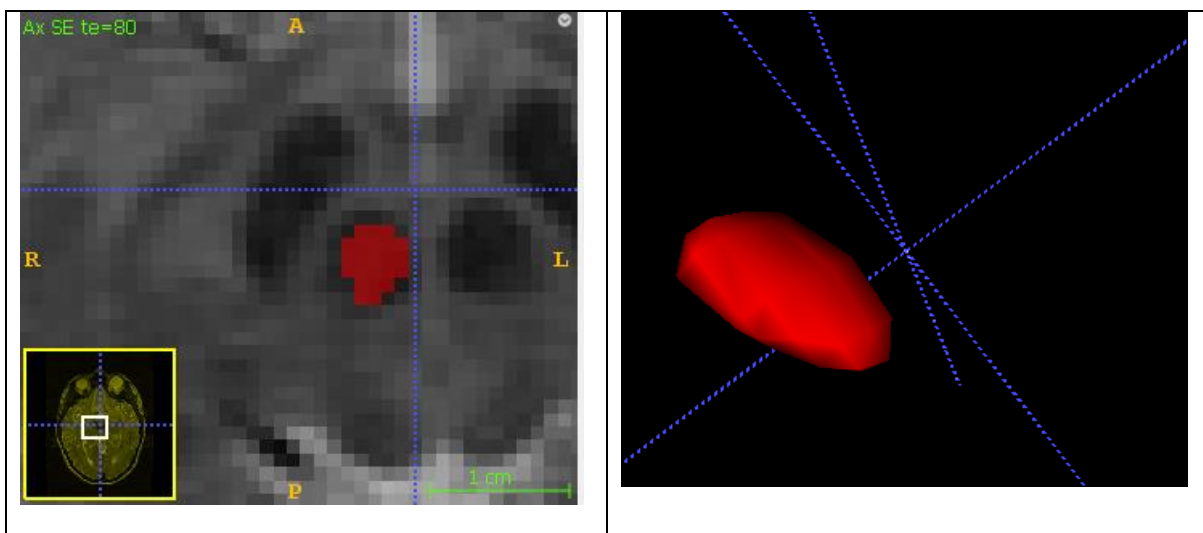


Figure 3.5.6.1 Left: Segmentation of the Red Nucleus (Left) for a study participant (Patient 1). Right: The 3D reconstruction produced with ITK-Snap. The segmentation is exported to ImageJ for analysis.

3.5.7 Image Processing

An RGB-combination of each echo time was used to check for alignment. This involves assigning each echo time to one of a red, blue and green channel, and re-combining these image stacks (see

Figure 3.5.7.1-2). In this way, areas of low attenuation will appear more white (due to an equal amount of R, G, B), while areas of high attenuation will appear more red. Further, areas of misalignment will become evident, aiding in image registration. See reference: (Toga & Thompson, 2001)

Patient 01

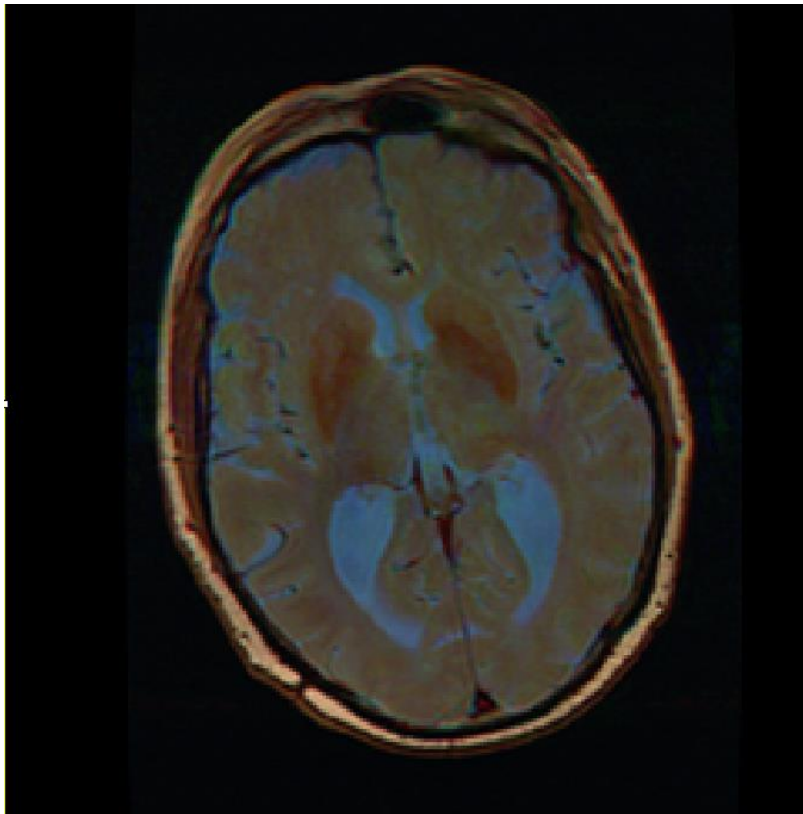
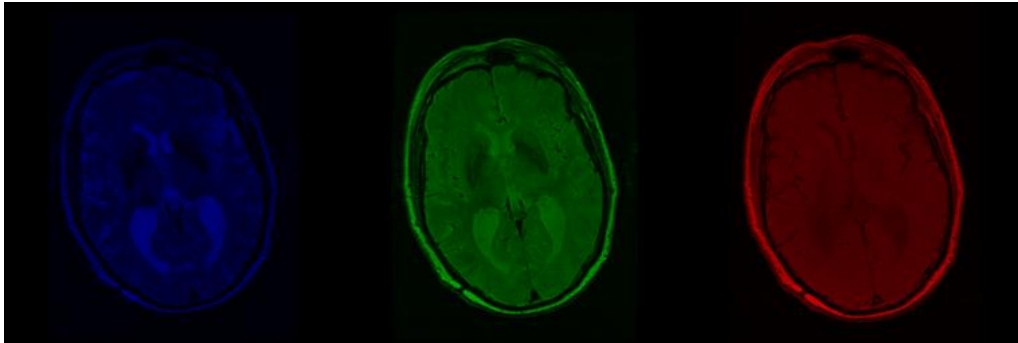


Figure 3.5.7.1: Top, image echo times split into Blue, Green and Red Channels. Bottom: Recombined image would be completely greyscale if the images were identical. Hues can help visually identify regions of faster decay as well as image registration issues.

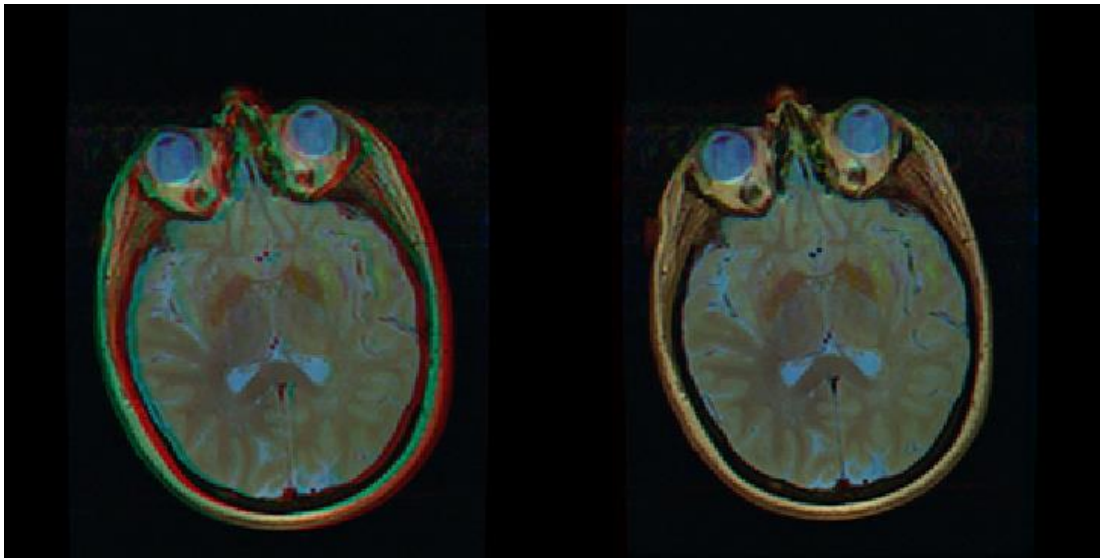


Figure 3.5.7.2 Before (left) and after (right) manual image registration. Splitting into three channels allows visual identification of mismatched image regions.

From figure 3.5.7.2, it is clear that there is misalignment between the echo times. This means that the patient moved slightly in between scans. It is therefore not possible to draw an ROI on one slice, and simply propagate it to another. This is a problem, as segmenting a low-echo time image is difficult due to low contrast, so the ideal approach is to first align the images, then segment on the highest contrast image (80ms), and then propagate ROIs through to the other echo time image stacks.

The image stack in figure 3.5.7.2 (Left) is fixed using lateral transformations in ImageJ (Right). The “red halo” effect is no longer seen.

Patients 4,5 and 7 did not appear to have obvious alignment issues, and so these stacks were used without additional transformation.

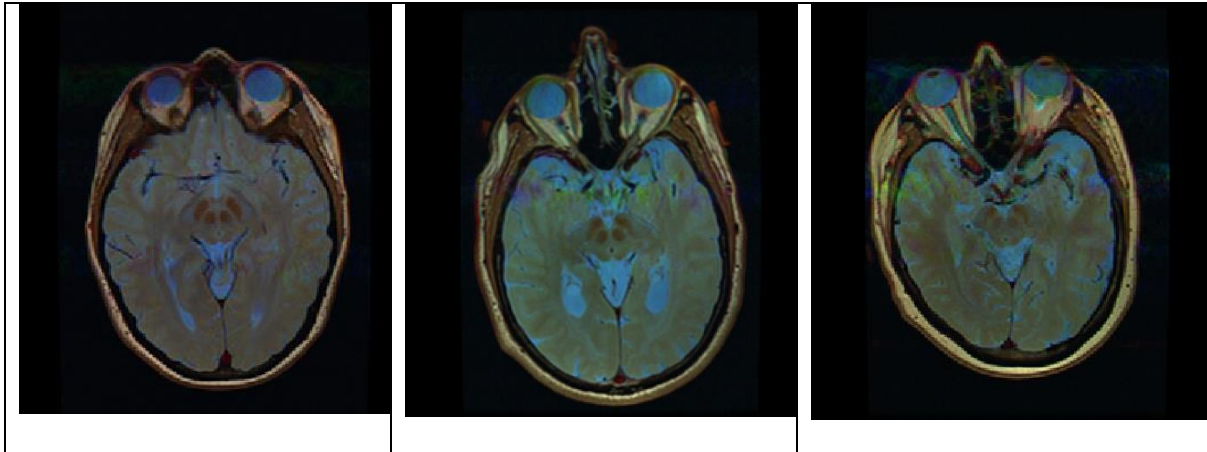


Figure 3.5.7.4: Patients 4,5, and 7 do not show significant registration mismatch.

3.6 Results

3.6.1 Results and data

The existence of a linear relationship (Wood et al., 2005),(House et al., 2007b) between R2 value and iron concentration in brain tissue, published values of healthy T2 (Haacke et al., 2005) and iron concentration measurement, along with linear equations determined from prior analysis allows iron concentration determination from R2 measurement (B. Hallgren & Sourander, 1958).

Using literature values for brain iron concentration (Haacke et al., 2005; Bo Hallgren & Sourander, 1960a) along with T2 relaxation times, a calibration curve is fit using linear regression.

$$[Fe] = 11500 * R2 - 74.6 \text{ for } R2 \text{ measured in } ms^{-1}$$

Standard Error of the Slope calculated as $4.0 s^{-1}$ and $r^2 = 0.80$.

Therefore we have calculated our required slope, $m = 11500 ms^{-1}$, in order to calculate iron concentration given an R2 value at 3T.

Sources of error are the slope of the linear fit (m), the R2 observed and R2 control values, and [Fe] control. Error propagation is used to determine error for final calculated concentration values.

3.6.1.1 T2 Values from image analysis

Brain images of each of the five participants were segmented into 8 regions as follows: Substantia Nigra Left (SN_L), Substantia Nigra Right (SN_R), Red Nucleus Left (RN_L), Red Nucleus Right (RN_R), Putamen Left (PT_L), Putamen Right (PT_R), Globus Pallidus Left (GP_L), Globus Pallidus Right (GP_R). Resulting data for each of the five patients are shown in tables 3.2-3.6.

Stated values for T2 are the mean of all values within the given ROI. Each pixel has three associated values (one for each echo time), which are used to fit the monoexponential decay and extract the T2 value, and the overall distribution is shown in more detail in 3.6.1.2.1-5 for each patient in a box plot.

Note: The original dataset had the five participants labelled as Patient 01, 03, 04, 05, 07. To avoid confusion and maintain consistency between our analysis and the original data, we have kept these labels throughout the study, despite there only being data for 5 patients (rather than relabelling the data to, for example, Patient 1, 2, 3, 4, 5). T2 values are presented in Table 3.6.1.1

Abbreviations: Substantia Nigra Left and Right (**SN_L, SN_R**), Red Nucleus Left and Right (**RN_L, RN_R**), Globus Pallidus Left and Right (**GP_L, GP_R**), Putamen Left and Right (**PT_L, PT_R**).

Measured T2 values (ms) \pm Standard Deviation						
<i>Region</i>	Patient 1	Patient 3	Patient 4	Patient 5	Patient 7	Control
<i>RN_L</i>	44 \pm 5	48 \pm 3	39 \pm 4	40 \pm 4	43 \pm 4	46 \pm 4
<i>RN_R</i>	38 \pm 5	48 \pm 4	40 \pm 5	41 \pm 5	45 \pm 4	46 \pm 4
<i>SN_L</i>	39 \pm 6	43 \pm 6	38 \pm 4	39 \pm 5	41 \pm 5	36 \pm 5
<i>SN_R</i>	41 \pm 5	43 \pm 5	36 \pm 4	40 \pm 6	41 \pm 5	36 \pm 5
<i>PUT_L</i>	43 \pm 8	59 \pm 6	46 \pm 4	50 \pm 6	51 \pm 4	52 \pm 2
<i>PUT_R</i>	45 \pm 4	58 \pm 9	46 \pm 4	48 \pm 5	47 \pm 5	52 \pm 2
<i>GP_L</i>	37 \pm 7	48 \pm 6	35 \pm 4	35 \pm 5	38 \pm 4	39 \pm 2
<i>GP_R</i>	35 \pm 5	42 \pm 7	34 \pm 4	39 \pm 6	39 \pm 6	39 \pm 2

Table 3.6.1.1: Measured T2 values across each of the 5 participants.

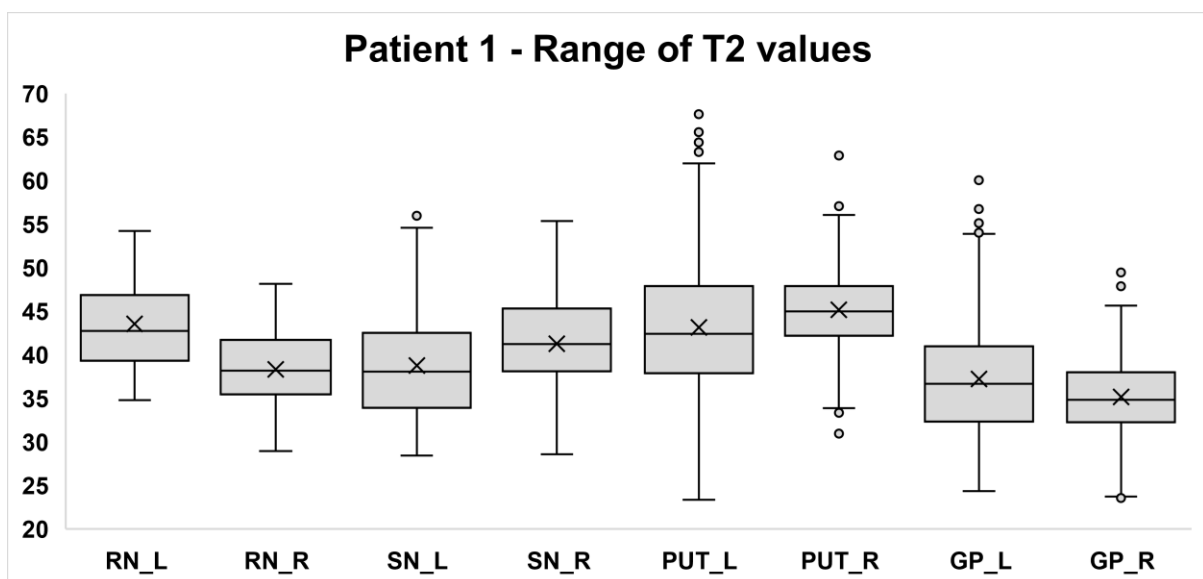
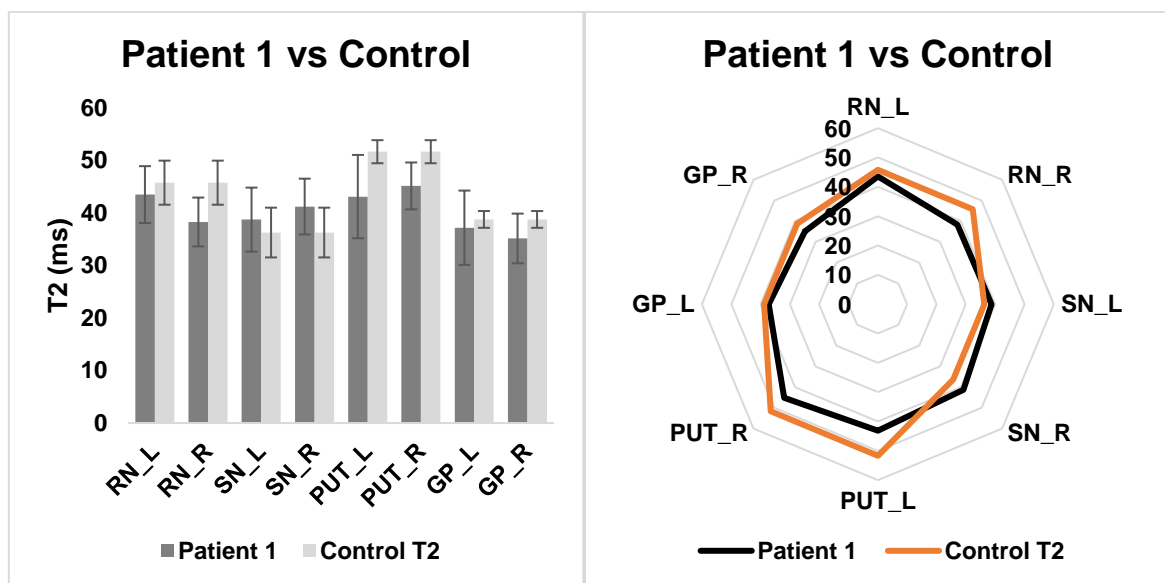
3.6.1.2 Descriptive statistics

3.6.1.2.1 Patient 1

Top left: comparison of T2 time (ms) with each brain region, compared to literature control.

Top right: The same data shown on a radar plot for clarity

Bottom: The distribution of T2 values displayed as a box plot for each region. Cross = mean, Middle line = median, box edges = interquartile range, whiskers = max values excluding outliers, circles = outliers.



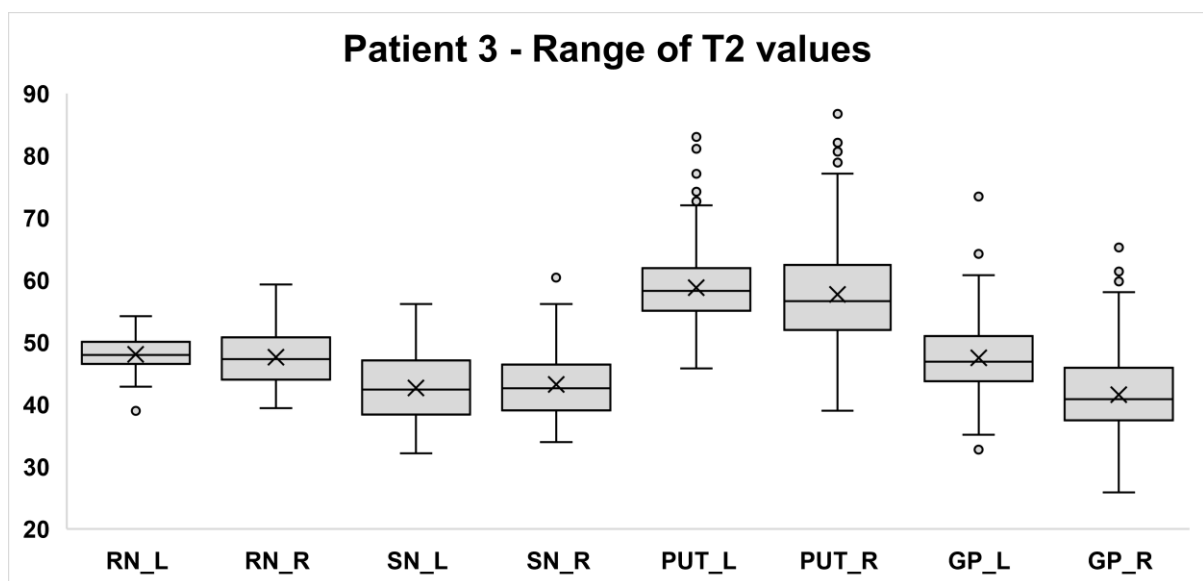
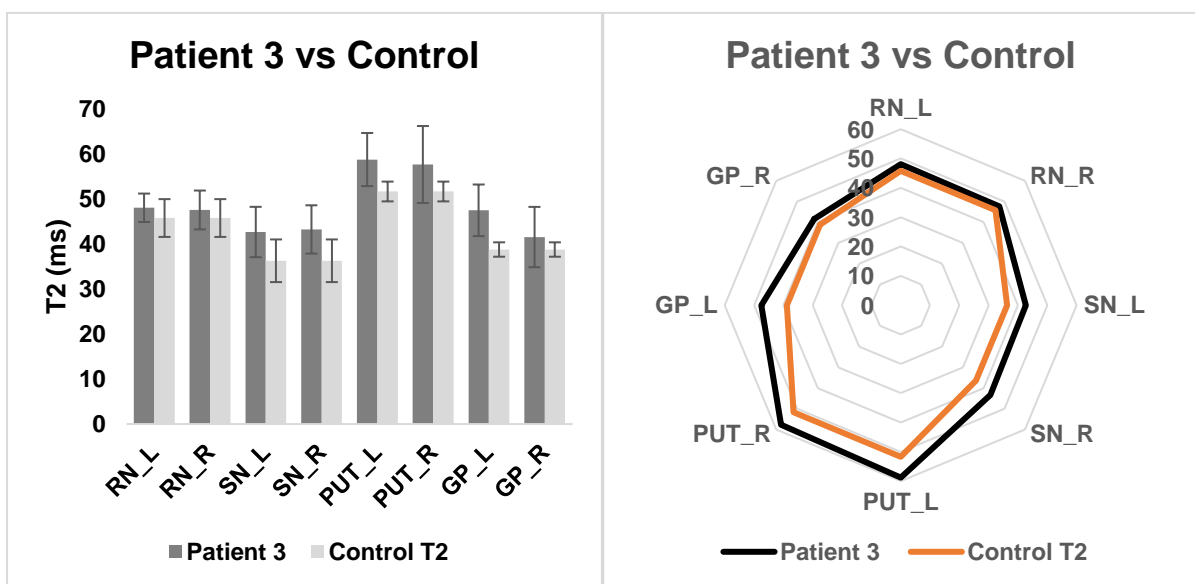
All regions normally distributed as tested with Shapiro Wilkes test ($p < 0.05$).

3.6.1.2.2 Patient 3

Top left: comparison of T2 time (ms) with each brain region, compared to literature control.

Top right: The same data shown on a radar plot for clarity

Bottom: The distribution of T2 values displayed as a box plot for each region. Cross = mean, Middle line = median, box edges = interquartile range, whiskers = max values excluding outliers, circles = outliers.



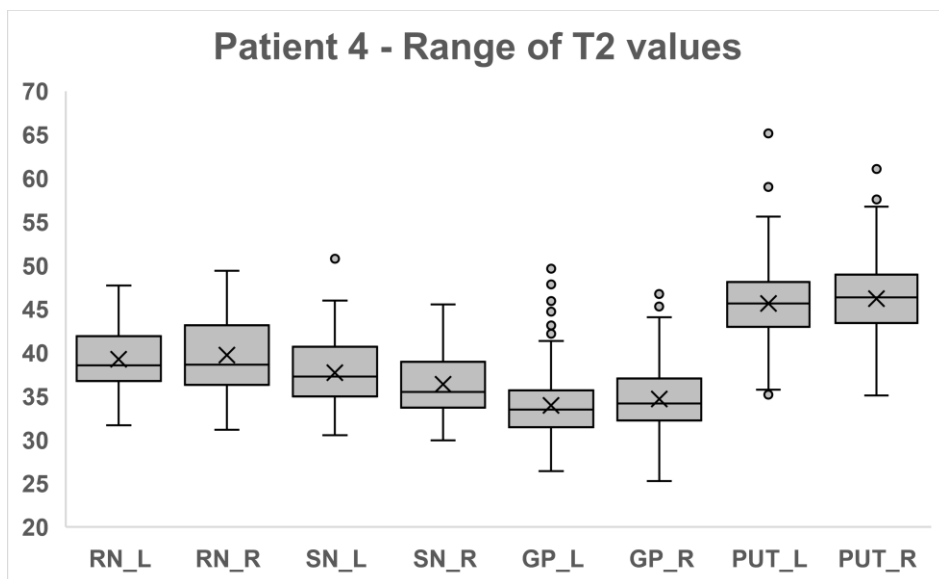
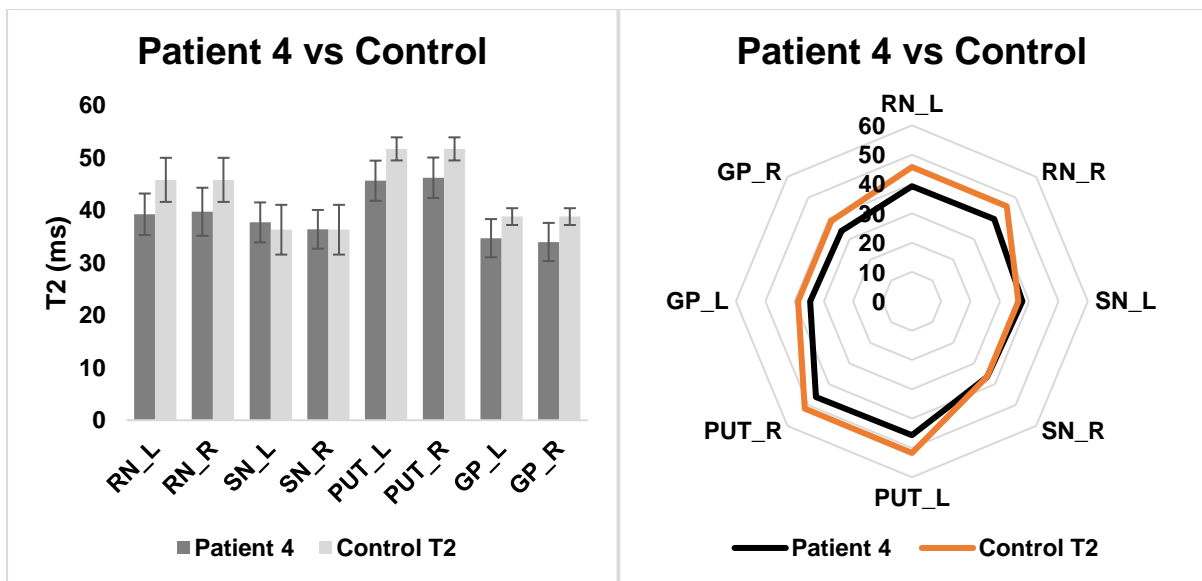
All regions normally distributed as tested with Shapiro Wilkes test ($p < 0.05$).

3.6.1.2.3 Patient 4

Top left: comparison of T2 time (ms) with each brain region, compared to literature control.

Top right: The same data shown on a radar plot for clarity

Bottom: The distribution of T2 values displayed as a box plot for each region. Cross = mean, Middle line = median, box edges = interquartile range, whiskers = max values excluding outliers, circles = outliers.



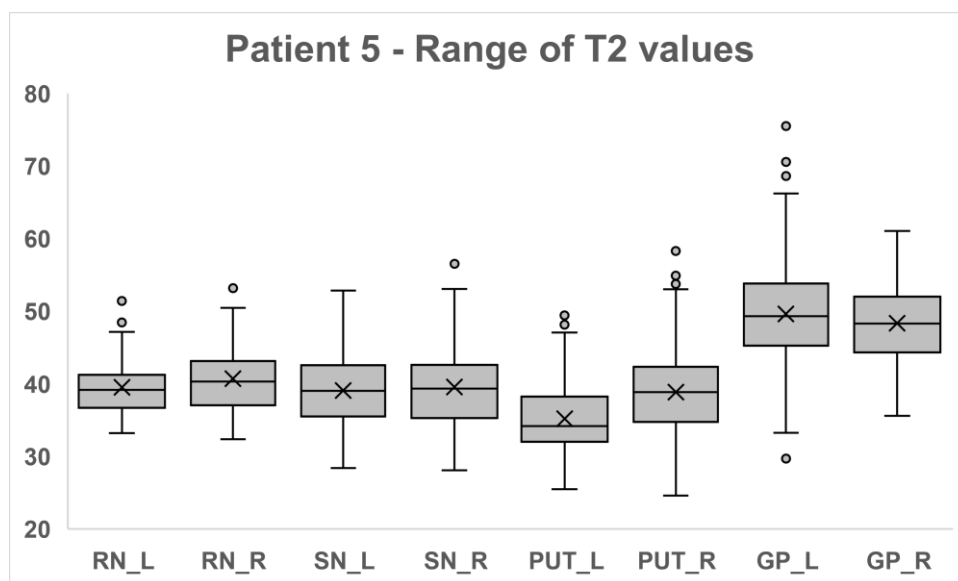
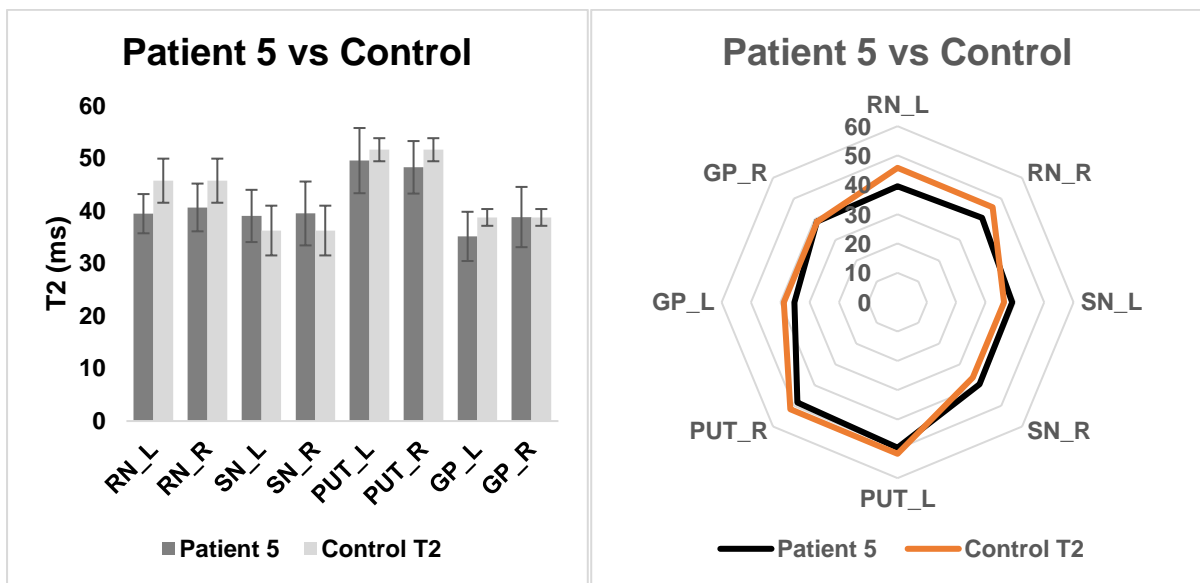
All regions normally distributed as tested with Shapiro Wilkes test ($p < 0.05$).

3.6.1.2.4 Patient 5

Top left: comparison of T2 time (ms) with each brain region, compared to literature control.

Top right: The same data shown on a radar plot for clarity

Bottom: The distribution of T2 values displayed as a box plot for each region. Cross = mean, Middle line = median, box edges = interquartile range, whiskers = max values excluding outliers, circles = outliers.



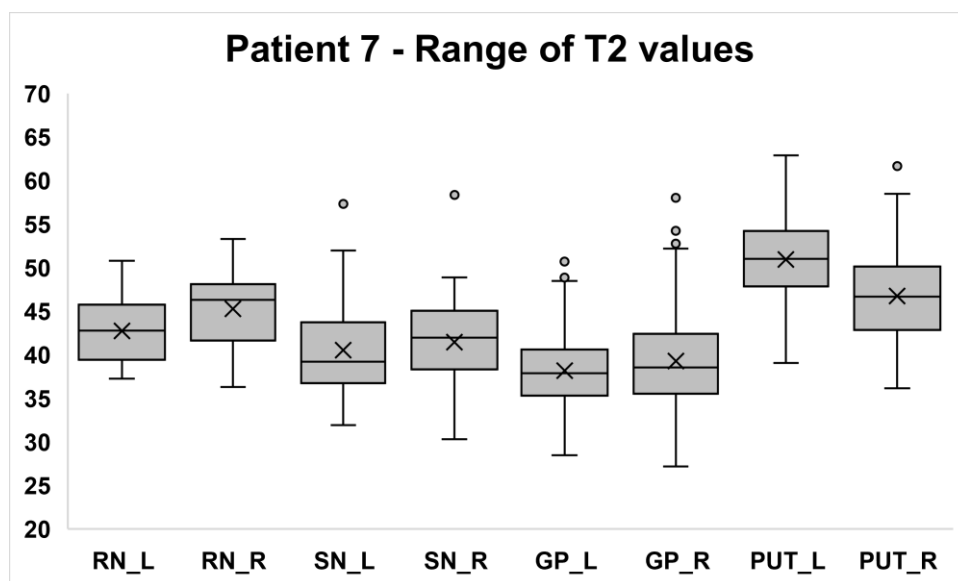
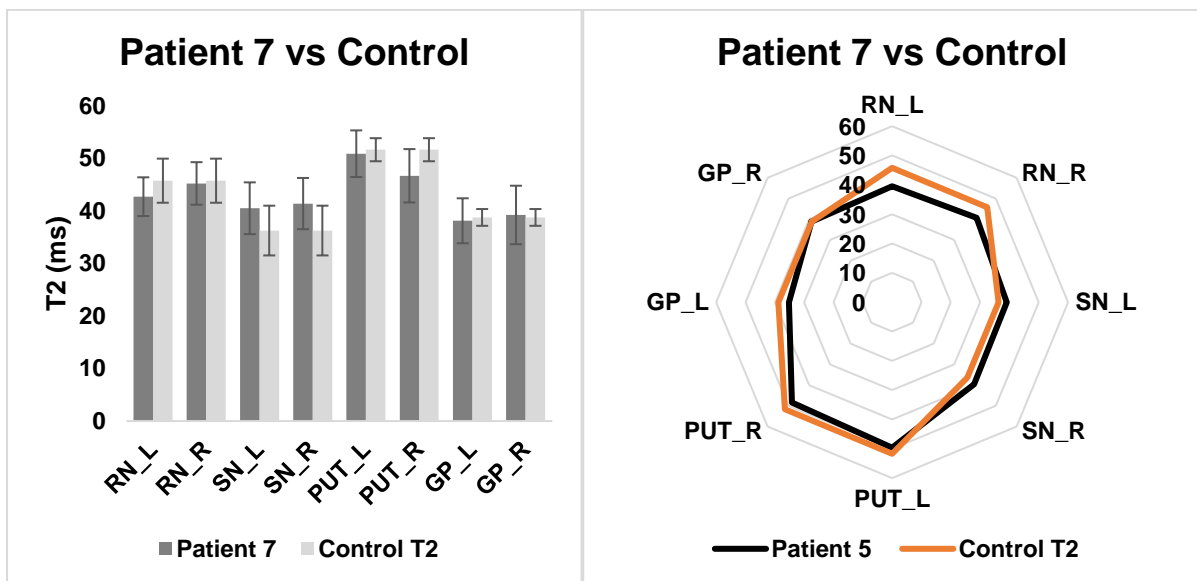
All regions normally distributed as tested with Shapiro Wilkes test ($p < 0.05$).

3.6.1.2.4 Patient 7

Top left: comparison of T2 time (ms) with each brain region, compared to literature control.

Top right: The same data shown on a radar plot for clarity

Bottom: The distribution of T2 values displayed as a box plot for each region. Cross = mean, Middle line = median, box edges = interquartile range, whiskers = max values excluding outliers, circles = outliers.



All regions normally distributed as tested with Shapiro Wilkes test ($p < 0.05$).

3.6.2 Analysis and Discussion

3.6.2.1 Calculation of [Fe] from T2

Iron values are calculated using the measured T2 relaxation rate according to the calibration determined in **Section 3.5.2**. Standard Deviation of the T2 value is used to provide a range in iron concentration, with error propagation used according to **Section 3.5.4**. Measured [Fe] values are shown in Table 3.6.2.1.1

Measured [Fe] values ($\mu\text{g/g}$)						
<i>Region</i>	Patient 1	Patient 3	Patient 4	Patient 5	Patient 7	Control
<i>RN_L</i>	190 \pm 110	165 \pm 99	218 \pm 118	216 \pm 117	194 \pm 109	176 \pm 104
<i>RN_R</i>	226 \pm 122	167 \pm 101	215 \pm 118	208 \pm 115	179 \pm 105	176 \pm 104
<i>SN_L</i>	222 \pm 124	195 \pm 113	231 \pm 122	220 \pm 121	209 \pm 116	242 \pm 129
<i>SN_R</i>	204 \pm 115	191 \pm 111	242 \pm 126	216 \pm 122	203 \pm 114	242 \pm 129
<i>PUT_L</i>	192 \pm 117	121 \pm 87	177 \pm 104	157 \pm 100	151 \pm 96	148 \pm 93
<i>PUT_R</i>	180 \pm 105	125 \pm 91	174 \pm 103	163 \pm 100	171 \pm 103	148 \pm 93
<i>GP_L</i>	234 \pm 133	167 \pm 103	257 \pm 131	252 \pm 132	227 \pm 122	222 \pm 116
<i>GP_R</i>	252 \pm 133	202 \pm 118	264 \pm 134	221 \pm 123	218 \pm 121	222 \pm 116

Table 3.6.2.1.1 Measured [Fe] values based on T2 value. Error displayed is propagated error.

In order to test for a significant effect, a one-sample t-test was used to compare the CICI patients cohort to the literature reference values in each brain region, shown in Table 3.6.2.1.2.

<i>Brain Region</i>	Mean	SD	Control	p-value
<i>RN_L</i>	197	19	176	0.13
<i>RN_R</i>	199	21	176	0.11
<i>SN_L</i>	215	27	242	0.16
<i>SN_R</i>	211	26	242	0.11
<i>PUT_L</i>	160	19	148	0.35
<i>PUT_R</i>	163	17	148	0.23
<i>GP_L</i>	228	30	222	0.77
<i>GP_R</i>	232	32	222	0.63

Table 3.6.2.1.2 Comparison table for mean region with literature value. P-value obtained from one-sample t-test.

No significant effect could be detected in any region, Red Nucleus, Substantia Nigra, Putamen or Globus Pallidus. Although mean value was higher, the large error term propagated through meant that we were unable to reject the null hypothesis. It is possible that with more data, either patients in cohort or having additional values for reference values would reduce the Standard Error of Slope in the linear fit, which may reduce overall error.

3.6.2.2 Sources of error

Factors that can influence the T2 measurement include patients moving in between scans causing loss of image registration, user error in drawing manual ROIs, as well as the experimental uncertainty associated with the scanner itself.

The largest effects will be produced from the lack of perfect image registration. For instance, the red nucleus is 5mm in diameter approximately. If a patient moves even 1 mm between scans, and this registration is not accounted for, up to 20% of the pixels in the exponential decay slice will be

misaligned and will instead be measuring neighbouring tissue. For this reason, extreme care is taken to ensure all images are registered correctly and ROIs propagated accurately, as well as ensuring as much as possible that the patient lies still in the scanner, with their head restrained in an MR head coil. Image registration was accounted for by manual adjustment of ROIs on every slice and at every echo time.

Given the results in this chapter and with the significance levels stated, this study cannot conclude whether there is evidence of an increase in brain iron concentration in Globus Pallidus, Red Nucleus, Putamen, or Substantia Nigra with having undergone chemotherapy.

As evidenced in Finnegan et al, however, this technique can indeed accurately determine iron concentration in the brain (Finnegan et al., 2019). The lack of significant effect here could be caused by multiple factors, including low sample size and poor image registration.

Finnegan et al found a high field relationship of:

$$R2 = 7.2 \times 10^{-5}[Fe] + 0.02$$

at 9.4T. No errors were specified.

Literature developed calibration curves in this study obtained the relationship (R2 in ms):

$$R2 = 9 \times 10^{-5}[Fe] + 0.006$$

at 3T, which is a rearrangement of the linear relationship:

$$[Fe] = 11500 \times R2 - 74.6$$

with error of slope = 4030, error in intercept estimated to be approximately the size of the offset i.e. 75.

The limitation of forming calibration curves from literature values are that there is a huge range of stated acceptable values, as summarised in a review paper by Tao et al in 2014 (Y. Tao et al., 2014). In order to obtain valid and interpretable FDRI results, it is necessary to consider the same individuals

under multiple field strengths, as the inter-patient variability of iron concentration makes comparison difficult.

Finally, there are other factors affecting T2 time aside from iron concentration, for example radicals in tissue. This is a real challenge of any real-world brain imaging study, and so any results will always have the caveat that effects from non-iron sources on T2 will be present, and not necessarily straightforward to quantify.

3.6.3 Future work - Improving the study methodology

This was a pilot study where the numbers were too small for it to be possible to attempt to draw statistically significant conclusions. However, it did provide an opportunity to test whether iron-sensitive sequences could be obtained from individuals with CICI, i.e., whether the participants could tolerate sequences of this duration without involuntary movement being a problem.

If this study were to be extended, it would be important to increase the number of participants, ideally through a multi-centre coordinated study of C patients and age- and gender-matched controls to enable robust investigation of iron-associated contrast as a function of disease. With sufficiently large cohort, the impact of the type of cancer, and the type of treatment received, could be explored as variables. Additionally, if there were access to routine healthy MRI brain scans of people which were later used if/when that individual developed CICI symptoms, though extremely logistically difficult to orchestrate, this would be the ideal paired test – this way, pre and post brain iron concentrations would belong to the same individual, and could be compared to pre- and post- measurements from a cohort of individuals who did not develop CICI, using a paired t-test.

This work was part of a feasibility study to see if the CICI patients could tolerate the scans, and to test the quality of the data obtained. Funding was not granted for the full follow-on study, but in future if this took place it would allow access to clinical data (e.g., motor function, measures of cognitive function, psychiatric assessments and evaluation) so that contrast changes in the brain areas affected are linked to clinical symptoms could be tested.

3.10 Individual contribution

This experiment was proposed by Prof Joanna Collingwood (University of Warwick), with support from Dr. Sarah Wayte (University Hospitals Coventry and Warwickshire, UHCW) and Professor Charles Hutchinson (UHCW). Images were acquired by Dr. Sarah Wayte, UHCW. Individual contributions by myself were:

1. Designed and carried out pilot study on my own brain, in order to determine whether 3 echo times would produce a measurement that was sufficiently close to the measurement made using 4 echo times
2. All image analysis, manual segmentation and thresholding.
3. All resulting data analysis from the experiment.

Chapter 4 - DECT Phantom Studies

4.1 Summary

Computed Tomography provides a fast method of acquiring clinical images in patients. While an MRI scan can take anywhere from 20 minutes to over an hour depending on patient requirements, with high costs associated with the time required as well as liquid helium for cooling the gradient coils, CT scans are completed in seconds.

In this chapter, studies are presented which aim to develop the technique of using DECT to provide accurate quantitative iron concentration data, validated with ICP-MS analysis of phantoms, in order to apply this principle to iron quantitation in the human brain for future work (*cadaver study detailed in Chapter 5*).

4.2 Introduction

Computed Tomography (CT) scans are cheap and fast ways of imaging the clinical patient. In recent years, Dual Energy CT (DECT) has become increasingly interesting on the research level for its ability to differentiate materials from one another from the spectral data acquired (Obaid et al., 2014),(E. S. H. Ibrahim et al., 2015). By scanning the patient or sample using two different X-ray energies, information relating to elemental composition can be obtained, whereas single energy CT limits the user to attributing attenuation changes to some unknown combination of materials – for example fat, tissue, trace metals, and water.

There are two main ways of achieving this effect currently; the first is by having two separate x-ray sources in a DECT configuration (a method employed by Siemens Medical Ltd.), and the second by Rapid kVp Switching, which as the name suggests, changes the energy of the photons being emitted quickly in order to obtain image data at near-simultaneous time points. This method is employed by GE Healthcare's Discovery scanner, which is the equipment used in this study.

DECT is starting to make headway in clinical trials. In 2012, a trial involving 38 patients and 43 controls showed that DECT had the ability to diagnose and stratify cirrhosis (Lv et al., 2012).

The typical iron concentration in the brain is lower than the liver, which is where much of the recent research has been focused (Tsurusaki et al., 2021)(Elbanna et al., 2020). The possibility to quantify iron in the brain using a cheap, fast, non-invasive technique is something that is widely sought after. Healthy liver iron is less than 2000 μ g/g, with Liver Iron Overload starting at anything above that. Brain iron on the other hand is approximately an order of magnitude less (Haacke et al., 2005; B. Hallgren & Sourander, 1958; Bo Hallgren & Sourander, 1960b).

Alzheimer's disease has been associated with iron, with ongoing debate over its role in terms of the pathogenesis of the disease. A prevailing view is that oxidative stress is one of the earliest hallmarks of the disease (Schipper, 2012) (Duce et al., 2010). Increased cortical iron has been established as a biomarker of the disease, even in its earliest stages. Chelation therapies being developed rely on early detection of AD, which at this stage relies mainly on waiting for a clinical diagnosis of Mild

Cognitive Impairment (MCI). Confirmation in the form of an MRI scan is a time consuming and expensive process. In this study we investigate the possibility of using Dual energy CT to provide spectral imaging which may allow iron quantification at the diagnostic stage. This early diagnosis would feed into prospective therapies for AD.

4.3 Literature Review

The relevant literature on this topic is broadly split into two main areas: Firstly, the use of monochromatic reconstructed images from DECT to make quantitative measurements in general – while not specific to detecting iron – are reviewed and understood. The approaches and methods described feed into the experimental design of the studies presented in this chapter where monochromatic reconstruction is used from DECT images in order to quantify iron concentration in phantoms. In this way the approach can be validated before subsequent studies (Chapter 5) aiming to apply this technique to iron detection in the human brain. Secondly, research into the uses of DECT for detecting iron in biological tissue, which is what is being attempted at neurologically relevant iron concentrations (this chapter) as well as in post-mortem cadaver brain tissue (chapter 5). In the literature, the use of DECT in quantifying iron in tissue has been limited to liver iron overload, where the iron concentrations can exceed 10 times the concentrations of the highest iron concentrations found in the brain (Ahmed et al., 2013; Sheth et al., 2019). Hemochromatosis, or iron overload disease, is a genetic disease of iron metabolism. The fundamental issue caused by the disease is increased iron uptake in the first part of the small intestine, the duodenum. Over the lifetime of the patient, iron accumulates in the body at an excessive rate, resulting in deposits of iron throughout the body (especially in the liver), and increases in serum transferrin saturation (Tsat) and ferritin. Common symptoms include the breakdown of cartilage in the joints and generalised fatigue. In some cases, hemochromatosis can lead to scarring of the liver (fibrosis), into the eventual replacing of the liver tissue with nodules and excessive scarring (cirrhosis), and ultimately hepatocellular cancer. (Batts, 2007)

Liver iron is typically measured by biopsy, with non-invasive alternatives being MRI. With MRI scans being both more expensive and hugely more time consuming than equivalent CT scans, DECT is investigated for its potential to replace MRI in situations where MRI may not be possible (presence of a pacemaker or metal implant in the patient, for example).

Ultimately, there is a gap in the literature looking specifically at brain iron and brain-iron-relevant iron concentrations with DECT, which the results of this chapter along with Chapter 5 aim to fill.

4.3.1 DECT for material specificity with monochromatic reconstruction

One of the key uses of DECT is the ability to produce virtual monochromatic CT images. The benefit of this process, as opposed to a polychromatic single energy system, is a reduction in artifact noise and ability to provide quantitative material-specific measurement (Ueguchi et al., 2018; Yu et al., 2012). In their 2018 study, Kumar et al. (V. Kumar et al., 2018) wished to investigate the presence of myocardial fibrosis, an accumulation of collagen in cardiac muscle, with a non-invasive analytical technique. They state that the current standard practice would be to use cardiac magnetic resonance (CMR). The motivation is that this technique cannot be used on every patient; specifically, it is unsuitable for patients with non-MR suitable implants, among other possible reasons. They investigate the possibility of using DECT as previous studies (Johnson 2017, Lamb 2015) have indicated sensitivity to collagen concentration change at appropriate energy levels.

The authors reconstruct the data into 11 different energies, 40keV to 140keV in increments of 10keV as shown in Figure 4.3.1 They plot the HU against energy for each phantom, shown in Figure 4.3.1.1. Unlike Ibrahim 2014, they do not use this data to produce linear relationships.

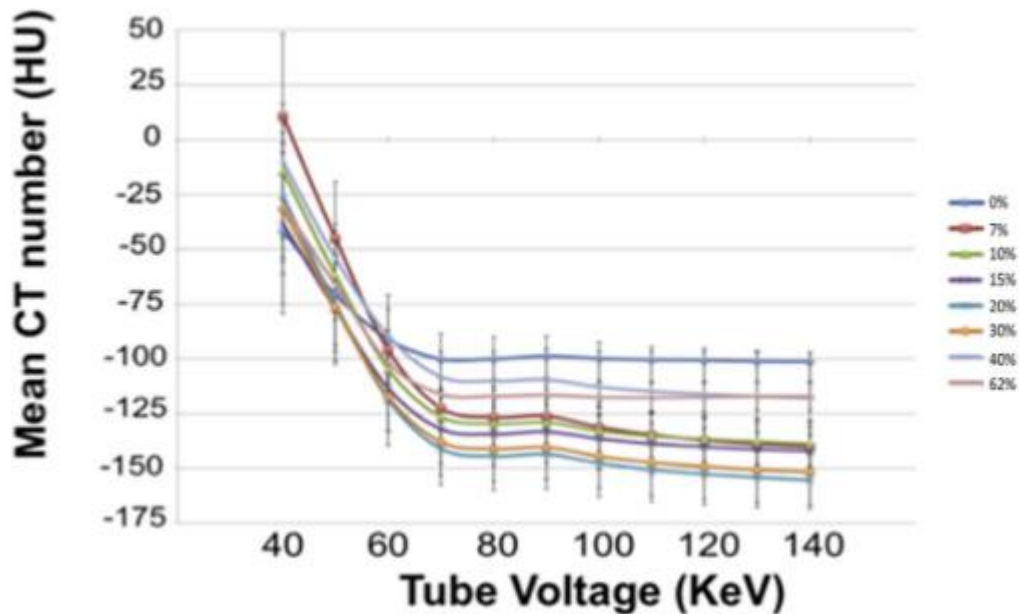


Figure 4.3.1.1 Reproduced from (V. Kumar et al., 2018) HU against monochromatic keV for each phantom. The authors did not use this data in order to plot HU against concentration over a range of energies, which would have allowed them to see which energy was best at determining concentration change among their sample size.

The authors reasoned that they wanted to compare using data acquired at all 11 energy levels as a grouping variable versus just using 70keV (since this most closely resembles a typical 120kVp single energy CT scan) - however if they had done a linear fit on a per-energy basis, it is possible that a particular energy may have been found to contain most of the sensitivity (most likely the lowest energy, 40keV) and that considerably better agreement with a *certain* single energy could be achieved rather than one chosen to resemble an alternative technique.

4.3.2 DECT iron

Research into DECT has specifically looked at quantifying iron in tissue, although not in the brain. A 2014 study (Tsai et al., 2014) observed that DECT may be used for the determination of iron concentration in the liver and heart, given that the authors were able to produce linear correlation between observed HU from monochromatic reconstructed images from DECT, with R2* values from

T2* relaxometry at 1.5 Tesla (Figure 4.3.2.1). Iron concentration values are assumed to be correct by the authors based on the target concentrations when making up the phantoms. No additional verification (e.g., with Mass Spectrometry) was performed to confirm the exact concentrations.

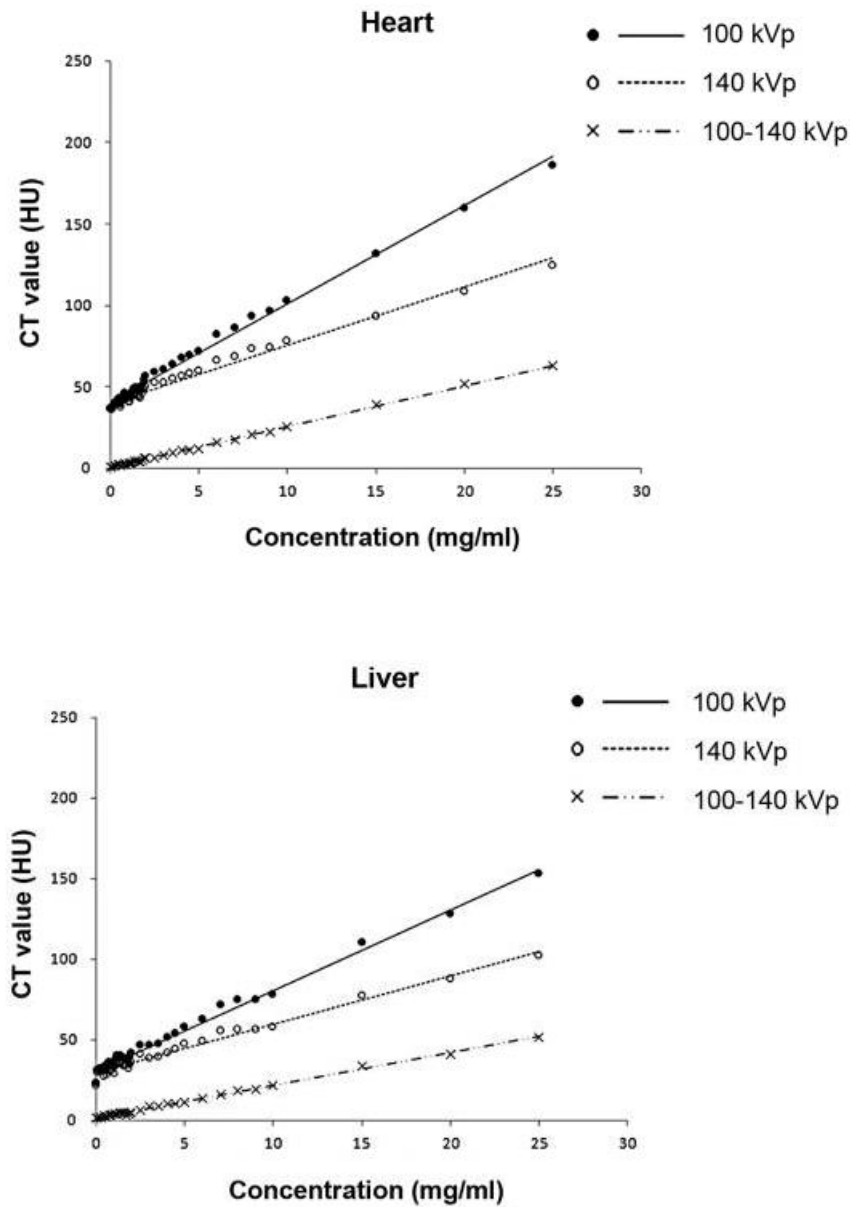


Figure 4.3.2.1 Reproduced from (Tsai et al., 2014) Linear relationship between HU and iron concentration in the heart (Top) and liver (Bottom). Note that CT value at 100 and 140kVp are shown, as well as their difference. The difference in energy forms a linear relationship going through the origin, i.e., the CT value for 0 concentration is equal at both energies.

This linear relationship between iron concentration and Hounsfield units has been corroborated in the literature (Abadia et al., 2017; Fischer, Gnannt, et al., 2011; E.-S. Ibrahim & Bowman, 2014; Luo et al., 2015).

In a 2014 study, Ibrahim et al. (E.-S. Ibrahim & Bowman, 2014) hypothesise that Dual Energy CT could be an alternative to T2* weighted MRI for determining iron concentration in tissue and compare the two techniques. They find that, in the concentration range they are looking in, DECT is a good alternative and can be used to determine iron concentration.

The methodology used in this study is well-designed to allow replication for neurologically relevant quantitative analysis; Agarose takes the place of human tissue, and each vial contains a different concentration of iron. The entire collection of 10 vials are then scanned using DECT and MRI, and results are compared. The main aim for this study was to determine whether or not DECT is suitable for detection myocardial iron overload, and as such the concentration ranges used reflect that. The iron concentrations used in this study are 0, 25, 50, ..., 225 $\mu\text{mol/g}$, or around 0, 1.4, 2.8, ..., 12.6 mg/g . This is far higher than the typical concentrations found in the human brain, which range from 150-300 $\mu\text{g/g}$.

The study concludes that R2* is strongly correlated with Hounsfield Units (HU) at all energy levels, i.e., in monochromatic reconstructions.

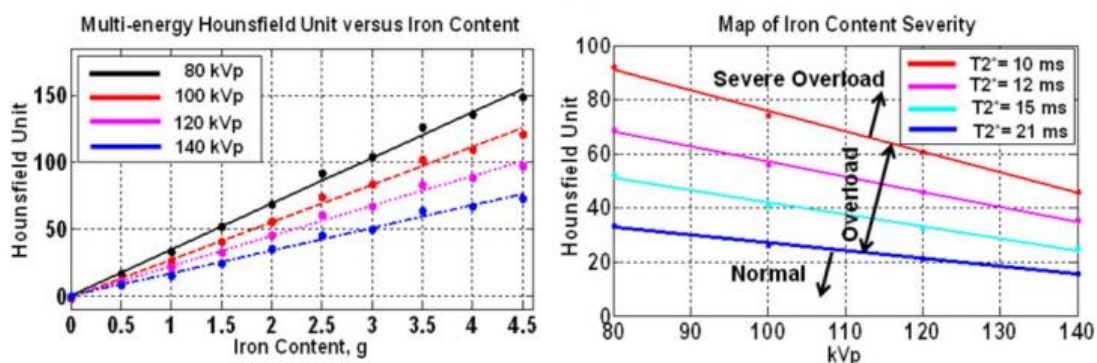


Figure 4.3.2.2 Reproduced from (E.-S. Ibrahim & Bowman, 2014) Linear relationship between iron content and HU depends on the energy level chosen in the monochromatic reconstructed image. (Right) The authors fit a linear model to the

data, whereas a mono-exponential fit would usually be most appropriate. If they had included energy levels down to 40keV it is possible that this mono-exponential relationship would be apparent.

Figure 4.3.2.2 shows that Ibrahim et al. were able to achieve increased levels of CT Number for increasing levels of iron concentration at all levels, with the lowest energy used (80kVp) exhibiting the highest sensitivity to iron concentration change.

DECT has also been used to quantify iron in animal models. Luo et al. (Luo et al., 2015) demonstrated in their 2015 paper that iron can be detected in rabbits at concentrations above 2mg/g.

The authors state that liver biopsy is the main method used to determine liver iron concentration, but that research has been done into the use of MRI to accurately quantify iron concentration. A common theme from the literature is the experimentation of DECT as a potential replacement technique for quantitative MRI. Once again, the difference between this study and the results presented later in this chapter is the concentration range of interest. A mixture of liver tissue and Ferric Nitrate ($\text{Fe}(\text{NO}_3)_3$) was made up for each test tube with concentrations ranging as follows:

0, 20, 40, 60, 80, 100, 120, 140, 160, 180, 200, and 400, 600, 800 $\mu\text{mol/g}$ of dry liver.

Note that the lowest (non-zero) concentration of 20 $\mu\text{mol/g}$ iron is around 1.1mg/g.

One set of phantoms contained only liver tissue and iron from the Ferric Nitrate, while the second set also contained goose fat to simulate the normal conditions found in the liver, i.e., the existence of fat. All phantoms were submerged in water.

CT images were obtained using a Siemens dual source DECT scanner. Single energy CT scans were obtained at 120kV, 210mAs. DECT images were obtained at 80 and 140kV. Images were reconstructed using the standard Siemens software at a slice thickness of 1.5mm. Siemens software “Liver VNC” was used to determine HU. Accurate liver iron content was determined by titration.

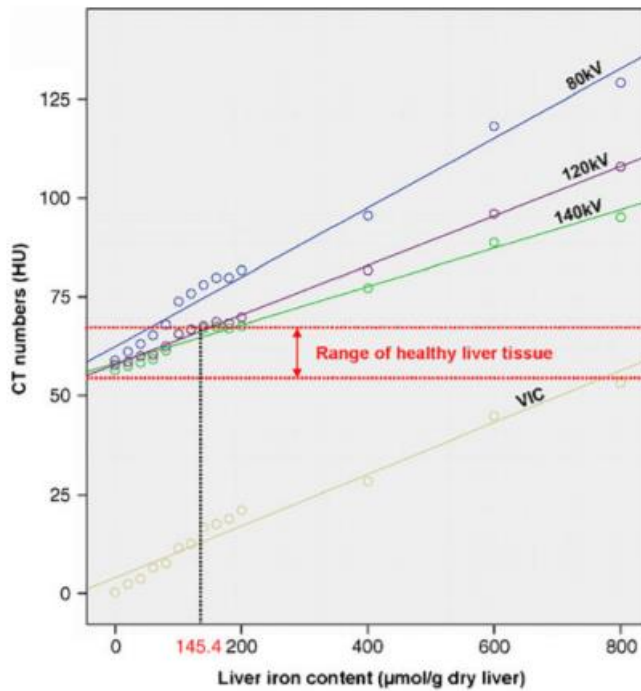


Figure 4.3.2.3: Reproduced from (Luo et al., 2015) Comparison of CT measurements at 80 kV, 140 kV and 120 kV with virtual iron content (VIC) measurements derived from dual-energy CT for iron quantification in fat-free phantoms.

The investigators found a positive linear relationship between liver iron content and HU across the monochromatic reconstructed images. In particular, Figure 4.3.2.3 shows that as energy is reduced, sensitivity change in iron concentration was also increased. The trade-off with lower energy is that contrast-to-noise ratio is decreased, for a given tube current. Figure 4.3.2.4 illustrates the increase in contrast-noise ratio (CNR) as kV is increased while keeping mA constant.

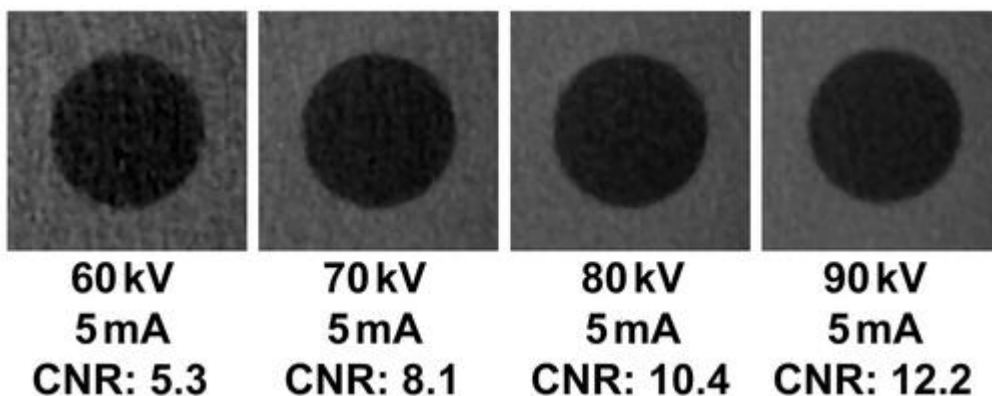


Figure 4.3.2.4: CNR increases with kV with mA held constant. Figure reproduced from (Pauwels et al., 2014).

Contrast-to-noise is determined using a cylindrical polymethyl methacrylate (PMMA) phantom, containing four materials (air, aluminium, polytetrafluoroethylene and low-density polyethylene).

Contrast-noise-ratio for a material, i , is defined in this paper as follows:

$$CNR_i = \frac{|MGV_i - MGV_{PMMA}|}{\sqrt{SD_i^2 - SD_{PMMA}^2}}$$

Where MGV = mean grey value, and SD = standard deviation.

Given our own use case, we would want to maximise sensitivity to iron as much as possible, and so the lowest possible energy should be used such that there is still sufficient CNR.

4.3.3 Detection limits

There is a fundamental minimum level of quantitation that is possible due to the fact that quantitative CT information comes directly from photon counts hitting the detector. This fundamental limit has been investigated in the literature. In Luo et al's 2015 study (Luo et al., 2015), while a lower limit of 20 μ mol//g was given, this was simply the lowest non-zero phantom concentration involved in the study.

The authors acknowledge that they did not investigate the lower end of the detection limit.

In 2019, Jacobsen et al. published a paper investigating the lower limits of iodine detection and quantification using DECT (Jacobsen et al., 2019). The limit of blank (LOB) was defined as the upper limit of the 95% confidence interval of the water sample. The limit of detection (LOD) was defined as the concentration with a 95% chance of having a signal above the LOB. The limit of quantification (LOQ) was defined as the lowest concentration where the coefficient of variation was less than 20%.

The authors determine that iodine could not be differentiated from a blank phantom at concentrations below 210 μ g/g. This investigation was repeated with the LOQ of iron (Jiang et al., 2021), where the authors determine that the LOQ of iron was 0.50/1.73/6.25 mg/ml in the small/medium/large phantoms respectively. ASIR (see section 4.3.4) was found to improve the LOQ by 11%. The result of this study is that for a small region of interest, it may be possible to determine iron concentration at

500µg/g. Though still higher than neurotypical iron concentration, this is approaching the concentrations found in the human brain.

4.3.4 ASIR

A highly cited paper from Hara (Hara et al., 2009) is one of the key pieces of literature discussing the use of ASIR in clinical CT and specifically the effects it has on dose and noise. The authors first scanned both a stock phantom at the standard dose and then at half that value (12.5 mGy), and then ASIR was used to scan 12 patients (7 male, 5 female) to compare image noise, low-contrast resolution, image quality and spatial resolution, with two radiologists (blinded to the technique used) rating images in each of those 4 categories from 1 (best) to 4 (worst). Hara concludes that by using ASIR, body CT dose index can be reduced by 32-65%.

For the phantom study, a stock phantom, the American College of Radiology (ACR) Phantom Gammex 464, was scanned using both the standard ACR guideline settings and then at half of the dose value (12.5mGy). Images were reconstructed with FBP and also ASIR, at values of 0-100% in intervals of 10%.

For the patient study of 12 individuals (seven men, five women; average age, 67.5 years; range, 53–86 years) who had all undergone routine-dose CT of either the abdomen, or the abdomen and pelvis together, a follow up low dose CT scan was done at most 10 months after the initial routine CT scan. Comparison scans were matched in terms of IV contrast agent and imaging settings.

The phantom study results along with original image caption from Hara et al. is shown in Figure

4.3.4.1

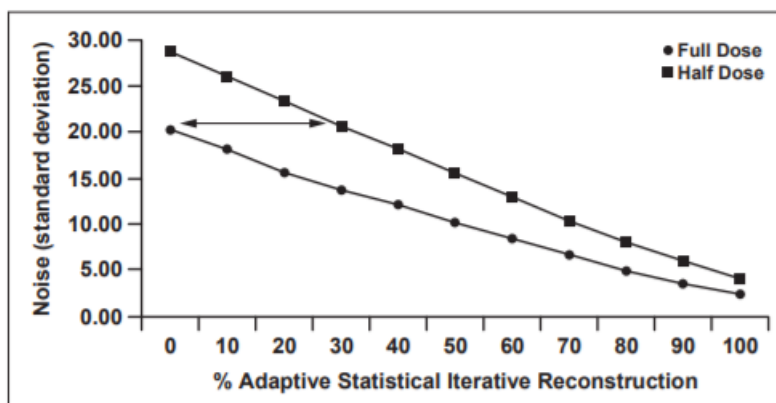


Figure 4.3.4.1: Reproduced from (Hara et al., 2009) Noise reduction in images reconstructed with adaptive statistical iterative reconstruction in phantom. Graph shows linear decrease in image noise (SD) as percentage adaptive statistical iterative reconstruction increases. Images acquired with 50% dose reduction (half dose) have 1.4 times SD value (28.57 compared with 20.39) without adaptive statistical iterative reconstruction. Reconstructing images with 30% adaptive statistical iterative reconstruction for half-dose acquisitions produces images with noise nearly equivalent to that of full dose images without adaptive statistical iterative reconstruction (double arrow) (SD 20.52 compared with 20.39).

Dose reduction from the patient study are shown in Table 4.3.4.1.

TABLE I: Comparison of Low-Dose CT and Routine-Dose CT of Same Patients

Patient No.	Type of Examination	IV Contrast Enhancement	Body Mass Index	Dose–Length Product (mGy·cm)			CT Dose Index		
				Routine Dose	Low Dose	Percentage Reduction	Routine Dose	Low Dose	Percentage Reduction
1	Abdomen	Yes	34	707	441	38	27	17	37
2	Abdomen	No	30	1,008	773	23	31	20	37
3	Abdomen, pelvis	Yes	28	1,209	886	27	26	18	32
4	Abdomen	Yes	25	376	305	19	14	9	35
5	Abdomen	Yes	25	848	502	41	26	15	44
6	Abdomen, pelvis	No	22	921	549	40	20	11	43
7	Abdomen, pelvis	Yes	22	860	548	36	18	11	39
8	Abdomen	Yes	20	396	197	50	13	6	52
9	Abdomen, pelvis	Yes	20	1,128	451	60	21	8	62
10	Abdomen	Yes	19	353	114	68	14	5	65
11	Abdomen, pelvis	Yes	19	1,198	442	63	26	9	65
12	Abdomen, pelvis	Yes	18	1,073	430	60	22	8	62
Average			24	840	470	44	22	11	48

Table 4.3.4.1: Reproduced from (Hara et al., 2009). Results of 12 patient study into CT dose index reduction as a result of using ASIR.

The reduction in noise due to ASIR is confirmed in Beister’s 2012 paper (Beister et al., 2012), where a brain image is reconstructed using FBP and ASIR and a standard deviation reduction from 28HU to 10HU is observed, shown in Figure 4.3.4.2.

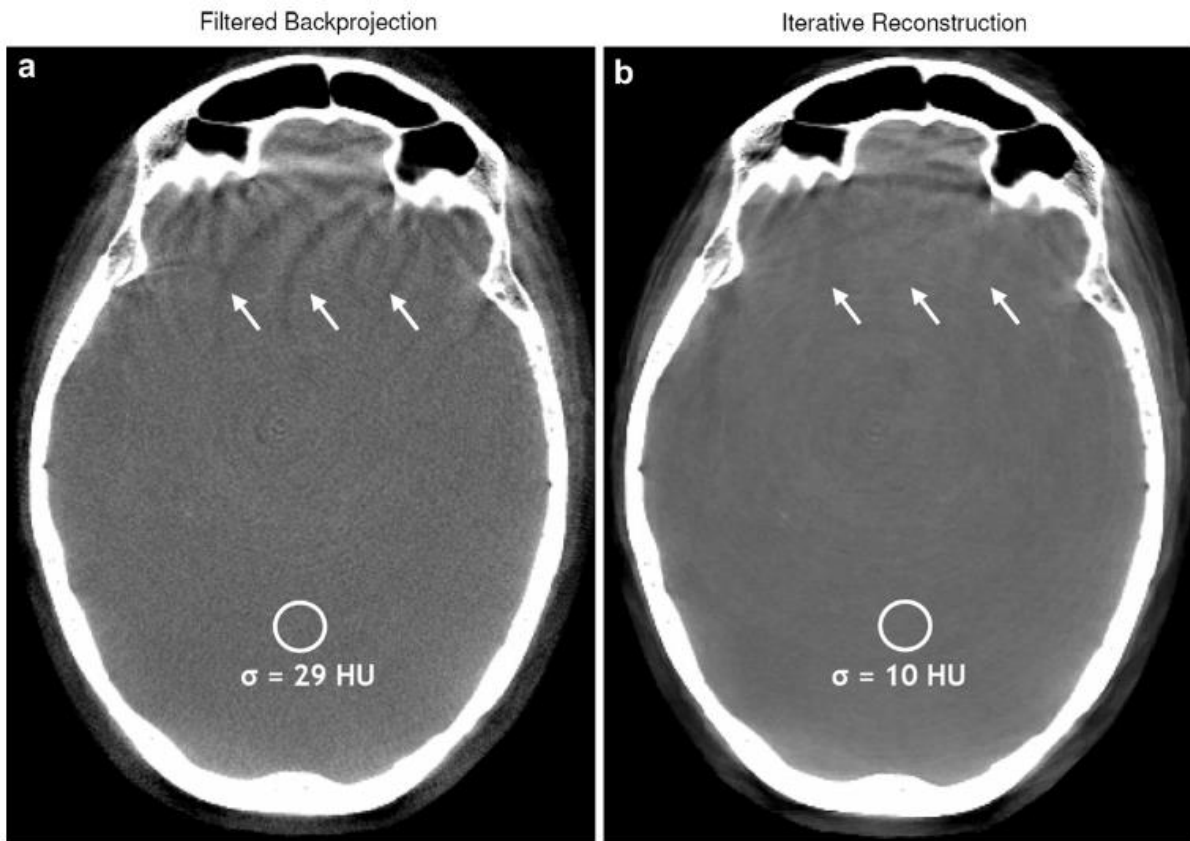


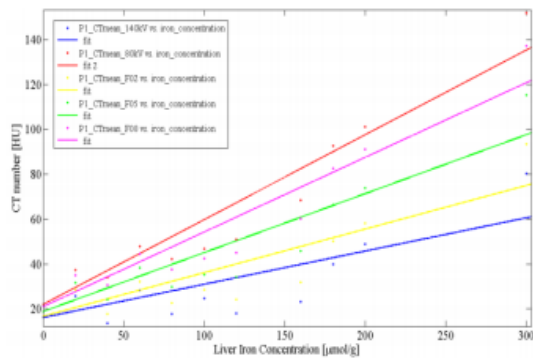
Figure 4.3.4.2: Reduction in noise due to ASIR observed in brain CT scan. Reproduced from (Beister et al., 2012)

4.3.5 CT Energy

In Malvarosa et al.'s study (Malvarosa et al., 2014), the influence of energy level on sensitivity to iron concentration was investigated. This study is important to our own study in this chapter not only because it is concerned with detecting iron with DECT in biologically relevant material and concentrations, but because the investigators are explicitly testing whether or not lower energy levels result in higher sensitivity to changes in iron concentration. The investigators do not, however, use full monochromatic reconstructions. Instead, they use the two energy sources from the Siemens dual source DECT scanned (80kVp and 140kVp) and use various weighted combinations of these to interpolate possible values. In our own study, spectral imaging is used to generate true monochromatic reconstructions as low as 40keV, which allows a more detailed analysis of low energy DECT for the detection of iron. The investigators combined ferric nitrate with homogenised liver in

11 test tubes with iron concentration within the liver as follows: 0, 20, 40, 60, 80, 100, 120, 160, 180, 200, and 300 $\mu\text{mol/g}$.

Phantoms were scanned using a Siemens Somatom dual source dual energy CT scanner. Relationship between measured liver iron concentration and HU is shown in Figure 4.3.5.1. They also investigated the impact of varying mAs.



CORRELATION COEFFICIENT (R) AND SENSITIVITY (S) AT THE DIFFERENT PROTOCOLS

Protocol	R			S [$\text{g}\cdot\mu\text{mol}^{-1}$]		
	1	2	3	1	2	3
80 kVp	0.97	0.96	0.97	0.41	0.39	0.43
F_0.8	0.96	0.95	0.96	0.36	0.39	0.39
F_0.5	0.94	0.93	0.94	0.30	0.29	0.31
F_0.2	0.90	0.89	0.89	0.23	0.23	0.24
140 kVp	0.86	0.86	0.84	0.19	0.19	0.19

Figure 4.3.5.1 Reproduced from (Malvarosa et al., 2014)(Left) The gradient of the linear fit increases as the energy level decreases. This is shown as the variable (S) in the Table 4.3 (Right).

The authors conclude that sensitivity goes down with increased energy. This is an important result and one that we verify in our own phantom study. In particular for our iron-based phantoms, the highest sensitivity was at 40keV which was the lowest available reconstruction, although noise is increased. It would have been interesting to see how they would have reconstructed their raw 80kVp and 140kVp into true monochromatic reconstructions with their available workstation software. The authors also conclude that varying mAs had no impact on the sensitivity of quantifying iron concentration (Malvarosa et al., 2014). This is not an expected result, as it would be expected that increased mAs would increase sensitivity to iron concentration changes.

4.4 Studies

To develop the process of iron quantification with DECT, and specifically the use of monochromatic reconstructed images, a number of pilot studies were carried out in order to inform future experimental design.

4.4.1 Layered experiment

4.4.1.1 Summary and aims

The aim of this experiment was to investigate whether monochromatic reconstructed images from DECT could be used to differentiate between neighbouring regions of different iron concentration. By forming a multi-layered gel with a different amount of Iron (III) Chloride in each layer, we can then image the final gel and see which of the layers shows a difference to the plain agarose in a DECT image. The intention was to replicate, to some degree, the environment that may be found in-vivo where areas of different iron concentration are in direct contact with one another. As long as the consistency and integrity of the agarose gels remained intact, it was thought that the iron content of each of the layers should remain consistent. Furthermore, this would allow us to see the effect of other nearby sources of iron. The experiment was designed as a test of the technique – if the resulting image analysis allowed us to check which layer a particular ROI was in by simply checking the resulting HU values, then the technique would be deemed a success.

4.4.1.2 Method

20mL of stock TAE 50x was added to 980mL of deionised water in a 1L bottle.

The stock solution of Iron (III) Chloride was made up to be 10x more concentrated than the highest concentration layer intended to be in the gel. 500mg of Iron (III) Chloride was weighed out and dissolved in 100mL of TAE.

To make each layer:

- 1) Add 1g Agarose powder to a 100mL conical flask.

- 2) Make up to the mark with TAE buffer and swirl gently.
- 3) Microwave for 3 minutes on full power.
- 4) Swirl gently and ensure there are no floating particles.
- 5) Microwave for 2 more minutes.
- 6) Add Iron (III) Chloride stock solution.

After microwaving, some solution will be lost to evaporation (approx. 20%). Make back up to the 100mL mark in the conical flask.

- 7) Pour first layer into 1L plastic beaker, which is the container for the gel. Place container in cold room and allow to set for 10-15 minutes.
- 8) Repeat the process until all concentrations are done.

The final product, pictured in Figure 4.4.1.2.1, was scanned at University Hospitals Coventry and Warwickshire on the GE Discovery HD Dual Energy CT scanner. Images using monochromatic reconstructions at 80keV and 140keV were used in subsequent calculations.



Figure 4.4.1.2.1: Layered agarose gel, with concentrations ranging from 0 to 7681 $\mu\text{g}/\text{mL}$ Iron (III) Chloride

4.4.1.3 Image Analysis

Monochromatic reconstructions at 80keV and 140keV are obtained and analysed to get HU values. ROIs are manually drawn in each of the 1cm horizontal regions, with 1mm either side just to ensure there is no overlap (resulting in an 8mm thick ROI for each layer). These ROIs are then projected through the image stack to give a 3-dimensional region. These regions are entirely enclosed by the material that is to be analysed. The mean pixel value of this 3D region is then calculated. Mean HU and Standard Deviation are recorded and shown in Table 4.5.

ImageJ is used to determine HU from the DICOM images. Metadata in the DICOM header is automatically interpreted by ImageJ and HU is presented in place of Pixel Value when selecting a region. These regions are saved, and HU numbers calculated pixel-wise, and averaged to obtain the overall HU reading for each region.

4.4.1.4 ICP-MS

In order to determine whether or not the result implied that the technique itself was incapable accurately quantifying iron concentration at lower concentrations, the experimental design was challenged. The layers were broken apart and analysed using ICP-MS. The results showed a large amount of inter-layer leeching that had occurred. Different concentrations in each layer were intended. The intended concentrations ranged from 0 to 5000 $\mu\text{g/g}$. Note that the resulting concentrations were not the same as intended, which was verified by ICP-MS, and that the highest concentration layer was excluded from analysis. The final concentrations of each layer, after a number of days had passed between creating the layered gel and the DECT scans, are shown in table 4.4.1.4.1:

Layer Number	Measured ($\mu\text{g/g}$)	SD
1	131.7	0.41
2	147.6	0.68
3	166.1	0.36
4	219.8	0.45
5	249.7	0.91
6	272.3	0.65
7	236.7	0.87
8	315.1	0.41
9	1141	0.76
10	2851	0.56
11	7681	0.44

Table 4.4.1.4.1: Iron concentrations in each layer at the time of ICP-MS analysis.

Additionally, the individual layers were segmented and placed into 15mL plastic polypropylene tubes and scanned at 9.4T using an MRI probe.

4.4.1.5 Results

Concentration ($\mu\text{g/g}$)	CT Number (HU)		SD	CT Number (HU)		SD
	80keV			140keV		
131.7	6.04	3.63	7.88	3.56		
147.6	6.98	3.26	8.35	3.24		
166.1	7.05	3.46	8.75	3.5		
219.8	6.82	3.49	8.2	3.42		
249.7	6.61	4.47	8.08	4.3		
272.3	6.59	3.45	7.91	3.48		
236.7	7.26	3.26	8.51	3.24		

315.1	6.73	3.49	8	3.58
1141	7.69	3.45	8.66	3.58
2851	8.46	3.06	8.98	3.03
7681	9.18	3.49	8.43	3.63

Table 4.4.1.5.1: Mean HU and corresponding standard deviation for 80keV and 140keV

monochromatic reconstructions of images taken for the layered agarose gel.

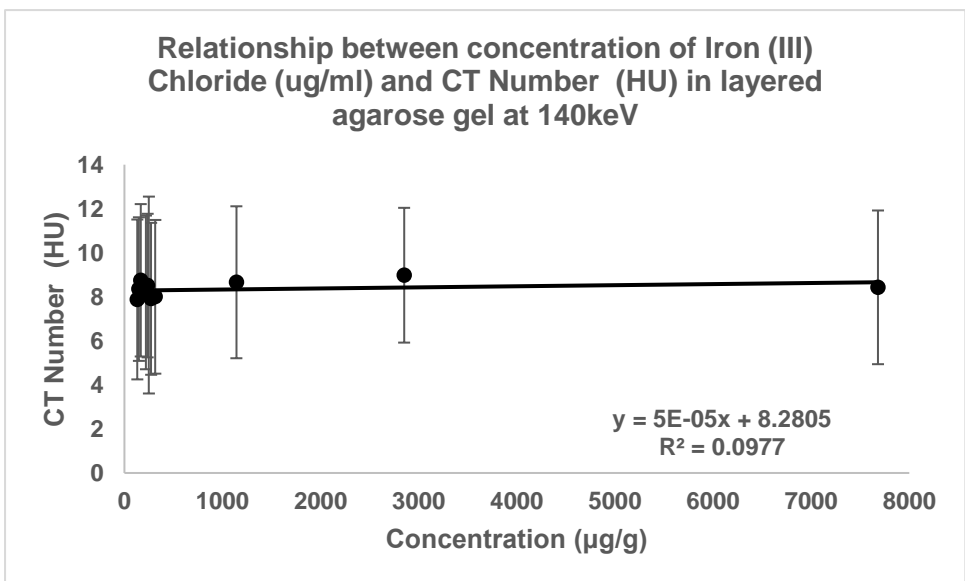
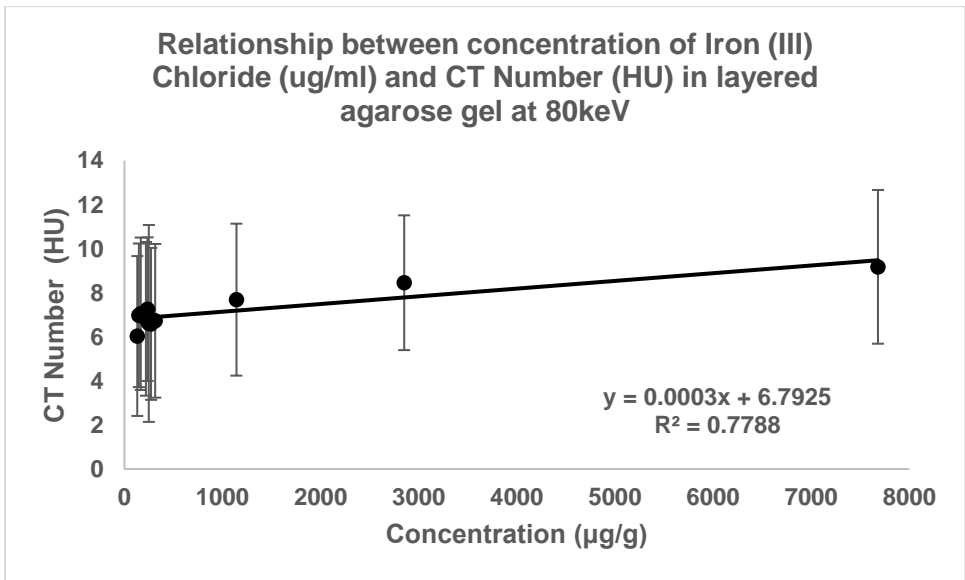


Figure 4.4.1.5.1: Layered agarose gel, with concentrations ranging from 0 to 7681 $\mu\text{g/mL}$ Iron (III) Chloride. Top: 80keV monochromatic reconstruction with $R^2=0.77$. Bottom: 140keV monochromatic reconstruction with $R^2=0.10$.

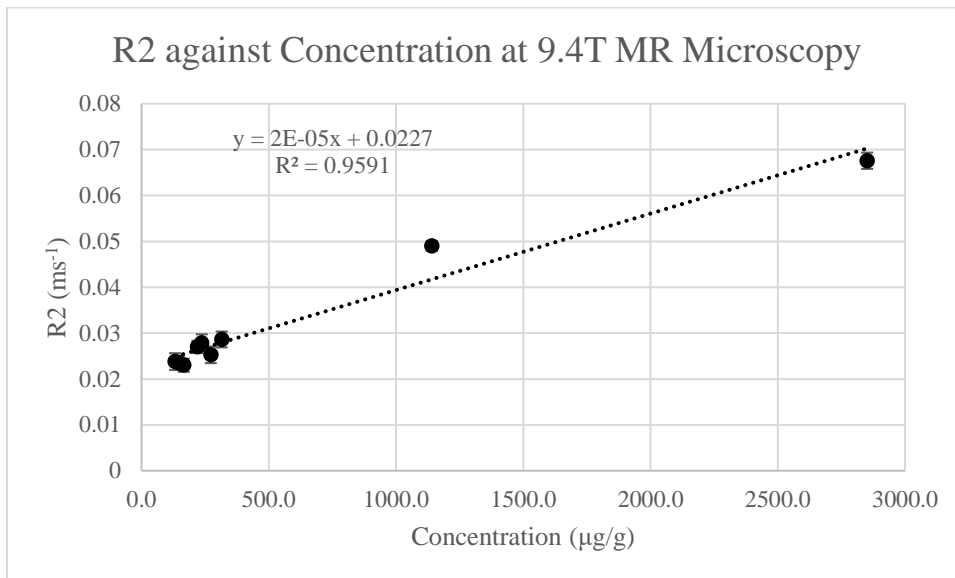


Figure 4.4.1.5.1: $R2$ against Concentration for each of the layered gels. It was not possible to fit an exponential decay for the highest concentration sample, due to the $T2$ signal decay at 9.4T being faster than the gap between the first and 2nd echo time. Concentration values verified with ICP-MS.

4.4.1.6 Discussion

Positive correlation between concentration and HU is observed in the 80keV reconstructed images, however the corresponding R^2 for 140keV is very low at 0.098, showing a very low percentage of the overall variance explained by concentration. At higher energy levels, the linear relationship is not as apparent. Even when the higher iron concentration layers are removed from the data leaving only the neurologically relevant concentrations in the analysis (0 to 315 $\mu\text{g/g}$), the correlation remains very low leaving $R^2=0.021$ for 80keV and $R^2=0.10$ for 140keV, implying that below 1mg/mL of Iron (III) Chloride, the DECT method cannot determine the difference between presence of FeCl_3 or no FeCl_3 at all (Figure 4.4.1.5.1).

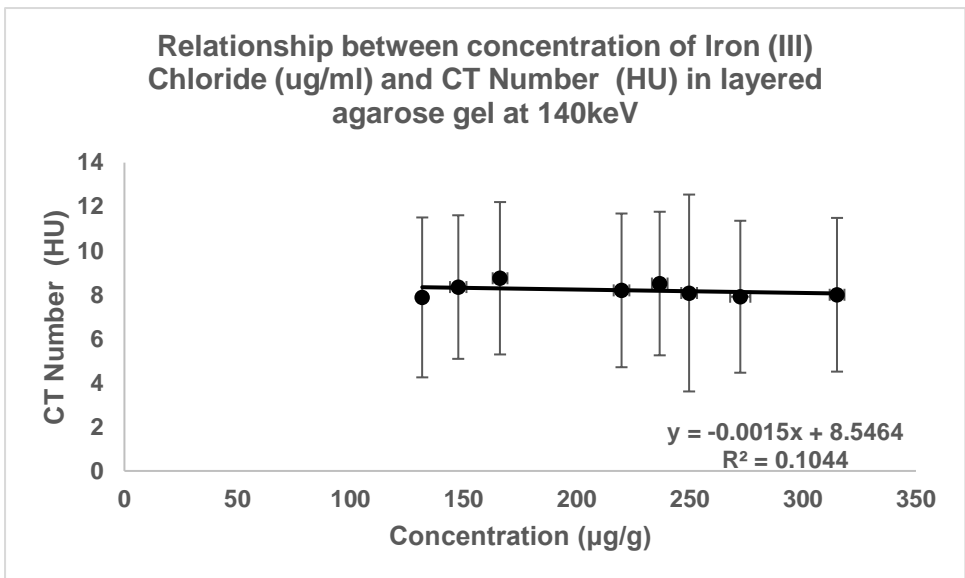
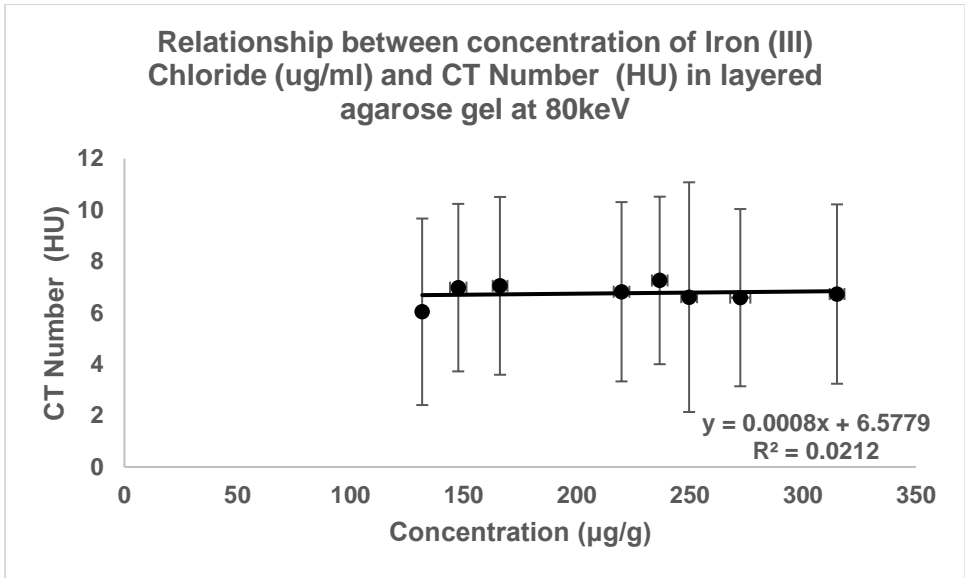


Figure 4.4.1.5.2: Concentrations ranging from 0 to 500µg/mL Iron (III) Chloride. Top: 80keV. Bottom: 140keV.

DECT was unable to specify a difference in Iron (III) Chloride concentration, even up to the highest concentrations shown in figures 4.4.1.5.1-2. The research of Jiang et al (Jiang et al., 2021) as discussed in Chapter 4.3.3 indicated a LOQ of 0.5mg/g, however this result was unable to reproduce the same level of specificity even above this limit. Additionally, the lowest and highest concentration datapoints for CT Number are both contained within 1SD of each other. There is no ability to determine concentration from HU value.

Data at 9.4T finds a linear fit of slope = 0.02, intercept 23ms. The intercept agrees closely with Finnegan's measurements at 9.4T (Mary E. Finnegan, 2013), finding the same order of magnitude for the slope (Finnegan's value = 0.07), and a similar intercept (Finnegan's value = 21ms).

In order to be detectable, there would need to exist a linear relationship with error small enough such that individual datapoints are at least 1SD away from neighbouring points.

To study the differences between the layers, 10 random ROIs were placed across the 1st, 4th, 8th and 11th layers. Their mean pixel intensity was recorded, and a t-test was performed to ascertain whether or not there was a significant difference in random sampling from each layer, as shown in table 4.4.1.5.2 and Figure 4.4.1.5.3.

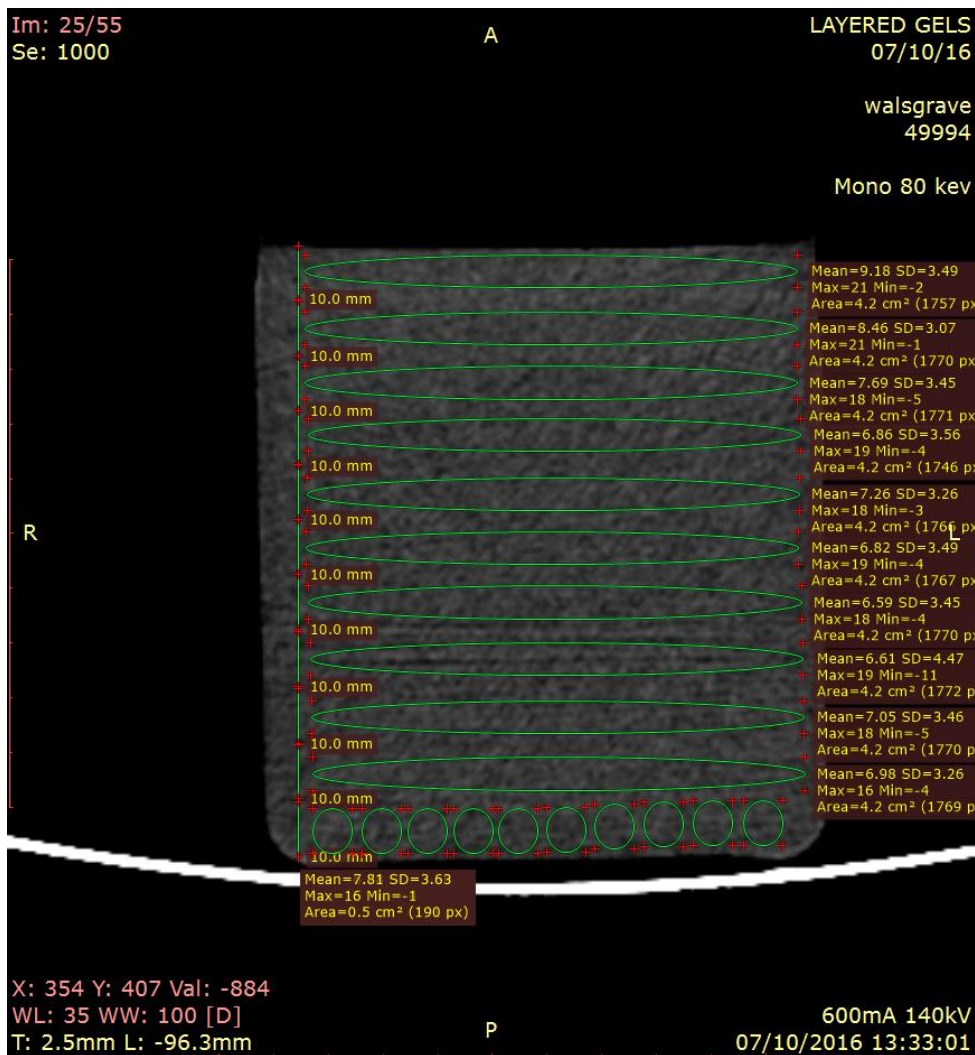


Figure 4.4.1.5.3: The bottom layer has 10 random circular samples taken from it. The same is done with the 4th, 8th and 11th layers. The 10 values for each layer are then compared using a t-test.

CT Number (HU)	CT Number (HU)	CT Number (HU)	CT Number (HU)
Layer 1	Layer 4	Layer 8	Layer 11
8.1 ± 3.6	5.6 ± 3.8	6.9 ± 3.7	8.9 ± 3.6
7.9 ± 3.4	8.1 ± 3.1	7.5 ± 3.1	8.3 ± 3.9
7.6 ± 3.2	7.2 ± 3.3	7.6 ± 3.3	9.6 ± 3.5
7.5 ± 3.1	7.1 ± 4.3	7.3 ± 3.6	8.9 ± 3.6
4.3 ± 3.8	6.0 ± 3.5	6.3 ± 3.2	6.9 ± 3.4
5.1 ± 3.6	6.5 ± 3.7	7.0 ± 3.5	8.9 ± 3.7
7.7 ± 4.2	5.1 ± 3.2	7.9 ± 3.1	8.2 ± 4.1
6.4 ± 3.7	6.9 ± 3.2	7.0 ± 3.4	10.1 ± 3.1
7.1 ± 3.6	7.3 ± 3.1	7.3 ± 3.6	10.3 ± 3.4
7.3 ± 3.0	5.6 ± 3.5	7.2 ± 4.4	8.3 ± 4.6
Mean ± SD:	Mean ± SD:	Mean ± SD:	Mean ± SD:
6.9 ± 3.5	6.5 ± 3.5	7.2 ± 3.5	8.9 ± 3.7
T-test p-value	0.24	0.26	0.0006

Table 4.4.1.5.2: 10 samples taken from each of the 4 layers indicated above, with mean HU from each compared across layers.

Each test is a one-sided t-test between the 0 layer and one of the other 3 layers.

The test statistic shows no statistically significant difference between the bottom layer (131.7 µg/mL agarose) and 219 µg/mL or 315 µg/mL of Iron (III) Chloride detectable by DECT. However, there was a significant difference between 131.7 and 7681 µg/mL at the 0.1% confidence level. While these results seem to indicate an inherent detection limit on the technique itself, it may also be due to non-ideal experimental design; the intention of the layered gel experiment was to recreate an environment where different iron concentrations are next to one another, but still self-contained and without any inter-space movement of iron. Retrospective analysis of the layers was conducted in order to test whether or not this was the case.

Analysis of the layers with MR Microscopy at 9.4T also took place. The highest concentration layer had a T2 signal decay that was faster than the gap between the first and 2nd echo time, which meant that fitting the mono-exponential decay was not possible. This is shown in Figure 4.4.1.6.1. By comparison to layer 10, the 2nd highest layer, the iron content is such that the signal does not decay before the first few echo times, as shown subsequently in figure 4.4.1.6.2.

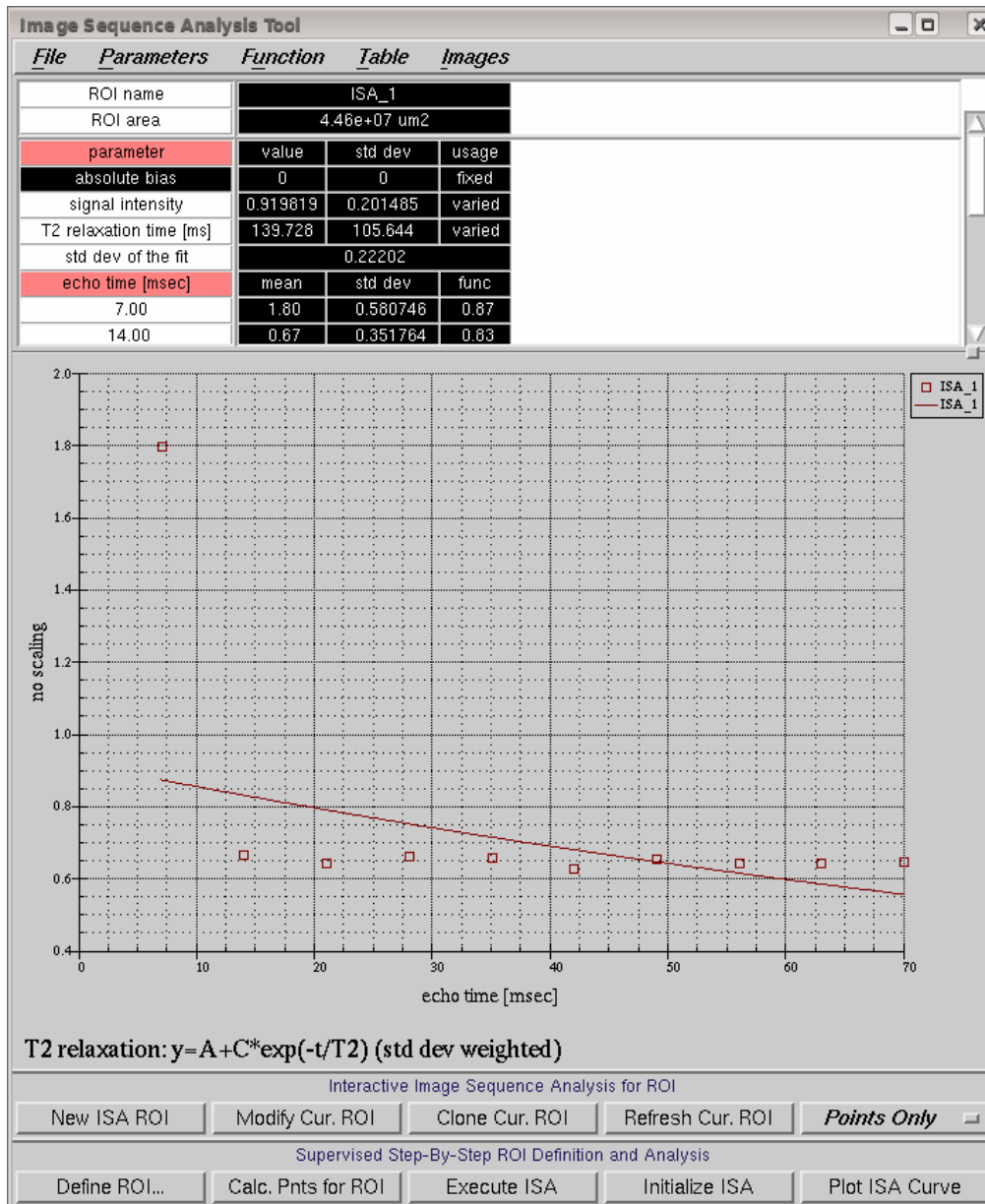


Figure 4.4.1.6.1a: Layer 11, with concentration = 7681 μ g/g. The MR signal at the 2nd echo time has already decayed to background. So no T2 measurement is possible for this layer.

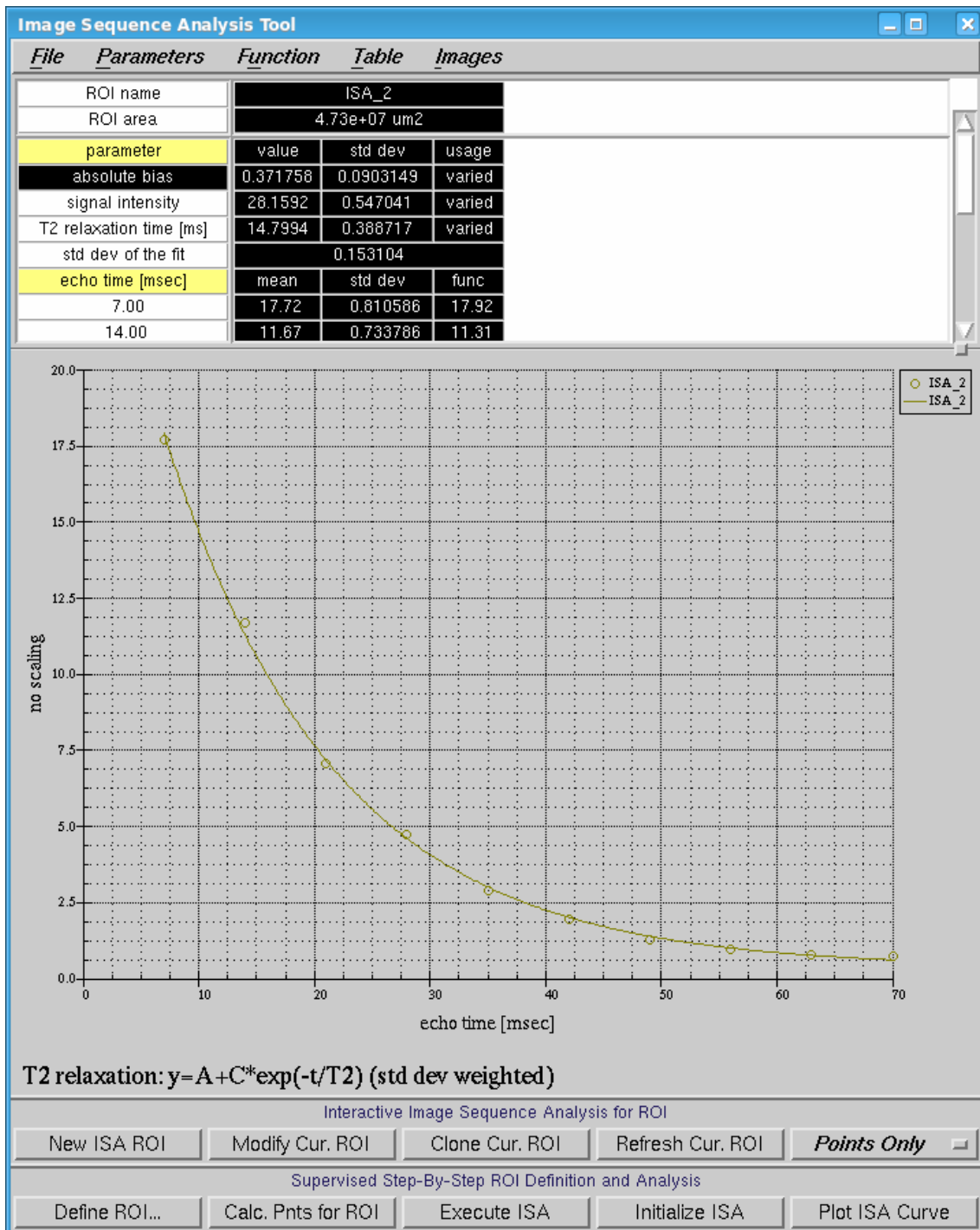


Figure 4.4.1.6.2: Layer 10 with concentration = 2851 $\mu\text{g/g}$. Note that measurement error in the signal is very small at high resolution high field MRI.

MR Microscopy at 9.4T was used to calculate R2, which was capable of determining iron concentration and distinguishing between each layer as predicted. A calibration curve was produced with linear regression with:

$$\text{slope} = 2 \times 10^{-5} \pm 1 \times 10^{-6} [\text{Fe}]^{-1} \text{ms}^{-1}, \text{intercept} = 0.023 \pm 0.001 \text{ms}^{-1}, \text{ shown in Figure}$$

4.4.1.5.1.

Future experimental design should reflect the limitations identified in this study regarding layered agarose phantoms, and as such, samples should remain separated for all future studies.

Systematic error may also have been present in constructing the phantoms. The method is detailed in 4.4.1.2. Further studies should include a measure of systematic by creating multiple copies of the phantoms, which would allow a quantitative analysis of the systematic error present. This was not possible due to limited scanner time on the clinical scanner, however an experimental design that allowed for the accurate scanning of multiple phantoms at once could have achieved this while using the same amount of scanner time. Additional work on ASIR could also provide a more appropriate monochromatic reconstruction energy which may also reduce artifacts and noise.

4.4.2 Agarose 5 gels

4.4.2.1 Summary and aims

To follow up on the layered gel experiment 5 separated agarose gels were made with varying iron concentrations. Each tube contained 50mL of agarose combined with an appropriate amount of Iron (III) Chloride to make up the desired concentration. Concentrations were within a normal neurological range as shown in table 4.4.2.3.1.

4.4.2.2 Method

Five agarose gels were made using stock TAE buffer, diluting with distilled water, and making five of the lower concentration samples up in separate tubes. In this way any possible motility-driven leeching between layers is avoided. Resulting HU values along with corresponding standard deviation values are shown in table 4.4.2.3.1. The process for creating the gels is the same as described in section 4.4.1.2.

4.4.2.3 Results

The five agarose gels were made using another stock TAE buffer, appropriately diluting with distilled water, and making five of the lower concentration samples up in separate tubes. In this way any possible motility-driven leeching between layers is avoided. Resulting HU values along with corresponding standard deviation values are shown in table 4.4.2.3.1.

Energy	0µg/g	80µg/g	120µg/g	180µg/g	250µg/g
80keV	4.66	6.69	6.42	6.56	6.39
140keV	6.46	8.68	8.54	8.84	9.3
SD	0µg/g	80µg/g	120µg/g	180µg/g	250µg/g
SD (80keV)	4.05	4.49	4.43	4.22	4.24
SD (140keV)	4.09	4.58	4.47	4.2	4.36

Table 4.4.2.3.1: HU values for each of the five agarose phantoms at 80 and 140keV, along with corresponding standard deviation values.

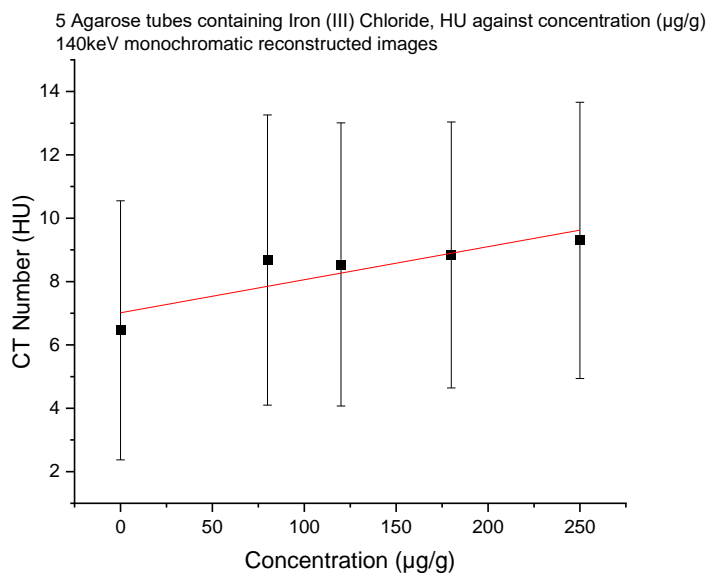
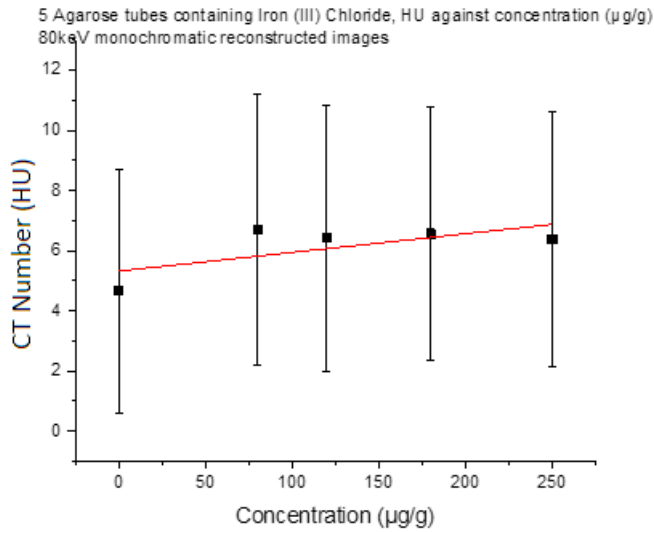


Figure 4.4.2.3.1: Top (previous page): CT Number (HU) against concentration for 5 phantoms using 80keV monochromatic reconstruction. Bottom (this page): As above but using 140keV monochromatic reconstruction.

4.4.2.4 Discussion

Linear fits to the data resulted in $R^2=0.49$ (80keV) and $R^2=0.78$ (140keV), indicating a stronger linear relationship than that found with the layered experiment (Figure 4.4.2.3.1). However, relatively large standard deviations on datapoints still render the outcome unclear. The large amount of uncertainty in the values makes drawing conclusions difficult from this data. It is unclear if the issue still remains as the low sensitivity to iron in the technique itself, or if the agarose adds an extra layer of complexity. A further study using aqueous phantoms is conducted in the next section.

One-way ANOVA analysis of both the 80keV and 140keV found that the differences in the mean were not significant ($p=0.55$ for 80keV, $p=0.26$ for 140keV).

This result also adds more evidence to the issue in the layered experiment *not* being solely due to inter-layer leaching, as this cannot have taken place in this experiment.

4.4.2.5 Conclusions

Separation of the phantoms did increase the quality of the data compared to the layered gel experiment, however the large uncertainty in the data still makes quantitative analysis impossible. It is therefore suggested that a study is done without agarose i.e., aqueous phantoms, to allow the best possible chance at quantitative analysis of iron concentration without any confounding factors.

For the main study in this chapter, the learnings of the previous studies are taken into account. Firstly, the phantoms themselves are aqueous solutions with ferric chloride used as the iron source. Secondly, the full range of the GE DECT scanner is used. While the previous studies have looked only at using 80keV and 140keV, the full spectrum of integer energies from 40 to 140keV are available as monochromatic reconstructions in the GE software. An analysis of the full range of energies will allow a more accurate analysis of whether or not DECT can detect iron at neurologically relevant iron concentrations.

A follow up study to this should be to investigate multiple energy levels and see if there is any dependency on energy. This is not possible to do at this time as monochromatic reconstructions were created at the time using the GSI software and the original data is no longer available – large multi-

energy data is routinely wiped from the hospital scanner system, and the NHS trust does not have capacity to retain data which was not used at that time.

Further, it was not possible to perform ICP-MS on these samples at the time of this experiment.

Future experimental design should ensure that this is always possible in order to obtain accurate iron concentrations for phantoms as well as experimental error in concentrations.

4.4.3 Aqueous Phantom Study

4.4.3.1 Summary and aims

The GE Discovery scanner has the capability to reconstruct any integer energy value between 40 and 140keV inclusive. In this study, we investigate the sensitivity to changes in iron concentration present at each energy level, in order to determine which energy levels should be used in quantitative analysis of reconstructed DECT images.

4.4.3.2 Method

Five 15mL aqueous phantoms were created using Ferric Chloride, $\text{FeCl}_3 \cdot 6\text{H}_2\text{O}$ as an iron source. ICP-MS was used for accurate determination of concentration.

The phantoms were placed on the tray table of the GE Discovery 750 W Dual Energy CT scanner using the alignment lasers to position them such that no air pockets were visible in the regions of interest. A GSI-9 protocol was used with 512x512 matrix size, 25cm field of view, 2.5mm slice thickness, 2.5mm slice interval, 600mAs and 2s rotation time.

The phantoms were analysed using ICP-MS, showing the concentrations to be 0, 215.5, 411.0, 512.7, 550.3 $\mu\text{g/g}$.

4.4.3.3 Results

Spectral imaging allows us to reconstruct images using 101 different energies (integer values between 40keV and 140keV inclusive). Element specific data are produced using a three-material decomposition algorithm built into the GSI workstation software. The precise mechanism of this algorithm is proprietary. Analysis is carried out by selection of regions of interest (ROIs) and analysing the resulting pixel intensity in Hounsfield Units (HU). Energy-specific CT Number data is made available by the GSI software. Regions of Interest (ROIs) were drawn inside each phantom on the GSI analysis workstation, being careful to avoid the plastic edges of the tubes and the pocket of air at the top of the tube. Eleven CT Number (HU) means were obtained for each phantom, one corresponding to each multiple of 10keV in the reconstruction range. Standard Deviation is provided

by the GSI software and is shown in Figures 1 and 2 as error bars. Comparing CT Number with energy (Fig1) showed that for each phantom, higher energy resulted in higher CT Number. The energy specific data for each phantom is shown in Fig 4.4.3.3.1. A higher gradient of linear fit for a particular energy implies a higher sensitivity to changes in iron concentration. Graphing was done using Origin (Origin Labs Ltd.) software, and data analysis was done using either Origin or MATLAB.

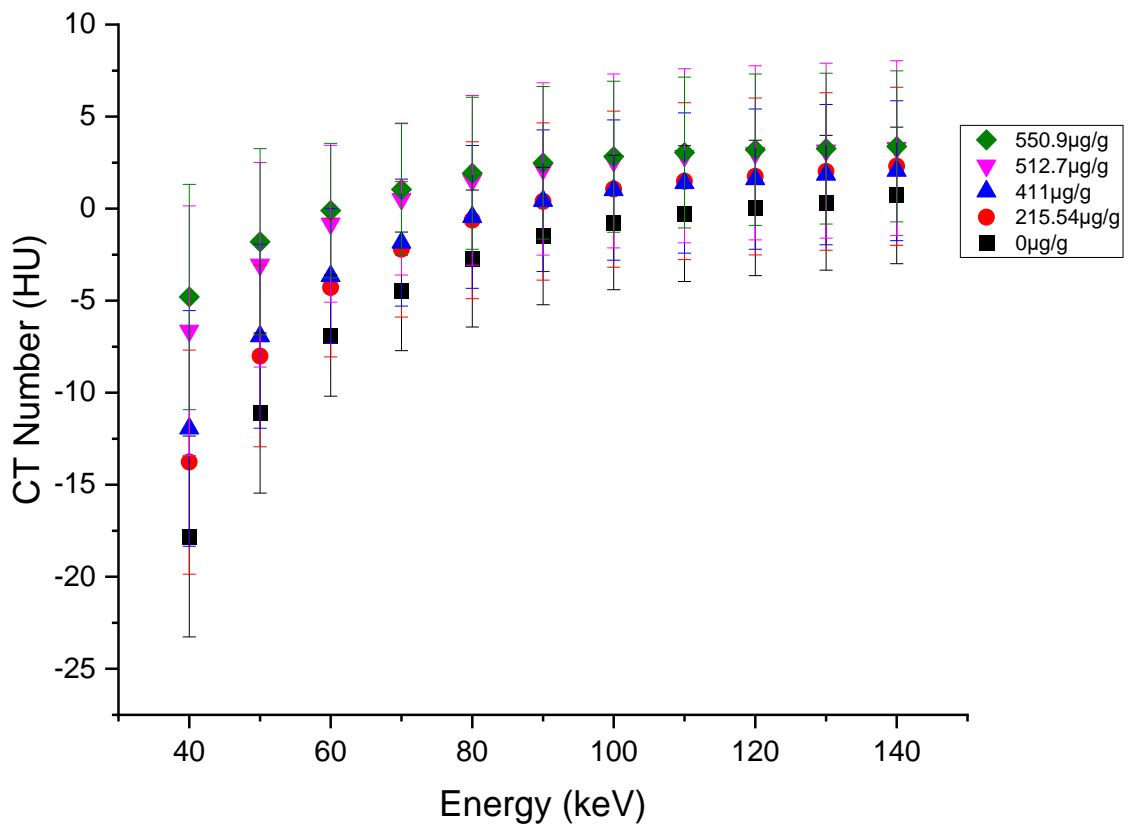


Figure 4.4.3.3.1 For each phantom, CT number was greater at higher energy.

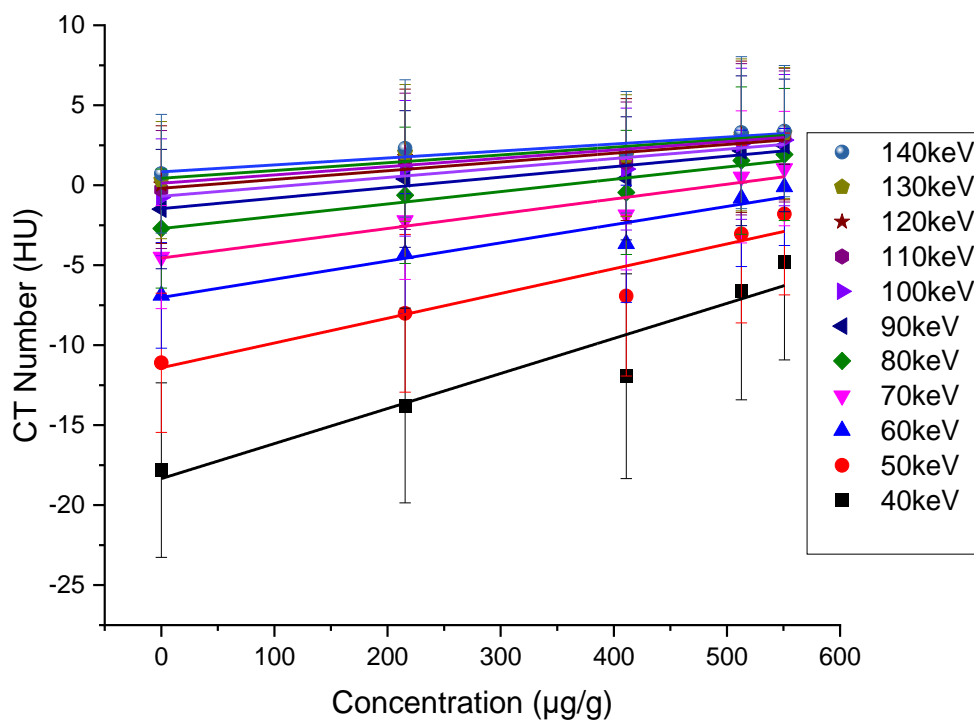


Figure 4.4.3.3.2 The same dataset from Figure 1, showing dependency of CT Number on iron concentration for a selected range of energies. For any given energy, CT Number was greater for higher concentration of iron. Note however that the gradient is greater for the lowest energies, indicating that the greatest scope for sensitivity to iron is at 40keV.

4.4.3.4 Analysis and Discussion

Figure 4.12 shows that for any given concentration of iron, the CT Number increases as the monochromatic reconstructed energy increases. However, the rate of increase with respect to energy is greatest at the low end, i.e., the CT Number increase from 40keV to 50keV is larger than that from 130keV to 140keV. No phantom had a lower CT Number than one with a higher concentration of iron, for all energies.

Figure 4.4.3.3.2 shows that the highest sensitivity to changes in iron concentration is found in 40keV monochromatic images, the lowest possible on the clinical scanner. As energy levels increase, the lines become less distinguishable – that is, the relative difference between CT numbers for a given sample, as energy increases, converges.

Error bars in Figures 1 and 2 show the standard deviation of the pixel intensity values in Hounsfield Units. Least squares regression was applied to the data to find energy dependent gradients of the linear fits, and these are shown in Fig 2. R2 of fits from Figure 1 range from 0.81 to 0.92. These fits were then analysed with another least-square regression to a standard exponential decay model, finding that the gradients themselves decay exponentially (R-Square = 0.99). This means that at higher energy, although differentiation is worse in any case, going even higher has a diminishing impact. Conversely, low energy gives the best possible detection for iron change and going lower still dramatically increases the sensitivity attained.

It should also be noted that originally, the target concentrations were different to the resulting outcome. It is possible that the resulting concentrations were different to expected due to user error in producing phantoms, due to contamination and/or degradation of the iron source (Iron (III) chloride). The Iron (III) Chloride used in the study was kept at room temperature sealed in a plastic container in the trace metals lab, department of Engineering, University of Warwick. Based on this, it is advised that phantom concentrations are verified using ICP-MS in general to ensure that not only are concentrations known, but also an error term can be obtained for more robust analysis of the resulting data.

4.4.3.4.1 CT Number behaving unexpectedly

An unexpected result of the aqueous phantom study is that attenuation appears to be less than 0 HU at energies lower than 140keV for blank (water). In fact, this is *CT Number* that is less than 0 HU.

It is important to distinguish between CT Number and beam attenuation. CT number is directly computed by the scanner. Attenuation might be inferred by a CT system which has been properly calibrated, however if this is not the case, then CT number itself may not represent actual attenuation values in terms of the *actual* physical process that is occurring.

The measurements in this study were repeated numerous times, and the same effect observed. The scanner is calibrated every day, according to the protocol outlined in Appendix 6. It is also possible

that the plastic tubing used to contain the phantoms have a detectable effect on the HU value obtained, which decreases to 0 effect as the CT energy increases towards 140keV. A paper on the establishment of HU values for reference QA phantoms in CT scanner found that adjusting the energy used in calibration could affect HU readings by up to 79HU (Sande et al., 2010). Additionally, they looked into particular materials and the impact that energy had on Hounsfield units, and saw that Polystyrene tubing had the same surprising effect observed here on 8 different scanners, where higher energy led to higher CT Number in aqueous samples. See Figure 4.4.3.4.1.1.

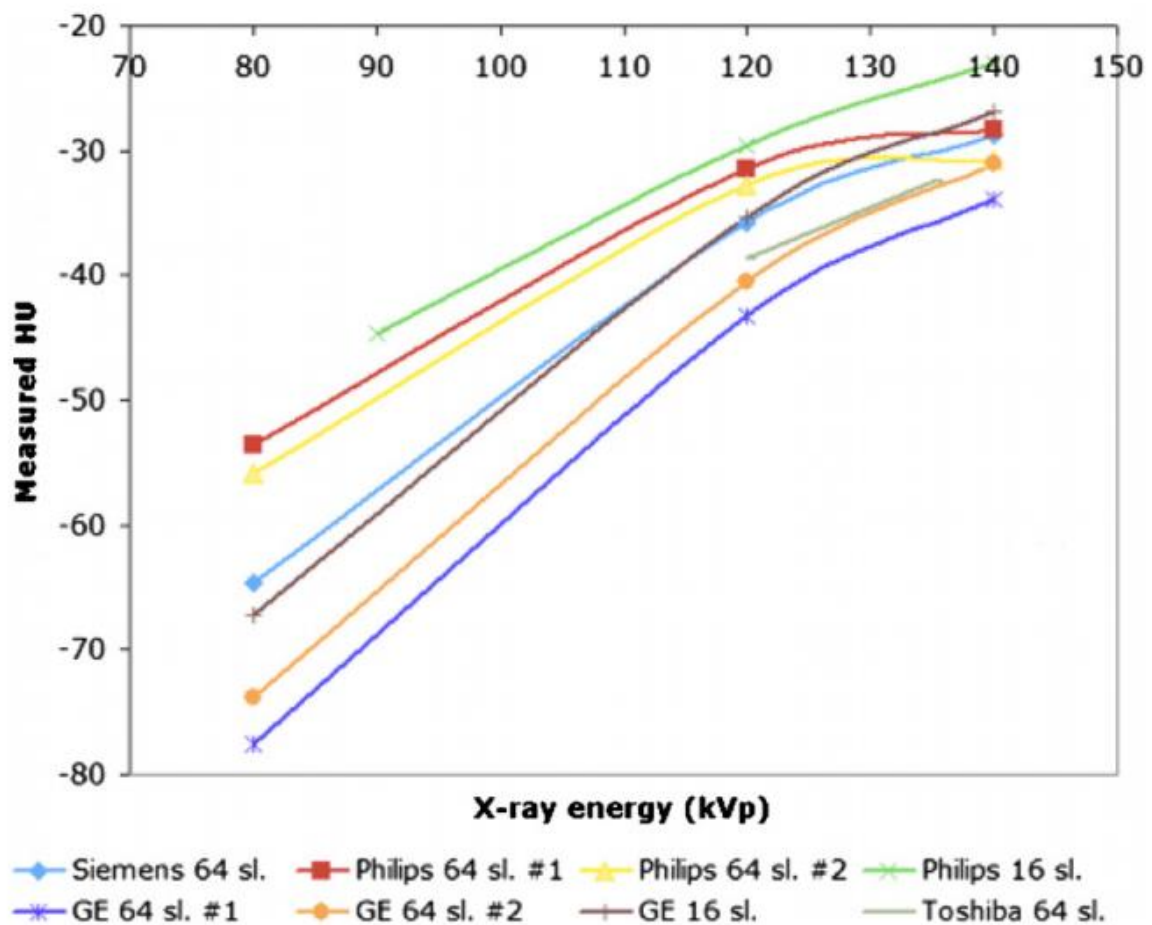


Figure 4.4.3.4.1.1: Research into measured HU variation with kVp across a range of CT manufacturers shows that increased energy can lead to increased CT Number in certain polymer-based phantoms – that is, the plastic casing of the aqueous phantom. In this figure, the sample is water, and the casing is made of polystyrene. Additionally, the phantom has $HU < 0$. Figure reproduced from (Sande et al., 2010)

A 2020 study by Suyudi et al (Suyudi et al., 2020) in which polypropylene phantoms (the material used for both the Aqueous Phantom Study (Chapter 4.4.3) and the ASIR study (Chapter 4.4.4)) also

observed higher energy radiation leading to higher Hounsfield Units (Suyudi et al., 2020). This is the opposite of the expected behaviour in tissue. It is possible that the polypropylene plastic tubing has a measurable effect on the CT beam due to interactions with the polymer itself.

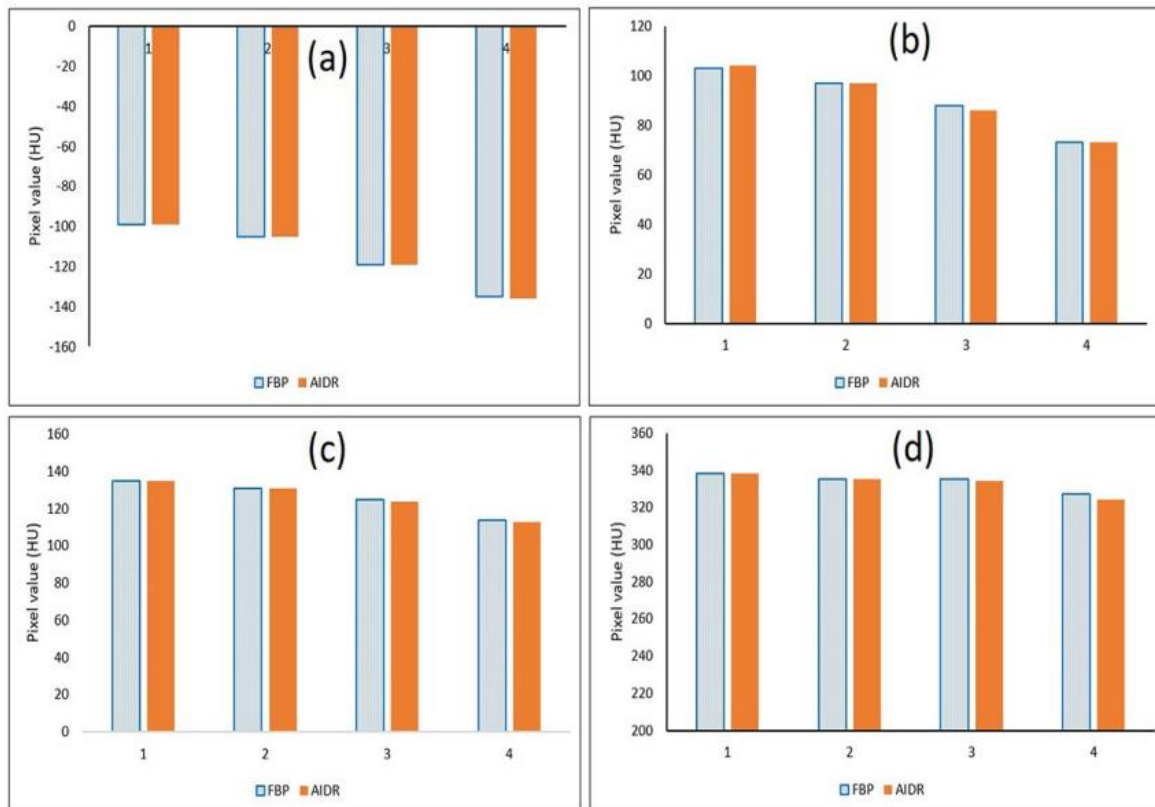


Figure 4.4.3.4.1.2: A comparison of HU values using two different methods of image reconstruction (filtered back projection, labelled FBP, and iterative reconstruction, labelled as AIDR). Image (a) is Polypropylene, (b) is nylon, (c) is acrylic, and (d) is Delrin. The numbers 1, 2, 3 and 4 refer to 135kVp, 120kVp, 100kVp and 80kVp respectively, i.e., the energy decreases from left to right, while the CT Number also decreases in each case. Figure reproduced from (Suyudi et al., 2020)

Quoting directly from Suyudi et al, referring to Figure 4.4.3.4.1.2: “The figure also shows that for all objects, the HU values decrease slightly for a lower usage of tube voltage from 135 kVp to 80 kVp” i.e., lower energy leading to lower CT Number. It should also be noted that polypropylene is the only material in this study which exhibits values below 0 HU for all measures.

Investigations into the reconstruction method as well as calibration procedure of the clinical scanner found that clinical scanner calibration passes when water is between -5 and +5 HU, so there is a range of potential values that a daily calibration can take. Additionally, this calibration is done at 80kVp, 100kVp, and 120kVp. The monochromatic reconstructed images, while theoretically producing images that are analogous to those which *would* have been captured from a single-energy CT source at the given energy, are not directly calibrated. Further studies should ensure that if 40keV monochromatic images are to be used for quantitative analysis, calibration of the scanner takes into account this low energy monochromatic reconstruction, or a method is available for adjusting the CT numbers in post-processing.

4.4.3.5 Conclusions

These results do not immediately suggest that DECT can detect iron concentration changes at human physiological and pathophysiological levels. However, there are elements of the study that are promising, namely that there exists a method of obtaining higher sensitivity by choosing lower energy monochromatic reconstructions, and that at 40keV, it may be possible to distinguish between iron concentrations. The linear fit has appropriate sensitivity and error, although there are a number of unexpected behaviours that may conflate the results. The impact of the polypropylene tube, if that is indeed an issue, is not quantifiable with this data alone. An intermediate study for the future would be to create a set of phantoms that are made of another material which interacts more weakly with the CT beam itself. Of particular importance is the exponentially decaying gradient (Fig 3), showing that lower energy X-rays are more sensitive to changes in iron concentration. By comparison with healthy human brain tissue, which will be mostly organic matter with a very low k-edge ($\sim 0.2\text{keV}$) (Minasian et al., 2013), it may be possible to identify and quantify iron concentration in regions of the human brain far more quickly and cheaply than comparable MRI techniques. This has widespread application in early detection of neurodegenerative disease, and merits further study in-vitro for potential clinical application.

4.4.4 ASIR study

4.4.4.1 Summary

A further crucial aspect of CT imaging that may play a role in image quality, and in particular the ability to quantitatively analyse CT images for the determination of iron concentration, is image reconstruction. This chapter aims to investigate the effects that Adaptive Statistical Iterative Reconstruction (ASIR) in DECT imaging has on quantitative concentration measurement from DICOM image analysis, as compared to standard filtered back projection (FBP) reconstruction methods. Six phantoms were produced of 0, 100, 200, 300, 400, 500 $\mu\text{g/g}$ Iron (III) Chloride (aq). These were scanned on a GE Discovery 750HD Dual Energy CT scanner, with no ASIR and 50% ASIR. The linear model fits the ASIR data more closely ($R^2 = 0.96$) than the non-ASIR data ($R^2 = 0.64$) suggesting that the ASIR images produce pixel data that more accurately describes the concentration of each phantom.

4.4.4.2 Introduction

Quantitative analysis of CT images fundamentally depends on a high level of certainty over the value assigned to each pixel in the final image by the reconstruction algorithm (Shepp & Vardi, 1982). Historically, CT images were produced from the raw data by the method of filtered back projection (FBP). With increasing awareness of the risks of CT dosage (Kim et al., 2011) as well as the desire for higher quality images, coupled with powerful modern computers, iterative reconstruction (IR) is finally viable as an alternative and superior reconstruction method without being overly time consuming.

As described earlier in Chapter 2, filtered back projection (FBP) works by looking at an object in the path of an X-Ray beam from many different angles and using the resulting information on X-Ray CT Number at each angle to construct an image. This is a fast and reliable method, but one which is prone to artifacts and image contamination (Jiahua Fan, 2014).

Iterative reconstruction methods are not a new idea (Hara et al., 2009); Indeed it is the advent of faster computers and in particular parallelisation of tasks (Wang et al., 2016) that has allowed these methods

to have any kind of clinical relevance. Even still, clinicians can expect anywhere from 10 to 100 times longer reconstruction time than a typical FBP method(Wang et al., 2016).

One potential application for ASIR is in quantitative analysis of trace metals in humans. DECT is to be potentially used in the future as an independent technique for iron concentration determination, without using MRI to locate regions of interest, then the increased image quality and X-Ray dose reduction from ASIR will play a role in accurate quantitative analysis.

ASIR works by first generating a standard FBP image via the traditional means, which serves as the starting point for the process, followed by forward projection which generates new images to be tested against the initial condition. After many iterations, the forward projection images will have a “best” one, i.e., the one which minimises the difference to the initial FBP image, but without the associated noise. This process is shown in Figure 4.4.4.2.1.

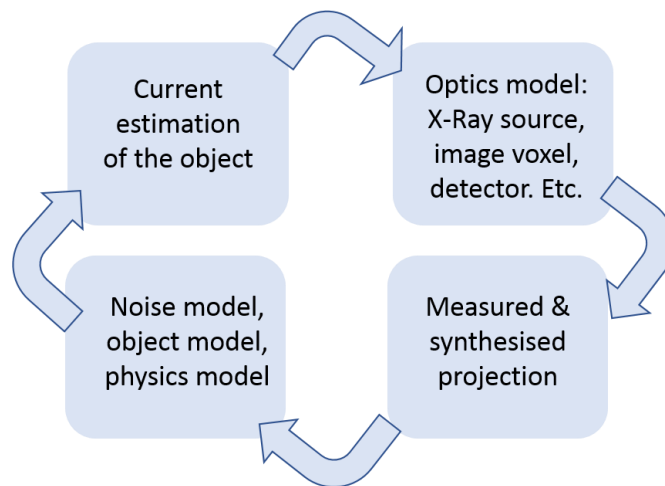


Figure 4.4.4.2.1: Flow diagram of ASIR process. Based on the same diagram in GE Healthcare white paper, Reproduced from (Jiahua Fan, 2014)

Accurate optics modelling is mainly responsible for the increased image quality and spatial resolution of ASIR images. This allows a lower dose to be used for comparable quality, or equivalently a higher image quality for the same dose. Accurate noise modelling is what mainly contributes to noise reduction, and dose reduction of up to 82% has been observed with no loss in image quality when compared to traditional FBP images(Jiahua Fan, 2014).

In 2019, Rodriguez-Granillo et al (Rodriguez-Granillo et al., 2019) published a study that identified the benefits of low keV monochromatic reconstructions, and attempted to use ASIR to reduce noise.

The authors state that low monochromatic energy levels (40 keV) derived from delayed enhancement dual energy cardiac computed tomography (DE-DECT) allow the evaluation of myocardial infarcts (MI) among stable patients, although at the expense of high image noise. They further state that the application of adaptive statistical iterative reconstruction (ASIR) to 40-keV DE-DECT might improve image quality and detection of MI in stable patients.”

In the same way, the result from 4.4.3 that 40keV reconstructions may have superior diagnostic potential is what has influenced the attempt to use ASIR to reduce image noise to aid diagnostic ability. ASIR reduced image noise, but qualitative assessment of image quality and diagnostic confidence did not significantly improve.

In this study, we aim to improve quantitative ability of DECT at 40keV by using 50% ASIR.

4.4.4.3 Materials and methods

Six phantoms were chosen for analysis produced of 0, 100, 200, 300, 400, 500 Iron (III) Chloride (aq). Water was chosen as the medium because of its appropriateness as a brain-tissue equivalent material (Ferreira et al., 2010). Each phantom was in a 15mL polypropylene test tube. These six phantoms were placed lying flat in a GE Discovery 750HD Dual Energy CT scanner, and scanned twice; once using preset GSI-30, 2.5mm slice thickness, no ASIR, and secondly using the same settings but with 50% ASIR. Regions of interest were drawn in each of the 6 test tubes, carefully avoiding the edges to minimise the risk of partial volume effects.

The GE 750HD DECT scanner is capable of applying ASIR from 0% to 100% in 10% increments. For this study, a midpoint of 50% ASIR is chosen.

4.4.4.4 Results

These data are used to test a linear relationship, which is the expected and assumed underlying model(E. S. H. Ibrahim et al., 2015). In order to conduct quantitative DECT, a robust and predictable model needs to be available from the reconstruction. A strong linear relationship which closely

matches the data is imperative for further application as an effective calibration curve. In this section we test which of the two reconstruction methods gives rise to a stronger linear fit, implying that this method is less prone to noise and indicating appropriateness to quantitative analysis.

Figure 4.4.4.4.1 shows the CT Number (HU) plotted against concentration for each phantom, and at both 0% and 50% ASIR. Each region of interest (ROI) contained 678 pixels, and so the standard error of the mean (SEM) was calculated by the formula $\frac{SD}{\sqrt{n}}$ where SD is the standard deviation of pixel values in the ROI, and n is the number of pixels. The standard error of the mean describes how the measured mean deviates from the true mean of a population. Table 4.4.4.4.1 shows the values observed.

Phantom concentration ($\mu\text{g/g}$)	CT Number (HU) (0% ASIR)	SEM	CT Number (HU) (50% ASIR)	SEM
0	-11.8	± 7.1	-10.4	± 7.3
100	-7.75	± 7.4	-7.44	± 7.0
200	-5.77	± 7.0	-6.44	± 7.2
300	-2.1	± 7.0	-3.29	± 7.3
400	-0.86	± 7.3	-1.96	± 7.1
500	-3.95	± 7.1	-0.97	± 7.2

Table 4.4.4.4.1: Mean CT Number values and standard error of the mean for each of the 6 phantoms with 0% ASIR and with 50% ASIR.

Figure 4.4.4.4.1 shows the linear fits to the data. A statistics summary for these linear fits is shown in Table 4.4.4.4.2.

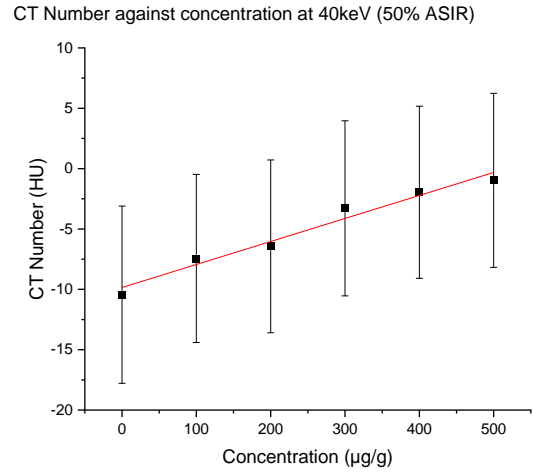
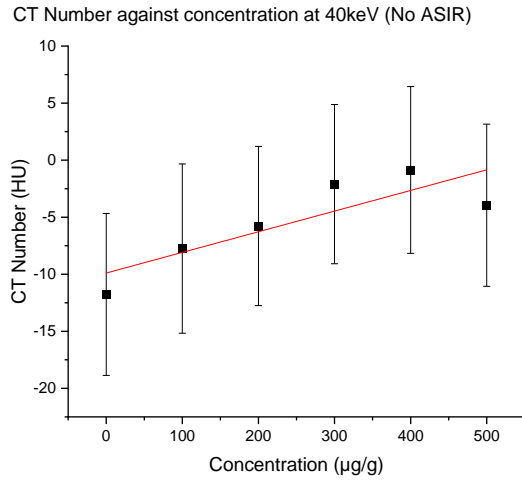


Figure 4.4.4.4.1: The result of scanning with (Left) 0% ASIR, and (Right) 50% ASIR. Error bars show the standard error of the mean within the chosen region of interest. R^2 (0% ASIR) = 0.64, R^2 (50% ASIR) = 0.96

ASIR	Gradient	Intercept	R^2	RSS
0%	0.01 ± 0.006	-9.9 ± 1.7	0.64	300.2
50%	0.02 ± 0.001	-9.9 ± 0.5	0.96	25.7

Table 4.4.4.4.2: Statistics of the linear fit shown in Figure 4.4.4.4.1. RSS = residual sum of squares

4.4.4.5 Discussion

Graphing and statistical analysis was done in OriginPro 2016 (Origin Labs Ltd). It is important to note that the phantoms themselves are not touched or interfered with in-between the non-ASIR and the ASIR scans, thus any difference in pixel value is entirely due to the ASIR.

50% ASIR enabled the same set of phantoms to exhibit a stronger linear fit, improving R^2 from 0.64 to 0.96. Residuals are plotted in Figure 4.4.4.3, showing no systematic error or bias.

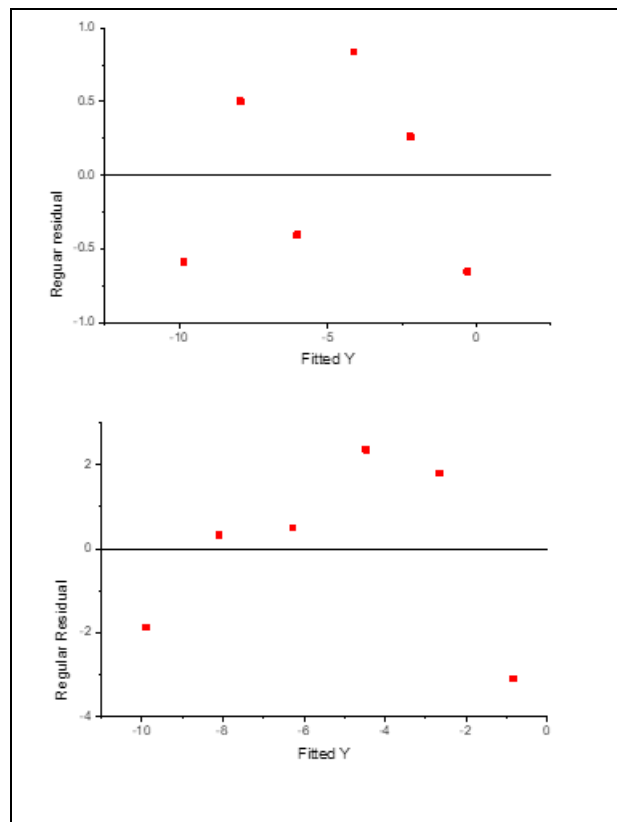


Figure 4.4.4.3: Residual plot for both No-ASIR (top) and 50% ASIR (bottom).

In 4.4.4.1, the 500 $\mu\text{g/g}$ datapoint behaves differently to the other datapoints, i.e., mean CT Number is lower despite concentration being higher. This value is still well within the standard error shown; however, this point “moves” closer to the linear regression once ASIR is applied. All datapoints are within the standard deviation of the first and last datapoint. This means that this result could be due to noise or other error. Further, error in iron concentrations is not possible to obtain without a corroborating analytical technique such as ICP-MS, which was not possible to carry out at the time of this experiment. This should be included in any future work related to this study.

The results in this section provide some limited evidence for increased accuracy attained when using iterative reconstruction for DECT images that are being used for quantitative analysis, specifically that the use of ASIR moves the data towards the expected underlying linear model. Studies have shown (Widmann et al., 2017; D. Zhang et al., 2011) that the use of ASIR should not have a negative impact on spatial resolution, so this protocol is appropriate for use in a further study and should not have negative impact on scanning protocol. The standard deviation of each region did not significantly change. SEM remained very similar (all values within 0.27-0.28). Other studies in the literature which observe a similar effect of no significant change to SD (or SEM) when using ASIR (Vorona et al., 2013). A 2020 paper from Sherif et al looking at paediatric brain imaging showed a difference in signal-to-noise between 60% and 80% ASIR, but again this difference was not significant (Sherif et al., 2020).

Phantoms in this study contained only one variable, namely the concentration of Iron (III) Chloride, and so CT Number changes can be attributed to this concentration change. However, in-vivo further study would use spectral imaging elemental assignment in tandem with ASIR. This is not possible to achieve retroactively, and so this should inform future study design. This has potential application in diagnostic imaging, where in particular MRI diagnosis of neurodegenerative disease is sometimes impossible due to some of the patients being unable to have an MRI scan because of metal implants, or the patient being unable to lay still for the extended period of time required for a typical clinical MRI scan. In this capacity, DECT scans have a distinct advantage in that they only take 2.0s for the scan to complete, and there is no magnetic field involved meaning patients with implants can still be scanned.

A drawback of CT is that each scan delivers a dose of radiation, which can be potentially harmful in the long-term. ASIR is the latest advancement in dose reduction in clinical CT, allowing an equivalent image to FBP to be constructed with up to 82% dose reduction (Jiahua Fan, 2014). In this study, dosage was not reduced, and instead image quality was increased. Naturally, an investigator may also choose to strike a balance between these two and conduct a study using a lower than standard dose, while achieving higher than standard image quality.

This study would be strengthened in the future by using the same ICP-MS technique for phantom concentration verification as was performed for the study outlined in 4.4.3.

Further information could be obtained as to the strength of ASIR in this area by looking at more than one application i.e., 50%. While this is not possible in retrospect, a study can obtain ASIR reconstructions at varying levels (0 to 100%, increments of 10%) and this is limited only by computation time, not by scanner time. Thus, this should be investigated further in future work.

The measured values in this study informed the study design for the cadaver work in chapter 5, suggesting that use of ASIR 50% was better than not using ASIR. This result would be strengthened further by understanding and experimenting with the impact of progressively increasing the level of ASIR.

4.5 MRI Phantom Study

An MRI phantom study was carried out using a 400MHz 9.4T NMR spectrometer with MR probe. This process allowed analysis of iron-based phantoms in a lab environment outside of the clinical setting.

4.5.1 Summary and aims

In order to test whether or not iron chloride phantoms would exhibit the expected linear relationship between iron concentration and R2 relaxation rate, an MR microscopy experiment setup looked at acquiring ten single-echo images from TE=10ms to TE=100ms in increments of 10ms, using iron chloride (aq) with iron concentration ranging from 0 to 250µg/g.

4.5.2 Method

4.5.2.1 MR Microscopy

MR Microscopy (MRM) is physically equivalent to MRI, but at a resolution scale down to 100 microns. High field strengths are used to enable spatial resolution below 100µm (Ly, 2011). While MRM is a useful technique for imaging small in-vivo features, e.g., brain anatomy in mice, it is also a useful quantitative MRI technique.

4.5.2.2 Image acquisition

Six 15mL aqueous phantoms were created using Ferric Chloride, FeCl₃.6H₂O as an iron source. Concentrations were 0 (water), 50, 100, 150, 200, 250 µg/g.

Each individual phantom was first scanned using a localizer sequence, to ensure accurate spatial registration of the phantom. Figure 4.6.2.1 shows the before/after of the localizer scan for one example sample. Once the localizer scan has located the image, crosshairs are displayed showing the centre of the imaging FOV. The operator can then manually box-select the region of interest using a square, and this region becomes the FOV, which ensures that the object to be imaged is not only central within the FOV, but also entirely contained within it.

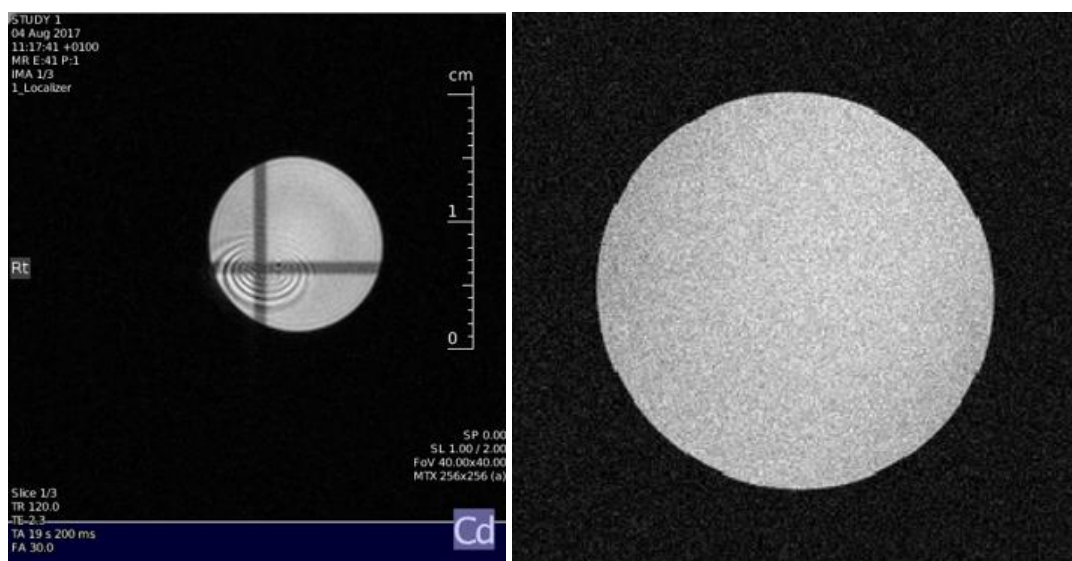


Figure 4.5.2.2.1: Left: The result of the localizer scan. The phantom is off centre within the imaging probe. The sequence for the localiser is not optimised for a clean image, simply as a fast and practical image registration tool for the spectrometer operator, so there are image artifacts present in the localiser image. Right: The final image as obtained once the image registration is complete.

Once the sample is correctly located, tuning sequences were used to ensure a clean mono-exponential free induction decay, shown in Figure 4.5.2.2. Before imaging, the probes were tuned and matched to the ^1H channel. The software TopSpin was used to manually shim the gradients until a smooth free induction decay (FID) of maximum size, and a symmetrical, as narrow as possible water peak with a full-width-half-maximum (FWHM) of below 60 Hz was achieved. The software ParaVision, proprietary software provided by Bruker along with the MR probe, was used to capture MR images.

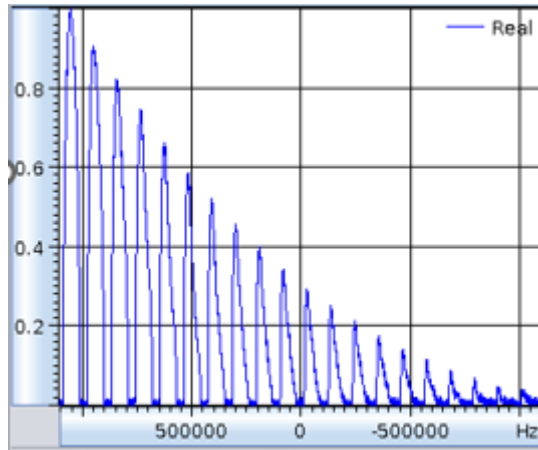


Figure 4.5.2.2.2: Free induction decay follows a mono-exponential decay when the scanner is correctly tuned via the shim coils.

4.5.3 Results

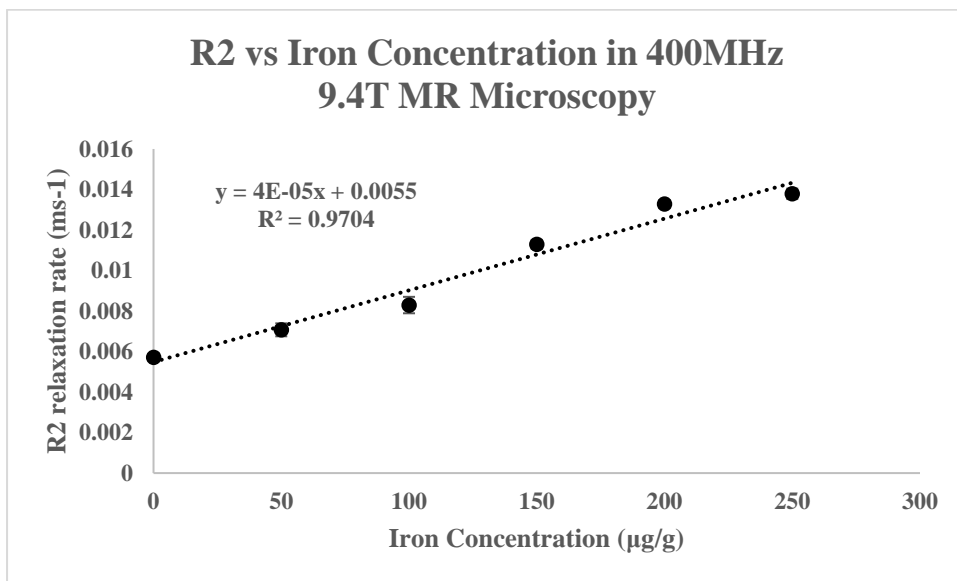


Figure 4.5.3.1: Results of phantom study at high field 9.4T MRI.

R2 relaxation rate was obtained from a mono-exponential decay fit to each of the ten echo times, shown in Figure 4.5.3.2.

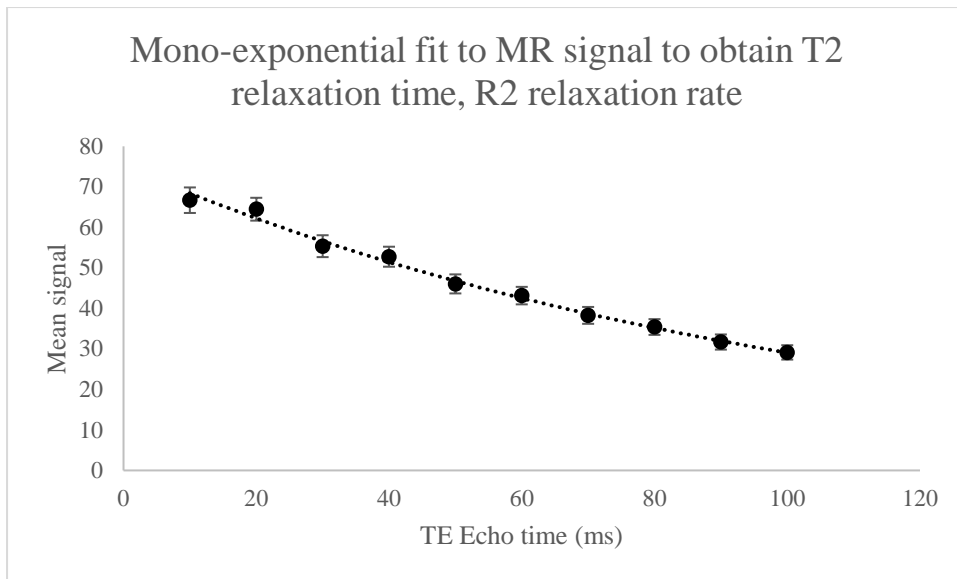


Figure 4.5.3.2: One example mono-exponential decay used to obtain T2 and hence R2 measurement. The data is reproduced from a ParaVision report that is generated by ParaVision software.

4.5.4 Analysis and discussion

As expected, at high field, error in R2 is low due to the high resolution and low relative SD for T2 values. A strong linear relationship is detected, with $R^2 = 0.97$ indicating that 97% of the variance in R2 is explained by the independent variable, iron concentration.

However, error in phantom concentration was not calculated. In order to be more certain of the error within the phantom concentrations, it was determined that ICP-MS should be used in future experimental design to accurately determine the concentration of each phantom. This was subsequently done for the layered gels experiment (4.4.1) and aqueous phantom study (section 4.4.3).

Finally, this is a model system with aqueous iron solutions in a highly controlled high-field environment, which does not precisely mimic the complexity and additional effects found in human tissue.

4.6 Discussion and further work

Phantom studies on MicroCT could help in being able to observe systematic error, as this would not be limited by hospital availability. Further, MicroCT devices are capable of scanning at single

energies and at lower than clinical energy levels (lower than 40keV). This could lead to additional energy-dependent studies being conducted, and a better understanding of the energy-attenuation relationship present in these phantoms.

An additional study using a medium even closer to human brain would be a good bridging step between this preliminary work and work with cadaveric human tissue. This was not possible due to time constraints using the clinical scanner, and so the human tissue cadaver study was prioritised.

A potential way of measuring the effect of brain tissue would be to use post-mortem animal tissue. The study design would involve scanning this tissue using DECT and obtaining CT Number values (HU) for each sample, and then using ICP-MS to directly measure the exact concentration of each sample. This would provide an even closer representation to using the technique in humans, and would allow full access to the tissue afterwards for accurate iron concentration determination.

Luo et al (Luo et al., 2015) carried out DECT using monochromatic reconstruction images on rabbits in order to detect liver iron concentration. The concentration range was significantly higher than neurologically relevant iron concentration range in human brain regions, nonetheless, successive studies that optimise the experimental design would be benefitted from having to also accommodate the matrix effects of living tissue. At present, the jump between phantoms and human tissue is very large, and additional bridging steps would aid progress in this area.

In June 2022, Lui et al (Leening P. Liu1, 2 et al., 2022) released a pre-print study where the spectral performance of DECT systems at 50keV and 150keV monochromatic reconstructions were used on tissue-like phantoms containing iron. However, iron concentration ranged from 5mg/mL to 11mg/mL, which is typical for liver iron overload (Fischer, Reiner, et al., 2011) but over 10x higher than expected values for brain iron (Barbosa et al., 2015). Phantom studies continue to be published in this space regarding DECT but still not at neurologically relevant iron concentration. The inability to quantify iron at these levels is consistent with the literature, in that no studies have been published which have demonstrated this ability. Toia et al (Toia et al., 2021) have suggested a lower limit of

detection that may allow for accurate brain iron determination, however the error on their estimate is large (200µg/g - 600µg/g).

The % of ASIR chosen was the midpoint of the available ASIR protocols, with freedom to experiment with this limited by time available on the clinical scanner. A further study into optimising the chosen level from 0% to 100% would be beneficial to understand what level of ASIR is most beneficial. In a 2018 paper, Tang et al looked at ASIR from 10% to 100% for subjective diagnostic ability. They determined that 50%-70% was the best range for diagnostic purposes, (H. Tang et al., 2018). It would be useful to compare the subjective radiographer-reported “best” images from a diagnostic point of view, with a statistical analysis of the images generated from each.

Additionally, ICP-MS (or another analytical technique) was not performed to confirm the concentration of iron present in all studies, meaning there may be some amount of systematic error in producing the phantoms. This should be addressed in the future and experimental planning and design should ensure that ICP-MS phantom concentration analysis always takes place.

Overall, at neurologically relevant iron concentration ranges, the 50% ASIR technique combined with low 40keV monochromatic reconstructions appears to show the highest realistic chance of any ability to quantify brain iron concentration. Further work on Cadavers will therefore use this study protocol.

4.7 Individual contribution

All phantom studies were developed by myself, including all experimental design, research, sample preparation in the lab, transport to the University Hospital and scanning on the clinical scanners, as well as all experimentation and analysis of the layered gel experiment using 9.4T MR Microscopy at Milburn House, University of Warwick. All data analysis was my own. Support was provided by Dr Sarah Wayte in operating the clinical scanner safely.

Chapter 5 - Cadaver Study

5.1 Summary

In order to attempt to create a reliable calibration curve measuring iron concentration human brain tissue against measured CT Number in HU, two cohorts of 4 cadaveric human heads were obtained from University Hospitals Coventry and Warwickshire. Ethical approval for this study was obtained from BSREC (See appendix 2).

Images of each head were taken using both DECT and MRI. MRI was used in order to accurately determine iron concentration in the brain regions of interest, which were Globus Pallidus, Red Nucleus, Putamen, and Substantia Nigra, each both left and right, i.e., 8 regions in total per sample.

Four of the samples (all from the first cohort) had sufficiently intact tissue structure in the cadaveric tissue to produce images that could be analysed in detail, and quantitative measurements taken, on both DECT and MRI.

No relationship could be detected between CT Number (HU) and iron concentration in any of the 4 samples. Large sources of noise from both attempting the imaging technique at neurologically relevant iron concentrations which may be below the detection limit, as well as the presence of putrefactive gas build-up in the cadaveric tissue, are discussed as possible causes.

It is concluded that at present, this technique is not suitable for determining brain iron concentration in cadaveric human tissue. To confirm this result, a human trial scanning participants on both DECT and MRI would be required.

5.2 Introduction

The results from the DECT Phantom study chapter indicate that DECT imaging, and specifically monochromatic reconstructions, can be used as a quantitative analytical method for determining iron concentration in an aqueous iron phantom in some conditions. As discussed, existing DECT studies (Luo et al., 2015) have been able to produce quantitative analysis of iron concentration in liver iron

overload, albeit at higher concentration levels than those found in typical physiological and pathophysiological brain regions.

This chapter describes the development towards a novel proof-of-concept for DECT imaging of the human brain in order to determine region-specific iron concentration, in a way that is analogous to the current standard practice non-invasive methods – QSM and T2 relaxometry. The results are somewhat inconclusive; various conflicting matrix effects found in the brain appear to make the technique inadequate for iron determination, but this is difficult to know for certain due to large quantities of gas found within the cadaveric heads which make the DECT images difficult to analyse.

Two cohorts of 4 cadaveric heads were scanned and analysed using both DECT and T2 Relaxometry on two separate occasions. The data from cohort 1 is presented in this chapter for analysis and discussion. Cohort 2 had significant damage and putrefactive gas build-up preventing any analysis.

This study was granted ethical approval by the University of Warwick Biomedical & Scientific Research Ethics Committee (BSREC), see Appendix 2.

5.3 Literature review

5.3.1 Imaging in post-mortem tissue

Post-mortem analysis is a crucial technique that has enabled advances in medical science and understanding for millennia, however there are a number of issues that arise specifically in this space which are relevant to this study.

Persson et al showed in their 2008 study that DECT provides improved soft-tissue discrimination and visualisation as compared to single energy traditional CT (Persson et al., 2008).

A 2012 review article from Lundstrom et al (Lundström et al., 2012) outlines many of the key issues facing research studies that use post mortem tissue specifically in clinical imaging, i.e. clinical MRI and CT.

In clinical pmMRI (post-mortem MRI), the main issue is temperature(Lundström et al., 2012). Cadavers are typically frozen and the temperature is not only below room temperature, but changes over the course of a typical MRI scan. The current state-of-the-art for post-mortem CT and MRI is outlined by Persson et al in a 2011 paper (Persson et al., 2011). The authors identify that DECT is the best possible approach for pmCT (post-mortem CT), while a T1 weighted MRI sequence gives the best possible image contrast for MRI. However, in the case of this study, we need to use MRI for quantitative iron measurement and so T2 weighted image sequences are required.

In clinical pmCT (post-mortem CT), the main issue is putrefactive gas build-up (Lundström et al., 2012). Within insufficient freezing, putrefactive gas build-up over 2-3 days can completely block the possibility to obtain sufficient images for visual inspection. Post-mortem quantitative DECT is not documented in the wider literature, and this is the first study of this type. However, it is likely that this putrefactive gas build-up, if present in the cadaveric heads in this study, would greatly impair or entirely block the possibility for quantitative analysis.

5.3.2 In-vivo DECT

While a quantitative DECT study into human brain iron has not been conducted before, some key areas of literature are important to understand in order to place this study into context within the wider existing literature. There are two main areas that need to be understood in order to draw meaningful conclusions from this study: first, the properties of post-mortem tissue under CT and MRI scanning, particularly in the brain. As the deceased tissue decays, putrefactive gas continually degrades the tissue and therefore the image quality, limiting the extent to which conclusions can be drawn about the donor's neurological tissue when they were still alive. Second, the effects of freezing and defrosting on neurological tissue. Tissue degradation from the thawing process may produce images that are significantly distorted or contain large volumes of artefacts, making quantitative analysis more complicated.

A 2012 study (A. B. Smith et al., 2012) set out to retrospectively classify and describe the range of effects that can be expected to be present in a CT scan of a human brain after death, with the primary purpose being one of caution: specifically, to educate and aid investigators into not confusing expected post-mortem tissue features for pre-mortem neurological pathology. Imaging of post-mortem tissue, sometimes referred to as *Virtual Post-Mortem*, has seen some use as a complementary technique to traditional autopsy (Levy et al., 2006). Not only can imaging provide additional insights to post-mortem study, but it can also direct an investigator to a specific location in the body that may require close inspection.

If virtual post-mortem is to be of use, it is crucial to understand the natural physiological processes that affect neurological tissue directly after death. A retrospective review of 33 post-mortem CT head scans was undertaken, with none of the participants having suffered head or face trauma related to their cause of death. 24 died from other bodily trauma, and the other 9 died from other causes (all cardiovascular related). All subjects were scanned within 72 hours of death, allowing the investigators to study and catalogue the immediate degradation effects of the brain after death.

Imaging was performed on a LightSpeed 16 Xtra (GE Healthcare, Milwaukee, Wisconsin). Whole body (head to toe) images were acquired using helical CT imaging in the axial plane. Slice thickness of 1.2mm and slice interval of 1.3mm was used, and scanning energy was 120kVp with 480mAs.

There are two findings from this paper that are of high importance to this study. The first is that in post-mortem tissue, the integrity of the sulci within the brain is deteriorated, and the grey-white distinction is significantly reduced, as shown in Figure 5.3.1.1. This makes image segmentation extremely difficult, meaning the segmentation needs to be a manual process of careful measurement from known landmarks e.g., the eye sockets, and the maximal length of the head.



Figure 5.3.1.1: This non-contrast CT image shows loss of the grey-white differentiation, as well as an inability to see the sulci of the brain. Figure reproduced from (A. B. Smith et al., 2012)

The second finding is the presence of putrefactive gas in the brain, as shown in figure 5.3.1.2. The authors warn that this should not be confused for pathological gas build-up. The effects of putrefaction have been known for a long time, and the gases released along with their role in the breakdown of tissue were categorised by Andrjevski in 1928 by carefully isolating each gas and testing its effects on agar plates (Andrjevski, 1928).

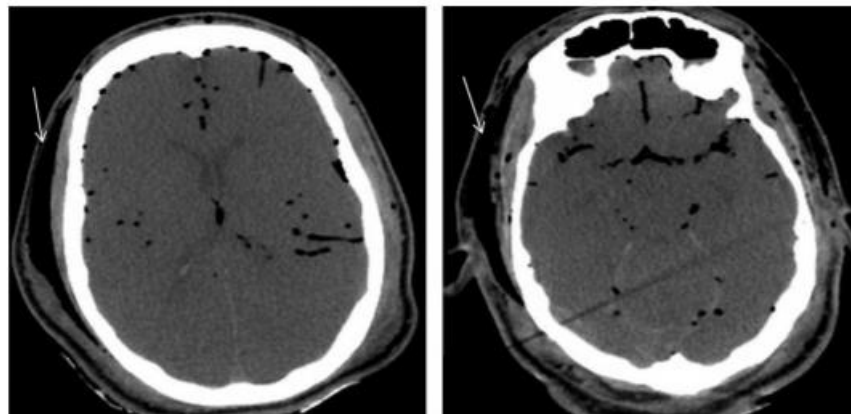


Figure 5.3.1.2: The black spots in the above images are pockets of putrefactive gas that are present in the brain tissue.

Figure reproduced from (A. B. Smith et al., 2012).

Offiah and Dean et al. document the putrefactive changes in the body after death, as well as after standard post-mortem preservation protocol, and include multi-modal imaging on both MRI and CT

for comparison. FLAIR, T1 weighted, and T2 weighted MRI is used in the study, as well as single energy CT.

Relevant to the study presented in this thesis, the effects of temperature on T2 signal are described.

Figure 5.3.1.3 shows an axial T2 weighted image of the thorax from a cadaver that was moved from a mortuary to the scanner with minimal transfer time. The lower temperature suppresses the typically higher T2 signal of the fat.

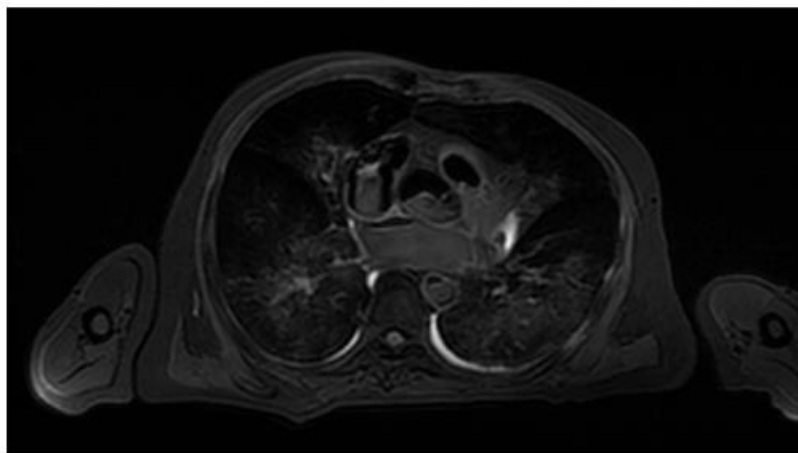


Figure 5.3.1.3: Axial T2 weighted fast spin-echo MRI sequence of a cadaver with temperature reduced due to storage in a mortuary. Figure reproduced from (A. B. Smith et al., 2012)

Further, T2 signal decay is significantly faster in frozen tissue. In fact, Kobayashi et al. showed in their 2010 paper that T2 signal decay is linearly proportional to temperature (Kobayashi et al., 2010).

5.4 Method

The techniques developed from phantom studies were applied to two groups of 4 cadaveric heads (total n=8). The second cohort of heads had severe damage and putrefactive gas making analysis impossible (see discussion of this chapter). The first cohort of 4 heads were used for analysis.

Based on our previously observed results in relation to both the use of low energy (40keV) monochromatic reconstructions, we aim to determine the accuracy to which DECT can be used to quantitatively assess iron concentration in the cadaveric heads. The CT protocol therefore mimics the

ASIR phantom study, using 40keV monochromatic reconstructed images for analysis, and 50% ASIR on the GE 750W DECT scanner.

T2 relaxation time was calculated from MR images and was compared with known age-corrected data to determine iron concentration, and monochromatic reconstructions of DECT images were analysed and compared to see if there was a correlation between the MRI and DECT images. In addition to this, ASIR data was collected at the same time as each DECT scan in order to compare the accuracy and analytical merit of using ASIR in quantitative DECT for human brain scans.

This study was granted ethical approval by the University of Warwick Biomedical & Scientific Research Ethics Committee (BSREC), see appendix 2.

The four samples came from deceased patients who were of ages 89-99 and with varying degrees of neurodegenerative disease, outlined in Table 5.4.1.

PATIENT	INFORMATION
PATIENT A	94-year-old male. 1-3 years of dementia before death. Diagnosed Parkinson’s Disease.
PATIENT B	95-year-old female. 1-3 years of dementia before death. Cause of death listed as senile brain degeneration.
PATIENT C	99-year-old male. 3-10 years of memory loss and confusion – dementia listed as secondary cause of death.
PATIENT D	89-year-old male. Alzheimer’s Disease diagnosed.

Table 5.4.1: The four heads used in the study for analysis.

Elevated Iron levels are expected in each of the 4 patients, given their advanced age and presence of dementia symptoms.

The heads were placed in the gantry of a GE Discovery MR750w 3T MRI scanner located at University Hospitals Coventry and Warwickshire, Coventry, UK, using a head coil for MR imaging. The scan parameters are listed in Table 5.4.2.

PARAMETER	VALUE
SLICE THICKNESS (MM)	2.5
REPETITION TIME (MS)	2500
ECHO TIME (MS)	10, 45, 80
NUMBER OF AVERAGES	1
IMAGING FREQUENCY (MHZ)	127.8
IMAGED NUCLEUS	1H
MAGNETIC FIELD STRENGTH (T)	3
SPACING BETWEEN SLICES (MM)	2.5
PIXEL BANDWIDTH (HZ)	244.141
ROWS	256
COLUMNS	256

Table 5.4.2: MRI scan parameters for study

The samples were also scanned using Dual Energy CT on a GE 750HD DECT scanner. Scan parameters using GSI preset 9, the highest mAs possible with the scanner, are listed in Table 5.4.3.

PARAMETER	VALUE
SLICE THICKNESS (MM)	2.5
SLICE INTERVAL (MM)	0
MAS	600
NUMBER OF AVERAGES	1
FIELD OF VIEW	25cm
MATRIX SIZE	512

Table 5.4.3: DECT parameters used in study

5.5 Image processing

5.5.1 ITK-Snap ROIs

3D regions of interest were generated and propagated throughout the brains in order to quantitatively measure MRI and DECT pixel values. Full range of ROIs are in appendix 7.

3D ROIs are generated and applied to image stacks on both MRI and DECT. Image registration is done manually using the skull as a rigid body.

See figure 5.5.1.1 for an example of a 3D region of interest generated from Patient A. The remainder of all regions is in Appendix 7.

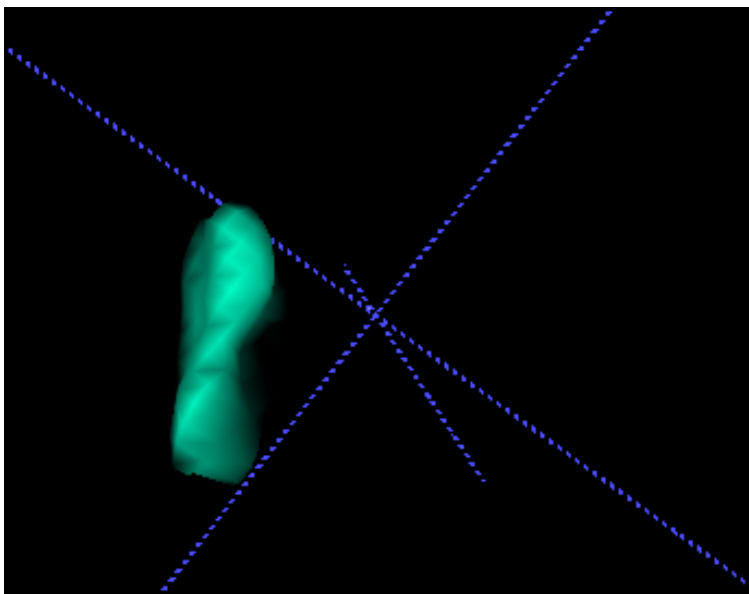


Figure 5.5.1.1: Substantia Nigra segmentation from Patient A. This region is then exported to ImageJ for analysis.

5.5.2 Thresholding

In order to attempt to gain as much valuable information from the images as possible, a threshold filter was placed on the images. A histogram of pixel values was produced for each image, as shown in figure 5.5.2.1.

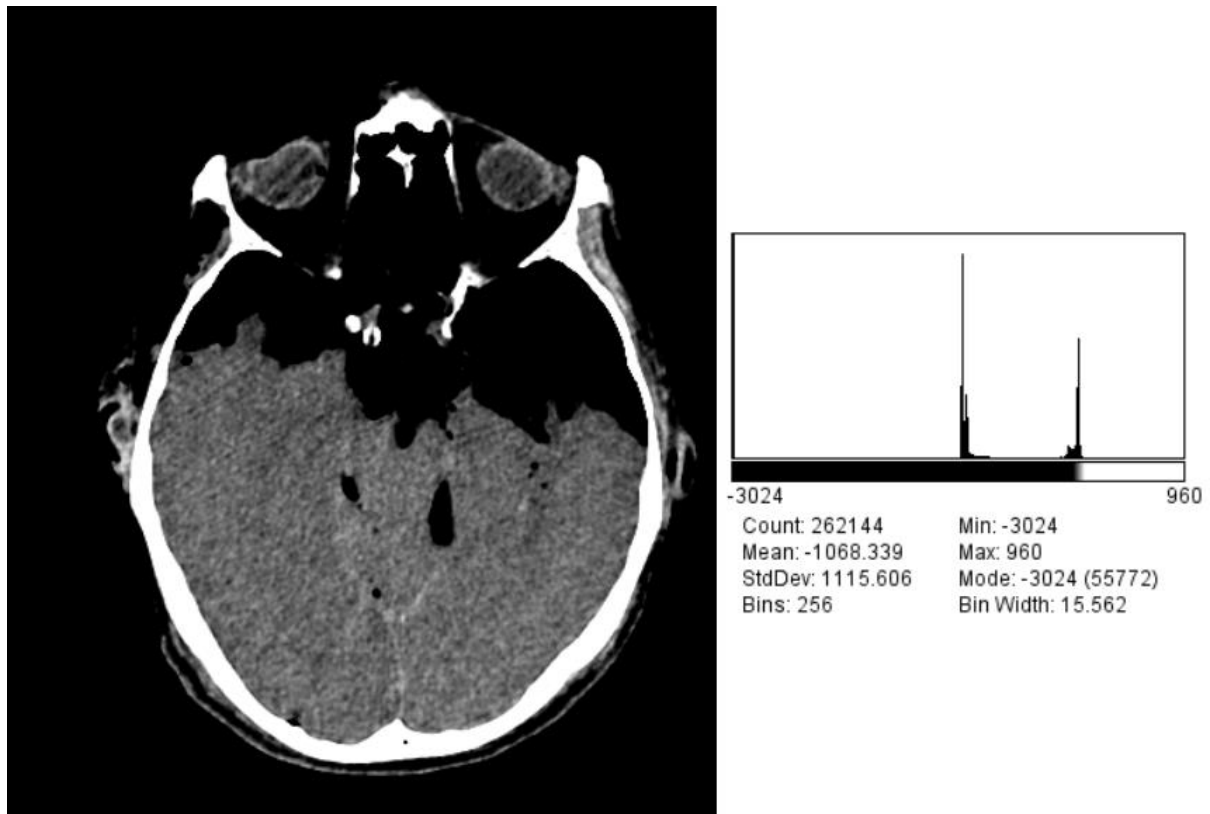


Figure 5.5.2.1: (Left) The slice of the brain of Patient B which was used for analysis of Globus Pallidus and Putamen. (Right) a histogram showing the total distribution of pixels in the image. By thresholding all pixels in the leftmost peak, all “noise” pixels are effectively removed from the image.

This histogram represents the total pixel distribution, not just in regions of interest. This was used to determine a background reading to be used as a lower threshold, and pixels below this value were excluded from the analysis. The same ROIs were then used on the thresholded images. A threshold value of -50 was used in order to remove some of the lower value pixels.

The second cohort had substantial damage, as shown in figures 5.5.2.1a-h.

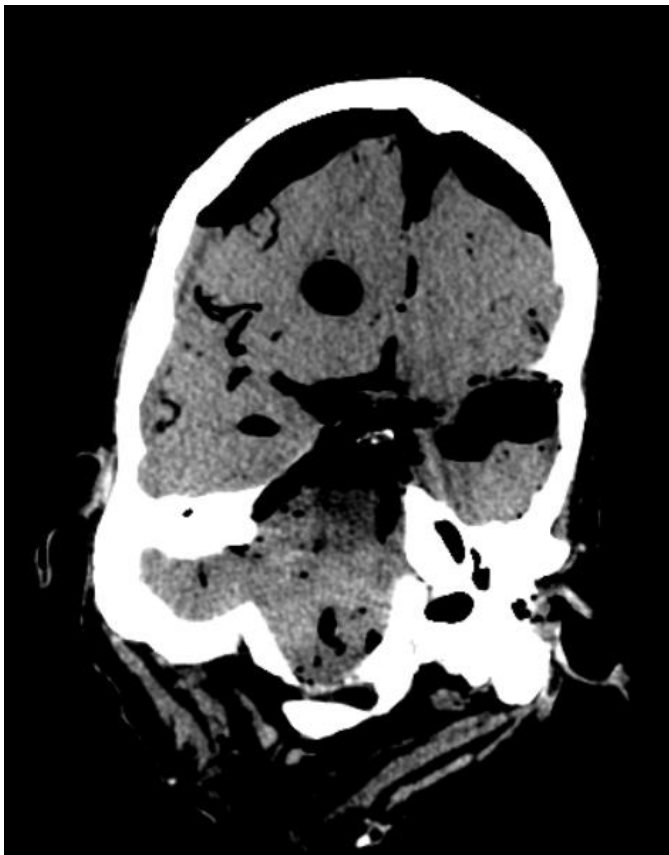
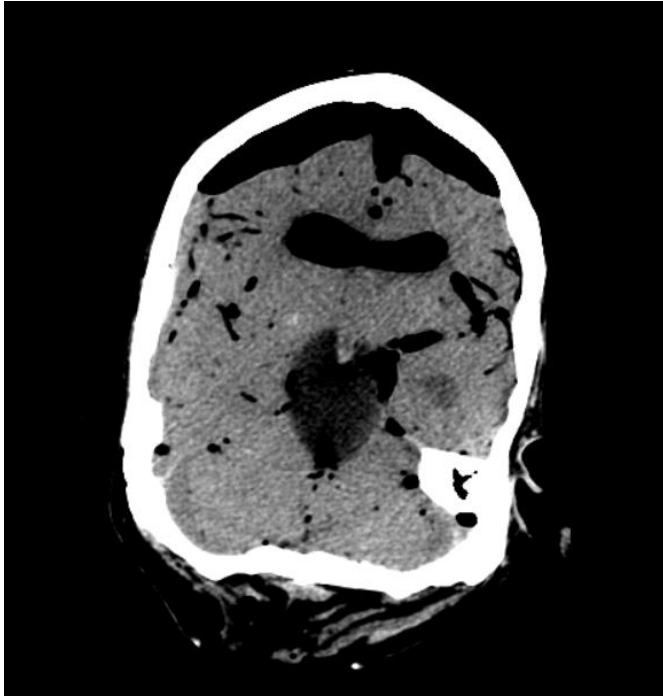


Figure 5.5.2.1 a, b: Patient E, large areas of damage and gas.

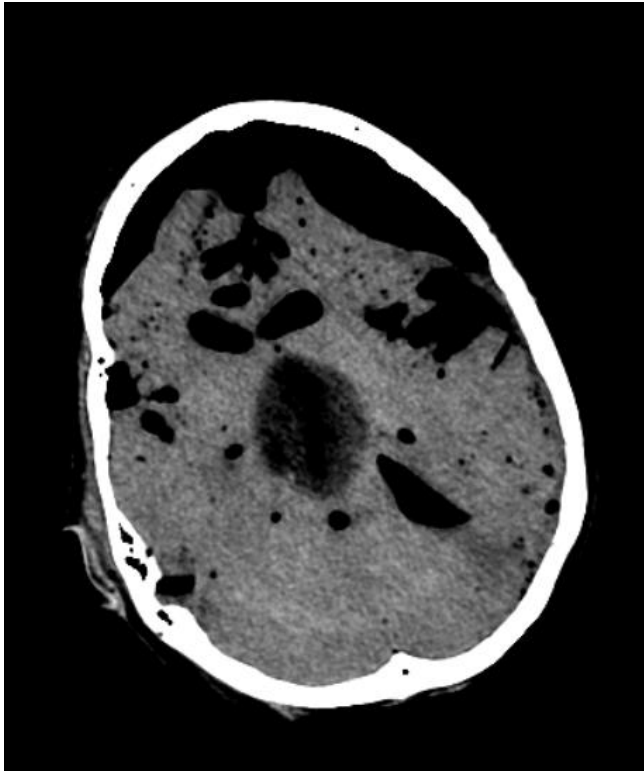


Figure 5.5.2.1 c, d: Patient F, large areas of damage and gas.

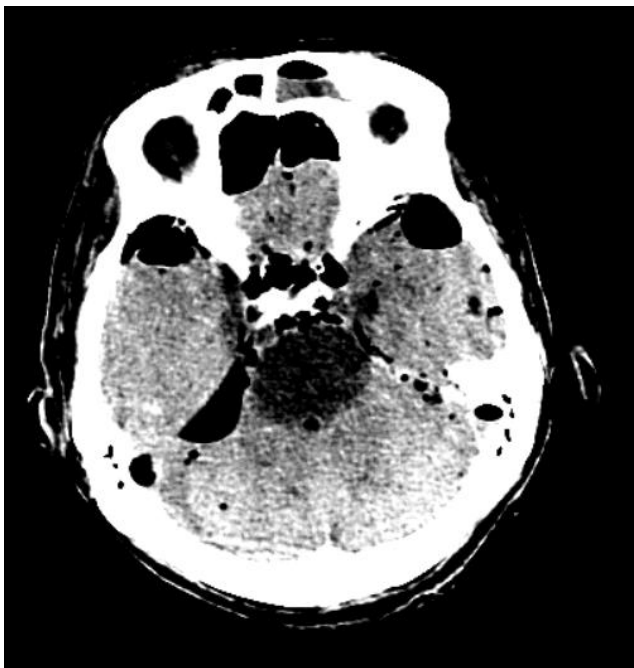
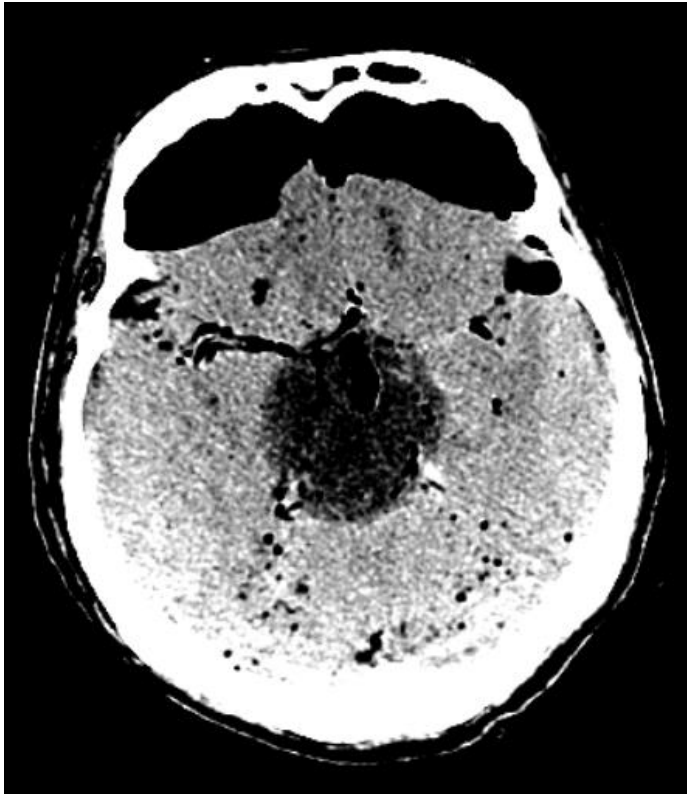


Figure 5.5.2.1e, f: Patient G, large areas of damage and gas.



Figure 5.5.2.1g, h: Patient H, large areas of damage and gas.

Analysis on the images was difficult due to some ROIs being entirely excluded due to putrefactive gas. Post-thresholded images also proved unsuccessful in mitigating the effect of the damage.

Therefore, the 2nd cohort of images (Samples E, F, G, H) was not used for analysis.

5.6 Results

With the aid of a radiologist consultant (Dr. Olu Adesanya, 15+ years' experience), slices are corroborated between MR and DECT images on a per-cadaver basis. The images obtained in this study were subject to a large amount of gas from decomposition, and so large black spots appear frequently. In events that ROIs overlap with these spots, the data shows a large drop in HU. These spots were excluded from the analysis by the thresholding technique outlined in 5.5.2.

MR and DECT images of the same cadaveric head are opened in ImageJ alongside one another. A duplicate stack is made of the DECT image, as this is the image set that cannot be transformed in order to preserve pixel information.

A transparent overlay of the MRI data is placed over the duplicate DECT stack. Using the translation and rotation tools in ImageJ, this image is manipulated such that all visible features that can be used for landmarking (namely the eyes and boundary of the head) are aligned. The overlay MR image is then saved as an ROI.

This ROI is then applied to a blank image, and further ROIs are then drawn on it. The benefit of this method is that ROIs can be drawn on the high contrast and higher detailed MR images, and we know that the overlaid MR image has already been aligned with the DECT image, so any ROIs drawn can be saved and applied to the DECT image in the exact location of the brain feature. An example of this manual segmentation is shown in Figure 5.6.1

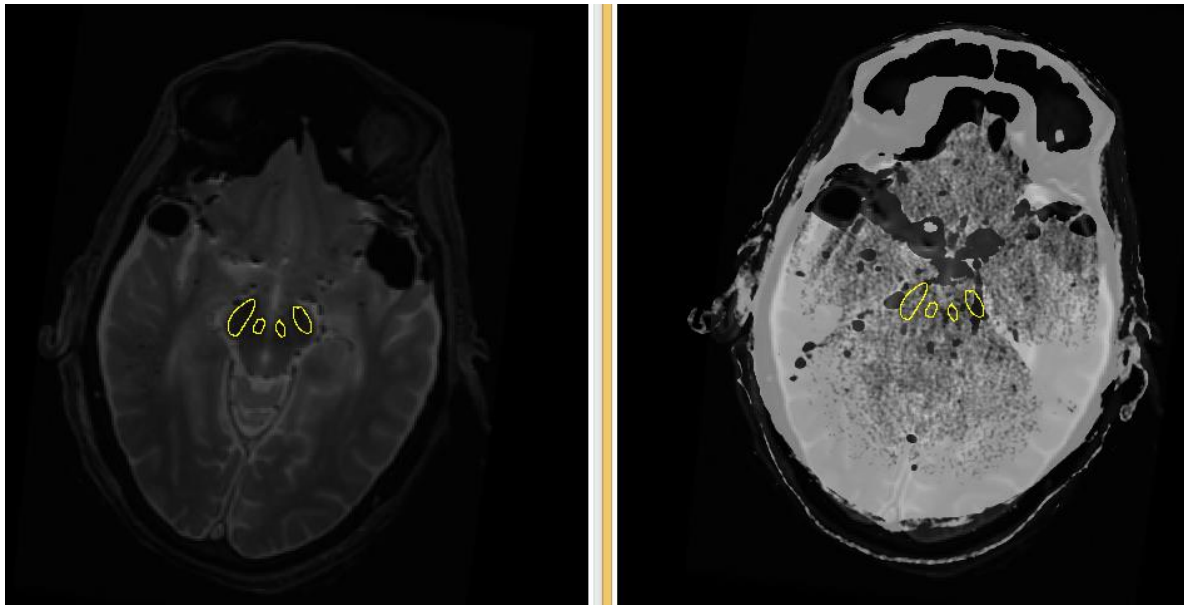


Figure 5.6.1: Images are manually registered using a transparent overlay, and ROIs are drawn on the MR image from the 3D regions produced from ITK-Snap 3D reconstructions. These then correspond to the same location on the DECT image. Shown above: Red Nucleus and Substantia Nigra.

5.6.1 T2 calculation from MRI

The relationship between T2 and iron concentration was introduced in Chapter 3 – ChemoBrain, and the same process is used to link detected T2 values in Table 5.6.1.1 with determined iron concentration values from T2 measurement in table 5.6.1.2 along with associated error.

Data acquired at 3T, using the same equipment as previously introduced in Chapter 3, namely GE Discovery 750W 3T MRI Scanner located at University Hospitals Coventry and Warwickshire.

Region	T2 (ms)	T2 (ms)	T2 (ms)	T2 (ms)
	Patient A	Patient B	Patient C	Patient D
<i>RN_L</i>	53±6	36±3	40±4	43±4
<i>RN_R</i>	55±5	39±4	42±4	39±5
<i>SN_L</i>	58±6	46±5	46±4	53±5
<i>SN_R</i>	61±5	40±5	51±4	57±6
<i>PUT_L</i>	63±8	44±6	58±3	41±6
<i>PUT_R</i>	61±4	39±8	46±3	39±5
<i>GP_L</i>	66±7	45±6	66±4	61±5
<i>GP_R</i>	63±5	50±6	62±4	55±5

Table 5.6.1.1: T2 relaxation time found in brain regions of cadaveric heads. This data is then used to produce corresponding iron concentration values shown in Table 5.6.1.2. Given to 2sf

Region	Iron	Iron	Iron	Iron
	Concentration	Concentration	Concentration	Concentration
	($\mu\text{g/g}$)	($\mu\text{g/g}$)	($\mu\text{g/g}$)	($\mu\text{g/g}$)
	Patient A	Patient B	Patient C	Patient D
<i>RN_L</i>	142±109	244±137	213±128	193±122
<i>RN_R</i>	134±106	218±130	199±125	221±133
<i>SN_L</i>	125±105	177±119	174±117	143±109
<i>SN_R</i>	115±102	211±130	152±110	129±106
<i>PUT_L</i>	109±101	185±122	123±103	204±129
<i>PUT_R</i>	115±101	220±142	177±117	223±134
<i>GP_L</i>	99±98	182±122	100±97	115±101
<i>GP_R</i>	107±99	154±113	112±100	133±106

Table 5.6.1.2: Calculated Iron concentration ($\mu\text{g/g}$) in each patient and each brain region

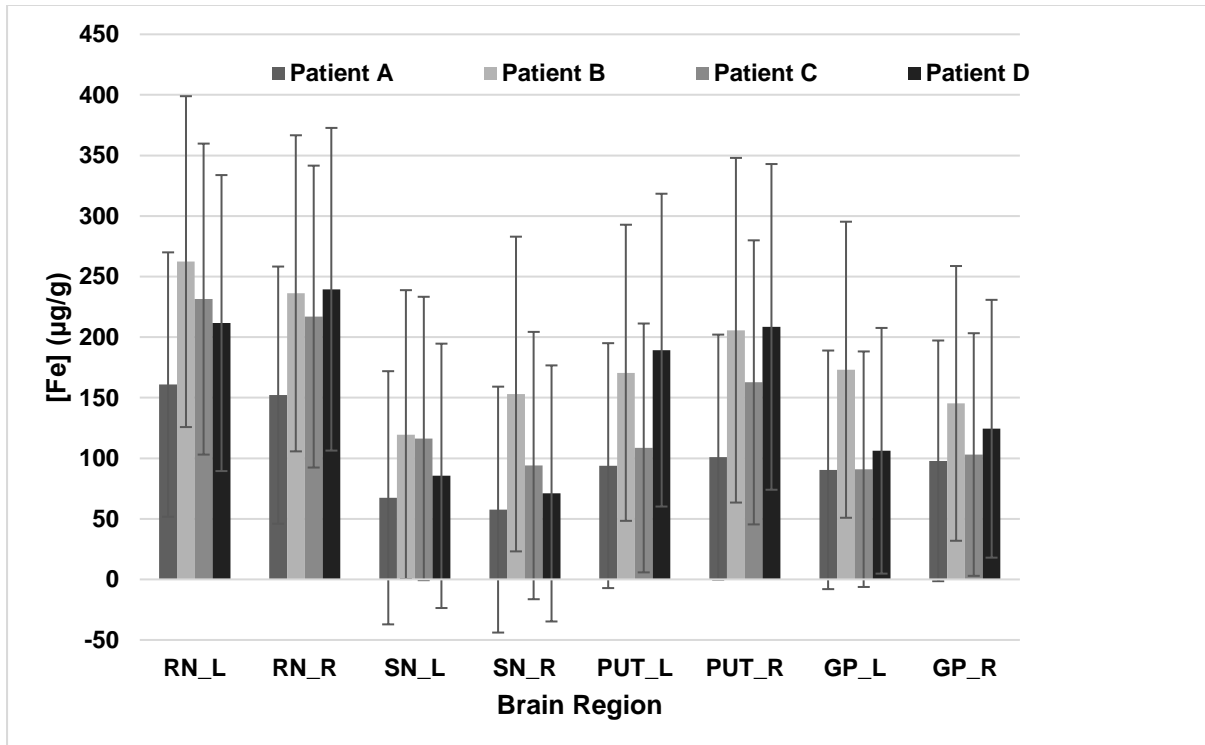


Figure 5.6.1.1: Brain iron concentration calculated from T2 relaxation times for each head and for each brain region.

Figure 5.6.1.1 shows the brain iron levels in each patient and in each region that were calculated using T2 data from Table 5.6.1.2, along with propagated error values. As in Chapter 3, error propagation used the established linear calibration curve relating R2 with Iron concentration, and applied the following formula to calculated propagated error:

$$(\Delta[Fe]_{Observed})^2 = (R2)^2(\Delta m)^2 + m^2(\Delta R2)^2 + (\Delta c)^2$$

5.6.2 Dual energy CT Results

For each patient, DECT images were manually segmented as described above and individual pixel values within each ROI are plotted in Figures 5.6.2.1a-d. The distribution is shown as a box plot, to illustrate the spread of values found in each region. For comparison with MRI, the mean is used.

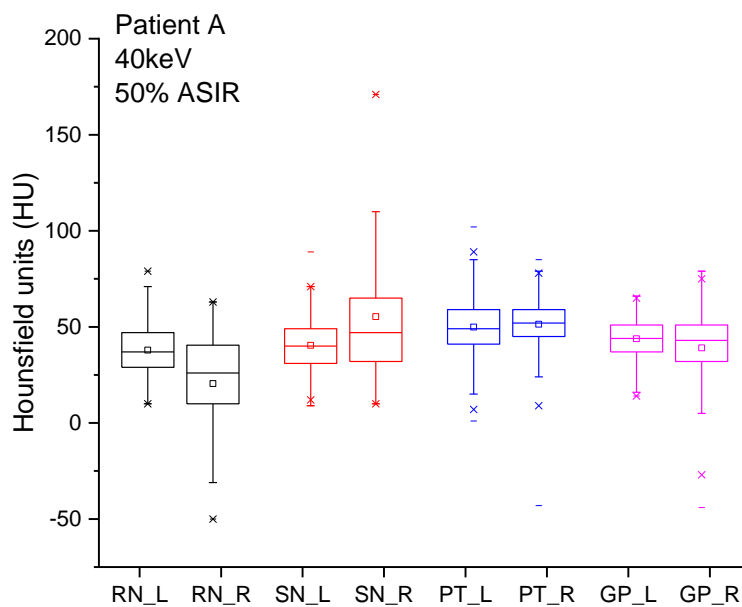


Figure 5.6.2.1a: Distribution of pixel values in each ROI on DECT images for patient A.

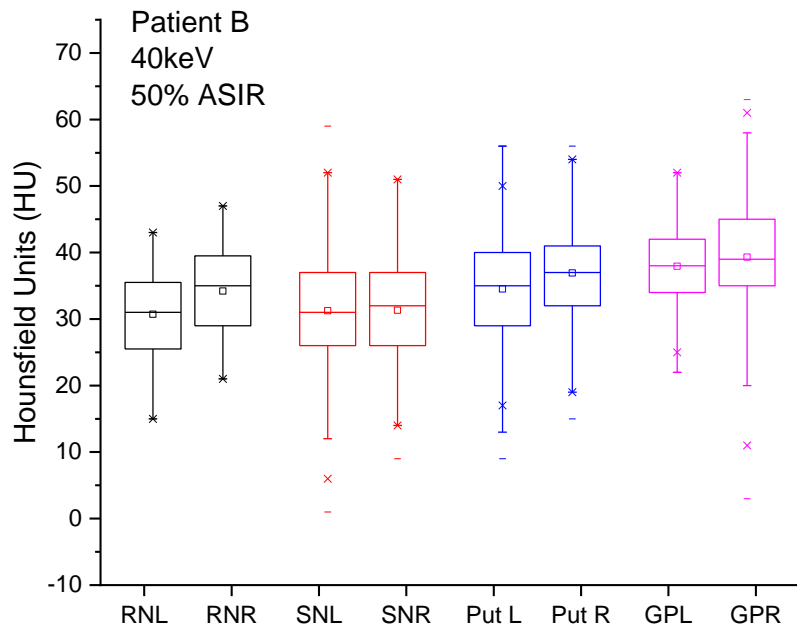


Figure 5.6.2.1b: Distribution of pixel values in each ROI on DECT images for patient B.

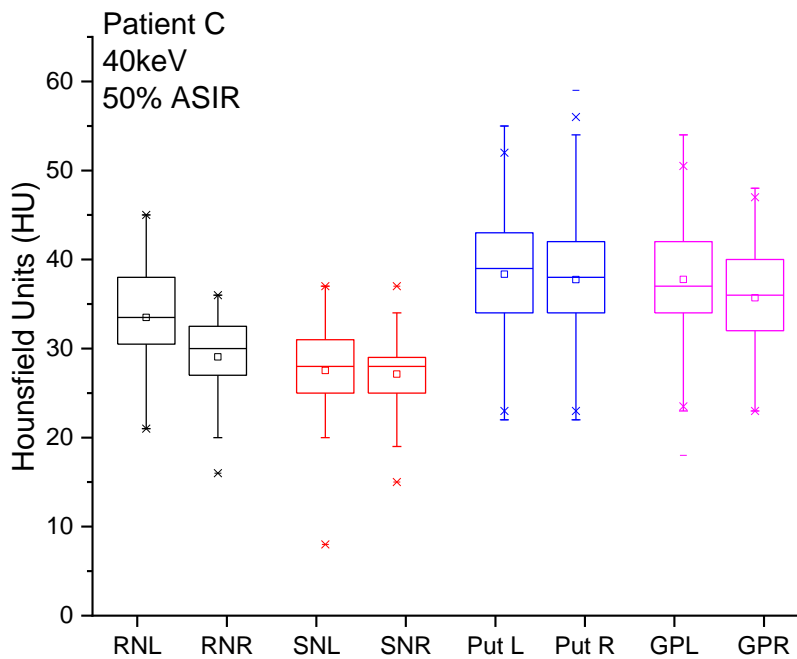


Figure 5.6.2.1c: Distribution of pixel values in each ROI on DECT images for patient C.

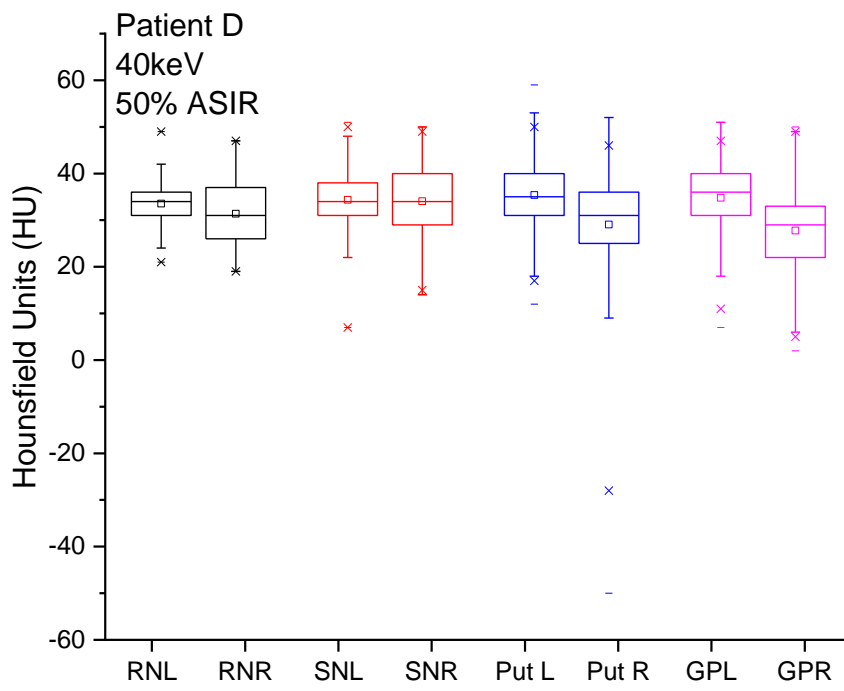


Figure 5.6.2.1d: Distribution of pixel values in each ROI on DECT images for patient D.

5.7 Analysis

5.7.1 Results and figures

Concentration of brain regions are calculated from T2 data and plotted against CT Number (HU) for each patient. This data is shown in Figures 5.7.1.1-a-d.

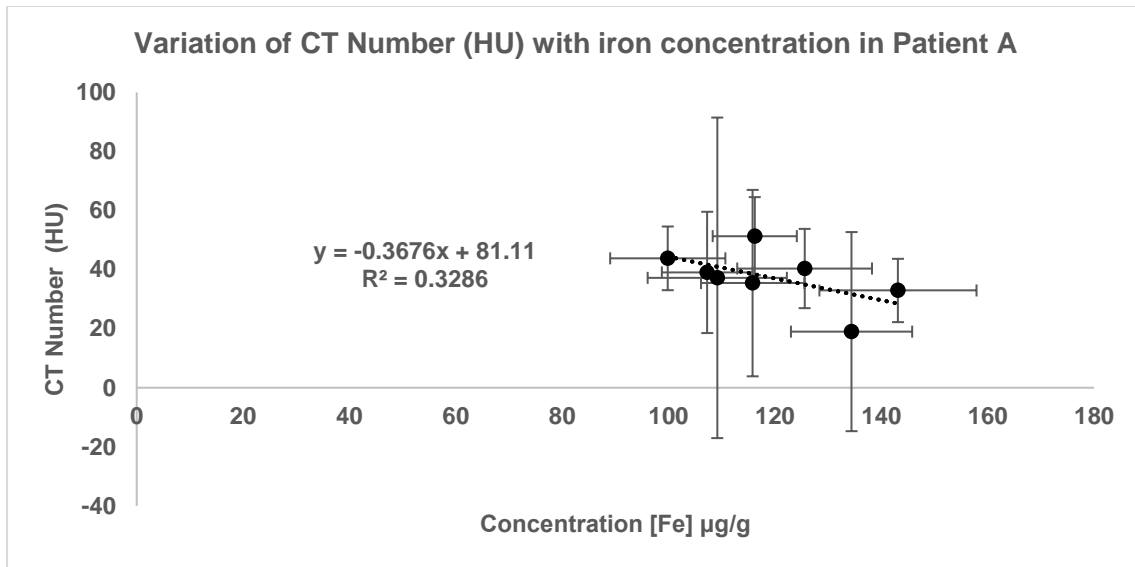


Figure 5.7.1.1a: CT Number against [Fe] concentration in 40keV (50% ASIR) DECT images for patient A.

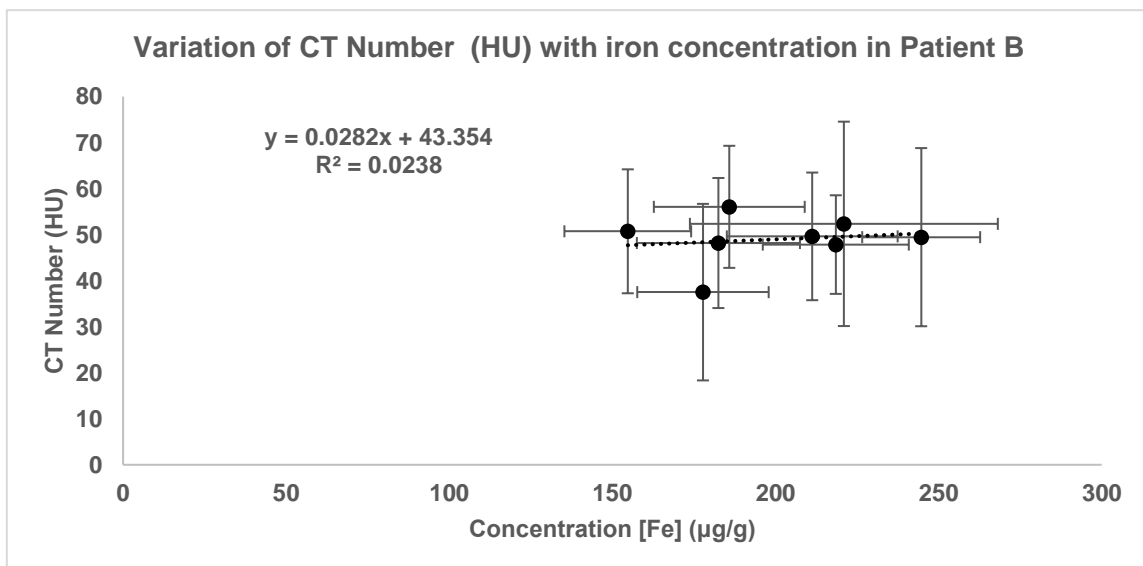


Figure 5.7.1.1b: CT Number against [Fe] concentration in 40keV (50% ASIR) DECT images for patient B.

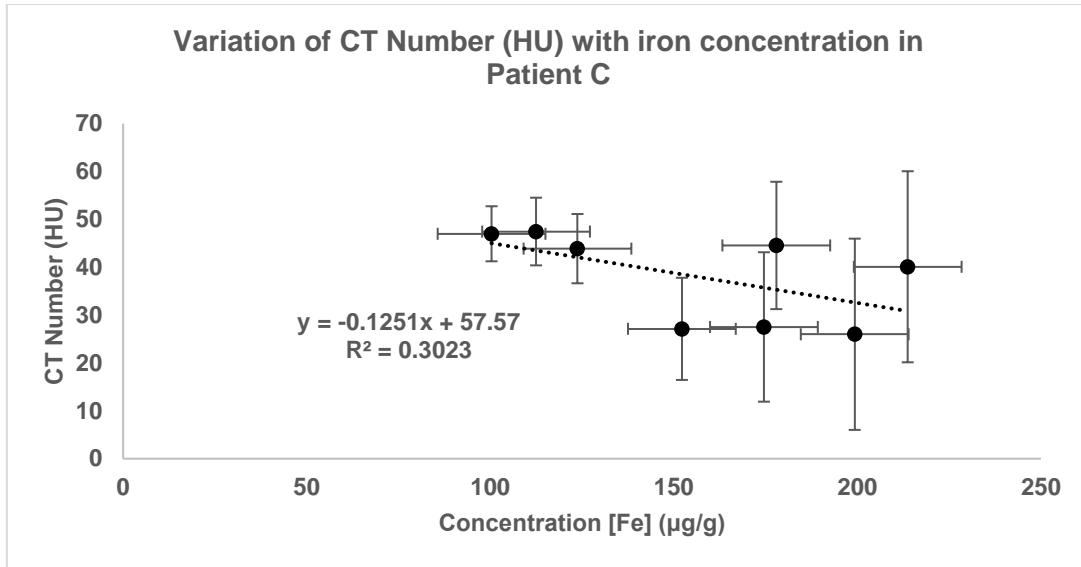


Figure 5.7.1.1c: CT Number against [Fe] concentration in 40keV (50% ASIR) DECT images for patient C.

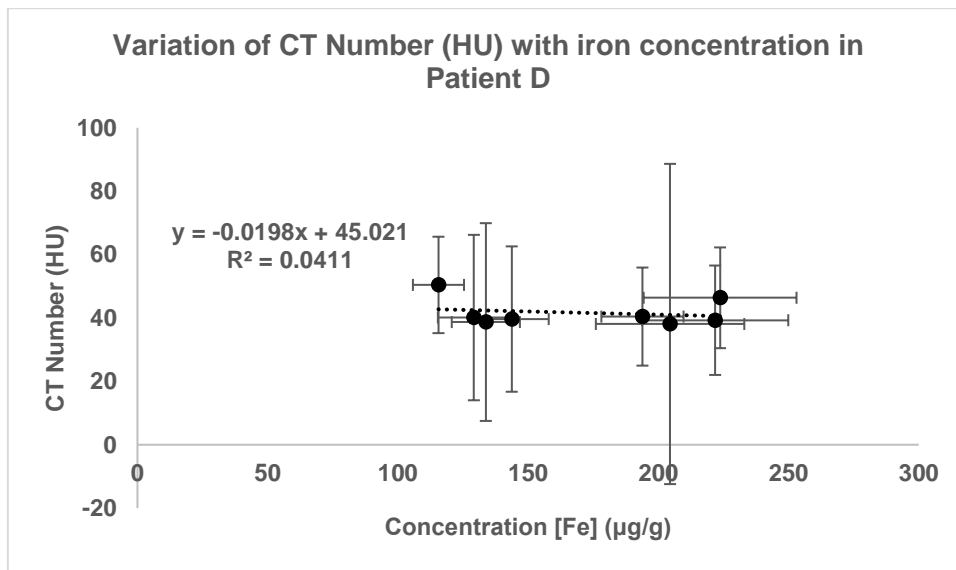


Figure 5.7.1.1d: CT Number against [Fe] concentration in 40keV (50% ASIR) DECT images for patient D.

5.7.2 Comparing DECT and MRI data

Figures 5.7.1.1a-d show the resulting plots of concentration against HU. As determined in phantom studies and literature reviews of other quantitative DECT studies, the expectation is that higher

concentration should lead to higher attenuation, however this was not observable in this data based on analysis of CT Numbers.

Another look at this data is shown in Figures 5.7.2.1-a-d, which show HU against R2. Again, no relationship is observed.

For each patient, the average HU value for a given region was plotted as a scatter, once for GSI9 and once for GSI30. Each point in the chart corresponds to a pair of values for one specific brain region – one value being the R2 value in that region as determined by the T2 relaxometry experiment, and the other being the HU value as determined by the respective DECT experiment.

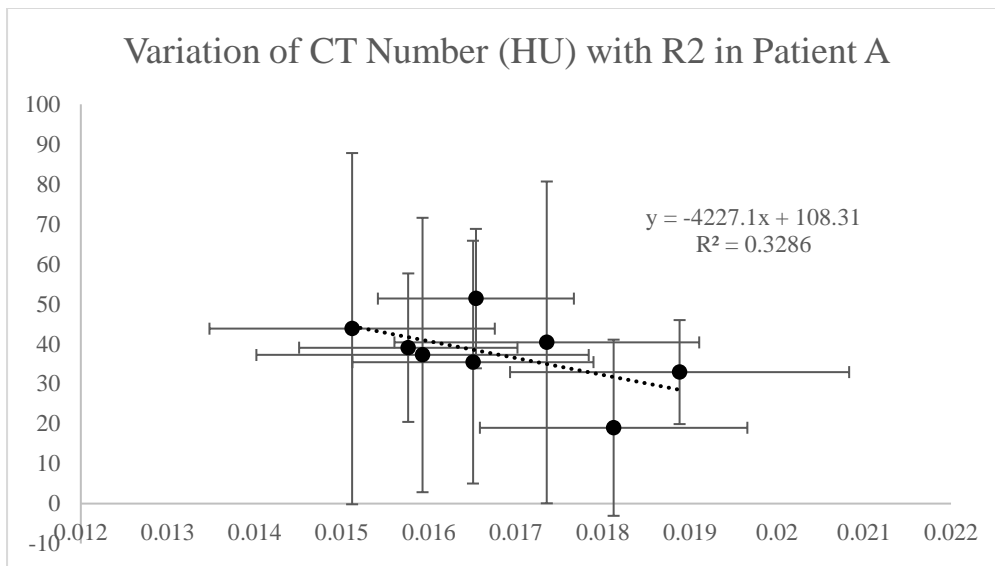


Figure 5.7.2.1a: CT Number against R2 in 40keV (50% ASIR) DECT images for patient A

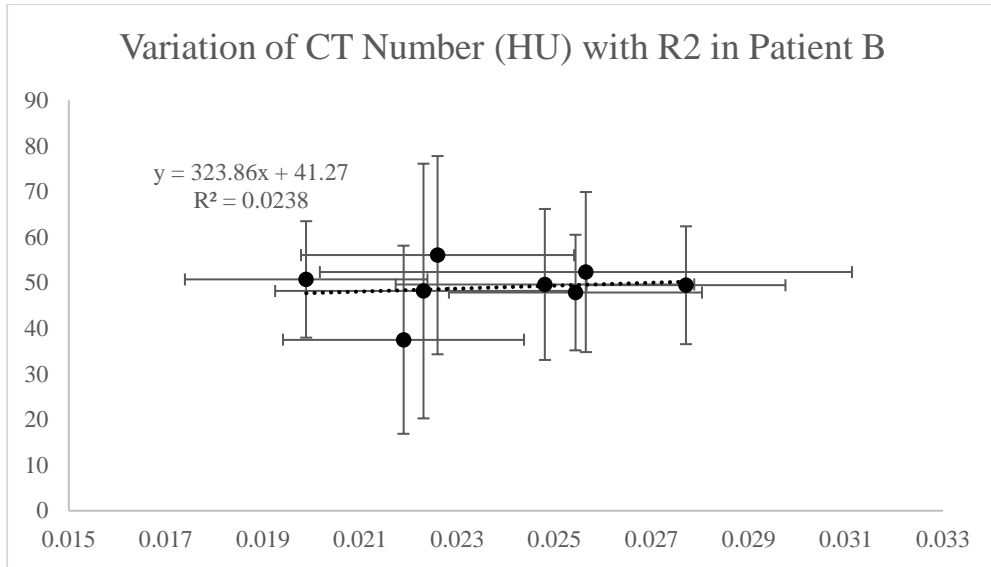


Figure 5.7.2.1b: CT Number against R2 in 40keV (50% ASIR) DECT images for patient B

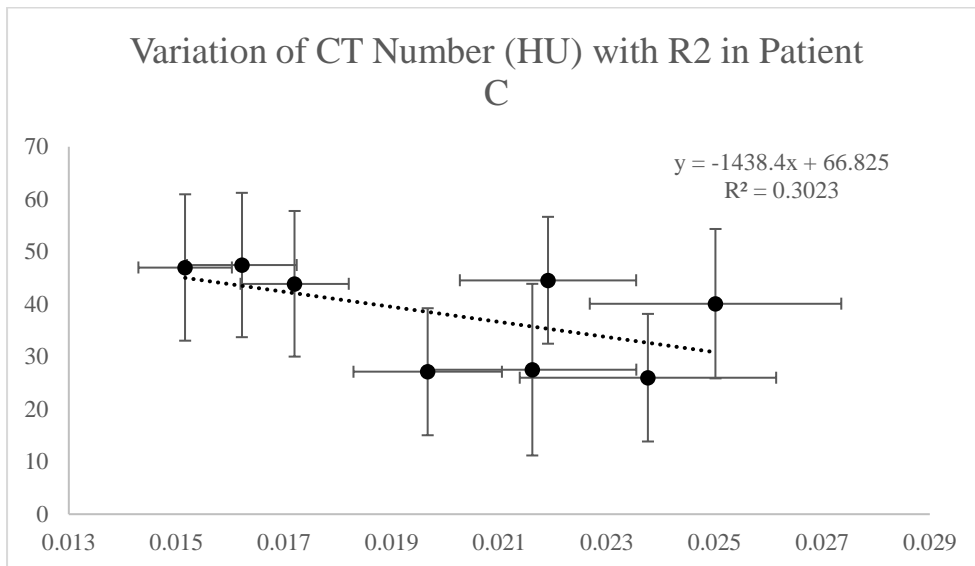


Figure 5.7.2.1c: CT Number against R2 in 40keV (50% ASIR) DECT images for patient C

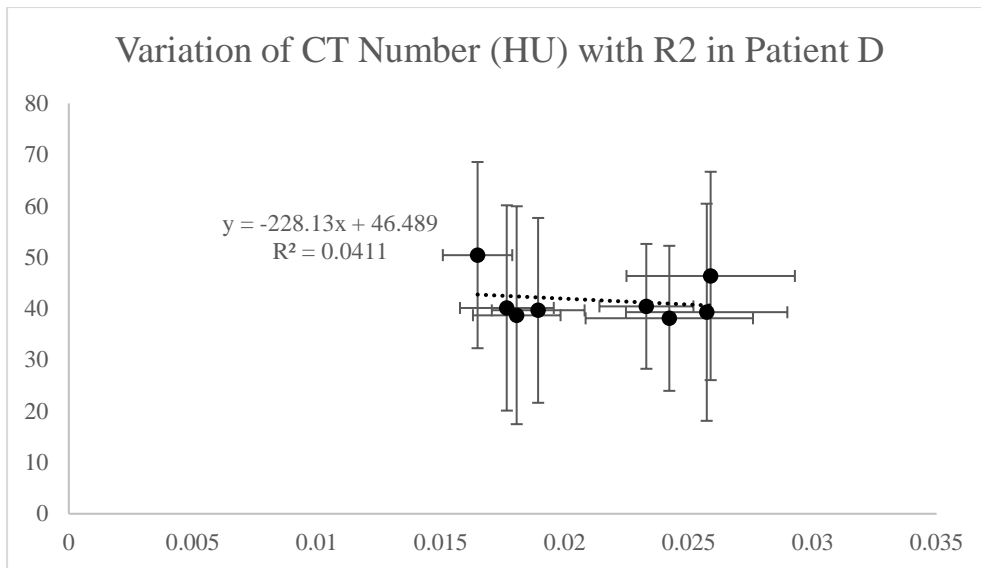


Figure 5.7.2.1d: CT Number against R2 in 40keV (50% ASIR) DECT images for patient D

The data shown in Figures 5.7.1.1 and 5.7.2.1 do not show the expected positive linear correlation. R^2 values are low indicating a low amount of variance explained by variation in concentration. Error in iron concentration is also high, meaning there is error in both directions on the calibration curve.

5.7.3 Statistical Analysis

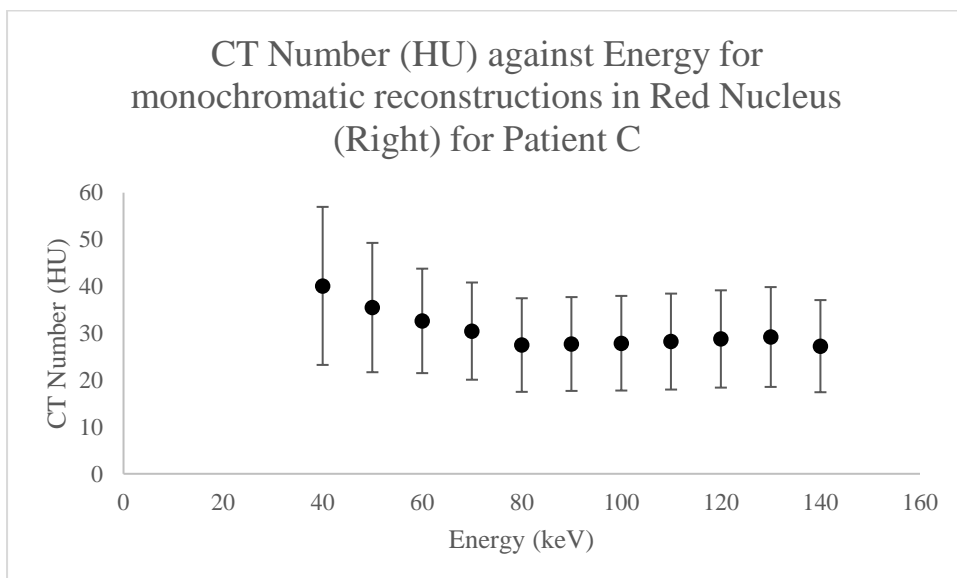
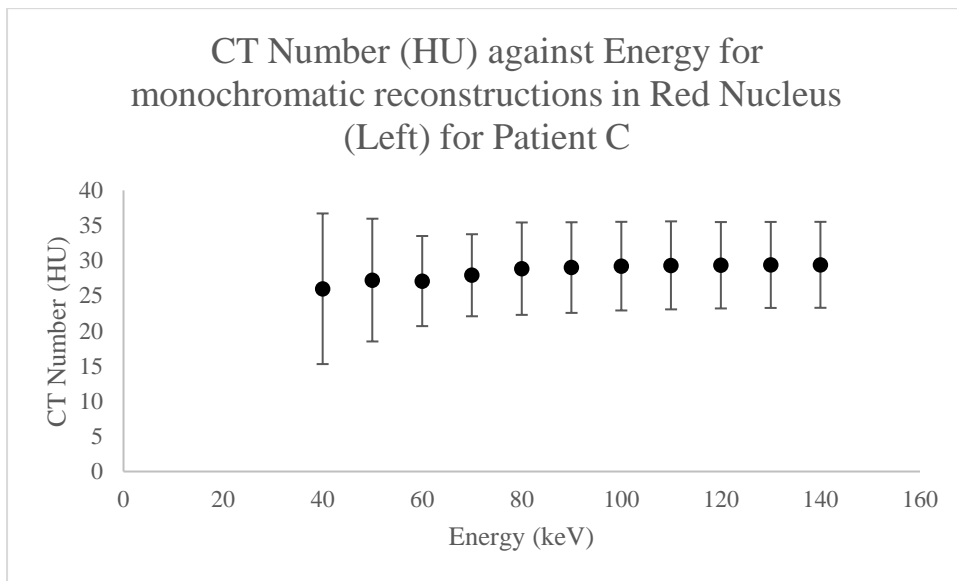
Linear regression trendlines on Figures 5.7.1.1a-d and 5.7.2.1a-d do not show the necessary positive linear correlation to show a positive relationship between HU and Iron Concentration. In Figures 5.7.1.1a and 5.7.1.1c, there is a slight negative correlation with $R^2 = 0.33$ and 0.30 respectively, and for 5.7.1.1b and 5.7.1.1d there is a positive correlation ($R^2 = 0.02$) and negative correlation ($R^2 = 0.04$) respectively. The low values of R^2 indicate that a low amount of the variance of the dependent variable is explained by the independent variable (iron concentration).

For each of the four samples, the lowest-concentration CT Number value was within 1SD of the highest, and vice versa (see error bars displayed on Figures 5.7.1a-d).

5.7.4 Spectral imaging consideration of brain images

40keV was chosen as the energy which exhibited the highest sensitivity to changes in iron concentration in phantom studies.

Monochromatic reconstructions were analysed for each brain region. Red Nucleus (Left and Right) is shown in figure 5.7.4.1 for Patient C as an example.

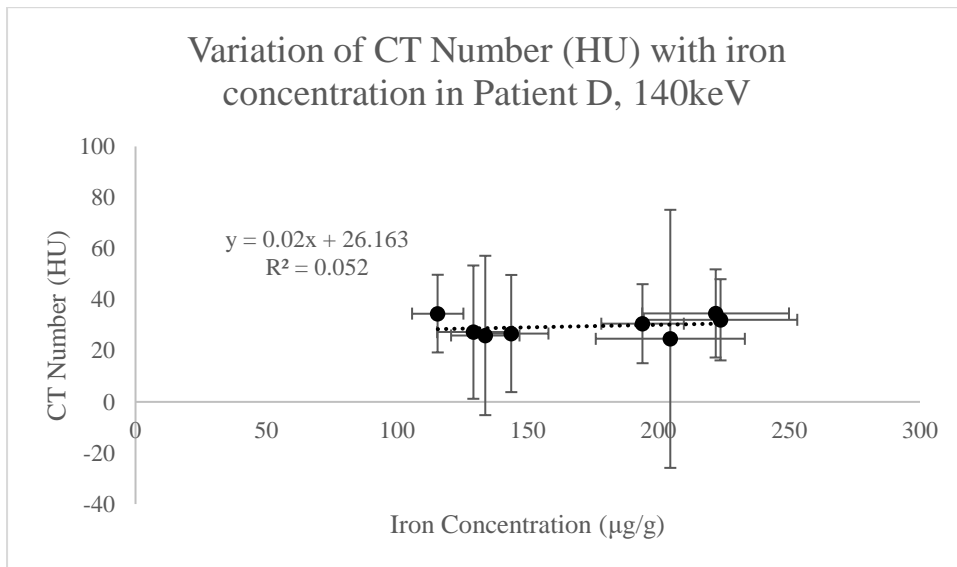


CT Numbers at 40keV were contained within error bounds of CT Numbers at 140keV and vice versa.

In general, a slight decrease in HU is observed for higher energy, with some exceptions e.g., Patient

C, Red Nucleus Left which showed minimal change in CT Number across energy levels, but this is within error, and it cannot be deduced from this data whether this is signal or noise due to the associated error.

The HU – Iron concentration plot for patient D is shown in Figure 5.7.4.2 as an example, showing no correlation between CT Number (HU) and iron concentration even at higher energy.



5.8 Discussion

5.8.1 Practical limitations

This study was carried out due to the difficulty of a full live patient study comparing DECT and T2 relaxometry. It proved difficult to get ethical approval and recruit volunteers for the study for this PhD, and so a cadaver study was proposed instead. It was hoped that this would be a reasonable compromise and that equivalent data would be brought forward. The difficulties with frozen and decaying tissue were known, however it was not expected that they would be so profound and have such an impact on the data. Cohort 2, as shown in figures 5.8a-h, produced images that were entirely unsuitable for analysis on DECT due to large amounts of damage and putrefactive gas. Cohort 1, although better, still suffered from some major issues, which made data analysis difficult, as shown in

figure 6.7. Despite these setbacks, this novel study into whether or not DECT can be used as a neurological quantitative analytical technique for iron detection still produced some interesting results, which may aid future experimental design, however no quantitative use of DECT has been proven in neurological tissue.

5.8.2 Accurate iron determination

As with the phantom studies, ICP-MS could be used to analyse dissected brain tissue regions and accurately determine iron content. Ethical and biosafety approvals were not available for this aspect of the study to take place and so this was not possible, however, a previous researcher in the group (Dr Mary Finnegan) did follow this protocol for her PhD looking at comparison of brain regions on high field 9.4T MRI. Figure 5.8.3.1 is reproduced from her PhD thesis, showing how the segmentation was mapped using MR imaging and then the samples underwent ICP-MS for accurate concentration determination. If approval had been granted this would have been the ideal approach, however in lieu of this, the MR technique of determining iron concentration was instead used.

This technique itself also has limitations which are specific to the cadaver environment. Temperature was not possible to control in the clinical environment, however it should be measured in the future – both the ambient temperature, and if another cadaver study would be done, the tissue temperature of the cadavers.

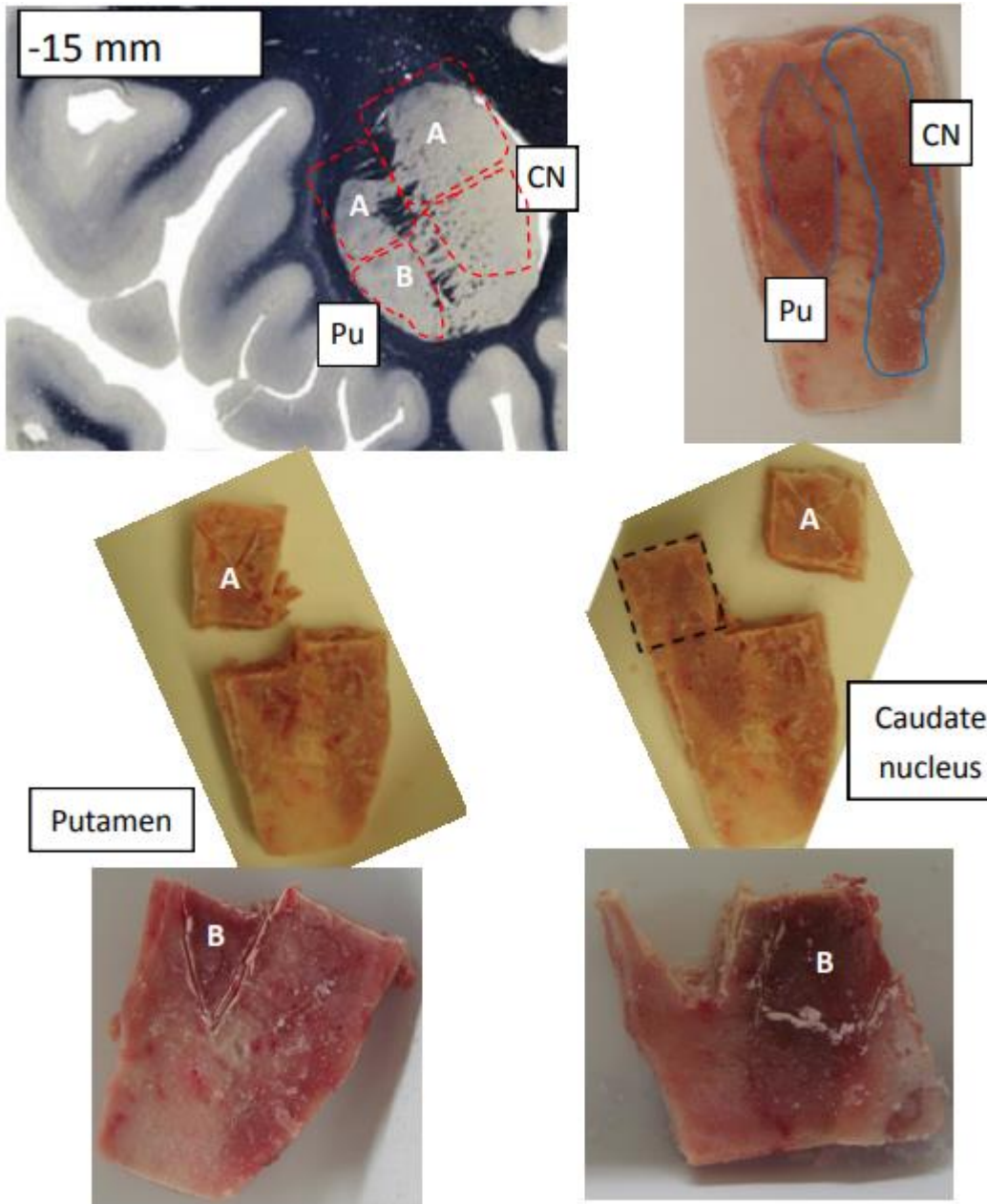


Figure 5.8.3.1: Reproduced from Dr Mary Finnegan's PhD thesis, a former group member, showing how the segmentation was mapped using MR imaging and then the samples underwent ICP-MS for accurate concentration determination.

5.8.3 Additional sources of error

Another consideration in the clinical setting is additional error sources and quantifying these. Individual, additional studies would need to be done to determine the error associated with temperature variation within the tissue as it changed from freezing to room temperature over the

course of the study. Further, it would be ideal if the matrix effects of the surrounding tissue and fluid could be quantified.

Free radical formation is posited in the neurodegenerative disease pathway (George Bartzokis et al., 2004; Carocci et al., 2018; Chauhan & Chauhan, 2006), however this may also then have an effect on MR signal due to their paramagnetism. Ahn et al (Ahn et al., 2019) used MRI to measure free radical production in an in-vivo mouse study. A technique that determines the degree of free radical production could be used to understand the impact of this disease pathway on the MR signal, and could be accounted for alongside any increased iron concentration.

5.9 Conclusions

DECT was unable to correlate with R2 values obtained from T2 relaxometry in human cadaveric heads at 5% confidence level.

These results form a novel set of experimental data, which have never been attempted before. It was not possible to draw statistically significant conclusions from data acquired, however further experimental design can be heavily influenced from this novel research.

One key limiting factor was the gas build-up found in the post-mortem tissue. While some of this effect was dealt with by thresholding (i.e., pixels that contain only gas, which would present with very negative CT numbers, can be manually excluded from analysis by image post-processing), it is not clear what effect gas can have on the tissue that remains above the threshold. For instance, if a given region produces a CT number of 100, it is not clear what if any effect the nearby or potentially present gas has on that measurement.

5.9.1 Other literature

Investigations into quantitative DECT continue to be studied in the literature, though there has not been any step towards detection neurologically relevant iron concentrations, or in studying neurological tissue. A 2021 study (Toia et al., 2021) into the lower limits of detection of trace metals

Iron, Copper and Zinc using DECT identified that iron could be detected at concentrations as low as 220µg/mL, while brain iron is frequently found at concentrations of 100-300µg/g (Barbosa et al., 2015; B. Hallgren & Sourander, 1958). Toia et al used medium and large torso-shaped aqueous phantoms in their study, and a comparison of FBP and ASiR was also used. This is shown in figure 5.9.1.1

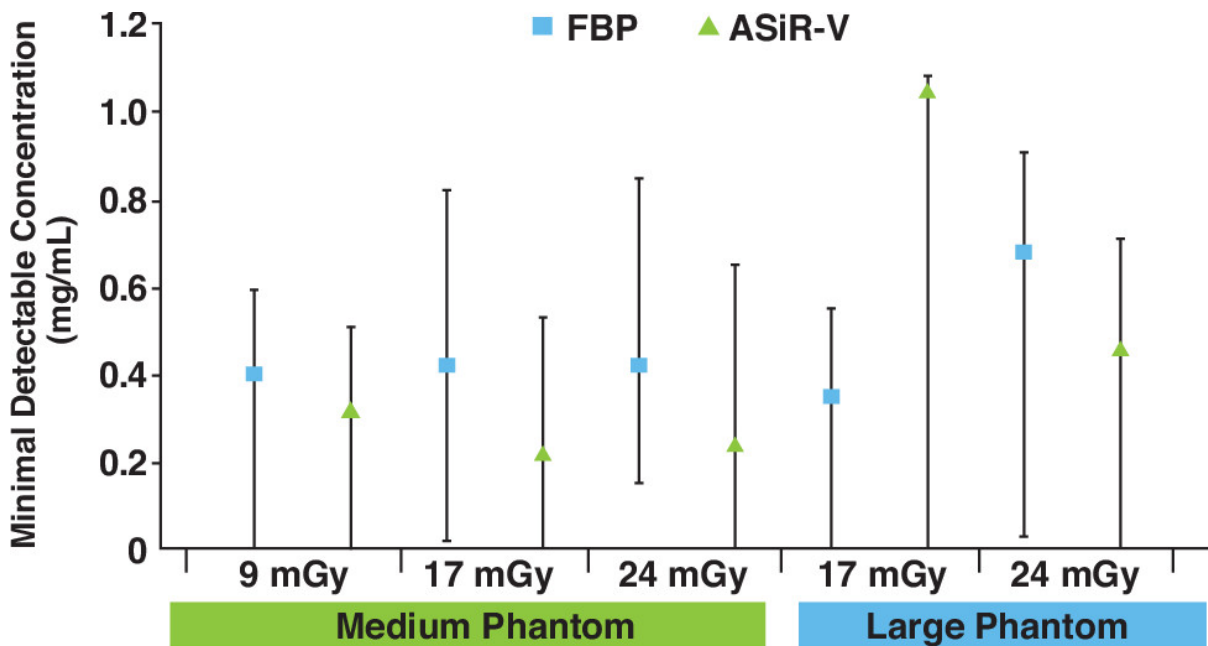


Figure 5.9.1.1 ASiR was able to lower the detection limit to 220µg/g. DECT was used and averaging was used on 80keV and 140keV images to get final figures. Figure reproduced from (Toia et al., 2021)

While this study was targeted at developing quantitative DECT for use in abdominal scans, in particular for quantifying iron concentration in liver iron overload, this does indicate that there may still be limited scope for iron concentration detection in neurological tissue, given that typical iron concentration (especially in neurodegenerative disease in patients with advanced age) is above 220µg/g. However, this was the limit of detection for one protocol specifically, and error shown for the minimum detectable concentration in this paper indicate that this value could be as high as 600µg/g. If the results from this chapter are to be taken forward and linked to literature such as Toia et al, it is important that the side-effects of cadaveric tissue are not present, as detection is severely limited by tissue quality. A trial in living tissue would be more appropriate, whether in animal studies or human trials with living participants.

5.10 Further work

One of the key limitations to this study was lack of full access to the human tissue. That is, other than the designated scanning time (which took place on one evening, 5th September 2018), there was no further access possible to the cadaveric heads to allow for dissection and elemental analysis using ICP-MS to determine true iron content in the brain regions studied. If this were possible this would have added very valuable information to the study as the error associated with the MR measurement would be mitigated, and instead CT Number could be compared directly with ICP-MS -measured iron content.

Some additional issues to overcome include tissue preservation. It was difficult to measure the brain regions of interest from the frozen human brain tissue, as already discussed due to build-up of gas and deformity of brain regions. An animal study would avoid this issue, e.g., using Micro CT to image rodents, which would also be more practical in allowing for ICP-MS determination of concentration post-mortem. High field MR Microscopy could be used to corroborate the iron detection, and this protocol could be developed further for clinical use.

Another potential avenue is contrast agents. It was not practical in this study to use contrast agents (due to working with cadavers) however this could be achieved with an animal study.

Scope for work with post-mortem human tissue more optimally preserved for analysis but numbers of cases will always be limited, and there are biosafety challenges and ethical approvals required to continue/expand this line of work.

Development of registration strategies to improve data correlation between information obtained on different platforms and with different spatial registrations would also be a great benefit, including auto-segmentation methods.

Another area of research is to apply alternative methods of iron measurement. In work subsequent to this thesis, PhD student Jierong Luo in the Trace Metals in Medicine Laboratory (supervised by Prof Collingwood) established a Quantitative Susceptibility Mapping (QSM) protocol on a 9.4T

(microscopy) and 3T (clinical) scanners so that in future QSM measurement of tissue susceptibility can be performed, which has been shown to give robust indications of tissue iron concentration in most regions of the brain.

Finally, there is scope to expand elemental analysis. Looking at DECT for other elements, e.g., Calcium is a potential avenue for analytical studies.

5.11 Individual contribution

All of the work in this chapter is my own. I was responsible, with support from my two supervisors, for writing the experiment brief, applying for BSREC ethical approval, for liaising with the hospital and for scanning the human cadaver heads at UHCW. All data analysis, image segmentation, thresholding was done by myself.

Chapter 6 - Conclusions and Future Work

6.1 Summary

This work provides the first attempt at quantitative DECT in human cadaveric neurological tissue. Relationship between iron concentration and CT Number determined from monochromatic reconstruction images from DECT was not possible to establish.

Chapter 3 outlined the results of a patient study using T2 relaxometry to attempt to correlate iron concentration in Globus Pallidus, Substantia Nigra, Red Nucleus, and Putamen brain regions with the presence of chemo brain symptoms. The study was unable to provide evidence of statistically significantly increased levels of iron in the brain regions of the CICI patients.

There were a number of assumptions in the study, which could be challenged with further work. First, the assumption that each participant had a normal level of brain iron before ChemoBrain symptoms. There is no way to know that this is true for our particular study. To be sure of this, a longitudinal study would be needed where a cohort of people that are undergoing chemotherapy have an MRI scan and their brain iron accurately measured. For those who proceed to get ChemoBrain, they can be recalled for further study at regular intervals, and those that do not can be used as controls. The investigator would then be able to compare the increase in iron concentration between the group that developed ChemoBrain and the group that did not and identify any significant differences between them.

In addition, it is not evident that the MRI method used was the best possible way to obtain iron concentration values non-invasively. One example is Quantitative Susceptibility Mapping (QSM). Santin et al found in their 2017 paper that QSM is a technique that is capable of identifying Parkinson's Disease, and that it can replace R2* mapping for iron quantification (Santin et al., 2017). QSM has been shown to allow discrimination between tissues with different susceptibilities including iron, microbleeds and calcification (Santin et al., 2017). Furthermore, Barbosa et al. found that QSM was more sensitive to iron concentration changes in the human brain than R2 or R2* mapping (Barbosa et al., 2015). A future study should aim to employ the state of the art in non-invasive

quantitative iron concentration determination. Alternatively, if a post-mortem study would be used, accurate iron concentration could be determined with ICP-MS which would enable the production of a calibration curve that can be used with clinical patients.

In 2021, Bernstein et al (Bernstein et al., 2021) published an fMRI (functional MRI) meta-analysis, proposing that lower activations of brain regions which were observed in fMRI scans of CICI patients reflect a dysfunction either in mobility or attention span, and that this is attributed to depletion of neurons.

A longitudinal study of the effect of CICI on brain iron would be required to determine whether there is a measurable effect of either cancer or chemotherapy on brain iron concentration in neurodegenerative-disease-relevant brain regions.

Chapter 4 outlined the DECT process and how it was built up from application to phantoms, use of monochromatic reconstructions in identifying the key energy level that would yield the maximum sensitivity to iron (i.e., the minimum available, 40keV), and finally applying it to low concentration phantoms in neurologically relevant concentration ranges.

A key part of the CT process is the image reconstruction. As outlined in Chapter 2, standard practice is to use filtered back projection to produce CT images, however newer methods are becoming feasible as more computing power allows us access to previously impossible techniques, such as iterative reconstruction.

The GE scanner used in this thesis has the capability for Adaptive Statistical Iterative Reconstruction (ASIR) built in, and CT images were reconstructed using both the standard and ASIR methods. Some of the initial preparatory and investigative work was done as part of this PhD and are detailed in Section 4.4.

Results from this chapter indicated that DECT lacked the specificity required to detect iron at neurologically relevant iron concentration levels due to large amounts of image noise, even in aqueous phantoms. Additional image acquisition techniques could be considered to reduce noise, such as multi-image acquisition. Averaging signals from multiple readings increase the signal to noise

ratio, SNR. SNR ratio grows as a function of the square root of n , where n is the number of repeated measures. Scanning time at the University Hospital was always a limiting factor in the studies presented in this thesis and so multiple acquisitions were not possible, but this would be a good study to attempt to reduce image noise and investigate whether this detection limit could be approached using neurological tissue.

Additional phantom studies could be used to further develop the techniques.

Work has been done with phantom studies replicating human torso, heart, or liver tissue, for example by Tsai et al (Tsai et al., 2014). Further development of phantom work should investigate varying the levels of ASIR used in this study. While 50% proved to be better than not using ASIR at all, it was not studied how this effect changes as a higher percentage is used. With a full understanding of the level of ASIR that produces the lowest noise while contributing the highest quantitative power, phantom studies can be optimised for lower detection limits of iron.

Chapter 5 applied the developed DECT technique, along with 40keV monochromatic reconstruction analysis, to human cadaveric heads. This novel study into a part of anatomy previously unconsidered for DECT yielded a negative result; it was not evident that the technique could quantify iron concentration in brain regions studied. A number of complexities in the experimental design were present.

Firstly, the cadaveric heads were not as suitable for analysis as initially thought. Significant damage and putrefactive gas build-up prevented accurate analysis of images, which may have contributed to the lack of correlation seen between MRI and DECT data. If no accurate MRI determination of iron concentration could be found, then there is no ability to use this as a reference value to determine the relationship between CT Number and concentration. The proposed human trial using clinical participants would avoid this issue – and this is the recommendation for advancing the technique further. It would still be a worthwhile exercise to carry this study forward and attempt the same analysis outlined in chapter 5 on live patient data for a conclusive result.

This thesis has employed both established and novel analytical techniques to human brain iron quantification. The results of the cadaver study (Chapter 5) will need further investigation to establish whether it is the technique's sensitivity to neurological tissue that has prevented a significant relationship between DECT and T2 Relaxation from being found, or if the post-mortem tissue decay and decomposition that confounded the results. DECT was used for the first time to attempt to establish a linear relationship at neurologically relevant concentration levels of iron in phantoms (chapter 4).

At present, using the DECT technique in the human brain is limited by the inability to accurately isolate regions of interest using only a CT scan. Image quality is too poor for even experienced radiologists to confidently ascertain which regions are which without using a side-by-side MRI scan. Further, even with the MR image data available for accurate location mapping on the CT images, it was shown that the CT numbers obtained do not correlate with the iron concentrations found using those same MRI scans.

In 2021, Peng et al (Peng et al., 2021) published another animal study which illustrates the capability for DECT to establish liver iron concentration, again at much higher concentration than is present in human neurological tissue.

6.2 Future work experimental designs

A priority for future work would be to develop the DECT technique to the point of being able to test it on living patients, avoiding the issues with putrefactive gas build-up in cadavers. Additional phantom studies, which mimic neurological tissue more closely, would also be useful in this regard and would provide further clarity and understanding of precisely what the difficulties are when imaging brain tissue.

The issue of region-of-interest localisation is also a difficulty. A potentially useful combination may be some sort of combined high-detail scout image, using MR or another imaging technique, and subsequently running a DECT scan. This would require significantly different hardware to anything

that is available on the market at the moment but would circumvent the issue of the difficulty of getting high resolution CT images of the brain.

Another interesting avenue is the more recent advancement of machine learning and specifically deep learning for automatic image registration. This thesis used radiologist-guided and brain-atlas-guided manual segmentation to find areas of interest within images, whereas a deep learning algorithm could be trained to recognise shapes, features and patterns to reliably locate brain features automatically and with a high degree of accuracy. This has already become an area of active research (Gibson et al., 2018; Zaharchuk et al., 2018), and there is evidence to suggest that this will become a key area of focus in segmentation and therefore in accurate quantitative medical imaging.

A natural progression of the technique to avoid the issue of low detection limit is to first develop and extend the field in the area of liver iron overload. Many of the same complexities with human body matrix effects are present, but the increased iron concentration would allow accurate determination of the best energies, parameters and scan settings to use to maximise iron signal. Extending the study design, whether through animal studies or use of tissue-like phantoms, could then ensure that as neurological iron levels are approached, the technique itself is repeatable, consistent and reliable. At present, there are too many confounding effects at play to develop the brain-iron technique in isolation.

In 2021, Gassenmaier et al (Gassenmaier et al., 2021) produced a paper comparing DECT with multi-echo MRI in quantifying liver fat concentration in 11 patients.

This is the avenue that this research should take going forward – to establish optimal clinical settings and parameters for the accurate determination of liver iron overload, before any work can be extended to lower and lower concentration regions found in the brain.

While a DECT-based quantitative iron scanning protocol, valid at neurologically relevant iron concentrations, would be of huge diagnostic benefit, the results in this thesis provide evidence that it is unlikely to be achievable with the current state of the art. Therefore, alternative research avenues

should be explored first to develop the techniques as far as possible, before scaling down to neurologically relevant iron concentration ranges is considered.

References

- Abadia, A. F., Grant, K. L., Carey, K. E., Bolch, W. E., & Morin, R. L. (2017). Spatial Distribution of Iron Within the Normal Human Liver Using Dual-Source Dual-Energy CT Imaging. *Investigative Radiology*. <https://doi.org/10.1097/RLI.0000000000000393>
- AD Elster. (2021). *MR Artifacts: Why does the phase wrap-around artefact occur?* MRIQuestions.Com.
- Agilent. (2022). *ICPMS Food Safety Training PDF*. https://www.agilent.com/cs/library/training/public/6_ICPMS_FoodSafety_Training.pdf
- Ahmed, J., Ahmad, N., Jankharia, B., Krishnan, P., & Merchant, R. H. (2013). Effect of deferasirox chelation on liver iron and total body iron concentration. *Indian Journal of Pediatrics*. <https://doi.org/10.1007/s12098-013-1030-y>
- Ahn, B., Smith, N., Saunders, D., Ranjit, R., Kneis, P., Towner, R. A., & Van Remmen, H. (2019). Using MRI to measure in vivo free radical production and perfusion dynamics in a mouse model of elevated oxidative stress and neurogenic atrophy. *Redox Biology*. <https://doi.org/10.1016/j.redox.2019.101308>
- Alkinoos, A., Manousos, K., Nicolas, F., Kyriaki Rafailia, K., Konstantinos, P., & Panagiotis, B. (2016). Reorganization of brain networks after spinal cord injury: a qualitative synthesis of the literature. *Frontiers in Human Neuroscience*. <https://doi.org/10.3389/conf.fnhum.2016.220.00036>
- Alvarez, R. E., & MacOvski, A. (1976). Energy-selective reconstructions in X-ray computerised tomography. *Physics in Medicine and Biology*. <https://doi.org/10.1088/0031-9155/21/5/002>
- Andrjevski, P. (1928). THE INFLUENCE OF PUTREFACTIVE GASES ON B. ANTHRACIS. *Journal of Bacteriology*.
- Ayton, S., Portbury, S., Kalinowski, P., Agarwal, P., Diouf, I., Schneider, J. A., Morris, M. C., & Bush, A. I. (2021). Regional brain iron associated with deterioration in Alzheimer's disease: A

large cohort study and theoretical significance. *Alzheimer's and Dementia*.

<https://doi.org/10.1002/alz.12282>

Bacci, G. (2001). Relationship between dose-intensity of treatment and outcome for patients with osteosarcoma of the extremity treated with neoadjuvant chemotherapy. *Oncology Reports*.

<https://doi.org/10.3892/or.8.4.883>

Barbosa, J. H. O., Santos, A. C., Tumas, V., Liu, M., Zheng, W., Haacke, E. M., & Salmon, C. E. G. (2015). Quantifying brain iron deposition in patients with Parkinson's disease using quantitative susceptibility mapping, R2 and R2*. *Magnetic Resonance Imaging*.

<https://doi.org/10.1016/j.mri.2015.02.021>

Bartzokis, G., & Tishler, T. A. (2000). MRI evaluation of basal ganglia ferritin iron and neurotoxicity in Alzheimer's and Huntington's disease. *Cellular and Molecular Biology (Noisy-Le-Grand, France)*.

Bartzokis, G, Sultzer, D., Cummings, J., Holt, L. E., Hance, D. B., Henderson, V. W., & Mintz, J. (2000). In vivo evaluation of brain iron in Alzheimer disease using magnetic resonance imaging. *Archives of General Psychiatry*, 57(1), 47–53. <https://doi.org/10.1001/archpsyc.57.1.47>

Bartzokis, G, Sultzer, D., Mintz, J., Holt, L. E., Marx, P., Phelan, C. K., & Marder, S. R. (1994). In vivo evaluation of brain iron in Alzheimer's disease and normal subjects using MRI. *Biol Psychiatry*, 35(7), 480–487.

Bartzokis, George, Cummings, J. L., Markham, C. H., Marmarelis, P. Z., Treciokas, L. J., Tishler, T. A., Marder, S. R., & Mintz, J. (1999). MRI evaluation of brain iron in earlier- and later-onset Parkinson's disease and normal subjects. *Magnetic Resonance Imaging*, 17(2), 213–222. [https://doi.org/10.1016/S0730-725X\(98\)00155-6](https://doi.org/10.1016/S0730-725X(98)00155-6)

Bartzokis, George, Tishler, T. A., Shin, I. S., Lu, P. H., & Cummings, J. L. (2004). Brain ferritin iron as a risk factor for age at onset in neurodegenerative diseases. *Annals of the New York Academy of Sciences*. <https://doi.org/10.1196/annals.1306.019>

- Batts, K. P. (2007). Iron overload syndromes and the liver. *Modern Pathology*.
<https://doi.org/10.1038/modpathol.3800715>
- Bauminger, E. R., Barcikowska, M., Friedman, A., Galazka-Friedman, J., Hechel, D., & Nowik, I. (1994). Does iron play a role in Parkinson's disease? *Hyperfine Interactions*.
<https://doi.org/10.1007/BF02064618>
- Beister, M., Kolditz, D., & Kalender, W. A. (2012). Iterative reconstruction methods in X-ray CT. In *Physica Medica*. <https://doi.org/10.1016/j.ejmp.2012.01.003>
- Bergouignan, L., Lefranc, J. P., Chupin, M., Morel, N., Spano, J. P., & Fossati, P. (2011). Breast cancer affects both the hippocampus volume and the episodic autobiographical memory retrieval. *PLoS ONE*. <https://doi.org/10.1371/journal.pone.0025349>
- Bernstein, L. J., Edelstein, K., Sharma, A., & Alain, C. (2021). Chemo-brain: An activation likelihood estimation meta-analysis of functional magnetic resonance imaging studies. In *Neuroscience and Biobehavioral Reviews*. <https://doi.org/10.1016/j.neubiorev.2021.08.024>
- Birkel, C., Birkel-Toeglhofer, A. M., Kames, C., Goessler, W., Haybaeck, J., Fazekas, F., Ropele, S., & Rauscher, A. (2020). The influence of iron oxidation state on quantitative MRI parameters in post mortem human brain. *NeuroImage*. <https://doi.org/10.1016/j.neuroimage.2020.117080>
- Bloch, F., Hansen, W. W., & Packard, M. (1946). The nuclear induction experiment. *Physical Review*.
<https://doi.org/10.1103/PhysRev.70.474>
- Blommaert, J., Schroyen, G., Vandenbulcke, M., Radwan, A., Smeets, A., Peeters, R., Sleurs, C., Neven, P., Wildiers, H., Amant, F., Sunaert, S., & Deprez, S. (2019). Age-dependent brain volume and neuropsychological changes after chemotherapy in breast cancer patients. *Human Brain Mapping*. <https://doi.org/10.1002/hbm.24753>
- Bock, J., Doenitz, A., Andreesen, R., Reichle, A., & Hennemann, B. (2006). Pericarditis after high-dose chemotherapy: More frequent than expected? *Onkologie*.
<https://doi.org/10.1159/000093528>

- Boykoff, N., Moieni, M., & Subramanian, S. K. (2009). Confronting chemobrain: an in-depth look at survivors' reports of impact on work, social networks, and health care response. *Journal of Cancer Survivorship : Research and Practice*, 3(4), 223–232. <https://doi.org/10.1007/s11764-009-0098-x>
- Brar, S., Henderson, D., Schenck, J., & Zimmerman, E. A. (2009). Iron accumulation in the substantia nigra of patients with Alzheimer disease and parkinsonism. *Archives of Neurology*. <https://doi.org/10.1001/archneurol.2008.586>
- Brooks, D. J., Luthert, P., Gadian, D., & Marsden, C. D. (1989). Does signal-attenuation of high-field T2-weighted MRI of the brain reflect regional cerebral iron deposition? Observations on the relationship between regional cerebral water proton T2 values and iron levels. *Journal of Neurology Neurosurgery and Psychiatry*. <https://doi.org/10.1136/jnnp.52.1.108>
- Brooks, R. A., Vymazal, J., Baumgarner, C. D., Tran, V., & Bulte, J. W. M. (1995). Comparison of t2 relaxation in blood, brain, and ferritin. *Journal of Magnetic Resonance Imaging*. <https://doi.org/10.1002/jmri.1880050414>
- Brown, M. S., Simon, J. H., Stemmer, S. M., Stears, J. C., Scherzinger, A., Cagnoni, P. J., & Jones, R. B. (1995). MR and proton spectroscopy of white matter disease induced by high-dose chemotherapy with bone marrow transplant in advanced breast carcinoma. *American Journal of Neuroradiology*.
- Brown, Mark S., Stemmer, S. M., Simon, J. H., Stears, J. C., Jones, R. B., Cagnoni, P. J., & Sheeder, J. L. (1998). White matter disease induced by high-dose chemotherapy: Longitudinal study with MR imaging and proton spectroscopy. *American Journal of Neuroradiology*.
- Bubba, T. (2019). *Mathematics of X-ray Tomography*. https://www.fips.fi/slides/Bubba_SummerSchoolVFIP2019_1.Pdf.
- Cardoso, C. V., de Barros, M. P., Bachi, A. L. L., Bernardi, M. M., Kirsten, T. B., de Fátima Monteiro Martins, M., Rocha, P. R. D. A., da Silva Rodrigues, P., & Bondan, E. F. (2020). Chemobrain in

- rats: Behavioral, morphological, oxidative and inflammatory effects of doxorubicin administration. *Behavioural Brain Research*. <https://doi.org/10.1016/j.bbr.2019.112233>
- Carocci, A., Catalano, A., Sinicropi, M. S., & Genchi, G. (2018). Oxidative stress and neurodegeneration: the involvement of iron. In *BioMetals*. <https://doi.org/10.1007/s10534-018-0126-2>
- Cetkovská, P., Pizinger, K., & Cetkovský, P. (2002). High-dose cytosine arabinoside-induced cutaneous reactions. *Journal of the European Academy of Dermatology and Venereology*. <https://doi.org/10.1046/j.1468-3083.2002.00395.x>
- Chaddock-Heyman, L., Mackenzie, M. J., Zuniga, K., Cooke, G. E., Awick, E., Roberts, S., Erickson, K. I., McAuley, E., & Kramer, A. F. (2015). Higher cardiorespiratory fitness levels are associated with greater hippocampal volume in breast cancer survivors. *Frontiers in Human Neuroscience*. <https://doi.org/10.3389/fnhum.2015.00465>
- Chauhan, V., & Chauhan, A. (2006). Oxidative stress in Alzheimer's disease. In *Pathophysiology* (Vol. 13, Issue 3, pp. 195–208). <https://doi.org/10.1016/j.pathophys.2006.05.004>
- Chemnitzer, R. (2019). Strategies for achieving the lowest possible detection limits in ICP-MS. *Spectroscopy (Santa Monica)*.
- Chen, B. T., Jin, T., Patel, S. K., Ye, N., Sun, C. L., Ma, H., Rockne, R. C., Root, J. C., Saykin, A. J., Ahles, T. A., Holodny, A. I., Prakash, N., Mortimer, J., Waisman, J., Yuan, Y., Li, D., Somlo, G., Vazquez, J., Levi, A., ... Hurria, A. (2018). Gray matter density reduction associated with adjuvant chemotherapy in older women with breast cancer. *Breast Cancer Research and Treatment*. <https://doi.org/10.1007/s10549-018-4911-y>
- Chen, X., He, X., Tao, L., Li, J., Wu, J., Zhu, C., Yu, F., Zhang, L., Zhang, J., Qiu, B., Yu, Y., & Wang, K. (2017). The working memory and dorsolateral prefrontal-hippocampal functional connectivity changes in long-term survival breast cancer patients treated with tamoxifen. *International Journal of Neuropsychopharmacology*. <https://doi.org/10.1093/ijnp/pyx008>

- Chen, Y., Jungsuwadee, P., Vore, M., Butterfield, D. A., & St. Clair, D. K. (2007). Collateral damage in cancer chemotherapy: Oxidative stress in nontargeted tissues. In *Molecular Interventions*.
<https://doi.org/10.1124/mi.7.3.6>
- Collingwood, J. F., & Davidson, M. R. (2014). The role of iron in neurodegenerative disorders: Insights and opportunities with synchrotron light. In *Frontiers in Pharmacology*.
<https://doi.org/10.3389/fphar.2014.00191>
- Collingwood, J., Finnegan, M., Arya, Z., Hagen, J., Chen, S., Chowdhury, A., Wayte, S., Ngandwe, E., Visanji, N., Dobson, J., Gowland, P., Hazrati, L., & Hutchinson, C. (2014). MRI evaluation of the relationship between R2, R2*, and tissue iron in the human basal ganglia. *International Society for Magnetic Resonance in Medicine Annual Meeting*.
<http://publications.diamond.ac.uk/pubman/viewpublication?publicationId=4964>
- Degremont, A., Jain, R., Philippou, E., & Latunde-Dada, G. O. (2021). Brain iron concentrations in the pathophysiology of children with attention deficit/hyperactivity disorder: A systematic review. *Nutrition Reviews*. <https://doi.org/10.1093/nutrit/nuaa065>
- Deture, M. A., & Dickson, D. W. (2019). The neuropathological diagnosis of Alzheimer's disease. In *Molecular Neurodegeneration*. <https://doi.org/10.1186/s13024-019-0333-5>
- Dias, V., Junn, E., & Mouradian, M. M. (2013). The role of oxidative stress in parkinson's disease. In *Journal of Parkinson's Disease*. <https://doi.org/10.3233/JPD-130230>
- DICOM Nema. (2016). *dicom.nema.org DICOM Headers*.
https://dicom.nema.org/medical/dicom/2016a/output/chtml/part03/sect_C.8.2.html
- Drayer, B., Burger, P., & Hurwitz, B. (1987). Reduced signal intensity on MR images of thalamus and putamen in multiple sclerosis: Increased iron content? *American Journal of Neuroradiology*.
- Duce, J. A., Tsatsanis, A., Cater, M. A., James, S. A., Robb, E., Wikke, K., Leong, S. L., Perez, K., Johanssen, T., Greenough, M. A., Cho, H. H., Galatis, D., Moir, R. D., Masters, C. L., McLean, C., Tanzi, R. E., Cappai, R., Barnham, K. J., Ciccotosto, G. D., ... Bush, A. I. (2010). Iron-

- Export Ferroxidase Activity of β -Amyloid Precursor Protein is Inhibited by Zinc in Alzheimer's Disease. *Cell*, 142(6), 857–867. <https://doi.org/10.1016/j.cell.2010.08.014>
- El-Agamy, S. E., Abdel-Aziz, A. K., Esmat, A., & Azab, S. S. (2019). Chemotherapy and cognition: comprehensive review on doxorubicin-induced chemobrain. In *Cancer Chemotherapy and Pharmacology*. <https://doi.org/10.1007/s00280-019-03827-0>
- Elbanna, K. Y., Mansoori, B., Mileto, A., Rogalla, P., & S. Guimarães, L. (2020). Dual-energy CT in diffuse liver disease: is there a role? *Abdominal Radiology*. <https://doi.org/10.1007/s00261-020-02702-4>
- Everett, J., Collingwood, J. F., Tjendana-Tjhin, V., Brooks, J., Lermyte, F., Plascencia-Villa, G., Hands-Portman, I., Dobson, J., Perry, G., & Telling, N. D. (2018). Nanoscale synchrotron X-ray speciation of iron and calcium compounds in amyloid plaque cores from Alzheimer's disease subjects. *Nanoscale*. <https://doi.org/10.1039/c7nr06794a>
- FCRPhysics. (2012). *No Title*. <https://sites.google.com/site/frcrphysicsnotes/production-of-x-rays>
- Ferguson, R. J., McDonald, B. C., Saykin, A. J., & Ahles, T. A. (2007). Brain structure and function differences in monozygotic twins: Possible effects of breast cancer chemotherapy. *Journal of Clinical Oncology*. <https://doi.org/10.1200/JCO.2007.10.8639>
- Ferreira, C. C., Ximenes Filho, R. E. M., Vieira, J. W., Tomal, A., Poletti, M. E., Garcia, C. A. B., & Maia, A. F. (2010). Evaluation of tissue-equivalent materials to be used as human brain tissue substitute in dosimetry for diagnostic radiology. *Nuclear Instruments and Methods in Physics Research, Section B: Beam Interactions with Materials and Atoms*, 268(16), 2515–2521. <https://doi.org/10.1016/j.nimb.2010.05.051>
- Finnegan, M. E., Visanji, N. P., Romero-Canelon, I., House, E., Rajan, S., Mosselmans, J. F. W., Hazrati, L. N., Dobson, J., & Collingwood, J. F. (2019). Synchrotron XRF imaging of Alzheimer's disease basal ganglia reveals linear dependence of high-field magnetic resonance microscopy on tissue iron concentration. *Journal of Neuroscience Methods*.

<https://doi.org/10.1016/j.jneumeth.2019.03.002>

Fischer, M. A., Gnannt, R., Raptis, D., Reiner, C. S., Clavien, P. A., Schmidt, B., Leschka, S.,

Alkadhi, H., & Goetti, R. (2011). Quantification of liver fat in the presence of iron and iodine:

An ex-vivo dual-energy CT study. *Investigative Radiology*.

<https://doi.org/10.1097/RLI.0b013e31820e1486>

Fischer, M. A., Reiner, C. S., Raptis, D., Donati, O., Goetti, R., Clavien, P. A., & Alkadhi, H. (2011).

Quantification of liver iron content with CT-added value of dual-energy. *European Radiology*.

<https://doi.org/10.1007/s00330-011-2119-1>

Gaa, J., Weidauer, S., Requardt, M., Kiefer, B., Lanfermann, H., & Zanella, F. E. (2004). Comparison

of intracranial 3D-ToF-MRA with and without parallel acquisition techniques at 1.5T and 3.0T:

Preliminary results. *Acta Radiologica*. <https://doi.org/10.1080/02841850410004229>

Gaman, A. M., Uzoni, A., Popa-Wagner, A., Andrei, A., & Petcu, E. B. (2016). The role of oxidative

stress in etiopathogenesis of chemotherapy induced cognitive impairment (CICI)-"Chemobrain".

In *Aging and Disease*. <https://doi.org/10.14336/AD.2015.1022>

Gao, Y., Tan, M. S., Wang, H. F., Zhang, W., Wang, Z. X., Jiang, T., Yu, J. T., & Tan, L. (2016).

ZCWPW1 is associated with late-onset Alzheimer's disease in han Chinese: A replication study

and meta-analyses. *Oncotarget*. <https://doi.org/10.18632/oncotarget.7945>

Garaventa, A., Rondelli, R., Lanino, E., Dallorso, S., Dini, G., Bonetti, F., Arrighini, A., Santoro, N.,

Rossetti, F., Miniero, R., Andolina, M., Amici, A., Indolfi, P., Lo Curto, M., Favre, C., Paolucci,

P., Pession, A., & De Bernardi, B. (1996). Myeloablative therapy and bone marrow rescue in

advanced neuroblastoma. Report from the Italian Bone Marrow Transplant Registry. Italian

Association of Pediatric Hematology-Oncology, BMT Group. *Bone Marrow Transplantation*.

Gassenmaier, S., Kähm, K., Walter, S. S., Machann, J., Nikolaou, K., & Bongers, M. N. (2021).

Quantification of liver and muscular fat using contrast-enhanced Dual Source Dual Energy

Computed Tomography compared to an established multi-echo Dixon MRI sequence. *European*

Journal of Radiology. <https://doi.org/10.1016/j.ejrad.2021.109845>

GE-Healthcare. (2009). *Discovery MR750, a 3.0T system*.

<https://www.gehealthcare.com/products/magnetic-resonance-imaging/3-0t/discovery-mr750>

GE-Healthcare. (2011). *Discovery 750HD User Manual*.

<https://www.manualsdir.com/manuals/254620/ge-healthcare-discovery-mr750w-30t.html?download>

Gelman, N., Gorell, J. M., Barker, P. B., Savage, R. M., Spickler, E. M., Windham, J. P., & Knight, R. A. (1999). MR imaging of human brain at 3.0 T: Preliminary report on transverse relaxation rates and relation to estimated iron content. *Radiology*.

<https://doi.org/10.1148/radiology.210.3.r99fe41759>

Ghadery, C., Pirpamer, L., Hofer, E., Langkammer, C., Petrovic, K., Loitfelder, M., Schwingenschuh, P., Seiler, S., Duering, M., Jouvent, E., Schmidt, H., Fazekas, F., Mangin, J. F., Chabriat, H., Dichgans, M., Ropele, S., & Schmidt, R. (2015). R2* mapping for brain iron: Associations with cognition in normal aging. *Neurobiology of Aging*.

<https://doi.org/10.1016/j.neurobiolaging.2014.09.013>

Gibson, E., Li, W., Sudre, C., Fidon, L., Shakir, D. I., Wang, G., Eaton-Rosen, Z., Gray, R., Doel, T., Hu, Y., Whyntie, T., Nachev, P., Modat, M., Barratt, D. C., Ourselin, S., Cardoso, M. J., & Vercauteren, T. (2018). NiftyNet: a deep-learning platform for medical imaging. *Computer Methods and Programs in Biomedicine*. <https://doi.org/10.1016/j.cmpb.2018.01.025>

Glenner, G. G., & Wong, C. W. (1984). Alzheimer's disease and Down's syndrome: Sharing of a unique cerebrovascular amyloid fibril protein. *Biochemical and Biophysical Research Communications*. [https://doi.org/10.1016/0006-291X\(84\)91209-9](https://doi.org/10.1016/0006-291X(84)91209-9)

Glover, P., & Mansfield, S. P. (2002). Limits to magnetic resonance microscopy. *Reports on Progress in Physics*. <https://doi.org/10.1088/0034-4885/65/10/203>

Goate, A., Chartier-Harlin, M. C., Mullan, M., Brown, J., Crawford, F., Fidani, L., Giuffra, L.,

- Haynes, A., Irving, N., James, L., Mant, R., Newton, P., Rooke, K., Roques, P., Talbot, C., Pericak-Vance, M., Roses, A., Williamson, R., Rossor, M., ... Hardy, J. (1991). Segregation of a missense mutation in the amyloid precursor protein gene with familial Alzheimer's disease. *Nature*. <https://doi.org/10.1038/349704a0>
- Goodwin, J. F., & Murphy, B. (1966). The colorimetric determination of iron in biological material with reference to its measurement during chelation therapy. *Clinical Chemistry*. <https://doi.org/10.1093/clinchem/12.2.58>
- Gossuin, Y., Burtea, C., Monseux, A., Toubreau, G., Roch, A., Muller, R. N., & Gillis, P. (2004). Ferritin-induced relaxation in tissues: An in vitro study. *Journal of Magnetic Resonance Imaging*. <https://doi.org/10.1002/jmri.20152>
- Griffiths, P. D., Dobson, B. R., Jones, G. R., & Clarke, D. T. (1999). Iron in the basal ganglia in Parkinson's disease. An in vitro study using extended X-ray absorption fine structure and cryo-electron microscopy. *Brain*. <https://doi.org/10.1093/brain/122.4.667>
- H.C., M. (2014). An overview of chemotherapy-related cognitive dysfunction, or "chemobrain." *Oncology (Williston Park, N.Y.)*, 28(9), 797–804. <http://ovidsp.ovid.com/ovidweb.cgi?T=JS&PAGE=reference&D=emed13&NEWS=N&AN=25224480>
- Haacke, E. M., Cheng, N. Y. C., House, M. J., Liu, Q., Neelavalli, J., Ogg, R. J., Khan, A., Ayaz, M., Kirsch, W., & Obenaus, A. (2005). Imaging iron stores in the brain using magnetic resonance imaging. *Magnetic Resonance Imaging*. <https://doi.org/10.1016/j.mri.2004.10.001>
- Hahn, E. L. (1950). Nuclear induction due to free larmor precession [18]. In *Physical Review*. <https://doi.org/10.1103/PhysRev.77.297.2>
- Hallgren, B., & Sourander, P. (1958). THE EFFECT OF AGE ON THE NON???HAEMIN IRON IN THE HUMAN BRAIN. *Journal of Neurochemistry*, 3(1), 41–51. <https://doi.org/10.1111/j.1471-4159.1958.tb12607.x>

- Hallgren, Bo, & Sourander, P. (1960a). The nonhemin iron in the cerebral cortex in Alzheimer's disease. *Journal of Neurochemistry*, 5, 307–310. <https://doi.org/10.1111/j.1471-4159.1960.tb13369.x>
- Hallgren, Bo, & Sourander, P. (1960b). The nonhemin iron in the cerebral cortex in Alzheimer's disease. *Journal of Neurochemistry*, 5, 307–310. <https://doi.org/10.1111/j.1471-4159.1960.tb13369.x>
- Hara, A. K., Paden, R. G., Silva, A. C., Kujak, J. L., Lawder, H. J., & Pavlicek, W. (2009). Iterative reconstruction technique for reducing body radiation dose at CT: Feasibility study. *American Journal of Roentgenology*, 193(3), 764–771. <https://doi.org/10.2214/AJR.09.2397>
- Hardy, J., & Selkoe, D. J. (2002). The amyloid hypothesis of Alzheimer's disease: Progress and problems on the road to therapeutics. In *Science*. <https://doi.org/10.1126/science.1072994>
- Hardy, P. A., Gash, D., Yokel, R., Andersen, A., Ai, Y., & Zhang, Z. (2005). Correlation of R2 with total iron concentration in the brains of rhesus monkeys. *Journal of Magnetic Resonance Imaging*, 21(2), 118–127. <https://doi.org/10.1002/jmri.20244>
- Hawrylycz, M. J., Lein, E. S., Guillozet-Bongaarts, A. L., Shen, E. H., Ng, L., Miller, J. A., Van De Lagemaat, L. N., Smith, K. A., Ebbert, A., Riley, Z. L., Abajian, C., Beckmann, C. F., Bernard, A., Bertagnolli, D., Boe, A. F., Cartagena, P. M., Mallar Chakravarty, M., Chapin, M., Chong, J., ... Jones, A. R. (2012). An anatomically comprehensive atlas of the adult human brain transcriptome. *Nature*. <https://doi.org/10.1038/nature11405>
- Herman, G. T. (2009). Fundamentals of Computerized Tomography. In *Scientific American*. <https://doi.org/10.1038/scientificamerican0471-56>
- Herrup, K. (2015). The case for rejecting the amyloid cascade hypothesis. *Nature Neuroscience*. <https://doi.org/10.1038/nn.4017>
- House, M. J., Pierre, T. G. S., & McLean, C. (2008). 1.4T study of proton magnetic relaxation rates, iron concentrations, and plaque burden in Alzheimer's disease and control postmortem brain

- tissue. *Magnetic Resonance in Medicine*. <https://doi.org/10.1002/mrm.21586>
- House, M. J., St. Pierre, T. G., Kowdley, K. V., Montine, T., Connor, J., Beard, J., Berger, J., Siddaiah, N., Shankland, E., & Jin, L. W. (2007a). Correlation of proton transverse relaxation rates (R2) with iron concentrations in postmortem brain tissue from Alzheimer's disease patients. *Magnetic Resonance in Medicine*, *57*(1), 172–180. <https://doi.org/10.1002/mrm.21118>
- House, M. J., St. Pierre, T. G., Kowdley, K. V., Montine, T., Connor, J., Beard, J., Berger, J., Siddaiah, N., Shankland, E., & Jin, L. W. (2007b). Correlation of proton transverse relaxation rates (R2) with iron concentrations in postmortem brain tissue from Alzheimer's disease patients. *Magnetic Resonance in Medicine*, *57*(1), 172–180. <https://doi.org/10.1002/mrm.21118>
- Hubbell, J. H. (1996). *X-Ray Mass Attenuation Coefficients. NIST Standard Reference Database 126*. <Http://Physics.Nist.Gov/PhysRefData/XrayMassCoef/>.
- Huntington's Disease - Core Concepts and Current Advances. (2012). In *Huntington's Disease - Core Concepts and Current Advances*. <https://doi.org/10.5772/1470>
- Ibrahim, E.-S., & Bowman, A. (2014). Evaluation of iron overload: dual-energy computed tomography versus magnetic resonance imaging. *Journal of Cardiovascular Magnetic Resonance*, *16*(1), 92.
- Ibrahim, E. S. H., Cernigliaro, J. G., Pooley, R. A., Bridges, M. D., Giesbrandt, J. G., Williams, J. C., & Haley, W. E. (2015). Detection of different kidney stone types: An ex vivo comparison of ultrashort echo time MRI to reference standard CT. *Clinical Imaging*, *40*(1), 90–95. <https://doi.org/10.1016/j.clinimag.2015.09.005>
- Inagaki, M., Yoshikawa, E., Matsuoka, Y., Sugawara, Y., Nakano, T., Akechi, T., Wada, N., Imoto, S., Murakami, K., Uchitomi, Y., Kobayakawa, M., Akizuki, N., & Fujimori, M. (2007). Smaller regional volumes of brain gray and white matter demonstrated in breast cancer survivors exposed to adjuvant chemotherapy. *Cancer*. <https://doi.org/10.1002/cncr.22368>
- Iseki, E., Matsushita, M., Kosaka, K., Kondo, H., Ishii, T., & Amano, N. (1989). Distribution and

- morphology of brain stem plaques in Alzheimer's disease. *Acta Neuropathologica*.
<https://doi.org/10.1007/BF00688200>
- Jacobsen, M. C., Cressman, E. N. K., Tamm, E. P., Baluya, D. L., Duan, X., Cody, D. D., Schellingerhout, D., & Layman, R. R. (2019). Dual-energy CT: Lower limits of iodine detection and quantification. *Radiology*. <https://doi.org/10.1148/radiol.2019182870>
- Jellinger, K., Paulus, W., Grundke-Iqbal, I., Riederer, P., & Youdim, M. B. H. (1990). Brain iron and ferritin in Parkinson's and Alzheimer's diseases. *Journal of Neural Transmission - Parkinson's Disease and Dementia Section*, 2(4), 327–340. <https://doi.org/10.1007/BF02252926>
- Jezzard, P. (2006). Shim Coil Design, Limitations and Implications. *Abstracts from the International Society of Magnetic Resonance in Medicine (ISMRM) Annual Meeting*.
- Jiahua Fan, M. Y. (2014). *Benefits of ASiR-V* Reconstruction for Reducing Patient Radiation Dose and Preserving Diagnostic Quality in CT Exams*.
- Jiang, X., Hintenlang, D. E., & White, R. D. (2021). Lower limit of iron quantification using dual-energy CT — a phantom study. *Journal of Applied Clinical Medical Physics*.
<https://doi.org/10.1002/acm2.13124>
- Johnson, K. (1999). *Harvard Brain Atlas*. <http://www.med.harvard.edu/aanlib/>
- Johnson, T. R. C. (2012). Dual-energy CT: general principles. *AJR. American Journal of Roentgenology*, 199(5 Suppl). <https://doi.org/10.2214/AJR.12.9116>
- Joshi, G., Sultana, R., Tangpong, J., Cole, M. P., St. Clair, D. K., Vore, M., Estus, S., & Butterfield, D. A. (2005). Free radical mediated oxidative stress and toxic side effects in brain induced by the anti cancer drug adriamycin: Insight into chemobrain. *Free Radical Research*.
<https://doi.org/10.1080/10715760500143478>
- Kamalian, S., Lev, M. H., & Gupta, R. (2016). Computed tomography imaging and angiography – principles. In *Handbook of Clinical Neurology*. <https://doi.org/10.1016/B978-0-444-53485-9.00001-5>

- Karçaaltincaba, M., & Aktaş, A. (2011). Dual-energy CT revisited with multidetector CT: Review of principles and clinical applications. In *Diagnostic and Interventional Radiology*.
<https://doi.org/10.4261/1305-3825.DIR.3860-10.0>
- Ke, Y., & Qian, Z. M. (2003). Iron misregulation in the brain: A primary cause of neurodegenerative disorders. In *Lancet Neurology*. [https://doi.org/10.1016/S1474-4422\(03\)00353-3](https://doi.org/10.1016/S1474-4422(03)00353-3)
- Kim, S. Y., Lee, K. H., Kim, K., Kim, T. Y., Lee, H. S., Hwang, S., Song, K. J., Kang, H. S., Kim, Y. H., & Rhee, J. E. (2011). Acute Appendicitis in Young Adults: Low- versus Standard-Radiation-Dose Contrast-enhanced Abdominal CT for Diagnosis. *Radiology*, 260(2), 437–445.
<https://doi.org/10.1148/radiol.11102247>
- Kobayashi, T., Isobe, T., Shiotani, S., Saito, H., Saotome, K., Kaga, K., Miyamoto, K., Kikuchi, K., Hayakawa, H., Akutsu, H., & Homma, K. (2010). Postmortem magnetic resonance imaging dealing with low temperature objects. In *Magnetic Resonance in Medical Sciences*.
<https://doi.org/10.2463/mrms.9.101>
- Koeppen, A. H. (1995). The history of iron in the brain. *Journal of the Neurological Sciences*.
[https://doi.org/10.1016/0022-510X\(95\)00202-D](https://doi.org/10.1016/0022-510X(95)00202-D)
- Koppelmans, V., Breteler, M. M. B., Boogerd, W., Seynaeve, C., Gundy, C., & Schagen, S. B. (2012). Neuropsychological performance in survivors of breast cancer more than 20 years after adjuvant chemotherapy. *Journal of Clinical Oncology*. <https://doi.org/10.1200/JCO.2011.37.0189>
- Kovalchuk, A., & Kolb, B. (2017). Chemo brain: From discerning mechanisms to lifting the brain fog—An aging connection. In *Cell Cycle*. <https://doi.org/10.1080/15384101.2017.1334022>
- Kruer, M. C., Boddart, N., Schneider, A., Houlden, H., Bhatia, K. P., Gregory, A., Anderson, J. C., Rooney, W. D., Hogarth, P., & Hayflick, S. J. (2012). Neuroimaging features of neurodegeneration with brain iron accumulation. In *American Journal of Neuroradiology* (Vol. 33, Issue 3, pp. 407–414). <https://doi.org/10.3174/ajnr.A2677>
- Kumar, P., Bulk, M., Webb, A., Van Der Weerd, L., Oosterkamp, T. H., Huber, M., & Bossoni, L.

- (2016). A novel approach to quantify different iron forms in ex-vivo human brain tissue. *Scientific Reports*. <https://doi.org/10.1038/srep38916>
- Kumar, V., McElhanon, K. E., Min, J. K., He, X., Xu, Z., Beck, E. X., Simonetti, O. P., Weisleder, N., & Raman, S. V. (2018). Non-contrast estimation of diffuse myocardial fibrosis with dual energy CT: A phantom study. *Journal of Cardiovascular Computed Tomography*. <https://doi.org/10.1016/j.jcct.2017.12.002>
- Langkammer, C., Ropele, S., Pirpamer, L., Fazekas, F., & Schmidt, R. (2014). MRI for iron mapping in Alzheimer's disease. *Neurodegenerative Diseases*. <https://doi.org/10.1159/000353756>
- Lanoiselée, H. M., Nicolas, G., Wallon, D., Rovelet-Lecrux, A., Lacour, M., Rousseau, S., Richard, A. C., Pasquier, F., Rollin-Sillaire, A., Martinaud, O., Quillard-Muraine, M., de la Sayette, V., Boutoleau-Bretonniere, C., Etcharry-Bouyx, F., Chauviré, V., Sarazin, M., le Ber, I., Epelbaum, S., Jonveaux, T., ... Champion, D. (2017). APP, PSEN1, and PSEN2 mutations in early-onset Alzheimer disease: A genetic screening study of familial and sporadic cases. *PLoS Medicine*. <https://doi.org/10.1371/journal.pmed.1002270>
- LaVaute, T., Smith, S., Cooperman, S., Iwai, K., Land, W., Meyron-Holtz, E., Drake, S. K., Miller, G., Abu-Asab, M., Tsokos, M., Switzer, R., Grinberg, A., Love, P., Tresser, N., & Rouault, T. A. (2001). Targeted deletion of the gene encoding iron regulatory protein-2 causes misregulation of iron metabolism and neurodegenerative disease in mice. *Nature Genetics*. <https://doi.org/10.1038/84859>
- Leening P. Liu^{1, 2}, N. S., Halliburton³, S. S., Meyer¹, S., Perkins³, A., Litt¹, H. I., Kauczor⁴, H. U., Leiner⁵, T., Stiller^{4*}, W., & Noël^{1*}, P. B. (2022). Spectral performance evaluation of a second-generation spectral detector CT. *MedRxiv Preprint Doi*: <https://doi.org/10.1101/2022.06.03.22275935>. <https://doi.org/10.1101/2022.06.03.22275935>
- Leng, S., Bruesewitz, M., Tao, S., Rajendran, K., Halaweish, A. F., Campeau, N. G., Fletcher, J. G., & McCollough, C. H. (2019). Photon-counting detector CT: System design and clinical

- applications of an emerging technology. *Radiographics*. <https://doi.org/10.1148/rg.2019180115>
- Levy-Lahad, E., Wasco, W., Poorkaj, P., Romano, D. M., Oshima, J., Pettingell, W. H., Yu, C. E., Jondro, P. D., Schmidt, S. D., Wang, K., Crowley, A. C., Fu, Y. H., Guenette, S. Y., Galas, D., Nemens, E., Wijsman, E. M., Bird, T. D., Schellenberg, G. D., & Tanzi, R. E. (1995). Candidate gene for the chromosome 1 familial Alzheimer's disease locus. *Science*. <https://doi.org/10.1126/science.7638622>
- Levy, A. D., Abbott, R. M., Mallak, C. T., Getz, J. M., Harcke, H. T., Champion, H. R., & Pearse, L. A. (2006). Virtual autopsy: Preliminary experience in high-velocity gunshot wound victims. In *Radiology*. <https://doi.org/10.1148/radiol.2402050972>
- Lewis, M. M., Du, G., Kidacki, M., Patel, N., Shaffer, M. L., Mailman, R. B., & Huang, X. (2013). Higher iron in the red nucleus marks Parkinson's dyskinesia. *Neurobiology of Aging*. <https://doi.org/10.1016/j.neurobiolaging.2012.10.025>
- Li, C. S. R. (2000). Impairment of motor imagery in putamen lesions in humans. *Neuroscience Letters*. [https://doi.org/10.1016/S0304-3940\(00\)01164-2](https://doi.org/10.1016/S0304-3940(00)01164-2)
- Li, M., & Caeyenberghs, K. (2018). Longitudinal assessment of chemotherapy-induced changes in brain and cognitive functioning: A systematic review. In *Neuroscience and Biobehavioral Reviews*. <https://doi.org/10.1016/j.neubiorev.2018.05.019>
- Li, Q., Wu, X., Xu, L., Chen, K., & Yao, L. (2018). Classification of Alzheimer's disease, mild cognitive impairment, and cognitively unimpaired individuals using multi-feature kernel discriminant dictionary learning. *Frontiers in Computational Neuroscience*. <https://doi.org/10.3389/fncom.2017.00117>
- Li, S., Yuan, S., Zhao, Q., Wang, B., Wang, X., & Li, K. (2018). Quercetin enhances chemotherapeutic effect of doxorubicin against human breast cancer cells while reducing toxic side effects of it. *Biomedicine and Pharmacotherapy*. <https://doi.org/10.1016/j.biopha.2018.02.055>

- Loeffler, D. A., Connor, J. R., Juneau, P. L., Snyder, B. S., Kanaley, L., DeMaggio, A. J., Nguyen, H., Brickman, C. M., & LeWitt, P. A. (1995). Transferrin and Iron in Normal, Alzheimer's Disease, and Parkinson's Disease Brain Regions. *Journal of Neurochemistry*.
<https://doi.org/10.1046/j.1471-4159.1995.65020710.x>
- Lovell, M. A., Robertson, J. D., Teesdale, W. J., Campbell, J. L., & Markesbery, W. R. (1998). Copper, iron and zinc in Alzheimer's disease senile plaques. *Journal of the Neurological Sciences*. [https://doi.org/10.1016/S0022-510X\(98\)00092-6](https://doi.org/10.1016/S0022-510X(98)00092-6)
- Lundström, C., Persson, A., Ross, S., Ljung, P., Lindholm, S., Gyllensvärd, F., & Ynnerman, A. (2012). State-of-the-art of visualization in post-mortem imaging. In *APMIS*.
<https://doi.org/10.1111/j.1600-0463.2011.02857.x>
- Luo, X. F., Yang, Y., Yan, J., Xie, X. Q., Zhang, H., Chai, W. M., Wang, L., Schmidt, B., & Yan, F. H. (2015). Virtual iron concentration imaging based on dual-energy CT for noninvasive quantification and grading of liver iron content: An iron overload rabbit model study. *European Radiology*, 25(9), 2657–2664. <https://doi.org/10.1007/s00330-015-3693-4>
- Lv, P., Lin, X., Gao, J., & Chen, K. (2012). Spectral CT: preliminary studies in the liver cirrhosis. *Korean Journal of Radiology : Official Journal of the Korean Radiological Society*, 13(4), 434–442. <https://doi.org/10.3348/kjr.2012.13.4.434>
- Ly, S. (2011). Magnetic Resonance Microscopy (MRM). *Embryo Project Encyclopedia*.
- Makin, S. (2018). The amyloid hypothesis on trial. *Nature*. <https://doi.org/10.1038/d41586-018-05719-4>
- Malvarosa, I., Massaroni, C., Liguori, C., Paul, J., Beomonte Zobel, B., Saccomandi, P., Vogl, T. J., Silvestri, S., & Schena, E. (2014). Estimation of liver iron concentration by dual energy CT images: Influence of X-ray energy on sensitivity. *2014 36th Annual International Conference of the IEEE Engineering in Medicine and Biology Society, EMBC 2014*.
<https://doi.org/10.1109/EMBC.2014.6944779>

- Mary E. Finnegan. (2013). *Investigation of the relationship between iron and high field MRI in healthy and Alzheimer's disease tissue*. <http://webcat.warwick.ac.uk/record=b2721556~S1>
- McCollough, C. H., Leng, S., Yu, L., & Fletcher, J. G. (2015). Dual- and multi-energy CT: Principles, technical approaches, and clinical applications. *Radiology*.
<https://doi.org/10.1148/radiol.2015142631>
- Minasian, S. G., Keith, J. M., Batista, E. R., Boland, K. S., Kozimor, S. A., Martin, R. L., Shuh, D. K., Tyliczszak, T., & Vernon, L. J. (2013). Carbon K-edge X-ray absorption spectroscopy and time-dependent density functional theory examination of metal-carbon bonding in metallocene dichlorides. *Journal of the American Chemical Society*, *135*(39), 14731–14740.
<https://doi.org/10.1021/ja405844j>
- N Flay, R. L. (2012). Application of the optical transfer function in x-ray computed tomography - a review. *NPL Report*.
- Nieboer, P., de Vries, E. G. E., Mulder, N. H., & van der Graaf, W. T. A. (2005). Relevance of high-dose chemotherapy in solid tumours. *Cancer Treatment Reviews*.
<https://doi.org/10.1016/j.ctrv.2005.02.002>
- Oakley, A. E., Collingwood, J. F., Dobson, J., Love, G., Perrott, H. R., Edwardson, J. A., Elstner, M., & Morris, C. M. (2007). Individual dopaminergic neurons show raised iron levels in Parkinson disease. *Neurology*. <https://doi.org/10.1212/01.wnl.0000262033.01945.9a>
- Obaid, D. R., Calvert, P. A., Gopalan, D., Parker, R. A., West, N. E. J., Goddard, M., Rudd, J. H. F., & Bennett, M. R. (2014). Dual-energy computed tomography imaging to determine atherosclerotic plaque composition: A prospective study with tissue validation. *Journal of Cardiovascular Computed Tomography*, *8*(3), 230–237.
<https://doi.org/10.1016/j.jcct.2014.04.007>
- Ordidge, R. J., Gorell, J. M., Deniau, J. C., Knight, R. A., & Helpert, J. A. (1994). Assessment of relative brain iron concentrations using T2-weighted and T2*-weighted MRI at 3 Tesla.

Magnetic Resonance in Medicine. <https://doi.org/10.1002/mrm.1910320309>

- Palmqvist, S., Zetterberg, H., Mattsson, N., Johansson, P., Minthon, L., Blennow, K., Olsson, M., & Hansson, O. (2015). Detailed comparison of amyloid PET and CSF biomarkers for identifying early Alzheimer disease. *Neurology*. <https://doi.org/10.1212/WNL.0000000000001991>
- Pauwels, R., Silkosessak, O., Jacobs, R., Bogaerts, R., Bosmans, H., & Panmekiate, S. (2014). A pragmatic approach to determine the optimal kVp in cone beam CT: Balancing contrast-to-noise ratio and radiation dose. *Dentomaxillofacial Radiology*. <https://doi.org/10.1259/dmfr.20140059>
- Peng, Y., Ye, J., Liu, C., Jia, H., Sun, J., Ling, J., Prince, M., Li, C., & Luo, X. (2021). Simultaneous hepatic iron and fat quantification with dual-energy CT in a rabbit model of coexisting iron and fat. *Quantitative Imaging in Medicine and Surgery*. <https://doi.org/10.21037/qims-20-902>
- Perl, D. P., & Good, P. F. (1992). Comparative techniques for determining cellular iron distribution in brain tissues. *Annals of Neurology*. <https://doi.org/10.1002/ana.410320713>
- Perrier, J., Viard, A., Levy, C., Morel, N., Allouache, D., Noal, S., Joly, F., Eustache, F., & Giffard, B. (2020). Longitudinal investigation of cognitive deficits in breast cancer patients and their gray matter correlates: impact of education level. *Brain Imaging and Behavior*. <https://doi.org/10.1007/s11682-018-9991-0>
- Persson, A., Jackowski, C., Engström, E., & Zachrisson, H. (2008). Advances of dual source, dual-energy imaging in postmortem CT. *European Journal of Radiology*. <https://doi.org/10.1016/j.ejrad.2008.05.008>
- Persson, A., Lindblom, M., & Jackowski, C. (2011). A state-of-the-art pipeline for postmortem CT and MRI visualization: From data acquisition to interactive image interpretation at autopsy. *Acta Radiologica*. <https://doi.org/10.1258/ar.2011.100460>
- Petersilka, M., Bruder, H., Krauss, B., Stierstorfer, K., & Flohr, T. G. (2008). Technical principles of dual source CT. *European Journal of Radiology*, 68(3), 362–368. <https://doi.org/10.1016/j.ejrad.2008.08.013>

- Peukert, X., Steindorf, K., Schagen, S. B., Runz, A., Meyer, P., & Zimmer, P. (2020). Hippocampus—Related Cognitive and Affective Impairments in Patients With Breast Cancer—A Systematic Review. *Frontiers in Oncology*. <https://doi.org/10.3389/fonc.2020.00147>
- Purcell, E. M., Pound, R. V., & Bloembergen, N. (1946). Nuclear magnetic resonance absorption in hydrogen gas [17]. In *Physical Review*. <https://doi.org/10.1103/PhysRev.70.986>
- Quemet, A., Brennetot, R., Chevalier, E., Prian, E., Laridon, A. L., Mariet, C., Fichet, P., Laszak, I., & Goutelard, F. (2012). Analysis of twenty five impurities in uranium matrix by ICP-MS with iron measurement optimized by using reaction collision cell, cold plasma or medium resolution. *Talanta*. <https://doi.org/10.1016/j.talanta.2012.05.041>
- Ramos, P., Santos, A., Pinto, N. R., Mendes, R., Magalhães, T., & Almeida, A. (2014). Iron levels in the human brain: A post-mortem study of anatomical region differences and age-related changes. *Journal of Trace Elements in Medicine and Biology*. <https://doi.org/10.1016/j.jtemb.2013.08.001>
- Reif, D. W. (1992). Ferritin as a source of iron for oxidative damage. *Free Radical Biology and Medicine*. [https://doi.org/10.1016/0891-5849\(92\)90091-T](https://doi.org/10.1016/0891-5849(92)90091-T)
- Reitz, C. (2012). Alzheimer's disease and the amyloid cascade hypothesis: A critical review. In *International Journal of Alzheimer's Disease*. <https://doi.org/10.1155/2012/369808>
- Rodriguez-Granillo, G. A., Deviggiano, A., Capunay, C., De Zan, M., Fernandez-Pereira, C., & Carrascosa, P. (2019). Role of Iterative Reconstruction Algorithm for the Assessment of Myocardial Infarction with Dual Energy Computed Tomography. *Academic Radiology*. <https://doi.org/10.1016/j.acra.2018.10.019>
- Roméo, F., & Hoult, D. I. (1984). Magnet field profiling: Analysis and correcting coil design. *Magnetic Resonance in Medicine*. <https://doi.org/10.1002/mrm.1910010107>
- Ronald, J. A., Chen, Y., Bernas, L., Kitzler, H. H., Rogers, K. A., Hegele, R. A., & Rutt, B. K. (2009). Clinical field-strength MRI of amyloid plaques induced by low-level cholesterol feeding in

- rabbits. *Brain*. <https://doi.org/10.1093/brain/awp031>
- Sande, E. P. S., Martinsen, A. C. T., Hole, E. O., & Olerud, H. M. (2010). Interphantom and interscanner variations for Hounsfield units-establishment of reference values for HU in a commercial QA phantom. *Physics in Medicine and Biology*. <https://doi.org/10.1088/0031-9155/55/17/015>
- Santin, M. D., Didier, M., Valabrègue, R., Yahia Cherif, L., García-Lorenzo, D., Loureiro de Sousa, P., Bardinet, E., & Lehericy, S. (2017). Reproducibility of R² * and quantitative susceptibility mapping (QSM) reconstruction methods in the basal ganglia of healthy subjects. *NMR in Biomedicine*. <https://doi.org/10.1002/nbm.3491>
- Schenck, J. F. (2003). Magnetic resonance imaging of brain iron. *Journal of the Neurological Sciences*. [https://doi.org/10.1016/S0022-510X\(02\)00431-8](https://doi.org/10.1016/S0022-510X(02)00431-8)
- Schipper, H. M. (2012). Neurodegeneration with brain iron accumulation - Clinical syndromes and neuroimaging. In *Biochimica et Biophysica Acta - Molecular Basis of Disease* (Vol. 1822, Issue 3, pp. 350–360). <https://doi.org/10.1016/j.bbadis.2011.06.016>
- Seger, C. A., & Cincotta, C. M. (2005). The roles of the caudate nucleus in human classification learning. *Journal of Neuroscience*. <https://doi.org/10.1523/JNEUROSCI.3401-04.2005>
- Shepp, L. A., & Vardi, Y. (1982). Maximum Likelihood Reconstruction for Emission Tomography. *IEEE Transactions on Medical Imaging*, 1(2), 113–122. <https://doi.org/10.1109/TMI.1982.4307558>
- Sherif, F. M., Said, A. M., Elsayed, Y. N., & Elmogy, S. A. (2020). Value of using adaptive statistical iterative reconstruction-V (ASIR-V) technology in pediatric head CT dose reduction. *Egyptian Journal of Radiology and Nuclear Medicine*. <https://doi.org/10.1186/s43055-020-00291-2>
- Sherrington, R., Rogaev, E. I., Liang, Y., Rogaeva, E. A., Levesque, G., Ikeda, M., Chi, H., Lin, C., Li, G., Holman, K., Tsuda, T., Mar, L., Foncin, J. F., Bruni, A. C., Montesi, M. P., Sorbi, S., Rainero, I., Pinessi, L., Nee, L., ... St George-Hyslop, P. H. (1995). Cloning of a gene bearing

missense mutations in early-onset familial Alzheimer's disease. *Nature*.

<https://doi.org/10.1038/375754a0>

Sheth, S., Allen, C. J., Farrell, D. E., Tripp, J. H., Jafari, R., Wang, Y., & Brittenham, G. M. (2019).

Measurement of the liver iron concentration in transfusional iron overload by MRI R2* and by high-transition-temperature superconducting magnetic susceptometry. *Clinical Imaging*.

<https://doi.org/10.1016/j.clinimag.2019.01.012>

Simó, M., Rifà-Ros, X., Rodriguez-Fornells, A., & Bruna, J. (2013). Chemobrain: A systematic

review of structural and functional neuroimaging studies. In *Neuroscience and Biobehavioral*

Reviews. <https://doi.org/10.1016/j.neubiorev.2013.04.015>

Smith, A. B., Lattin, G. E., Berran, P., & Harcke, H. T. (2012). Common and expected postmortem

CT observations involving the brain: Mimics of antemortem pathology. *American Journal of*

Neuroradiology. <https://doi.org/10.3174/ajnr.A2966>

Smith, R. L., Shi, X., & Estlin, E. J. (2012). Chemotherapy dose-intensity and survival for childhood

medulloblastoma. *Anticancer Research*.

Spence, H., McNeil, C. J., & Waiter, G. D. (2020). The impact of brain iron accumulation on

cognition: A systematic review. In *PLoS ONE*. <https://doi.org/10.1371/journal.pone.0240697>

St Pierre, T. G., Clark, P. R., & Chua-anusorn, W. (2004). Single spin-echo proton transverse

relaxometry of iron-loaded liver. In *NMR in Biomedicine*. <https://doi.org/10.1002/nbm.905>

Suyudi, I., Anam, C., Sutanto, H., Triadyaksa, P., & Fujibuchi, T. (2020). Comparisons of hounsfield

unit linearity between images reconstructed using an adaptive iterative dose reduction (AIDR)

and a filter back-projection (FBP) techniques. *Journal of Biomedical Physics and Engineering*.

<https://doi.org/10.31661/jbpe.v0i0.1912-1013>

Svensson, E., Aurell, Y., Jacobsson, L. T. H., Landgren, A., Sigurdardottir, V., & Dehlin, M. (2020).

Dual energy CT findings in gout with rapid kilovoltage-switching source with gemstone

scintillator detector. *BMC Rheumatology*. <https://doi.org/10.1186/s41927-019-0104-5>

- Tan, M. S., Yu, J. T., Jiang, T., Zhu, X. C., Wang, H. F., Zhang, W., Wang, Y. L., Jiang, W., & Tan, L. (2013). NLRP3 polymorphisms are associated with late-onset Alzheimer's disease in Han Chinese. *Journal of Neuroimmunology*. <https://doi.org/10.1016/j.jneuroim.2013.10.002>
- Tang, H., Yu, N., Jia, Y., Yu, Y., Duan, H., Han, D., Ma, G., Ren, C., & He, T. (2018). Assessment of noise reduction potential and image quality improvement of a new generation adaptive statistical iterative reconstruction (ASIR-V) in chest CT. *British Journal of Radiology*. <https://doi.org/10.1259/bjr.20170521>
- Tang, X., Cai, F., Ding, D. X., Zhang, L. L., Cai, X. Y., & Fang, Q. (2018). Magnetic resonance imaging relaxation time in Alzheimer's disease. In *Brain Research Bulletin*. <https://doi.org/10.1016/j.brainresbull.2018.05.004>
- Tao, G., Huang, J., Moorthy, B., Wang, C., Hu, M., Gao, S., & Ghose, R. (2020). Potential role of drug metabolizing enzymes in chemotherapy-induced gastrointestinal toxicity and hepatotoxicity. In *Expert Opinion on Drug Metabolism and Toxicology*. <https://doi.org/10.1080/17425255.2020.1815705>
- Tao, Y., Wang, Y., Rogers, J. T., & Wang, F. (2014). Perturbed iron distribution in Alzheimer's disease serum, cerebrospinal fluid, and selected brain regions: A systematic review and meta-analysis. *Journal of Alzheimer's Disease*. <https://doi.org/10.3233/JAD-140396>
- Tavčar, P., Sonc, M., & Kmetec, V. (2010). Problems of High-Dose Methotrexate in Oncological Patients. *Zdravstveno Varstvo*. <https://doi.org/10.2478/v10152-010-0017-6>
- Ter-Pogossian, M. M. (1984). Image Reconstruction from Projections, The Fundamentals of Computerized Tomography by G. T. Herman . *Medical Physics*. <https://doi.org/10.1118/1.595466>
- Thompson, K. J., Shoham, S., & Connor, J. R. (2001). Iron and neurodegenerative disorders. *Brain Research Bulletin*. [https://doi.org/10.1016/S0361-9230\(01\)00510-X](https://doi.org/10.1016/S0361-9230(01)00510-X)
- Toga, A. W., & Thompson, P. M. (2001). The role of image registration in brain mapping. *Image and*

Vision Computing. [https://doi.org/10.1016/s0262-8856\(00\)00055-x](https://doi.org/10.1016/s0262-8856(00)00055-x)

- Toia, G. V., Alessio, A. M., & Mileto, A. (2021). Use of dual-energy CT for quantification of essential trace metals (iron, copper, and zinc): Proof of concept. *American Journal of Roentgenology*. <https://doi.org/10.2214/AJR.20.23138>
- Tsai, Y. S., Chen, J. S., Wang, C. K., Lu, C. H., Cheng, C. N., Kuo, C. S., Liu, Y. S., & Tsai, H. M. (2014). Quantitative assessment of iron in heart and liver phantoms using dual-energy computed tomography. *Experimental and Therapeutic Medicine*. <https://doi.org/10.3892/etm.2014.1813>
- Tsurusaki, M., Sofue, K., Hori, M., Sasaki, K., Ishii, K., Murakami, T., & Kudo, M. (2021). Dual-energy computed tomography of the liver: Uses in clinical practices and applications. In *Diagnostics*. <https://doi.org/10.3390/diagnostics11020161>
- Ueguchi, T., Ogihara, R., & Yamada, S. (2018). Accuracy of Dual-Energy Virtual Monochromatic CT Numbers: Comparison between the Single-Source Projection-Based and Dual-Source Image-Based Methods. *Academic Radiology*. <https://doi.org/10.1016/j.acra.2018.02.022>
- Vogt, N. (2016). Biophysics: Unraveling magnetogenetics. In *Nature Methods*. <https://doi.org/10.1038/nmeth.4060>
- Vorona, G. A., Zuccoli, G., Sutcavage, T., Clayton, B. L., Ceschin, R. C., & Panigrahy, A. (2013). The use of adaptive statistical iterative reconstruction in pediatric head CT: A feasibility study. *American Journal of Neuroradiology*. <https://doi.org/10.3174/ajnr.A3122>
- Vymazal, J., Brooks, R. A., Patronas, N., Hajek, M., Bulte, J. W. M., & Di Chiro, G. (1995). Magnetic resonance imaging of brain iron in health and disease. *Journal of the Neurological Sciences*. [https://doi.org/10.1016/0022-510X\(95\)00204-F](https://doi.org/10.1016/0022-510X(95)00204-F)
- Vymazal, J., Zak, O., Bulte, J. W. M., Aisen, P., & Brooks, R. A. (1996). T1 and T2 of ferritin solutions: Effect of loading factor. *Magnetic Resonance in Medicine*. <https://doi.org/10.1002/mrm.1910360111>
- Walker, C. H., Drew, B. A., Antoon, J. W., Kalueff, A. V., & Beckman, B. S. (2012). Neurocognitive

- effects of chemotherapy and endocrine therapies in the treatment of breast cancer: Recent perspectives. *Cancer Investigation*. <https://doi.org/10.3109/07357907.2011.636116>
- Wang, X., Sabne, A., Kisner, S., Raghunathan, A., Bouman, C., & Midkiff, S. (2016). High performance model based image reconstruction. *Proceedings of the 21st ACM SIGPLAN Symposium on Principles and Practice of Parallel Programming - PPOPP '16*, 1–12. <https://doi.org/10.1145/2851141.2851163>
- Ward, R. J., Zucca, F. A., Duyn, J. H., Crichton, R. R., & Zecca, L. (2014). The role of iron in brain ageing and neurodegenerative disorders. In *The Lancet Neurology*. [https://doi.org/10.1016/S1474-4422\(14\)70117-6](https://doi.org/10.1016/S1474-4422(14)70117-6)
- Wardlaw, J. M., Brindle, W., Casado, A. M., Shuler, K., Henderson, M., Thomas, B., MacFarlane, J., Maniega, S. M., Lymer, K., Morris, Z., Pernet, C., Nailon, W., Ahearn, T., Mumuni, A. N., Mugruza, C., McLean, J., Chakirova, G., Tao, Y., Simpson, J., ... Hernandez, M. C. V. (2012). A systematic review of the utility of 1.5 versus 3 Tesla magnetic resonance brain imaging in clinical practice and research. In *European Radiology*. <https://doi.org/10.1007/s00330-012-2500-8>
- Wattjes, M. P., & Barkhof, F. (2012). Diagnostic relevance of high field MRI in clinical neuroradiology: The advantages and challenges of driving a sports car. In *European Radiology*. <https://doi.org/10.1007/s00330-012-2552-9>
- Weishaupt, D. (2003). *How does MRI work?*
- Widmann, G., Bischel, A., Stratis, A., Bosmans, H., Jacobs, R., Gassner, E. M., Puelacher, W., & Pauwels, R. (2017). Spatial and contrast resolution of ultralow dose dentomaxillofacial CT imaging using iterative reconstruction technology. *Dentomaxillofacial Radiology*. <https://doi.org/10.1259/dmfr.20160452>
- Wieneke, M. H., & Dienst, E. R. (1995). Neuropsychological assessment of cognitive functioning following chemotherapy for breast cancer. *Psycho-Oncology*.

<https://doi.org/10.1002/pon.2960040108>

- Wood, J. C., Enriquez, C., Ghugre, N., Tyzka, J. M., Carson, S., Nelson, M. D., & Coates, T. D. (2005). MRI R2 and R2* mapping accurately estimates hepatic iron concentration in transfusion-dependent thalassemia and sickle cell disease patients. *Blood*, *106*(4), 1460–1465. <https://doi.org/10.1182/blood-2004-10-3982>
- World Health Organisation, T. (2018). *Cancer*. WHO Website. https://www.who.int/health-topics/cancer#tab=tab_1
- Yiannopoulou, K. G., Anastasiou, A. I., Zachariou, V., & Pelidou, S. H. (2019). Reasons for failed trials of disease-modifying treatments for alzheimer disease and their contribution in recent research. In *Biomedicines*. <https://doi.org/10.3390/biomedicines7040097>
- Yoshikawa, E., Matsuoka, Y., Inagaki, M., Nakano, T., Akechi, T., Kobayakawa, M., Fujimori, M., Nakaya, N., Akizuki, N., Imoto, S., Murakami, K., & Uchitomi, Y. (2005). No adverse effects of adjuvant chemotherapy on hippocampal volume in Japanese breast cancer survivors. *Breast Cancer Research and Treatment*. <https://doi.org/10.1007/s10549-005-1412-6>
- Yoshizumi, T. (2011). Dual Energy CT in Clinical Practice. *Medical Physics*. <https://doi.org/10.1118/1.3642476>
- Yu, L., Leng, S., & McCollough, C. H. (2012). Dual-energy CT-based monochromatic imaging. In *AJR. American journal of roentgenology*. <https://doi.org/10.2214/ajr.12.9121>
- Yushkevich, P. A., Piven, J., Hazlett, H. C., Smith, R. G., Ho, S., Gee, J. C., & Gerig, G. (2006). User-guided 3D active contour segmentation of anatomical structures: Significantly improved efficiency and reliability. *NeuroImage*. <https://doi.org/10.1016/j.neuroimage.2006.01.015>
- Zaharchuk, G., Gong, E., Wintermark, M., Rubin, D., & Langlotz, C. P. (2018). Deep learning in neuroradiology. In *American Journal of Neuroradiology*. <https://doi.org/10.3174/ajnr.A5543>
- Zecca, L., Youdim, M. B. H., Riederer, P., Connor, J. R., & Crichton, R. R. (2004). Iron, brain ageing and neurodegenerative disorders. In *Nature Reviews Neuroscience* (Vol. 5, Issue 11, pp. 863–

873). <https://doi.org/10.1038/nrn1537>

Zhang, D., li, X., & Liu, B. (2011). WE-C-110-02: Influence of ASIR on Spatial Resolution: A Study for Objects of Varying Contrast Levels. *Medical Physics*. <https://doi.org/10.1118/1.3613341>

Zhang, Da, Li, X., & Liu, B. (2011). Objective characterization of GE Discovery CT750 HD scanner: Gemstone spectral imaging mode. *Medical Physics*. <https://doi.org/10.1118/1.3551999>

Zhu, W. Z., Zhong, W. De, Wang, W., Zhan, C. J., Wang, C. Y., Qi, J. P., Wang, J. Z., & Lei, T. (2009). Quantitative MR phase-corrected imaging to investigate increased brain iron deposition of patients with Alzheimer disease. *Radiology*. <https://doi.org/10.1148/radiol.2532082324>

Appendices

Appendix 1



Health Research Authority

Professor Annie Young
Professor of Nursing
University of Warwick
Coventry
CV4 7AL

Email: hra.approval@nhs.net

22 June 2016

Dear Professor Young

Letter of HRA Approval

Study title:	A pre-pilot exploration to develop interventions for a randomised controlled trial in chemobrain
IRAS project ID:	148558
REC reference:	16/WM/0173
Sponsor	University of Warwick

I am pleased to confirm that HRA Approval has been given for the above referenced study, on the basis described in the application form, protocol, supporting documentation and any clarifications noted in this letter.

Participation of NHS Organisations in England

The sponsor should now provide a copy of this letter to all participating NHS organisations in England.

Appendix B provides important information for sponsors and participating NHS organisations in England for arranging and confirming capacity and capability. **Please read *Appendix B* carefully**, in particular the following sections:

- *Participating NHS organisations in England* – this clarifies the types of participating organisations in the study and whether or not all organisations will be undertaking the same activities
- *Confirmation of capacity and capability* - this confirms whether or not each type of participating NHS organisation in England is expected to give formal confirmation of capacity and capability. Where formal confirmation is not expected, the section also provides details on the time limit given to participating organisations to opt out of the study, or request additional time, before their participation is assumed.
- *Allocation of responsibilities and rights are agreed and documented (4.1 of HRA assessment criteria)* - this provides detail on the form of agreement to be used in the study to confirm capacity and capability, where applicable.

Further information on funding, HR processes, and compliance with HRA criteria and standards is also provided.

It is critical that you involve both the research management function (e.g. R&D office) supporting each organisation and the local research team (where there is one) in setting up your study. Contact details and further information about working with the research management function for each organisation can be accessed from www.hra.nhs.uk/hra-approval.

Appendices

The HRA Approval letter contains the following appendices:

- A – List of documents reviewed during HRA assessment
- B – Summary of HRA assessment

After HRA Approval

The document "*After Ethical Review – guidance for sponsors and investigators*", issued with your REC favourable opinion, gives detailed guidance on reporting expectations for studies, including:

- Registration of research
- Notifying amendments
- Notifying the end of the study

The HRA website also provides guidance on these topics, and is updated in the light of changes in reporting expectations or procedures.

In addition to the guidance in the above, please note the following:

- HRA Approval applies for the duration of your REC favourable opinion, unless otherwise notified in writing by the HRA.
- Substantial amendments should be submitted directly to the Research Ethics Committee, as detailed in the *After Ethical Review* document. Non-substantial amendments should be submitted for review by the HRA using the form provided on the [HRA website](#), and emailed to hra.amendments@nhs.net.
- The HRA will categorise amendments (substantial and non-substantial) and issue confirmation of continued HRA Approval. Further details can be found on the [HRA website](#).

Scope

HRA Approval provides an approval for research involving patients or staff in NHS organisations in England.

If your study involves NHS organisations in other countries in the UK, please contact the relevant national coordinating functions for support and advice. Further information can be found at <http://www.hra.nhs.uk/resources/applying-for-reviews/nhs-hsc-rd-review/>.

If there are participating non-NHS organisations, local agreement should be obtained in accordance with the procedures of the local participating non-NHS organisation.

IRAS project ID	148558
-----------------	--------

User Feedback

The Health Research Authority is continually striving to provide a high quality service to all applicants and sponsors. You are invited to give your view of the service you have received and the application procedure. If you wish to make your views known please email the HRA at hra.approval@nhs.net. Additionally, one of our staff would be happy to call and discuss your experience of HRA Approval.

HRA Training

We are pleased to welcome researchers and research management staff at our training days – see details at <http://www.hra.nhs.uk/hra-training/>

Your IRAS project ID is **148558**. Please quote this on all correspondence.

Yours sincerely

Nicola Gilzeane
Assessor

Email: hra.approval@nhs.net

Copy to:

Mrs Jane Prewett, University of Warwick, Sponsor Contact
wmssponsorship@warwick.ac.uk

Ms Ceri Jones, University Hospitals Coventry & Warwickshire NHS Trust, Lead NHS R&D Contact
ceri.jones@uhcw.nhs.uk

Appendix A - List of Documents

The final document set assessed and approved by HRA Approval is listed below.

Document	Version	Date
Covering letter on headed paper		
Evidence of Sponsor insurance or indemnity (non NHS Sponsors only) [Liability and Clinical Trials Warwick]		30 July 2015
GP/consultant information sheets or letters [Pre-CB GP Information Letter - Patients]	2.0	04 May 2016
GP/consultant information sheets or letters [Pre-CB GP Information letter - supporters]	2.0	04 May 2016
Interview schedules or topic guides for participants [Pre-CB Interview topic guide]	1.0	03 February 2016
Interview schedules or topic guides for participants [Pre-CB MAAT Observation Guide]	1.0	03 February 2016
Interview schedules or topic guides for participants [Pre-CB Supporters Workshop Topic Guide]	1.0	03 February 2016
Interview schedules or topic guides for participants [MAAT survivor workbook]		
IRAS Application Form [IRAS_Form_23032016]		23 March 2016
Letter from sponsor [Letter Confirming Sponsorship]	1.0	03 February 2016
Other [Site Agreement Warwick University]		
Other [Delegation Log]		12 April 2016
Other [Study Task Key]		12 April 2016
Other [Schedule of Events]	2	15 May 2016
Other [Statement of Activities]	1.0	29 April 2016
Other [Notification of Non-substantial Amendment]		21 June 2016
Participant consent form [Pre-Cb Patient Consent Form v2.0 04-May-2016]	2.0	04 May 2016
Participant consent form [Pre-CB Supporter Consent Form]	2.0	04 May 2016
Participant information sheet (PIS) [Pre-CB Supporter Information sheet]	2.0	04 May 2016
Participant information sheet (PIS) [Pre-CB Patient Information Sheet]	2.0	04 May 2016
Research protocol or project proposal [Pre-CB Protocol]	2.0	04 May 2016
Summary CV for Chief Investigator (CI) [Pre-CB CI Annie Young CV]		30 January 2016
Validated questionnaire [BIPQ assessment]		
Validated questionnaire [FACT-Cog outcome measure]		
Validated questionnaire [Minimental Digit Span Assessment]		
Validated questionnaire [Ministroop]		
Validated questionnaire [PASAT manual]		
Validated questionnaire [Rasch Self Efficacy Assessment]		
Validated questionnaire [Work Limitations Questionnaire]		
Validated questionnaire [Trail Making Test questionnaire]		

Appendix B - Summary of HRA Assessment

This appendix provides assurance to you, the sponsor and the NHS in England that the study, as reviewed for HRA Approval, is compliant with relevant standards. It also provides information and clarification, where appropriate, to participating NHS organisations in England to assist in assessing and arranging capacity and capability.

For information on how the sponsor should be working with participating NHS organisations in England, please refer to the *participating NHS organisations, capacity and capability and Allocation of responsibilities and rights are agreed and documented (4.1 of HRA assessment criteria)* sections in this appendix.

The following person is the sponsor contact for the purpose of addressing participating organisation questions relating to the study:

Jane Prewett (024 765 22746, wmssponsorship@warwick.ac.uk)

HRA assessment criteria

Section	HRA Assessment Criteria	Compliant with Standards	Comments
1.1	IRAS application completed correctly	Yes	There are no sites listed in Part C of the IRAS application, the applicant has confirmed University Hospitals Coventry and Warwickshire NHS Trust as a site.
2.1	Participant information/consent documents and consent process	Yes	A non-substantial amendment was submitted following REC approval to update the Supporter Information Sheet to bring it in line with HRA standards.
3.1	Protocol assessment	Yes	No comments
4.1	Allocation of responsibilities and rights are agreed and documented	Yes	The applicant has confirmed that they have chosen to use their own site agreement to act as agreement of an NHS organisation to participate.
4.2	Insurance/indemnity arrangements assessed	Yes	Where applicable, independent contractors (e.g. General Practitioners) should ensure that the professional

Section	HRA Assessment Criteria	Compliant with Standards	Comments
			indemnity provided by their medical defence organisation covers the activities expected of them for this research study
4.3	Financial arrangements assessed	Yes	The applicant has confirmed in the site agreement provided that funding will be provided to sites for MRI scans
5.1	Compliance with the Data Protection Act and data security issues assessed	Yes	No comments
5.2	CTIMPS – Arrangements for compliance with the Clinical Trials Regulations assessed	Not Applicable	No comments
5.3	Compliance with any applicable laws or regulations	Yes	No comments
6.1	NHS Research Ethics Committee favourable opinion received for applicable studies	Yes	No comments
6.2	CTIMPS – Clinical Trials Authorisation (CTA) letter received	Not Applicable	No comments
6.3	Devices – MHRA notice of no objection received	Not Applicable	No comments
6.4	Other regulatory approvals and authorisations received	Not Applicable	No comments

Participating NHS Organisations in England

This provides detail on the types of participating NHS organisations in the study and a statement as to whether the activities at all organisations are the same or different.

There is only one site type for this study as all participating NHS organisations will be undertaking the same activity.

The Chief Investigator or sponsor should share relevant study documents with participating NHS organisations in England in order to put arrangements in place to deliver the study. The documents should be sent to both the local study team, where applicable, and the office providing the research management function at the participating organisation. For NIHR CRN Portfolio studies, the Local LCRN contact should also be copied into this correspondence. For further guidance on working with participating NHS organisations please see the HRA website.

If chief investigators, sponsors or principal investigators are asked to complete site level forms for participating NHS organisations in England which are not provided in IRAS or on the HRA website, the chief investigator, sponsor or principal investigator should notify the HRA immediately at hra.approval@nhs.net. The HRA will work with these organisations to achieve a consistent approach to information provision.

Confirmation of Capacity and Capability

This describes whether formal confirmation of capacity and capability is expected from participating NHS organisations in England.

Participating NHS organisations in England **will be expected to formally confirm their capacity and capability to host this research.**

- Following issue of this letter, participating NHS organisations in England may now confirm to the sponsor their capacity and capability to host this research, when ready to do so. How capacity and capability will be confirmed is detailed in the *Allocation of responsibilities and rights are agreed and documented (4.1 of HRA assessment criteria)* section of this appendix.
- The [Assessing, Arranging, and Confirming](#) document on the HRA website provides further information for the sponsor and NHS organisations on assessing, arranging and confirming capacity and capability.

Principal Investigator Suitability

This confirms whether the sponsor position on whether a PI, LC or neither should be in place is correct for each type of participating NHS organisation in England and the minimum expectations for education, training and experience that PIs should meet (where applicable).

A Principal Investigator will be required at sites. The applicant has confirmed that a PI has been identified at University Hospital Coventry and Warwickshire NHS Trust.

GCP training is not a generic training expectation, in line with the [HRA statement on training expectations](#).

HR Good Practice Resource Pack Expectations

This confirms the HR Good Practice Resource Pack expectations for the study and the pre-engagement checks that should and should not be undertaken

Where external research staff access sites and contractual arrangements are not already in place, letters of access will be required. Where letters of access are required sites are to confirm the necessary Occupational Health and DBS checks are in place.

Other Information to Aid Study Set-up

This details any other information that may be helpful to sponsors and participating NHS organisations in England to aid study set-up.

The applicant has indicated that they do not intend to apply for inclusion on the NIHR CRN Portfolio.

Appendix 2



BIOMEDICAL & SCIENTIFIC RESEARCH ETHICS

COMMITTEE (BSREC)

STUDY PROTOCOL

Can spectral CT quantify brain iron concentration in cadaveric brains?

Ziedo Solomon, Dr Joanna F Collingwood and Dr Sarah C Wayte

Lay Summary

The concentration of iron in various regions of the human brain has been demonstrated to increase with age, in particular for those suffering from Alzheimer's and Parkinson's disease(Bo Hallgren &

Sourander, 1960b). Non-invasive measurement of brain iron is typically carried out using an MRI scan, however a number of drawbacks exist which can make this option unsuitable. As ageing is a key risk factor, the presence of metal implants is more likely, preventing MRI scans. Furthermore, patients must lie still for around 30 minutes for the MRI scan to complete, which can be difficult for someone suffering from a neurodegenerative disease.

The development of Dual Energy CT (DECT) (also known as Spectral Imaging), which works by acquiring CT images using two different X-Ray energies, allows specific elemental analysis by comparing the attenuation at each energy level rather than just one. The aim of this research is to assess if Spectral CT can quantify brain iron concentrations with the same accuracy as MRI on up to ten cadaveric heads. The benefits would be that a patient unable to have an MRI scan due to metal implants would not be prevented from having a DECT scan, and importantly these DECT scans take just a few seconds.

Background

MRI techniques have been validated as a means of quantifying iron concentration in the human brain, which have been shown to increase with age, as well as with Alzheimer's and Parkinson's disease (G Bartzokis et al., 1994, 2000; George Bartzokis et al., 1999; Zecca et al., 2004). Relatively recently Spectral CT (E.-S. Ibrahim & Bowman, 2014) was demonstrated *in vitro* as a method of quantifying iron concentrations at the levels found in diseased hearts and livers (Petersilka et al., 2008). However, to our knowledge, spectral CT has not been shown before as a method for quantitative iron concentration analysis at the low levels found in the human brain.

Research carried out at University Hospitals Coventry and Warwickshire NHS Trust (UHCW) with test tubes containing various concentrations of ferritin and Iron (III) Chloride have shown that it may be possible to quantify human brain concentration levels of iron using spectral CT.

Aims/Objectives

In this study, the cadaveric heads would be scanned both using DECT and MRI, obtaining Spectral CT data and quantitative MRI data. The subsequent analysis will show if the DECT data agrees with the gold standard MRI technique.

Methodology

Study population and design

Up to ten cadaveric heads, with the majority aged fifty years or over will be scanned using Spectral CT and quantitative MRI scanning.

In 2014, *Collingwood et al.* (J. Collingwood et al., 2014) investigated the relationship between iron concentration in the human brain and MRI parameters including R_2 and R_2^* . In this study, 10 healthy male volunteers aged <40 years were used to produce data that confirmed an excellent linear correlation between R_2 and iron concentration at on a 3 Tesla clinical MRI scanner, with correlation coefficient $r^2 = 0.98$ and $p < 0.001$. The method in this study constitutes the Gold Standard technique against which our new DECT technique will be measured and compared. For this reason, **a sample size of 10 is both necessary and sufficient for this investigation.**

Furthermore, Figure 1 shows that brain iron concentration increases rapidly in younger people, with a plateauing effect as one gets older. That is to say that in our study, where we hope to obtain cadavers aged 50+, we can expect even *less* inter-participant brain iron concentration variability than the previous 2014 Collingwood et al study, where the 10 participants were aged 21-68.

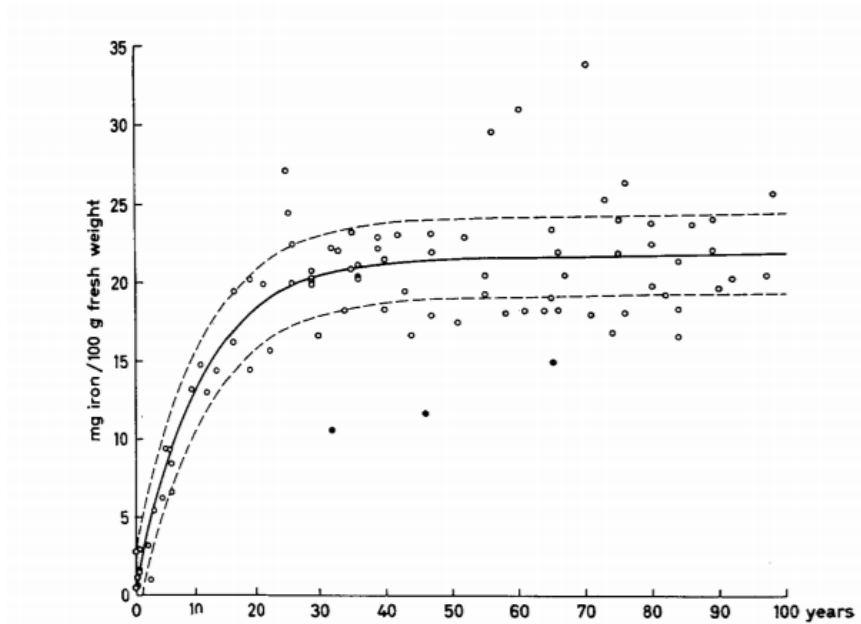


Figure 3: Brain iron in the Globus Pallidus as reported by Hallgren and Sourander (B. Hallgren & Sourander, 1958). The three filled circles (outliers) are cases where the patient had severe intestinal haemorrhage.

Inclusion/Exclusion criteria are as follows:

- **Include** Cadavers where the donor was age 50+ at time of death in order to be certain that enough natural iron accumulation will have occurred over the donor’s lifetime to provide a measurable effect with the two techniques.
- **Exclude** cadavers containing metal (clips, implant, etc) due to imaging artifacts that will occur on MRI.
- **Exclude** Cadavers with known head trauma or those which are likely to have suffered brain haemorrhages, as the high iron concentrations in blood clots may confound the iron concentration measurements.

The CT scanning is fast (2.0s rotation time), so could be performed on all ten heads in a single session and can be obtained with the heads in their standard storage state, i.e., frozen. MRI however is more time consuming, and the heads would need to be defrosted prior to scanning. Each head scan will take

around 40 minutes on MRI, meaning it is expected that a maximum of three could be scanned in any one session, and a number of MRI sessions would be required.

The handling of cadavers, cadaveric tissue and all related materials will be done only by Brain Burnett (Manager of Surgical Training Centre at Warwick Medical School) or one of his team or other members of staff at UHCW (radiographers and medical physicists).

Initial analysis on the resulting images and datasets from the CT and MRI scans will be done by PhD student Ziedo Solomon in the School of Engineering, University of Warwick.

Data Analysis/Outcome Measures

The Spectral CT images will be analysed to measure attenuation in multiple brain regions.

- The attenuation in Hounsfield units (HU) is measured, and in particular the attenuation due specifically to iron can be identified using Spectral CT.
- Iron concentration values obtained are then compared to the equivalent MRI measurement, which is taken using T2 relaxation time and correlated to iron concentration using known values.
- By comparing the experimental Spectral CT iron concentration values to data obtained from the more established MRI technique, it can be determined if the technique produces values that form a predictable linear relationship between concentration and attenuation, using the MRI data as our basis.
- Specifically, data points are determined by taking the MRI and DECT image slices and manually segmenting (drawing pixel-by-pixel regions around brain features) and using both GE Gemstone Imaging software and the open-source ImageJ software to calculate mean pixel value and standard deviation of pixel intensity. For the MRI images, relaxation time is

determined using the “MRI Processor” ImageJ plugin. Alternatively, this can be done manually using MATLAB.

- Data will be plotted as scatter plots with axes representing MRI Calculated concentration against DECT measured attenuation, and with linear regression (MATLAB) used establish the existence of a linear relationship between the two, tested using a paired t-test.
- Data will also be plotted as Bland-Altman plots to show the correlation of MRI and DECT measured brain iron concentration.
- Image analysis (ImageJ) carried out on the DECT and MRI slices will be used to determine standard deviation of pixel value in each of the sets of images, allowing noise to be compared between the two imaging modalities (MRI and DECT) with an ANOVA F-test.
- This result, if confirmed, would support the validation of Spectral CT as an alternative fast iron concentration measurement for diagnostic purposes, and can serve as a baseline pilot study for a full clinical trial.

Ethical Considerations:

Informed Consent

The Anatomy and Surgical Training Centre based at University Hospitals Coventry and Warwickshire is fully licensed (HTA licence 30019) to conduct research, surgical and medical education on human tissue.

This study does not require NHS ethical approval.

For each donor, a tissue request form is submitted, detailing exact use of the donor. An example form

is attached to this submission (Titled “Appendix 1 – Tissue Request Form”). In this case, the cadaveric tissue allocated for this research work would include all details of GF0245

Participant Confidentiality and Data Security

Each cadaveric head will be allocated a unique project reference number by Dr. Sarah Wayte, who will only be told the age, sex and neurological status of each cadaver, where the only neurological information required is to confirm the absence of known conditions that may have led to extreme localised or systemic iron accumulation (e.g., major head trauma or rare disorders such as neuroferritinopathy). The project reference number will be used to obtain both the CT and MRI imaging.

The images and associated analysis will also be retained in the Engineering Department at the University of Warwick on Dr Collingwood's password-protected group server space for a maximum of ten years to meet the University of Warwick research integrity standards.

The images will be stored on the Radiology Physics Department hard drive at UHCW for a maximum of ten years after the study completion. This drive is stored in a locked filing cabinet.

Financing:

The PhD project that this research will contribute to is funded by the EPSRC through the Molecular Analytical Sciences Centre for Doctoral Training (MAS CDT) at the University of Warwick.

CT and MRI scanner instrument time is provided as an in-kind contribution to the PhD through a formal partnership between University Hospital Coventry and Warwickshire and MAS CDT. The cadavers are also provided by UHCW.

Dissemination and Implementation:

The results will form part of Ziedo Solomon's PhD thesis, which is focused on non-invasive quantitative analysis of trace metals in the human brain. The intention is that these results will be published in peer reviewed journals and presented at conferences.

References:

1. Hallgren, B. & Sourander, P. The nonhemin iron in the cerebral cortex in Alzheimer's disease. *J. Neurochem.* 5, 307–310 (1960).
2. Zecca, L., Youdim, M. B. H., Riederer, P., Connor, J. R. & Crichton, R. R. Iron, brain ageing and neurodegenerative disorders. *Nature Reviews Neuroscience* 5, 863–873 (2004).
3. Bartzokis, G. et al. In vivo evaluation of brain iron in Alzheimer's disease and normal subjects using MRI. *Biol Psychiatry* 35, 480–487 (1994).
4. Bartzokis, G. et al. In vivo evaluation of brain iron in Alzheimer disease using magnetic resonance imaging. *Arch. Gen. Psychiatry* 57, 47–53 (2000).
5. Bartzokis, G. et al. MRI evaluation of brain iron in earlier- and later-onset Parkinson's disease and normal subjects. *Magn. Reson. Imaging* 17, 213–222 (1999).
6. Ibrahim, E.-S. & Bowman, A. Evaluation of iron overload: dual-energy computed tomography versus magnetic resonance imaging. *J. Cardiovasc. Magn. Reson.* 16, 92 (2014).
7. Petersilka, M., Bruder, H., Krauss, B., Stierstorfer, K. & Flohr, T. G. Technical principles of dual source CT. *Eur. J. Radiol.* 68, 362–368 (2008).
8. Collingwood, J. et al. MRI evaluation of the relationship between R2, R2*, and tissue iron in the human basal ganglia. in *International Society for Magnetic Resonance in Medicine Annual Meeting* (2014).
9. Hallgren, B. & Sourander, P. THE EFFECT OF AGE ON THE NON-HAEMIN IRON IN THE HUMAN BRAIN. *J. Neurochem.* 3, 41–51 (1958).

PRIVATE
Mr Ziedo Solomon
Chemistry
University of Warwick
Coventry
CV4 7AL

5 September 2018

Dear Mr Solomon

Study Title and BSREC Reference: *Can spectral CT quantify brain iron concentration in cadaveric brains?* REGO-2018-2200

Thank you for submitting the revisions to the above-named study to the University of Warwick's Biomedical and Scientific Research Ethics Sub-Committee for approval.

I am pleased to confirm that approval is granted.

In undertaking your study, you are required to comply with the University of Warwick's *Research Data Management Policy*, details of which may be found on the Research and Impact Services' webpages, under "Codes of Practice & Policies" » "Research Code of Practice" » "Data & Records" » "Research Data Management Policy", at: http://www2.warwick.ac.uk/services/ris/research_integrity/code_of_practice_and_policies/research_code_of_practice/datacollection_retention/research_data_mgt_policy

You are also required to comply with the University of Warwick's *Information Classification and Handling Procedure*, details of which may be found on the University's Governance webpages, under "Governance" » "Information Security" » "Information Classification and Handling Procedure", at:

<http://www2.warwick.ac.uk/services/gov/informationsecurity/handling>.

Investigators should familiarise themselves with the classifications of information defined therein, and the requirements for the storage and transportation of information within the different classifications:

Information Classifications:

<http://www2.warwick.ac.uk/services/gov/informationsecurity/handling/classifications>

Handling Electronic Information:


<http://www2.warwick.ac.uk/services/gov/informationsecurity/handling/electronic/>

Handling Paper or other media

<http://www2.warwick.ac.uk/services/gov/informationsecurity/handling/paper/>.

Please also be aware that BSREC grants **ethical approval** for studies. **The seeking and obtaining of all other necessary approvals is the responsibility of the investigator.**


These other approvals may include, but are not limited to:

- 
1. Any necessary agreements, approvals, or permissions required in order to comply with the University of Warwick's Financial Regulations and Procedures.
 2. Any necessary approval or permission required in order to comply with the University of Warwick's Quality Management System and Standard Operating Procedures for the governance, acquisition, storage, use, and disposal of human samples for research.
 3. All relevant University, Faculty, and Divisional/Departmental approvals, if an employee or student of the University of Warwick.
 4. Approval from the applicant's academic supervisor and course/module leader (as appropriate), if a student of the University of Warwick.
 5. NHS Trust R&D Management Approval, for research studies undertaken in NHS Trusts.
 6. NHS Trust Clinical Audit Approval, for clinical audit studies undertaken in NHS Trusts.
 7. Approval from Departmental or Divisional Heads, as required under local procedures, within Health and Social Care organisations hosting the study.
 8. Local ethical approval for studies undertaken overseas, or in other HE institutions in the UK.
 9. Approval from Heads (or delegates thereof) of UK Medical Schools, for studies involving medical students as participants.
 10. Permission from Warwick Medical School to access medical students or medical student data for research or evaluation purposes.
 11. NHS Trust Caldicott Guardian Approval, for studies where identifiable data is being transferred outside of the direct clinical care team. Individual NHS Trust procedures vary in their implementation of Caldicott guidance, and local guidance must be sought.
 12. Any other approval required by the institution hosting the study, or by the applicant's employer.

There is no requirement to supply documentary evidence of any of the above to BSREC, but applicants should hold such evidence in their Study Master File for University of Warwick auditing and monitoring purposes. You may be required to supply evidence of any necessary approvals to other University functions, e.g. The Finance Office, Research & Impact Services (RIS), or your Department/School.

May I take this opportunity to wish you success with your study, and to remind you that any Substantial Amendments to your study require approval from BSREC before they may be implemented.

Yours sincerely

pp. 

Dr David Ellard
Chair
Biomedical and Scientific
Research Ethics Sub-Committee

**Biomedical and Scientific
Research Ethics Sub-Committee**
Research & Impact Services
University of Warwick
Coventry, CV4 8UW.
E: BSREC@Warwick.ac.uk

[http://www2.warwick.ac.uk/services/
ris/research_integrity/researchethics
committees/biomed](http://www2.warwick.ac.uk/services/ris/research_integrity/researchethicscommittees/biomed)

Appendix 3

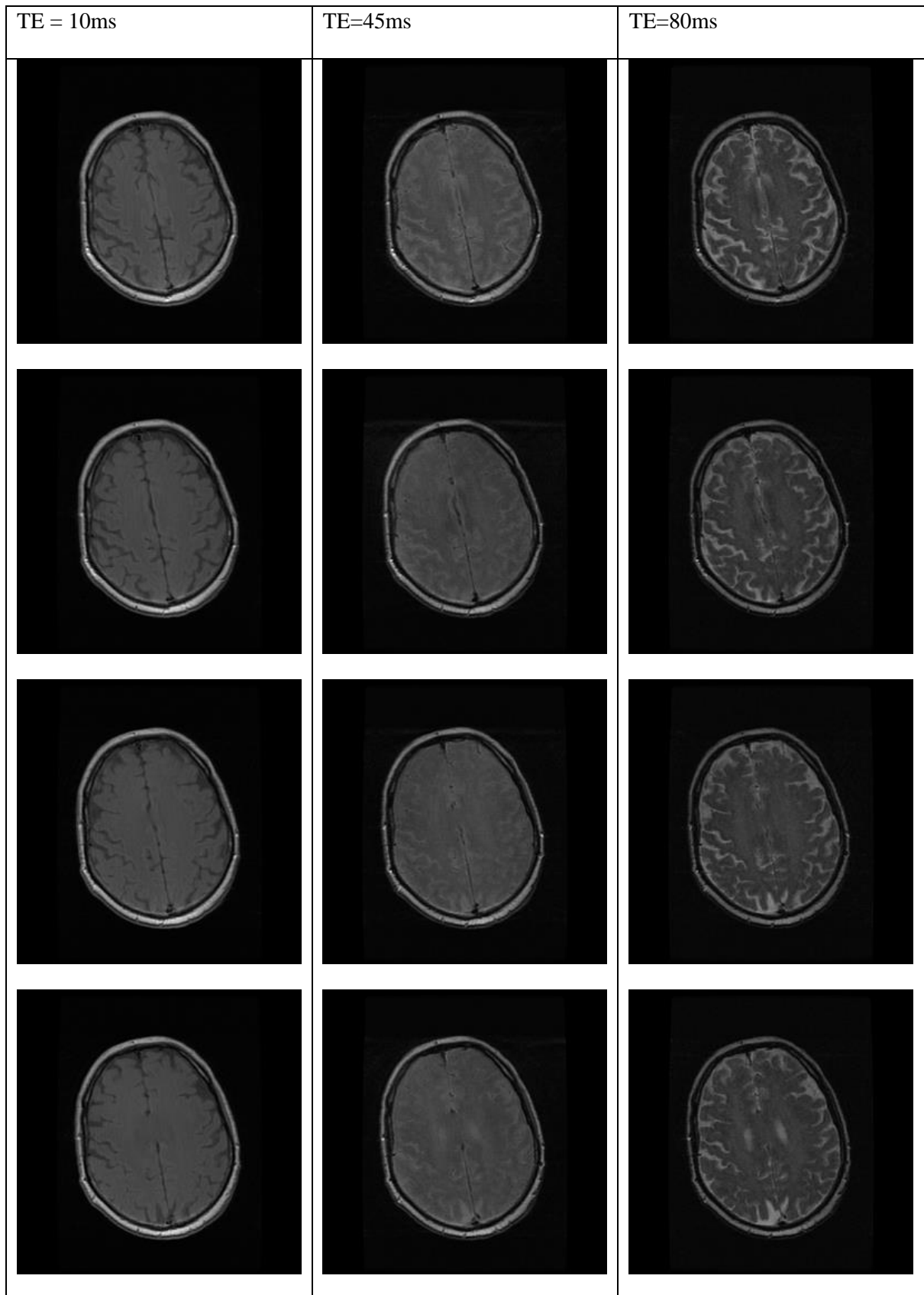
My own brain scanned using 4 echo times. These images were analysed in order to determine whether an accurate T2 measure could be made while skipping one of the echo times, in order to make the experiment itself more feasible (each echo time requires a person to be still in the scanner for an additional 6.5 minutes).

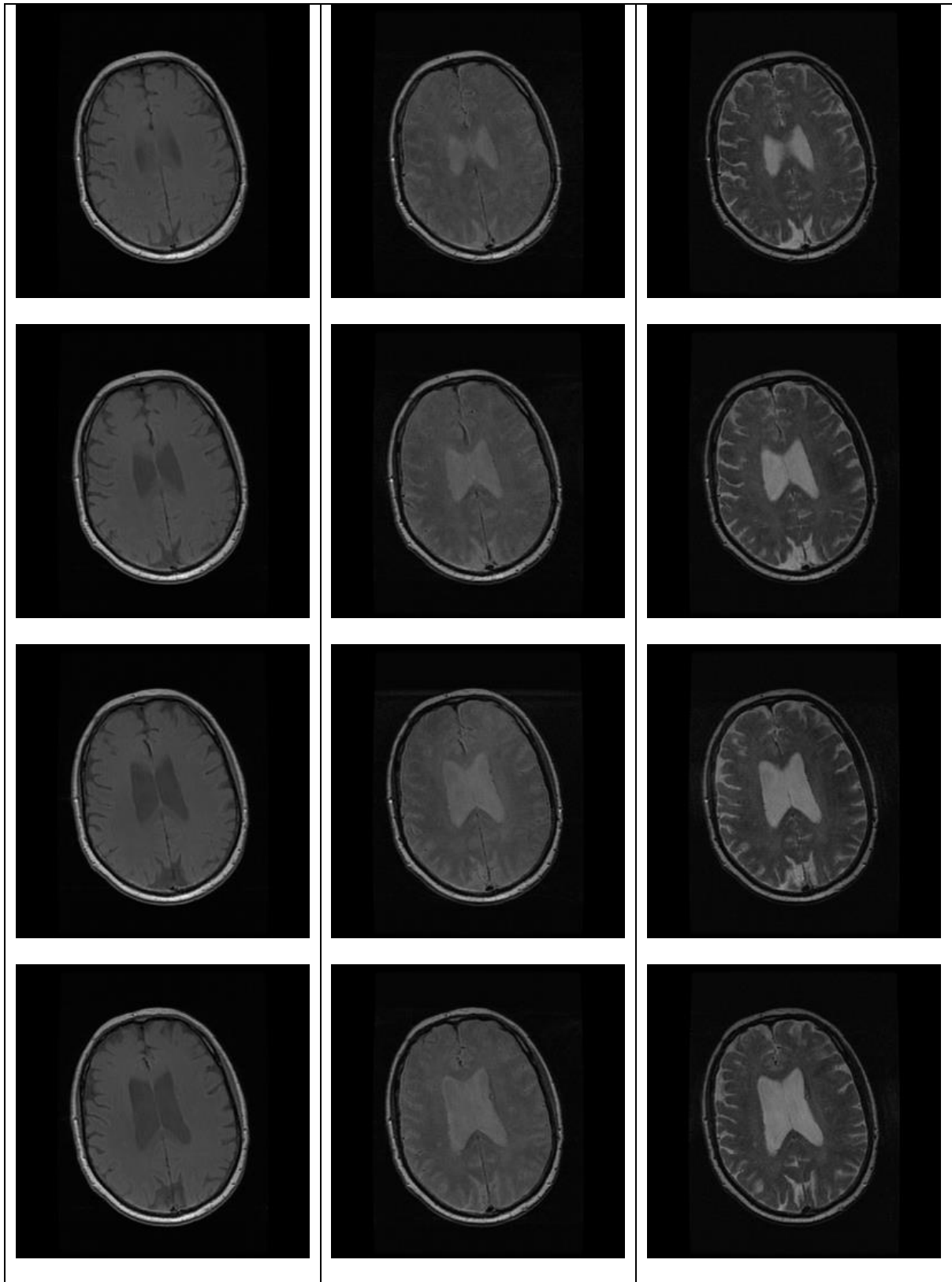
Appendix 4

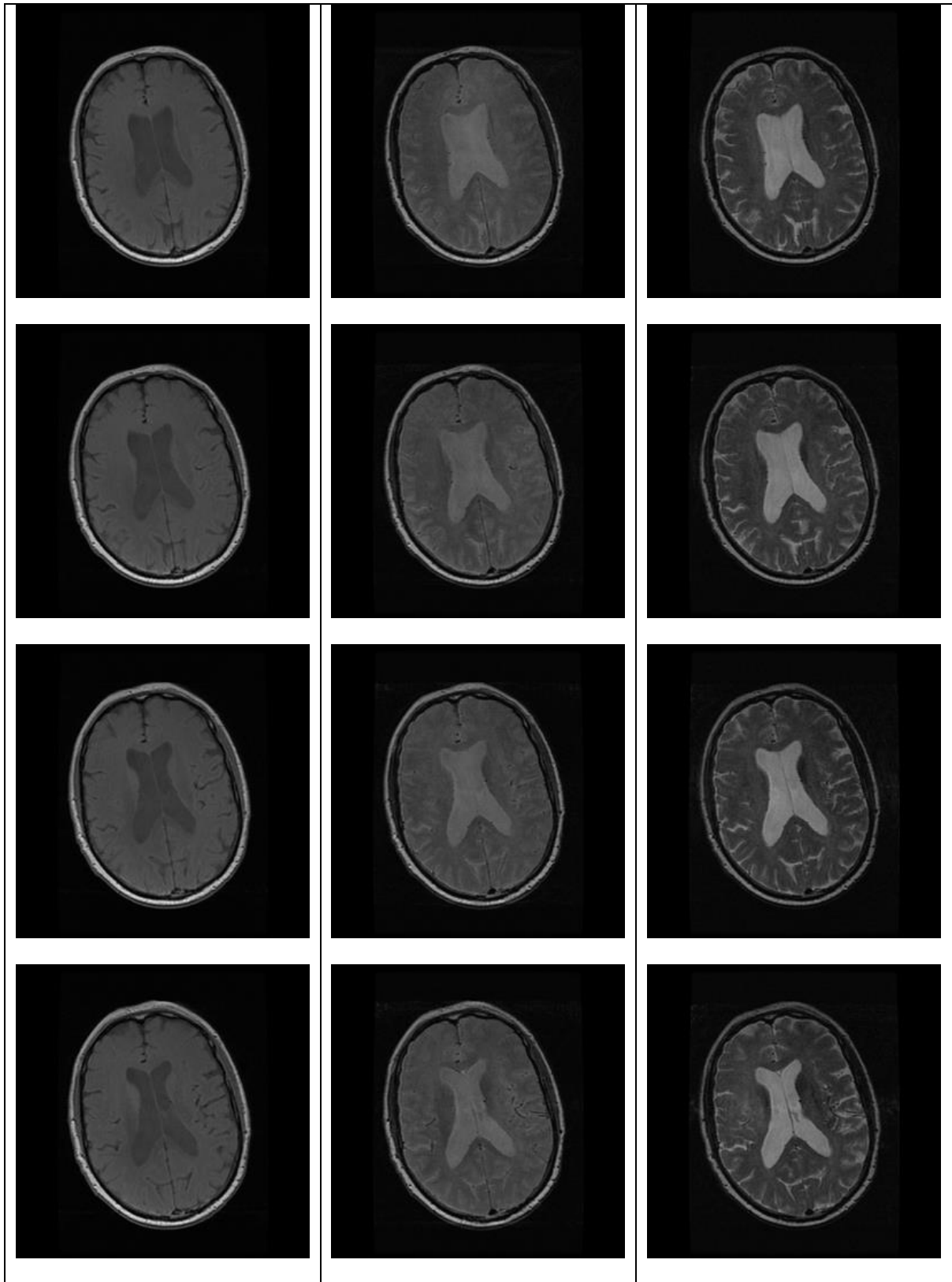
Chemobrain study images, all slices and each echo time

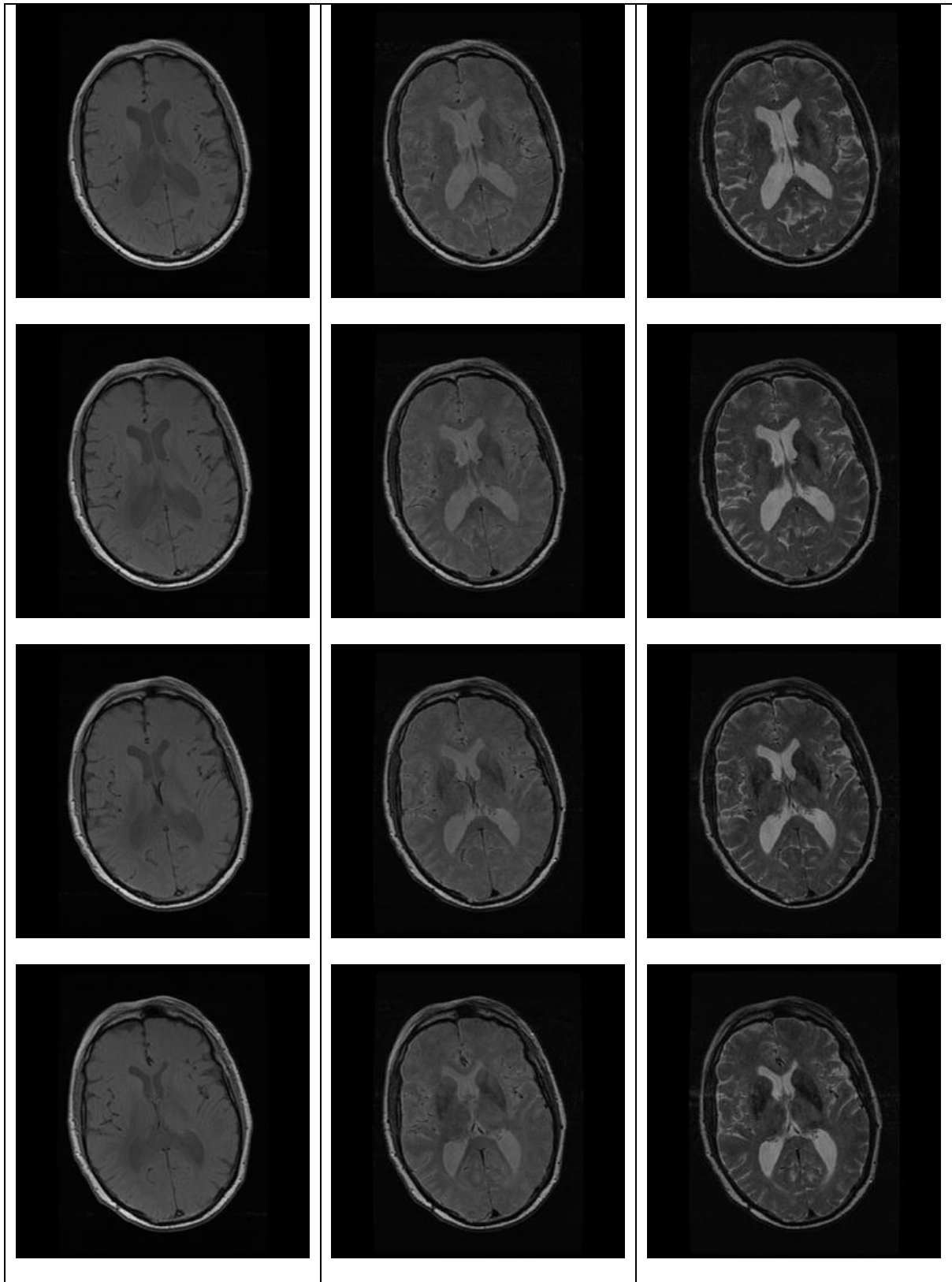
All region segmentations

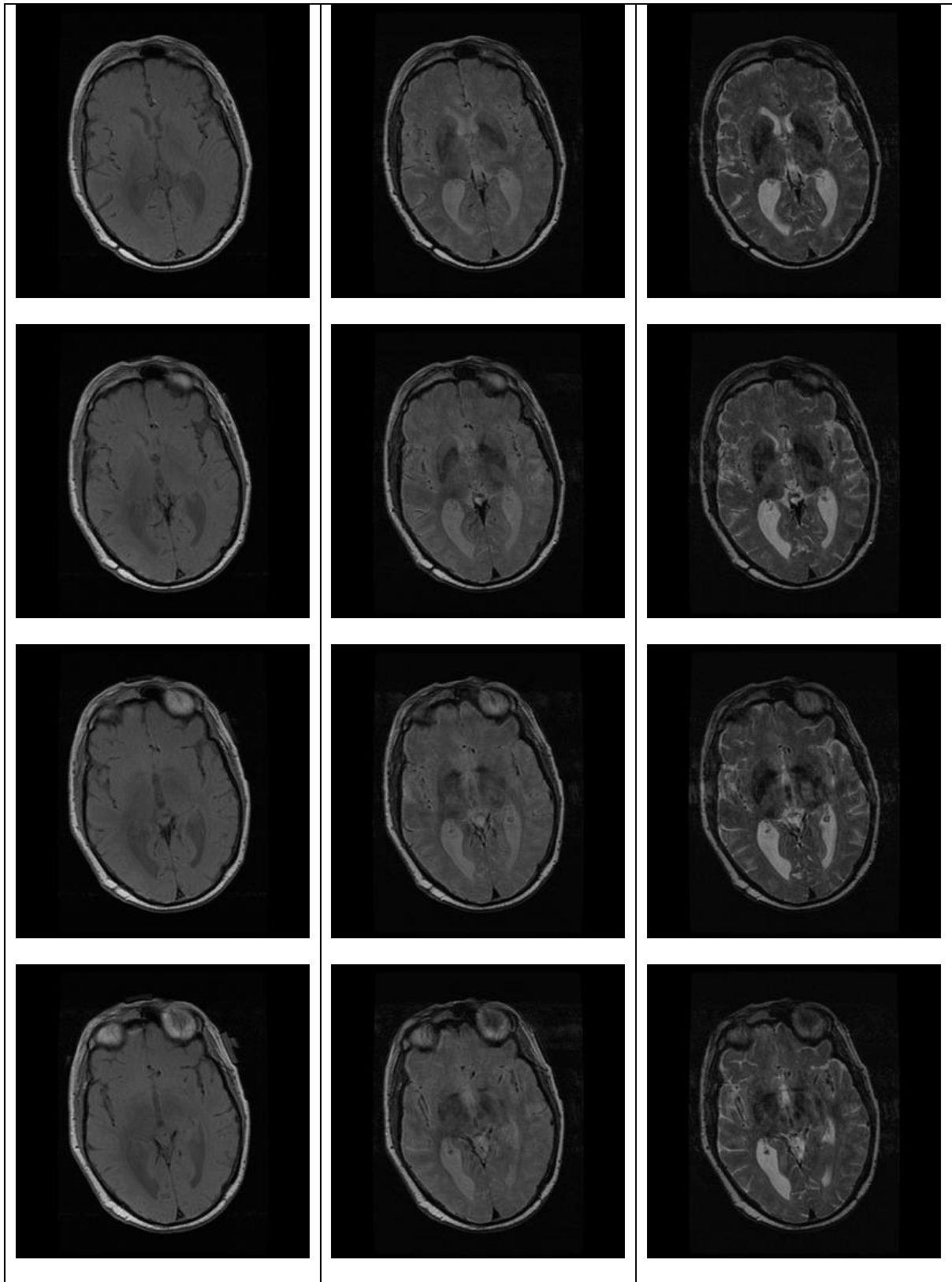
Patient 01

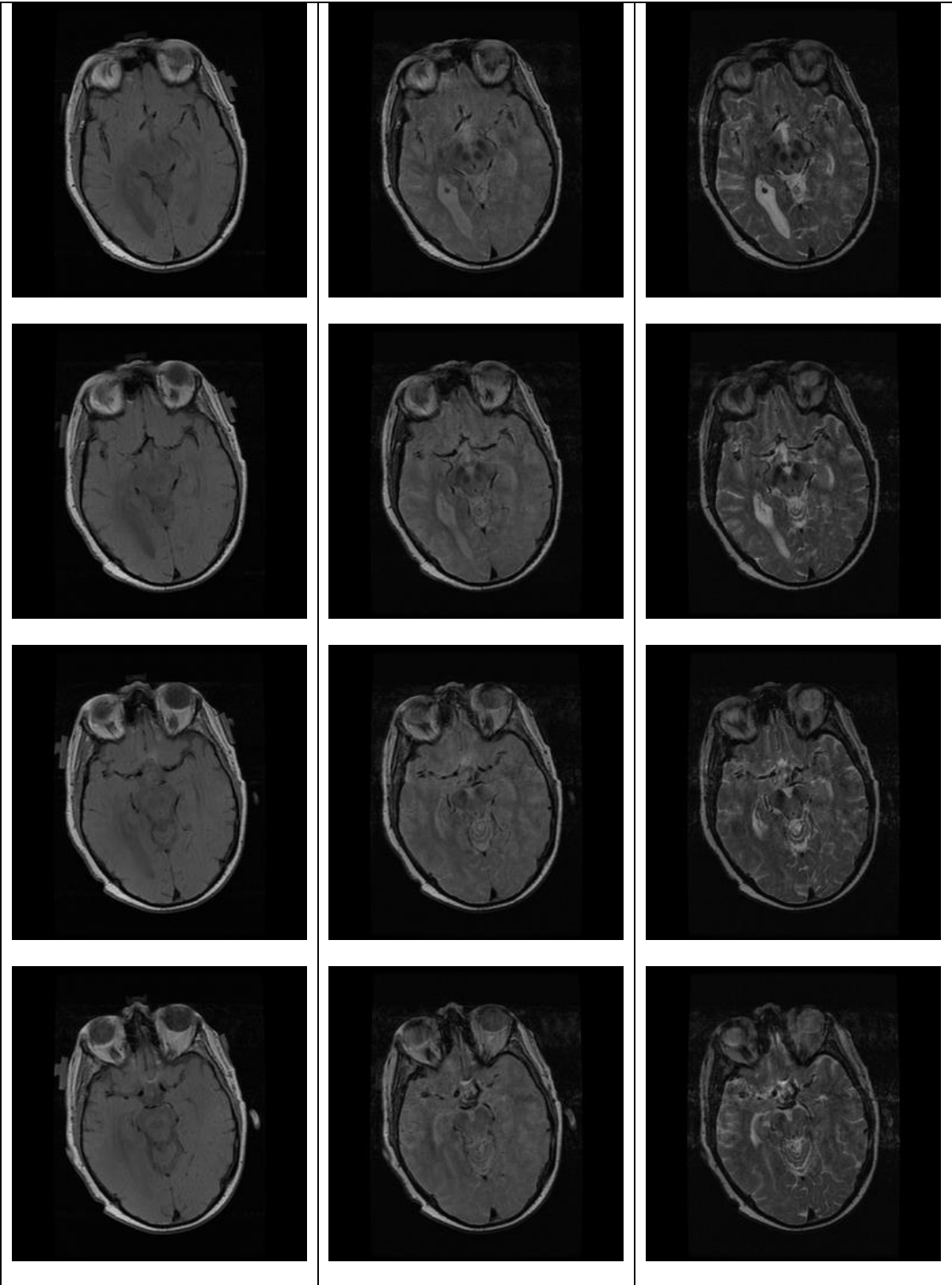


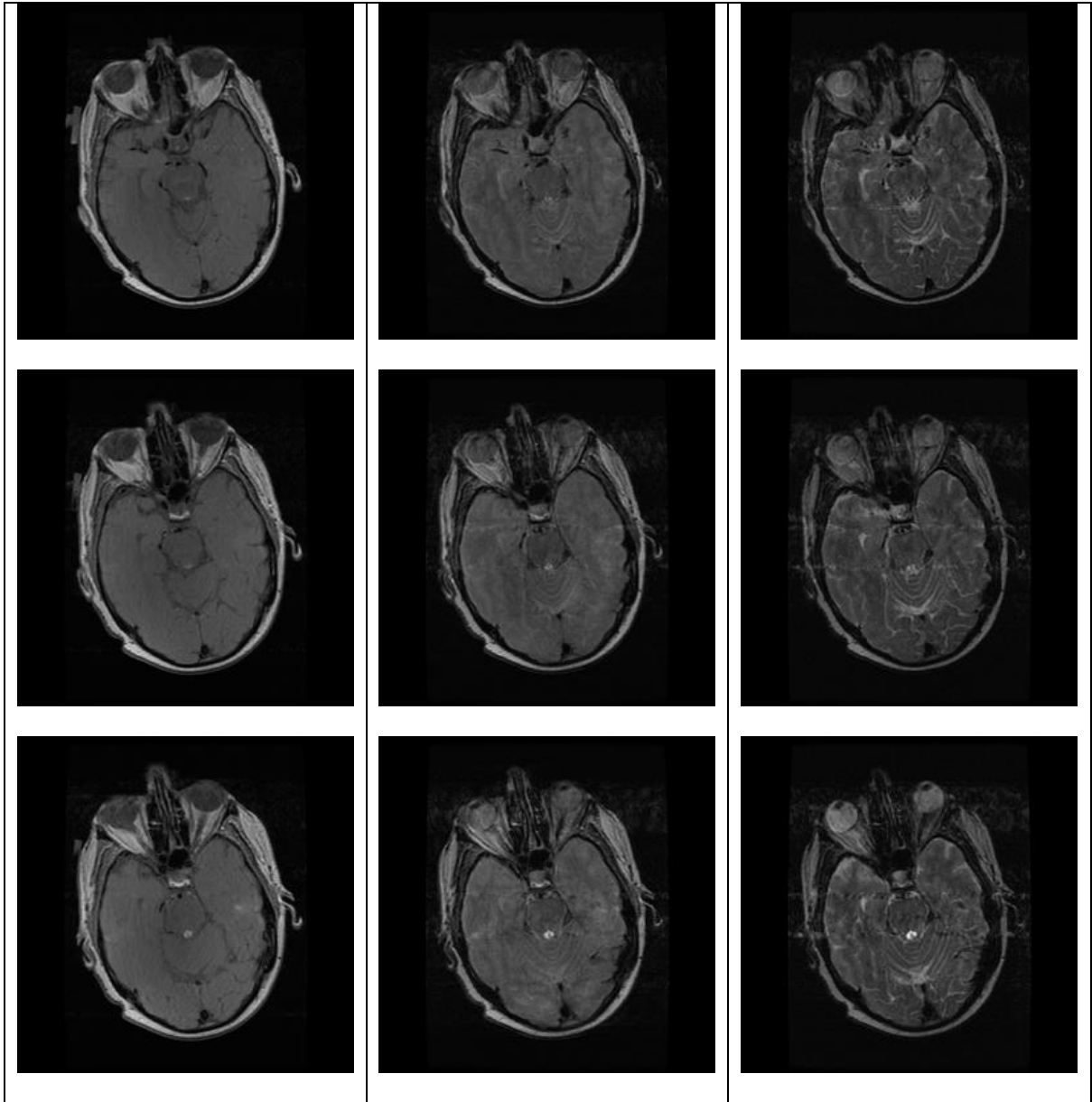




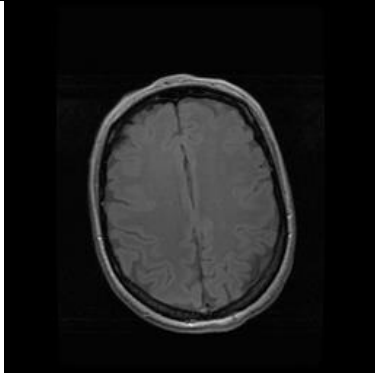
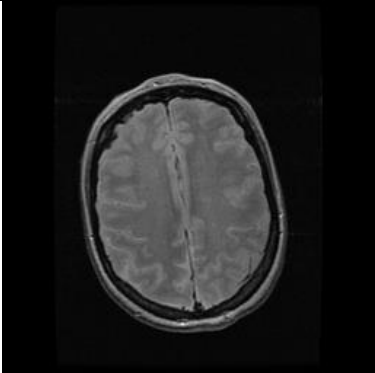
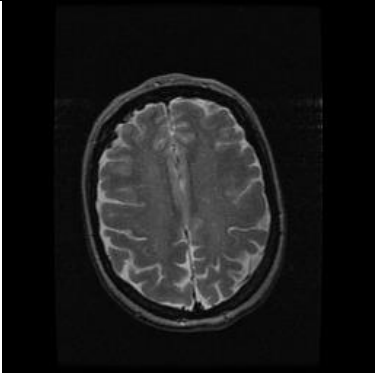
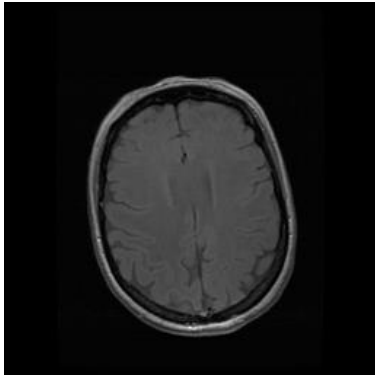
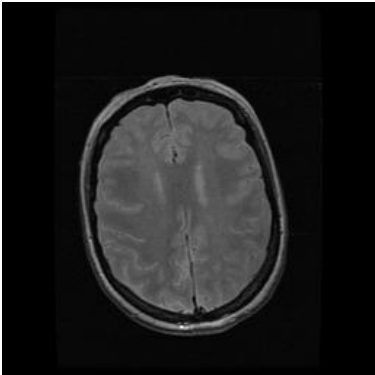
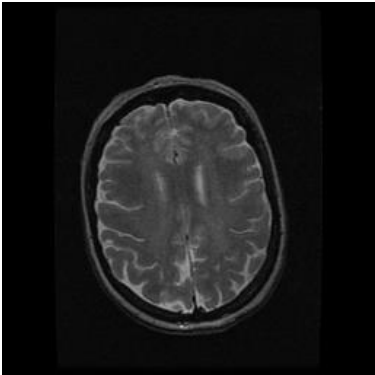
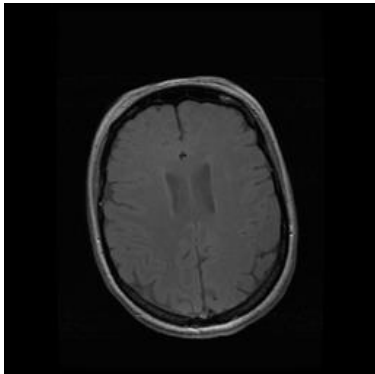
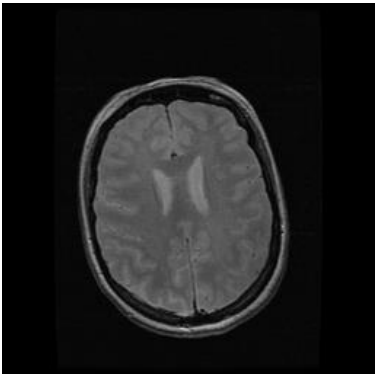
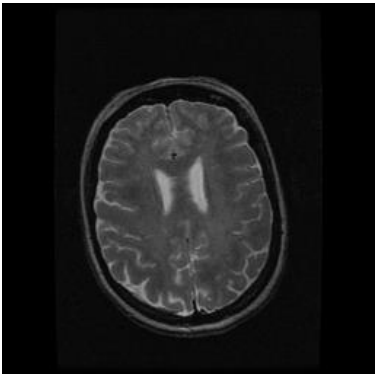
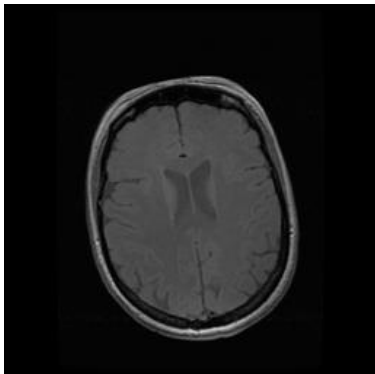
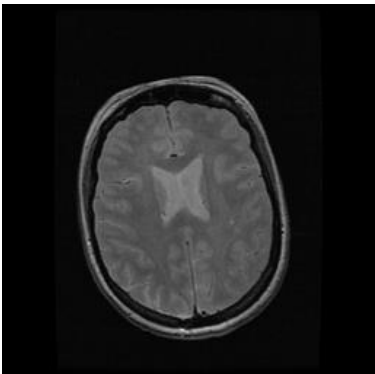
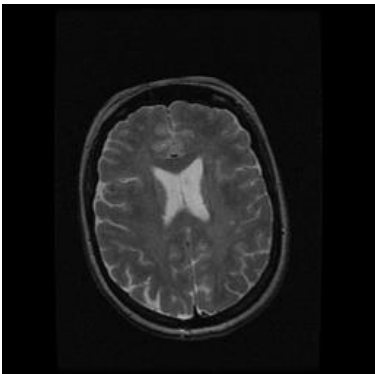


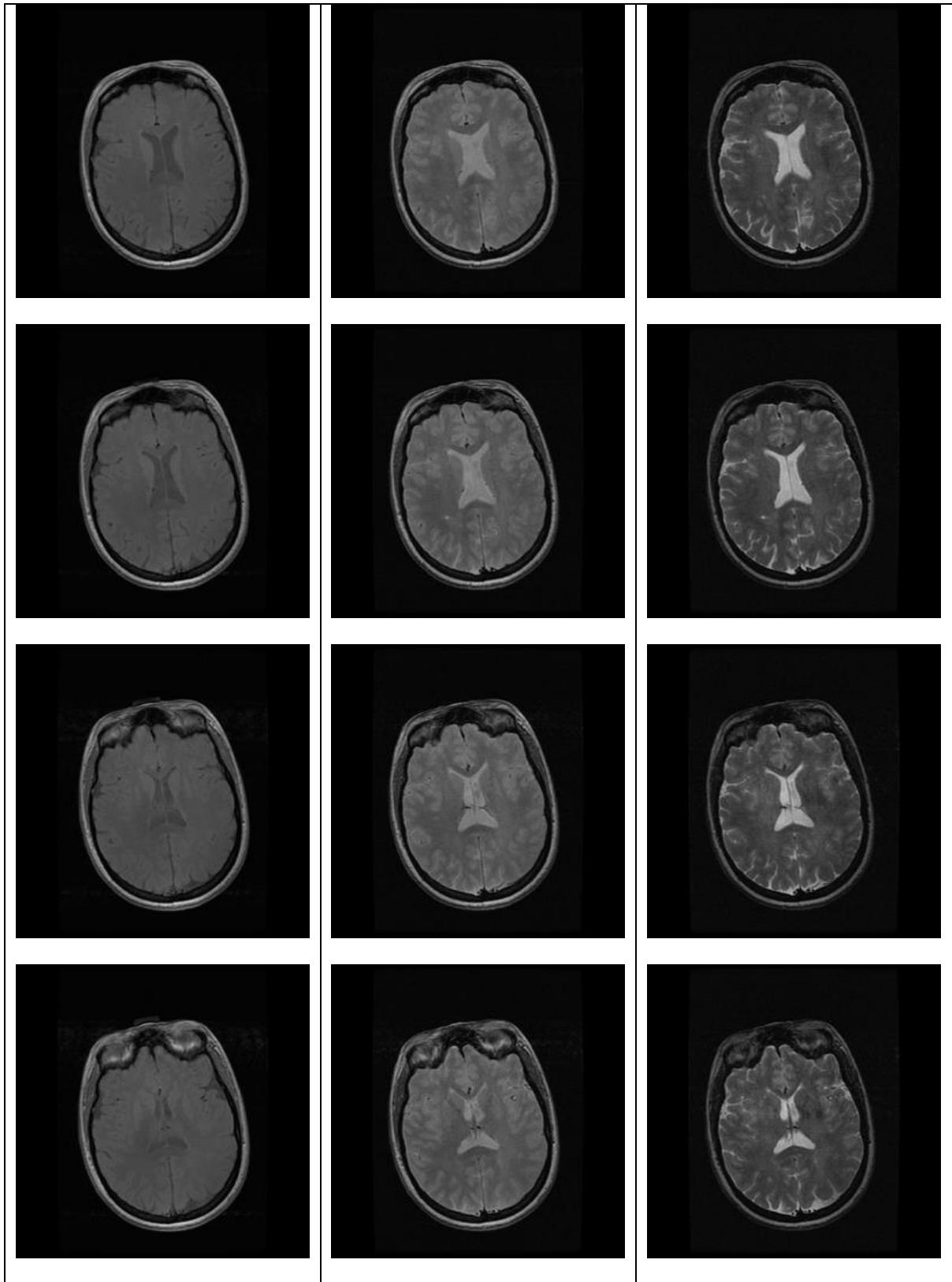


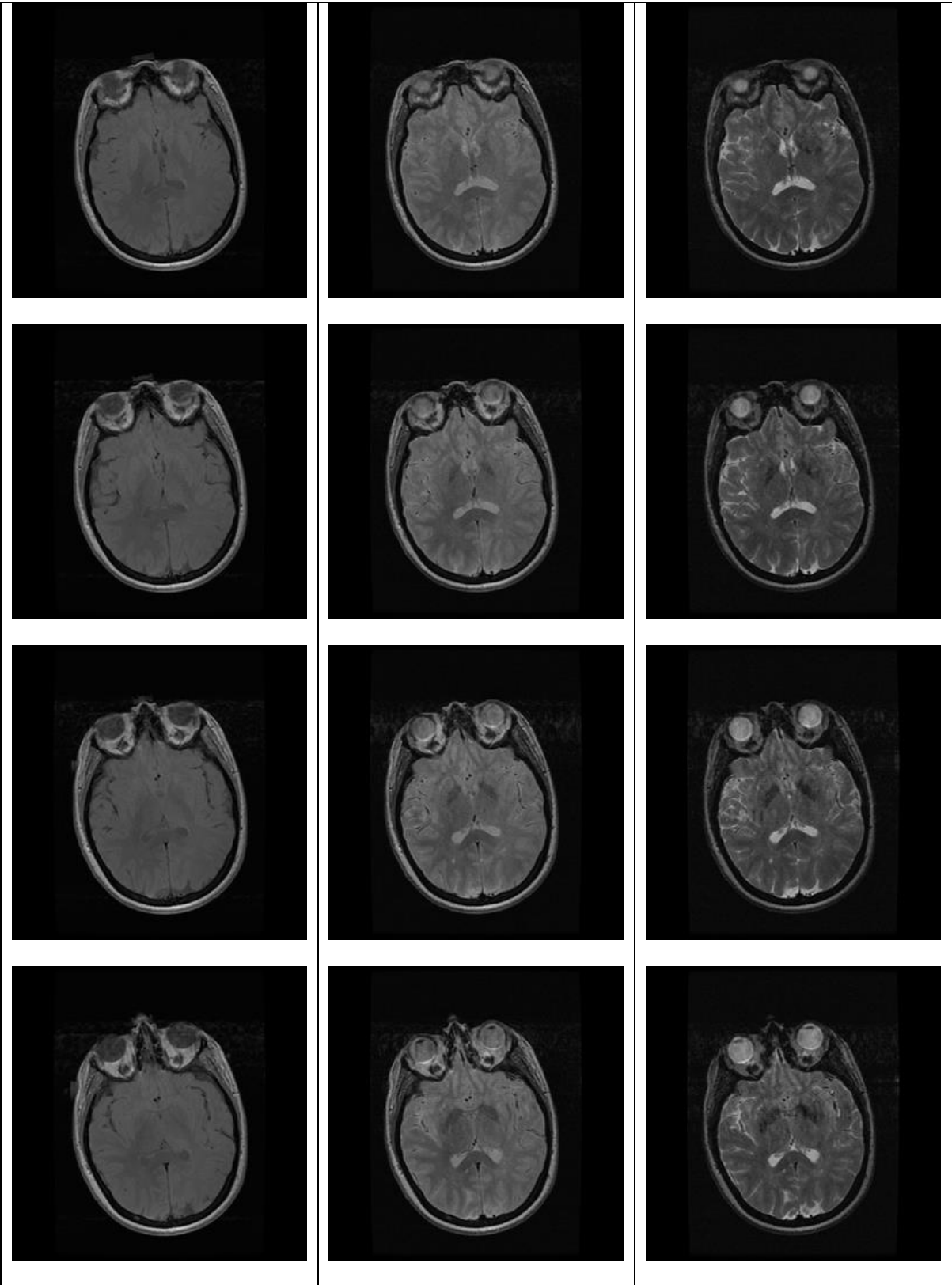


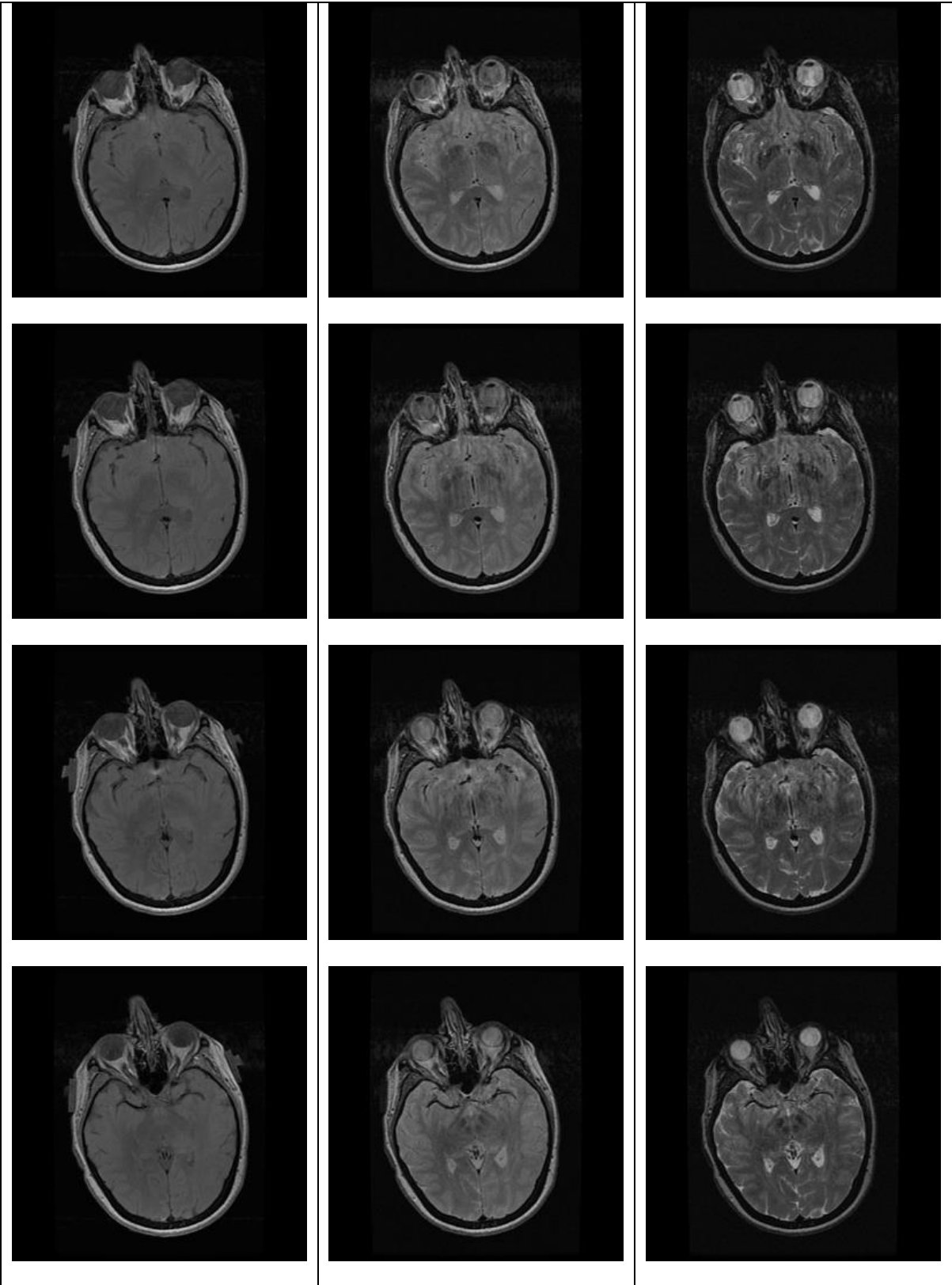


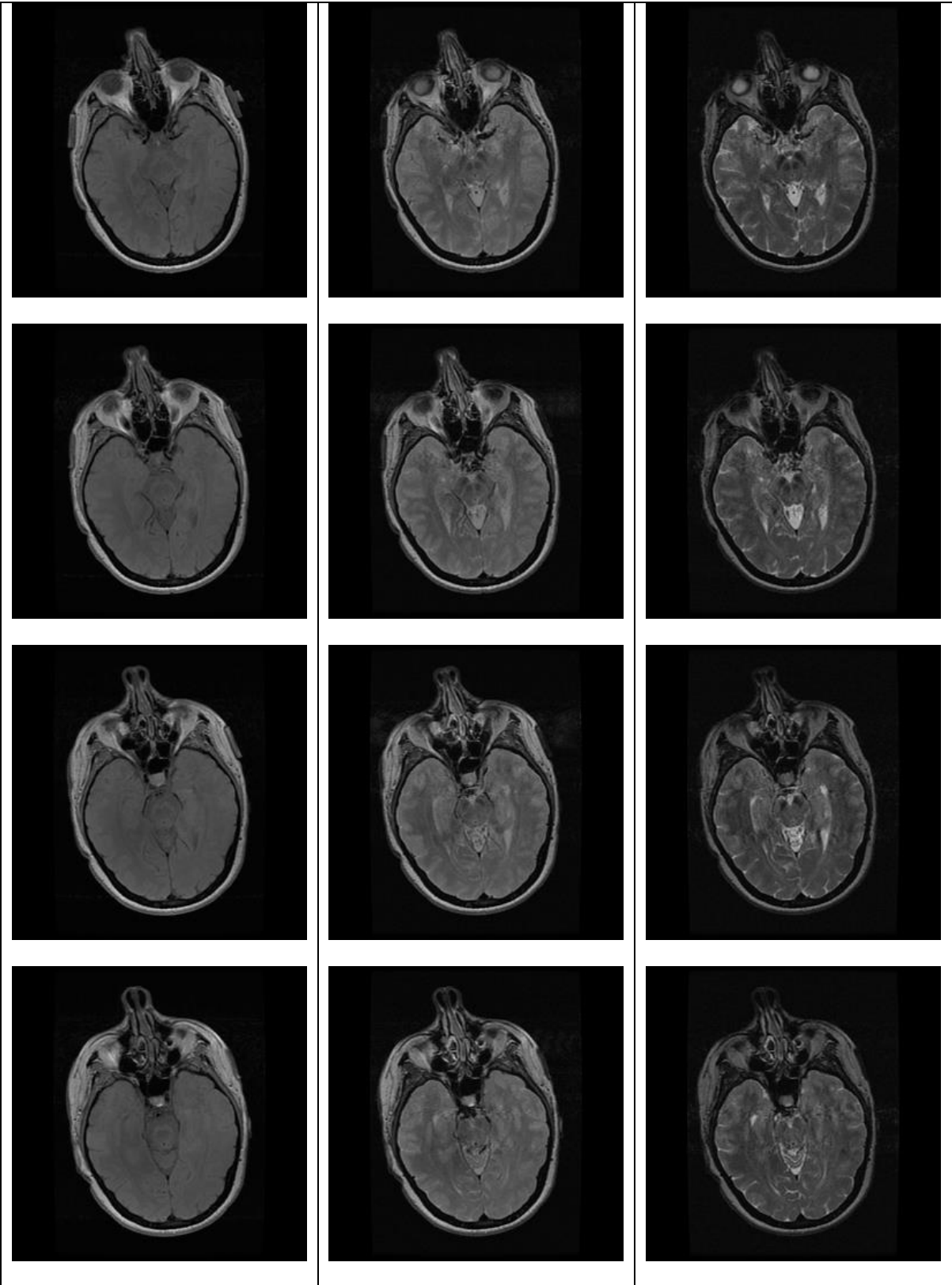
Patient 03

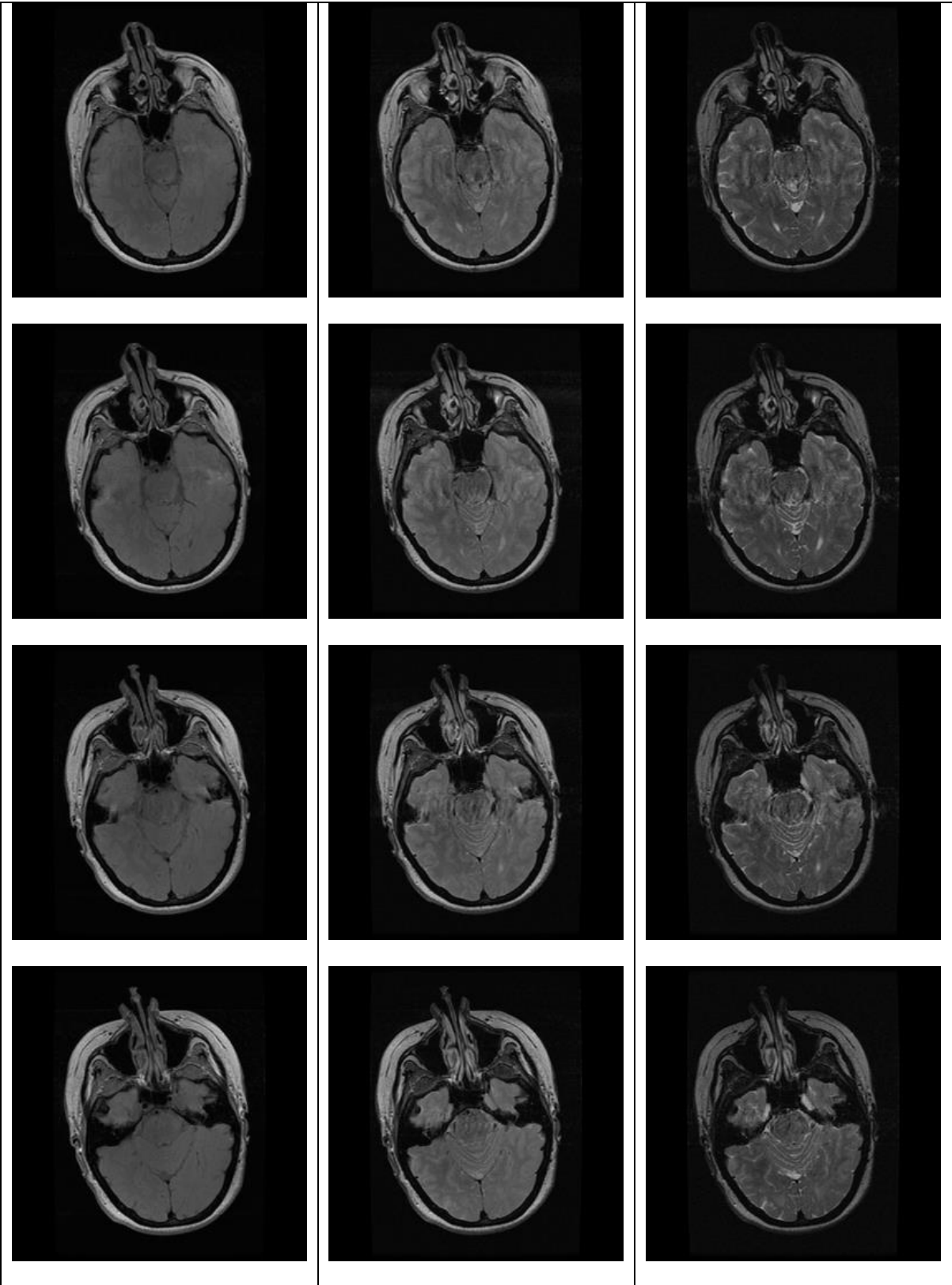
TE=10ms	TE=45ms	TE=80ms
		
		
		
		

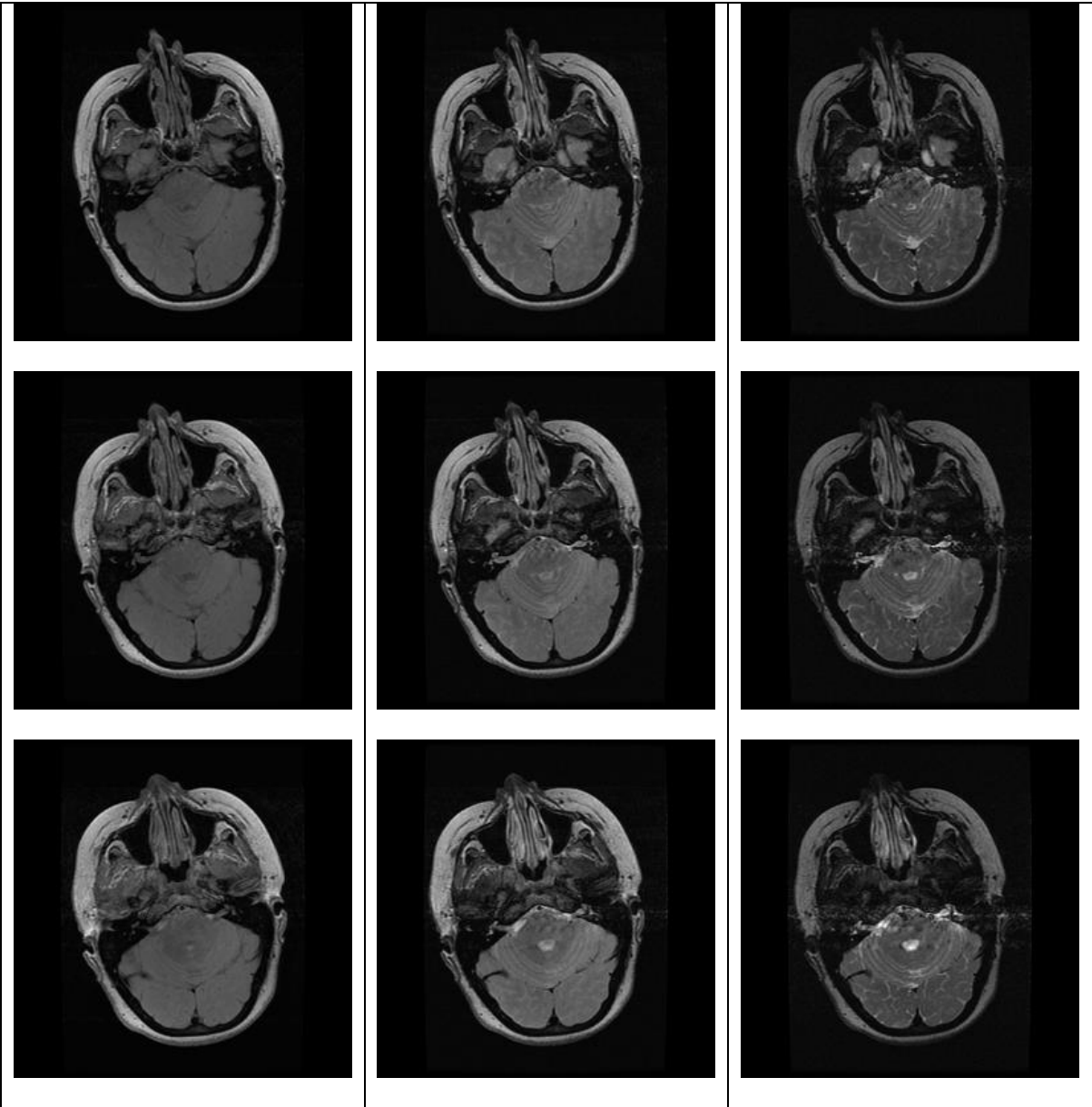




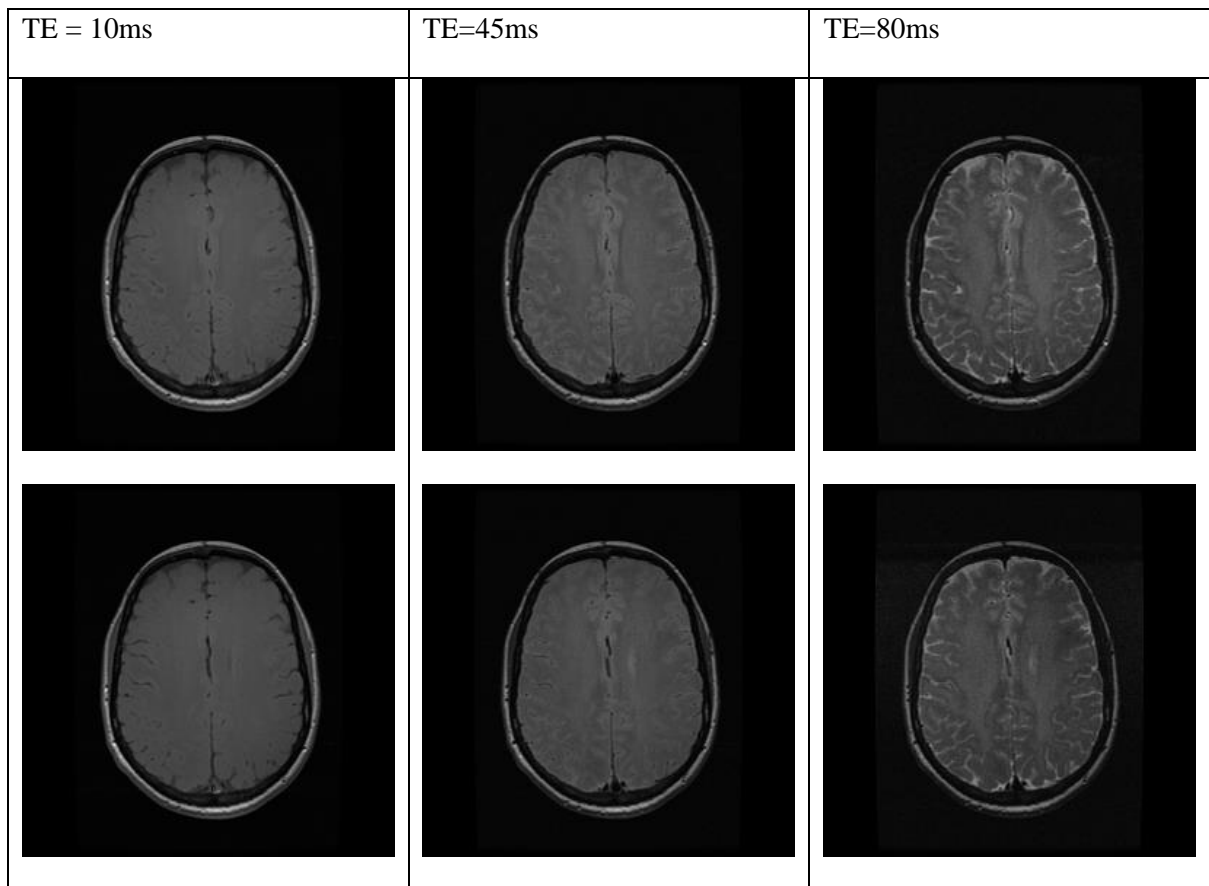


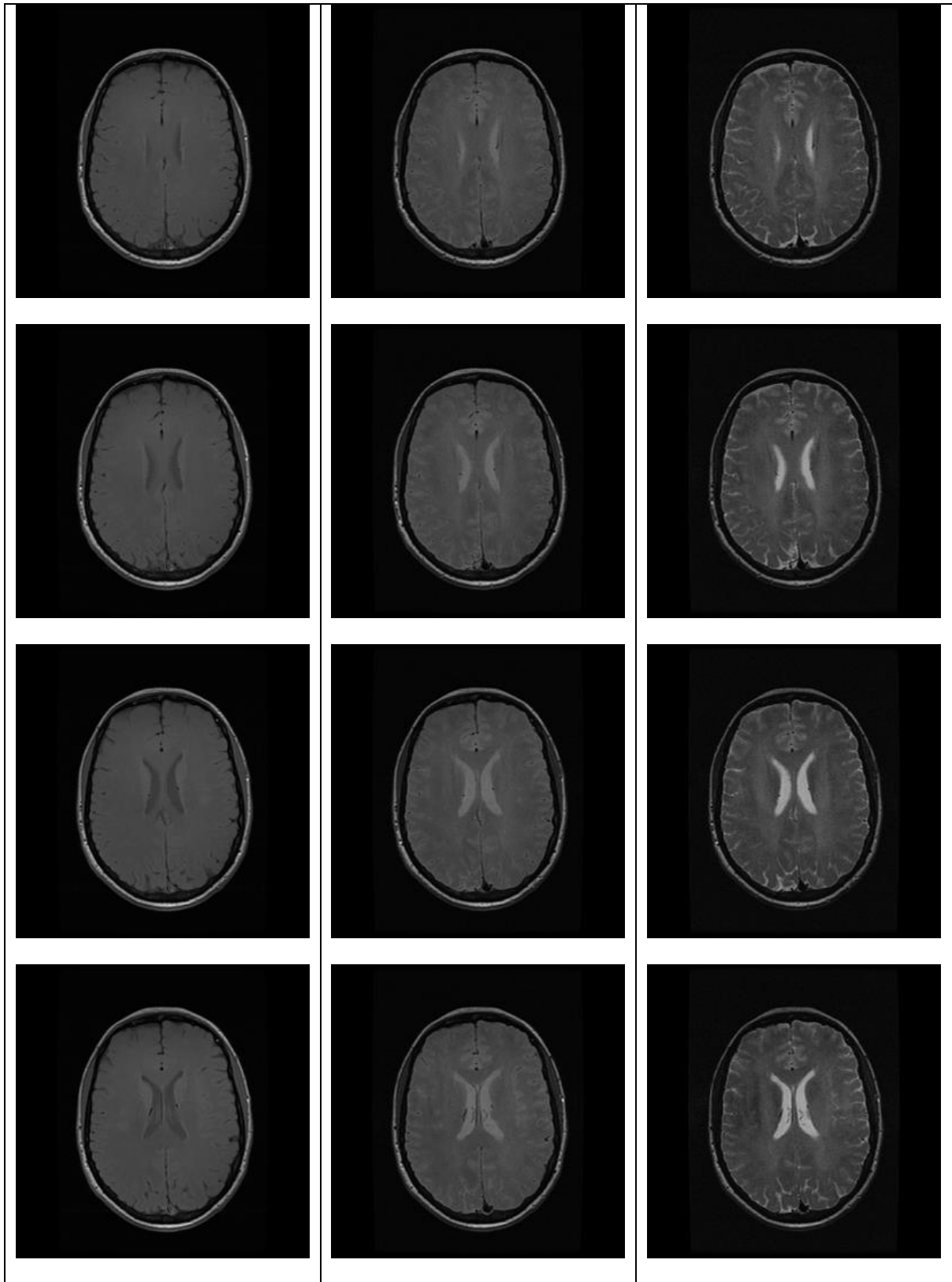


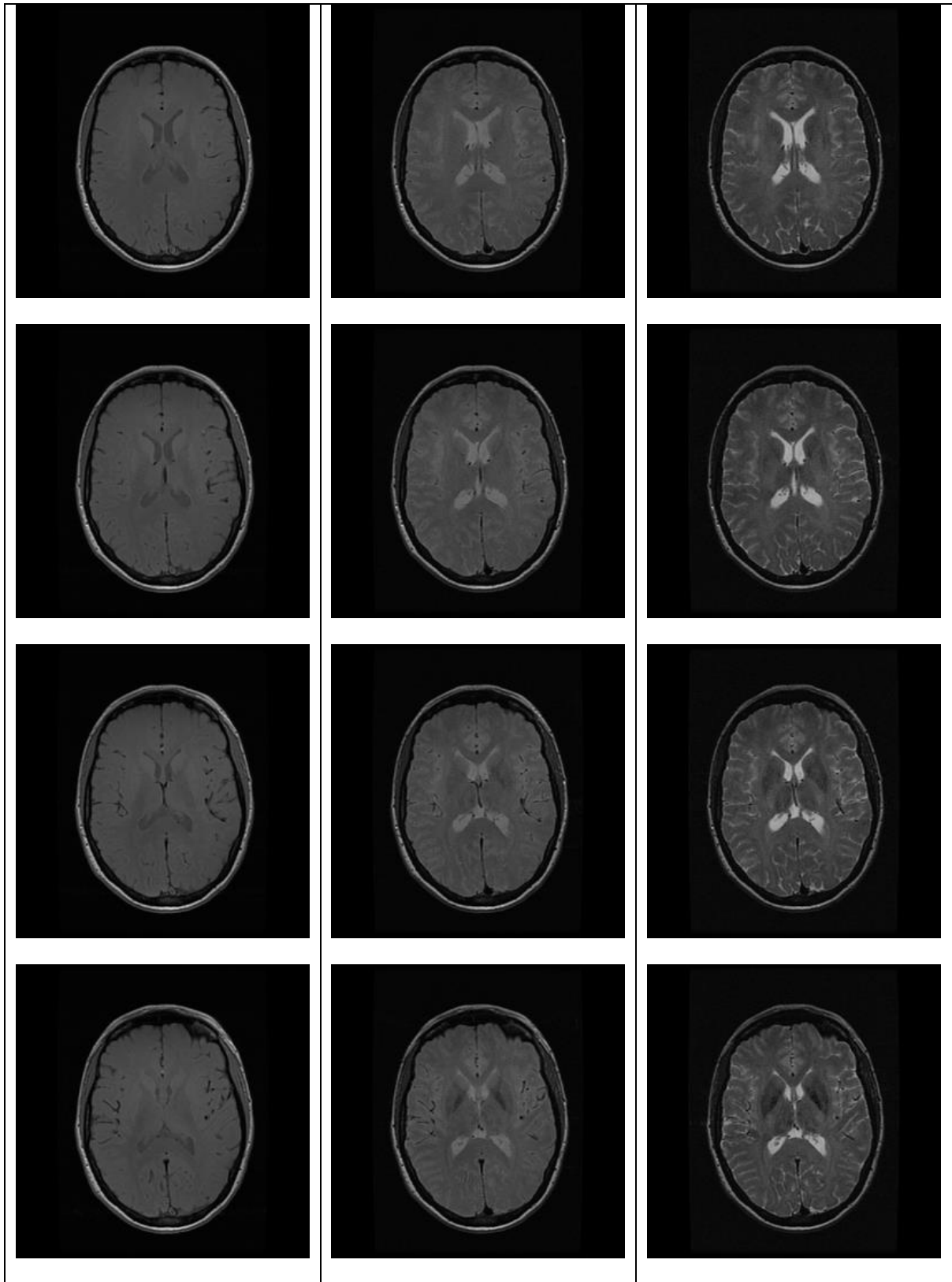


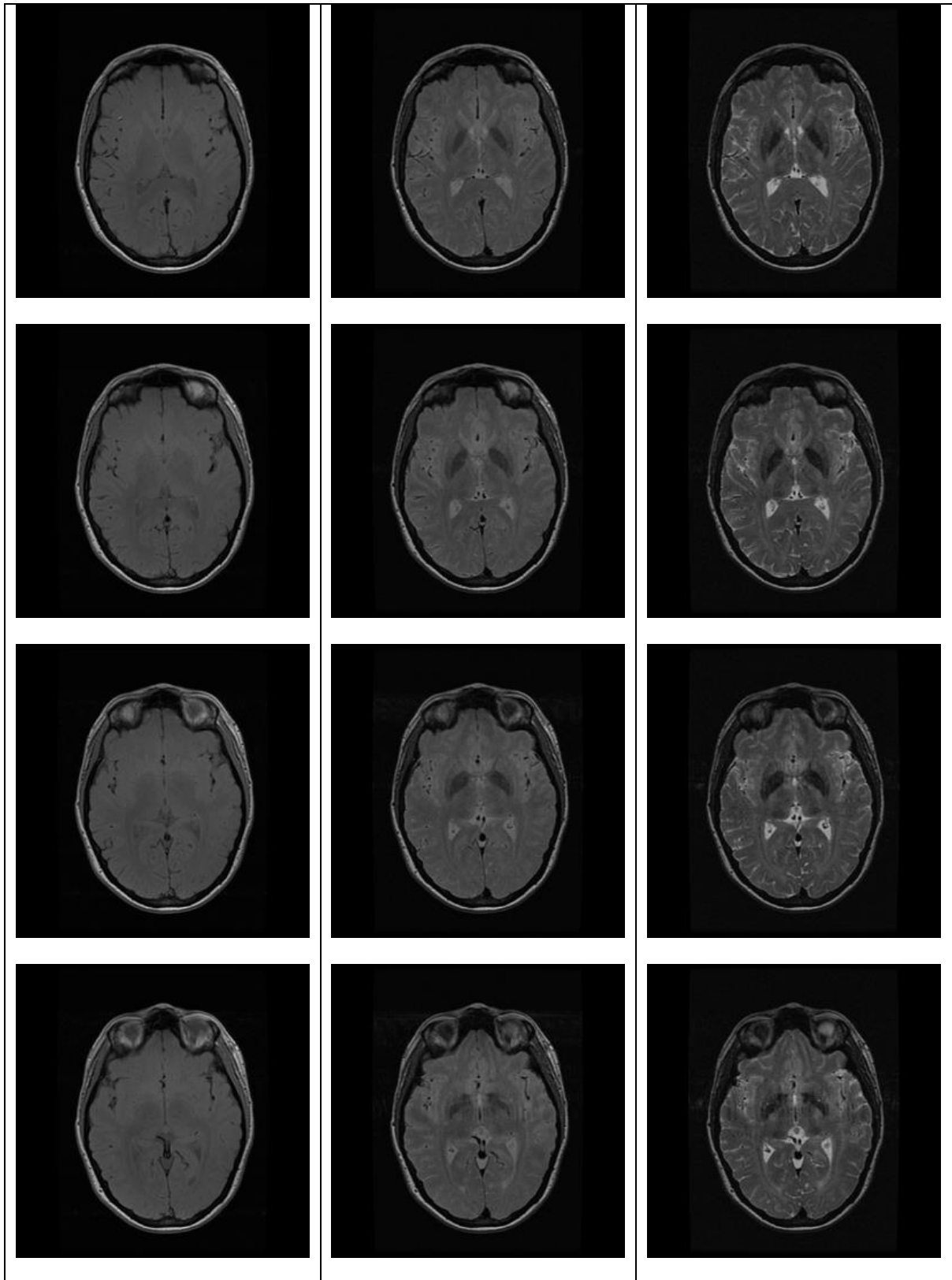


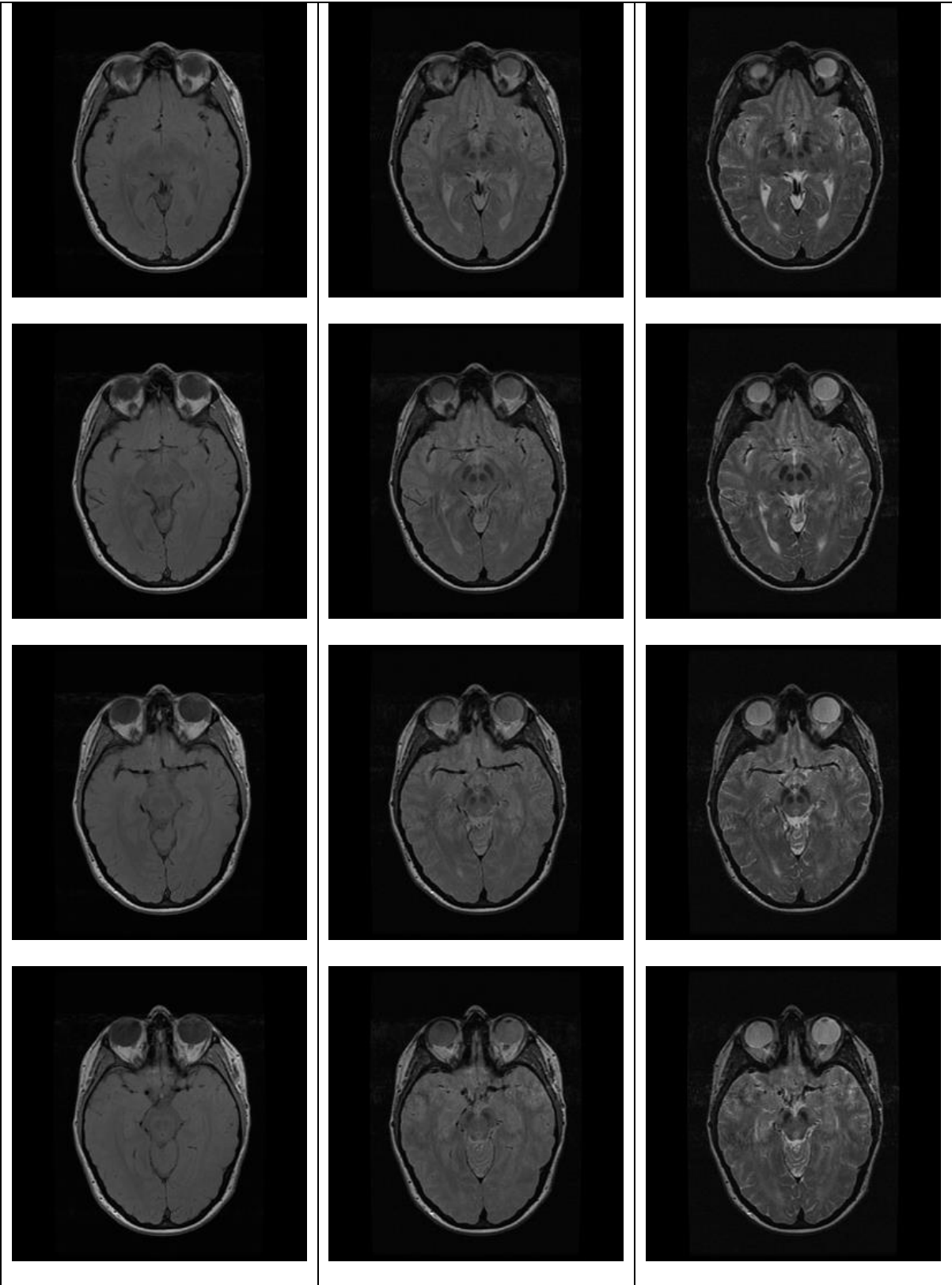
Patient 04

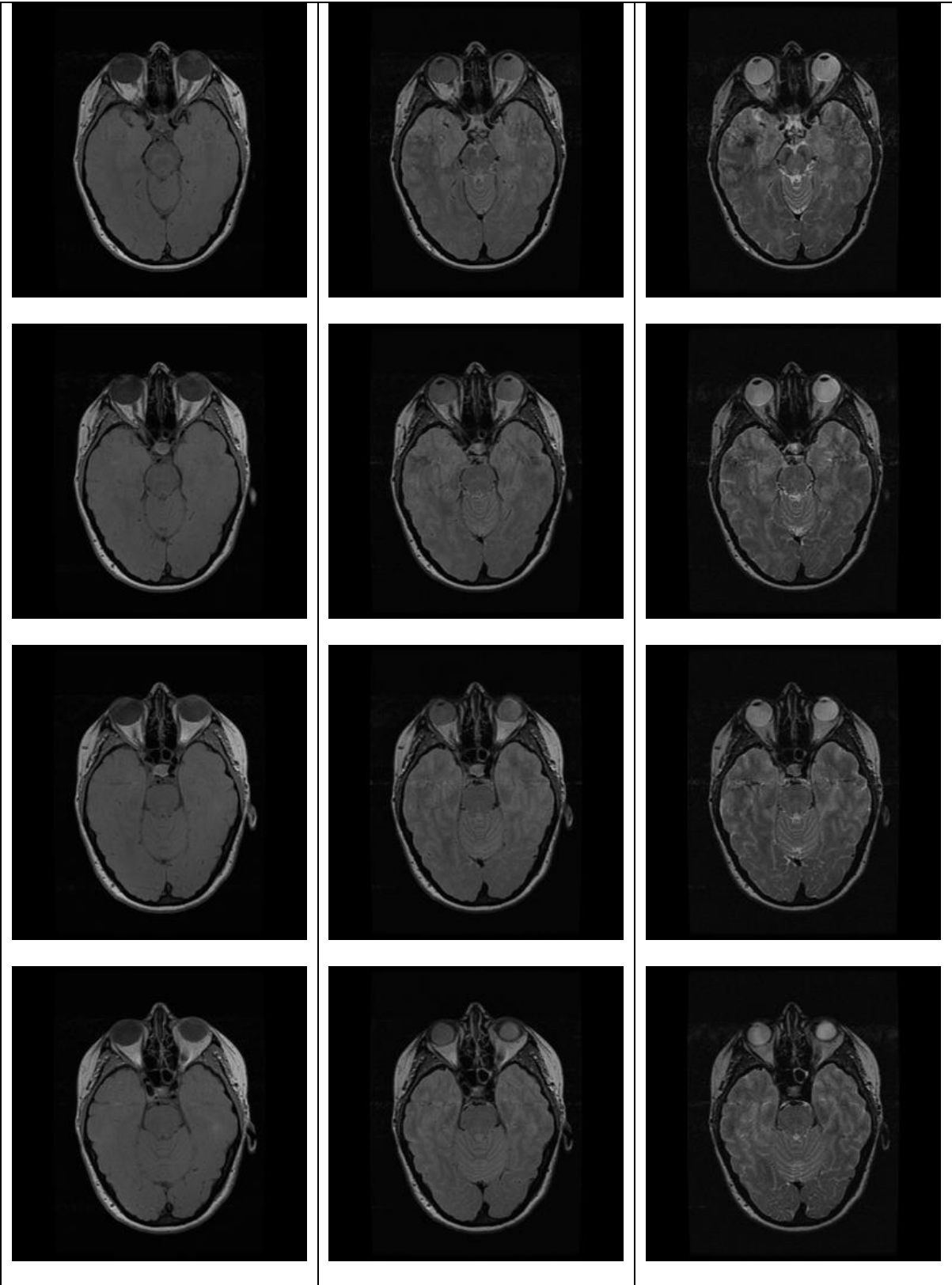


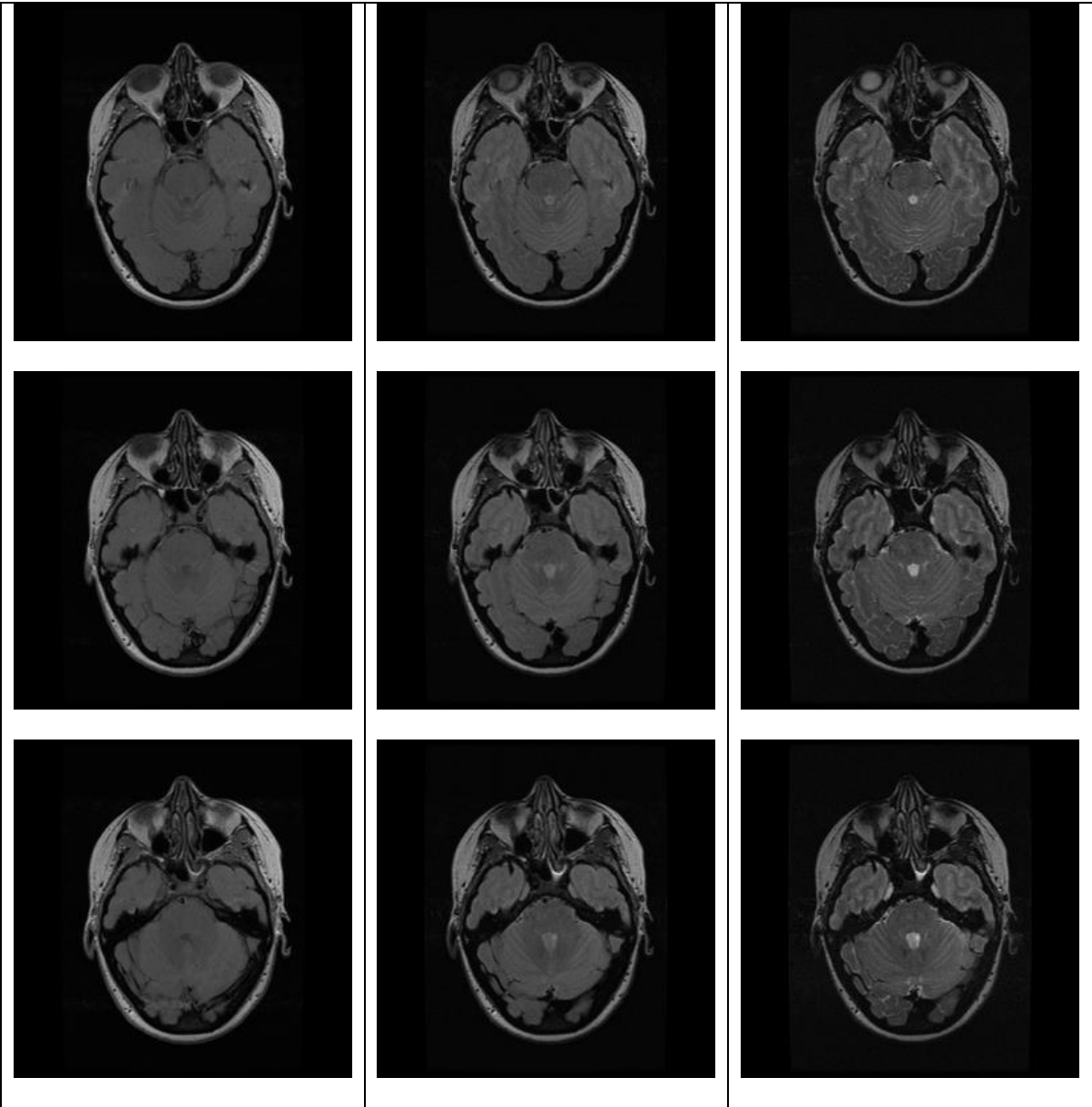


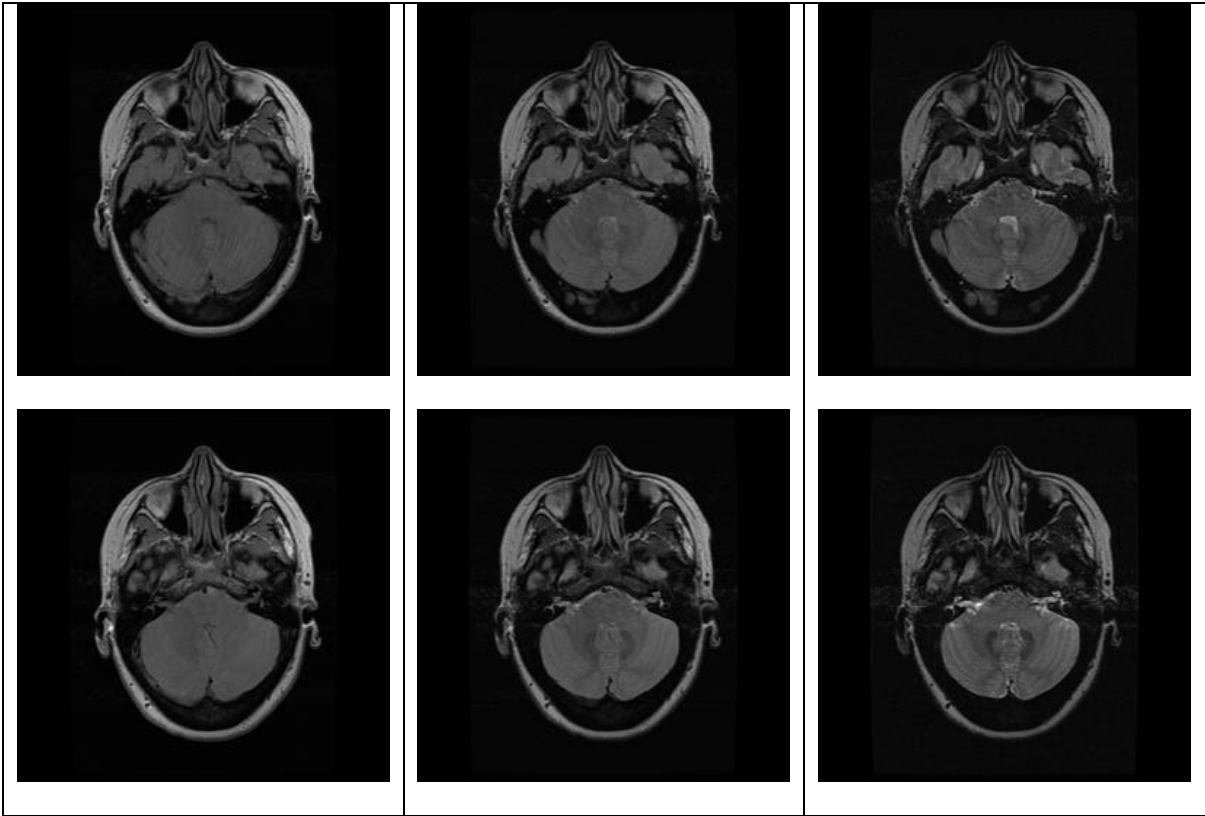




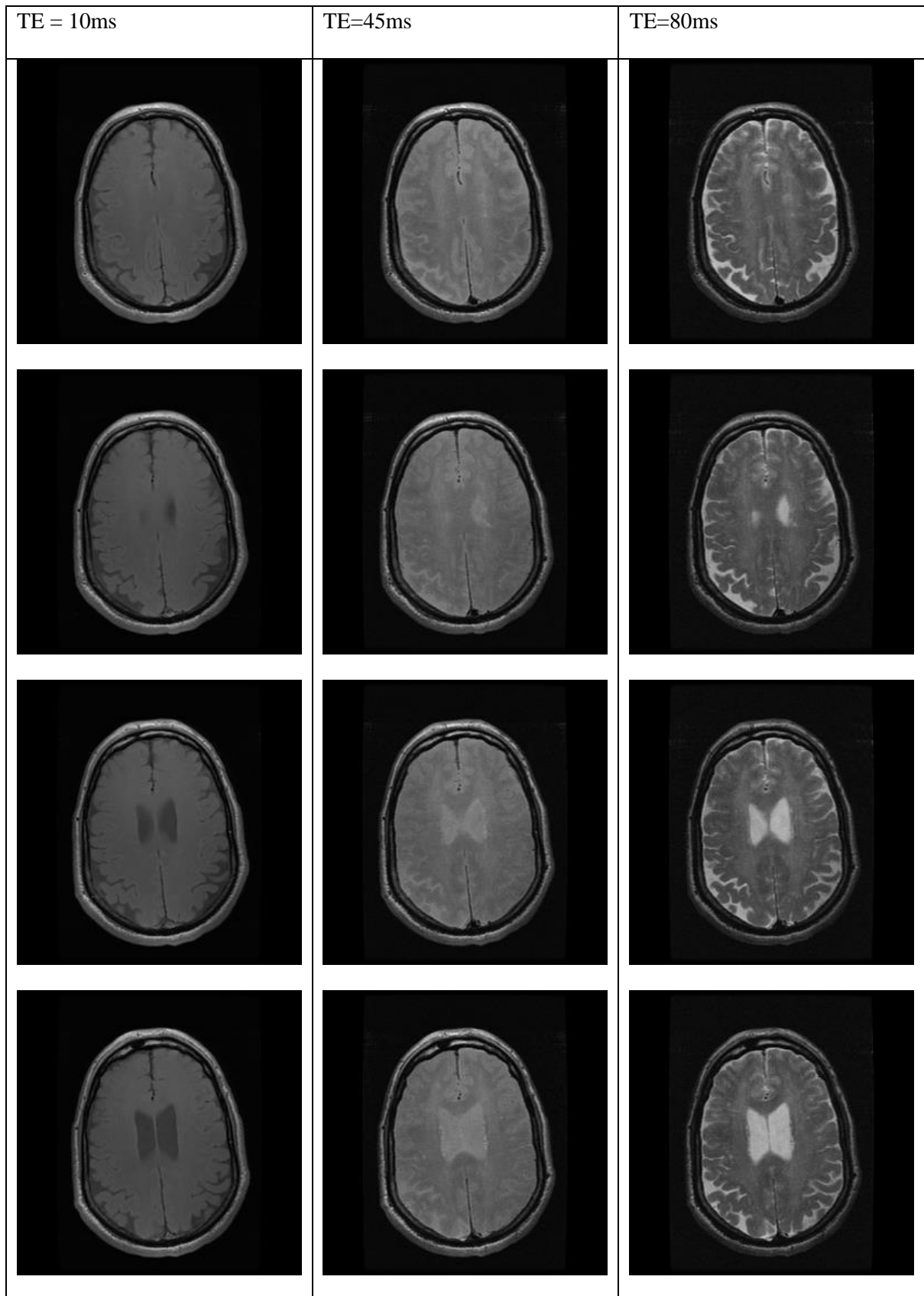


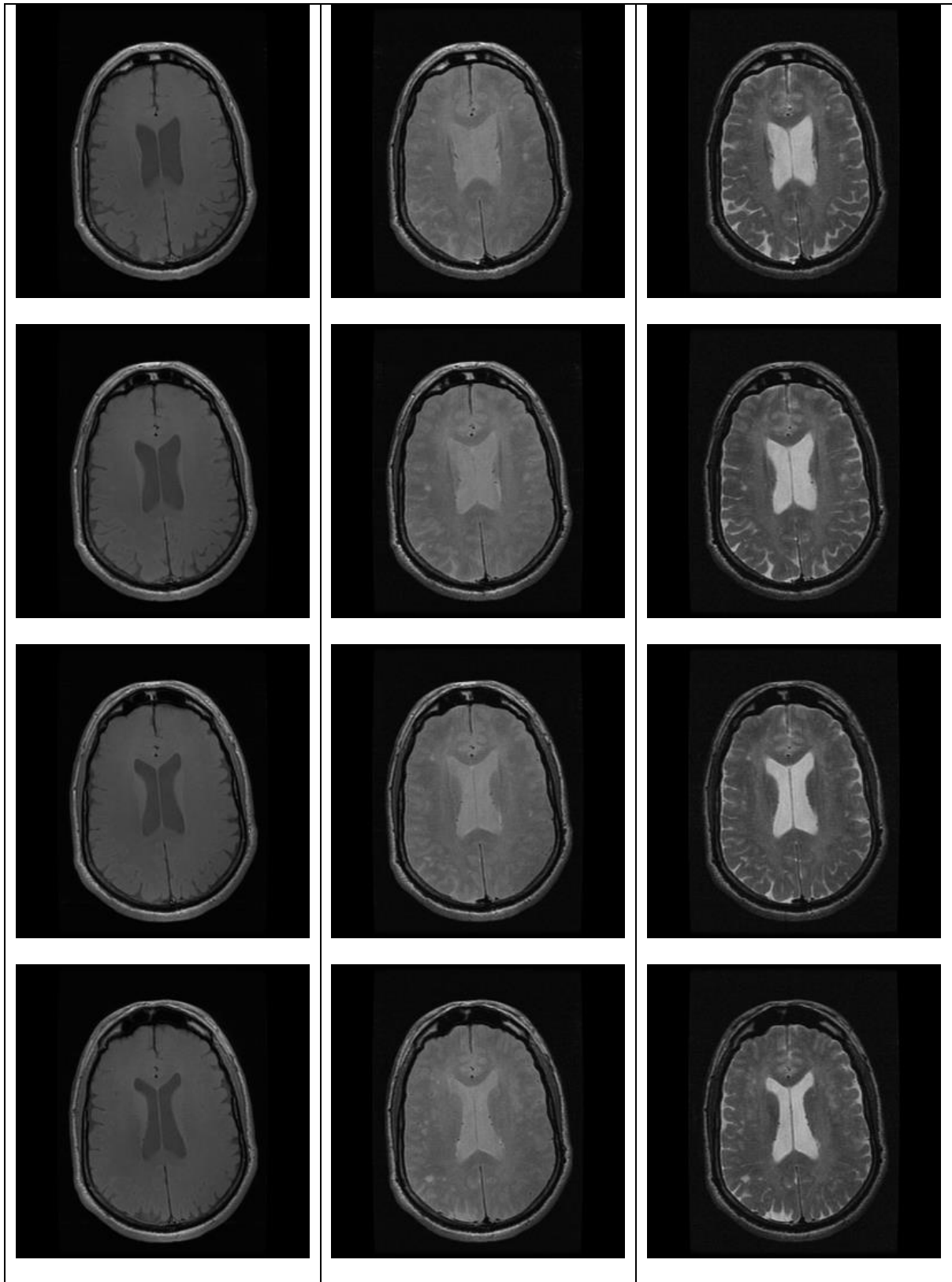


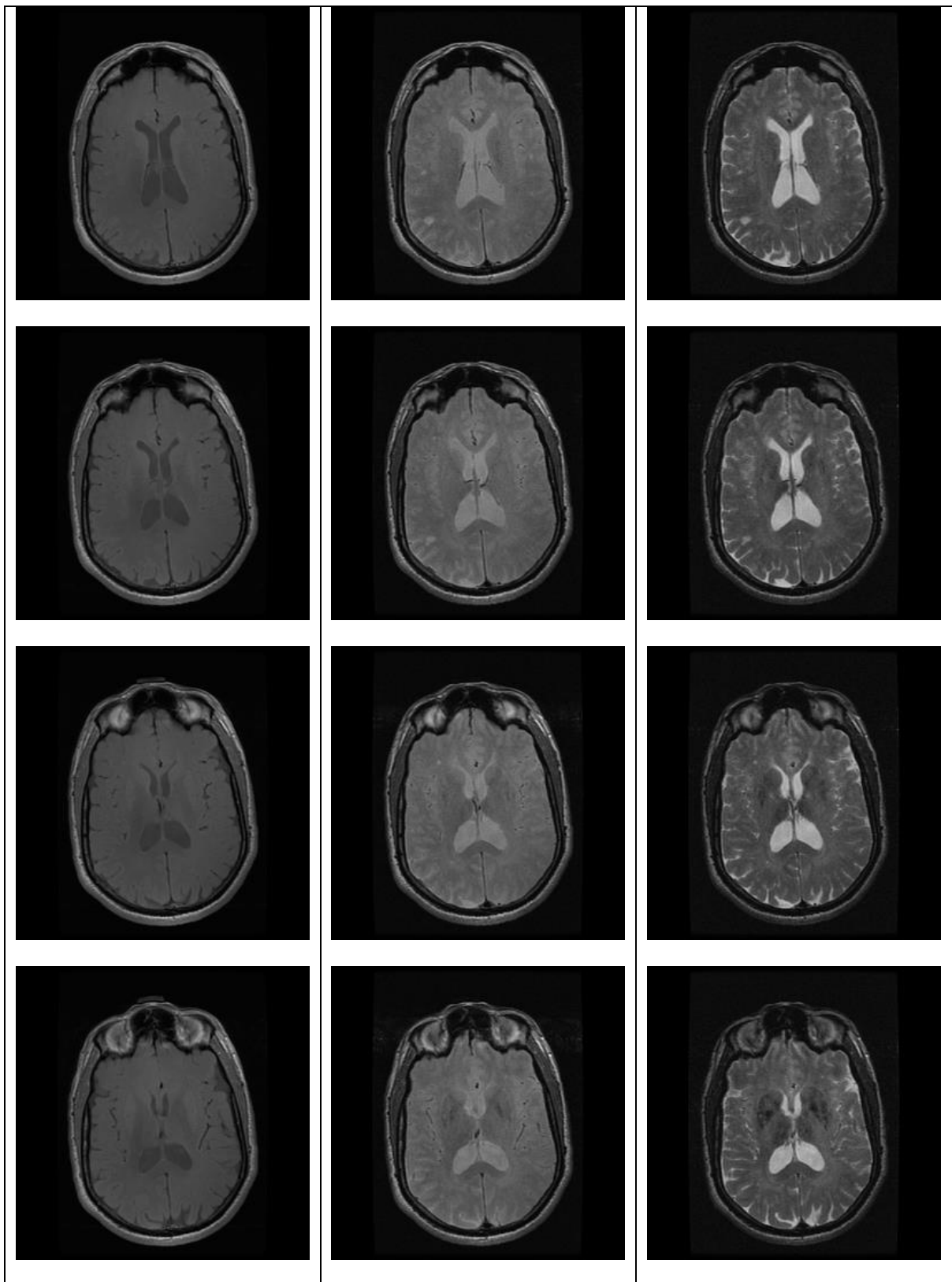


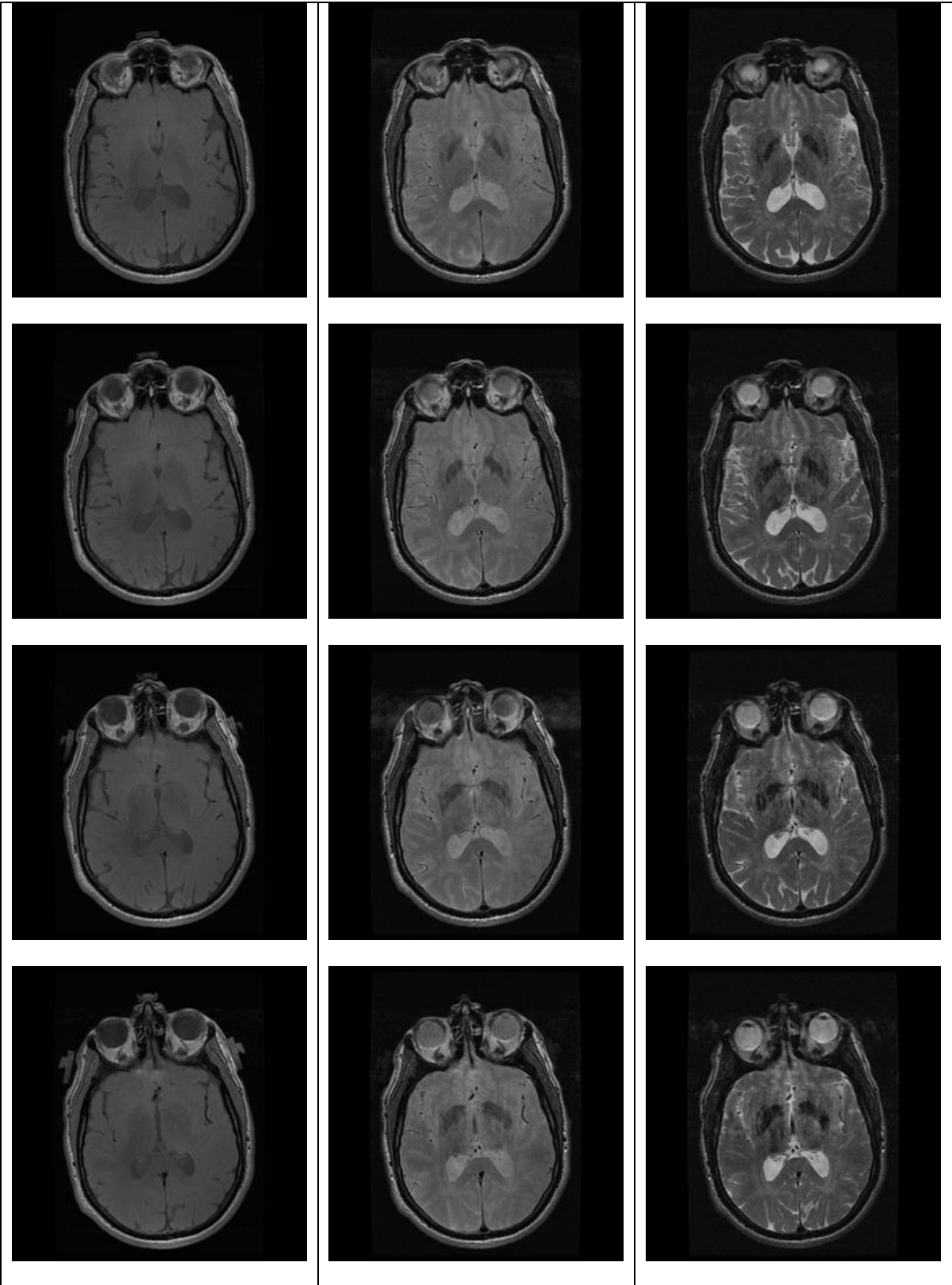


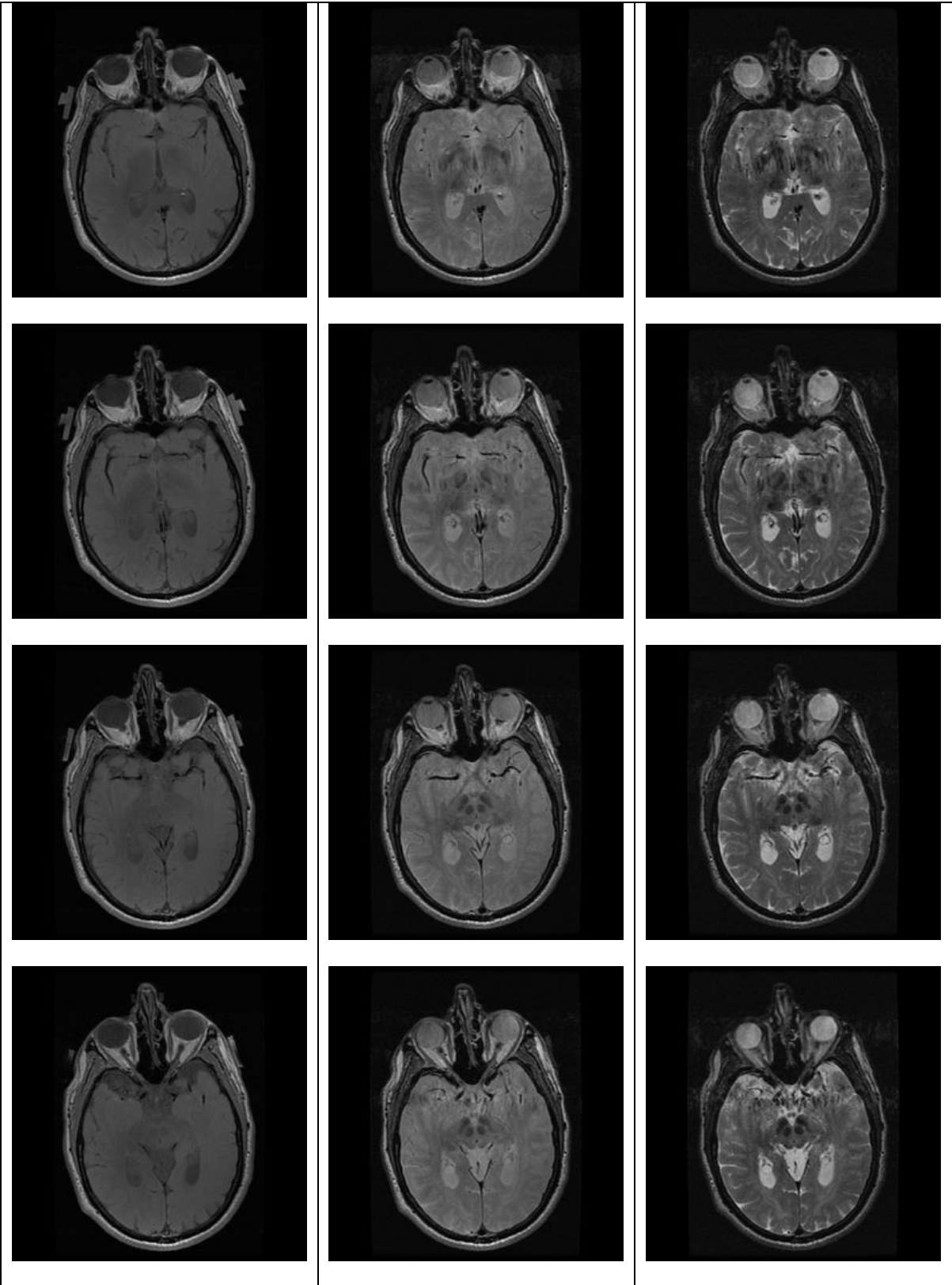
Patient 05

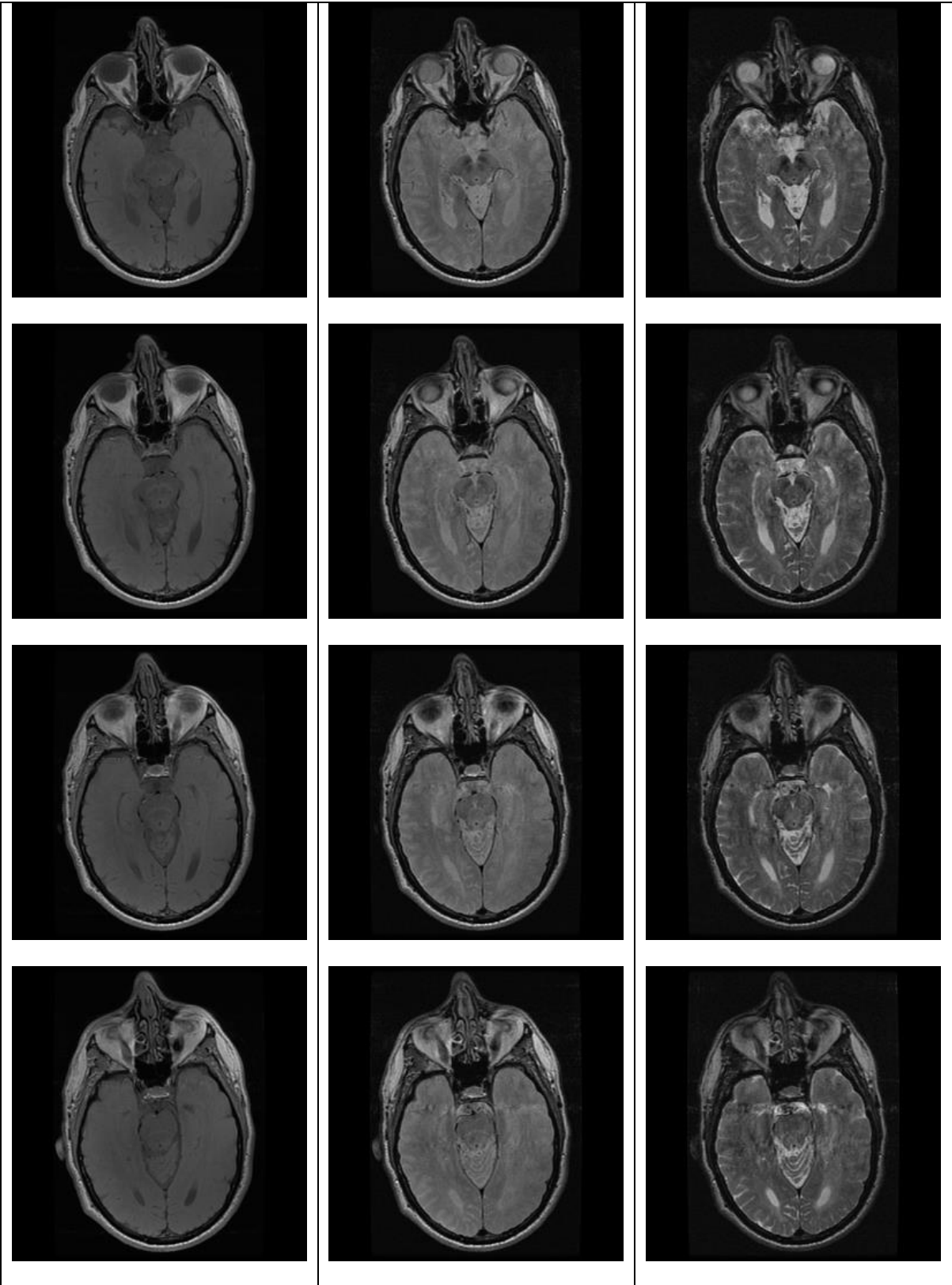


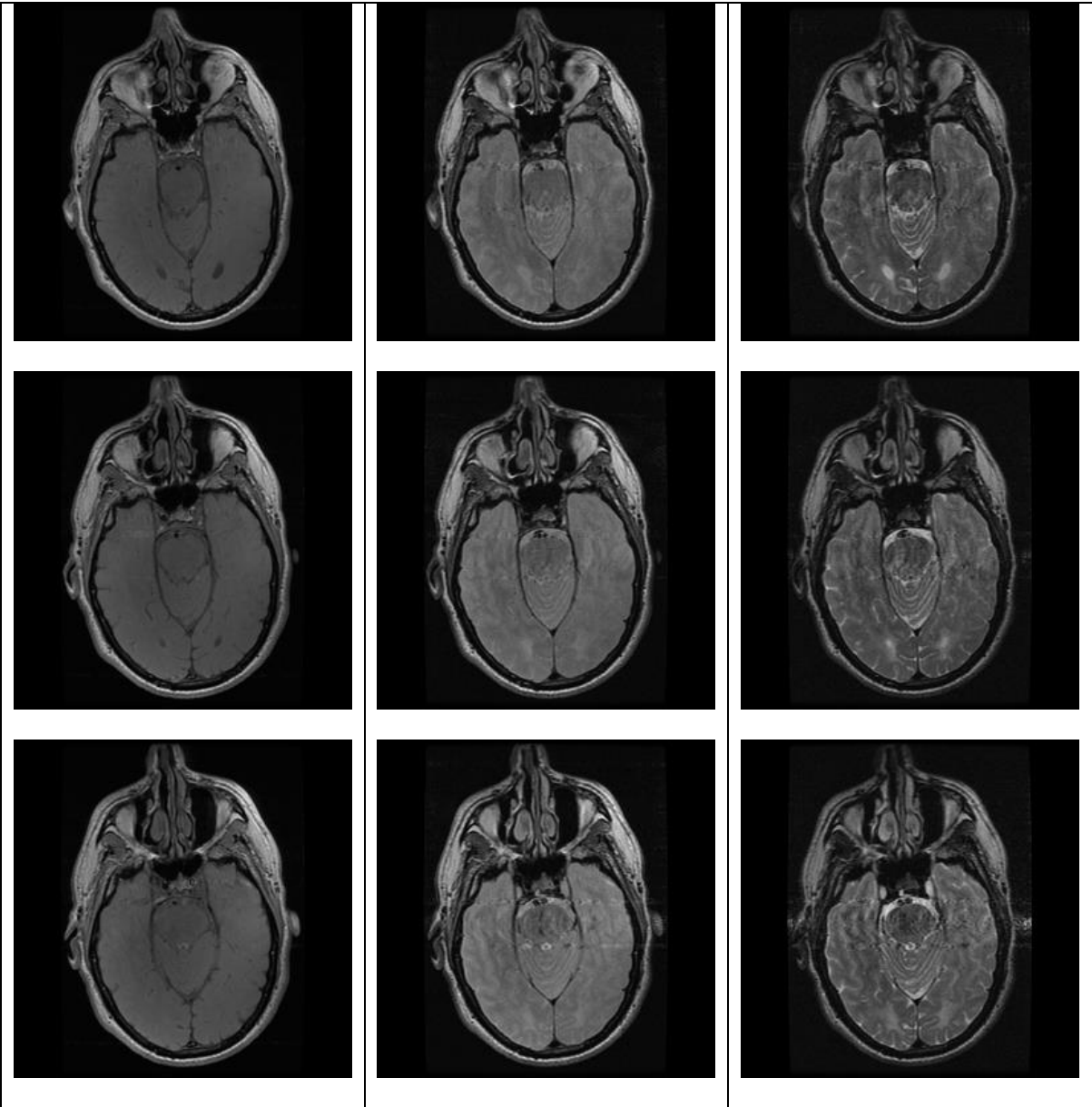




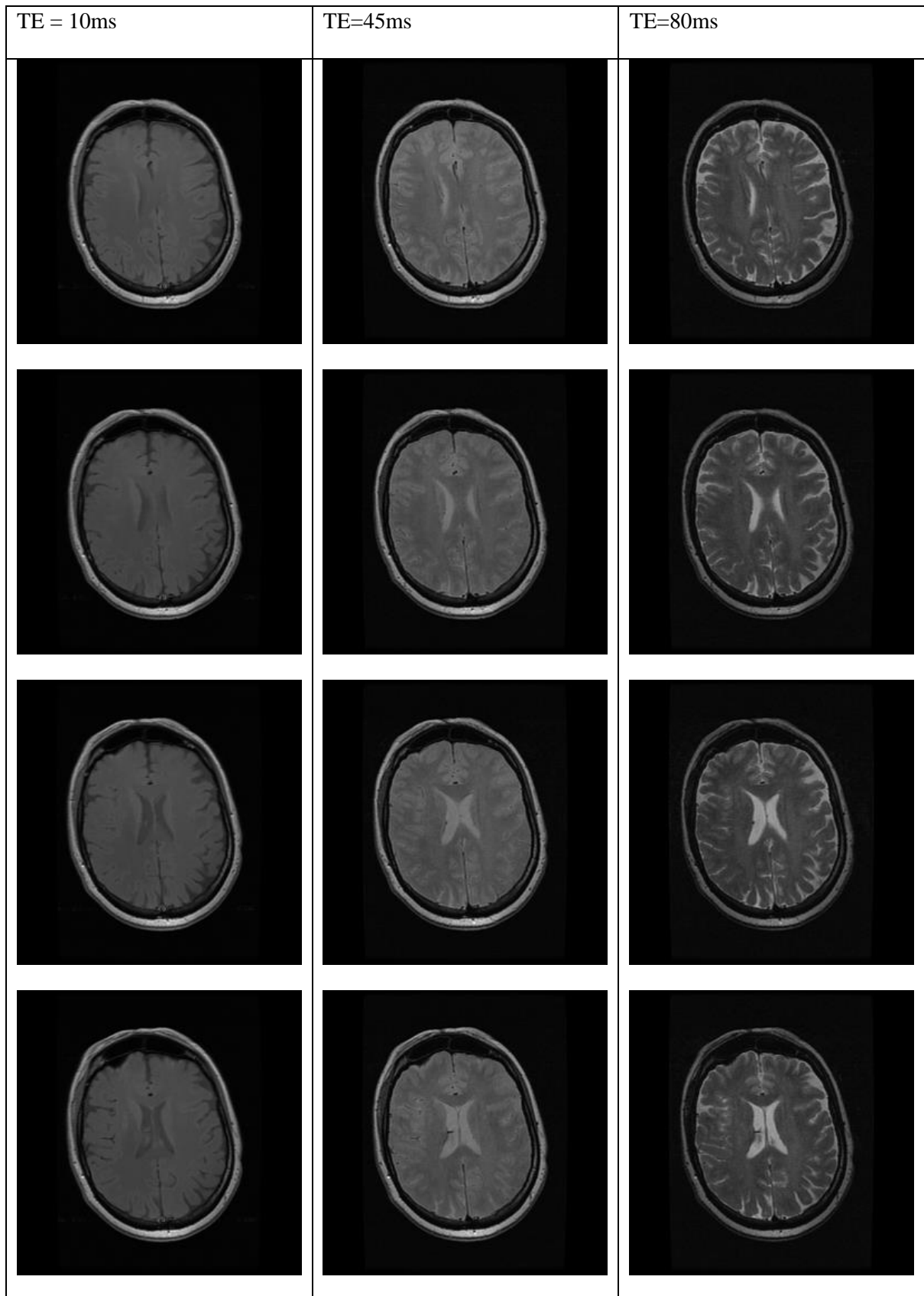


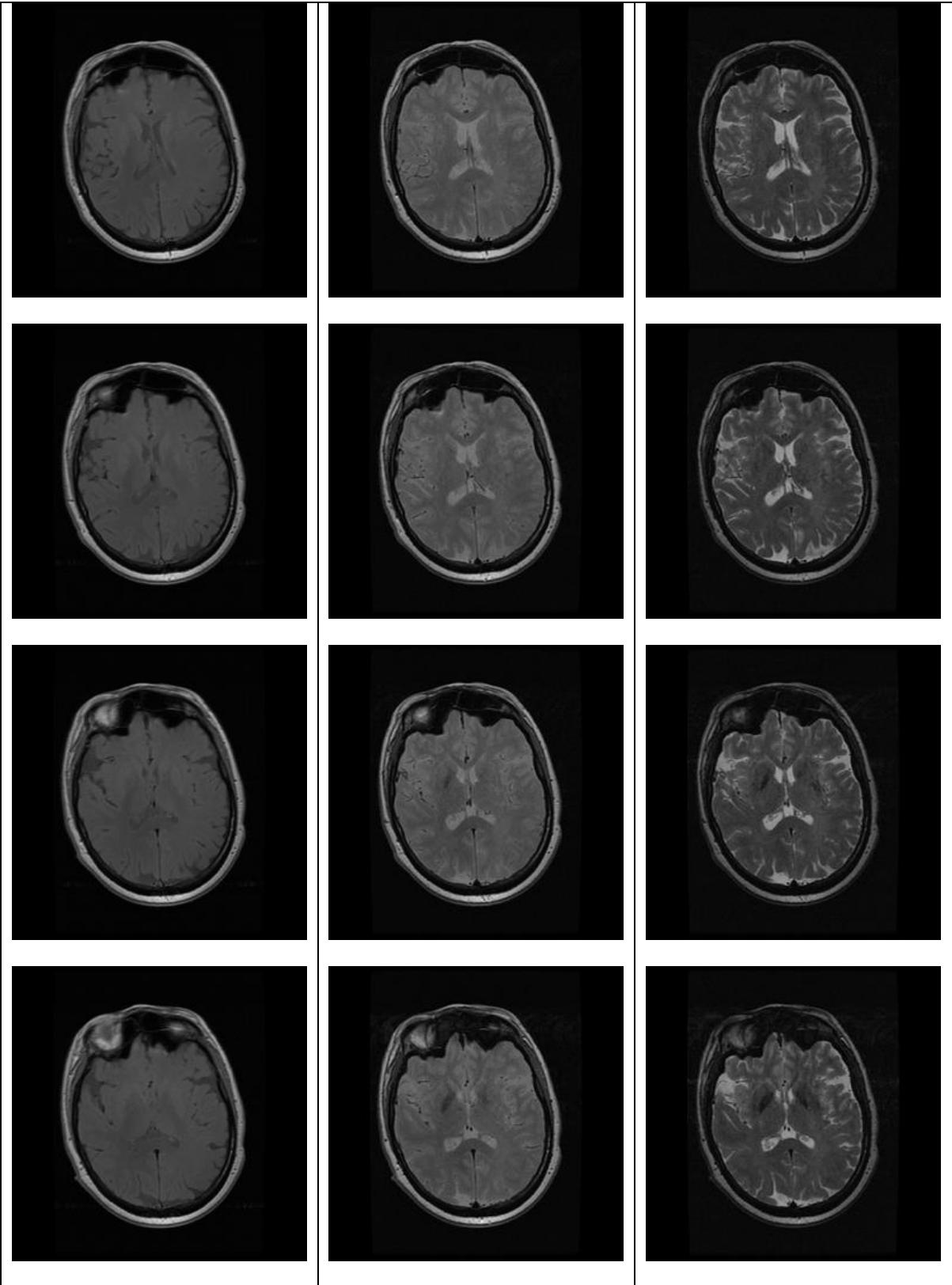


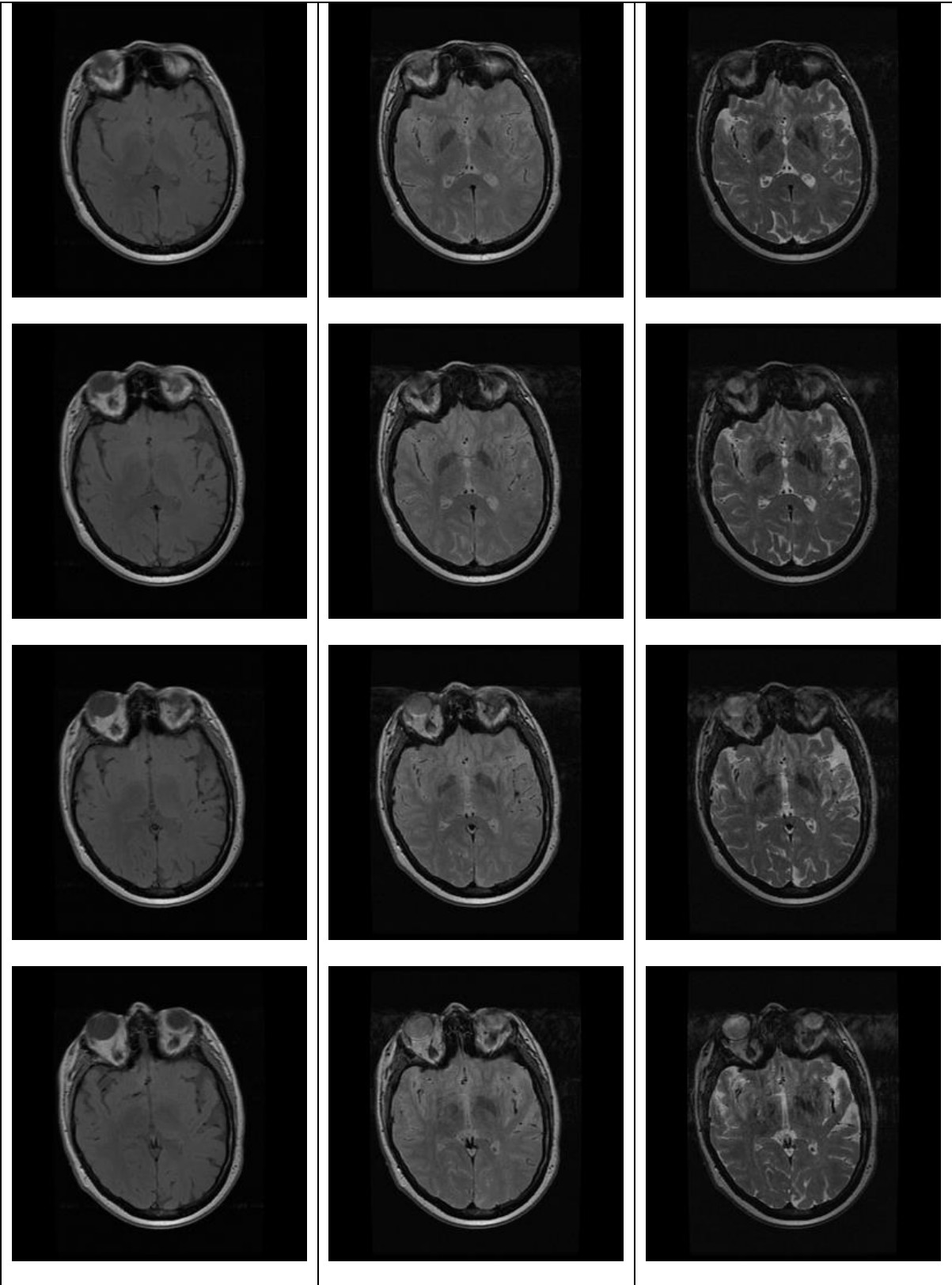


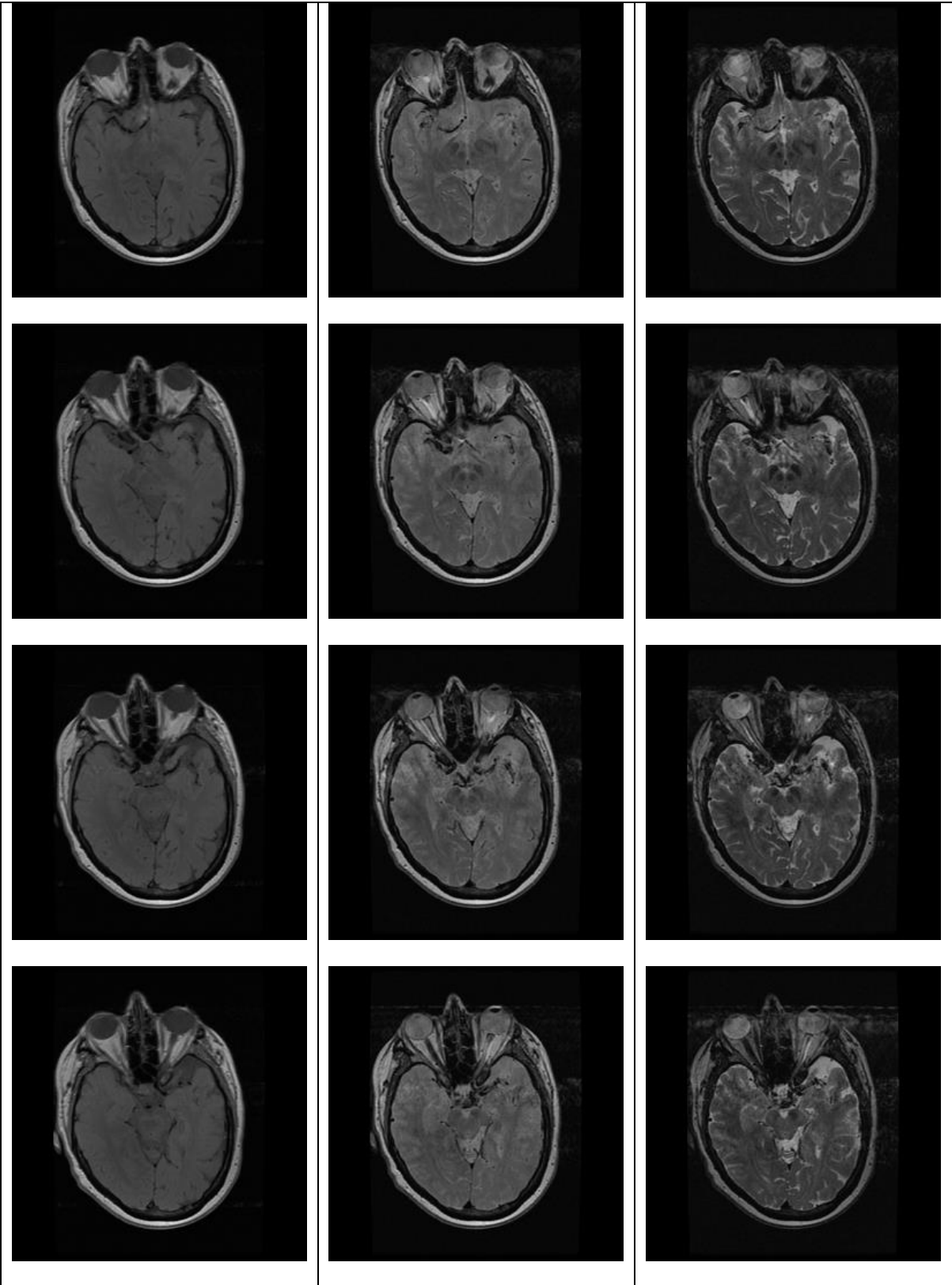


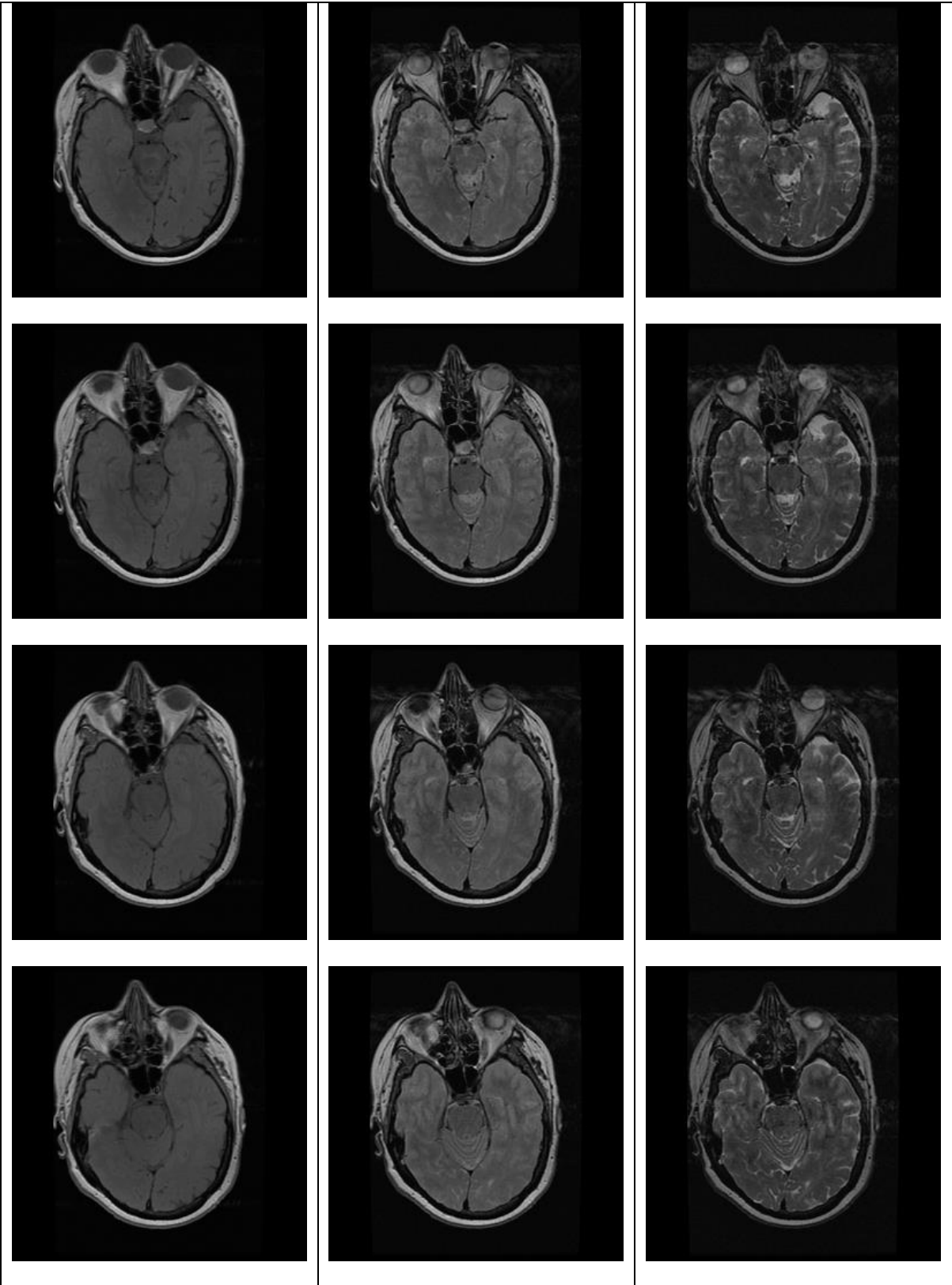
Patient 07

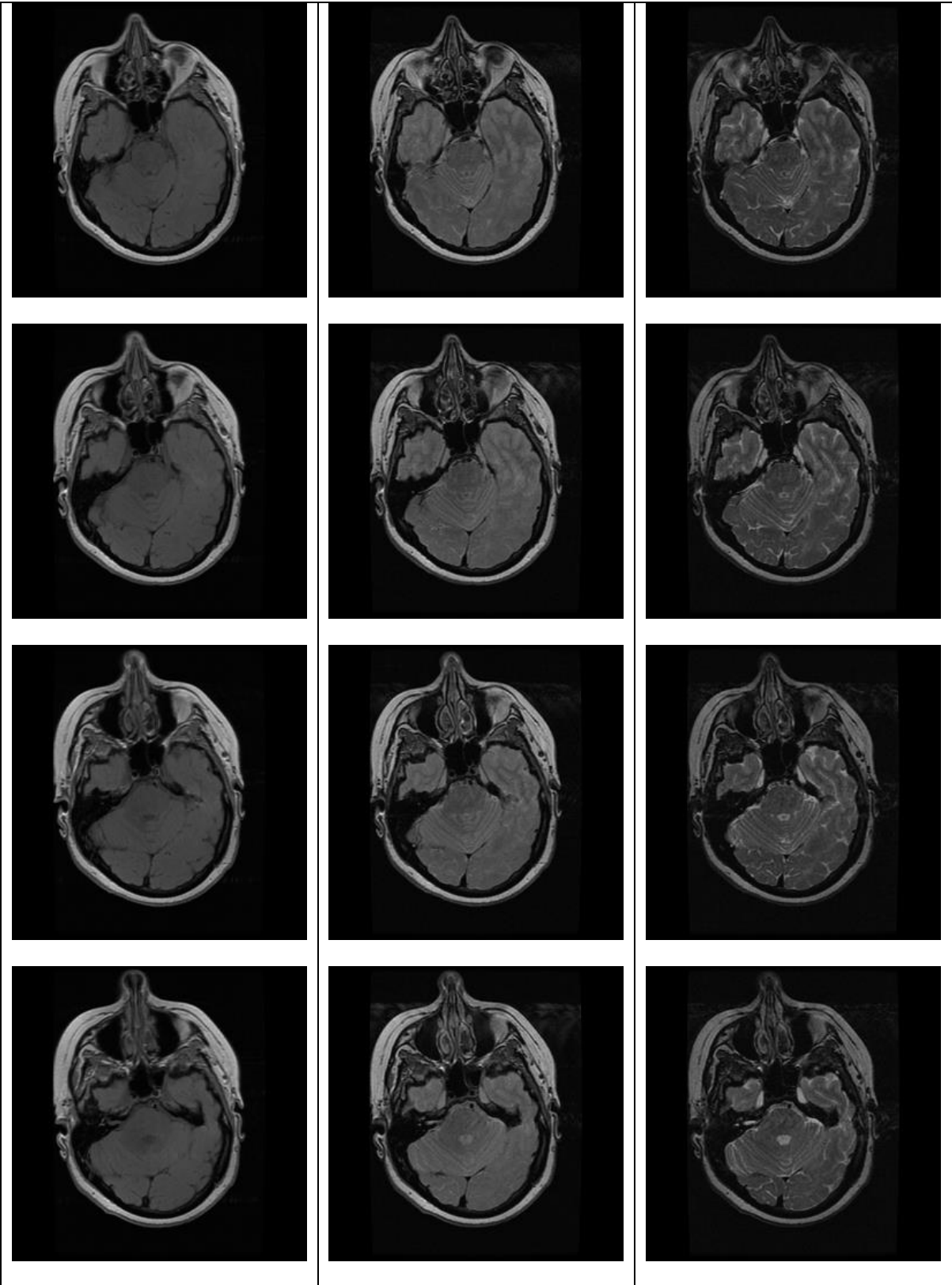


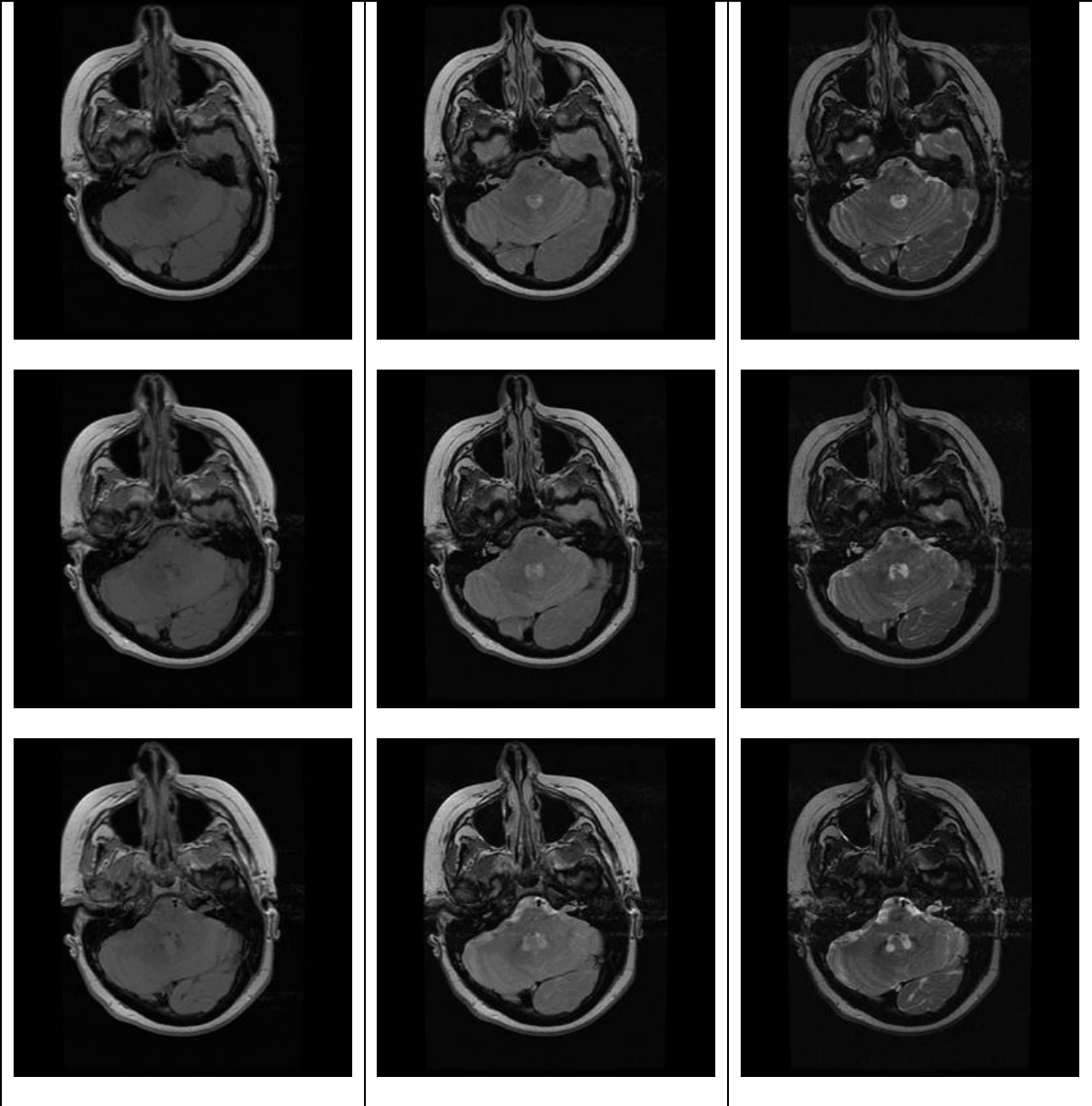




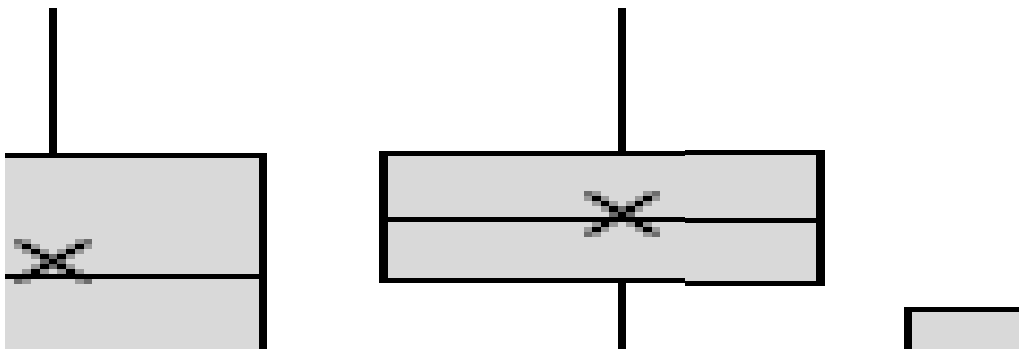


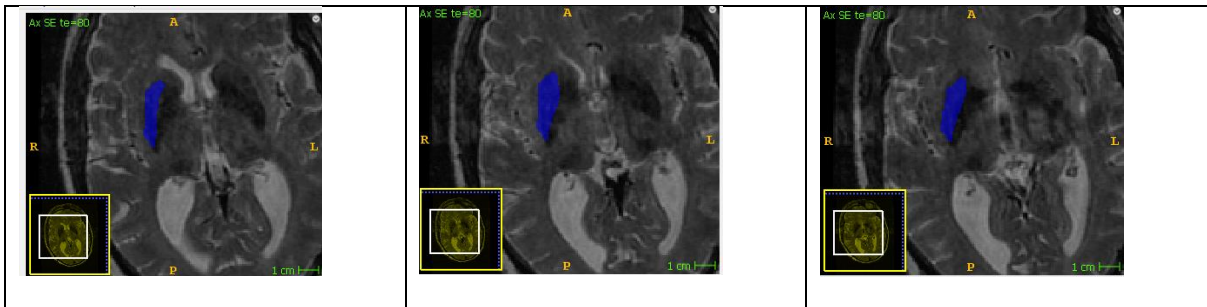
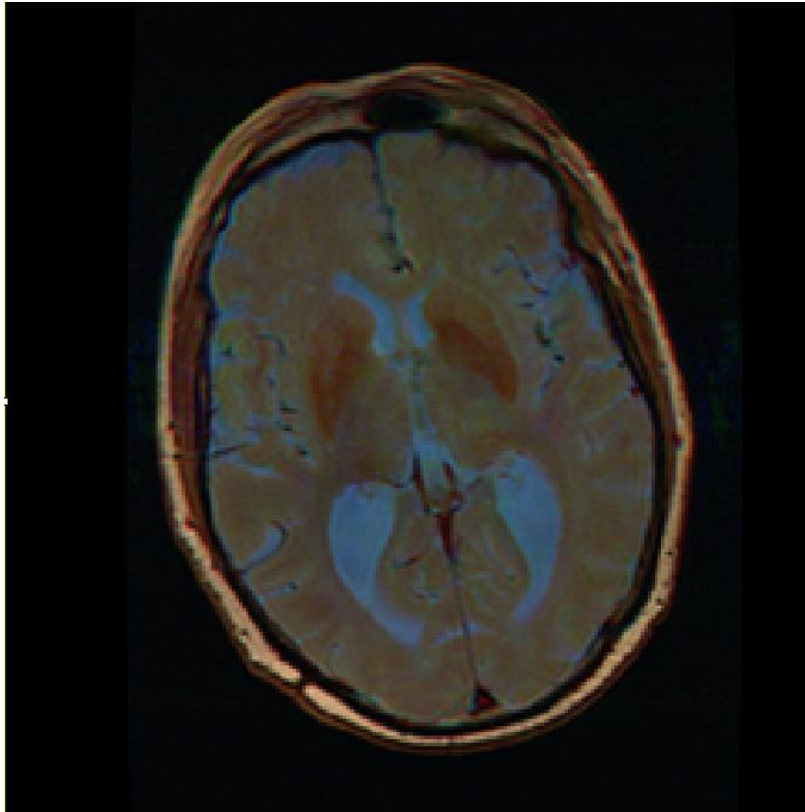




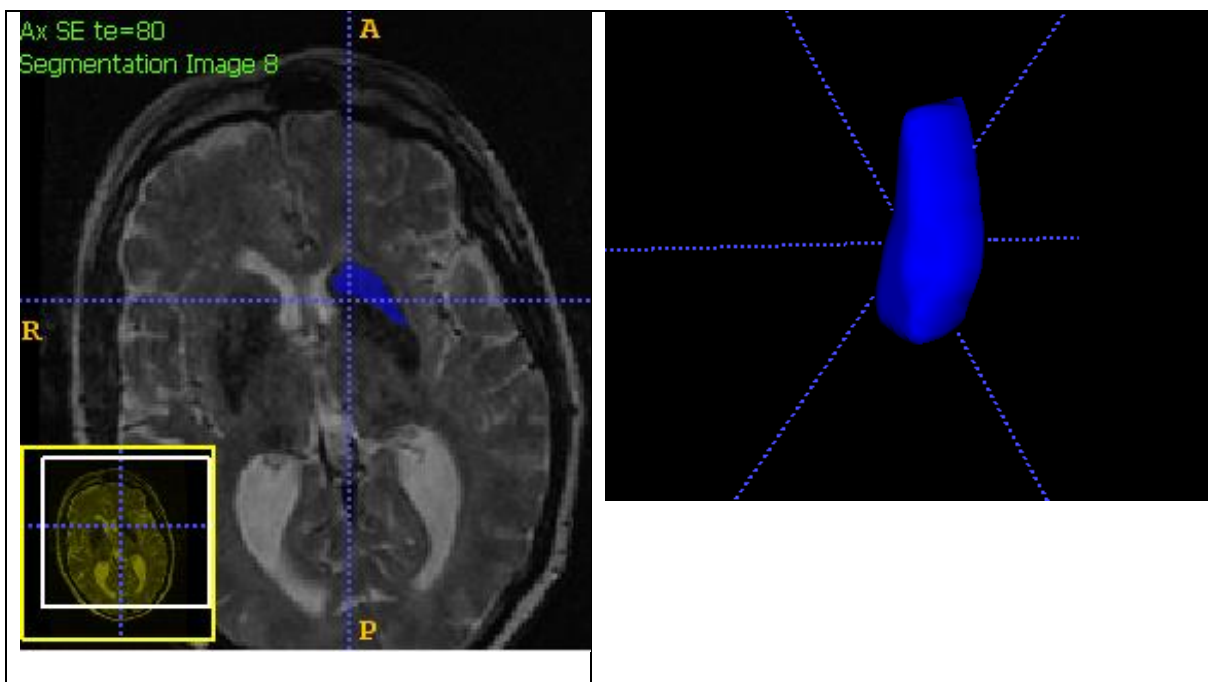
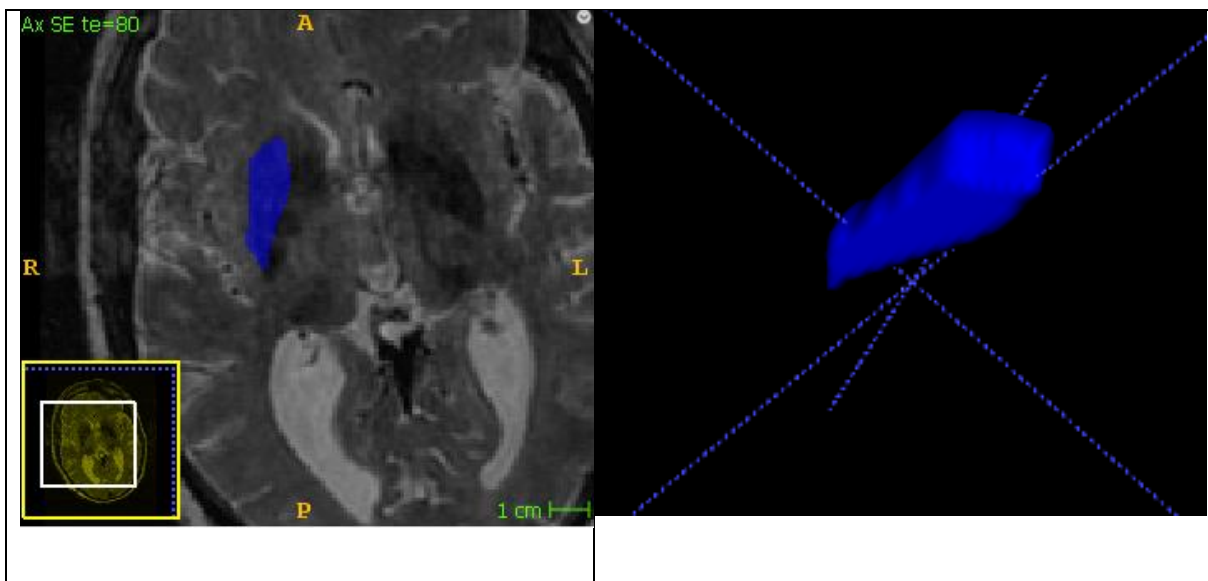


Patient 1

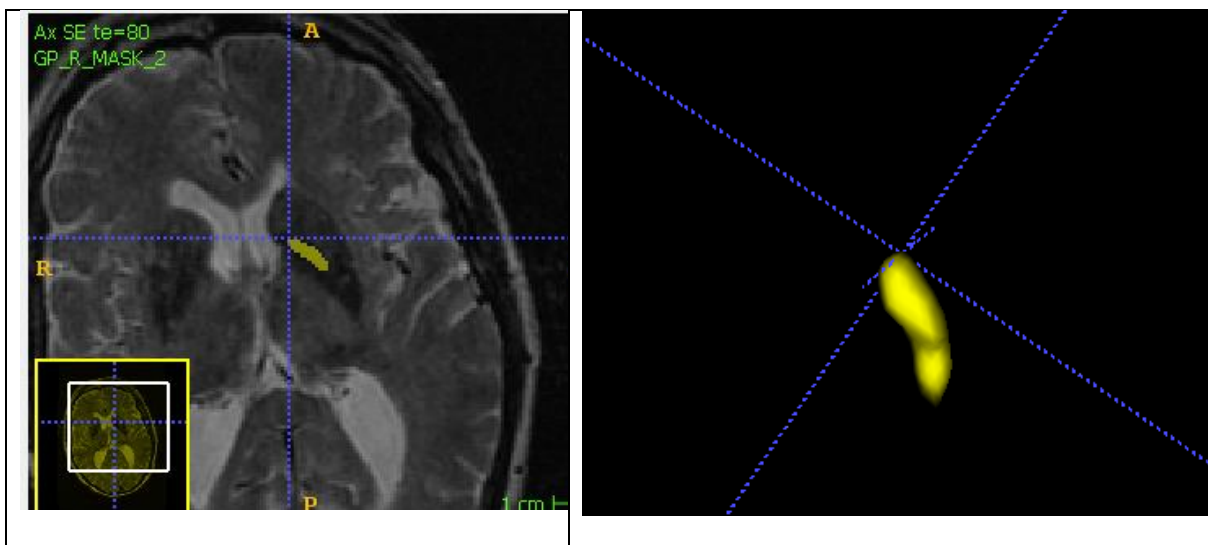
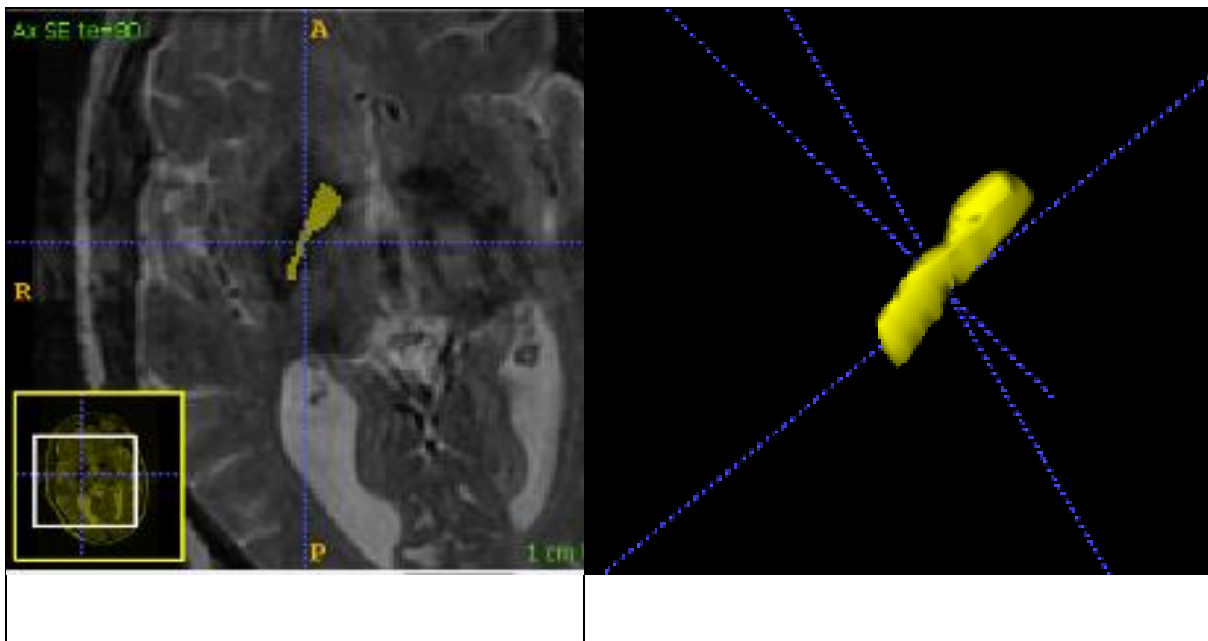




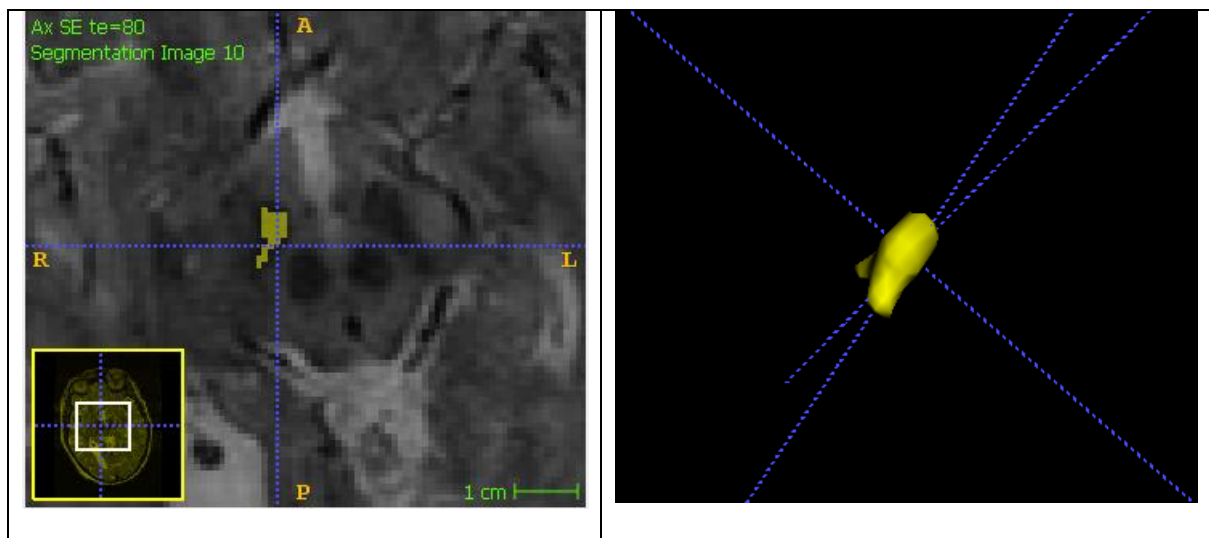
Putamen

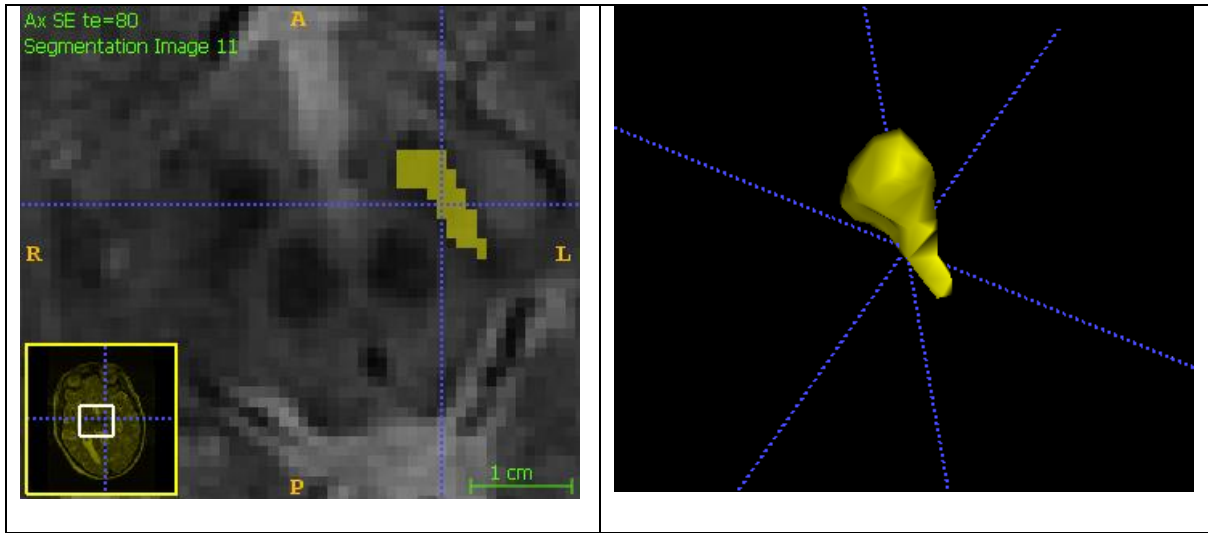


Globus Pallidus



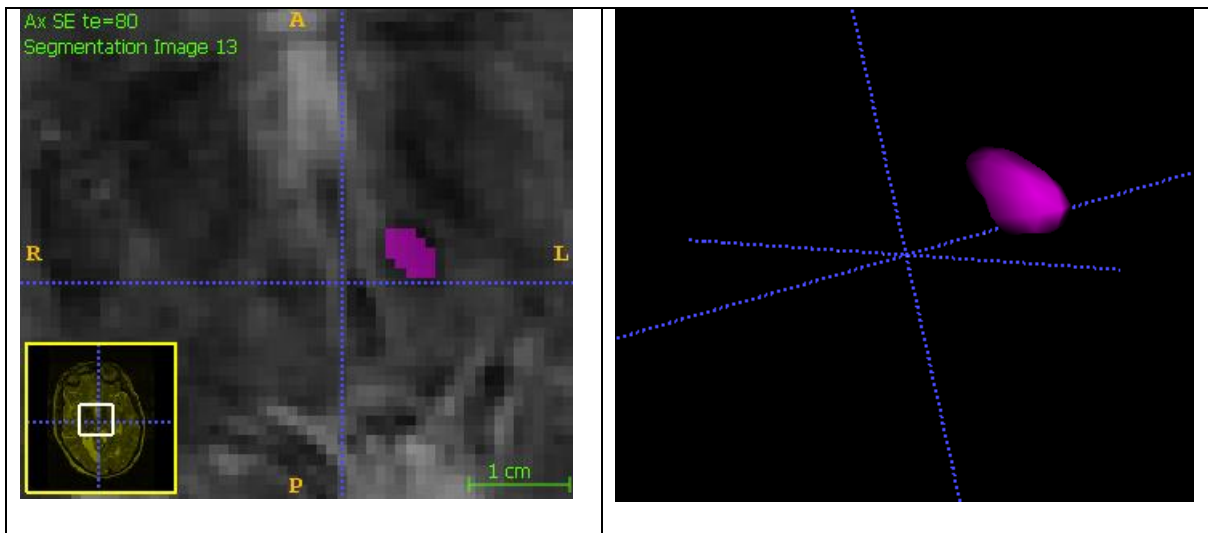
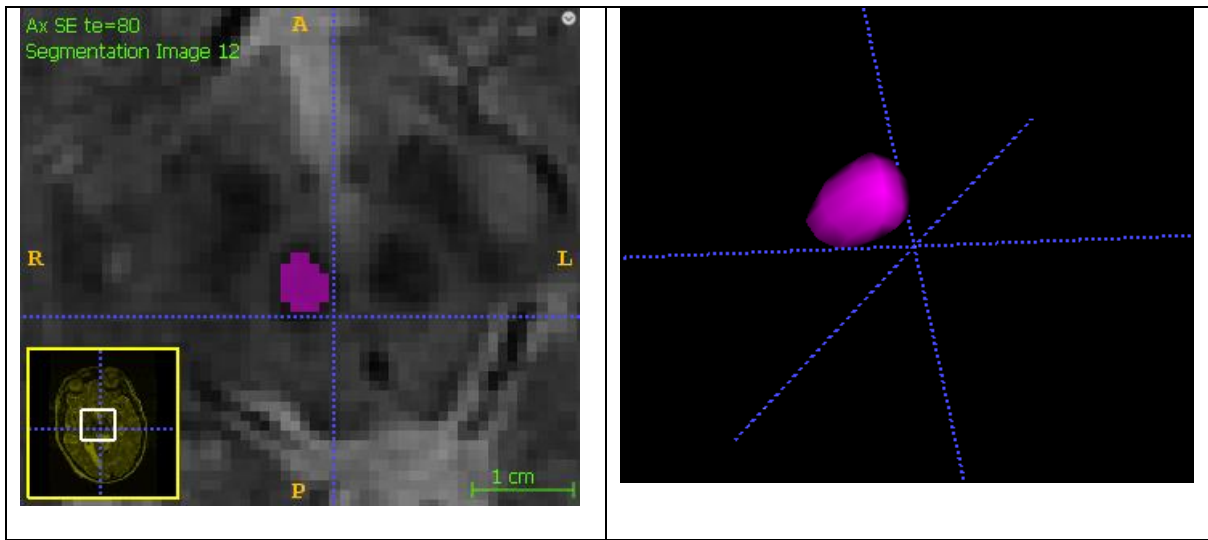
SN



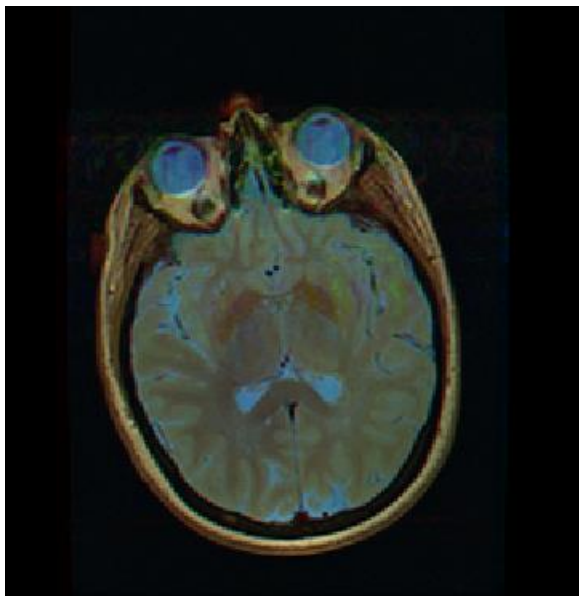
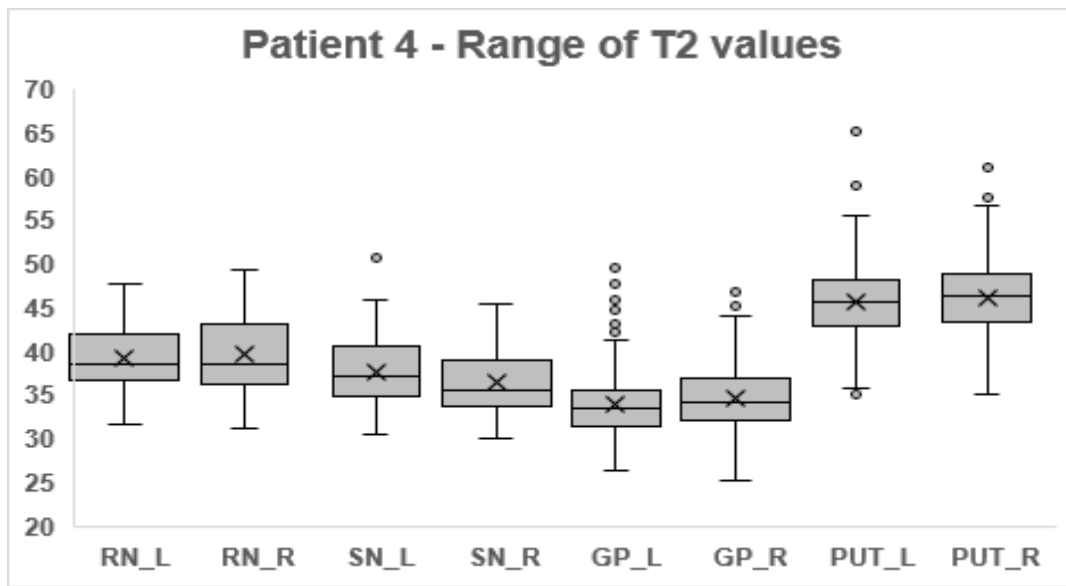


#

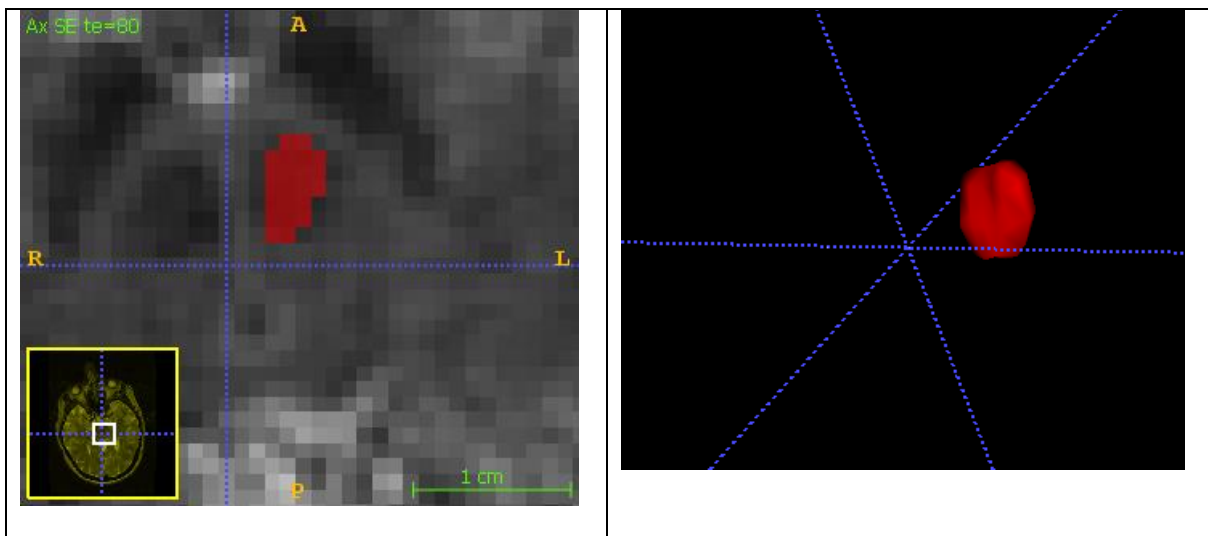
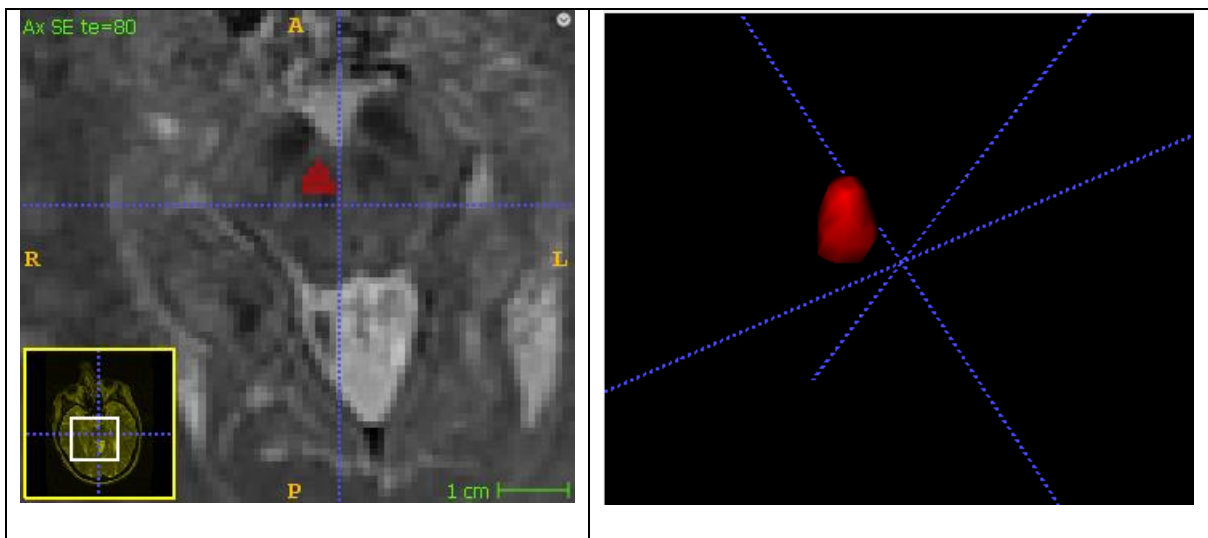
Red Nucleus



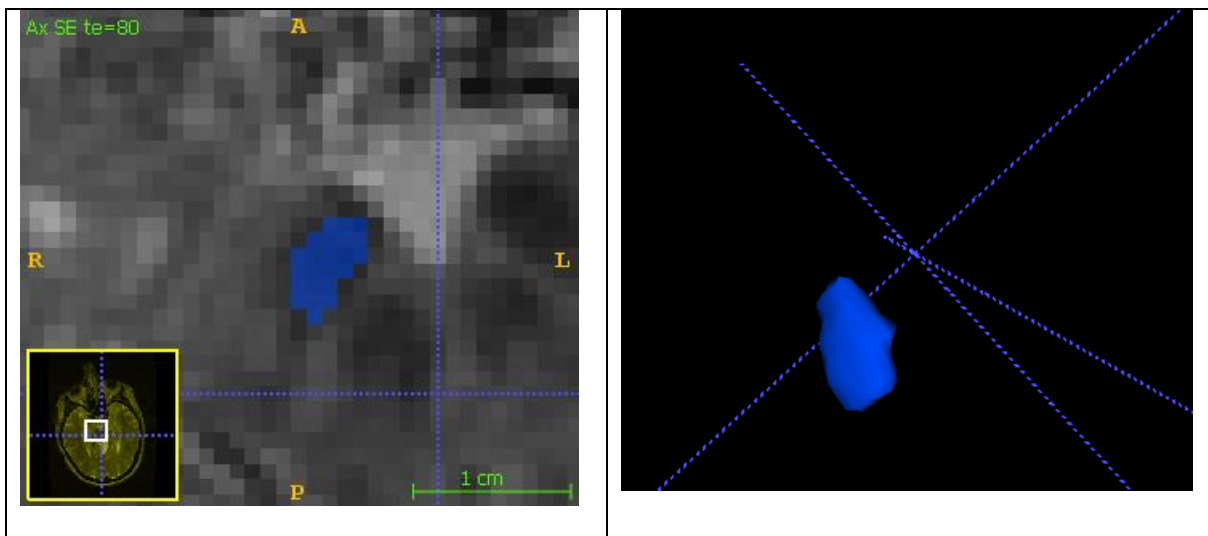
Patient 3

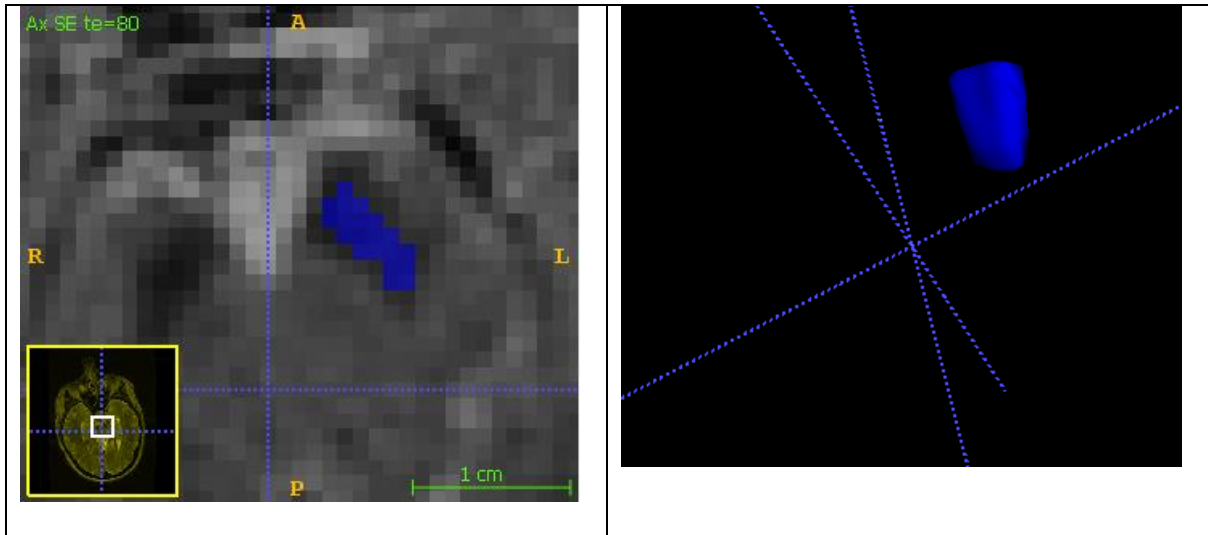


Red Nucleus

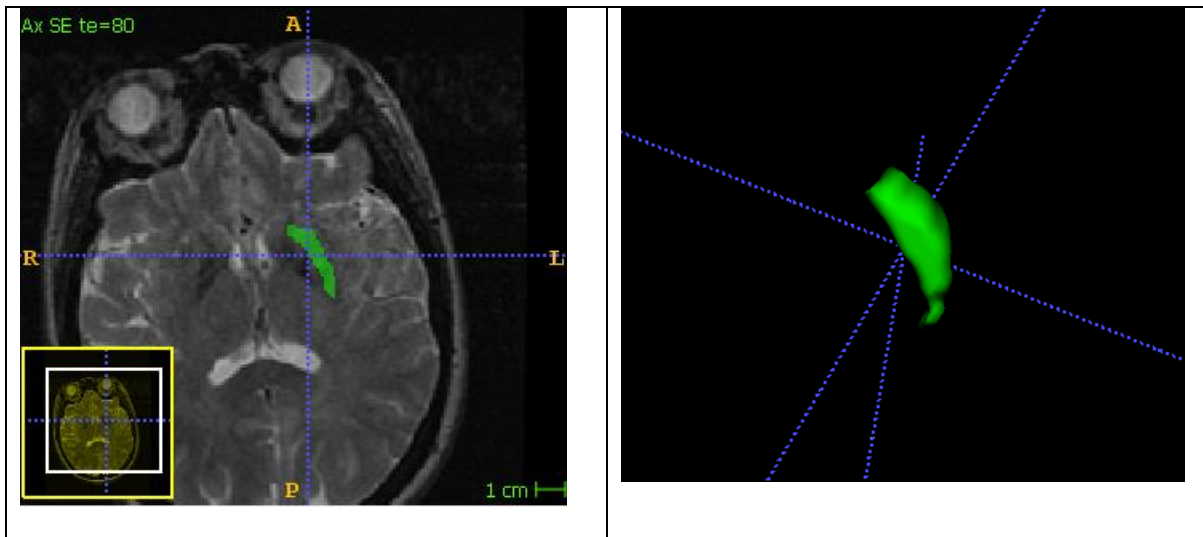
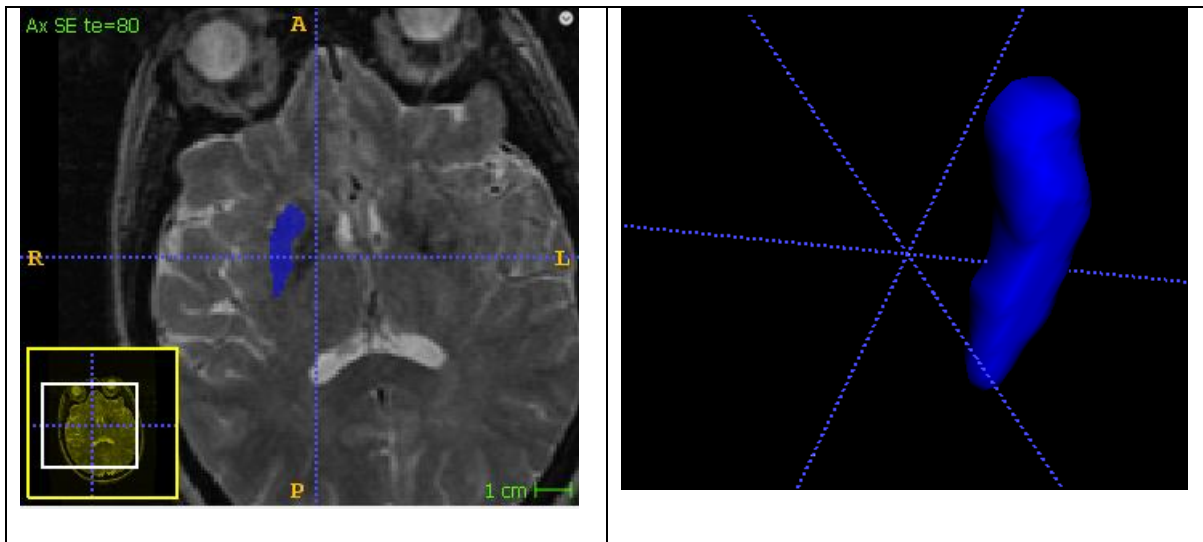


SN

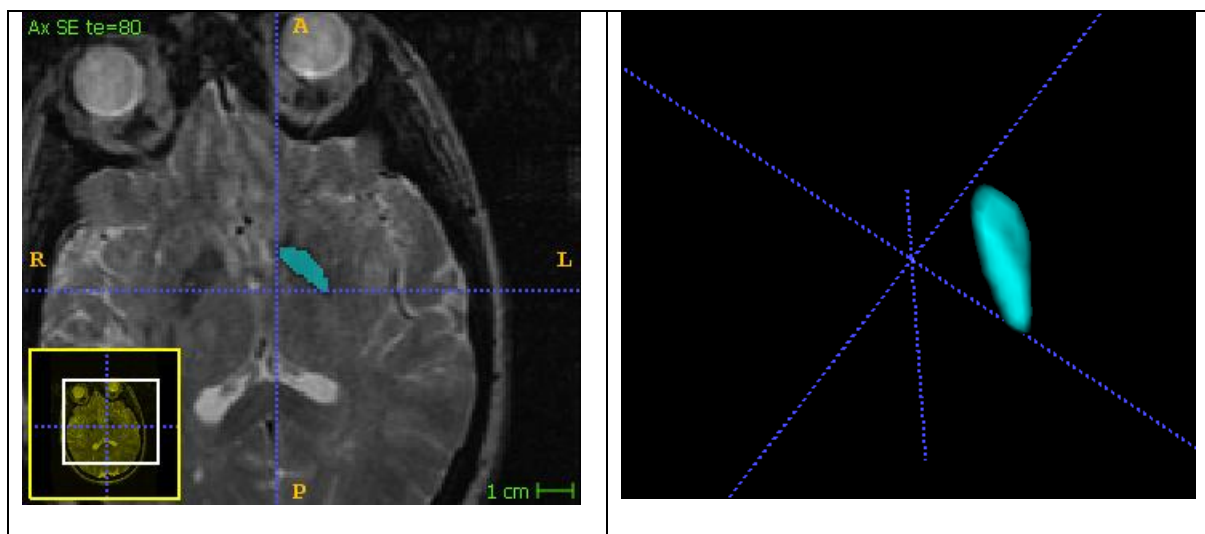
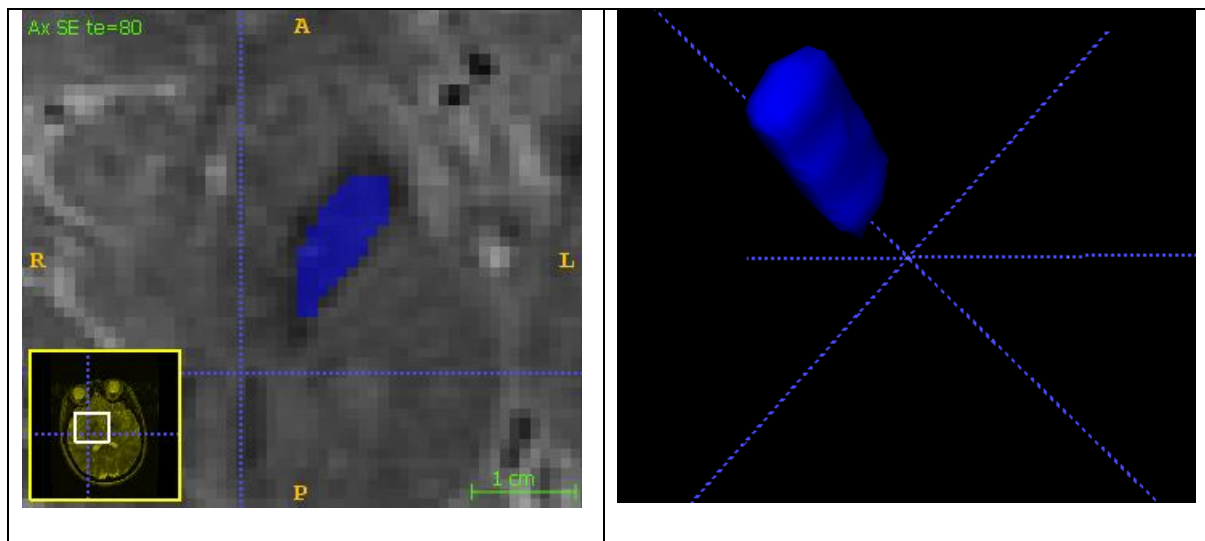




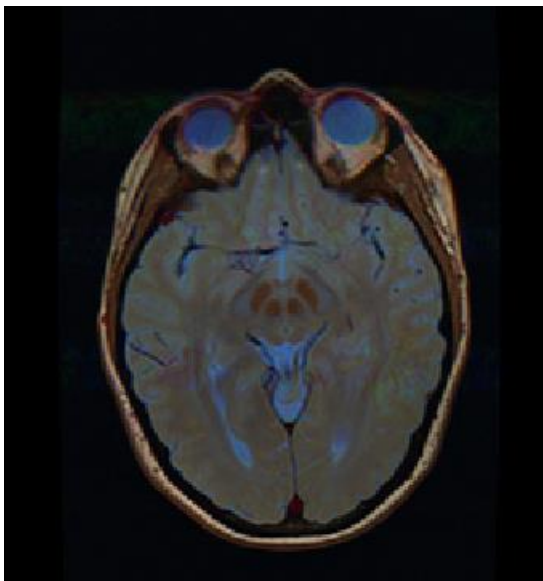
Putamen



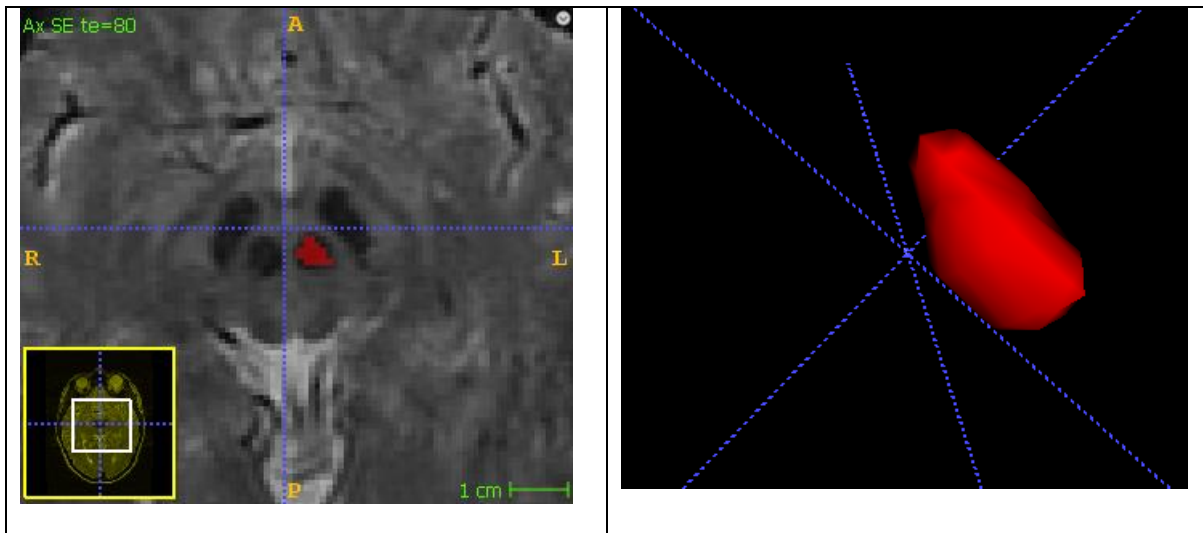
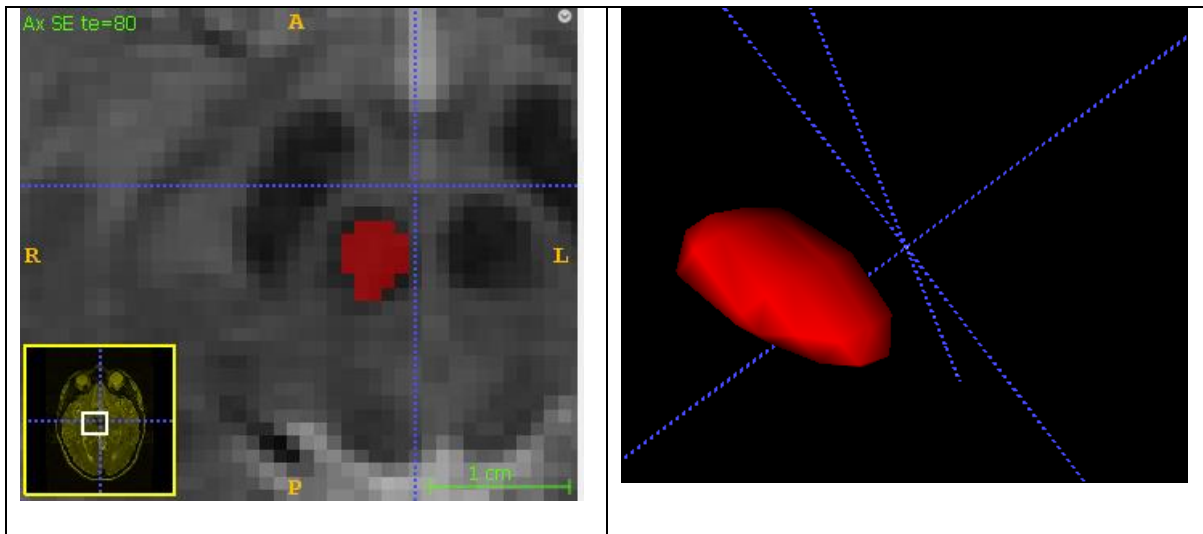
GP



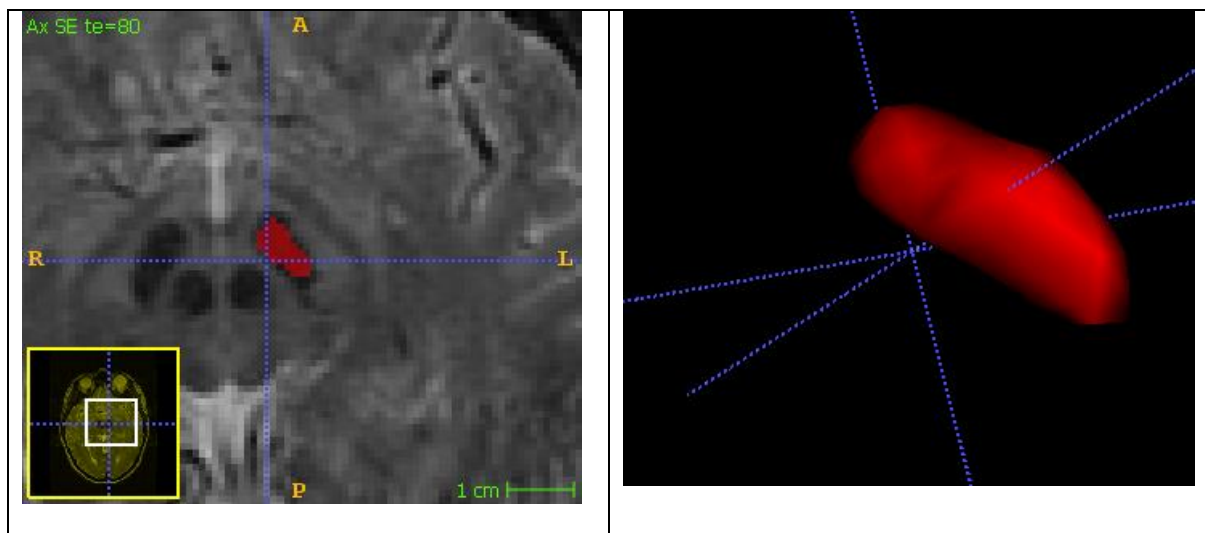
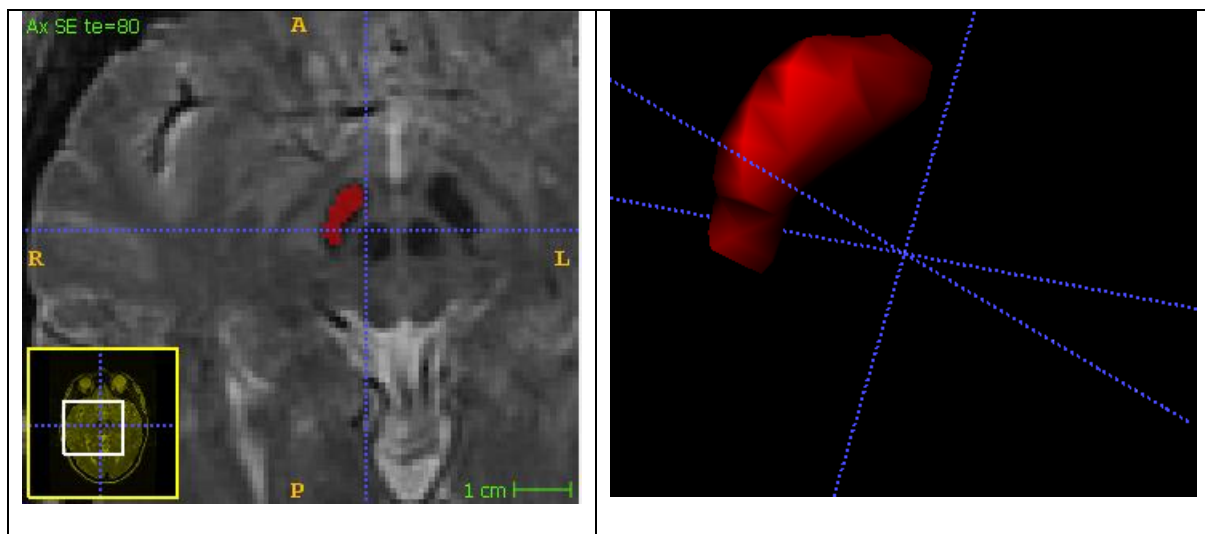
Patient 4



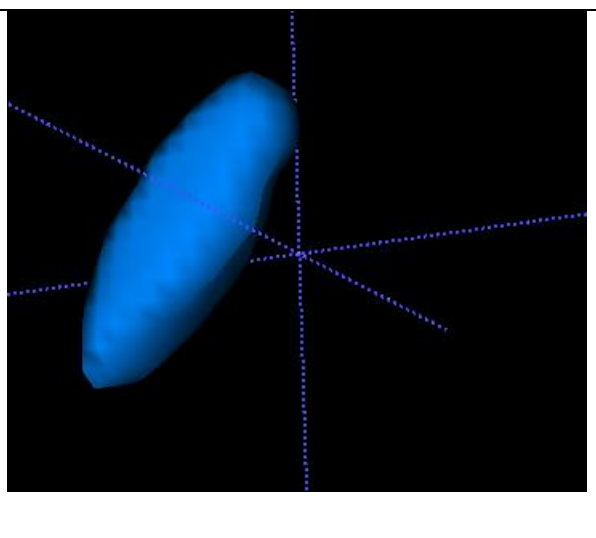
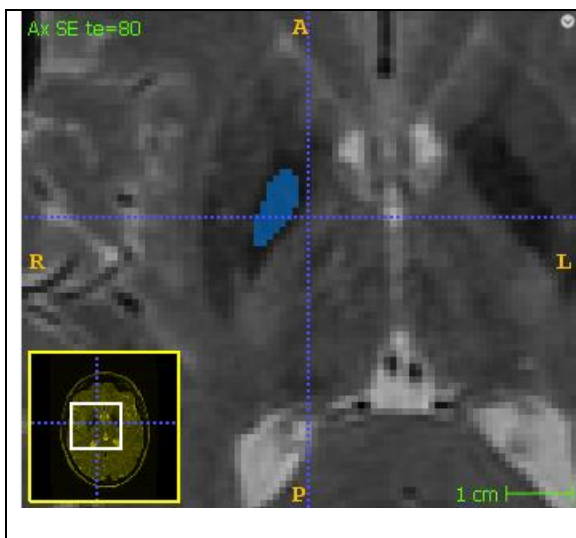
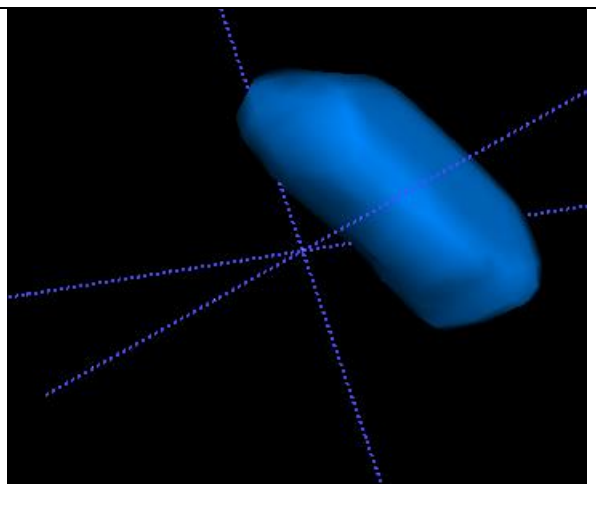
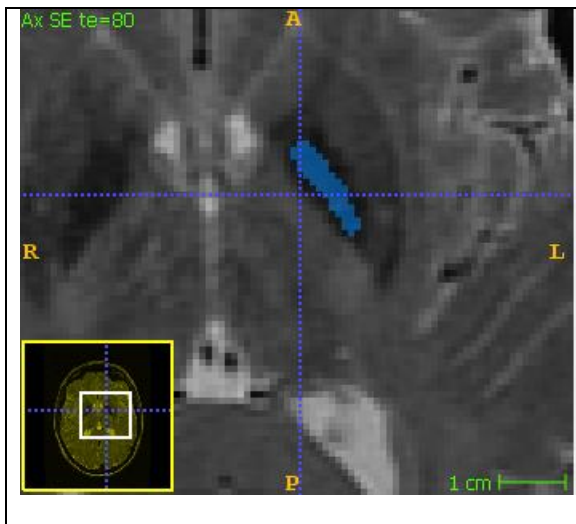
RN



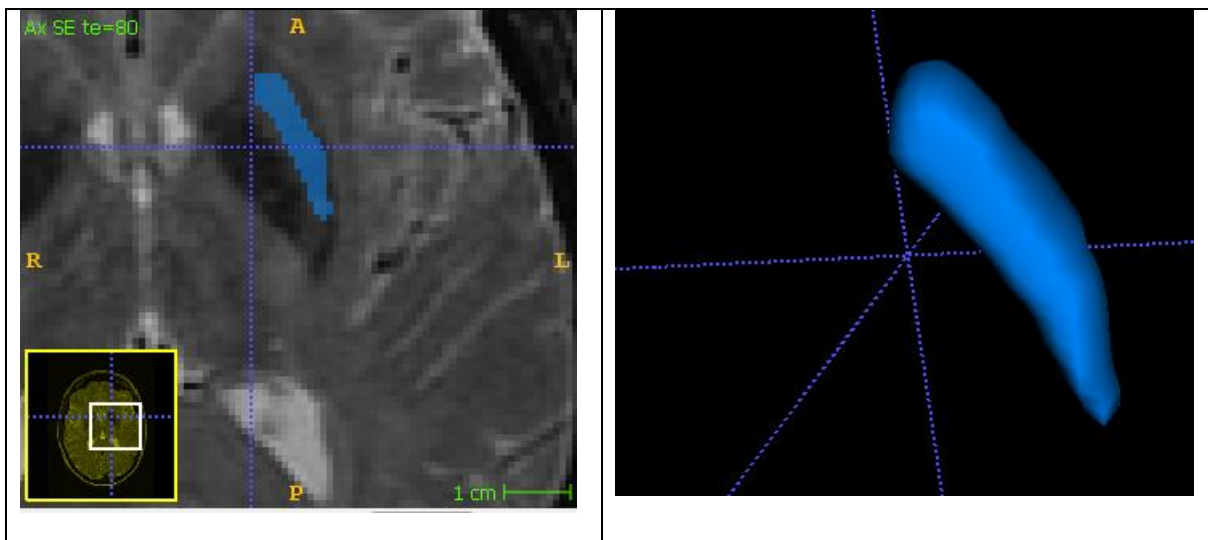
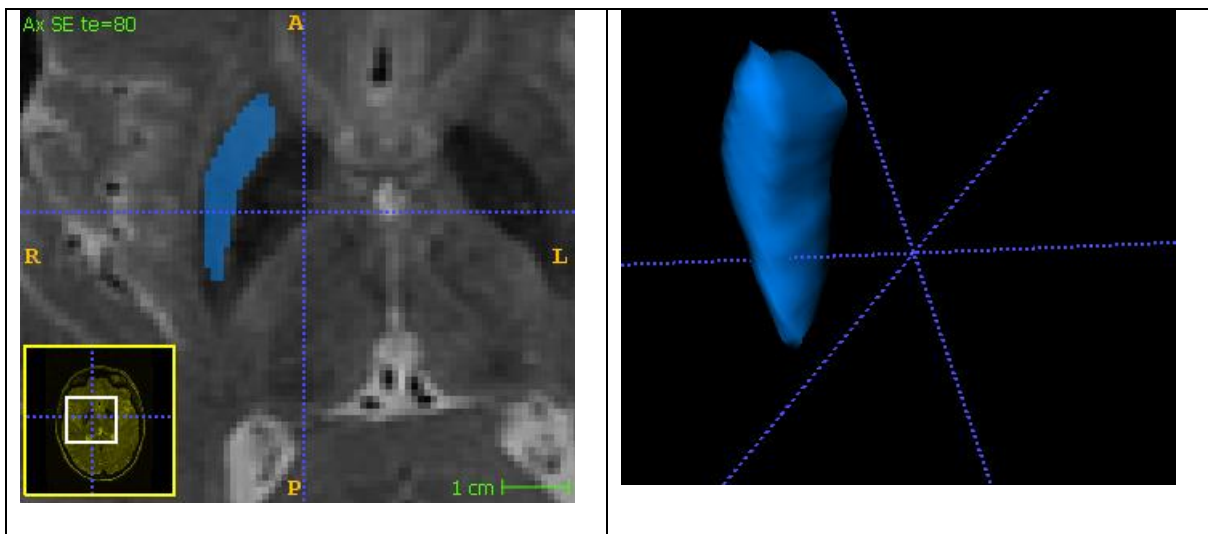
SN



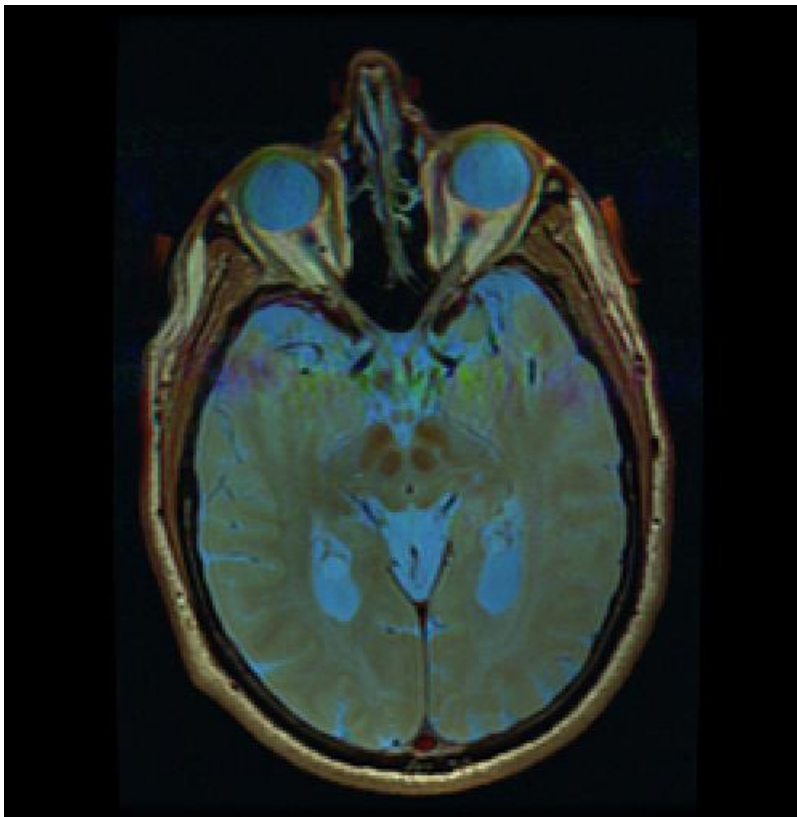
Gp



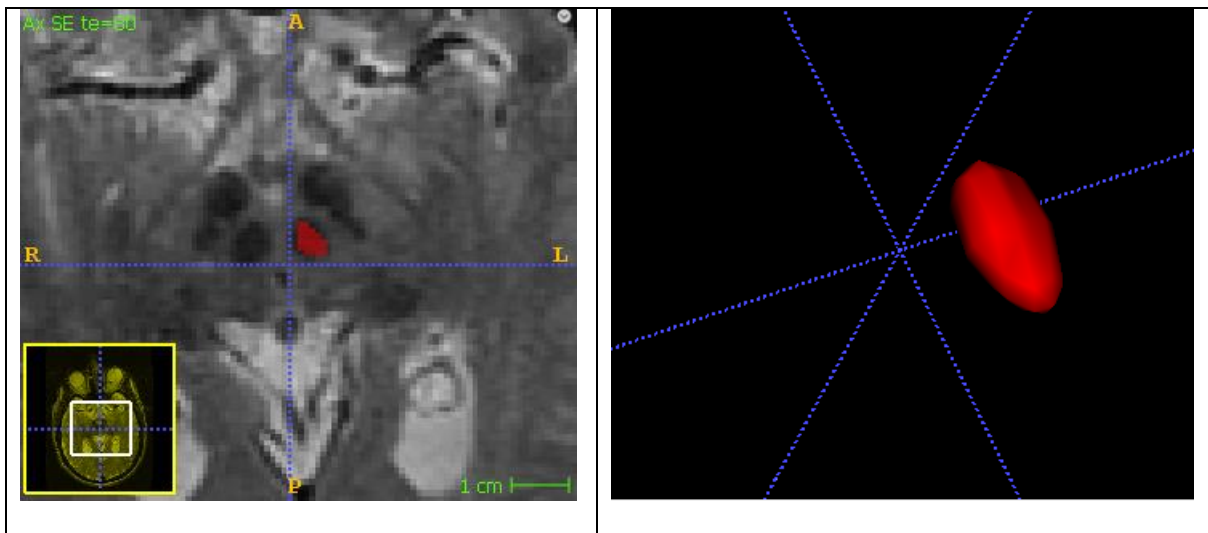
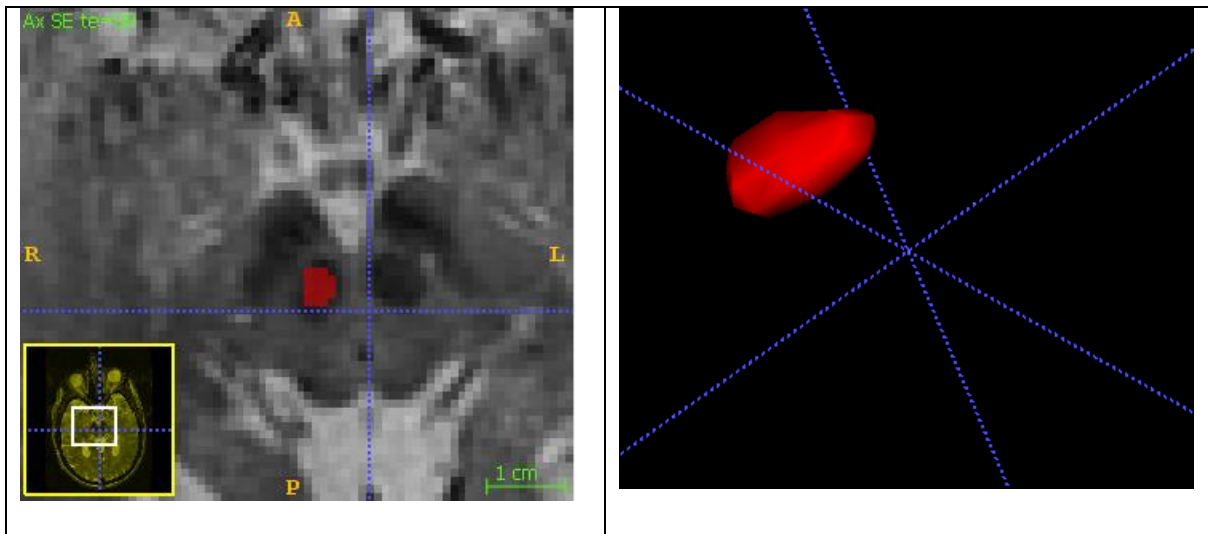
Put



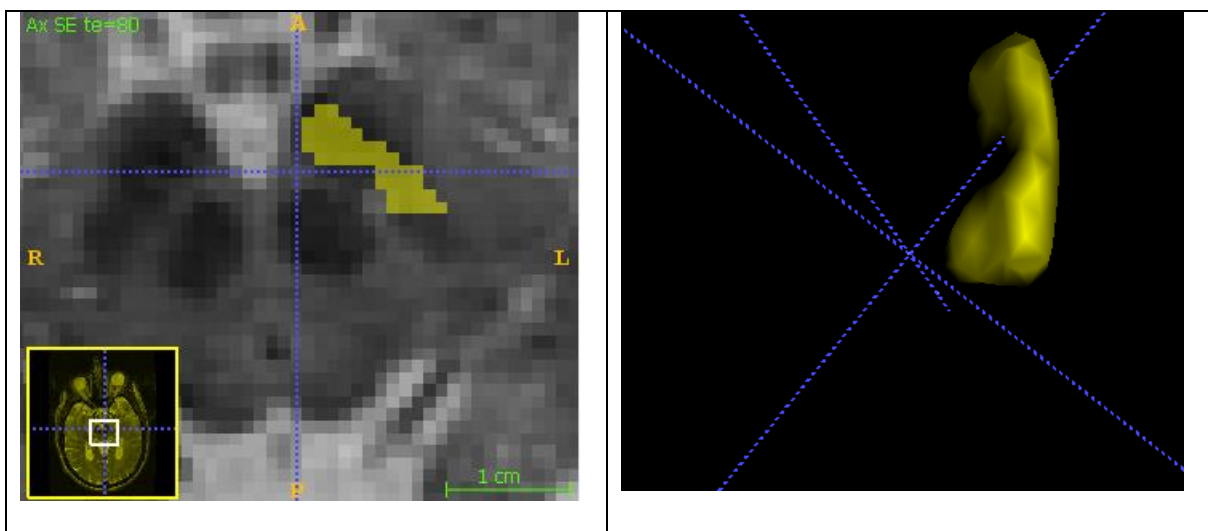
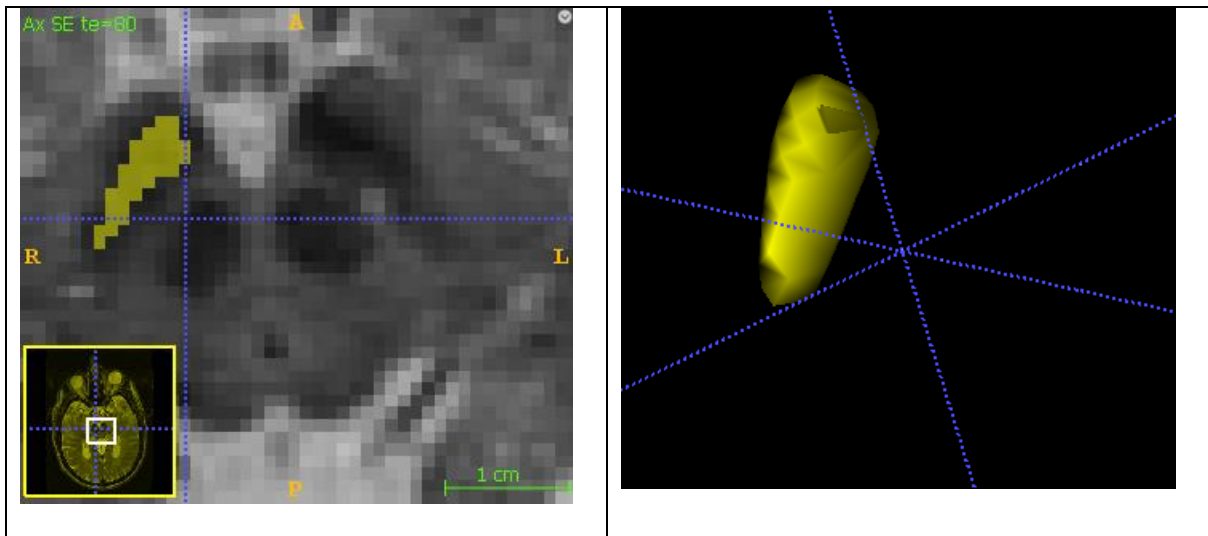
Patient 5



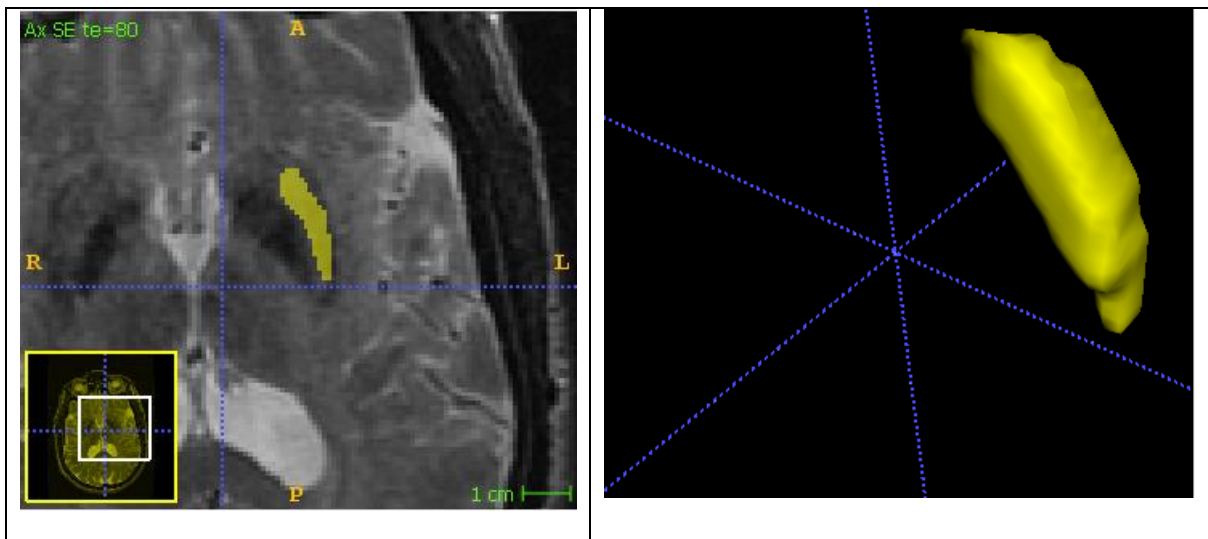
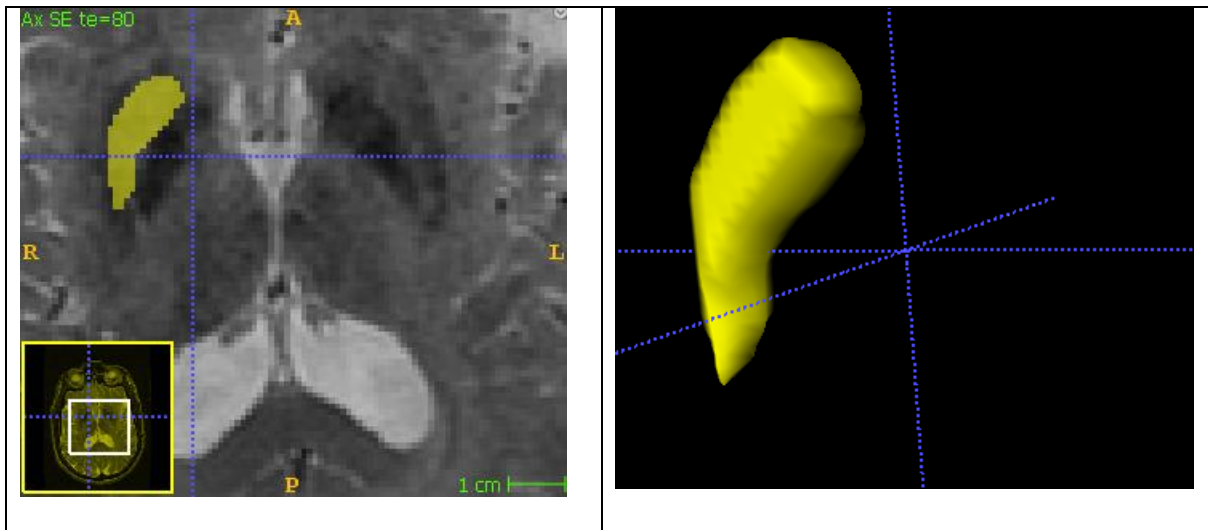
Rn



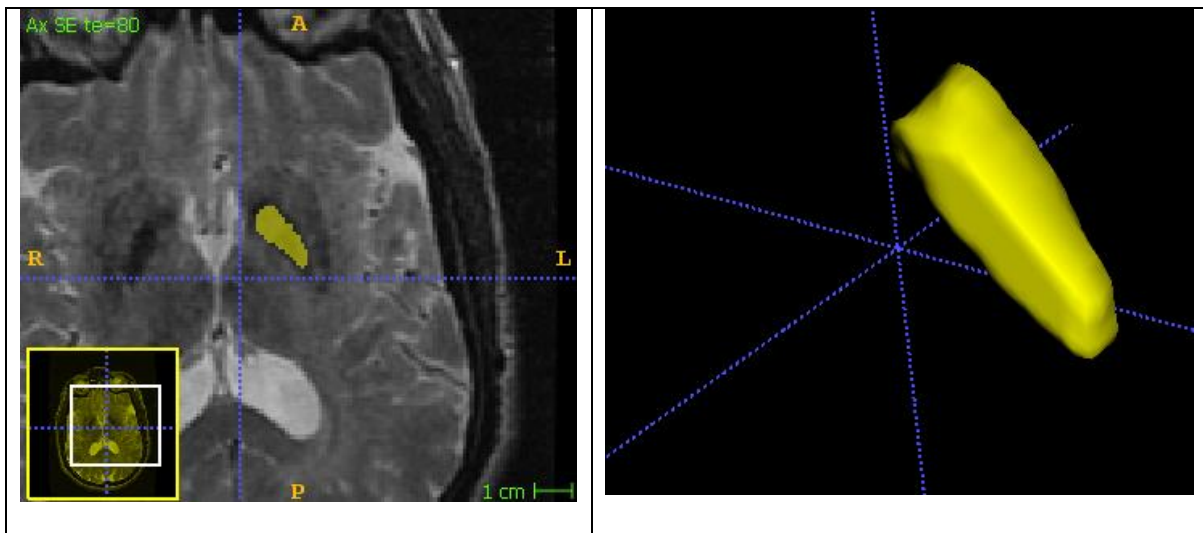
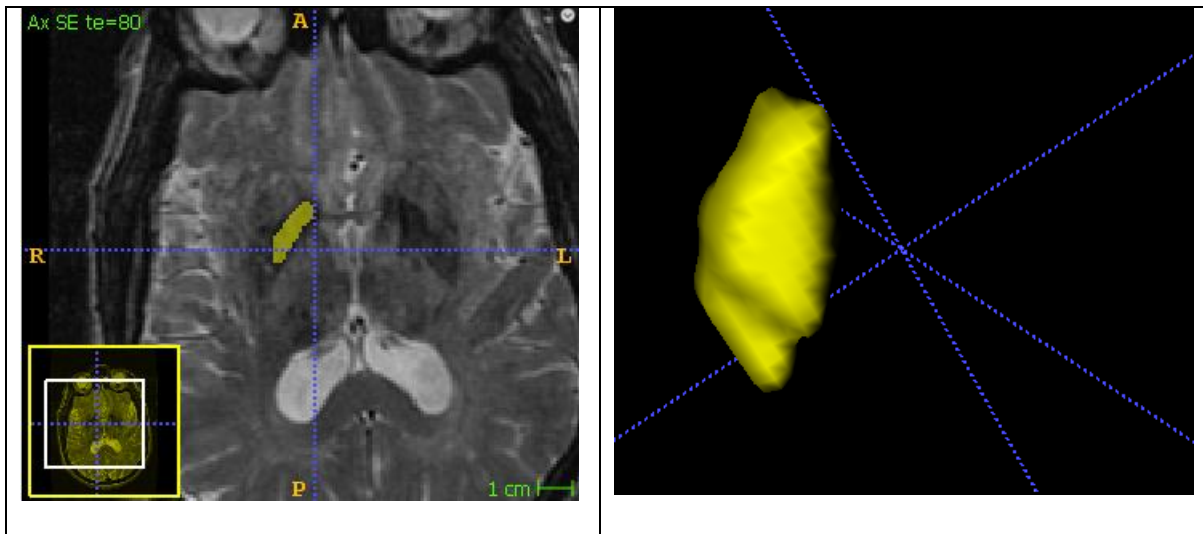
Sn



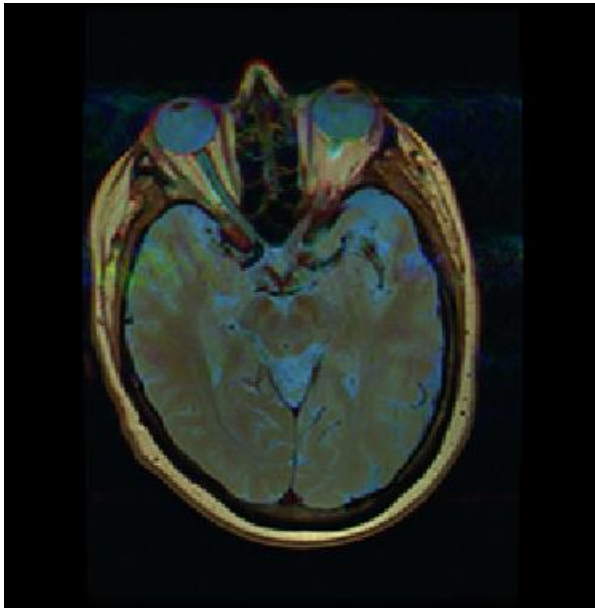
Put



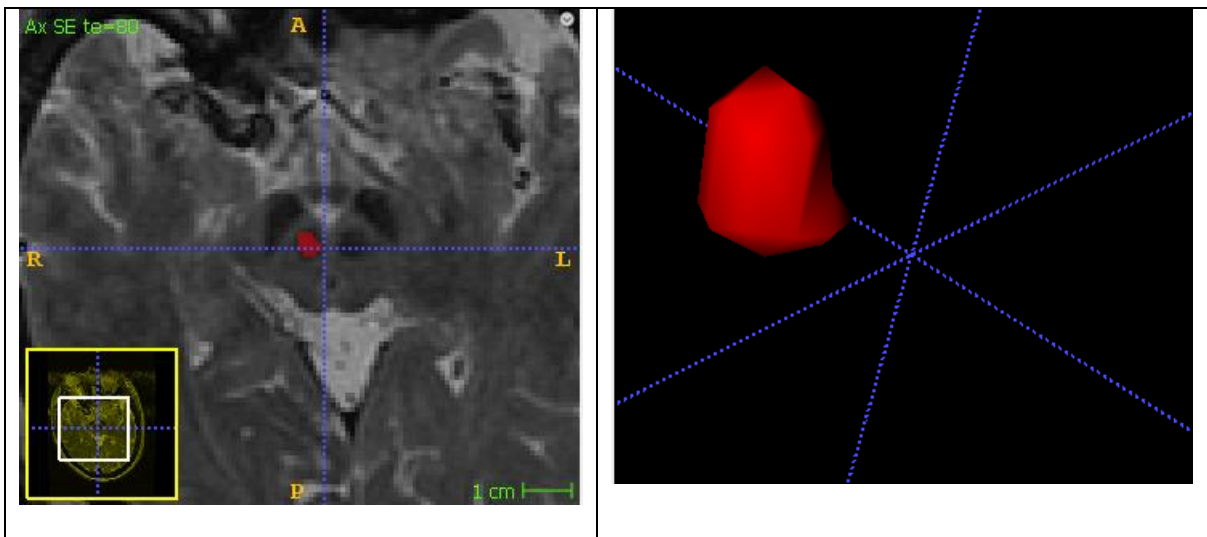
Gp

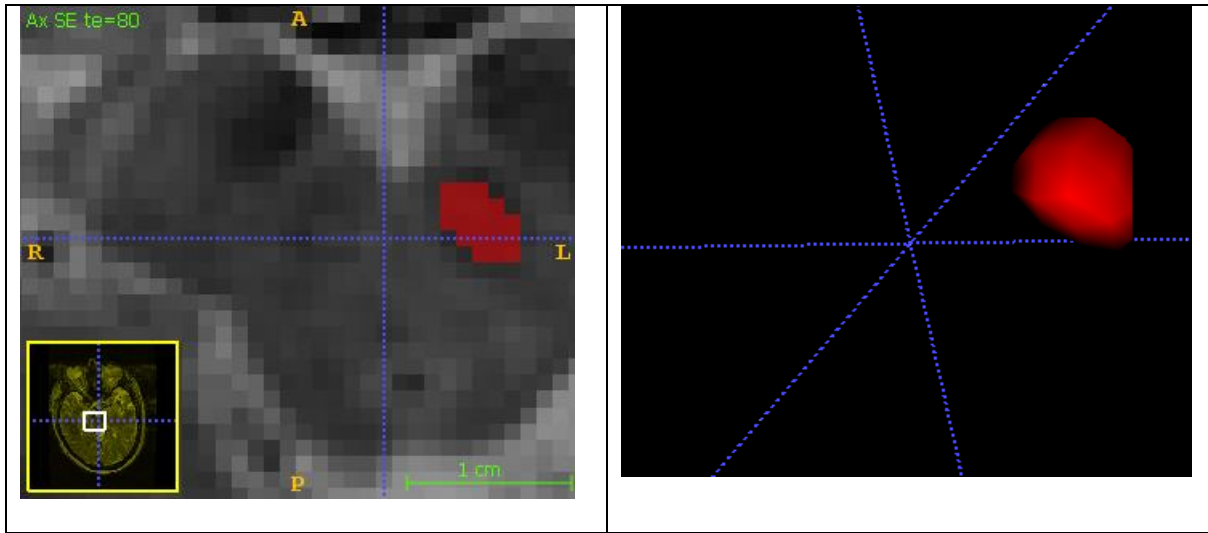


Patient 7

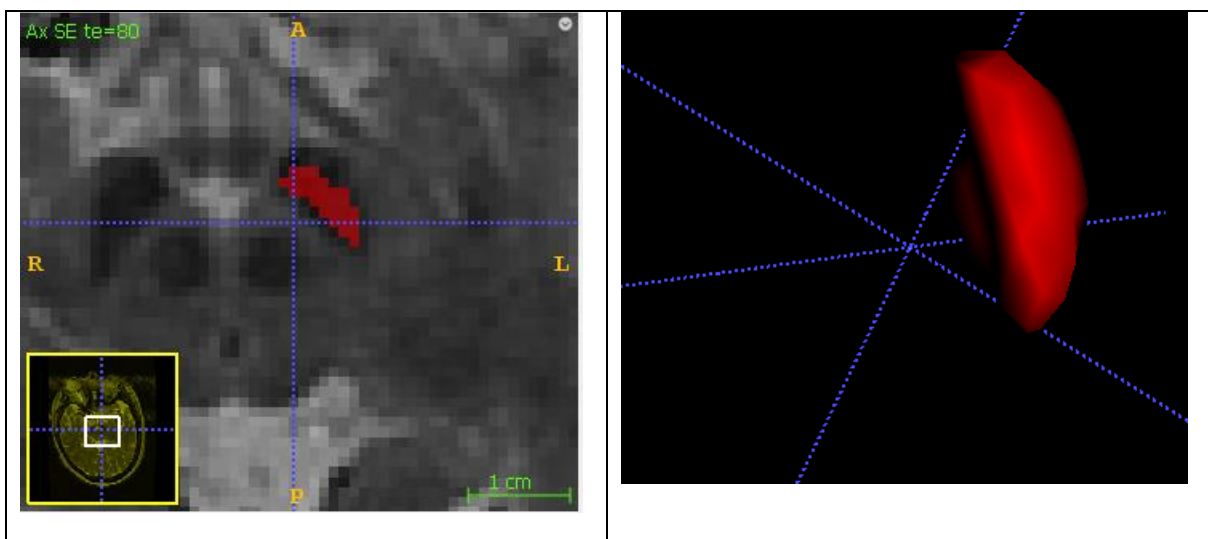
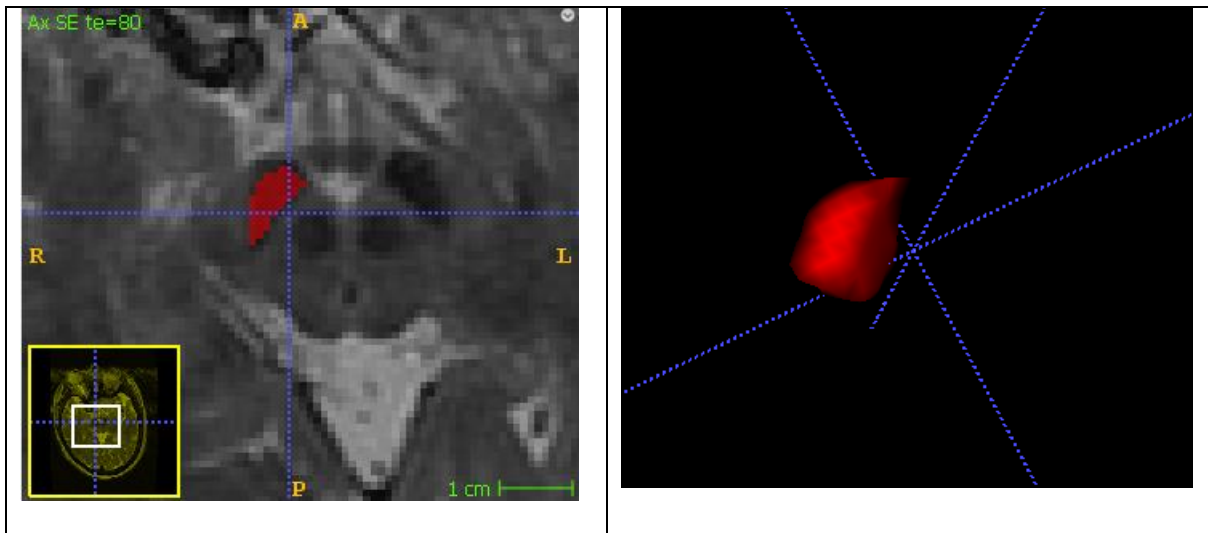


RN

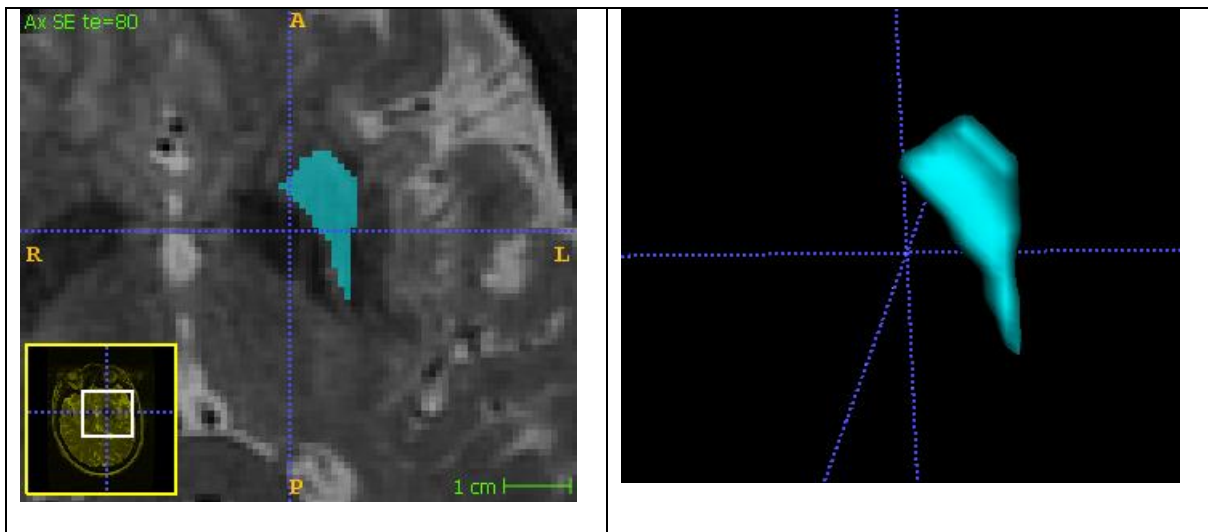
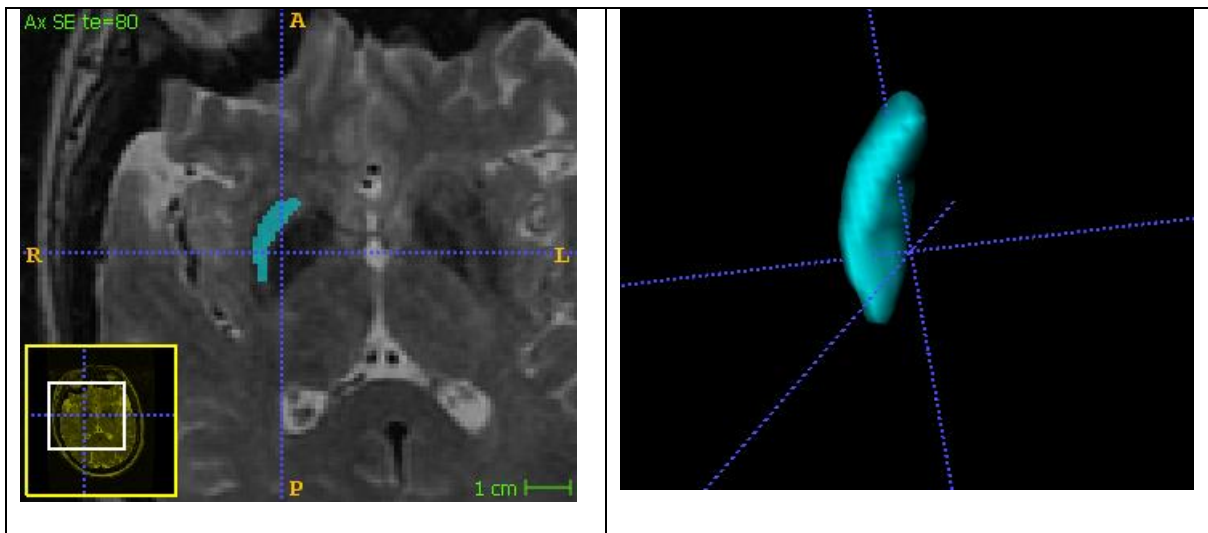




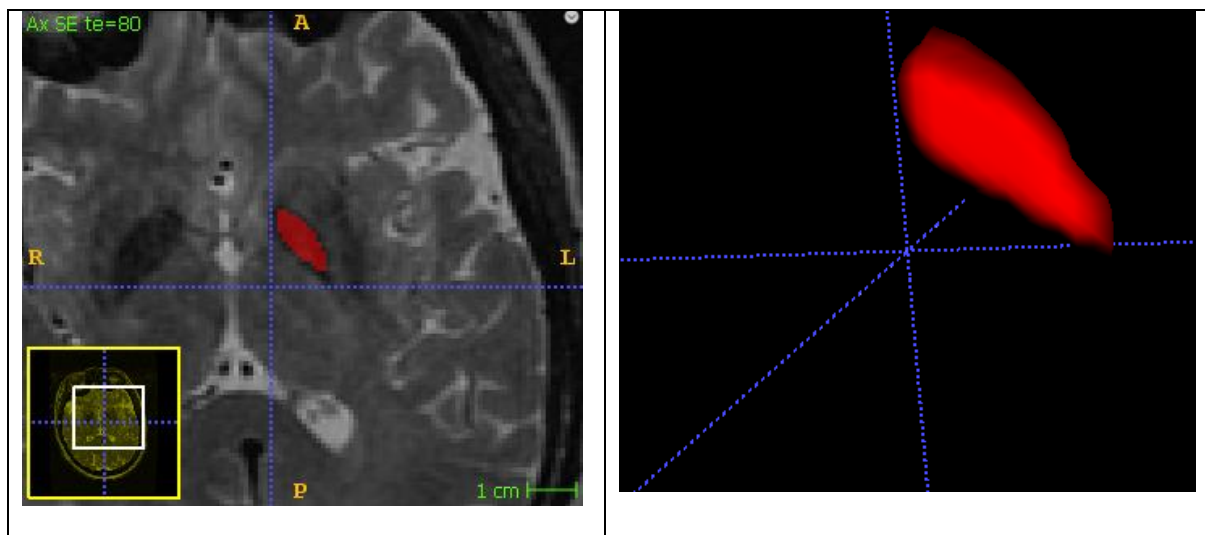
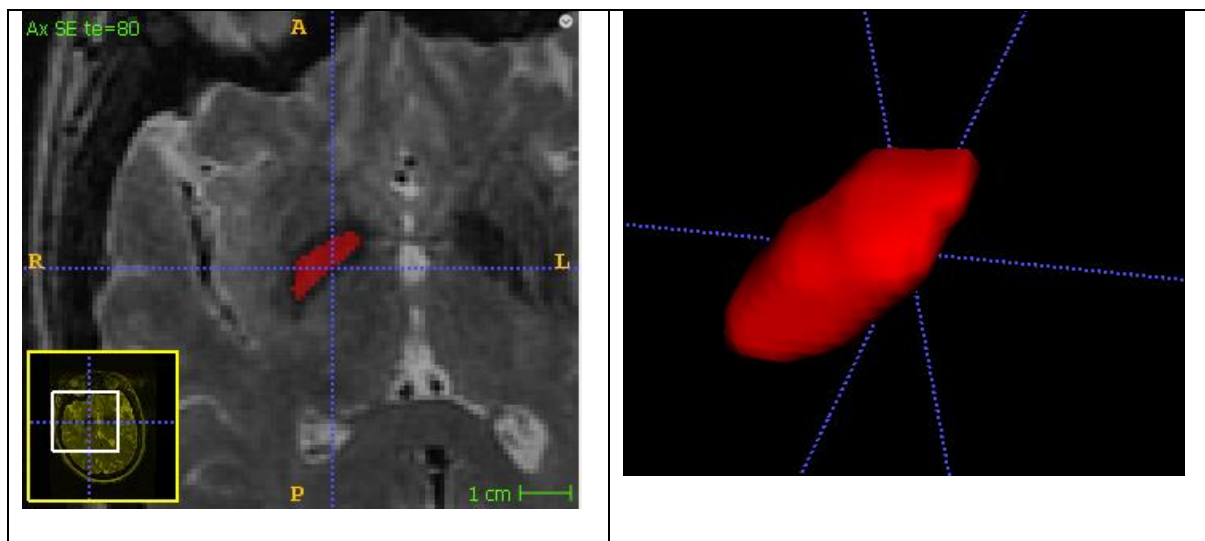
SN



PUT

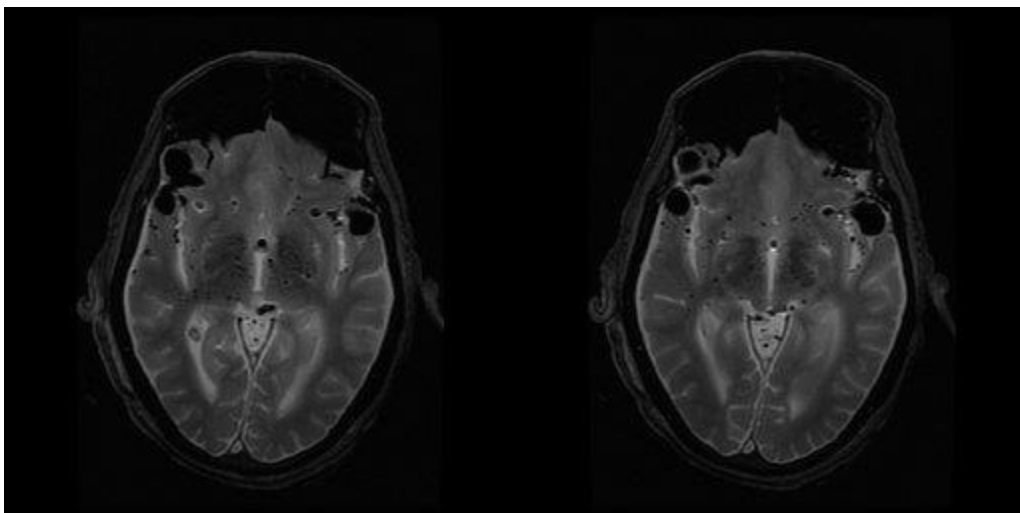
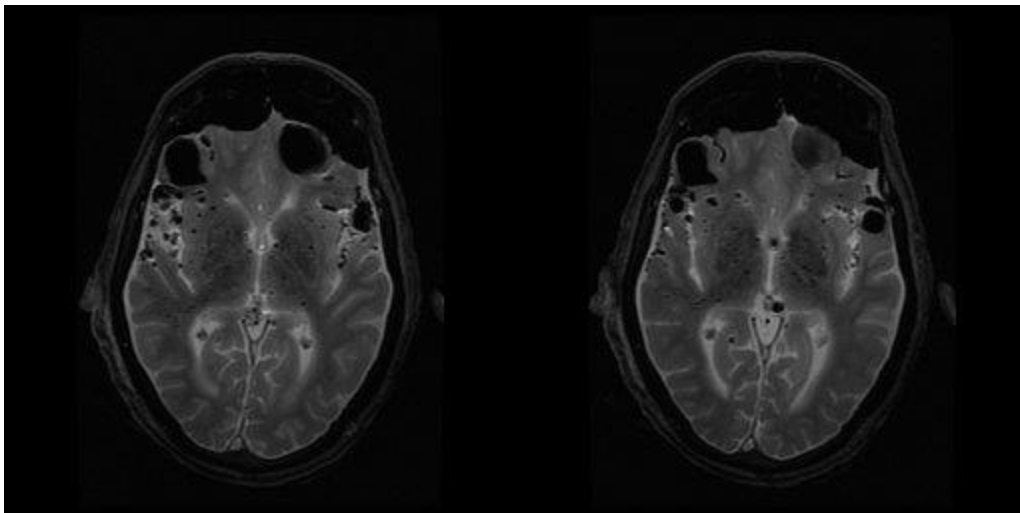
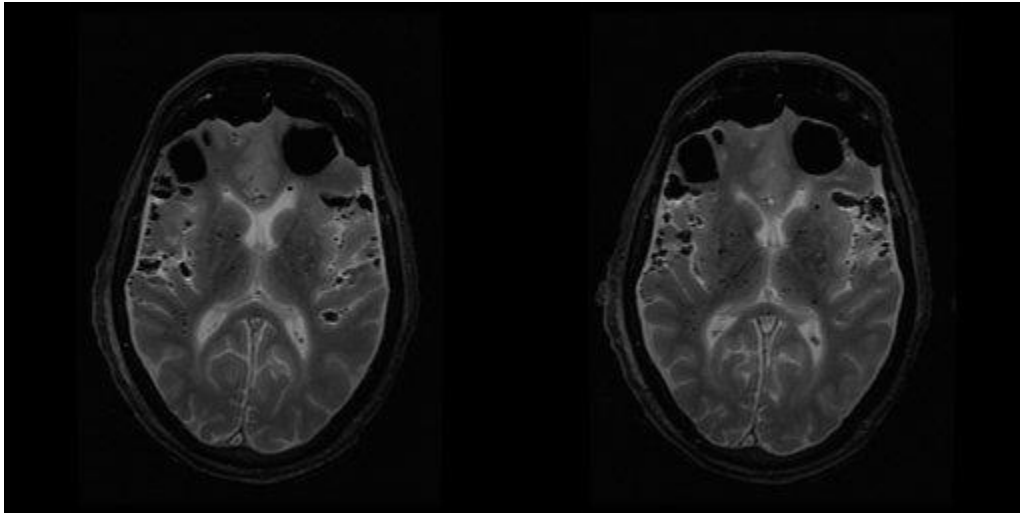


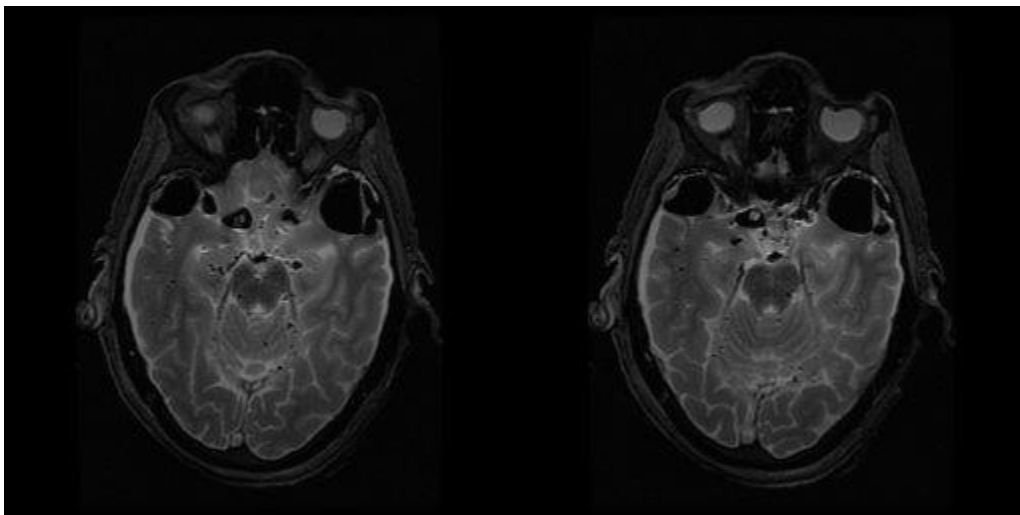
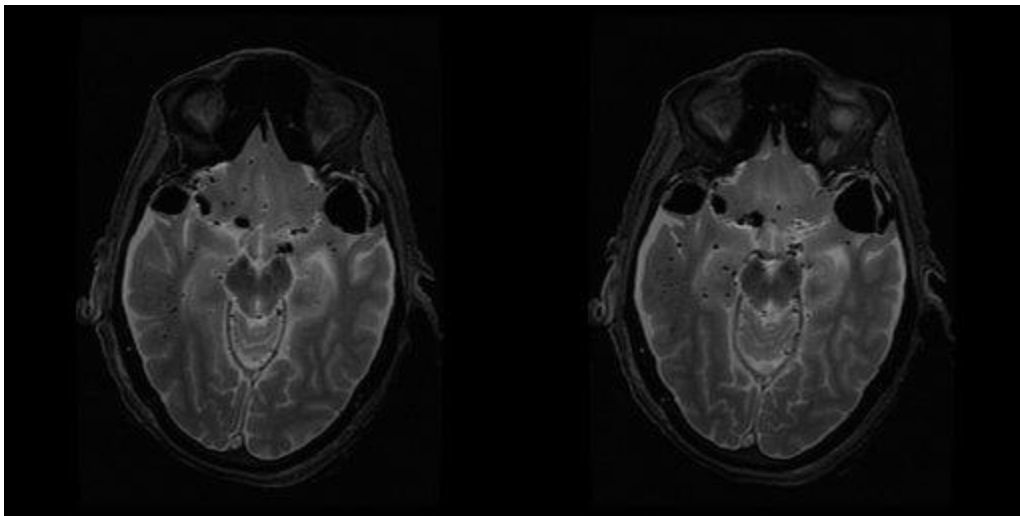
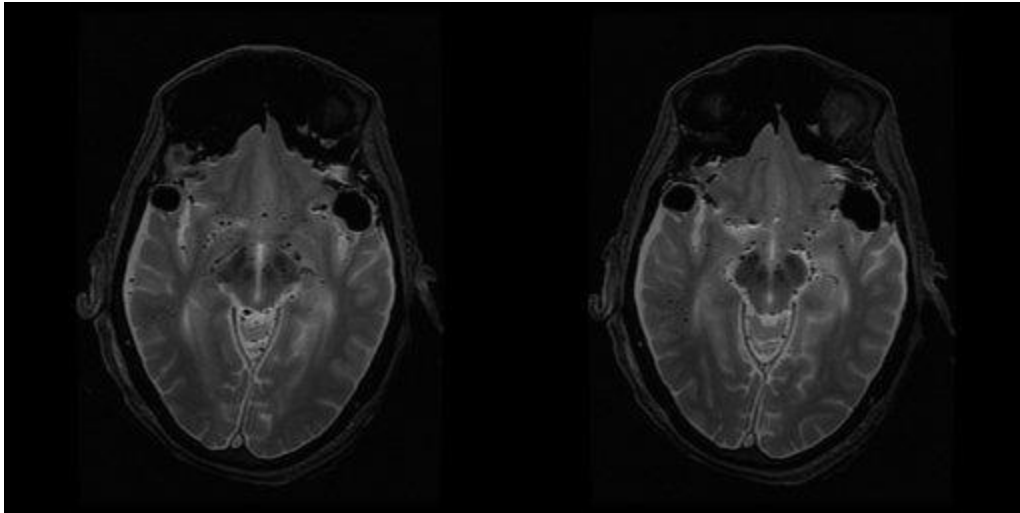
GP

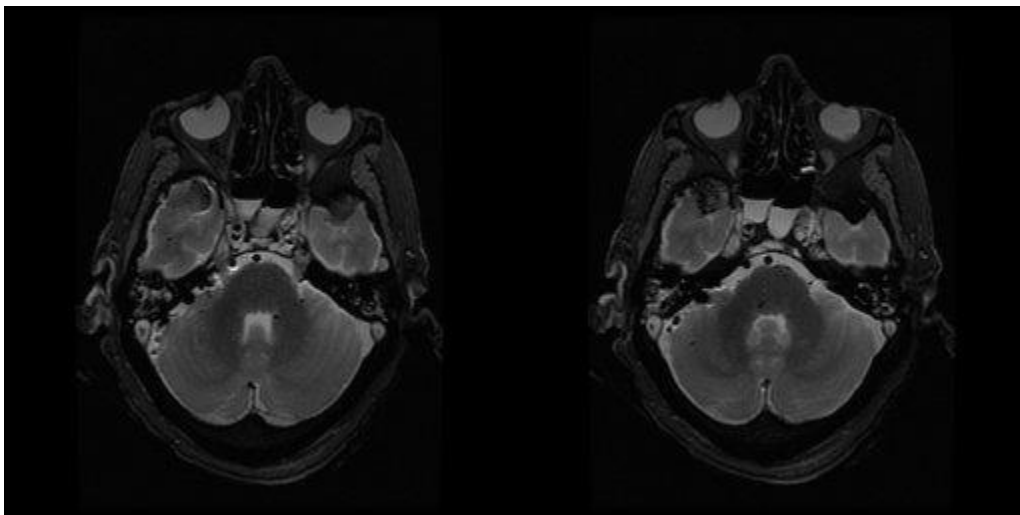
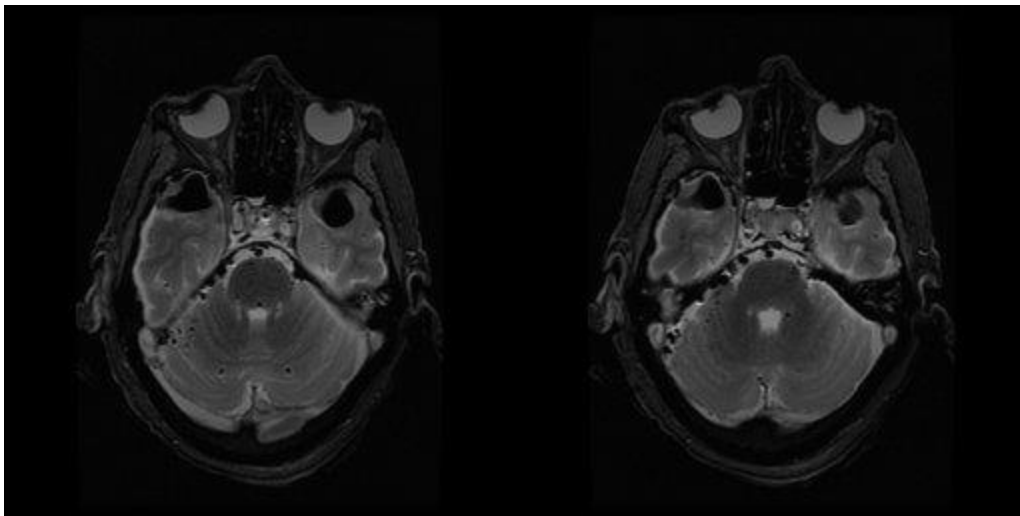
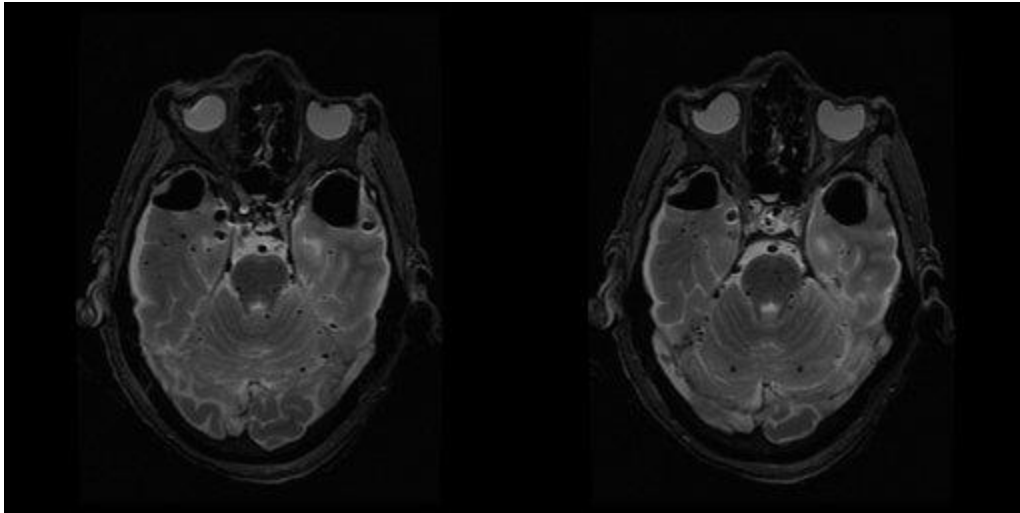


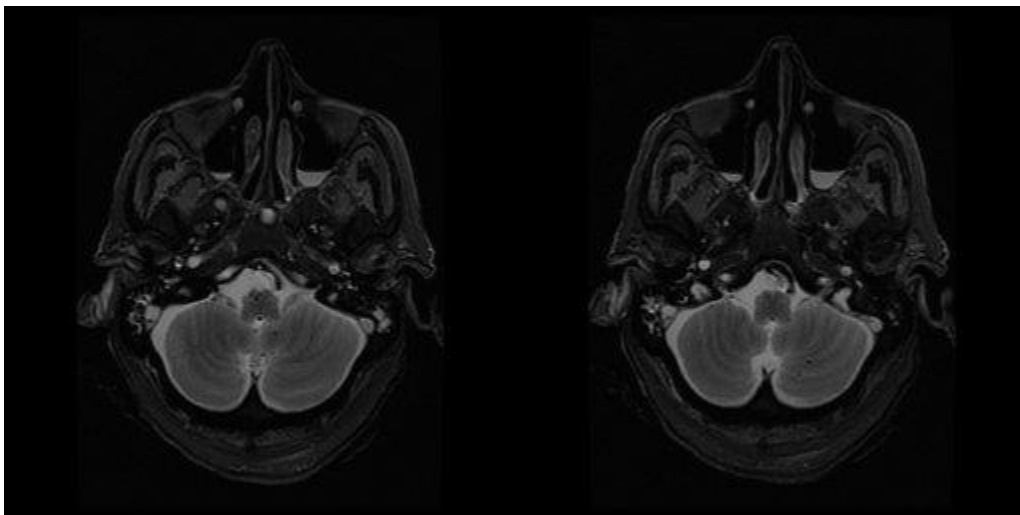
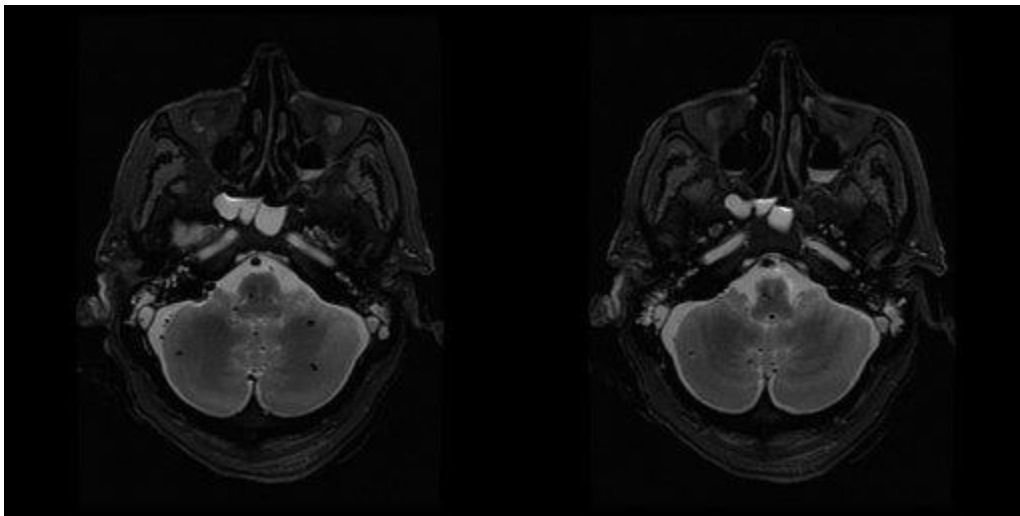
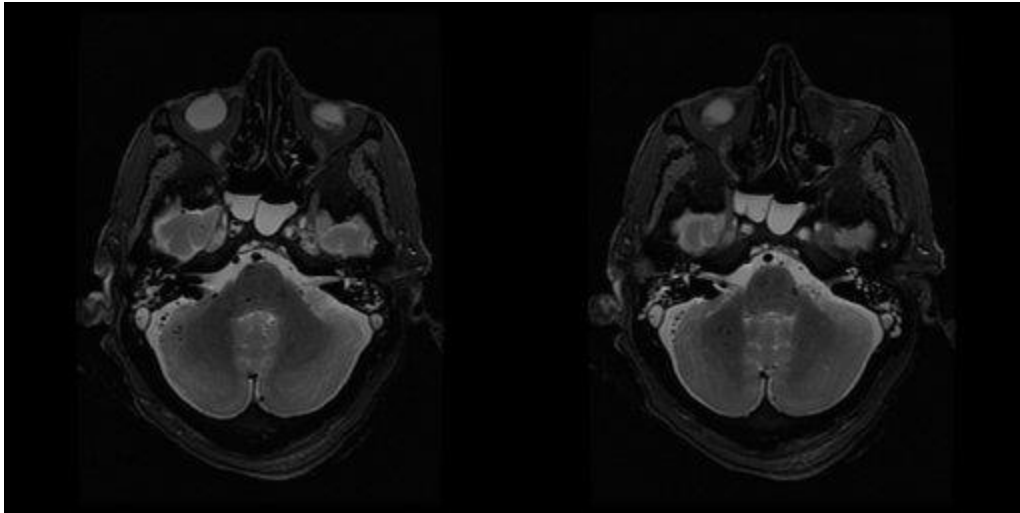
Appendix 5

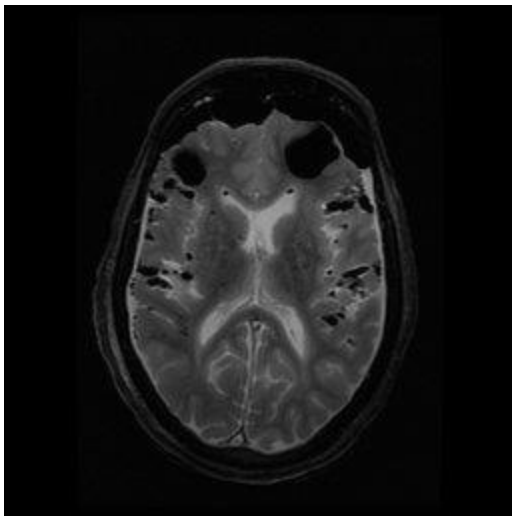
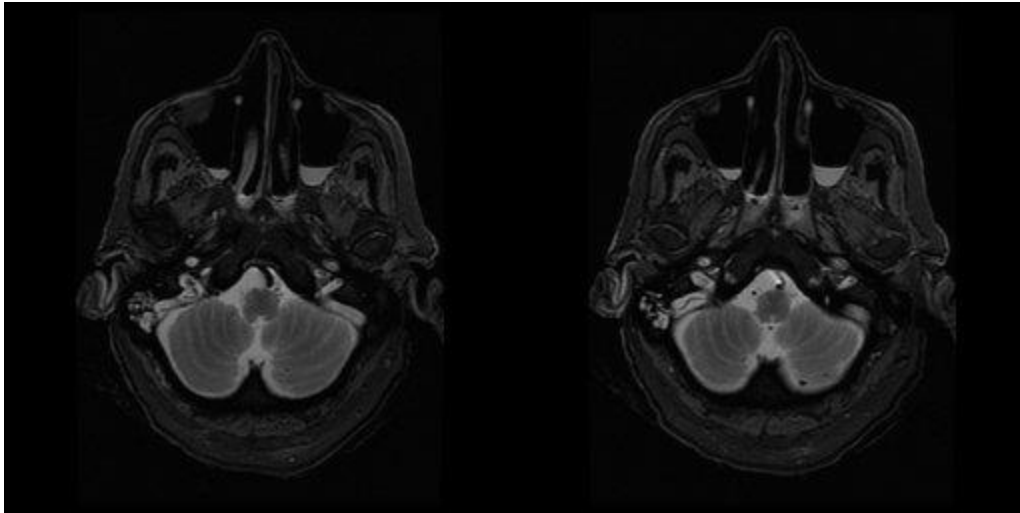
5.1 Patient A



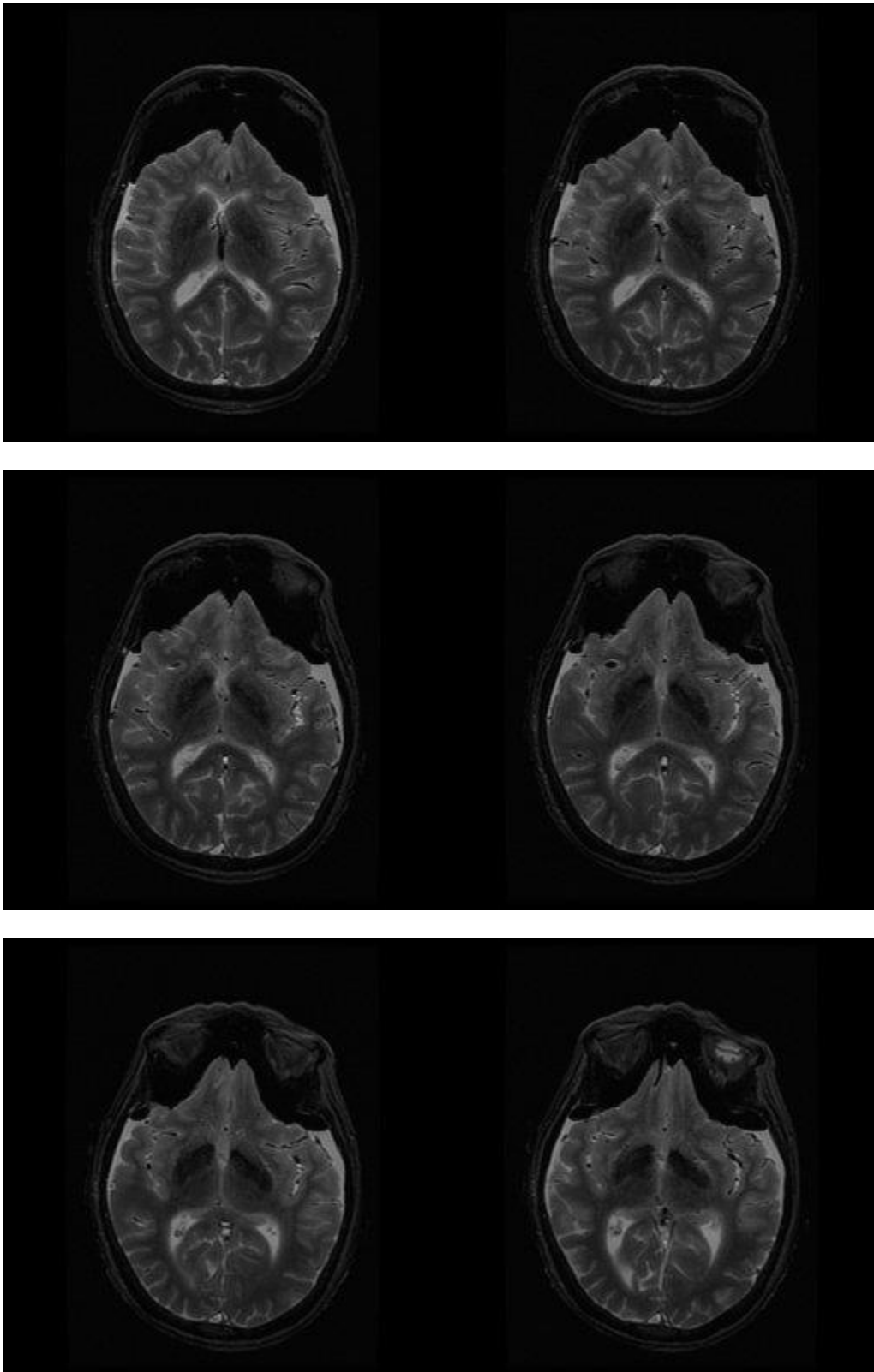


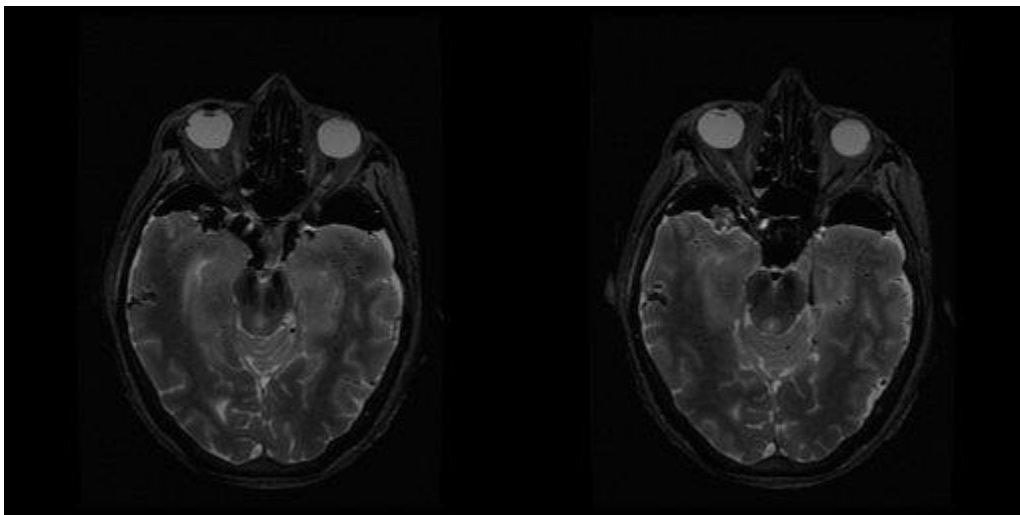
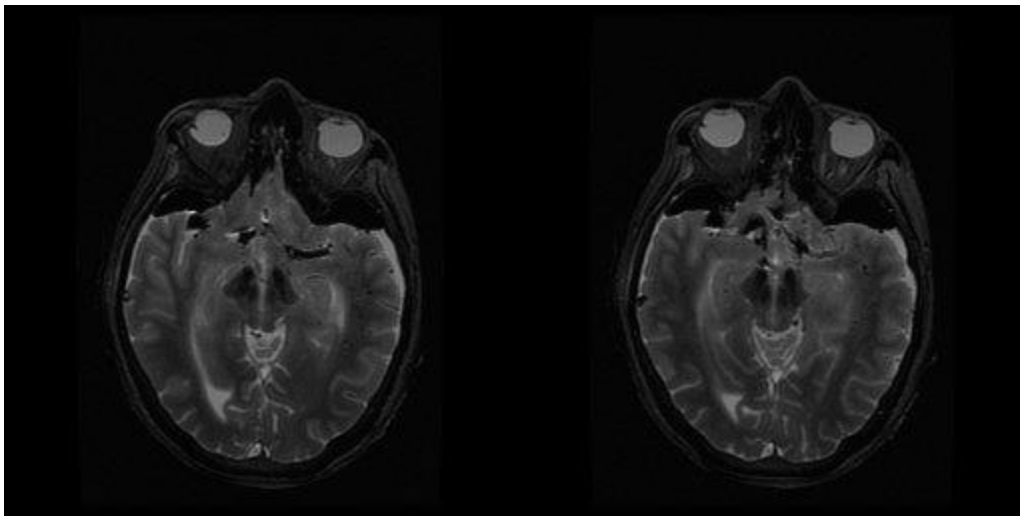
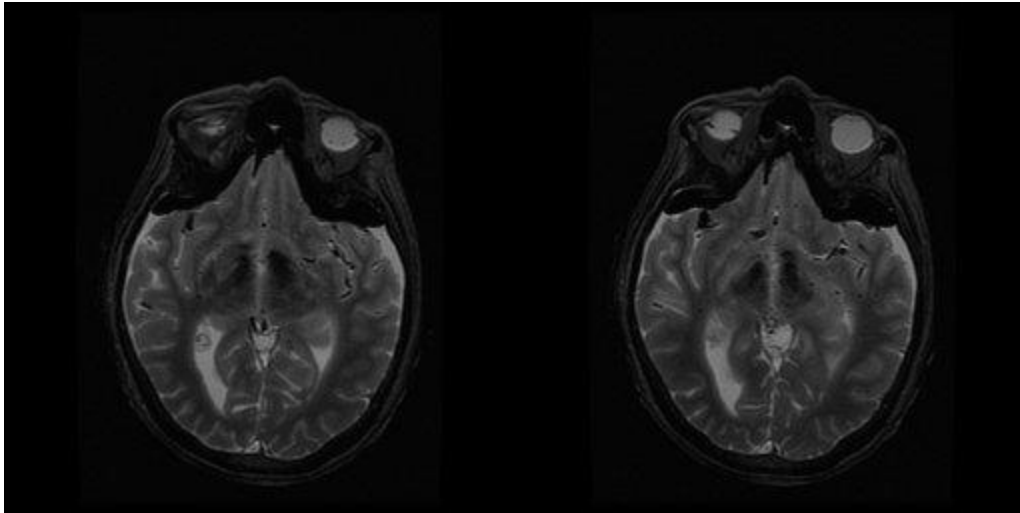


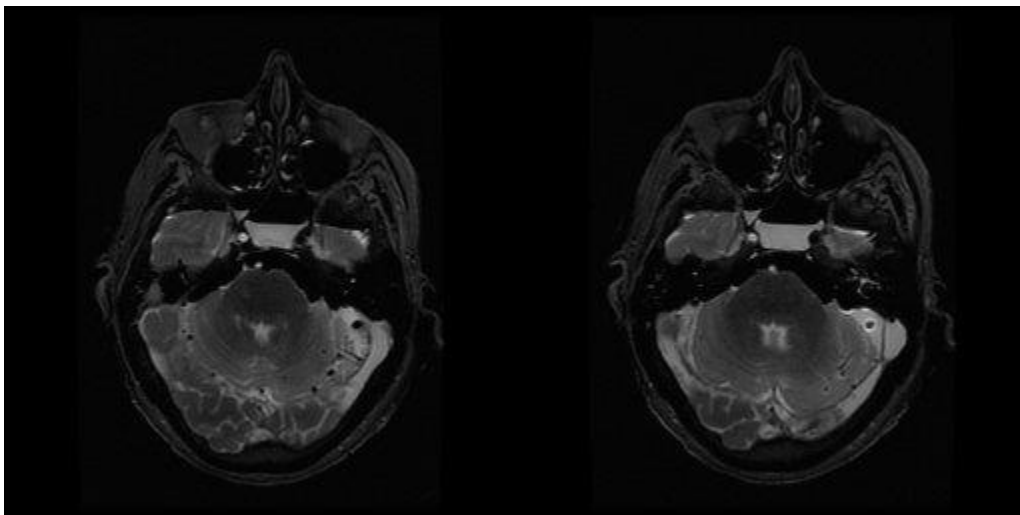
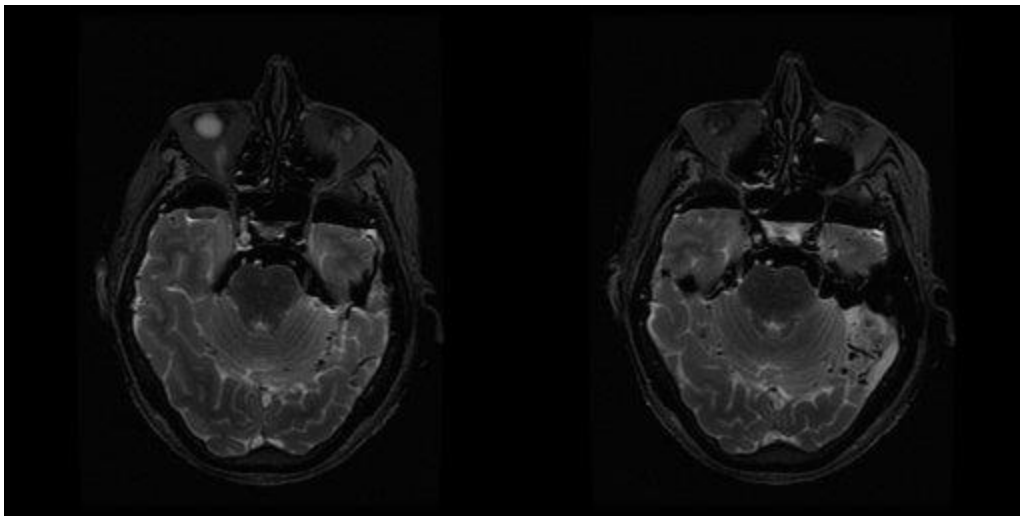
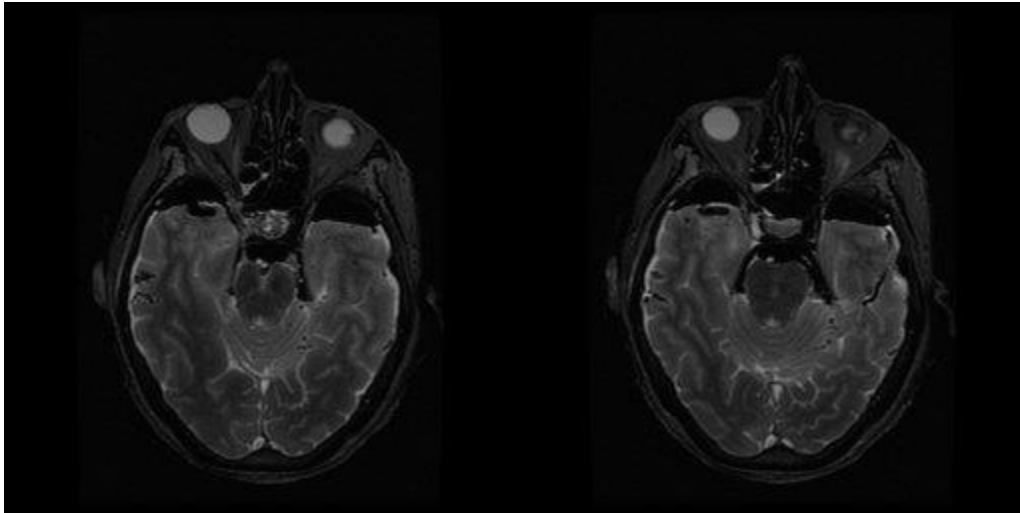


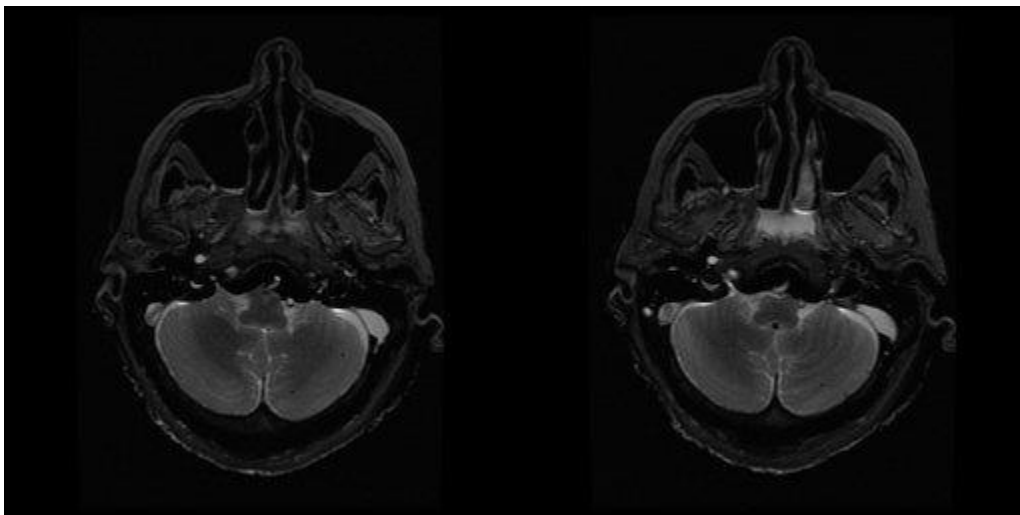
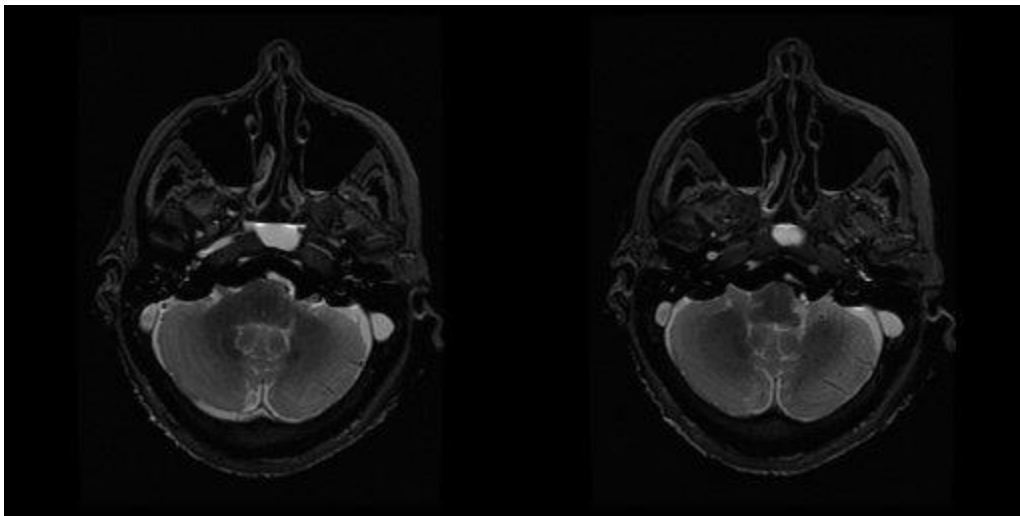
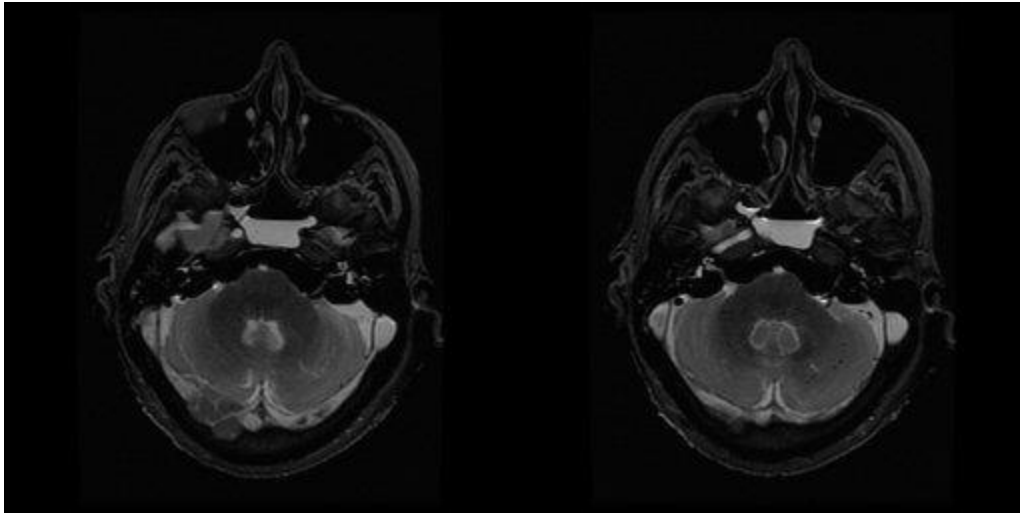


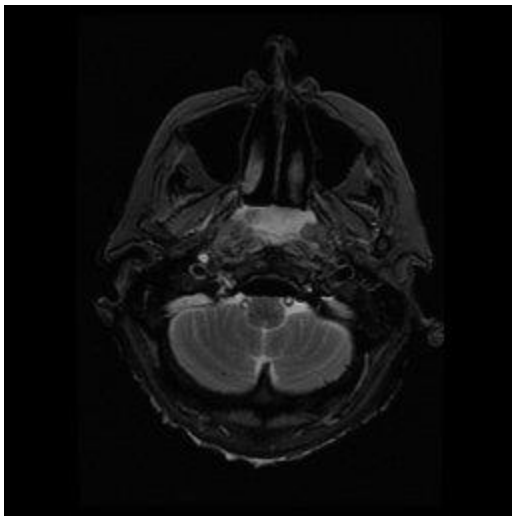
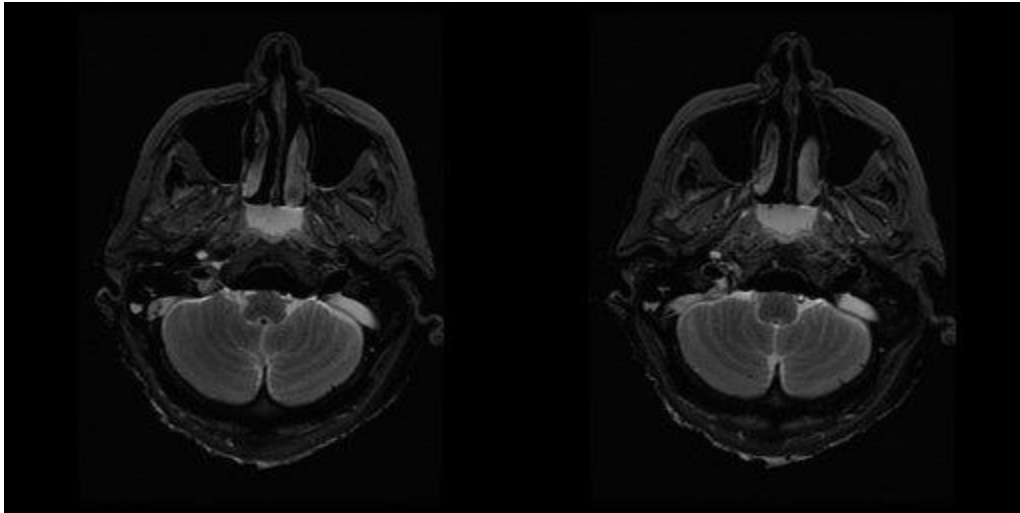
5.2 Patient B



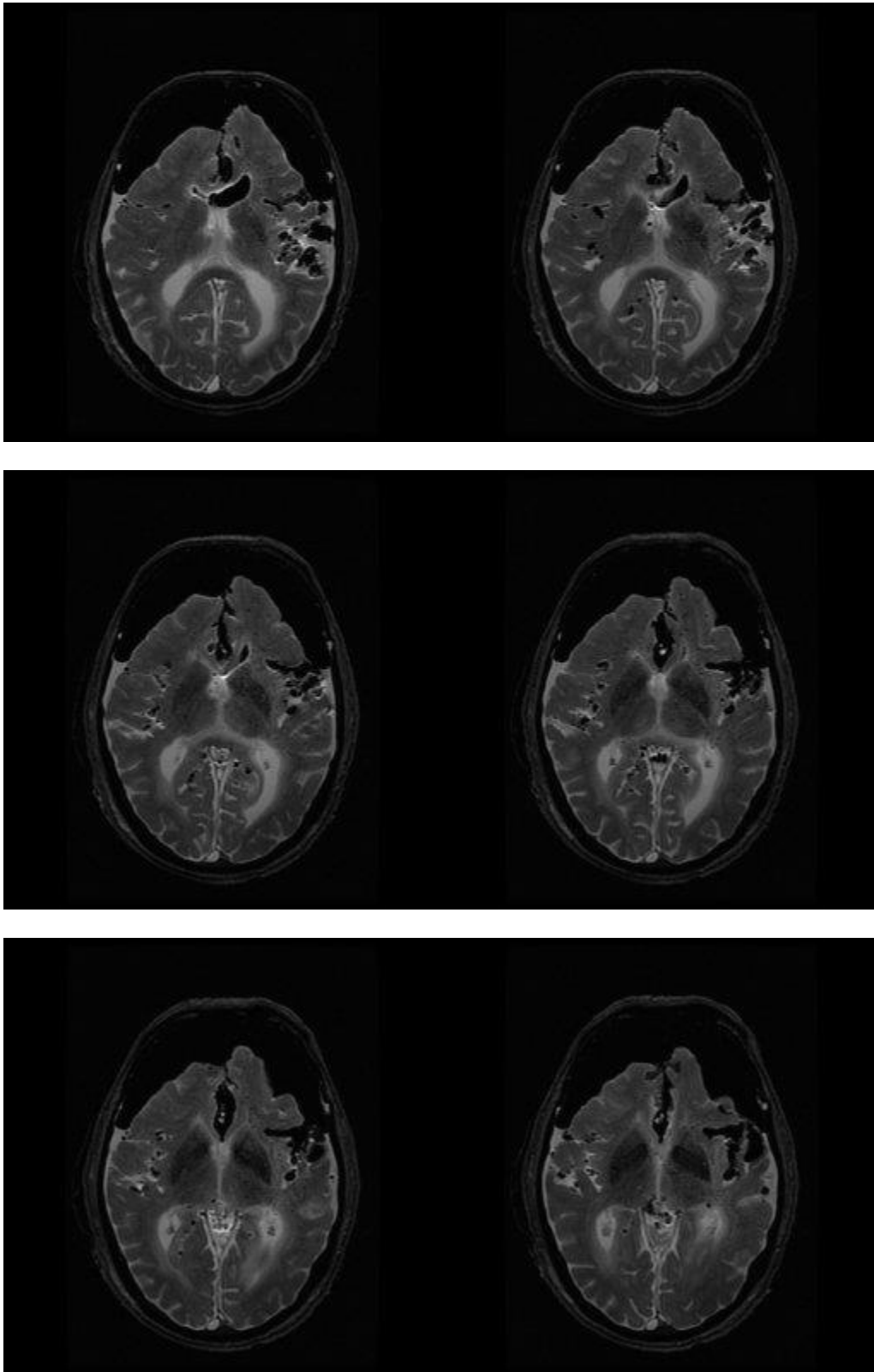


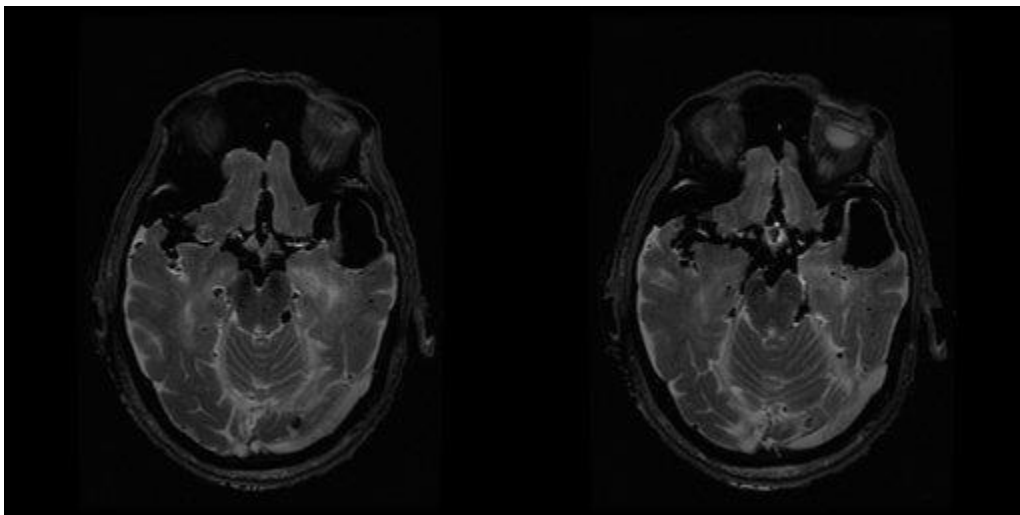
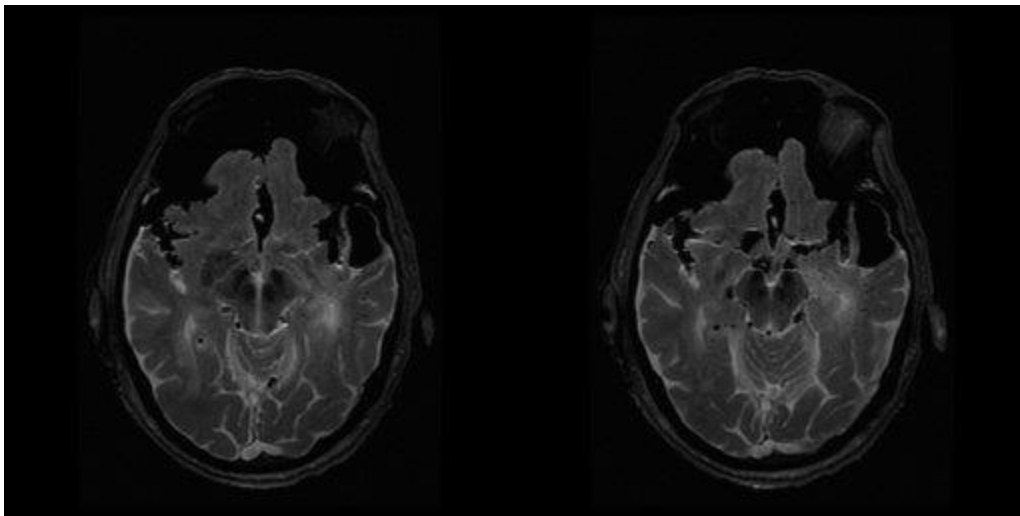
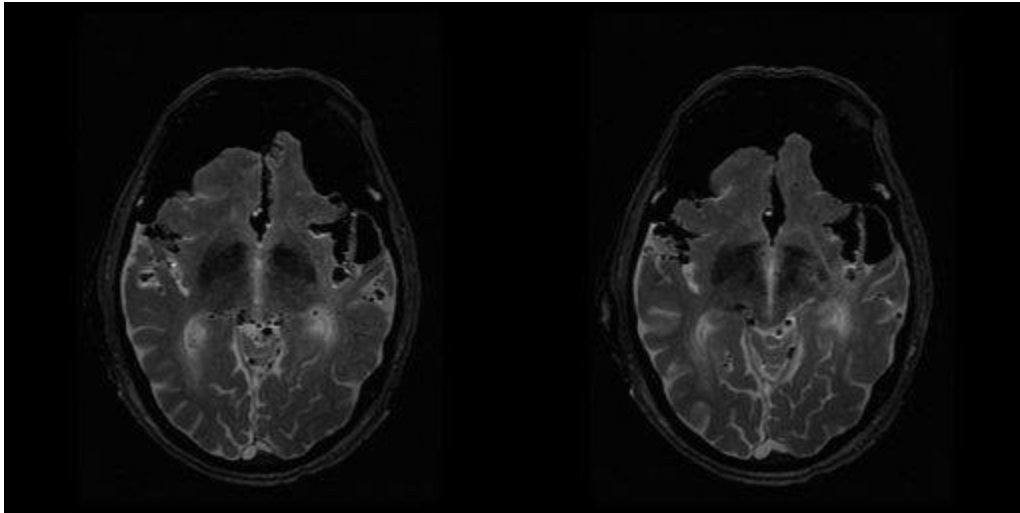


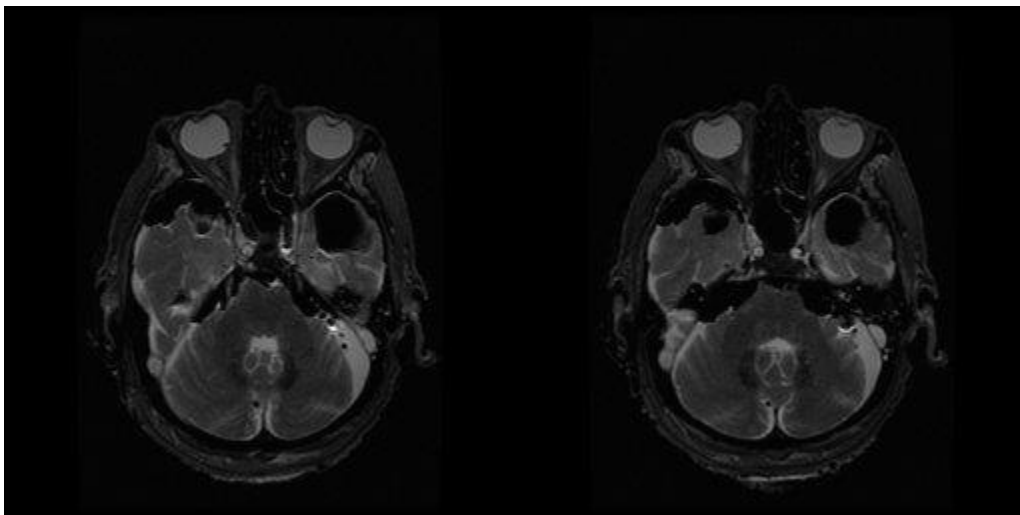
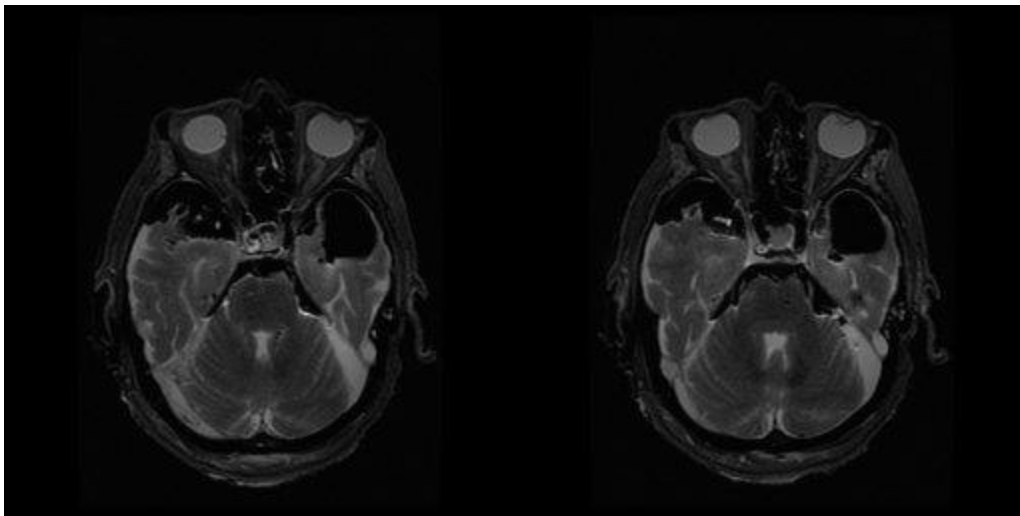
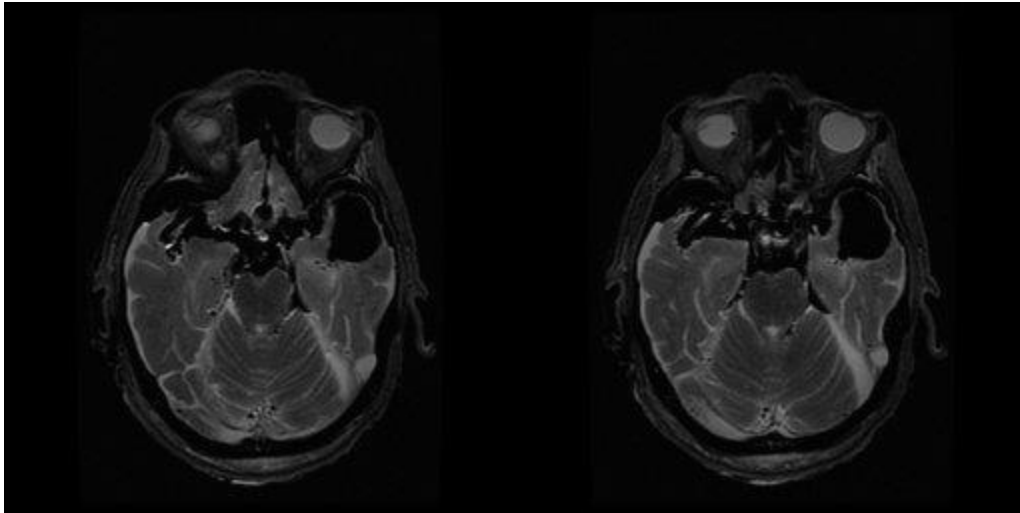


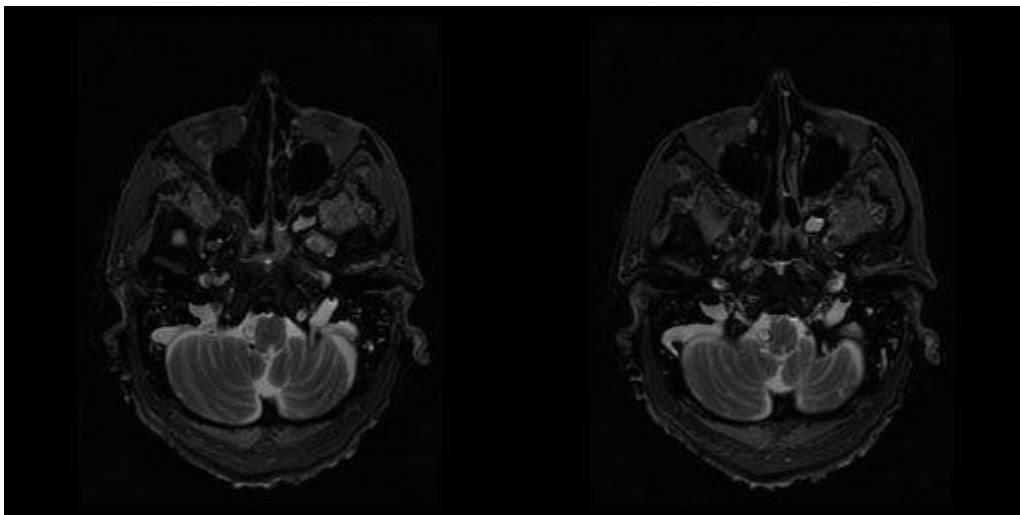
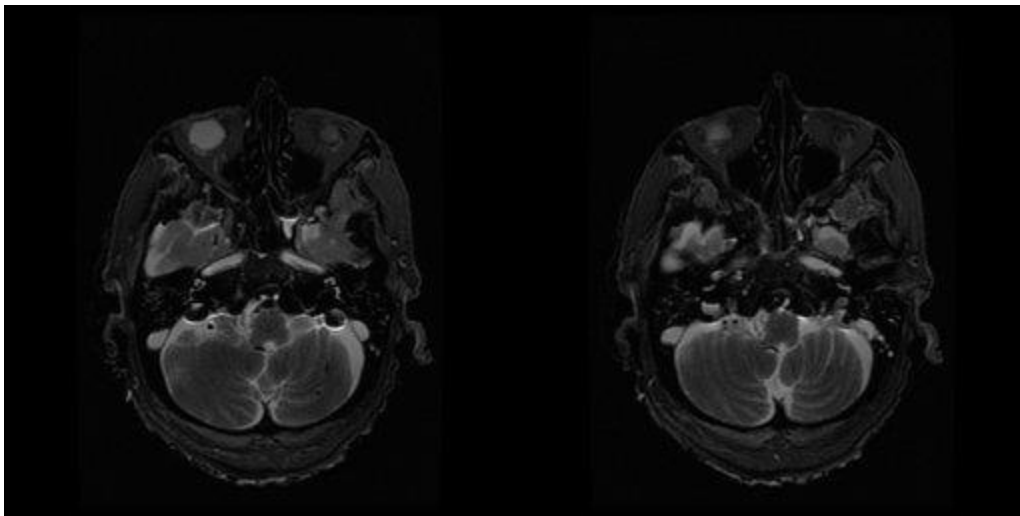
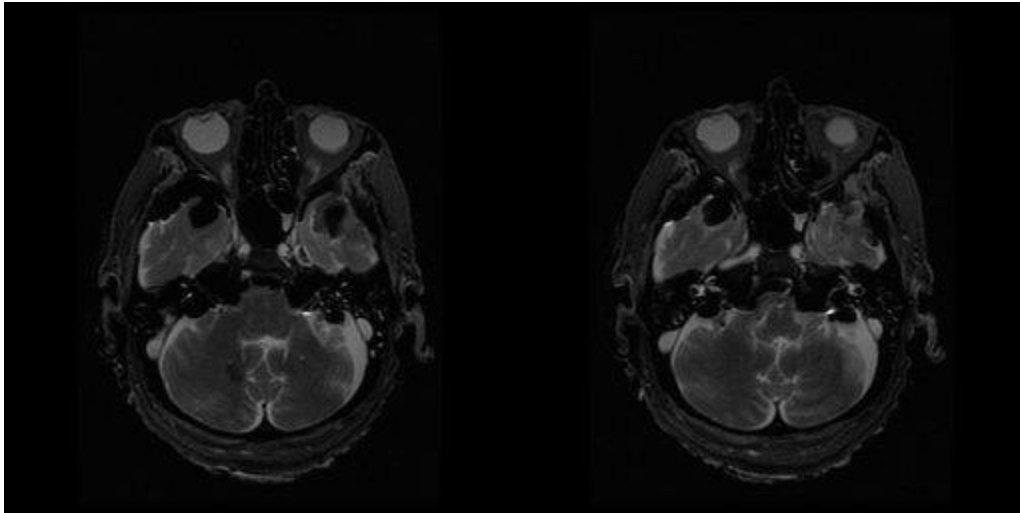


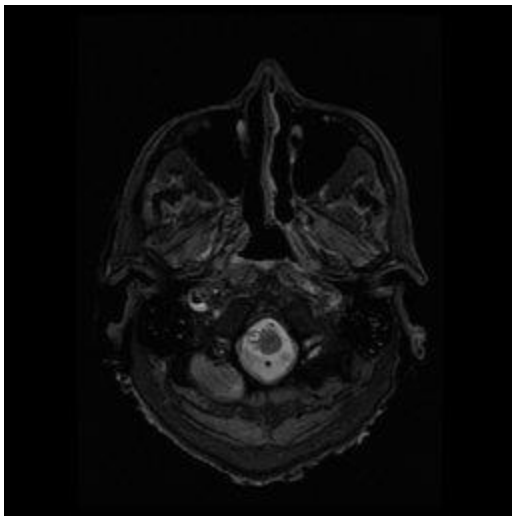
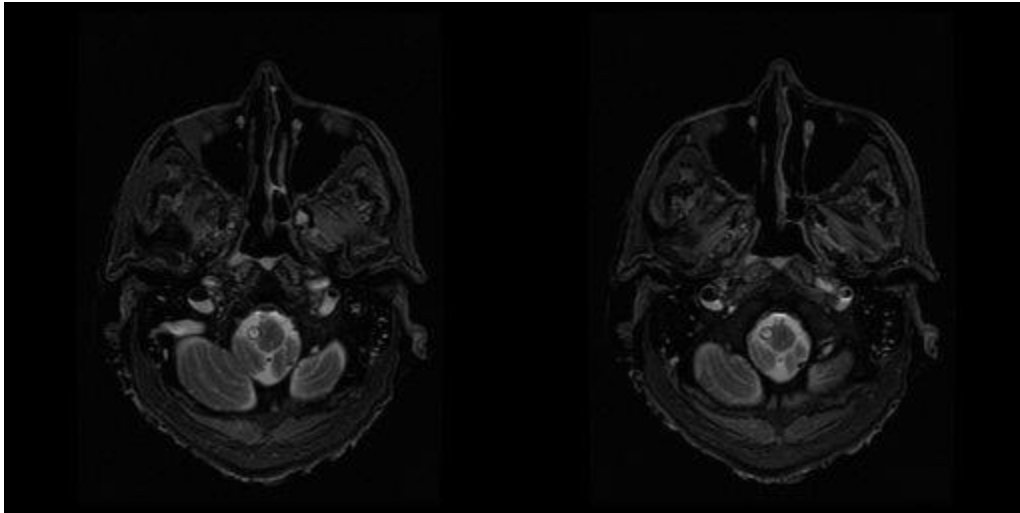
5.3 Patient C



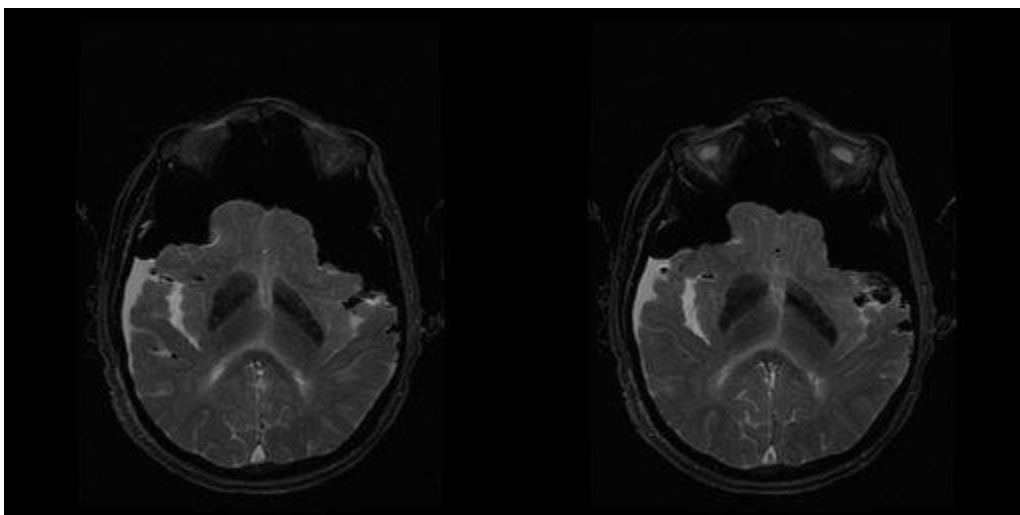
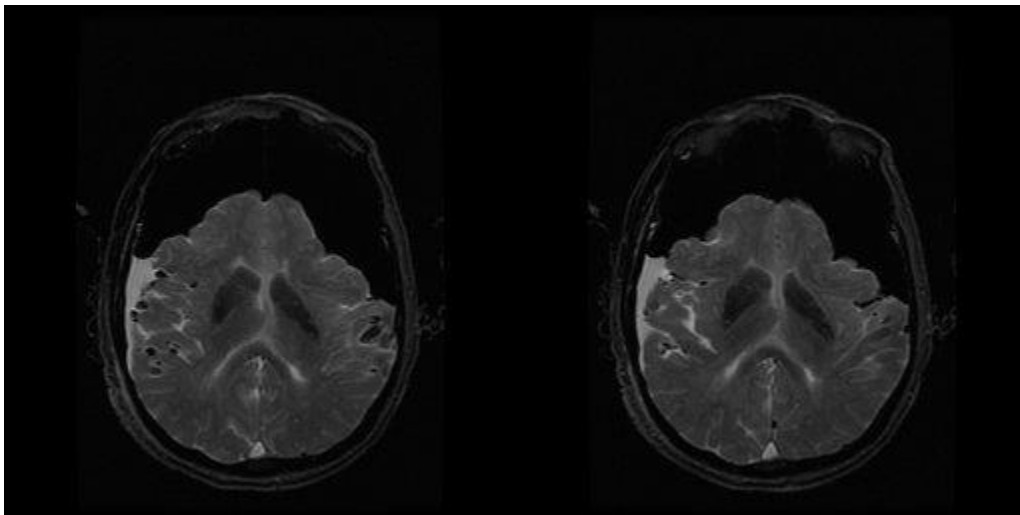
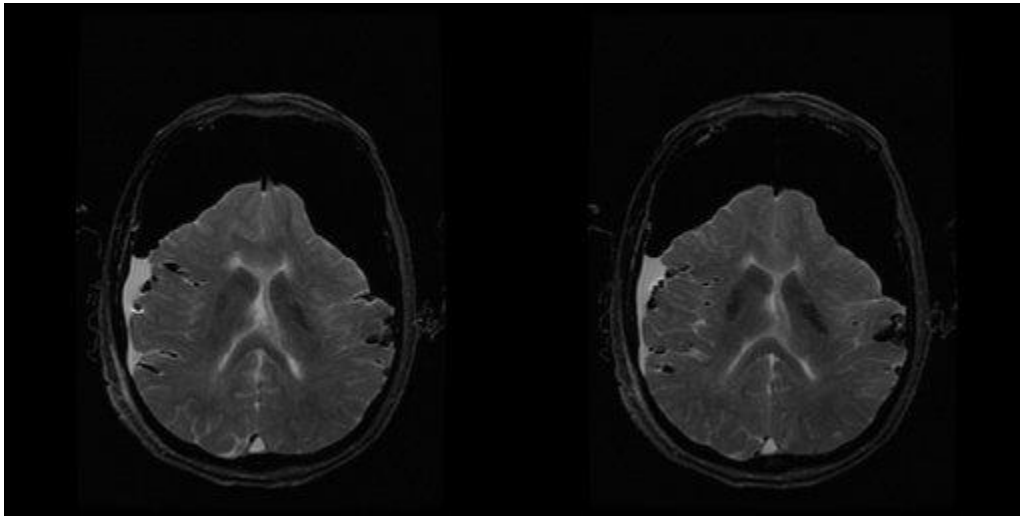


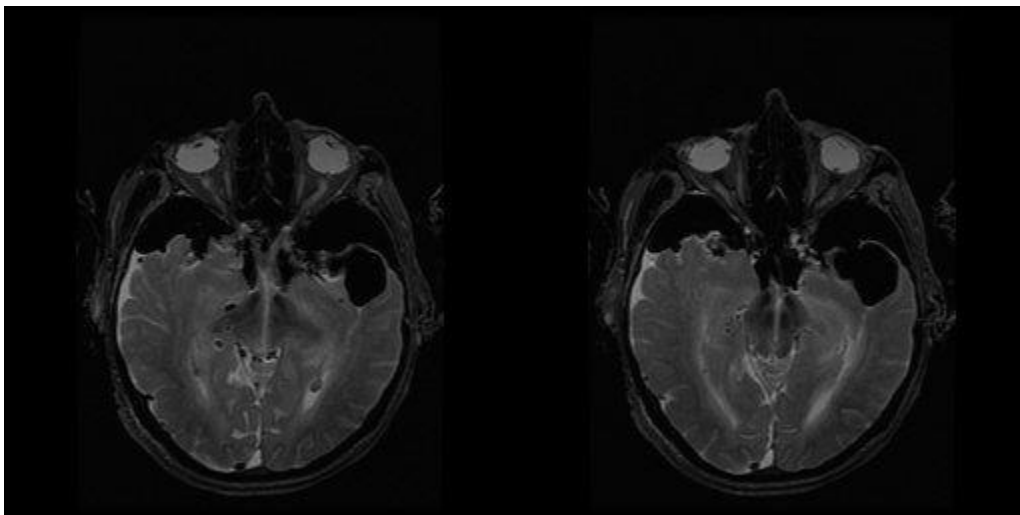
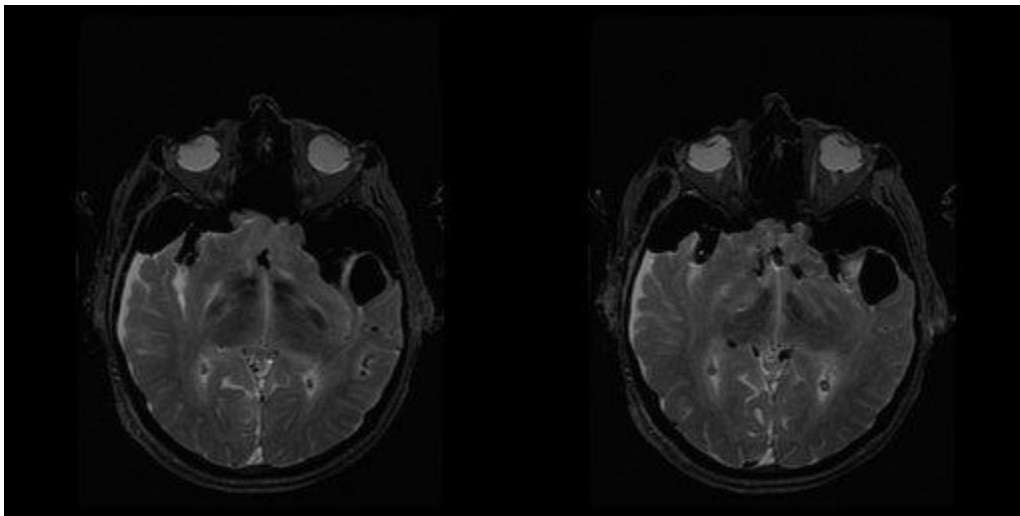
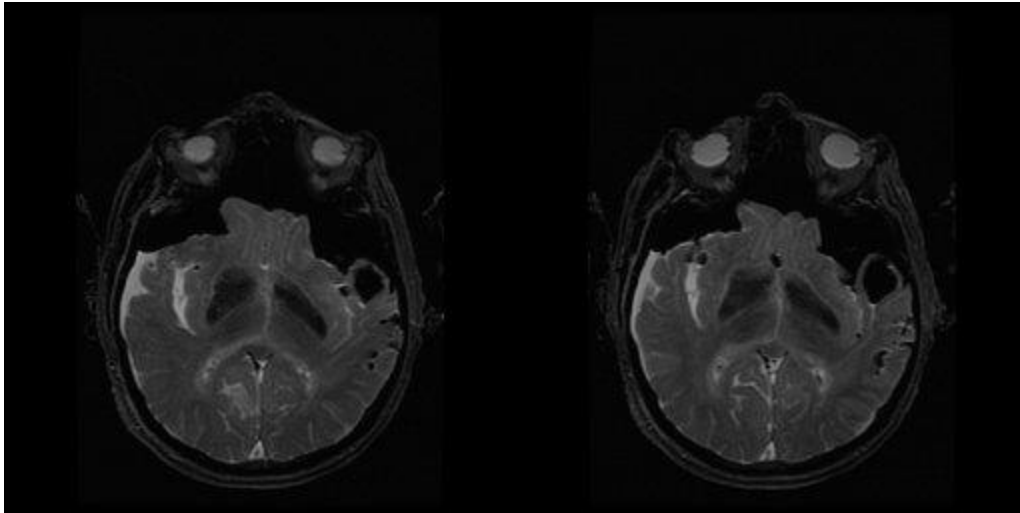


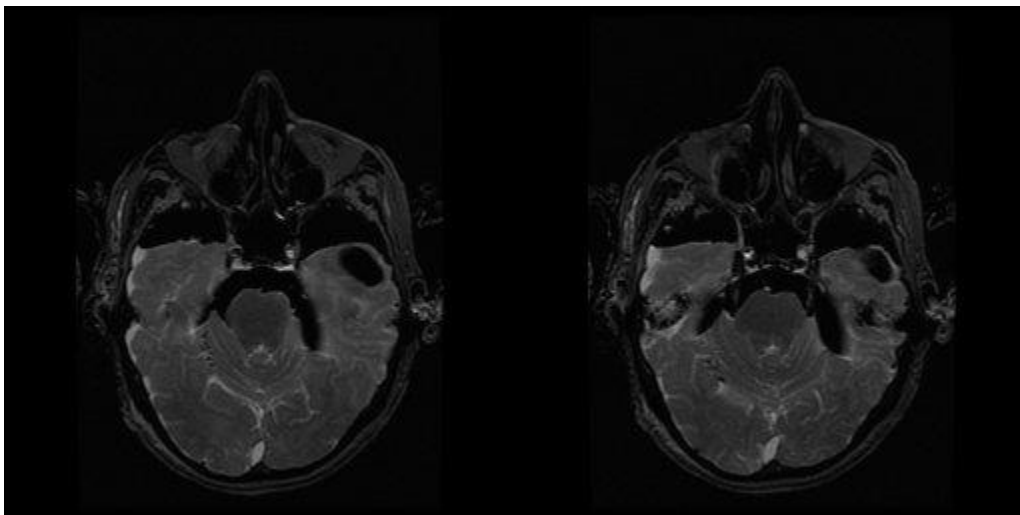
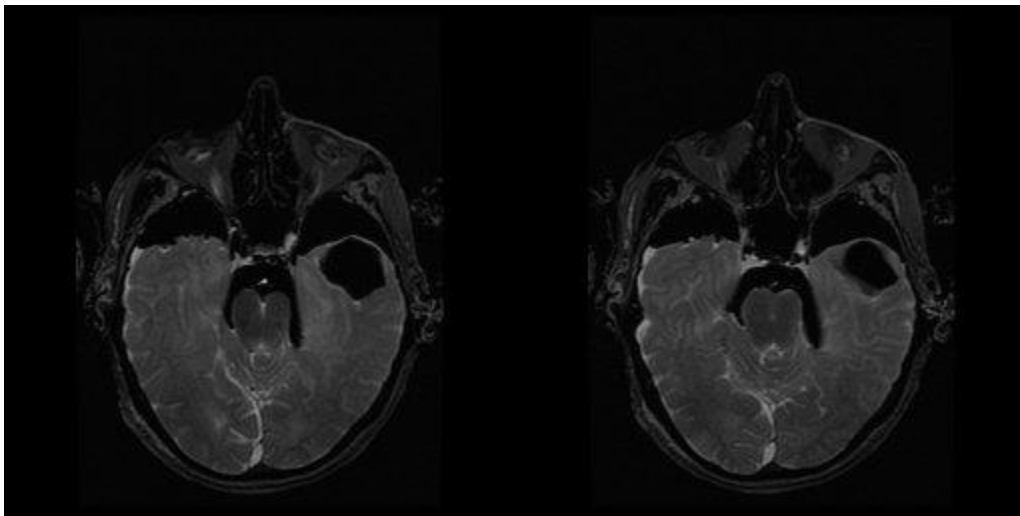
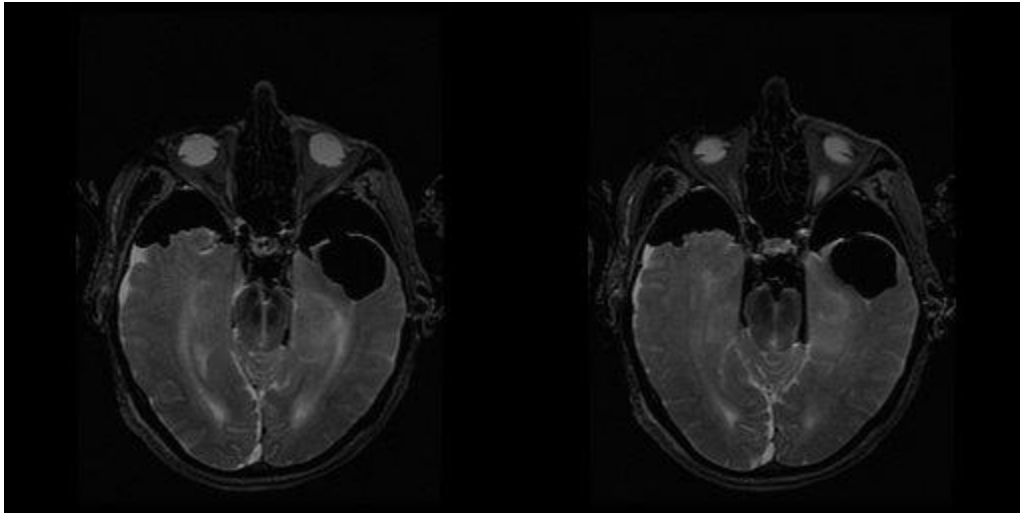


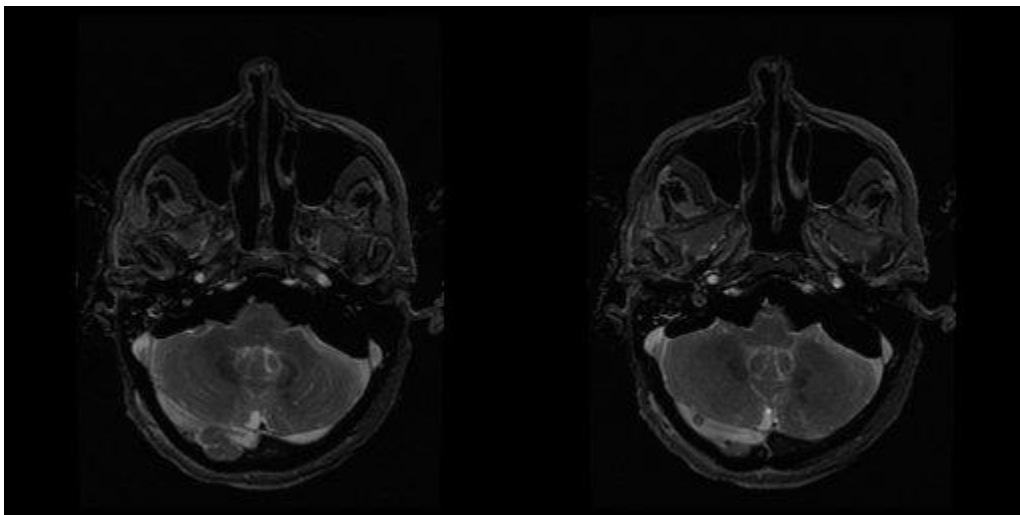
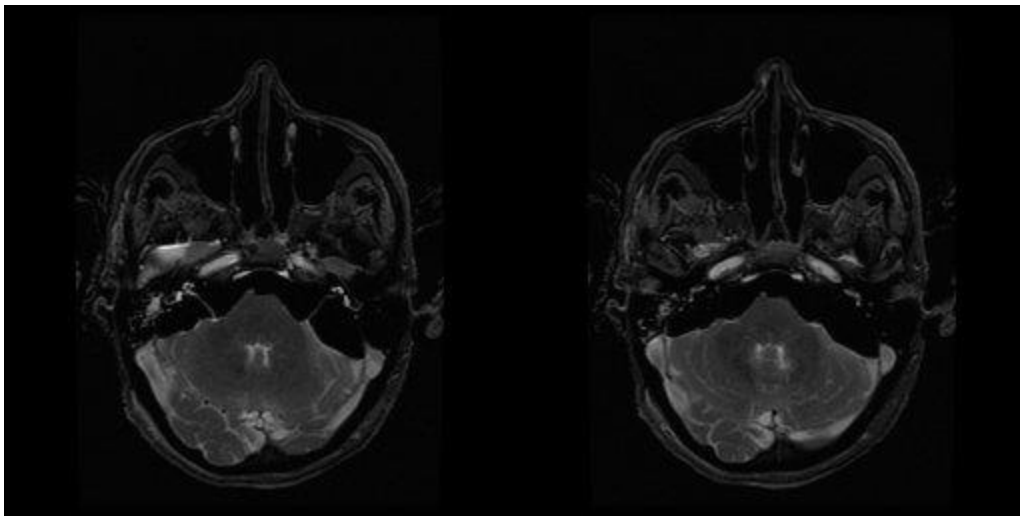
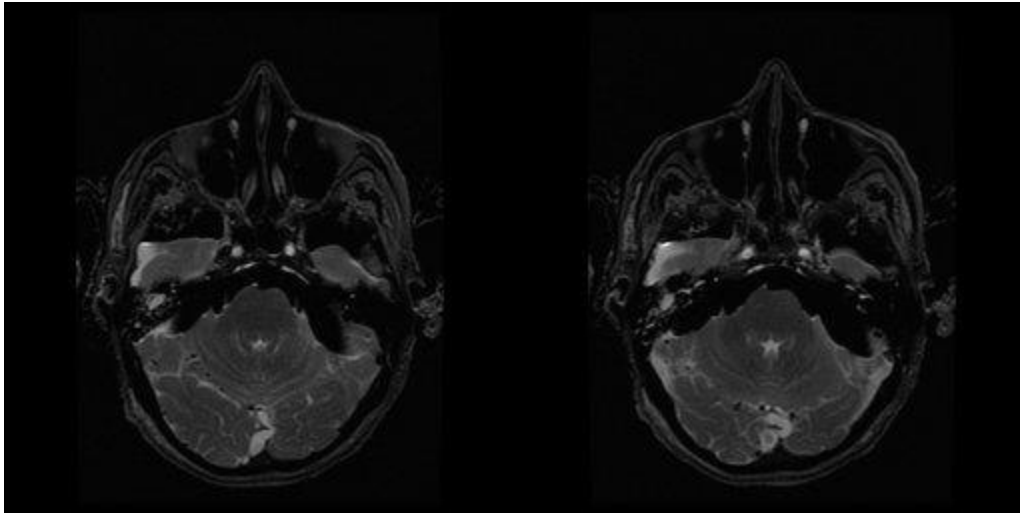


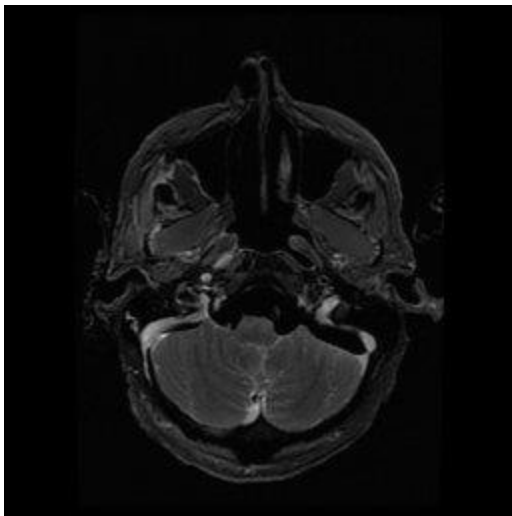
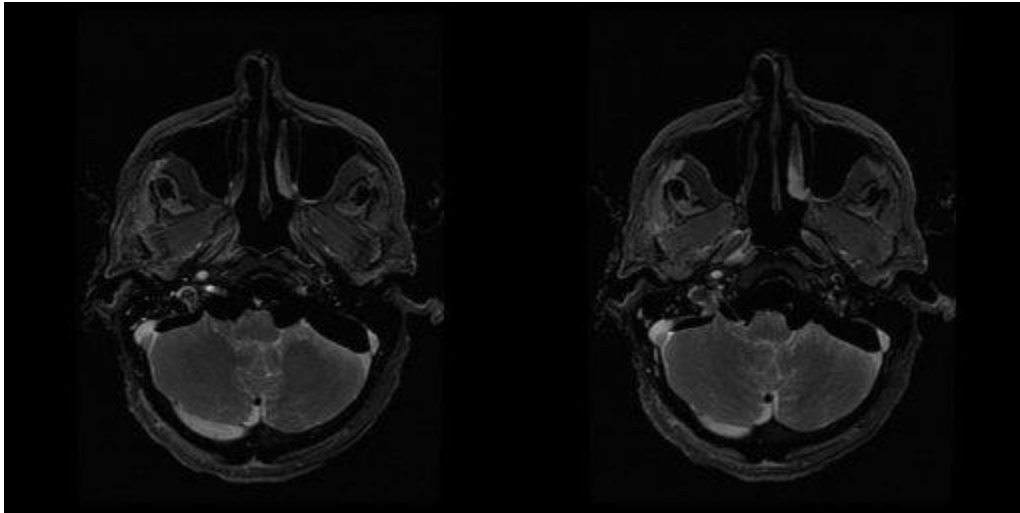
5.4 Patient D











Radiology Department: CT

CT Daily Quality Control Work Instructions

Scope

The daily testing of all CT scanners is required for each of the CT units at University Hospital in Coventry & Hospital of St. Cross in Rugby

Responsibilities

Radiographer's using the unit prior to the start of clinical use that day should carry out the checks described in these instructions. If any of the results from the checks show that the unit is not within tolerance, then it is the radiographer's responsibility to take action and notify the lead/senior radiographer in CT.

Instructions

The CT daily checks should be recorded on the relevant CT Daily Checks form.

The first step is to record the date and initials of the operator who is carrying out the QC. After the scanner has run up, the daily air calibration should be carried out and this step recorded (the daily air cal. automatically includes the tube warm-up)

Position the GE QC holder and phantom on the CT couch. The phantom should be aligned with the **external** laser lights in each direction (See Image A). Adjustments can be made using the three directional handles on the holder.

When this has been completed, zero the phantom to the **external** lights and drive the table into the gantry until the phantom is aligned with the **internal** lasers. At this point record the S/I position of the table in the **table accuracy column** and then **re-zero to internal laser**.

Create a new patient on the scanner with patient ID “Test” and then select protocol 10.1 Daily QA. Follow the protocol; scout the phantom, checking the position of the proposed scan is similar to Image B. When this is completed carry out the scan.

Now, the images from scan should be reviewed using the browser; firstly look at image 3, can both long lines (see Image C) be seen? If this is not the case the phantom may need to be re-aligned. Record the result of this test.

At image 20, create an ROI that is centred in the phantom & has an approx. area of 7000mm².

From the bottom left of the screen record the mA for that image and on the bottom right of the screen record the mean CT number (m) and Standard deviation (SD) value.

Compare all the results to the remedial tolerances stated & indicate if the result is a pass or fail. If any of the testing fails, then the overall result is a fail, you should notify the lead or a senior CT Radiographer and then a decision should be made to contact Radiology physics (27500/1).

Setting Baselines

As the testing of this unit is looking at the reproducibility of the CT scanner over a length of time, the baselines are important in identifying that the scanner has a problem. Therefore, if changes to the scanner are made new baselines may need to be set. The CT daily QC should be carried out on three occasions and the average value for mA, mean CT number & Standard deviation should be recorded and the tolerance box updated at the top of the QC form.

Troubleshooting – Steps to be taken to verify results prior to action.

- Repeat the measurement that has failed and double check the exposure factors.

- Ensure the correct equipment is used and setup is as directed in this Work Instruction.
- If possible, ask a colleague to carry out the repeat measurements.

Daily QC protocol settings on GE CT scanners:

Protocol Name: Daily QC 10.1

Scout: 120kV, 10mA, Orientation = 90 scout range is S130 to I100,

Scan: Axial, 120kV, SFoV = Head, 1s rotation, 8i x 2.5mm, Smart mA enabled, Noise index = 5, mA range is 10 to 500, ASiR = 40% (dose reduction = 40%), scan range I5 to S52.5.

Image A: GE phantom alignment with lasers



Image B: Scout of GE phantom

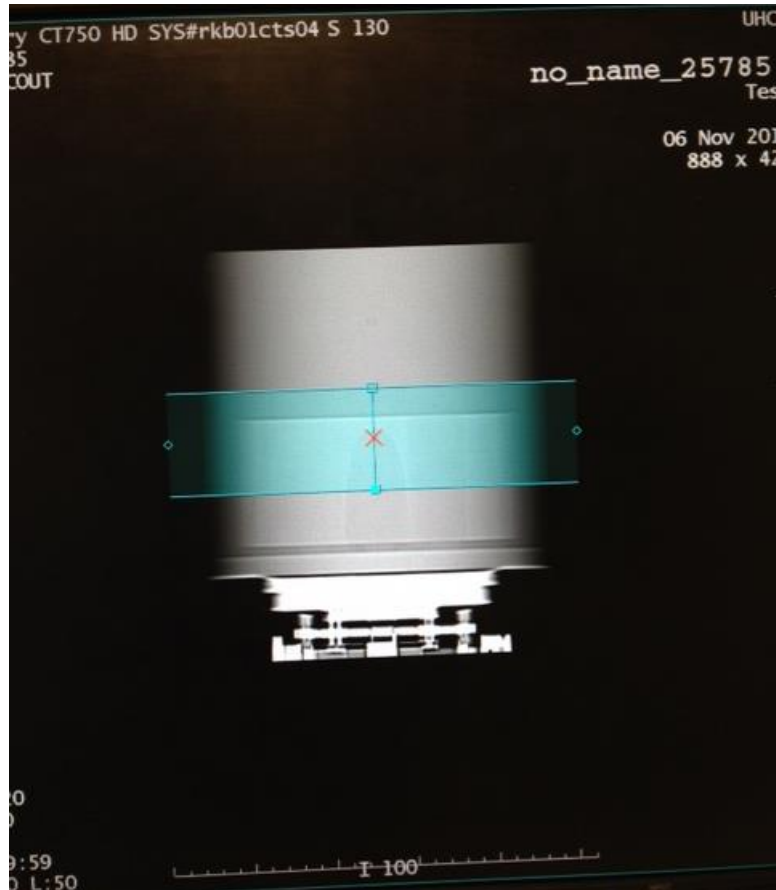
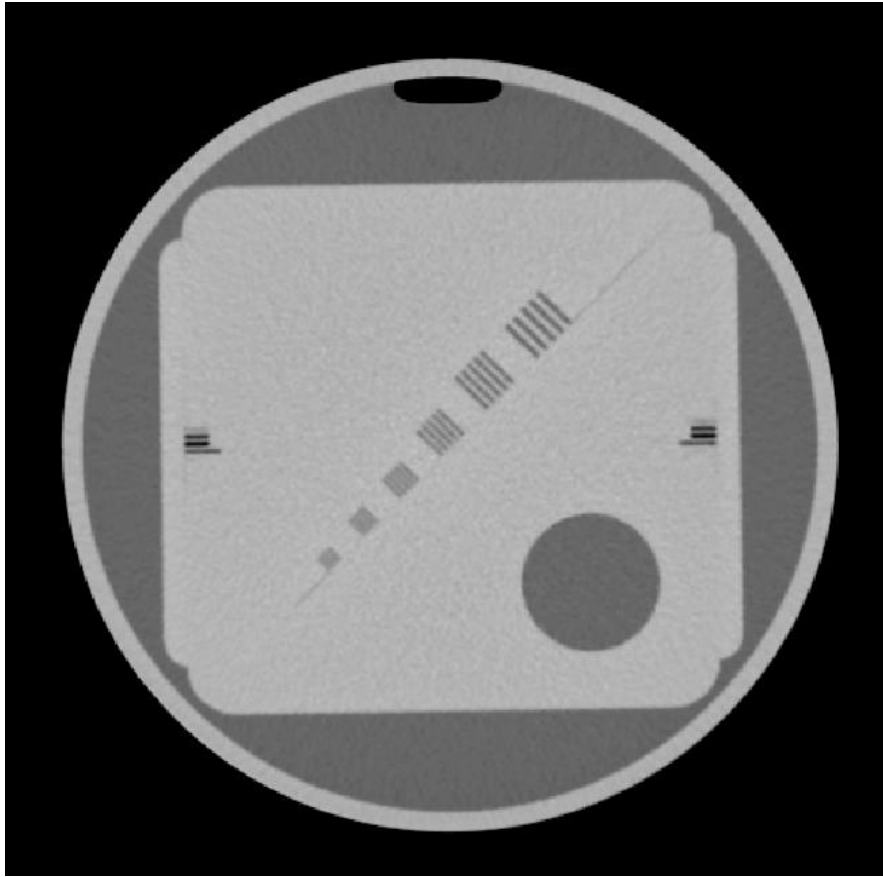


Image C: Image of GE phantom to check positioning of the phantom



Radiology Department: CT

CT Daily Quality Control Form

Unit Assessed	ED CT (GE Revolution EVO)
----------------------	-----------------------------------

Factors to be assessed	Tolerance Range		
	Lower Limit	Baseline	Upper Limit
Image long lines are visible	1	2	3
mA +/- 5%	323	340	357
Mean HU +/- 5HU	- 4.0	1.0	6.0
SD +/- 10%	2.64	2.93	3.22

Date	Initials	Air Cal done? (Y/N)	Table accuracy (mm)	On which image are long lines	Record from Slice 20			Overall Result? (Pass/Fail)	Action required? (Y/N)
					mA	Mean HU	SD		

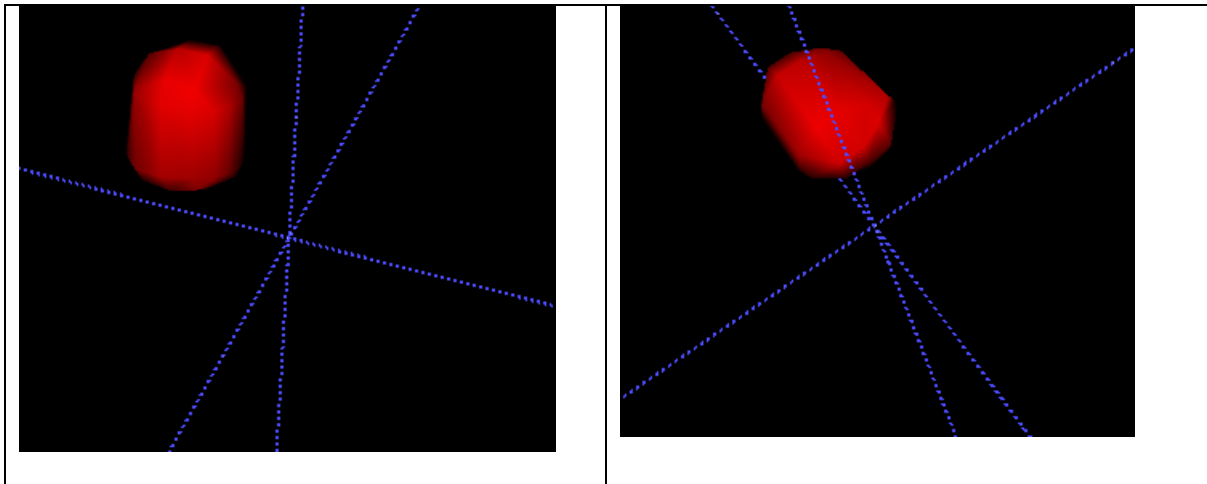
These checks follow the guidance provided by IPEM report 91: Recommended Standards for Routine Performance Testing of Diagnostic X-ray Imaging Systems, IPEM 2005.

Appendix 7

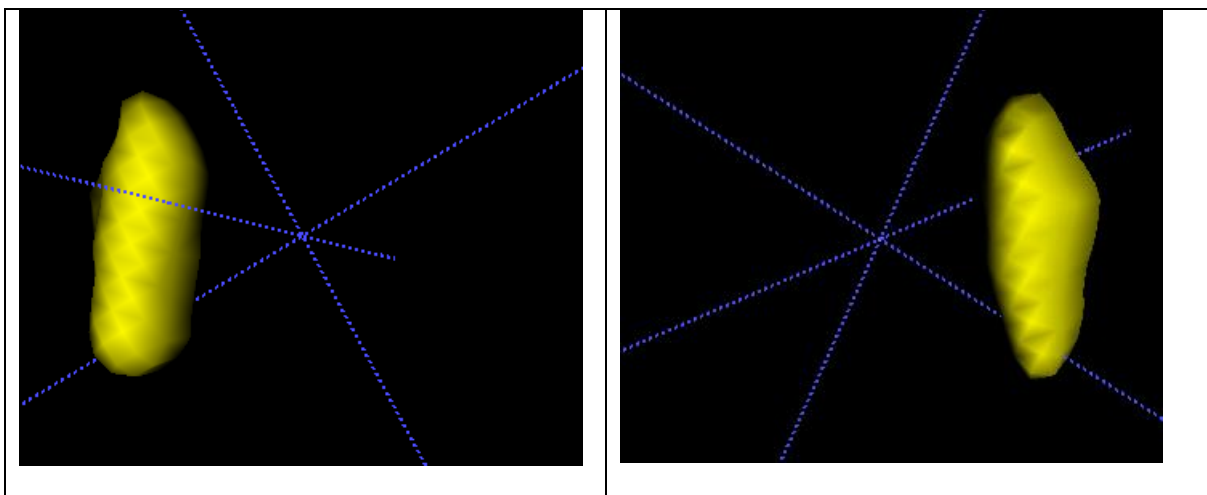
ROIs

Patient A

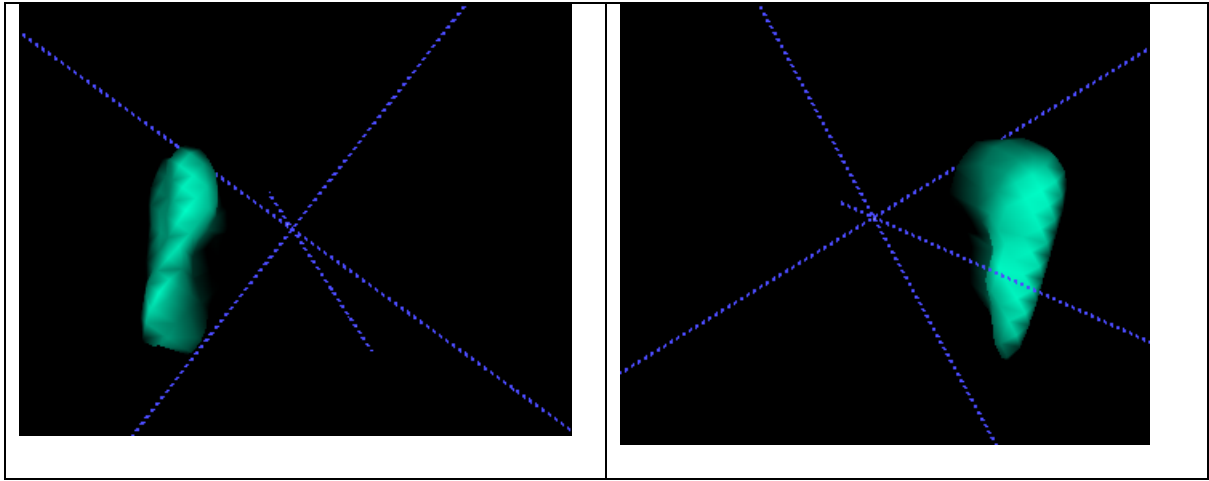
RN



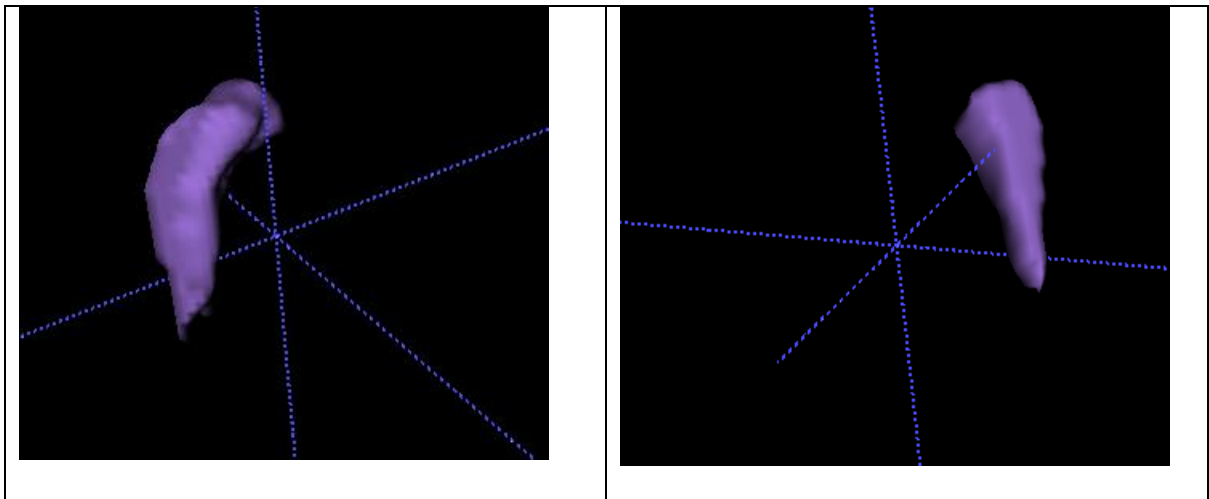
SN



GP



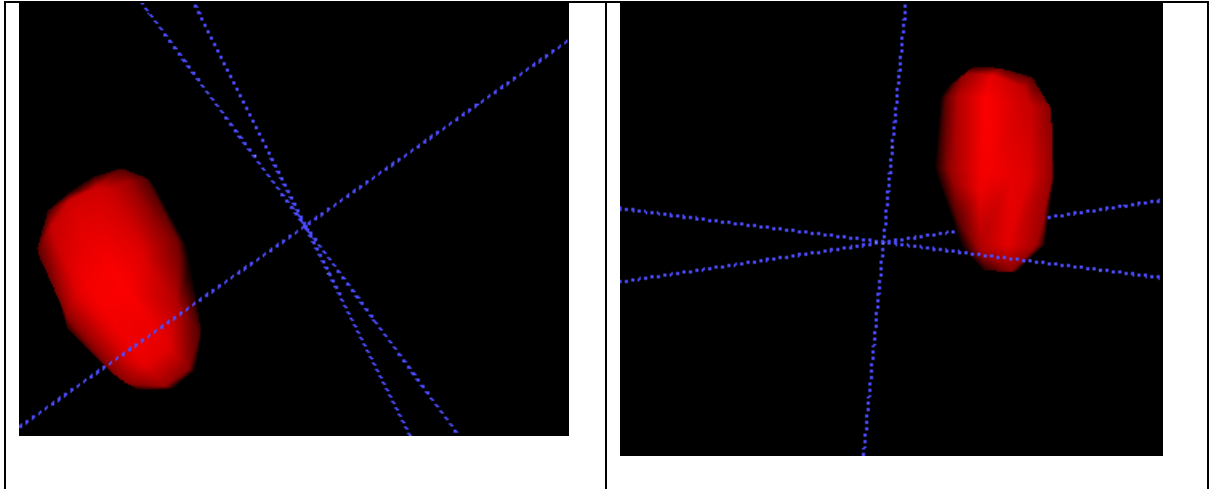
Put



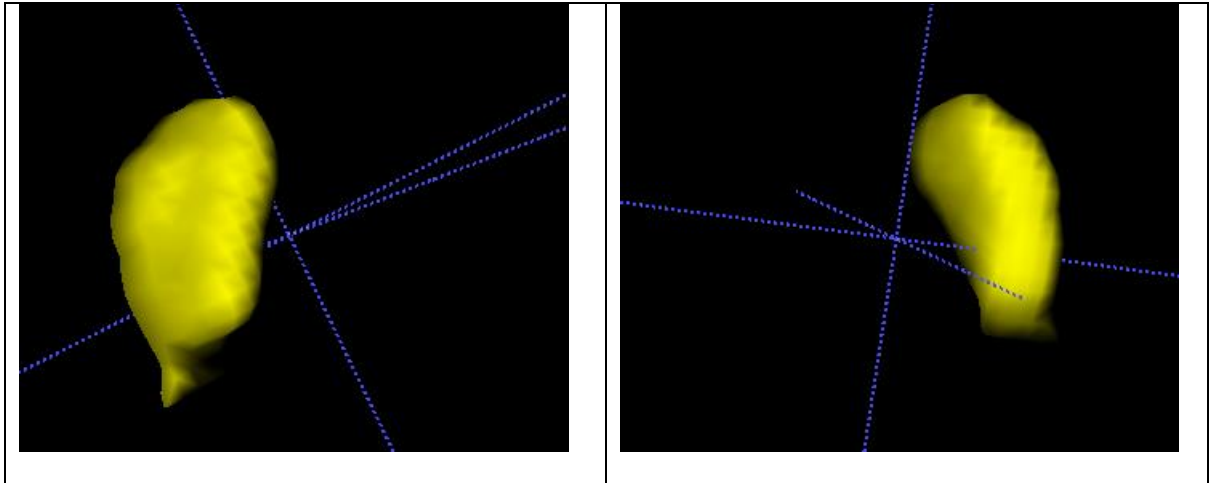
ROIs

Patient B

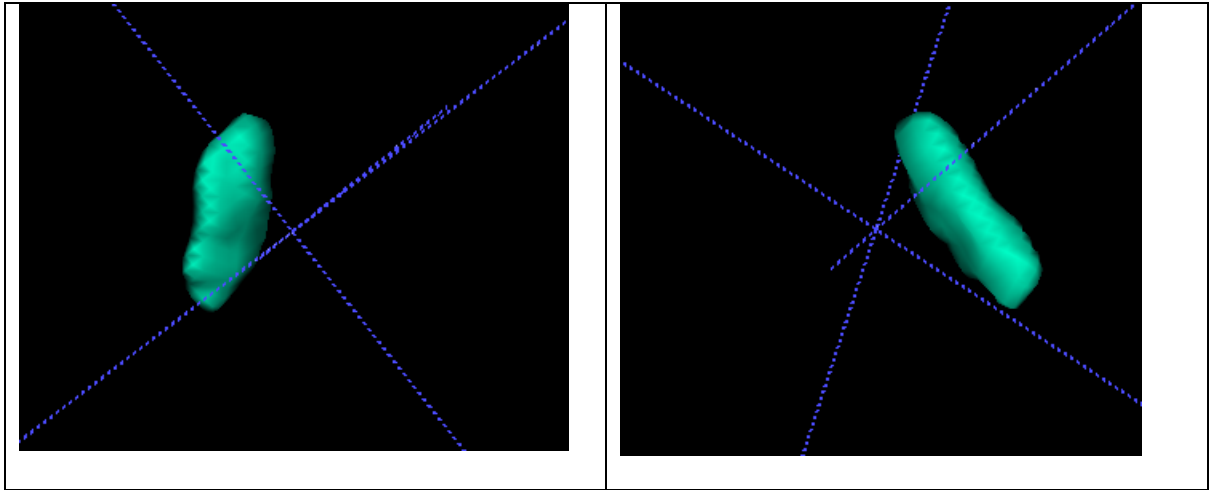
RN



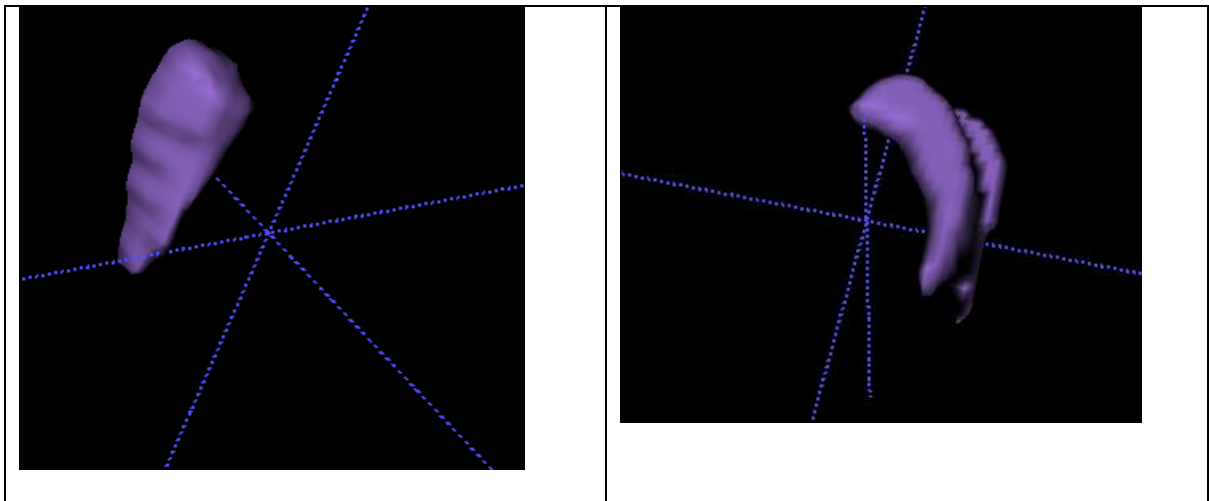
SN



GP



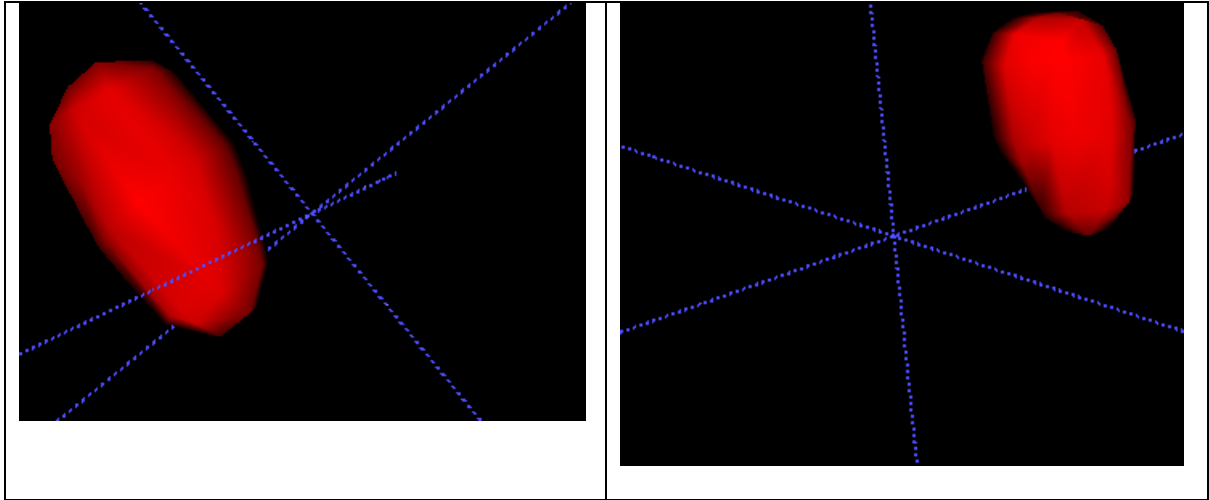
Put



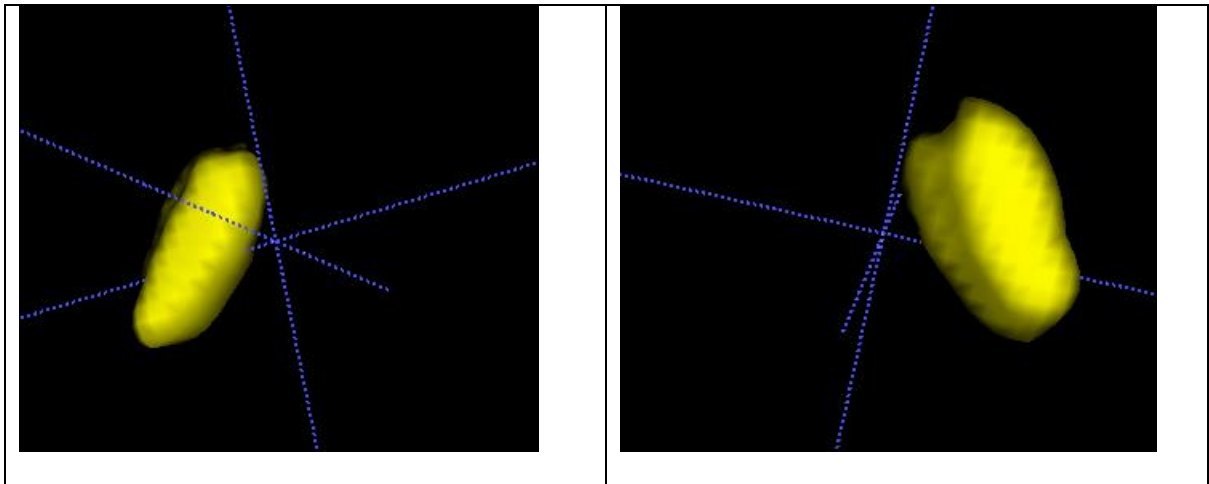
ROIs

Patient C

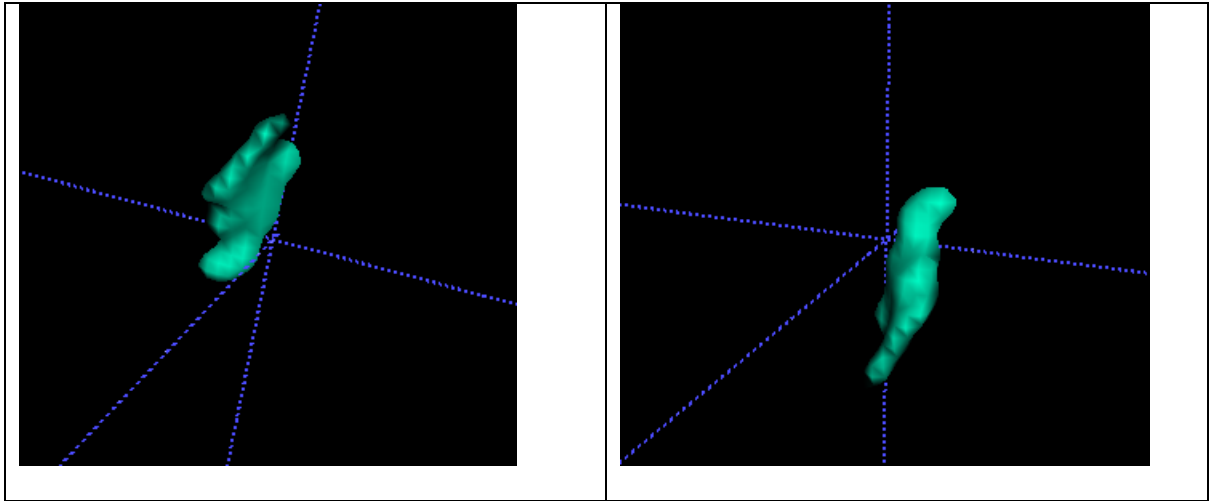
RN



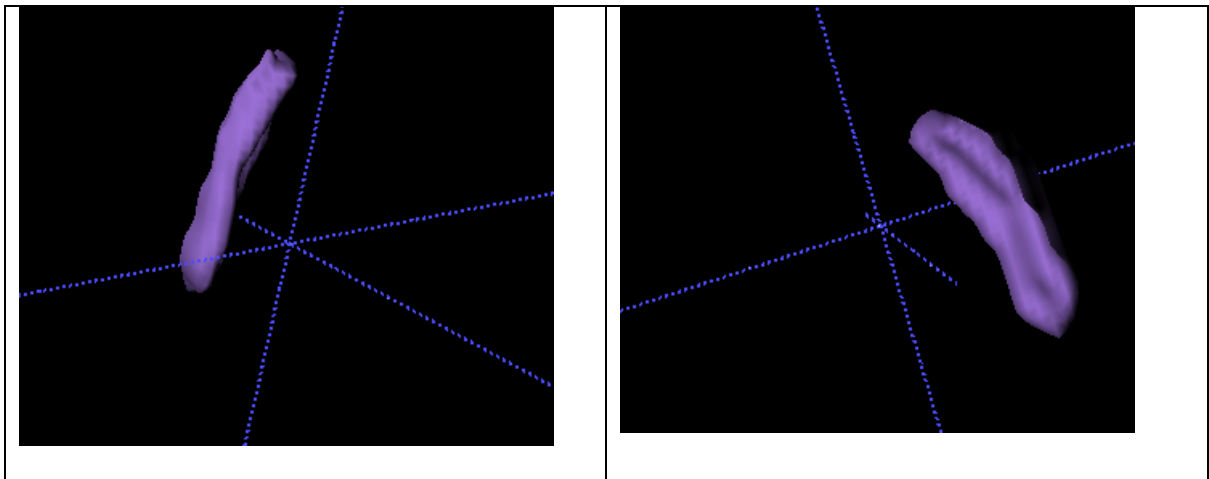
SN



GP



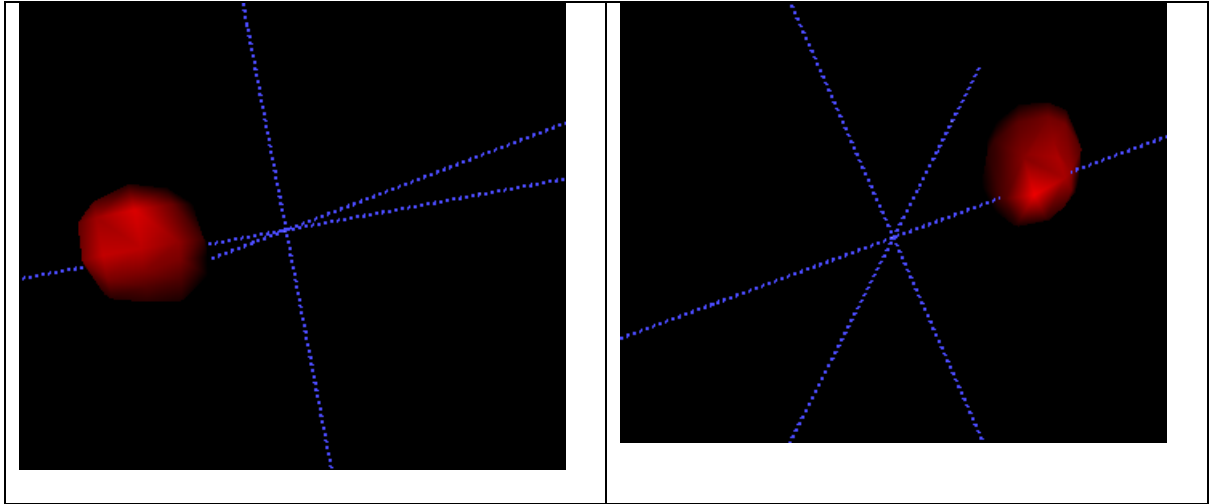
Put



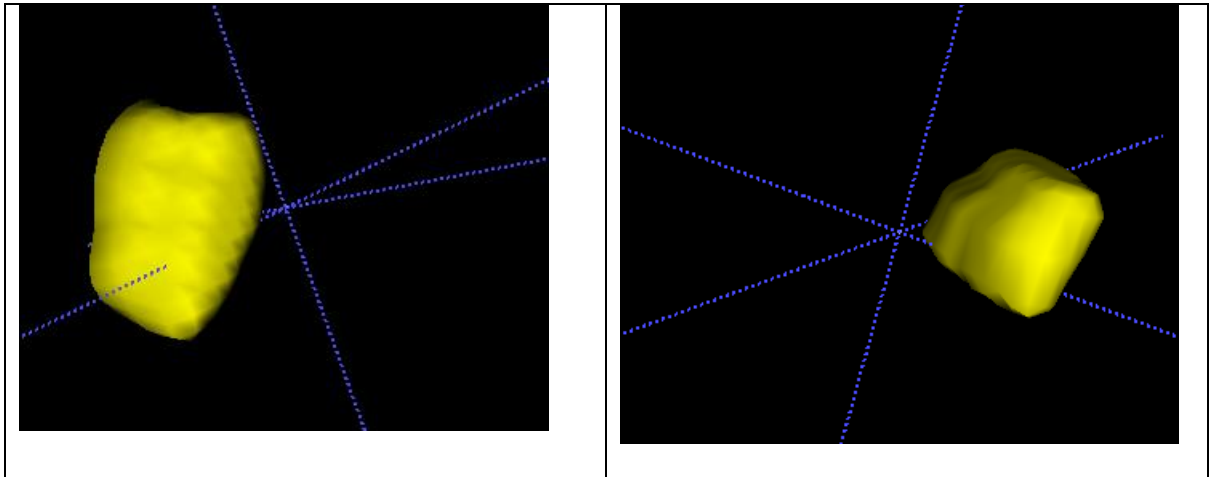
ROIs

Patient D

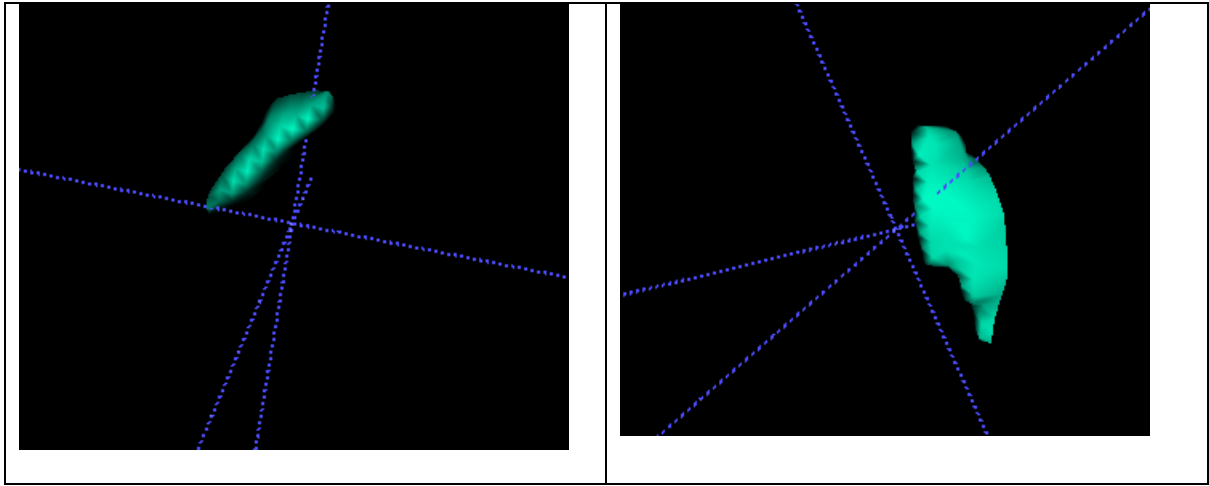
RN



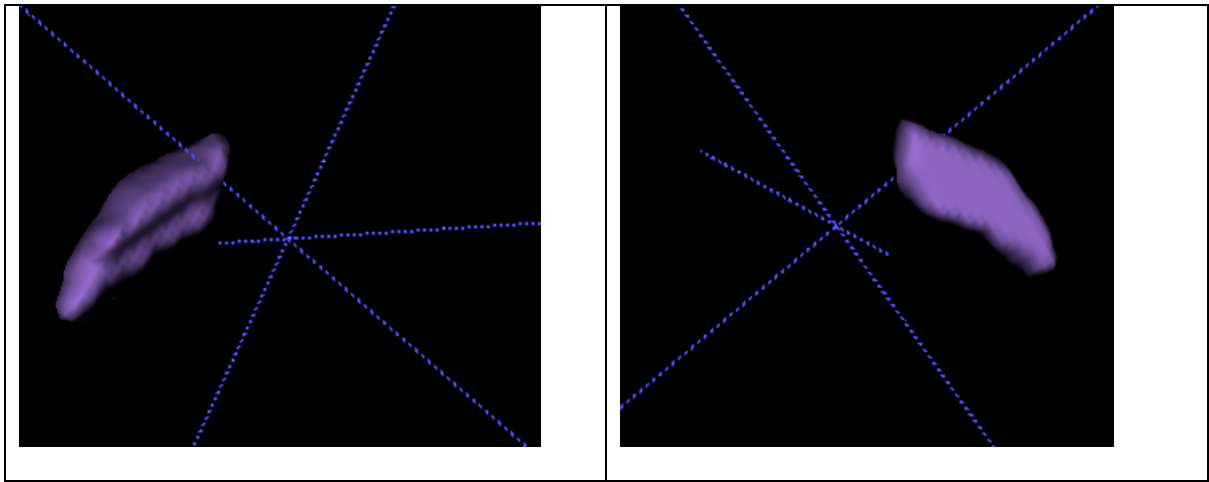
SN



GP



Put



Appendix 8

ASIR study images

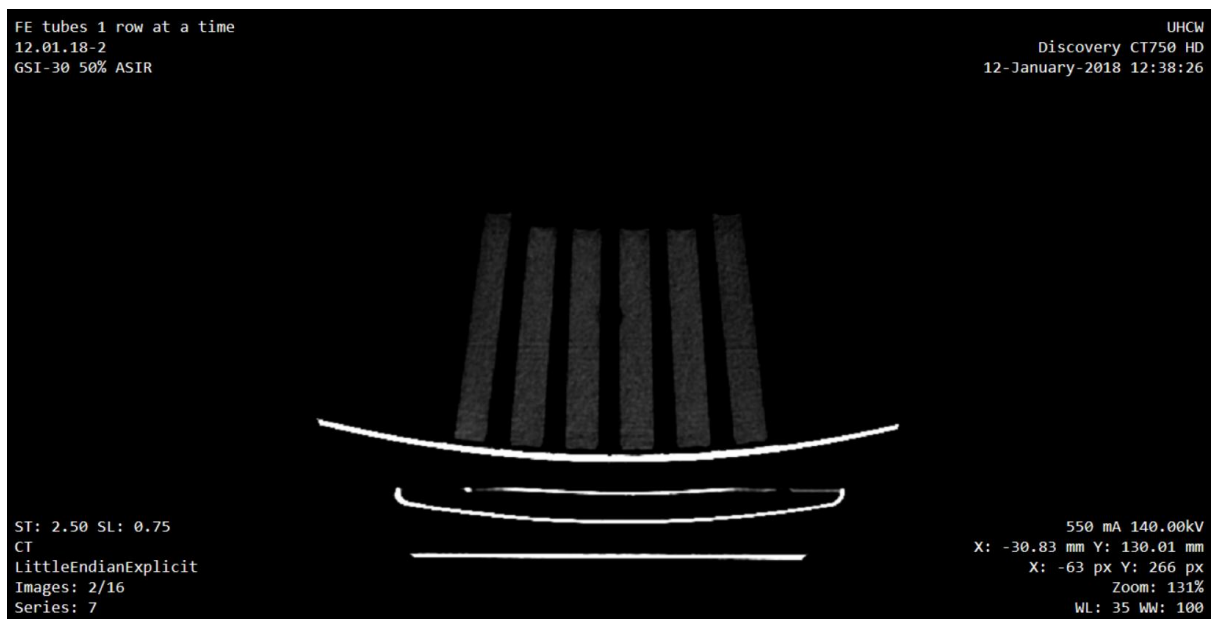
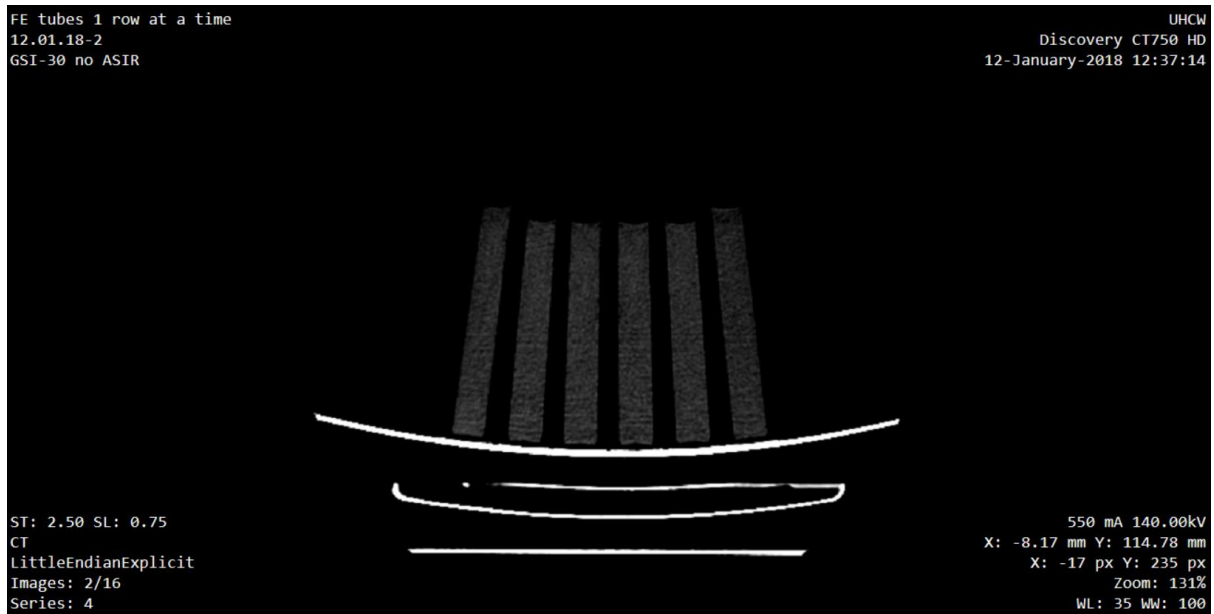


Figure A8.1: 0, 100, ..., 500 μ g/g phantoms left to right.